Research Topics

Advanced materials and models in the establishment and repair of pathological microenvironment

Edited by
Behnam Akhavan, Zuhao Li, Zhonghan Wang
and Antonella Motta

Published in
Frontiers in Bioengineering and Biotechnology

ISSN 1664-8714
ISBN 978-2-8325-4889-9
DOI 10.3389/978-2-8325-4889-9

About Frontiers

Frontiers is more than just an open access publisher of scholarly articles: it is a pioneering approach to the world of academia, radically improving the way scholarly research is managed. The grand vision of Frontiers is a world where all people have an equal opportunity to seek, share and generate knowledge. Frontiers provides immediate and permanent online open access to all its publications, but this alone is not enough to realize our grand goals.

Frontiers journal series

The Frontiers journal series is a multi-tier and interdisciplinary set of open-access, online journals, promising a paradigm shift from the current review, selection and dissemination processes in academic publishing. All Frontiers journals are driven by researchers for researchers; therefore, they constitute a service to the scholarly community. At the same time, the *Frontiers journal series* operates on a revolutionary invention, the tiered publishing system, initially addressing specific communities of scholars, and gradually climbing up to broader public understanding, thus serving the interests of the lay society, too.

Dedication to quality

Each Frontiers article is a landmark of the highest quality, thanks to genuinely collaborative interactions between authors and review editors, who include some of the world's best academicians. Research must be certified by peers before entering a stream of knowledge that may eventually reach the public - and shape society; therefore, Frontiers only applies the most rigorous and unbiased reviews. Frontiers revolutionizes research publishing by freely delivering the most outstanding research, evaluated with no bias from both the academic and social point of view. By applying the most advanced information technologies, Frontiers is catapulting scholarly publishing into a new generation.

What are Frontiers Research Topics?

Frontiers Research Topics are very popular trademarks of the *Frontiers journals series*: they are collections of at least ten articles, all centered on a particular subject. With their unique mix of varied contributions from Original Research to Review Articles, Frontiers Research Topics unify the most influential researchers, the latest key findings and historical advances in a hot research area.

Find out more on how to host your own Frontiers Research Topic or contribute to one as an author by contacting the Frontiers editorial office: frontiersin.org/about/contact

Advanced materials and models in the establishment and repair of pathological microenvironment

Topic editors
Behnam Akhavan — The University of Newcastle, Australia
Zuhao Li — Shanghai Jiao Tong University, China
Zhonghan Wang — Second Affiliated Hospital of Jilin University, China
Antonella Motta — University of Trento, Italy

Citation
Akhavan, B., Li, Z., Wang, Z., Motta, A., eds. (2024). *Advanced materials and models in the establishment and repair of pathological microenvironment*.
Lausanne: Frontiers Media SA. doi: 10.3389/978-2-8325-4889-9

Table of contents

frontiers | Frontiers in Bioengineering and Biotechnology

TYPE Review
PUBLISHED 13 March 2023
DOI 10.3389/fbioe.2023.1154301

OPEN ACCESS

EDITED BY
Zuhao Li,
Jilin University, China

REVIEWED BY
Xuan Mei,
Harvard Medical School, United States
Yu Wang,
Changchun Institute of Applied Chemistry (CAS), China

*CORRESPONDENCE
Chunli Yao,
ycl@jlu.edu.cn

†These authors have contributed equally to this work

SPECIALTY SECTION
This article was submitted to Tissue Engineering and Regenerative Medicine, a section of the journal Frontiers in Bioengineering and Biotechnology

RECEIVED 30 January 2023
ACCEPTED 02 March 2023
PUBLISHED 13 March 2023

CITATION
Zhang Z, Qi Z, Kong W, Zhang R and Yao C (2023), Applications of MXene and its modified materials in skin wound repair.
Front. Bioeng. Biotechnol. 11:1154301.
doi: 10.3389/fbioe.2023.1154301

Applications of MXene and its modified materials in skin wound repair

Ziyan Zhang[1†], Zhiping Qi[1†], Weijian Kong[2], Renfeng Zhang[2] and Chunli Yao[3]*

[1]Department of Orthopedic Surgery, The Second Hospital of Jilin University, Changchun, China, [2]The Second Hospital of Jilin University, Changchun, China, [3]Department of Dermatology, The Second Hospital of Jilin University, Changchun, China

The rapid healing and repair of skin wounds has been receiving much clinical attention. Covering the wound with wound dressing to promote wound healing is currently the main treatment for skin wound repair. However, the performance of wound dressing prepared by a single material is limited and cannot meet the requirements of complex conditions for wound healing. MXene is a new two-dimensional material with electrical conductivity, antibacterial and photothermal properties and other physical and biological properties, which has a wide range of applications in the field of biomedicine. Based on the pathophysiological process of wound healing and the properties of ideal wound dressing, this review will introduce the preparation and modification methods of MXene, systematically summarize and review the application status and mechanism of MXene in skin wound healing, and provide guidance for subsequent researchers to further apply MXene in the design of skin wound dressing.

KEYWORDS

skin wound repair, MXene, biocompatibility, conductivity, antibacterial

1 Introduction

With the rapid development of society, the incidence of skin injury caused by trauma, disease and other factors in life is increasing (LeBlanc et al., 2019). Skin is an important protective organ of the human body. Maintaining its integrity can provide a physical barrier for the body to prevent the invasion of foreign harmful substances, reduce the loss of water and electrolyte, and maintain the stability of the internal environment (Dąbrowska et al., 2018; Swaney and Kalan, 2021). Therefore, it is very important to promote rapid healing of skin wound. Wound dressing can cover the surface of the wound to protect the wound, reduce the impact of external factors and stimulation on the wound, and protect the smooth healing of the wound (Obagi et al., 2019). However, skin wound healing is a continuous and dynamic process, during which neutrophils, fibroblasts, epithelial cells, growth factors, cytokines and other cells and factors interact to regulate (Velnar et al., 2009; Golebiewska and Poole, 2015). At the same time, in the process of wound healing, it is also necessary to maintain a sterile, breathable, moist stable and appropriate microenvironment to ensure the smooth evolution of each stage of the whole healing process (Pereira and Bártolo, 2016; Wang et al., 2018). The wound dressing formed by a single or a combination of two matrix materials cannot meet many requirements for skin healing. In order to solve this problem, in addition to re-designing matrix materials with more comprehensive and excellent performance, it has become a feasible and effective method to use growth factors or nanomaterials to modify matrix materials to improve the overall performance of wound dressings.

MXene is a new kind of metallic nitrogen and carbon compound, which has a two-dimensional lamellar structure similar to graphene and black phosphorus (Naguib et al., 2012). The abundant functional groups on its surface give it more abundant physical and chemical properties and biological properties. MXene has good biocompatibility, electrical conductivity and mechanical properties, but also can produce photothermal effect under NIR conditions, which makes it widely used in biological fields such as biosensing, tumor therapy, tracer imaging and so on (Naguib et al., 2012; Carey and Barsoum, 2021; Chen et al., 2021; Fadahunsi et al., 2022). In addition, researchers also found that MXene has good antibacterial activity and certain scavenging ability of active oxygen species (Jastrzębska et al., 2017; Wang et al., 2023). These biological characteristics are highly consistent with the properties required by wound dressings, making MXene become a hot material for modification of skin wound dressings in recent years (Li et al., 2022a; Liu et al., 2022a; Yang et al., 2022a). However, there has been no systematic review on the mechanism and application of MXene in skin wound repair. In this paper, we will introduce the preparation and modification methods of the emerging material MXene based on the pathophysiological changes of skin wound healing and the properties of the ideal wound dressing, and systematically review the role and application of MXene in the process of skin wound healing (Scheme 1). To provide reference for further application of MXene in skin wound dressing design by subsequent researchers.

2 Characteristics and properties of wounds healing

2.1 Normal skin structure and function

Skin is the largest organ of the human body. The skin is composed of epidermis, dermis and subcutaneous tissue from the outside to inside. According to the differentiation stage and characteristics of keratinocytes, the epidermis can be divided into four layers, from deep to shallow, which are basal layer, spinous layer, granular layer and stratum corneum. The basal layer is located at the bottom of the epidermis and consists of a cylindrical layer of epidermal stem cells, also known as basal cells. These basal cells have the ability to proliferate and differentiate, and can maintain the stability of their numbers (Prost-Squarcioni, 2006; Li et al., 2010). Spinous cells have strong protein synthesis function and can synthesize a large amount of keratin and lamellar granules. Keratinoid also distributed in the upper cells of the spinous layer, which together with the intercellular desmosomes can closely connect the spinous cells and prevent the entry of external water, thus providing protection and isolation (Wertz, 2018).

The cells in the granulosa layer are supplemented by the spinous cells in the upper part of the spinous layer. When the cells in the granulosa layer migrate to the stratum corneum, almost all the cellular structures in the cells are destroyed, and the cells turn into keratinocytes. The stratum corneum, at the top of the epidermis, is composed of protein-rich keratinocytes and the extracellular lipids that surround them. The stratum corneum is an important functional layer for the skin to resist mechanical damage, prevent water loss and environmental soluble substances from penetrating the skin (Jiao et al., 2022). In addition, there is a zona pellucida composed of 2-3 layers of flattened cells between the granular layer and the cuticle layer in the palm and plantar, called the pellucida (Elias, 2012). Based on the basal cells in the basal layer, the cells in the whole epidermis migrate outward continuously through the proliferation and differentiation of the basal cells to provide supplement for the cells in each layer and realize self-renewal and self-repair to a certain extent.

The dermis is mainly composed of connective tissue that contains nerves, blood vessels, lymphatics, muscles, and skin appendages (Woodley, 2017). The dermis can be divided into papillary layer and reticular layer from shallow to deep. The papillary layer protrudes outwards to the epidermal layer and contains rich capillaries and nerve endings, which can provide adequate nutrition for the epidermal layer (Arda et al., 2014). The mesh layer contains a large number of collagen fibers and elastic fibers. The interwoven fiber tissues provide toughness and elasticity for the skin, ensure that the skin has a certain mechanical strength and toughness, and play a protective role for the tissues and organs in the body (Usansky et al., 2021).

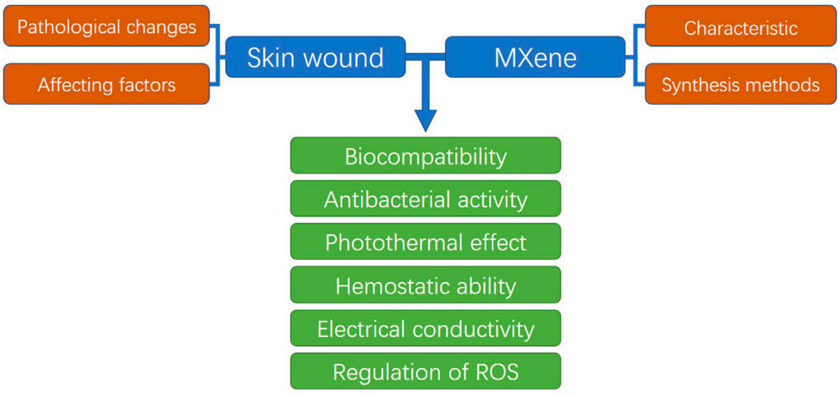

SCHEME 1
Schematic diagram of this review.

2.2 Pathophysiological changes of skin wound healing

After skin injury occurs, the body completes skin wound repair through a series of continuous pathophysiological changes. The whole process can be roughly divided into four stages as shown in Figure 1: hemostatic stage, inflammatory stage, proliferative stage and remodeling stage (Wilkinson and Hardman, 2020). After the occurrence of skin injury, the capillaries and arteriolar arteries in the injured area are broken, and the exposed vascular endothelial cells and the foreign substances causing the injury jointly activate the internal and external coagulation cascade, prompting platelet activation and accumulation to the injured site (Velnar et al., 2009). Through the release of endogenous ADP and thromboxane A2 in the platelets, the platelets undergo irreversible coagulation and form platelet thrombosis (Golebiewska and Poole, 2015). Platelet thrombus, together with fibrin, fibronectin, further constitute insoluble clots that act as wound packing and hemostasis (Broughton et al., 2006). In addition, clots composed of platelets and proteins can also provide attachment scaffolds for immune cells, release a variety of cytokines and inflammatory factors, promote the migration and aggregation of inflammatory cells and activate inflammatory response (Cooke, 2019).

Under the induction of inflammatory factors, neutrophils first gather to the injured area, phagocytosis and release reactive oxygen species, antimicrobial peptides, proteolytic enzymes to engulf and remove necrotic tissues and pathogens (Li et al., 2007). Neutrophils also continue to release pro-inflammatory factors, further stimulating the aggregation of neutrophils and macrophages to the injured area (Paquet and Piérard, 1996; Rodero and Khosrotehrani, 2010). With the removal of necrotic tissue and pathogens from the injured area, the number of neutrophils gradually decreases. Most neutrophils are squeezed out from the wound area, and the remaining neutrophils are gradually removed by recruited macrophages through endocytosis (SingerHealing, 2022). As the inflammatory response progresses, macrophages shift from a pro-inflammatory phenotype to an anti-inflammatory phenotype at the end of inflammation by releasing a variety of growth factors that promote angiogenesis, fibroplasia, and skin re-epithelialization (Hunt et al., 2000).

When the wound repair entered the proliferative stage, keratinocytes, fibroblasts and endothelial cells began to proliferate under the action of EGF, FGF, VEGF and other growth factors (Werner and Grose, 2003; Lichtman et al., 2016). The keratinocytes at the wound edge become more polar and migratory and begin to migrate to the injured area where they proliferate and differentiate to form a new upper layer, which known as re-epithelialization (Rousselle et al., 2019). At the same time, fibroblasts synthesize a large amount of type III collagen, proteoglycan and fibronectin to form extracellular matrix, which provides skeleton structure for cell migration and proliferation to the injured area (Bártolo et al., 2022). Under the action of growth factors such as VEGF, endothelial cells migrate to the injured area and proliferate to form a new capillary network (Park et al., 2017). Together with the newly

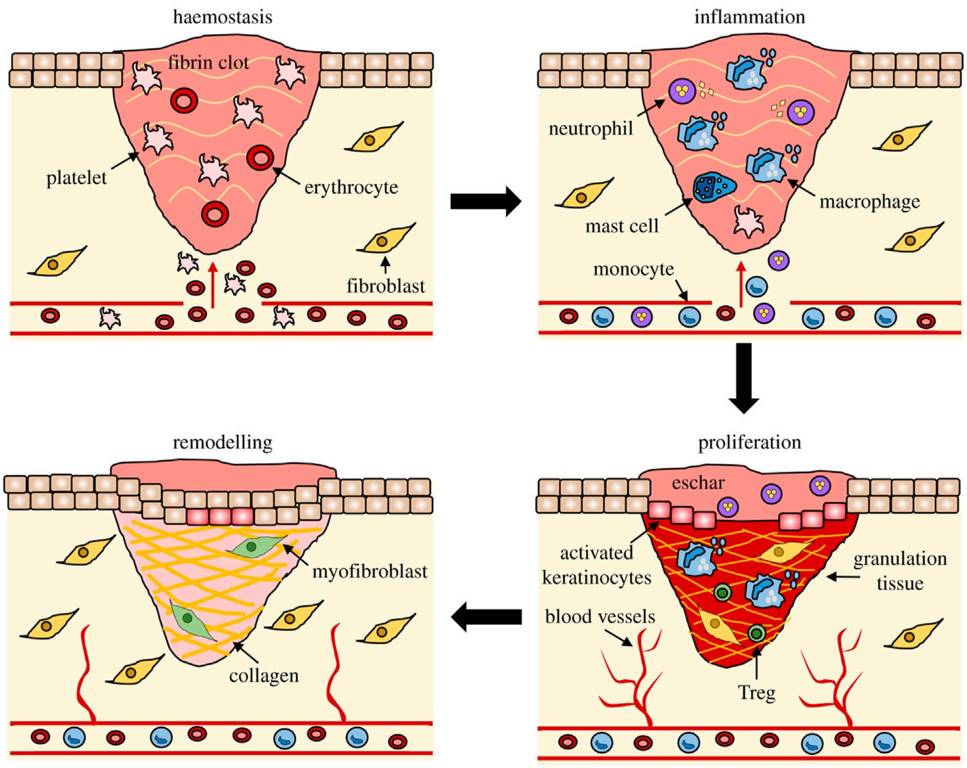

FIGURE 1
The stages of wound repair and their major cellular components (Wilkinson and Hardman, 2020).

generated extracellular matrix and keratinocytes in the wound, constitute granulation tissue.

Wound healing begins to enter the remodeling stage at 2–3 weeks after injury, which is mainly the remodeling of new tissue and the formation of scar tissue. The new granulation tissue is mainly composed of type III collagen with low elastic tension, while the normal skin tissue is mainly composed of type I collagen with higher tensile strength (Rippa et al., 2019; Wikslund et al., 2022). Therefore, under the action of fibroblasts and collagenase, collagen in granulation tissue is constantly degraded and regenerated to form higher strength type I collagen, thus providing scar tissue with mechanical strength close to that of normal skin tissue (Churko and Laird, 2013). At the same time, the excess capillaries and residual inflammatory cells formed in the repair process will be gradually eliminated by apoptosis, and eventually scar tissue will be formed (Kimura and Tsuji, 2021).

2.3 Related factors affecting skin wound healing

Under physiological conditions, the wound repair process can be completed in about 2 weeks. The factors affecting wound healing can be divided into endogenous factors and exogenous factors according to different sources (Table 1). Common endogenous factors include age, nutritional status, physical health status, hormone level and genetic factors (Winter 2006). With the increase of age, the proliferation activity of keratinocytes and basal cells in the epidermis of the skin decreases, so it is more prone to damage under the influence of external injuries (Boismal et al., 2020). At the same time, the decrease in the activity of macrophages and the decrease in the release of growth factors and cytokines caused by aging prolongs the time of proliferation, which leads to the prolongation of the wound healing process and the increase of the time required (Bonté et al., 2019).

In addition to the slowing down of tissue renewal caused by aging, the health status of the body also affects wound healing. Some chronic diseases such as diabetes can affect the abnormal formation of micro vessels during wound healing, resulting in delayed skin re-epithelialization and abnormal extracellular matrix remodeling. Vitamins, essential fatty acids and other nutrients also play a key role in wound healing. Lack of these nutrients can lead to prolonged wound healing and an increased risk of infection (Pullar et al., 2017). Proper supplements of vitamins and fatty acids such as vitamin A, vitamin C and n-3 fatty acids can speed up wound healing (Huang et al., 2018a; VanBuren and Everts, 2022). Hormones also have a certain impact on the healing of skin wounds. Glucocorticoid can inhibit the inflammatory response, slow down the aggregation of neutrophils and macrophages to the wound during the inflammatory period, and prolong the wound healing time (Hengge et al., 2006). Estrogen can promote the re-epithelialization of keratinocytes and angiogenesis of endothelial cells, and accelerate wound healing (Wilkinson and Hardman, 2017). Insulin controls blood sugar levels to achieve normal wound healing, avoiding microvascular abnormalities caused by hyperglycemia and energy supply disorders caused by hypoglycemia (Hrynyk and Neufeld, 2014; Yu et al., 2019). Finally, wound healing is also affected by genetic factors. For example, people with cicatricial constitution may produce excessive scar of wound fiber due to excessive deposition of collagen, thus forming scar healing (Amadeu et al., 2004).

TABLE 1 Factors affecting skin wound healing.

Endogenous factors	Exogenous factors
Age	Drinking
Hormone	Infection
Nutrition	Smoking
Chronic disease	
Heredity	

In addition to endogenous factors, exogenous factors also have significant influence on the healing of skin wounds. When the bacteria in the environment come into contact with the wound, the bacteria will gather and grow on the wound, release toxins and cause the necrosis of tissues and cells (Zulkowski, 2013). In the process of removing bacteria, inflammatory factors will be released excessively, resulting in the imbalance between growth factors and inflammatory factors, the inhibition of cell proliferation, and the delay of wound healing or prolonged wound healing (Scalise et al., 2015; Malone and Schultz, 2022). Smoking also has an obvious adverse effect on wound healing. Nicotine and NO in cigarettes can cause small blood vessel constriction, increase platelet adhesion, cause small blood vessel occlusion (Ortiz and Grando, 2012). Alcohol inhibits the body's immune response while reducing the level of collagen forming MMPs, which affects the normal healing of wound (Rosa et al., 2018).

3 Characteristics of wound dressing in skin wound healing

3.1 Types and main functions of wound dressings

As a kind of open wound, the external environment has obvious influence on the healing process of skin wound (Kruse et al., 2015; Kirchner et al., 2020). Early wound dressing is mainly made of gauze, cotton and other materials, applied to the wound can quickly stop bleeding, absorb exudation, help the wound drainage, reduce the chance of wound infection (Pereira and Bártolo, 2016; Farahani and Shafiee, 2021). However, these traditional wound dressings can not effectively maintain the moist wound environment (Aljghami et al., 2019). At the same time, there are still large pores in these traditional dressings, which cannot avoid the contact between bacteria in the air and the wound (Simões et al., 2018; Obagi et al., 2019). With the development of time, modern dressings represented by hydrogels, fiber dressings, foam dressings and film dressings are gradually applied in clinical practice (Walker et al., 2017; Liang et al., 2021a; Tan et al., 2022). These dressings can create a moist surface environment for the wound and prevent bacteria from passing through the dressing and entering the wound while ensuring gas exchange (Francesko et al., 2018). Fiber dressings such as alginate fiber dressings also have excellent absorbency and are able to fully absorb the wound exudation, keeping the wound relatively dry (Zhang and Zhao, 2020). Since wound healing is affected by many internal and external factors, it has become a new direction for the construction of wound dressings to modify or add a variety of bioactive substances to the existing matrix materials and make them have anti-inflammatory, antibacterial, promoting re-epithelialization and other biological functions (Zhao et al., 2017; Zhang et al., 2022a; Yao et al., 2023).

3.2 Properties of an ideal wound dressing

Although the properties of dressings is improving, there is still a certain gap compared with the healing effect of autologous skin transplantation (Herskovitz et al., 2016). An ideal wound dressing should be able to meet the needs of all aspects of the wound healing process and provide the most suitable internal and external environment for cell and tissue regeneration. Firstly, the dressing must have good biocompatibility in the selection of raw materials, and will not cause immune rejection or biological toxicity (Zhang et al., 2022a); At the same time, it should have relatively low economic cost, which is convenient for large-scale production and clinical application (Pagnamenta, 2017). The wound dressing constructed should be able to simulate the tissue structure of the skin, have appropriate mechanical strength, and be able to fit closely with the skin without adhesion to the wound, so as to avoid the occurrence of secondary damage (Alizadehgiashi et al., 2021). In addition, the wound dressing should also have good moisture, air permeability and water absorption, can fully absorb the wound exudate, to ensure the gas exchange between the wound and the outside world (Liang et al., 2021b; Yang et al., 2022a). Finally, the wound dressing should have a certain antibacterial and bactericidal ability, to minimize the occurrence of wound infection; And on this basis, it has the ability to promote cell proliferation and growth and skin regeneration (Jiang and Loo, 2021; Yuan et al., 2022). Obviously, a single kind of material cannot meet all the above needs. Therefore, it will be a future research trend to construct bioactive materials and tissue engineering dressings by adding bioactive substances or stem cells to matrix materials through multi-material combination.

4 Properties and preparation of MXene

4.1 Characteristics of MXene

MXene is a general term for a class of two-dimensional metal carbides, whose structure is generally $M_{n+1}X_n$, where M represents excessive metallic elements and X represents carbon, nitrogen, or a carbon-nitrogen complex (Naguib et al., 2012). MXene is usually obtained by etching the A atomic layer in the MAX phase of its

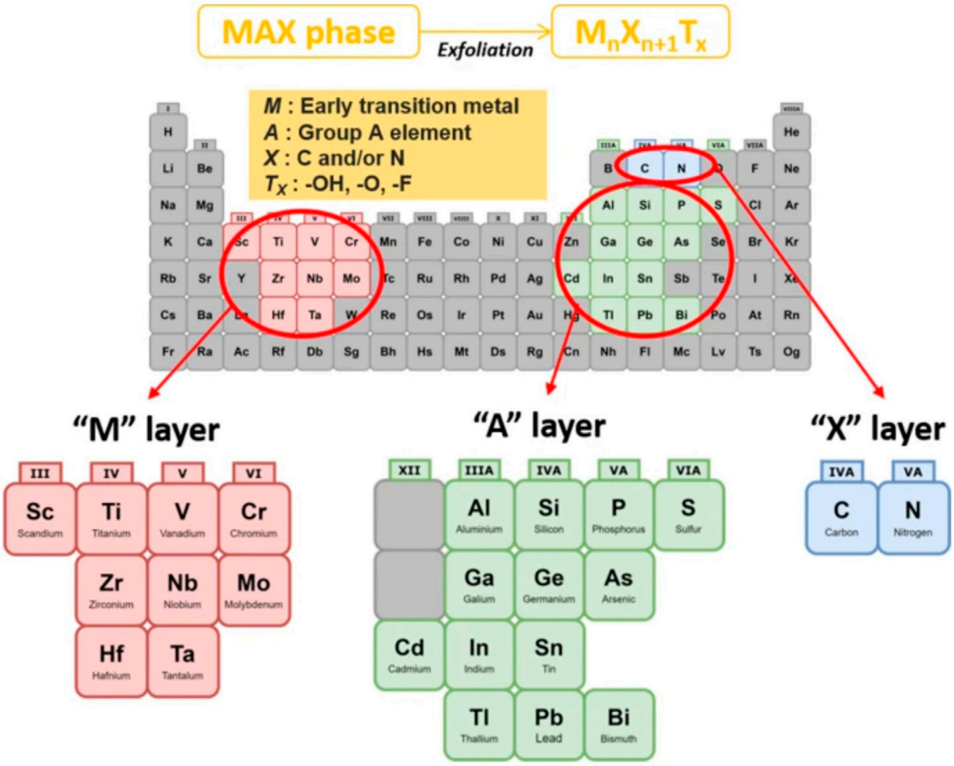

FIGURE 2
General element composition of MAX phase and MXene: M: early transition metal, A: Group A element, X: C and/or N, Tx: surface functional group (Zamhuri et al., 2021).

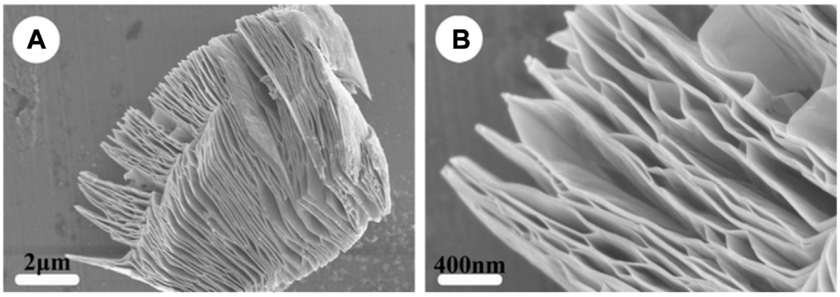

FIGURE 3
Structure of MXene. SEM images of **(A)** MXene-Ti3C2 and **(B)** the high-magnification of **(A)**. (Wang et al., 2015).

precursor. As shown in Figure 2 and Figure 3, MAX is communicated as $M_{n+1}AX_n$, where A represents an element of the third or fourth main group, usually Al and Si (Zamhuri et al., 2021). The M-A bond in MAX has the properties of a metallic bond with a weak force relative to the M-X bond, so the A phase in MAX can be etched out by a mixture of HF or HCl with fluorine salts, leaving the M atomic layer and X atomic layer to form two-dimensional $M_{n+1}X_n$. Since MXene prepared by liquid phase method has functional groups such as -OH, -O and -F, it is often written as $M_{n+1}X_nT_x$, where T stands for the surface functional groups in the compound and x indicates the number of such groups (Naguib et al., 2014).

Since Naguib et al. first discovered and synthesized MXene in 2012, dozens of different MXene have been prepared and applied in many fields, such as catalysis, sensor, energy storage, microwave absorption, biomedicine and so on (Pang et al., 2019; Soleymaniha et al., 2019; Huang et al., 2021). The transition metals, surface functional groups and unique two-dimensional lamellar structure of MXene give it a rich variety of properties. MXene composed of Ti, Ta and Nb in the transition elements has good stability and biocompatibility in animals, and does not cause obvious immune response and pathological changes in the body (Sundaram et al., 2020). Surface functional groups and electronegative layered structures provide MXene with good hydrophilicity (Lu et al., 2021). Compared with two-dimensional materials such as graphene, MXene has better water dispersion and hydrophilicity, and can be uniformly dispersed in water-based solvent to construct a hydrophilic composite material with good cytocompatibility and adhesion (Chen et al., 2017; Lin et al., 2021). The abundant surface functional groups also provide a large number of binding sites for MXene, which can be combined with other matrix materials, proteins, drugs and other biological macromolecules to achieve material modification and drug delivery, greatly expanding the application of MXene in the field of biomedicine (Huang et al., 2020a; Koyappayil et al., 2022). MXene also has an electrical conductivity close to that of graphene, and can vary between semiconductors and conductors according to the modification of its surface groups, meeting different electrical conductivity requirements of materials (Yin et al., 2021a; Riazi et al., 2021). The mechanical destruction of bacterial cell membranes by MXene's two-dimensional lamellar structure and the redox action of lipopolysaccharides by strong anions on cell membranes give MXene excellent antibacterial properties (Begum et al., 2020; Hao et al., 2022). In addition, MXene has strong light absorption in the NIR region, which makes MXene also promising in the field of photothermal therapy and imaging (Yin et al., 2021b; Jiang et al., 2022).

4.2 Preparation methods of MXene

4.2.1 Hydrofluoric acid etching method

Etching the MAX phase using acid is the most commonly used method for preparing block MXene (Zhang et al., 2022b). Etching the Max phase using acid is the most commonly used method for preparing block MXene, and among all candidates, HF was the earliest one being applied. Based on the difference of bonding force between M-A bond and M-X bond in MAX, HF targets the M-A bond in MAX, where high concentration of HF provides fluorine ions that binds selectively and tightly to A element (He et al., 2021a; Chen et al., 2021). By adjusting HF concentration and reaction time to control the degree of reaction, MXene two-dimensional laminates prepared by different MAX phases and MXene blocks of different thickness can be obtained. For example, when 40% HF is used for etching, Ti_3AlC_2 powder needs to be etched for 24 h to obtain multilayer Ti_3C_2 nanosheets (Awasthi et al., 2020), while Nb_2C can be prepared only by treating Nb_2AlC powder for 3 h (He et al., 2021b). However, it should be noted that MXene prepared by etching MAX phase with HF is mostly accordion-like multilayer structure. If single-layer two-dimensional MXene sheets need to be obtained, intercalator such as DMSO should be introduced into the reaction system or ultrasonic wave should be used for delamination stripping (Naguib et al., 2015; Rajavel et al., 2018). Due to the strong corrosion of HF, it is dangerous for operators (Ozcan et al., 2012). Meanwhile, the use of high concentration HF to treat MAX phase for a long time increases the defects in the prepared MXene layer and reduces the transverse size (Ghidiu et al., 2014). Therefore, the use of HCl to replace part of HF in the reaction system has also become a feasible preparation method (Wei et al., 2021; Yu et al., 2021).

4.2.2 *In situ* hydrofluoric acid etching

High safety risks exist in the preparation of MXene using HF, and additional intercalation agents are required in the preparation of monolayer two-dimensional MXene, which has led to the search for new safer and more efficient methods of MXene preparation. The substitution of M-A layer by the *in-situ* HF formation on the surface of the material by the combination of HCl and fluoride salt has become the mainstream preparation method (Baraneedharan et al., 2022; Kumar et al., 2022). In this method, LiF and HCl are usually used as etching agents. Cations in fluoride salts can also be used as intercalating agents to enable MXene to be stratified and stripped, so as to obtain single two-dimensional MXene, eliminating the need to introduce additional intercalating agents (Ghazaly et al., 2021; Sinha et al., 2021). Besides LiF, fluoride salts such as NaF, KF and NH4F exerts similar effects in the etching process (Liu et al., 2017a; Sun et al., 2023). In addition, given that neither HF nor fluoride brine solutions can substitute A layer in the preparation of nitride-based MAX, MAX is mixed with molten fluoride salt mixture in an argon atmosphere (Urbankowski et al., 2016).

4.2.3 Fluorine-free preparation method

Whether HF is used for direct etching or HF *in situ* etching, HF formation is inevitably involved in the reaction process. HF is very harmful to human body, and a small amount of HF direct contact can cause the necrosis of cell tissues and even lead to death (Kaminsky et al., 1990; Miranda et al., 2021). In addition, the introduction of fluoride ions in the reaction system will reduce the number of -OH, -O and other functional groups on the surface of MXene, which is not conducive to the further modification of MXene in the application of biomedicine (Huang et al., 2018b). Therefore, the construction of a fluorine-free MXene preparation method will be more conducive to the application of MXene in the biomedical field. Yang et al. designed a method for preparing Ti_3C_2 nanosheets using electrochemical etching of NH_4Cl and TMAOH (Yang et al., 2018). Two Ti_3AlC_2 nanosheets were used as anode and cathode respectively, during the etching process, chloride ion in the solution binds tightly to Al, consequently pure Ti_3C_2 is collected. Li et al. designed a NaOH-assisted hydrothermal process to prepare Ti_3C_2 and obtained a 92% purity Ti_3C_2 powder (Li et al., 2018). Since no fluoride ion is involved in the preparation process, the Ti_3C_2 collected in this way possess more active functional groups and have more potentiality for biological modification.

In addition to MXene obtained by treating MAX phase, MXene nanosheets can also be prepared by chemical vapor deposition (Li et al., 2021a; Thirumal et al., 2022). This method is mainly used to prepare some two-dimensional MXene that cannot be synthesized by etching or does not exist stable MAX precursor phase, such as TaC, TaN, etc (Liu et al., 2021). For example, Geng et al. used a CVD process catalyzed by molten copper to prepare Mo_2C thin layers on graphene surface *in situ* (Geng et al., 2017). Wang et al. heated Cu and Ta with acetylene gas to prepare TaC thin nanosheets (Wang et al., 2017). In summary, the current methods of preparing MXene can be roughly divided into two categories according to whether fluorine ions are involved in the reaction system. The method of preparing MXene using HF or *in-situ* synthesis of HF is relatively simple and easy to prepare and synthesize in large quantities. However, the biological security problems brought by fluorine ions need to be carefully applied. Fluorine-free preparation method has higher biosecurity and is more environmentally friendly because fluorine ion is not involved in the reaction system. However, its preparation process is more complex, and its yield has some disadvantages compared with traditional methods.

5 Application of MXene and its modified materials in skin wound healing

5.1 Biocompatibility

As a new material, good cytocompatibility and tissue non-toxicity are the prerequisite for its further application in the biomedical field. Up to now, there are dozens of two-dimensional transition metal compounds in the MXene family, but only Ti, Nb, Ta several transition elements and their compounds with relatively stable chemical properties can be applied in the field of biomedicine, and Ti_3C_2 is the main application in skin wound healing materials (Jastrzębska et al., 2017; Liu et al., 2022a). For Ti_3C_2, its biocompatibility is affected by many factors, such as concentration, size, synthesis method and administration route (Scheibe et al., 2019; Szuplewska et al., 2019). In general, MXene has no obvious toxic and side effects on most cell lines at low and medium concentration. However, when the concentration of MXene increases gradually, the activity of tumor cell lines will be significantly decreased. When the concentration of MXene reaches 500 mg/L, normal cell lines can still maintain 70% or even higher cell activity. On the other hand, the activity of tumor cell lines decreased significantly, and only about 20% of A549 cell line still had proliferative activity at this concentration (Jastrzębska et al., 2017). This phenomenon may be due to the fact that MXene produces reactive oxygen species that exceed the oxidative stress level of cancer cells, thus leading to apoptosis of cancer cells (Hu et al., 2010).

The morphology of MXene applied in biomaterials also has some influence on its biosafety. Zhou et al. found that the safe concentration of Ti_3C_2 QDs for human embryonic kidney cell 2,937 and MCF-7 cancer cells could reach 400 mg/L when they selected Ti_3C_2 QDS as the intervention material (Zhou et al., 2017). The oxidized Ti_3C_2 formed by the oxidation of the functional groups on the surface of Ti_3C_2 showed significant cytotoxicity (Jastrzebska et al., 2020). The size of the prepared MXene also has a certain influence on its cytocompatibility. Compared with large size Ti_3C_2 (500 nm) under the same conditions, small size Ti_3C_2 (1–100 nm) showed higher activity inhibition on cells, which may be caused by the ability of small size MXene to enter cells through endocytosis and induce autophagy dysfunction (Shi et al., 2020). However, although MXene may have some effects on cell activity *in vitro*, none of the results showed any potential organ pathological changes or toxic effects when MXene was applied *in vivo in vitro*, indicating that MXene has no toxic side effects on organisms, which provides a guarantee for its safe use *in vivo* (Liu et al., 2017b; Li et al., 2021b).

The process of skin wound healing is mainly realized by fibroblasts and keratinocytes. Whether MXene has toxic effects on these 2 cells determines whether it can be used in the modified design of skin wound dressings. Li et al. constructed an anisotropic MXene@ PVA hydrogel in which NIH3T3 cell lines grown in the hydrogel had a cell survival rate of over 90%, in addition, NIH3T3 cells in the hydrogel showed higher cellular activity compared to the control group (Li et al., 2022a). Wang et al. constructed a SF-coated MXene membrane and showed that human skin fibroblasts HSAS1 cells were

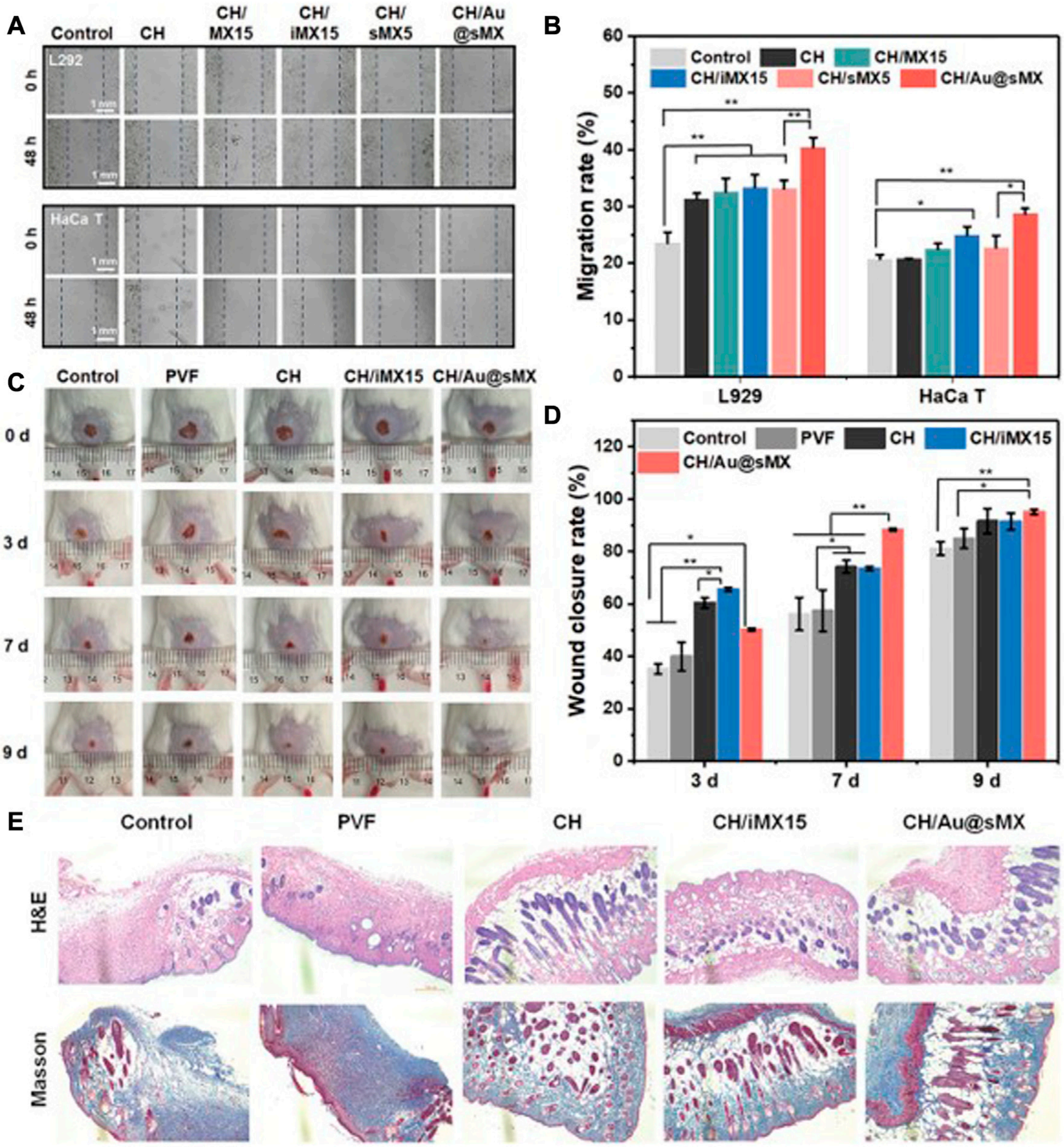

FIGURE 4
Biocompatibility of MXene-modified sponges *in vivo* and vitro **(A)** Representative images and **(B)** migration scratch assay of L292 and HaCaT at 48 and 0 h after scratching and treatment with 0.5 mg/ml of each sample. *In vivo* assessment of the sponges for wound healing **(C)** Photographic snapshots of temporal development of healing wounds for the different sponges in 0, 3, 7, and 9 days, respectively. **(D)** Wound closure rate of different sponges at different healing times **(E)** H&E staining and Masson staining images of the wound section at the 13th day for each group, respectively (Li et al., 2022b).

able to grow normally on the surface of the membrane and still showed 99% cellular activity after 6 days (Wang et al., 2020). These results indicated that MXene had good biosafety for fibroblasts, and did not affect the activity of fibroblasts. Li et al. inoculated HaCaT keratinocyte into MXene-containing chitin composite sponges, and Figure 4 showed that HaCaT keratinocyte migration was significantly enhanced in MXene-containing materials, with good cell survival (Li et al., 2022b). These results indicate that MXene has good cytocompatibility with the two key cells in skin injury and regeneration, and can promote fibroblast migration and wound healing to a certain extent.

5.2 Antibacterial activity

Wound infection is an important factor that leads to wound deterioration or delayed healing. For a wound healing dressing, it has certain antibacterial and even bactericidal properties to significantly reduce the chance of infection on the wound surface and promote the healing of the wound, especially the infected wound (Liu et al., 2022a; Li et al., 2022c; Yu et al., 2022). Traditional wound care methods for infected wounds usually use antibiotics to solve the problem of wound infection, but a wide variety of bacterial species and complex environment on the wound

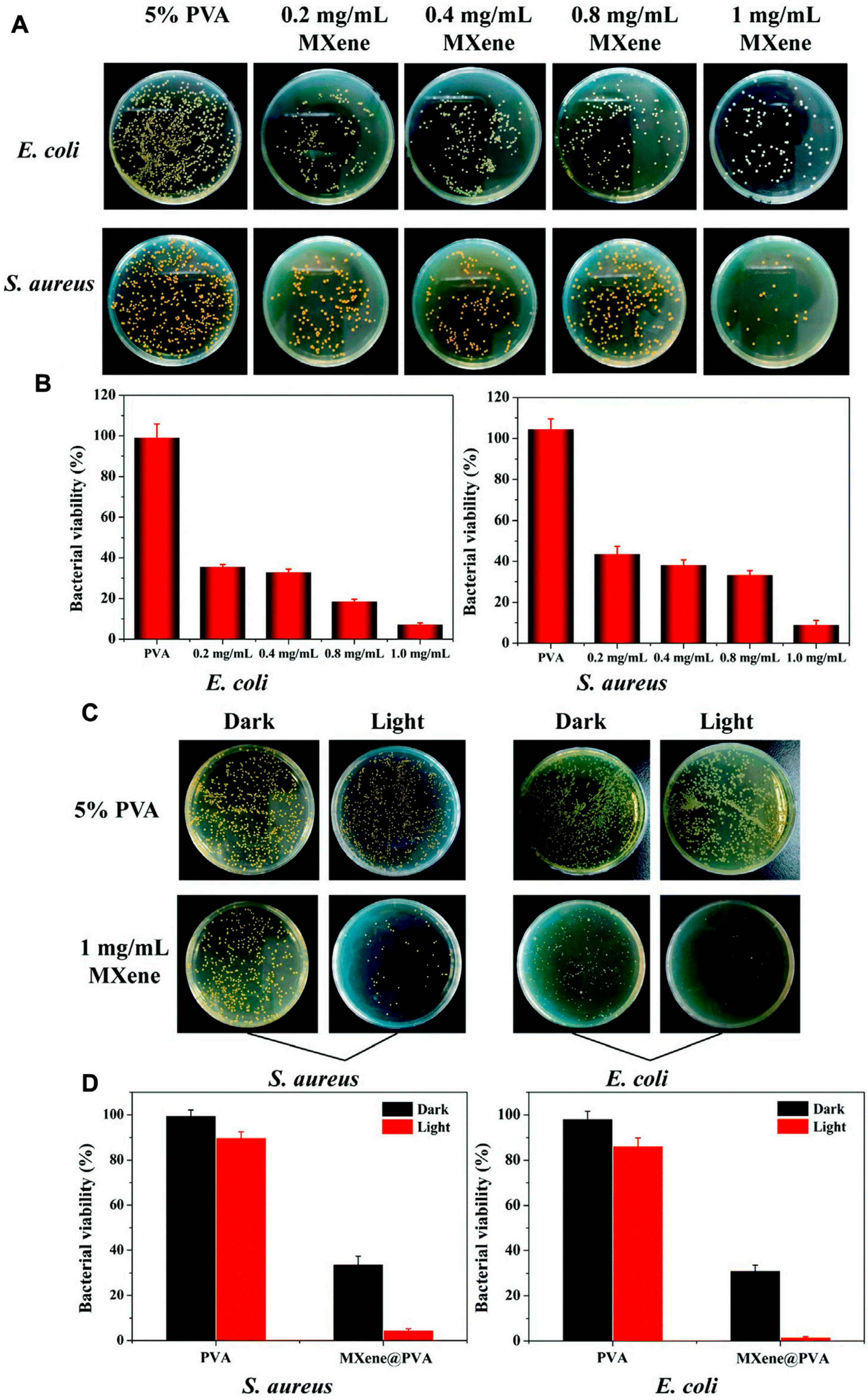

FIGURE 5
Antibacterial ability of MXene-modified MXene@PVA hydrogel **(A)** Photograph of bacterial colonies of *Escherichia coli* and *Staphylococcus aureus* treated with different concentrations of MXene. **(C)** Photograph of bacterial colonies formed by *Escherichia coli* and *Staphylococcus aureus* treated with the PVA hydrogel, the PVA hydrogel + NIR, MXene@PVA hydrogel (1 mg/ml MXene) and the MXene@PVA hydrogel (1 mg/ml MXene) + NIR. The power density was 1.5 W/cm^2, and the operation time was 10 min **(B)**; **(D)** corresponding survival rates for *Escherichia coli* and *Staphylococcus aureus* (Li et al., 2022a).

surface make it difficult for a single antibiotic to cover all bacterial species, and long-term use of broad-spectrum antibiotics is easy to lead to the colonization and growth of multi-drug-resistant bacteria such as MRSA, further increasing the difficulty of wound healing (Deurenberg and Stobberingh, 2008; Li et al., 2022c). MXene has a lamellar structure similar to graphene and more abundant surface groups, so the researchers hypothesized that MXene should also have some antibacterial properties. Rasool et al. investigated the antibacterial properties of MXene in 2016, and found that Ti_3C_2 had higher antibacterial efficiency against Gram-negative *Escherichia coli* and Gram-positive *Bacillus subtilis* compared to GO (Rasool et al., 2016). At the same time, Ti_3C_2 showed obvious dose-dependent bactericidal effect, and it was found that Ti_3C_2 could achieve 98% bactericidal killing rate at 200 μg/ml. TEM and SEM results showed that the cell membrane was destroyed under the action of Ti_3C_2, resulting in the release of cytoplasm from the bacteria. The authors speculate that this strong antibacterial activity may be caused by bacterial oxidative stress caused by electron transfer and the direct mechanical damage of MXene lamellar structure to the cell membrane (Mashtalir et al., 2014; Tian et al., 2014).

MXene can avoid the emergence of bacterial resistance through the mechanism of bacterial death caused by mechanical damage and oxidative stress, and can also maintain a good killing effect against multi-drug resistant bacteria, which makes more researchers apply MXene in the modification and construction of wound dressings (Figure 5). Mayerberger, E. A. et al. constructed a chitosan nanofiber loaded with MXene. When *E. coli* and *Staphylococcus aureus* were inoculated on the fibers, they showed a 95% and 62% reduction in the number of colonies formed, respectively, 4 hours after culture (Mayerberger et al., 2018). Rozmysłowska-Wojciechowska et al. constructed a MXene modified chitosan-hyaluronic acid hydrogel and demonstrated up to 90% growth inhibition against *E. coli* and *S. aureus* in hydrogels supplemented with only 1% MXene (Rozmysłowska-Wojciechowska et al., 2020). In addition to the antibacterial effect of MXene itself, the abundant functional groups on the surface of MXene give it great potential for modification, which can be combined with proteins, growth factors, nanoparticles and other molecules to play more roles. Zhang et al. fixed lysozyme onto the surface of MXene nanosheets. This composite demonstrated excellent MRSA killing ability and significantly promoted the healing of infected wound (Zhang et al., 2023).

5.3 Photothermal effect

Photothermal effect refers to the phenomenon of increasing temperature caused by the interaction between photon energy and lattice vibration after the material is irradiated by light, among which the photothermal effect caused by near-infrared radiation is the most obvious (Huang et al., 2020b; Meng et al., 2022). It is found that MXene has high photothermal conversion efficiency, and can achieve obvious temperature increase under the condition of low power NIR irradiation (Xu et al., 2020; Safaei and Shishehbore, 2021). Jin et al. found that for the constructed nanofiber hydrogel loaded with MXene, 0.5 W NIR irradiated for 5min could increase the material temperature from 23°C to 41°C, and the material temperature further rose to 61°C after 5 min irradiated with 1 W NIR (Jin et al., 2021). Such excellent photothermal effect provides a new design and application idea for the application of MXene in the design of skin wound dressing. On the one hand, MXene can make the material temperature rise to a higher temperature through the photothermal effect, at 40°C or higher temperature can significantly inhibit the growth activity of bacteria, and further enhance the antibacterial and bactericidal effect of the material together with the mechanical damage effect of MXene on bacteria. Wang et al. constructed a chitosan-MXene suspension and loaded it on PVDF membrane to form a multifunctional membrane. The antibacterial experiment results showed that the antibacterial ability of the multifunctional membrane combined with NIR was close to 100%, which was significantly improved compared with the simple material group without NIR irradiation (Wang et al., 2022). The results of animal experiments showed that on the 14th day of treatment, the healing rate of the infected wound reached 95% in the MXene combined with NIR irradiation group, which was higher than that in the material group without NIR irradiation. These results indicated that the photothermal effect of MXene could further enhance the antibacterial properties of MXene and promote the healing effect of MXene on infected wounds.

On the other hand, the photothermal effect of MXene can be used to regulate the properties of the materials, so as to realize the on-demand release and precise regulation of growth factors or other active substances in the materials. Yang et al. constructed a multi-stimulus response MXene@AgNPs hydrogel (Figure 6), which achieved precise controlled release of AgNPs through photo response and magnetic response, and avoided the cytotoxicity caused by high concentration of AgNPs in a short time while guaranteeing the bactericidal effect (Yang et al., 2022b). The results of animal experiments showed that the elevation of local temperature after NIR irradiation further enhanced the action depth of AgNPs and improved the therapeutic effect of the material on deep chronic infected wounds. Xu et al. constructed a multi-mode antibacterial platform based on MXene, which utilized the photothermal effect of MXene to achieve continuous and stable release of amoxicillin, and achieved better long-term antibacterial effect under the condition of low drug loading (Xu et al., 2021). Jin et al. constructed a temperature-responsive MXene nanoribbon loaded with vitamin E. The surface temperature of the material was raised by NIR irradiation to realize the dissolution and release of vitamin E, which effectively improved the wound healing function of the material (Jin et al., 2021).

5.4 Hemostatic ability

Blood vessels rupture after skin injury occurs, and rapid hemostasis in the early stage of injury to form clots is conducive to wound healing and reduce the risk of infection (Guo and Dipietro, 2010; Rodriguez-Merchan, 2012). MXene has a rich surface charge that promotes blood cell aggregation, activates platelet activation and clot formation (Liu et al., 2018; Wu et al., 2021). Li et al. constructed a MXene@PDA decorated chitosan nanofiber wound dressing, which was shown to have safe blood compatibility and induce higher blood cell and platelet adhesion *in vivo* and *in vitro* (Figure 7). The authors speculate that this is mainly due to the large number of hydroxyl groups in MXene@PDA, which can adhere to blood cells and platelets and induce blood cell aggregation, platelet activation, and clot formation through interaction with plasma fibrin (Li et al., 2022d). Zhou et al. constructed a conductive antibacterial hemostatic

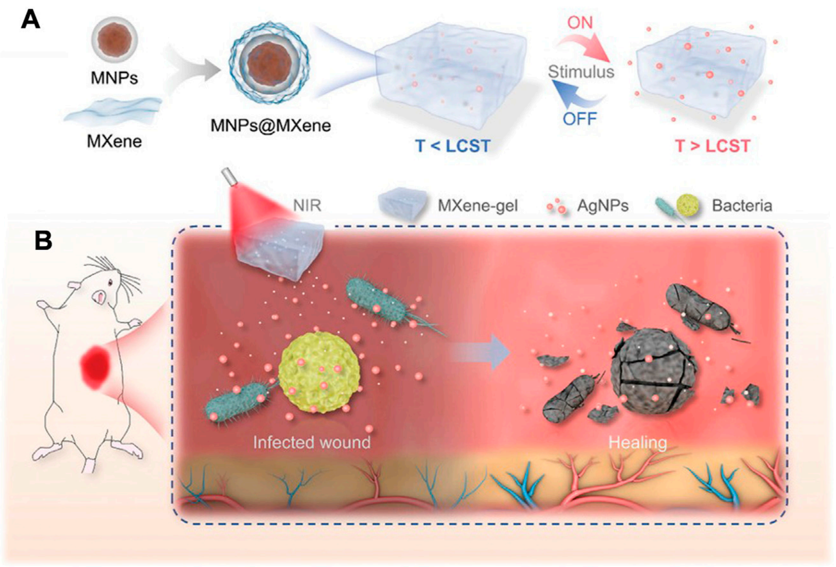

FIGURE 6
Schematic illustration of the preparation and application of NIR-responsive MXene-based hydrogel system. **(A)** The formation and drug release process of the MXene-based hydrogel system. **(B)** Deep chronic infected wound treated with NIR responsive AgNPs-loaded MXene-based hydrogel system. (Yang et al., 2022b).

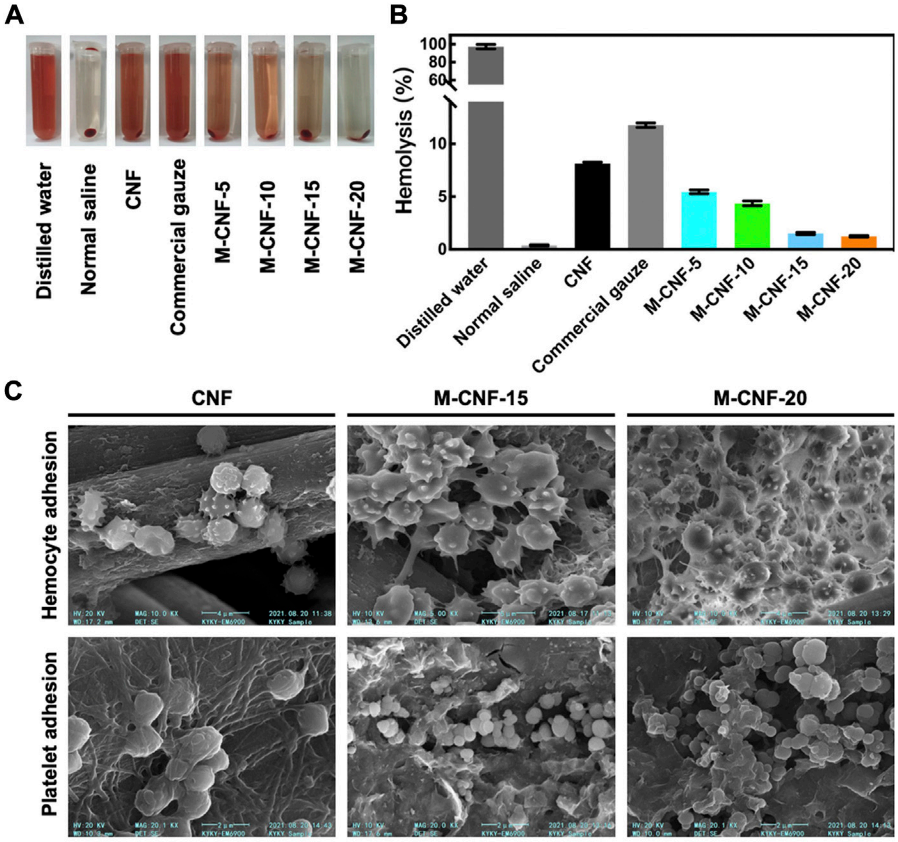

FIGURE 7
Hemostatic ability of MXene modified material M-CNF **(A, B)** Hemolysis image and hemolysis ratios of the M-CNF-x extracts. **(C)** SEM images of blood cells and platelets adhesion on the CNF, M-CNF-15 and M-CNF-20 surface (Li et al., 2022d).

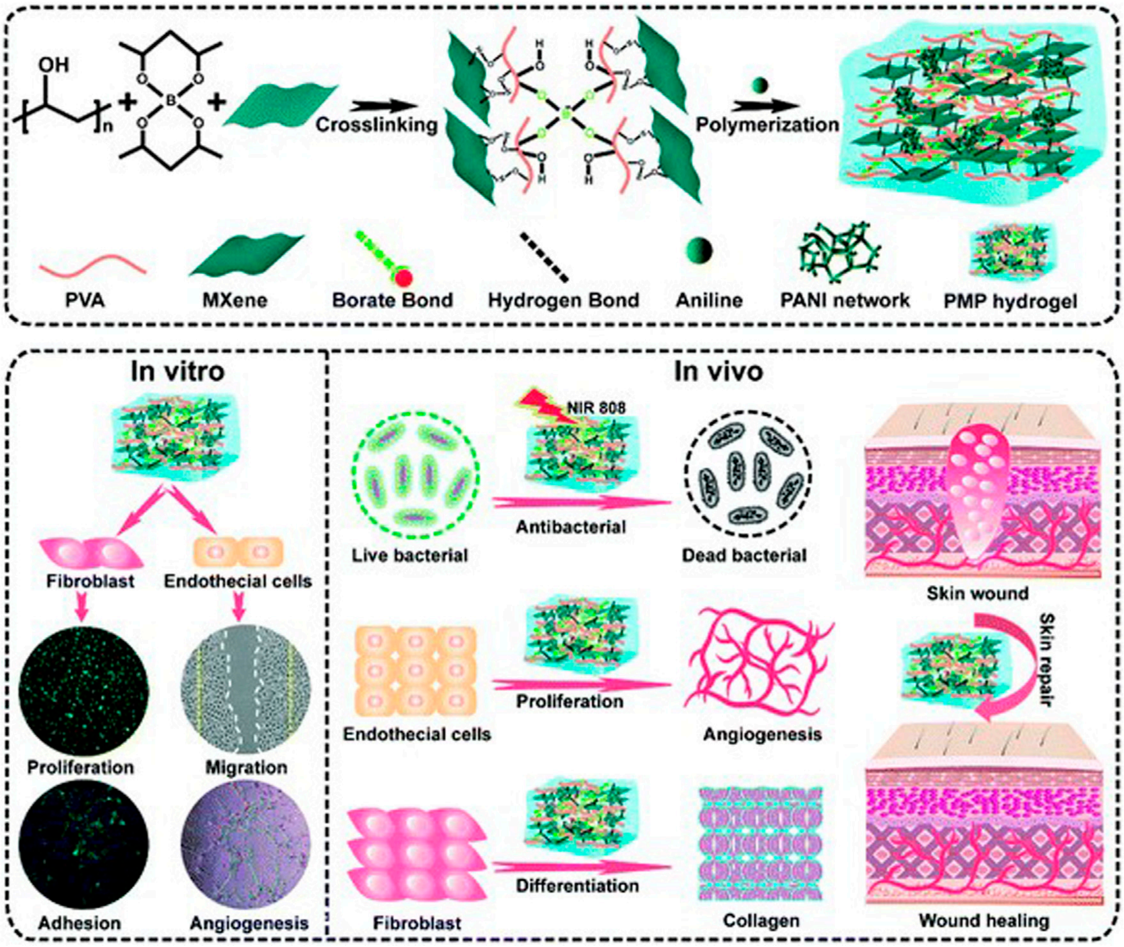

FIGURE 8
Schematic illustration of the fabrication of MXene-modified PMP hydrogels and their application in skin wound healing (Liu et al., 2022b).

multifunctional scaffold based on MXene nanosheets to promote wound healing in multidrug-resistant bacterial infections. The results showed that the MXene modified HPEM scaffold could significantly reduce the amount of wound bleeding, shorten the coagulation time, and demonstrate excellent hemostasis and coagulation ability. At the same time, the HPEM scaffold significantly accelerated the wound healing of MRSA-infected by effective anti-inflammatory effects, promoting cell proliferation and angiogenesis, stimulating granulation tissue formation, collagen deposition, vascular endothelial differentiation and angiogenesis (Zhou et al., 2021). Yang et al. designed a PCL-based MX@AgP bio-HJs antibacterial fiber membrane, which can realize sterilization, hemostasis, promote re-epithelialization and collagen deposition with the aid of NIR, providing a good regeneration microenvironment for wounds and promoting the healing of infected wounds (Yang et al., 2022c).

5.5 Electrical conductivity

Healthy skin can form a kind of "skin battery" function (Foulds and Barker, 1983; McCaig et al., 2005). When the skin is damaged to form a wound, the normal epithelial potential is immediately short-circuited, and the current flows out from the center of the wound to form a relatively stable current circuit at the edge of the wound, which is called the damaging endogenous electric field (Luo et al., 2021). A large number of studies have proved that the injurious endogenous electric field plays a vital role in the healing of skin injury (Isseroff and Dahle, 2012; Ashrafi et al., 2017; Verdes et al., 2022). As an exogenous electric field, bioelectrical stimulation can stimulate macrophages, lymphocytes and neutrophils to migrate to the wound in the early stage of skin wound healing (Demir et al., 2004), reduce the number of immune cells and cytokines in the late stage of healing (Weiss et al., 1989), increase the local tissue blood flow (Taşkan et al., 1997), reduce edema reaction (Gürgen et al., 2014), promote the migration and proliferation of fibroblasts and epithelial cells (Asadi et al., 2013), and accelerate the wound healing process (Franklin et al., 2016). Tang et al. constructed a chitosan-fibroin protein scaffold containing GO, which has good electrical conductivity. The experimental results showed that this scaffold combined with electrical stimulation could significantly improve the migration and proliferation of fibroblasts, and promote the healing of skin wounds (Tang et al., 2019).

As a two-dimensional nanosheet with similar structure to GO, MXene is endowed with good electrical conductivity by a large number

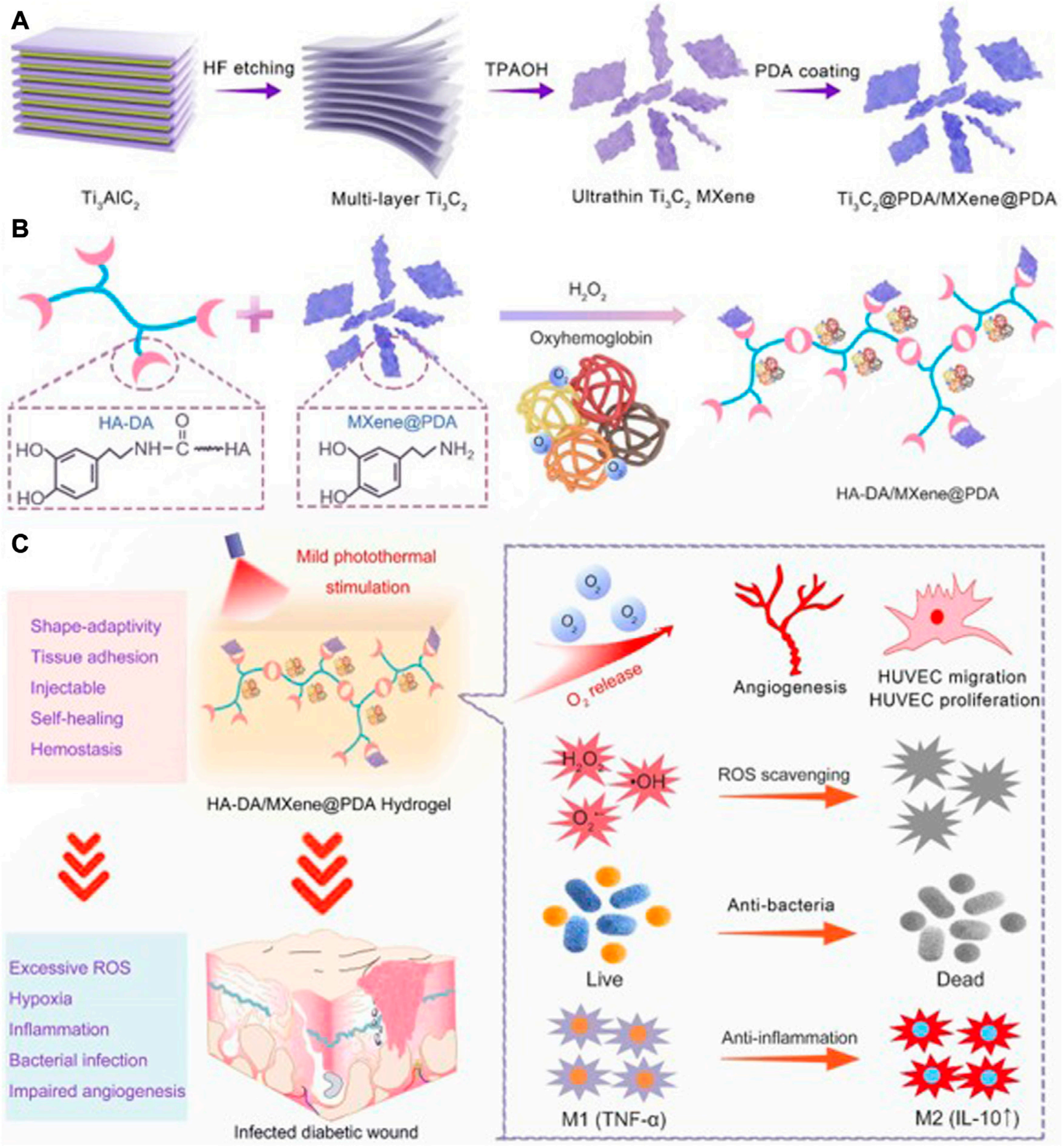

FIGURE 9
Schematic illustration of MXene@PDA Nanosheets. **(A)** Synthesis Diagram of MXene@PDA Nanosheets. **(B)** Schematic Illustrations of Injectable HA-DA/MXene@PDA Hydrogel Preparation. **(C)** Infected Diabetic Wound Healing Mechanism of HA-DA/MXene@PDA Hydrogel through Supplying O2, Scavenging ROS, Eradicating Bacteria, and Inhibiting Inflammation. (Li et al., 2022f).

of delocalized electrons. Mao et al. constructed a bacterial cellulose composite hydrogel containing MXene, which had good electrical and mechanical properties. The results of *in vitro* and *in vivo* experiments showed that the combination of hydrogel and electrical stimulation could significantly enhance the proliferation activity of NIH3T3 cells and accelerate the wound healing process compared with the group without electrical stimulation (Mao et al., 2020). Zhu et al. constructed an electroactive oxidized alginate/gelatin/MXene composite hydrogel. Compared with alginate/gelatin hydrogel alone, this composite material showed better mechanical properties and electroactivity. Meanwhile, it had good cytocompatibility to NIH3T3 cells and could promote the attachment and migration of fibroblasts (Zhu et al., 2022). Zheng et al. developed an injectable multifunctional hydrogel scaffold based on MXene@CeO2 nanocomposite material, which has good electrical conductivity, antioxidant capacity, antibacterial properties and mechanical properties. The multifunctional hydrogel can significantly promote the proliferation and migration of fibroblasts under the intervention of electrical stimulation. Animal experimental results showed that the composite significantly accelerated MDR wound healing by promoting granulation tissue formation, collagen deposition and re-epithelialization (Zheng et al., 2021). Liu et al. constructed a high-strength, conductive and antibacterial PVA hydrogel containing MXene and polyaniline (Figure 8). MXene in the hydrogel irradiated by NIR provided good antibacterial properties, while MXene and PANI endowed the material with excellent electrical conductivity. Applying electrical stimulation to the fibroblasts in the hydrogel can significantly promote their proliferation and migration. Animal experiments have shown that this multifunctional hydrogel can significantly accelerate skin wound healing by promoting angiogenesis and collagen deposition (Liu et al., 2022b).

5.6 Regulation of reactive oxygen species and inflammatory responses

In the process of skin wound healing, the local inflammatory response of the injury is in a dynamic balance. After injury, the local inflammatory response formed in the early stage of injury and the release of cytokines are conducive to the migration of macrophages, neutrophils and lymphocytes to the injured area, and accelerate the removal of wound cell debris and foreign substances (Golebiewska and Poole, 2015). When entering the proliferative and remodeling stages, a large number of inflammatory cells gathered in the injured area are gradually replaced by transplanted fibroblasts and epithelial cells, while the level of cytokines gradually decreases and various growth factors gradually increase, resulting in the formation of granulation tissue in the wound area, and the final healing is realized through remodeling (Dunnill et al., 2017; Deng et al., 2021). However, many factors such as diabetes, bacterial infection and other factors can interfere this immune response balance, which is characterized by excessive production of reactive oxygen species, pro-inflammatory cytokines and protease (Huang et al., 2020c; Tu et al., 2022). Excess ROS can cause oxidative damage to cells and tissues, inhibiting angiogenesis, granulation tissue formation, and wound healing (Wang et al., 2023). The use of wound dressings with reactive oxygen scavenging ability can reduce the inflammatory response of the wound and accelerate wound healing (Li et al., 2021c; Li et al., 2022e). MXene contains a large number of delocalized electrons, which can realize rapid conduction and delivery of electrons (Iravani et al., 2022). Meanwhile, the rich functional groups on the surface of MXene can also react with reactive oxygen species, so it has an excellent application prospect in reactive oxygen species scavenging (Iravani and Varma, 2022). Adding MXene to skin wound dressing can improve the overall scavenging ability of the material on reactive oxygen species.

Chen et al. constructed a temperature-sensitive Nb_2C hydrogel with antioxidant and antibacterial activities. The Nb_2C in this hydrogel can effectively remove reactive oxygen species and reduce oxidative damage of cells. Meanwhile, the hydrogel under NIR irradiation also has good antibacterial properties and can promote diabetic wound healing (Chen et al., 2022). Wei et al. constructed a new PAAM-based spongy macroporous hydrogel, in which MXene added to the hydrogel provided excellent antibacterial properties and active oxygen scavenging ability. The reactive oxygen scavenging rate of hydrogels containing MXene was up to 96% at 2 h. The authors speculated that this was mainly due to the removal of ROS by antioxidant phenol quinone groups in the MADA chain through redox reaction, and the removal effect was further enhanced by the electron transport capacity of MXene (Wei et al., 2022). Li et al. developed an injectable hydrogel based on HA-DA (Figure 9). MXene in the hydrogel showed excellent scavenging ability of reactive oxygen species and active nitrogen species, which could effectively reduce cellular inflammatory response and release of inflammatory factors, and promote the healing of diabetic infected wound (Li et al., 2022f).

6 Conclusion and perspectives

Skin wound healing is a continuous and complex dynamic process, which requires the joint action of a variety of cells, factors and appropriate microenvironment to achieve rapid and satisfactory healing. In order to give wound dressing a more comprehensive performance, as far as possible to meet the various needs of wound healing, the use of a variety of matrix materials combined with or add other materials to the matrix material for modification has become the main direction of wound dressing design. The rich physical and biological properties of MXene provide a good prospect for its application in the design and manufacture of wound dressing.

MXene represented by Ti_3C_2 has good biocompatibility. Adding MXene to the material can improve the overall mechanical properties and hemostatic ability of the material. The unique two-dimensional lamellar structure and abundant functional groups on the surface of MXene also give it excellent antibacterial properties, electrical conductivity and reactive oxygen scavenging ability, which can be further enhanced under the action of NIR. The rich functional groups on the surface of MXene also provide the potential for further modification, which further broadens the prospect of application in the design of materials for skin wound healing. The addition of MXene to wound dressings can significantly improve the overall performance of the material, giving the dressings antibacterial ability, electrical conductivity and reactive oxygen scavenging ability, and other properties conducive to skin wound healing

However, although MXene has many advantages in the application of skin wound healing and repair, there are still some shortcomings that need to be solved or improved. The existing preparation methods of MXene need to introduce hydrofluoric acid or its salt compounds, which has certain biosafety risks. When preparing MXene on a large scale, how to effectively ensure the homogeneity of the product for large-scale production and use is also a problem to be solved in the future. Although there are some potential problems in the large-scale preparation of MXene and the maintenance of the homogeneity of lamellar structure, we believe that with the continuous development of research, these problems will be able to find effective solutions, making MXene an ideal modified material for skin wound repair.

Author contributions

CY conceptualized the literatures, ZiZ and ZQ wrote the manuscript and designed the figures. WK and RZ provided input on the discussion of various sections. All authors contributed to the article and approved the submitted version.

Funding

This work was supported by National Natural Science Foundation of China (8200230). Health Special Project of Jilin Province (2020SCZT013). Science and Technology Proof of Concept Project of Jilin University (2022GN019). Natural Science Foundation of Jilin Provincial Science and Technology Department (20200201454JC) and Bethune Project of Jilin University (2022B43).

Conflict of interest

The authors declare that the research was conducted in the absence of any commercial or financial relationships that could be construed as a potential conflict of interest.

The handling editor ZL declared a shared parent affiliation with the authors at the time of review.

Publisher's note

References

Alizadehgiashi, M., Nemr, C. R., Chekini, M., Pinto Ramos, D., Mittal, N., Ahmed, S. U., et al. (2021). Multifunctional 3D-printed wound dressings. *ACS Nano* 15, 12375–12387. doi:10.1021/acsnano.1c04499

Aljghami, M. E., Saboor, S., and Amini-Nik, S. (2019). Emerging innovative wound dressings. *Ann. Biomed. Eng.* 47, 659–675. doi:10.1007/s10439-018-02186-w

Amadeu, T. P., Braune, A. S., Porto, L. C., Desmoulière, A., and Costa, A. M. (2004). Fibrillin-1 and elastin are differentially expressed in hypertrophic scars and keloids. *Wound Repair Regen.* 12, 169–174. doi:10.1111/j.1067-1927.2004.012209.x

Arda, O., Göksügür, N., and Tüzün, Y. (2014). Basic histological structure and functions of facial skin. *Clin. Dermatol* 32, 3–13. doi:10.1016/j.clindermatol.2013.05.021

Asadi, M. R., Torkaman, G., Hedayati, M., and Mofid, M. (2013). Role of sensory and motor intensity of electrical stimulation on fibroblastic growth factor-2 expression, inflammation, vascularization, and mechanical strength of full-thickness wounds. *J. Rehabil. Res. Dev.* 50, 489–498. doi:10.1682/jrrd.2012.04.0074

Ashrafi, M., Baguneid, M., Alonso-Rasgado, T., Rautemaa-Richardson, R., and Bayat, A. (2017). Cutaneous wound biofilm and the potential for electrical stimulation in management of the microbiome. *Future Microbiol.* 12, 337–357. doi:10.2217/fmb-2016-0204

Awasthi, G. P., Maharjan, B., Shrestha, S., Bhattarai, D. P., Yoon, D., Park, C. H., et al. (2020). Synthesis, characterizations, and biocompatibility evaluation of polycaprolactone-MXene electrospun fibers. *Colloids Surfaces a-Physicochemical Eng. Aspects* 586, 124282. doi:10.1016/j.colsurfa.2019.124282

Baraneedharan, P., Vadivel, S., C, A. A., Mohamed, S. B., and Rajendran, S. (2022). Advances in preparation, mechanism and applications of various carbon materials in environmental applications: A review. *Chemosphere* 300, 134596. doi:10.1016/j.chemosphere.2022.134596

Bártolo, I., Reis, R. L., Marques, A. P., and Cerqueira, M. T. (2022). Keratinocyte growth factor-based strategies for wound Re-epithelialization. *Tissue Eng. Part B Rev.* 28, 665–676. doi:10.1089/ten.TEB.2021.0030

Begum, S., Pramanik, A., Davis, D., Patibandla, S., Gates, K., Gao, Y., et al. (2020). 2D and heterostructure nanomaterial based strategies for combating drug-resistant bacteria. *ACS Omega* 5, 3116–3130. doi:10.1021/acsomega.9b03919

Boismal, F., Serror, K., Dobos, G., Zuelgaray, E., Bensussan, A., and Michel, L. (2020). Skin aging: Pathophysiology and innovative therapies. *Med. Sci. Paris.* 36, 1163–1172. doi:10.1051/medsci/2020232

Bonté, F., Girard, D., Archambault, J. C., and Desmoulière, A. (2019). Skin changes during ageing. *Subcell. Biochem* 91, 249–280. doi:10.1007/978-981-13-3681-2_10

Broughton, G., Janis, J. E., and Attinger, C. E. (2006). The basic science of wound healing. *Plast. Reconstr. Surg.* 117, 12s–34s. doi:10.1097/01.prs.0000225430.42531.c2

Carey, M., and Barsoum, M. W. (2021). MXene polymer nanocomposites: A review. *Mater. Today Adv.* 9, 100120. doi:10.1016/j.mtadv.2020.100120

Chen, J., Liu, Y., Cheng, G., Guo, J., Du, S., Qiu, J., et al. (2022). Tailored hydrogel delivering niobium carbide boosts ROS-scavenging and antimicrobial activities for diabetic wound healing. *Small* 18, 2201300. doi:10.1002/smll.202201300

Chen, K., Qiu, N., Deng, Q., Kang, M. H., Yang, H., Baek, J. U., et al. (2017). Cytocompatibility of Ti(3)AlC(2), Ti(3)SiC(2), and Ti(2)AlN: *In vitro* tests and first-principles calculations. *ACS Biomater. Sci. Eng.* 3, 2293–2301. doi:10.1021/acsbiomaterials.7b00432

Chen, X. Y., Zhao, Y., Li, L., Wang, Y., Wang, J., Xiong, J., et al. (2021). MXene/Polymer nanocomposites: Preparation, properties, and applications. *Polym. Rev.* 61, 80–115. doi:10.1080/15583724.2020.1729179

Churko, J. M., and Laird, D. W. (2013). Gap junction remodeling in skin repair following wounding and disease. *Physiol. (Bethesda)* 28, 190–198. doi:10.1152/physiol.00058.2012

Cooke, J. P. (2019). Inflammation and its role in regeneration and repair. *Circ. Res.* 124, 1166–1168. doi:10.1161/circresaha.118.314669

Dąbrowska, A. K., Spano, F., Derler, S., Adlhart, C., Spencer, N., and Rossi, R. (2018). The relationship between skin function, barrier properties, and body-dependent factors. *Skin. Res. Technol.* 24, 165–174. doi:10.1111/srt.12424

Demir, H., Balay, H., and Kirnap, M. (2004). A comparative study of the effects of electrical stimulation and laser treatment on experimental wound healing in rats. *J. Rehabil. Res. Dev.* 41, 147–154. doi:10.1682/jrrd.2004.02.0147

Deng, L., Du, C., Song, P., Chen, T., Rui, S., Armstrong, D. G., et al. (2021). The role of oxidative stress and antioxidants in diabetic wound healing. *Oxid. Med. Cell Longev.* 2021, 1–11. doi:10.1155/2021/8852759

Deurenberg, R. H., and Stobberingh, E. E. (2008). The evolution of *Staphylococcus aureus*. *Infect. Genet. Evol.* 8, 747–763. doi:10.1016/j.meegid.2008.07.007

Dunnill, C., Patton, T., Brennan, J., Barrett, J., Dryden, M., Cooke, J., et al. (2017). Reactive oxygen species (ROS) and wound healing: The functional role of ROS and emerging ROS-modulating technologies for augmentation of the healing process. *Int. Wound J.* 14, 89–96. doi:10.1111/iwj.12557

Elias, P. M. (2012). Structure and function of the stratum corneum extracellular matrix. *J. Investigative Dermatology* 132, 2131–2133. doi:10.1038/jid.2012.246

Fadahunsi, A. A., Li, C., Khan, M. I., and Ding, W. (2022). MXenes: State-of-the-art synthesis, composites and bioapplications. *J. Mater Chem. B* 10, 4331–4345. doi:10.1039/d2tb00289b

Farahani, M., and Shafiee, A. (2021). Wound healing: From passive to smart dressings. *Adv. Healthc. Mater* 10, e2100477. doi:10.1002/adhm.202100477

Foulds, I. S., and Barker, A. T. (1983). Human skin battery potentials and their possible role in wound healing. *Br. J. Dermatol* 109, 515–522. doi:10.1111/j.1365-2133.1983.tb07673.x

Francesko, A., Petkova, P., and Tzanov, T. (2018). Hydrogel dressings for advanced wound management. *Curr. Med. Chem.* 25, 5782–5797. doi:10.2174/0929867324666170920161246

Franklin, B. M., Maroudas, E., and Osborn, J. L. (2016). Sine-wave electrical stimulation initiates a voltage-gated potassium channel-dependent soft tissue response characterized by induction of hemocyte recruitment and collagen deposition. *Physiol. Rep.* 4, e12832. doi:10.14814/phy2.12832

Geng, D. C., Zhao, X., Chen, Z., Sun, W., Fu, W., Chen, J., et al. (2017). Direct synthesis of large-area 2D Mo2C on *in situ* grown graphene. *Adv. Mater.* 29, 1700072. doi:10.1002/adma.201700072

Ghazaly, A. E., Ahmed, H., Rezk, A. R., Halim, J., Persson, P. O. A., Yeo, L. Y., et al. (2021). Ultrafast, one-step, salt-solution-based acoustic synthesis of Ti(3)C(2) MXene. *ACS Nano* 15, 4287–4293. doi:10.1021/acsnano.0c07242

Ghidiu, M., Lukatskaya, M. R., Zhao, M. Q., Gogotsi, Y., and Barsoum, M. W. (2014). Conductive two-dimensional titanium carbide 'clay' with high volumetric capacitance. *Nature* 516, 78–81. doi:10.1038/nature13970

Golebiewska, E. M., and Poole, A. W. (2015). Platelet secretion: From haemostasis to wound healing and beyond. *Blood Rev.* 29, 153–162. doi:10.1016/j.blre.2014.10.003

Guo, S., and Dipietro, L. A. (2010). Factors affecting wound healing. *J. Dent. Res.* 89, 219–229. doi:10.1177/0022034509359125

Gürgen, S. G., Sayın, O., Cetin, F., and Tuç Yücel, A. (2014). Transcutaneous electrical nerve stimulation (TENS) accelerates cutaneous wound healing and inhibits pro-inflammatory cytokines. *Inflammation* 37, 775–784. doi:10.1007/s10753-013-9796-7

Hao, S., Han, H., Yang, Z., Chen, M., Jiang, Y., Lu, G., et al. (2022). Recent advancements on photothermal conversion and antibacterial applications over MXenes-based materials. *Nanomicro Lett.* 14, 178. doi:10.1007/s40820-022-00901-w

He, C., Yu, L. D., Yao, H. L., Chen, Y., and Hao, Y. Q. (2021b). Combinatorial photothermal 3D-printing scaffold and checkpoint blockade inhibits growth/metastasis of breast cancer to bone and accelerates osteogenesis. *Adv. Funct. Mater.* 31, 2006214. doi:10.1002/adfm.202006214

He, C., Sun, X., Zhang, H., Yuan, C., Wei, Y., and Li, J. (2021a). Preparation strategies and applications of MXene-polymer composites: A review. *Macromol. Rapid Commun.* 42, 2100324. doi:10.1002/marc.202100324

Hengge, U. R., Ruzicka, T., Schwartz, R. A., and Cork, M. J. (2006). Adverse effects of topical glucocorticosteroids. *J. Am. Acad. Dermatol* 54, 1–15. doi:10.1016/j.jaad.2005.01.010

Herskovitz, I., Hughes, O. B., Macquhae, F., Rakosi, A., and Kirsner, R. (2016). Epidermal skin grafting. *Int. Wound J.* 13 (3), 52–56. doi:10.1111/iwj.12631

Hrynyk, M., and Neufeld, R. J. (2014). Insulin and wound healing. *Burns* 40, 1433–1446. doi:10.1016/j.burns.2014.03.020

Hu, W., Peng, C., Luo, W., Lv, M., Li, X., Li, D., et al. (2010). Graphene-based antibacterial paper. *ACS Nano* 4, 4317–4323. doi:10.1021/nn101097v

Huang, H., Feng, W., and Chen, Y. (2021). Two-dimensional biomaterials: Material science, biological effect and biomedical engineering applications. *Chem. Soc. Rev.* 50, 11381–11485. doi:10.1039/d0cs01138j

Huang, H., Jiang, R., Feng, Y., Ouyang, H., Zhou, N., Zhang, X., et al. (2020a). Recent development and prospects of surface modification and biomedical applications of MXenes. *Nanoscale* 12, 1325–1338. doi:10.1039/c9nr07616f

Huang, H., Li, Z., Lin, J., Han, G., and Huang, P. (2018b). Two-dimensional transition metal carbides and nitrides (MXenes) for biomedical applications. *Chem. Soc. Rev.* 47, 5109–5124. doi:10.1039/C7CS00838D

Huang, H., Wang, P. W., Yang, S. C., Chou, W. L., and Fang, J. Y. (2018a). Cosmetic and therapeutic applications of fish oil's fatty acids on the skin. *Mar. Drugs* 16, 256. doi:10.3390/md16080256

Huang, H., Liang, P., Jiang, B., Zhang, P., Yu, W., Duan, M., et al. (2020c). Hyperbaric oxygen potentiates diabetic wound healing by promoting fibroblast cell proliferation and endothelial cell angiogenesis. *Life Sci.* 259, 118246. doi:10.1016/j.lfs.2020.118246

Huang, H., Cui, X., Li, S., Wei, J., Li, P., Wang, Y., et al. (2020b). Two-dimensional MXene-based materials for photothermal therapy. *Nanophotonics* 9, 2233–2249. doi:10.1515/nanoph-2019-0571

Hunt, T. K., Hopf, H., and Hussain, Z. (2000). Physiology of wound healing. *Adv. Skin. Wound Care* 13, 6–11.

Iravani, P., Iravani, S., and Varma, R. S. (2022). MXene-chitosan composites and their biomedical potentials. *Micromachines (Basel)* 13, 1383. doi:10.3390/mi13091383

Iravani, S., and Varma, R. S. (2022). Smart MXene quantum dot-based nanosystems for biomedical applications. *Nanomater. (Basel)* 12, 1200. doi:10.3390/nano12071200

Isseroff, R. R., and Dahle, S. E. (2012). Electrical stimulation therapy and wound healing: Where are we now? *Adv. Wound Care (New Rochelle)* 1, 238–243. doi:10.1089/wound.2011.0351

Jastrzebska, A. M., Szuplewska, A., Rozmyslowska-Wojciechowska, A., Chudy, M., Olszyna, A., Birowska, M., et al. (2020). On tuning the cytotoxicity of Ti3C2 (MXene) flakes to cancerous and benign cells by post-delamination surface modifications. *2d Mater.* 7, 025018. doi:10.1088/2053-1583/ab6a60

Jastrzębska, A. M., Szuplewska, A., Wojciechowski, T., Chudy, M., Ziemkowska, W., Chlubny, L., et al. (2017). *In vitro* studies on cytotoxicity of delaminated Ti3C2 MXene. *J. Hazard Mater* 339, 1–8. doi:10.1016/j.jhazmat.2017.06.004

Jiang, L., and Loo, S. C. J. (2021). Intelligent nanoparticle-based dressings for bacterial wound infections. *ACS Appl. Bio Mater* 4, 3849–3862. doi:10.1021/acsabm.0c01168

Jiang, S., Lin, J., and Huang, P. (2022). Nanomaterials for NIR-II photoacoustic imaging. *Adv. Healthc. Mater* 2022, e2202208. doi:10.1002/adhm.202202208

Jiao, Q., Yue, L., Zhi, L., Qi, Y., Yang, J., Zhou, C., et al. (2022). Studies on stratum corneum metabolism: Function, molecular mechanism and influencing factors. *J. Cosmet. Dermatol* 21, 3256–3264. doi:10.1111/jocd.15000

Jin, L., Guo, X., Gao, D., Wu, C., Hu, B., Tan, G., et al. (2021). NIR-responsive MXene nanobelts for wound healing. *Npg Asia Mater.* 13, 24. doi:10.1038/s41427-021-00289-w

Kaminsky, L. S., Mahoney, M. C., Leach, J., Melius, J., and Miller, M. J. (1990). Fluoride: Benefits and risks of exposure. *Crit. Rev. Oral Biol. Med.* 1, 261–281. doi:10.1177/10454411900010040501

Kimura, S., and Tsuji, T. (2021). Mechanical and immunological regulation in wound healing and skin reconstruction. *Int. J. Mol. Sci.* 22, 5474. doi:10.3390/ijms22115474

Kirchner, S., Lei, V., and MacLeod, A. S. (2020). The cutaneous wound innate immunological microenvironment. *Int. J. Mol. Sci.* 21, 8748. doi:10.3390/ijms21228748

Koyappayil, A., Chavan, S. G., Roh, Y. G., and Lee, M. H. (2022). Advances of MXenes; perspectives on biomedical research. *Biosens. (Basel)* 12, 454. doi:10.3390/bios12070454

Kruse, C. R., Nuutila, K., Lee, C. C., Kiwanuka, E., Singh, M., Caterson, E. J., et al. (2015). The external microenvironment of healing skin wounds. *Wound Repair Regen.* 23, 456–464. doi:10.1111/wrr.12303

Kumar, J. A., Prakash, P., Krithiga, T., Amarnath, D. J., Premkumar, J., Rajamohan, N., et al. (2022). Methods of synthesis, characteristics, and environmental applications of MXene: A comprehensive review. *Chemosphere* 286, 131607. doi:10.1016/j.chemosphere.2021.131607

LeBlanc, K., Langemo, D., Woo, K., Campos, H. M. H., Santos, V., and Holloway, S. (2019). Skin tears: Prevention and management. *Br. J. Community Nurs.* 24, S12–S18. doi:10.12968/bjcn.2019.24.Sup9.S12

Li, Y., Xian, J., Hong, J., Cao, X., Zhang, C., Deng, Q., et al. (2022c). Dual photothermal nanocomposites for drug-resistant infectious wound management. *Nanoscale* 14, 11284–11297. doi:10.1039/d2nr01998a

Li, Y., Dai, J., Yi, X., and Cheng, F. (2022d). Generation of cost-effective MXene@polydopamine-decorated chitosan nanofibrous wound dressing for promoting wound healing. *Biomater. Adv.* 140, 213055. doi:10.1016/j.bioadv.2022.213055

Li, J., Chen, J., and Kirsner, R. (2007). Pathophysiology of acute wound healing. *Clin. Dermatol* 25, 9–18. doi:10.1016/j.clindermatol.2006.09.007

Li, S., Li, Z., Liu, X., Li, C., Zheng, Y., Yeung, K. W. K., et al. (2021b). Interfacial engineering of Bi(2)S(3)/Ti(3)C(2)T(x) MXene based on work function for rapid photo-excited bacteria-killing. *Nat. Commun.* 12, 1224. doi:10.1038/s41467-021-21435-6

Li, L., Fukunaga-Kalabis, M., Yu, H., Xu, X., Kong, J., Lee, J. T., et al. (2010). Human dermal stem cells differentiate into functional epidermal melanocytes. *J. Cell Sci.* 123, 853–860. doi:10.1242/jcs.061598

Li, Y., Gu, B., Li, X., Tang, S., Zheng, L., Ruiz-Hitzky, E., et al. (2022b). MXene-enhanced chitin composite sponges with antibacterial and hemostatic activity for wound healing. *Adv. Healthc. Mater.* 11, 2102367. doi:10.1002/adhm.202102367

Li, S., Wang, J., Zhu, Z., Liu, D., Li, W., Sui, G., et al. (2021a). CVD carbon-coated carbonized loofah sponge loaded with a directionally arrayed MXene aerogel for electromagnetic interference shielding. *J. Mater. Chem. A* 9, 358–370. doi:10.1039/d0ta09337h

Li, T. F., Yao, L., Liu, Q., Gu, J., and Li, J. (2018). Fluorine-free synthesis of high-purity Ti $_3$ C $_2$ T $_{<i>x</i>}$ (T=OH, O) via alkali treatment. *Angew. Chemie-International Ed.* 57, 6115–6119. doi:10.1002/anie.201800887

Li, Y., Fu, R., Duan, Z., Zhu, C., and Fan, D. (2022f). Artificial nonenzymatic antioxidant MXene nanosheet-anchored injectable hydrogel as a mild photothermal-controlled oxygen release platform for diabetic wound healing. *ACS Nano* 16, 7486–7502. doi:10.1021/acsnano.1c10575

Li, Y., Han, M., Cai, Y., Jiang, B., Zhang, Y., Yuan, B., et al. (2022a). Muscle-inspired MXene/PVA hydrogel with high toughness and photothermal therapy for promoting bacteria-infected wound healing. *Biomaterials Sci.* 10, 1068–1082. doi:10.1039/D1BM01604K

Li, Y., Zhao, Y., Huang, H., Zhang, C., Liu, H., Wang, Z., et al. (2022e). A nanozyme-immobilized hydrogel with endogenous ROS-scavenging and oxygen generation abilities for significantly promoting oxidative diabetic wound healing. *Adv. Healthc. Mater.* 11, 2201524. doi:10.1002/adhm.202201524

Li, S., Zhao, Y., Liu, H., Ren, M., Wang, Z., Wang, X., et al. (2021c). pH-responsive hydrogel loaded with insulin as a bioactive dressing for enhancing diabetic wound healing. *Mater. Des.* 210, 110104. doi:10.1016/j.matdes.2021.110104

Liang, W., Lu, Q., Yu, F., Zhang, J., Xiao, C., Dou, X., et al. (2021b). A multifunctional green antibacterial rapid hemostasis composite wound dressing for wound healing. *Biomater. Sci.* 9, 7124–7133. doi:10.1039/d1bm01185e

Liang, W., He, J., and Guo, B. (2021a). Functional hydrogels as wound dressing to enhance wound healing. *ACS Nano* 15, 12687–12722. doi:10.1021/acsnano.1c04206

Lichtman, M. K., Otero-Vinas, M., and Falanga, V. (2016). Transforming growth factor beta (TGF-β) isoforms in wound healing and fibrosis. *Wound Repair Regen.* 24, 215–222. doi:10.1111/wrr.12398

Lin, X., Li, Z., Qiu, J., Wang, Q., Wang, J., Zhang, H., et al. (2021). Fascinating MXene nanomaterials: Emerging opportunities in the biomedical field. *Biomater. Sci.* 9, 5437–5471. doi:10.1039/d1bm00526j

Liu, C., Yao, W., Tian, M., Wei, J., Song, Q., and Qiao, W. (2018). Mussel-inspired degradable antibacterial polydopamine/silica nanoparticle for rapid hemostasis. *Biomaterials* 179, 83–95. doi:10.1016/j.biomaterials.2018.06.037

Liu, F. F., Zhou, A., Chen, J., Jia, J., Zhou, W., Wang, L., et al. (2017a). Preparation of Ti3C2 and Ti2C MXenes by fluoride salts etching and methane adsorptive properties. *Appl. Surf. Sci.* 416, 781–789. doi:10.1016/j.apsusc.2017.04.239

Liu, F. F., Zou, J., Tang, Q., Yang, X., Zhang, Y., Zhang, Q., et al. (2017b). Surface modified Ti(3)C(2) MXene nanosheets for tumor targeting photothermal/photodynamic/chemo synergistic therapy. *ACS Appl. Mater Interfaces* 9, 40077–40086. doi:10.1021/acsami.7b13421

Liu, S., Li, D., Wang, Y., Zhou, G., Ge, K., Jiang, L., et al. (2022b). Flexible, high-strength and multifunctional polyvinyl alcohol/MXene/polyaniline hydrogel enhancing skin wound healing. *Biomaterials Sci.* 10, 3585–3596. doi:10.1039/D2BM00575A

Liu, S., Gao, R., Yang, C., Feng, Z., Ou-Yang, W., Pan, X., et al. (2022a). ECM-mimetic immunomodulatory hydrogel for methicillin-resistant Staphylococcus aureus-infected chronic skin wound healing. *Sci. Adv.* 8, eabn7006. doi:10.1126/sciadv.abn7006

Liu, X. L., Dai, Y., Wang, Z. J., and Wu, J. (2021). Research progress on tantalum carbide coatings oncarbon materials. *New Carbon Mater.* 36, 1049–1059. doi:10.1016/s1872-5805(21)60101-4

Lu, B., Zhu, Z., Ma, B., Wang, W., Zhu, R., and Zhang, J. (2021). 2D MXene nanomaterials for versatile biomedical applications: Current trends and future prospects. *Small* 17, e2100946. doi:10.1002/smll.202100946

Luo, R., Dai, J., Zhang, J., and Li, Z. (2021). Accelerated skin wound healing by electrical stimulation. *Adv. Healthc. Mater.* 10, 2100557. doi:10.1002/adhm.202100557

Malone, M., and Schultz, G. (2022). Challenges in the diagnosis and management of wound infection. *Br. J. Dermatol* 187, 159–166. doi:10.1111/bjd.21612

Mao, L., Hu, S., Gao, Y., Wang, L., Zhao, W., Fu, L., et al. (2020). Biodegradable and electroactive regenerated bacterial cellulose/MXene (Ti $_3$ C $_2$ T *_x*) composite hydrogel as wound dressing for accelerating skin wound healing under electrical stimulation. *Adv. Healthc. Mater.* 9, 2000872. doi:10.1002/adhm.202000872

Mashtalir, O., Cook, K. M., Mochalin, V. N., Crowe, M., Barsoum, M. W., and Gogotsi, Y. (2014). Dye adsorption and decomposition on two-dimensional titanium carbide in aqueous media. *J. Mater. Chem. A* 2, 14334–14338. doi:10.1039/C4TA02638A

Mayerberger, E. A., Street, R. M., McDaniel, R. M., Barsoum, M. W., and Schauer, C. L. (2018). Antibacterial properties of electrospun Ti3C2Tz (MXene)/chitosan nanofibers. *RSC Adv.* 8, 35386–35394. doi:10.1039/C8RA06274A

McCaig, C. D., Rajnicek, A. M., Song, B., and Zhao, M. (2005). Controlling cell behavior electrically: Current views and future potential. *Physiol. Rev.* 85, 943–978. doi:10.1152/physrev.00020.2004

Meng, J. Q., An, Z. Y., Liu, Y. D., Sun, X. Y., and Li, J. (2022). MXene-based hydrogels towards the photothermal applications. *J. Phys. D-Applied Phys.* 55, 374003. doi:10.1088/1361-6463/ac79d9

Miranda, G. H. N., Alvarenga, M. O. P., Ferreira, M. K. M., Puty, B., Bittencourt, L. O., Fagundes, N. C. F., et al. (2021). A systematic review and meta-analysis of the association between fluoride exposure and neurological disorders. *Sci. Rep.* 11, 22659. doi:10.1038/s41598-021-99688-w

Naguib, M., Mashtalir, O., Carle, J., Presser, V., Lu, J., Hultman, L., et al. (2012). Two-dimensional transition metal carbides. *Acs Nano* 6, 1322–1331. doi:10.1021/nn204153h

Naguib, M., Mochalin, V. N., Barsoum, M. W., and Gogotsi, Y. (2014). 25th anniversary article: MXenes: A new family of two-dimensional materials. *Adv. Mater.* 26, 992–1005. doi:10.1002/adma.201304138

Naguib, M., Unocic, R. R., Armstrong, B. L., and Nanda, J. (2015). Large-scale delamination of multi-layers transition metal carbides and carbonitrides “MXenes”. *Dalton Trans.* 44, 9353–9358. doi:10.1039/c5dt01247c

Obagi, Z., Damiani, G., Grada, A., and Falanga, V. (2019). Principles of wound dressings: A review. *Surg. Technol. Int.* 35, 50–57.

Ortiz, A., and Grando, S. A. (2012). Smoking and the skin. *Int. J. Dermatol* 51, 250–262. doi:10.1111/j.1365-4632.2011.05205.x

Ozcan, M., Allahbeickaraghi, A., and Dündar, M. (2012). Possible hazardous effects of hydrofluoric acid and recommendations for treatment approach: A review. *Clin. Oral Investig.* 16, 15–23. doi:10.1007/s00784-011-0636-6

Pagnamenta, F. (2017). Evidence generation for wound care dressing selection: Reviewing the issues. *J. Wound Care* 26, 545–550. doi:10.12968/jowc.2017.26.9.545

Pang, J., Mendes, R. G., Bachmatiuk, A., Zhao, L., Ta, H. Q., Gemming, T., et al. (2019). Applications of 2D MXenes in energy conversion and storage systems. *Chem. Soc. Rev.* 48, 72–133. doi:10.1039/c8cs00324f

Paquet, P., and Piérard, G. E. (1996). lnterleukin-6 and the Skin. *Int. Arch. Allergy Immunol.* 109, 308–317. doi:10.1159/000237257

Park, J. W., Hwang, S. R., and Yoon, I. S. (2017). Advanced growth factor delivery systems in wound management and skin regeneration. *Molecules* 22, 1259. doi:10.3390/molecules22081259

Pereira, R. F., and Bártolo, P. J. (2016). Traditional therapies for skin wound healing. *Adv. Wound Care (New Rochelle)* 5, 208–229. doi:10.1089/wound.2013.0506

Prost-Squarcioni, C. (2006). Histologie de la peau et des follicules pileux. *Med. Sci. Paris.* 22, 131–137. doi:10.1051/medsci/2006222131

Pullar, J. M., Carr, A. C., and Vissers, M. C. M. (2017). The roles of vitamin C in skin health. *Nutrients* 9, 866. doi:10.3390/nu9080866

Rajavel, K., Ke, T., Yang, K., and Lin, D. H. (2018). Condition optimization for exfoliation of two dimensional titanium carbide (Ti_3C_2T _{*x*}). *Nanotechnology* 29, 095605. doi:10.1088/1361-6528/aaa687

Rasool, K., Helal, M., Ali, A., Ren, C. E., Gogotsi, Y., and Mahmoud, K. A. (2016). Antibacterial Activity of $Ti_3C_2T_{\text{<i>x</i>}}$ MXene. *ACS Nano* 10, 3674–3684. doi:10.1021/acsnano.6b00181

Riazi, H., Taghizadeh, G., and Soroush, M. (2021). MXene-based nanocomposite sensors. *ACS Omega* 6, 11103–11112. doi:10.1021/acsomega.0c05828

Rippa, A. L., Kalabusheva, E. P., and Vorotelyak, E. A. (2019). Regeneration of dermis: Scarring and cells involved. *Cells* 8, 607. doi:10.3390/cells8060607

Rodero, M. P., and Khosrotehrani, K. (2010). Skin wound healing modulation by macrophages. *Int. J. Clin. Exp. Pathol.* 3, 643–653.

Rodriguez-Merchan, E. C. (2012). Surgical wound healing in bleeding disorders. *Haemophilia* 18, 487–490. doi:10.1111/j.1365-2516.2012.02760.x

Rosa, D. F., Sarandy, M. M., Novaes, R. D., Freitas, M. B., do Carmo Gouveia Peluzio, M., and Goncalves, R. V. High-fat diet and alcohol intake promotes inflammation and impairs skin wound healing in wistar rats. *Mediat. Inflamm.* 2018, 1–12. doi:10.1155/2018/46585832018

Rousselle, P., Montmasson, M., and Garnier, C. (2019). Extracellular matrix contribution to skin wound re-epithelialization. *Matrix Biol.* 75-76, 12–26. doi:10.1016/j.matbio.2018.01.002

Rozmysłowska-Wojciechowska, A., Karwowska, E., Gloc, M., Wozniak, J., Petrus, M., Przybyszewski, B., et al. (2020). Controlling the porosity and biocidal properties of the chitosan-hyaluronate matrix hydrogel nanocomposites by the addition of 2D Ti3C2Tx MXene. *Materials* 13, 4587. doi:10.3390/ma13204587

Safaei, M., and Shishehbore, M. R. (2021). Energy conversion and optical applications of MXene quantum dots. *J. Mater. Sci.* 56, 17942–17978. doi:10.1007/s10853-021-06428-6

Scalise, A., Bianchi, A., Tartaglione, C., Bolletta, E., Pierangeli, M., Torresetti, M., et al. (2015). Microenvironment and microbiology of skin wounds: The role of bacterial biofilms and related factors. *Semin. Vasc. Surg.* 28, 151–159. doi:10.1053/j.semvascsurg.2016.01.003

Scheibe, B., Wychowaniec, J. K., Scheibe, M., Peplinska, B., Jarek, M., Nowaczyk, G., et al. (2019). Cytotoxicity assessment of Ti–Al–C based MAX phases and $Ti_3C_2T_{\text{<i>x</i>}}$ MXenes on human fibroblasts and cervical cancer cells. *ACS Biomater. Sci. Eng.* 5, 6557–6569. doi:10.1021/acsbiomaterials.9b01476

Shi, Y. E., Han, F., Xie, L., Zhang, C., Li, T., Wang, H., et al. (2020). A MXene of type Ti3C2Tx functionalized with copper nanoclusters for the fluorometric determination of glutathione. *Microchim. Acta* 187, 38. doi:10.1007/s00604-019-4000-x

Simões, D., Miguel, S. P., Ribeiro, M. P., Coutinho, P., Mendonca, A. G., and Correia, I. J. (2018). Recent advances on antimicrobial wound dressing: A review. *Eur. J. Pharm. Biopharm.* 127, 130–141. doi:10.1016/j.ejpb.2018.02.022

SingerHealing, A. J. (2022). Healing mechanisms in cutaneous wounds: Tipping the balance. *Tissue Eng. Part B Rev.* 28, 1151–1167. doi:10.1089/ten.TEB.2021.0114

Sinha, A., Ma, K., and Zhao, H. (2021). 2D Ti(3)C(2)T(x) flakes prepared by *in-situ* HF etchant for simultaneous screening of carbamate pesticides. *J. Colloid Interface Sci.* 590, 365–374. doi:10.1016/j.jcis.2021.01.063

Soleymaniha, M., Shahbazi, M. A., Rafieerad, A. R., Maleki, A., and Amiri, A. (2019). Promoting role of MXene nanosheets in biomedical Sciences: Therapeutic and biosensing innovations. *Adv. Healthc. Mater* 8, e1801137. doi:10.1002/adhm.201801137

Sun, J., Shengping Zhang, B. S., Alomar, M., Alqarni, A. S., Najla Alotaibi, M. S., Badriah Alshahrani, M. S., et al. (2023). Recent advances in the synthesis of MXene quantum dots. *Chem. Rec.* 2023, e202200268. doi:10.1002/tcr.202200268

Sundaram, A., Ponraj, J. S., Wang, C., Peng, W. K., Manavalan, R. K., Dhanabalan, S. C., et al. (2020). Engineering of 2D transition metal carbides and nitrides MXenes for cancer therapeutics and diagnostics. *J. Mater Chem. B* 8, 4990–5013. doi:10.1039/d0tb00251h

Swaney, M. H., and Kalan, L. R. (2021). Living in your skin: Microbes, molecules, and mechanisms. *Infect. Immun.* 89, 006955–e720. doi:10.1128/iai.00695-20

Szuplewska, A., Rozmyslowska-Wojciechowska, A., Pozniak, S., Wojciechowski, T., Birowska, M., Popielski, M., et al. (2019). Multilayered stable 2D nano-sheets of Ti(2) NT(x) MXene: Synthesis, characterization, and anticancer activity. *J. Nanobiotechnology* 17, 114. doi:10.1186/s12951-019-0545-4

Tan, G., Wang, L., Pan, W., and Chen, K. (2022). Polysaccharide electrospun nanofibers for wound healing applications. *Int. J. Nanomedicine* 17, 3913–3931. doi:10.2147/ijn.S371900

Tang, P., Han, L., Jia, Z., Wang, K., and Zhang, H. (2019). Mussel-Inspired electroactive and antioxidative scaffolds with incorporation of polydopamine-reduced graphene oxide for enhancing skin wound healing. *ACS Appl. Mater. Interfaces* 11, 7703–7714. doi:10.1021/acsami.8b18931

Taşkan, I., ??zyazgan, ??r., Tercan, M., Karda??, H. Y., Balkanli, S., Saraymen, R., et al. (1997). A comparative study of the effect of ultrasound and electrostimulation on wound healing in rats. *Plast. Reconstr. Surg.* 100, 966–972. doi:10.1097/00006534-199709001-00020

Thirumal, V., Yuvakkumar, R., Kumar, P. S., Ravi, G., Keerthana, S., and Velauthapillai, D. (2022). Facile single-step synthesis of MXene@CNTs hybrid nanocomposite by CVD method to remove hazardous pollutants. *Chemosphere* 286, 131733. doi:10.1016/j.chemosphere.2021.131733

Tian, T., Shi, X., Cheng, L., Luo, Y., Dong, Z., Gong, H., et al. (2014). Graphene-based nanocomposite as an effective, multifunctional, and recyclable antibacterial agent. *ACS Appl. Mater. Interfaces* 6, 8542–8548. doi:10.1021/am5022914

Tu, C., Lu, H., Zhou, T., Zhang, W., Deng, L., Cao, W., et al. (2022). Promoting the healing of infected diabetic wound by an anti-bacterial and nano-enzyme-containing hydrogel with inflammation-suppressing, ROS-scavenging, oxygen and nitric oxide-generating properties. *Biomaterials* 286, 121597. doi:10.1016/j.biomaterials.2022.121597

Urbankowski, P., Anasori, B., Makaryan, T., Er, D., Kota, S., Walsh, P. L., et al. (2016). Synthesis of two-dimensional titanium nitride Ti4N3 (MXene). *Nanoscale* 8, 11385–11391. doi:10.1039/c6nr02253g

Usansky, I., Jaworska, P., Asti, L., Kenny, F. N., Hobbs, C., Sofra, V., et al. (2021). A developmental basis for the anatomical diversity of dermis in homeostasis and wound repair. *J. Pathol.* 253, 315–325. doi:10.1002/path.5589

VanBuren, C. A., and Everts, H. B. (2022). Vitamin A in skin and hair: An update. *Nutrients* 14, 2952. doi:10.3390/nu14142952

Velnar, T., Bailey, T., and Smrkolj, V. (2009). The wound healing process: An overview of the cellular and molecular mechanisms. *J. Int. Med. Res.* 37, 1528–1542. doi:10.1177/147323000903700531

Verdes, M., Mace, K., Margetts, L., and Cartmell, S. (2022). Status and challenges of electrical stimulation use in chronic wound healing. *Curr. Opin. Biotechnol.* 75, 102710. doi:10.1016/j.copbio.2022.102710

Walker, R. M., Gillespie, B. M., Thalib, L., Higgins, N. S., and Whitty, J. A. (2017). Foam dressings for treating pressure ulcers. *Cochrane Database Syst. Rev.* 10, Cd011332. doi:10.1002/14651858.CD011332.pub2

Wang, D. Y., Wang, L., Lou, Z., Zheng, Y., Wang, K., Zhao, L., et al. (2020). Biomimetic, biocompatible and robust silk Fibroin-MXene film with stable 3D cross-link structure for flexible pressure sensors. *Nano Energy* 78, 105252. doi:10.1016/j.nanoen.2020.105252

Wang, F., Yang, C., Duan, C., Xiao, D., Tang, Y., and Zhu, J. (2015). An organ-like titanium carbide material (MXene) with multilayer structure encapsulating hemoglobin for a mediator-free biosensor. *J. Electrochem. Soc.* 162, B16–B21. doi:10.1149/2.0371501jes

Wang, G., Yang, F., Zhou, W., Xiao, N., Luo, M., and Tang, Z. (2023). The initiation of oxidative stress and therapeutic strategies in wound healing. *Biomed. Pharmacother.* 157, 114004. doi:10.1016/j.biopha.2022.114004

Wang, L. Y., Du, L., Wang, M., Wang, X., Tian, S., Chen, Y., et al. (2022). Chitosan for constructing stable polymer-inorganic suspensions and multifunctional membranes for wound healing. *Carbohydr. Polym.* 285, 119209. doi:10.1016/j.carbpol.2022.119209

Wang, P. H., Huang, B. S., Horng, H. C., Yeh, C. C., and Chen, Y. J. (2018). Wound healing. *J. Chin. Med. Assoc.* 81, 94–101. doi:10.1016/j.jcma.2017.11.002

Wang, Z. X., Kochat, V., Pandey, P., Kashyap, S., Chattopadhyay, S., Samanta, A., et al. (2017). Metal immiscibility route to synthesis of ultrathin carbides, borides, and nitrides. *Adv. Mater.* 29, 1700364. doi:10.1002/adma.201700364

Wei, C., Tang, P., Tang, Y., Liu, L., Lu, X., Yang, K., et al. (2022). Sponge-like macroporous hydrogel with antibacterial and ROS scavenging capabilities for diabetic wound regeneration. *Adv. Healthc. Mater.* 11, 2200717. doi:10.1002/adhm.202200717

Wei, Y., Zhang, P., Soomro, R. A., Zhu, Q., and Xu, B. (2021). Advances in the synthesis of 2D MXenes. *Adv. Mater* 33, e2103148. doi:10.1002/adma.202103148

Weiss, D. S., Eaglstein, W. H., and Falanga, V. (1989). Exogenous electric current can reduce the formation of hypertrophic scars. *J. Dermatol Surg. Oncol.* 15, 1272–1276. doi:10.1111/j.1524-4725.1989.tb03146.x

Werner, S., and Grose, R. (2003). Regulation of wound healing by growth factors and cytokines. *Physiol. Rev.* 83, 835–870. doi:10.1152/physrev.2003.83.3.835

Wertz, P. (2018). Epidermal lamellar granules. *Skin. Pharmacol. Physiol.* 31, 262–268. doi:10.1159/000491757

Wikslund, L. K., Kaljusto, M. L., Amundsen, V. S., and Kvernebo, K. (2022). Microvascular remodeling following skin injury. *Microcirculation* 29, e12755. doi:10.1111/micc.12755

Wilkinson, H. N., and Hardman, M. J. (2017). The role of estrogen in cutaneous ageing and repair. *Maturitas* 103, 60–64. doi:10.1016/j.maturitas.2017.06.026

Wilkinson, H. N., and Hardman, M. J. (2020). Wound healing: Cellular mechanisms and pathological outcomes. *Open Biol.* 10, 200223. doi:10.1098/rsob.200223

Winter, G. D. (2006). Some factors affecting skin and wound healing. *J. Tissue Viability* 16, 20–23. doi:10.1016/s0965-206x(06)62006-8

Woodley, D. T. (2017). Distinct fibroblasts in the papillary and reticular dermis: Implications for wound healing. *Dermatol Clin.* 35, 95–100. doi:10.1016/j.det.2016.07.004

Wu, Y. D., Zheng, W., Xiao, Y., Du, B., Zhang, X., Wen, M., et al. (2021). Multifunctional, robust, and porous PHBV-GO/MXene composite membranes with good hydrophilicity, antibacterial activity, and platelet adsorption performance. *Polymers* 13, 3748. doi:10.3390/polym13213748

Xu, D. X., Li, Z. D., Li, L. S., and Wang, J. (2020). Insights into the photothermal conversion of 2D MXene nanomaterials: Synthesis, mechanism, and applications. *Adv. Funct. Mater.* 30, 2000712. doi:10.1002/adfm.202000712

Xu, X., Wang, S., Wu, H., Liu, Y., Xu, F., and Zhao, J. (2021). A multimodal antimicrobial platform based on MXene for treatment of wound infection. *Colloids Surfaces B: Biointerfaces* 207, 111979. doi:10.1016/j.colsurfb.2021.111979

Yang, S., Lan, L., Gong, M., Yang, K., and Li, X. (2022a). An asymmetric wettable PCL/chitosan composite scaffold loaded with IGF-2 for wound dressing. *J. Biomater. Appl.* 37, 577–587. doi:10.1177/08853282221110315

Yang, S., Zhang, P., Wang, F., Ricciardulli, A. G., Lohe, M. R., Blom, P. W. M., et al. (2018). Fluoride-free synthesis of two-dimensional titanium carbide (MXene) using A binary aqueous system. *Angew. Chemie-International Ed.* 57, 15491–15495. doi:10.1002/anie.201809662

Yang, S., Zhang, C., Deng, D., Gu, Y., Wang, H., and Zhong, Q. (2022b). Multiple stimuli-responsive MXene-based hydrogel as intelligent drug delivery carriers for deep chronic wound healing. *Small* 18, 2104368. doi:10.1002/smll.202104368

Yang, S., Zhou, X., Chan, Y. K., Wang, Z., Li, L., Li, J., et al. (2022c). Photo-activated nanofibrous membrane with self-rechargeable antibacterial function for stubborn infected cutaneous regeneration. *Small* 18, 2105988. doi:10.1002/smll.202105988

Yao, H., Yuan, X., Wu, Z., Park, S., Zhang, W., Chong, H., et al. (2023). Fabrication and performance evaluation of gelatin/sodium alginate hydrogel-based macrophage and MSC cell-encapsulated paracrine system with potential application in wound healing. *Int. J. Mol. Sci.* 24, 1240. doi:10.3390/ijms24021240

Yin, J., Pan, S., Guo, X., Gao, Y., Zhu, D., Yang, Q., et al. (2021b). Nb(2)C MXene-functionalized scaffolds enables osteosarcoma phototherapy and angiogenesis/osteogenesis of bone defects. *Nanomicro Lett.* 13, 30. doi:10.1007/s40820-020-00547-6

Yin, J., Li, Y., Yao, X., Wang, Y., Jia, L., Liu, Q., et al. (2021a). MXenes for solar cells. *Nanomicro Lett.* 13, 78. doi:10.1007/s40820-021-00604-8

Yu, L. P., Zhou, X. H., Lu, L., Xu, L., and Wang, F. J. (2021). MXene/carbon nanotube hybrids: Synthesis, structures, properties, and applications. *ChemSusChem* 14, 5079–5111. doi:10.1002/cssc.202101614

Yu, R., Li, M., Li, Z., Pan, G., Liang, Y., and Guo, B. (2022). Supramolecular thermo-contracting adhesive hydrogel with self-removability simultaneously enhancing noninvasive wound closure and MRSA-infected wound healing. *Adv. Healthc. Mater* 11, e2102749. doi:10.1002/adhm.202102749

Yu, T., Gao, M., Yang, P., Liu, D., Wang, D., Song, F., et al. (2019). Insulin promotes macrophage phenotype transition through PI3K/Akt and PPAR-γ signaling during diabetic wound healing. *J. Cell Physiol.* 234, 4217–4231. doi:10.1002/jcp.27185

Yuan, Y., Ding, L., Chen, Y., Chen, G., Zhao, T., and Yu, Y. (2022). Nano-silver functionalized polysaccharides as a platform for wound dressings: A review. *Int. J. Biol. Macromol.* 194, 644–653. doi:10.1016/j.ijbiomac.2021.11.108

Zamhuri, A., Lim, G. P., Ma, N. L., Tee, K. S., and Soon, C. F. (2021). MXene in the lens of biomedical engineering: Synthesis, applications and future outlook. *Biomed. Eng. Online* 20, 33. doi:10.1186/s12938-021-00873-9

Zhang, D., Huang, L., Sun, D.-W., Pu, H., and Wei, Q. (2023). Bio-interface engineering of MXene nanosheets with immobilized lysozyme for light-enhanced enzymatic inactivation of methicillin-resistant *Staphylococcus aureus*. *Chem. Eng. J.* 452, 139078. doi:10.1016/j.cej.2022.139078

Zhang, M., and Zhao, X. (2020). Alginate hydrogel dressings for advanced wound management. *Int. J. Biol. Macromol.* 162, 1414–1428. doi:10.1016/j.ijbiomac.2020.07.311

Zhang, X., Wei, P., Yang, Z., Liu, Y., Yang, K., Cheng, Y., et al. (2022a). Current progress and outlook of nano-based hydrogel dressings for wound healing. *Pharmaceutics* 15, 68. doi:10.3390/pharmaceutics15010068

Zhang, X., Yan, Y., Qiu, H., Ma, Z., Ruan, K., and Gu, J. (2022b). A mini-review of MXene porous films: Preparation, mechanism and application. *J. Mater. Sci. Technol.* 103, 42–49. doi:10.1016/j.jmst.2021.08.001

Zhao, X., Wu, H., Guo, B., Dong, R., Qiu, Y., and Ma, P. X. (2017). Antibacterial anti-oxidant electroactive injectable hydrogel as self-healing wound dressing with hemostasis and adhesiveness for cutaneous wound healing. *Biomaterials* 122, 34–47. doi:10.1016/j.biomaterials.2017.01.011

Zheng, H., Wang, S., Cheng, F., He, X., Liu, Z., Wang, W., et al. (2021). Bioactive anti-inflammatory, antibacterial, conductive multifunctional scaffold based on MXene@CeO2 nanocomposites for infection-impaired skin multimodal therapy. *Chem. Eng. J.* 424, 130148. doi:10.1016/j.cej.2021.130148

Zhou, L., Wu, F., Yu, J., Deng, Q., Zhang, F., and Wang, G. (2017). Titanium carbide (Ti3C2Tx) MXene: A novel precursor to amphiphilic carbide-derived graphene quantum dots for fluorescent ink, light-emitting composite and bioimaging. *Carbon* 118, 50–57. doi:10.1016/j.carbon.2017.03.023

Zhou, L., Zheng, H., Liu, Z., Wang, S., Liu, Z., Chen, F., et al. (2021). Conductive antibacterial hemostatic multifunctional scaffolds based on $Ti_3C_2T_{<i>x</i>}$ MXene nanosheets for promoting multidrug-resistant bacteria-infected wound healing. *ACS Nano* 15, 2468–2480. doi:10.1021/acsnano.0c06287

Zhu, H., Dai, W., Wang, L., Yao, C., Wang, C., Gu, B., et al. (2022). Electroactive oxidized alginate/gelatin/MXene (Ti3C2Tx) composite hydrogel with improved biocompatibility and self-healing property. *Polymers* 14, 3908. doi:10.3390/polym14183908

Zulkowski, K. (2013). Skin bacteria: Implications for wound care. *Adv. Skin. Wound Care* 26, 231–236. doi:10.1097/01.ASW.0000428953.13223.fa

Frontiers in Bioengineering and Biotechnology

TYPE Original Research
PUBLISHED 09 May 2023
DOI 10.3389/fbioe.2023.1167623

EDITED BY
Antonella Motta,
University of Trento, Italy

REVIEWED BY
Fengyuan Zhao,
Peking University Third Hospital, China
Gloria Gallego-Ferrer,
Polytechnic University of Valencia, Spain

*CORRESPONDENCE
Piergiorgio Gentile,
✉ piergiorgio.gentile@newcastle.ac.uk

RECEIVED 16 February 2023
ACCEPTED 27 April 2023
PUBLISHED 09 May 2023

CITATION
Scalzone A, Cerqueni G, Wang XN, Dalgarno K, Mattioli-Belmonte M, Ferreira-Duarte AM and Gentile P (2023), A cytokine-induced spheroid-based *in vitro* model for studying osteoarthritis pathogenesis. *Front. Bioeng. Biotechnol.* 11:1167623. doi: 10.3389/fbioe.2023.1167623

A cytokine-induced spheroid-based *in vitro* model for studying osteoarthritis pathogenesis

Annachiara Scalzone[1,2], Giorgia Cerqueni[3], Xiao Nong Wang[4], Kenny Dalgarno[1], Monica Mattioli-Belmonte[3], Ana M. Ferreira-Duarte[1] and Piergiorgio Gentile[1]*

[1]School of Engineering, Newcastle University, Newcastle UponTyne, United Kingdom, [2]Center for Advanced Biomaterials for Healthcare@CRIB Istituto Italiano di Tecnologia, Napoli, Italy, [3]Department of Clinical and Molecular Sciences (DISCLIMO), Università Politecnica delle Marche, Ancona, Italy, [4]Translational and Clinical Research Institute, Newcastle University, Newcastle UponTyne, United Kingdom

Given the lack of *in vitro* models faithfully reproducing the osteoarthritis (OA) disease on-set, this work aimed at manufacturing a reliable and predictive *in vitro* cytokine-based Articular Cartilage (AC) model to study OA progression. Cell spheroids of primary human fetal chondrocytes (FCs) and h-TERT mesenchymal stem cells differentiated chondrocytes (Y201-C) were analysed in terms of growth kinetics, cells proliferation and apoptosis over 10 days of culture, in healthy condition or in presence of cytokines (interleukin-1ß, –6 and TNF-α). Then, the spheroids were assembled into chondrospheres using a bottom-up strategy, to obtain an *in vitro* cytokines-induced OA model. The resulting chondrospheres were evaluated for gene expression and anabolic ECM proteins. Compared to the healthy environment, the simulated OA environment induced chondrocyte hyperproliferation and apoptotic pathway, decreased expression of anabolic ECM proteins, and diminished biosynthetic activity, resembling features of early-stage OA. These characteristics were observed for both Y201-C and HC at high and low concentrations of cytokines. Both HC and Y201-C demonstrated the suitability for the manufacturing of a scaffold-free *in vitro* OA model to facilitate studies into OA pathogenesis and therapeutic strategies. Our approach provides a faithful reproduction of early-stage osteoarthritis, demonstrating the ability of obtaining different disease severity by tuning the concentration of OA-related cytokines. Given the advantages in easy access and more reproducible performance, Y201-C may represent a more favourable source of chondrocytes for establishing more standardized protocols to obtain OA models.

KEYWORDS

***in vitro* model, articular cartilage, osteoarthritis, cytokines, chondrocytes**

1 Introduction

Among different forms of joint diseases, the progressive degeneration of Articular Cartilage (AC) due to osteoarthritis (OA) is the most common and chronic, with a global prevalence of weight-bearing joints such as the hip and knee (Yuan et al., 2003; Cross et al., 2014). OA and the associated burden costs are revealing an increasing impact worldwide, representing a major public health challenge (Kloppenburg & Berenbaum, 2020). Being a "whole joint" disease, OA pathophysiology involves cellular changes, structural defects and dysfunction of all the joint compartments, i.e., cartilage, bone and synovium (Scanzello & Goldring, 2012; Rigoglou & Papavassiliou, 2013). In healthy AC, chondrocytes have an active biosynthetic activity, expressing and synthesizing anabolic markers like collagen type 2 (Coll II) and aggrecan. During OA, chondrocytes tend to both proliferate, possibly due to better access of chondrocytes to proliferative factors from the synovial fluid, caused by damages to the matrix itself, and to undergo an inappropriate hypertrophy-like maturation and become apoptotic (at late OA) (Blanco et al., 1998). Current studies have demonstrated a central role of the inflammatory process, mediated by pro-inflammatory mediators (i.e., cytokines and chemokines) in OA pathogenesis, which are responsible for the production of degradative enzymes (i.e., aggrecanases and collagenases) by chondrocytes while inhibiting their anabolic activity. These enzymes digest the extracellular matrix (ECM), causing aggrecan cleavage and Coll II fibrillation (Valdes, 2010).

Several therapeutic strategies have been exploited for OA treatment, based on the level of pain and degeneration of the diarthrodial joint. Amongst those, regenerative medicine approaches (i.e., autologous chondrocyte implantation, ACI) increased in popularity in the field in the last two decades. Particularly, a variation of ACI, called Chondrosphere® has been clinically approved and recommended by the NICE in 2017 for treating symptomatic AC defect up to 10 cm^2. Since OA progression is a complex, dynamic, and metabolically active process that involves the balance between anabolic and catabolic processes affecting the joint tissues, there is still a lack of knowledge about the OA evolution process and its internal mechanisms (Gikas et al., 2009).

In this scenario, reliable and predictive *in vitro* models of AC tissues in healthy and OA conditions play a critical role in advancing the understanding of the physiology, biology, and pathological progression of OA, and will contribute hugely to the development of novel regenerative treatments for OA (Grenier et al., 2014; Johnson et al., 2016). A variety of proinflammatory cytokines are commonly used to induce the ECM degradation seen in human OA which involves factors i.e., interleukins (IL-1α, IL-1β, IL-6, IL-8, IL-9) and tumour necrosis factor (TNF-α) (Gabriel et al., 2010; Novakofski et al., 2012; Sylvester et al., 2012). Amongst them IL-1β, TNF-α and IL-6 are the three cytokines mostly induced in OA pathogenesis and possess a synergic effect: (i) IL-1β, which was found to inhibit Coll II and proteoglycans (PGs) and stimulate the production of MMP1,3,13, (ii) IL-6 to activate NF-kB pathway and downregulate the enzymatic antioxidant defenses in chondrocytes with mitochondria; (iii) TNF-α, which can activate the NF-kB pathway, increase the expression of MMPs, inhibit anabolic molecules, and stimulate chondrocytes apoptosis (Fan et al., 2007; Calich et al., 2010; Meliconi et al., 2013; Löfgren et al., 2018). Particularly, lots of studies focused on IL-1β and successfully demonstrated the effect of therapeutic compounds on the OA-induced model; whereas TNF-α and IL-6, which play a main role in the pathophysiology of OA, have only been investigated in a few experimental trials (Bondeson et al., 2010; Goldring & Goldring, 2016). In addition, the concentration of cytokines used for *in vitro* studies up to date is lower than the ones detected in synovial fluid of OA patients, therefore it is hard to obtain a faithful representation of the native OA environment (Bartolotti et al., 2021). Despite several *in vitro* models having been developed and refined over the years, there is still no confirmed gold standard which can be applied when developing OA drug molecules and/or drug delivery systems.

Thus, this work aims to study the OA progression in a multiple cytokines-induced *in vitro* AC model. To this goal, a pathological model is designed by loading the cell media with a cocktail of cytokines including IL-1ß, IL-6 and TNF-α. The use of a combination of cytokines would induce OA-like cell and tissue responses to closely resemble the native disease, particularly taking into consideration the importance of synovium effects in the model design (Johnson et al., 2016). This pathological model was based on a reliable *in vitro* model of healthy AC, developed in our previous work (Scalzone et al., 2022b), whereas cytokines concentration was selected according to their prevalence in OA synovial fluid (Sohn et al., 2012). The main features which distinguish Healthy and OA conditions were analyzed with primary human fetal chondrocytes (FC) and Y201 TERT mesenchymal stem cells differentiated chondrocytes (Y201-C) using a pathological *in vitro* OA model.

2 Experimental section

2.1 Materials

All the reagents were obtained from Sigma-Aldrich (United Kingdom) unless differently stated. The ultrapure water employed (dH_2O) throughout the experiments was obtained with a Milli-Q Integral system equipped with a BioPak ultrafiltration cartridge (Millipore, Merck).

2.2 Cell culture: FCs and Y201-C

FC was cultured (Cell Application, United States) in ready-to-use Chondrocyte Growth Medium (PromoCell, United Kingdom) at 37°C in a humidified atmosphere incubator containing 5% CO_2. At 80% confluence, cells were detached with trypsin-EDTA (PAA-Laboratories GmbH, Germany) and subcultured to passage 6 for experiments. Human TERT immortalised bone marrow stromal cells (Y201) were supplied by Prof P. Genever (York University) and cultured at 37°C and 5% CO_2 in Dulbecco's Modified Eagle Medium (DMEM) with low glucose content, supplemented with 10% Foetal bovine serum (FBS), 2 mM L-glutamine and a 1% Penicillin/Streptomycin (P/S). After the expansion, cells were differentiated in chondrocytes (Y201-C), as previously reported (Scalzone et al., 2022b).

2.3 Manufacturing of *in vitro* OA model

Spheroids were formed as previously reported in our work (Scalzone et al., 2023). Briefly, FC (passage 6) and Y201-C (passage 15) were seeded in a round bottom non-tissue treated 96-well plate (ThermoFisher Scientific, United Kingdom) at a density of 2×10^5 cells/well, suspended in 150 µL of DMEM/F12 supplemented with 0.25% (w/v) methylcellulose (MC). Then, the multi-well plates were incubated at 37°C and 5% CO_2 for 10 days. After 1 day of culture, three different conditions were set for the spheroids, as reported in Table 1, and the media was changed every 2 days.

TABLE 1 Culture conditions for FC and Y201-C: High concentration of cytokines (OA-HC), Low concentration of cytokines (OA-LC) and Healthy.

Cytokines	High concentration (OA-HC)	Low concentration (OA-LC)	Healthy
IL-1β	5 ng/mL	1 ng/mL	-
TNF-α	5 ng/mL	1 ng/mL	-
IL-6	50 ng/mL	10 ng/mL	-

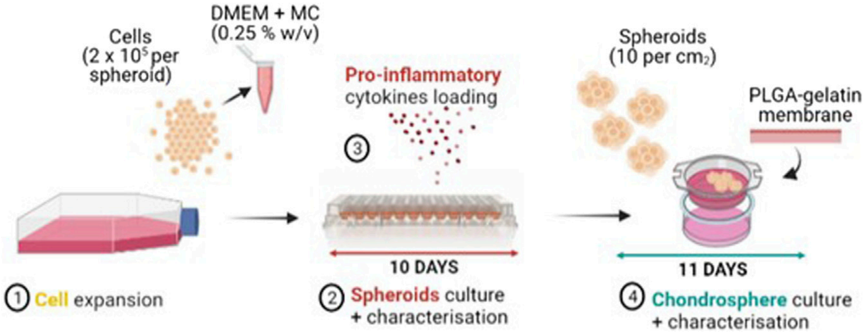

FIGURE 1
Manufacturing process of the OA *in vitro* model: FC and Y201-C cells expansion (1), Spheroids culture and characterization in a round bottom 96-well plate for 10 days (2) with the addition of IL-6, IL-1ß, TNF-α proinflammatory mediators at day 3 of spheroids culture (3), Chondrospheres culture and characterisation for further 11 days on a gelatin-coated electrospun PLGA membrane (4).

Following a procedure optimised in our previous work, after 10 days of spheroids culture, five single spheroids were transferred onto an electrospun poly(lactic-co-glycolic acid) (PLGA)-dopamine functionalised and gelatin-coated membranes, that were mounted in 48-multiwell CellCrowns™ (10 spheroids per cm^2 of membrane) to obtain chondrospheres, which were cultured in DMEM/F12 medium for further 11 days at 37°C in a humified atmosphere with 5% CO_2. The whole process for manufacturing the *in vitro* OA model is reported in Figure 1.

2.4 Spheroids growth kinetics during the culture

Spheroid growth kinetics was monitored over 10 days of culture for all conditions: Healthy, OA-HC and OA-LC. Images were taken on days 1, 4 and 10 with an EVOS M5000 microscope in phase-contrast brightfield. Spheroids morphometric analysis was performed by measuring diameters and areas of at least 4 spheroids for time points using ImageJ software. Results were analysed using GraphPad Prism software (GraphPad Software, Inc., La Jolla, CA).

2.5 Metabolic activity assessment

To evaluate cells metabolic activity MTS (3-(4,5-dimethylthiazol-2-yl)-5-(3-carboxymethoxyphenyl)-2-(4-sulfophenyl-2H-tetrazolium) assay (CellTiter 96® AQueous One Solution Cell Proliferation Assay, Promega, United Kingdom) was used. Each condition was analysed in triplicate on days 1, 4 and 10. MTS solution was prepared to dilute at 1:6 the CellTiter 96® AQueous One Solution Reagent in phenol red-free DMEM/F12 supplemented with 10% FBS and 1% P/S. 200 μL of MTS solution was added to each well that contained the spheroids and incubated at 37°C in a humidified 5% CO_2 atmosphere for 2.5 h and then 90 μL of the solution was transferred into a 96-well plate in duplicate for each sample. Absorbance was recorded at 490 nm using a Filter-based FLUOstar® Omega multi-mode reader (FLUOstar® Omega, Germany). The results were analysed using GraphPad Prism 9 software.

2.6 Gene expression analysis

For gene expression analysis, total RNA was extracted from spheroid and chondrosphere samples using miRNeasy Micro RNA Isolation Kit (Qiagen, United States), according to the manufacturer's protocol. The concentration and purity of the isolated RNA were measured using a spectrophotometer (NanoDrop™ 1,000, Thermo Fisher Scientific, United States). Reverse transcription was performed using the High-Capacity cDNA Reverse Transcription Kit (Thermo Fisher, United Kingdom), using a thermocycler (2,720 Thermal Cycler, Applied Biosystems, United States) based on cycles of 10 min at 25°C, 120 min at 37°C, 5 min at 85°C. Reverse Transcription quantitative real-time Polymerase Chain Reaction (RT-qPCR) was performed using TaqMan™ Fast Advanced Master Mix and

TaqMan™ *SOX9, ACAN, COL2A1, COL1A2, MMP13* and *ADAMTS5* probes (Thermo Fisher Scientific, United Kingdom). Gene expression raw data were acquired using QuantStudio™ 3 Real-Time PCR System (Thermo Fisher Scientific, United States). The expression of the genes of interest was normalized to Glyceraldehyde-3-phosphate dehydrogenase (*GAPDH)* and presented as a relative expression using the $2^{-(\Delta\Delta Ct)}$ method(Livak & Schmittgen, 2001). The expression levels of day 0 control conditions for FC and Y201-C were set to 1 then the expression levels of day 10 and day 21 conditions were presented as fold-change relative to the controls. The ratio of COL2A1/COL1A2 was evaluated as well on day 10 and day 21.

2.7 Histology and immunohistochemistry (IHC) assessment

Samples of both Y201-C and FC in all conditions on days 1, 7 and 21 were washed with PBS, moved to a 0.5 mL Eppendorf embedded in OCT Compound (Agar Scientific, United Kingdom) and snap frozen at −80°C until further use. Samples were cryosectioned using a CM1900 cryostat (Leica Biosystems, Germany) at −20°C at 5 µm thickness, let dry at room temperature for 2 h and kept frozen until analysis. To perform Histology and IHC, frozen slides were transferred to cold Acetone at −20°C for 10 min. Following this, the fixative was let evaporate for 15–20 min and the slides were washed twice with PBS to remove any trace of OCT compound.

Hematoxylin and Eosin (H&E), Picrosirius Red and Alcian Blue stainings were performed according to standard procedures (Scalzone et al., 2022a). Histology slides were let dry overnight under the fume hood and imaged the following day with EVOS M5000 Microscope in RGD Brightfield at × 20 and × 40 magnification. For IHC, fixed and washed tissue slices were permeabilised with Triton 100x solution (0.1% w/v in PBS), immersed in BSA (2% w/v in PBS) and incubated for 2 h at RT with primary antibodies rabbit Anti-Collagen II (ab34712 Abcam) or rabbit Anti-Ki-67 (NB500-170SS Bio-techne Ltd.) or mouse Anti-Aggrecan (ab3778 Abcam) respectively at 1:200, 1:100 and 1:50 in BSA solution. After washing in PBS, secondary antibodies solutions were added for 1 h: AlexaFluor-594 goat anti-rabbit IgG (H + L) (ab150080 Abcam) 1:500 in BSA solution to Anti-Collagen II slides, Fluorescein-labelled goat anti-rabbit IgG (H + L) (F2765, Thermo Fisher Scientific) 1:1,000 in BSA solution for Anti-Ki-67 and Goat anti-Mouse IgG (H&L) - Alexa Fluor™ 488 (A-11001, Thermo Fisher Scientific) 1:1,000 in BSA solution for Anti-Aggrecan slides. Finally, nuclei were counterstained with Hoechst solution (R37609 Thermo Fisher Scientific), according to the manufacturer's instructions, and a drop of Invitrogen ProLong Glass Antifade Mountant (Fisher Scientific, United Kingdom) was added to each slide and covered with a rectangular coverslip. Slides were let dry under the hood for 15 min and imaged using EVOS M5000 Microscope in fluorescence at × 40 magnification.

2.8 Statistical analysis

Tests were performed at least in triplicate for each sample. The results were represented as mean ± standard deviation. Differences between groups were determined using a One-way analysis of variance (ANOVA) with Tukey's multiple comparison test using levels of statistical significance of $p < 0.0001$ (****), $p < 0.001$ (***), $p < 0.05$(**) and $p < 0.01$(*).

3 Results

3.1 Spheroids growth kinetics and metabolic activity

Spheroids growth dynamics were analysed on days 1, 4 and 10 for both FC and Y201-C cells in Healthy, OA-LC and OA-HC conditions. From the images collected, it was noticed a gradual decrease in both healthy spheroids' size (Figure 2A), and a significant decrease in their diameter's dimension (Figures 2B, C). Particularly, the diameter of the FC spheroids significantly decreased from 1,610 ± 100 µm on day 1–1,005 ± 90 µm on day 10 ($p < 0.0001$), while Y201-C spheroid diameter significantly decreased from 1750 ± 90 µm on day 1–1,200 ± 70 µm at day 10 ($p < 0.0001$). In the OA spheroids condition, a different trend was observed for both FC and Y201-C, with a stable dimension of spheroids over the culture at low and high concentrations of cytokines. On day 10, FC spheroids achieved values of 1,450 ± 50 µm and 1,650 ± 50 µm for OA-LC and OA-HC samples, respectively. These values were significantly different ($p < 0.0001$) compared to the Healthy FC on day 10. Similarly, Y201-C spheroids in OA-LC and OA-HC conditions showed values of 1,600 ± 50 µm and 1850 ± 50 µm, respectively, significantly different ($p < 0.0001$) from Y201-C in Healthy conditions on day 10.

Cellular mitochondrial activity was estimated via MTS assay (Figure 3). FC spheroids metabolic activity decreased over culture ($p < 0.0001$) in all conditions: from 0.07 ± 0.03 on day 1 to 0.03 ± 0.02 in Healthy, 0.04 ± 0.01 in OA-LC and 0.05 ± 0.02 in OA-HC conditions at day 10. Y201-C spheroids metabolic activity showed a different trend, increasing statistically ($p < 0.0001$) from 0.08 ± 0.01 on day 1 to 0.13 ± 0.05, 0.14 ± 0.05 and 0.16 ± 0.07, respectively in Healthy, OA-LC and OA-HC conditions at day 10. Both FC and Y201-C showed higher metabolic activity for OA-HC samples compared to OA-LC ($p < 0.01$) and Healthy ($p < 0.05$) (Figures 3A, B).

3.2 Analyses of cell proliferation and apoptotic tendency

Proliferation and apoptosis were evaluated on cryosections on day 1 and day 21. Cellular proliferation was assessed via immunostaining for Ki-67 (an antigen associated with cellular proliferation) and cell nuclei were counterstained for DAPI (blue) (Figure 4). A brighter signal corresponding to Ki-67 staining was observed in both FC (Figure 4A) and Y201-C (Figure 4B) in OA conditions (both in OA-HC and OA-LC) on day 21, compared to the Healthy control on day 21 and compared to day 1 control. While few cells in a proliferative state were found on the construct edges in the Y201-C on days 1 and 21 in healthy conditions, compared to the FC.

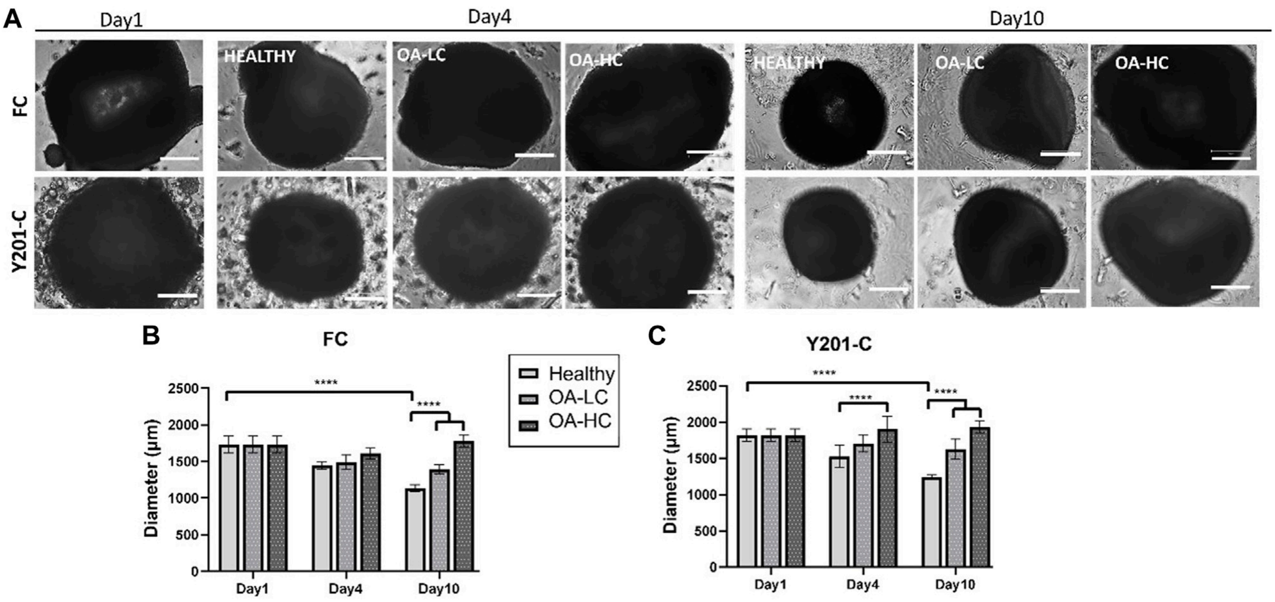

FIGURE 2
FC and Y201-C spheroids images on day 1, day 4 and day 10 in Healthy, OA-LC and OA-HC conditions. Scale bars:300 μm. **(A)** Spheroids diameter at different timepoints for FC **(B)** and Y201-C **(C)** at each condition. Statistics: ****$p < 0.0001$.

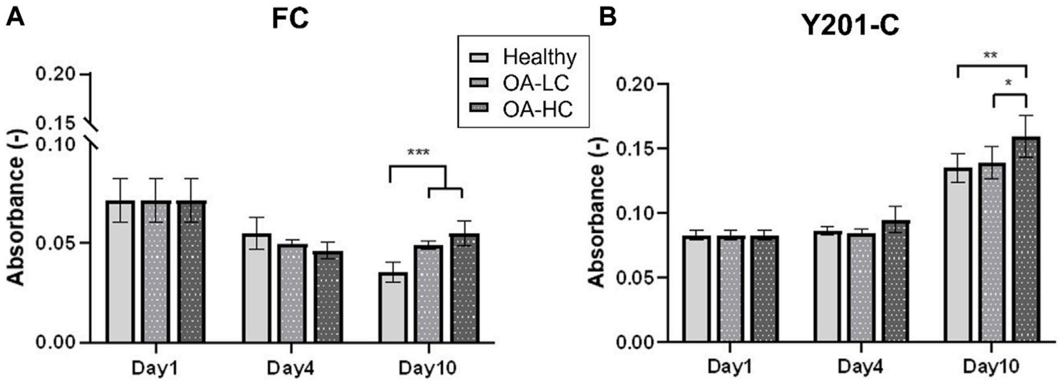

FIGURE 3
Analyses of cellular mitochondrial activity in Healthy, OA-LC and OA-HC conditions, for FC **(A)** and Y201-C **(B)**. Statistics: **$p < 0.05$ and *$p < 0.01$.

Chondrocytes' apoptotic features, typical of late-stage OA were analysed on cryosections at 21 days at high magnification (×63) staining cells nuclei with DAPI (Figure 5). Both, FC and Y201-C in a healthy state, showed typical rounded-shaped cell nuclei homogenously dispersed within the tissue slices (Figures 5A, B). While in OA condition (OA-LC and OA-HC), both cells showed heterogeneous nucleic acids organisation toward clustering structures (Figures 5C–F, circles). Also, in the OA condition, cells had fragmented and pyknotic nuclei.

3.3 Gene expression analysis

The expression of anabolic (*SOX9, COL2A1, ACAN* and *COL1A2*) and Catabolic (*MMP13* and *ADAMTS-5*) markers was analysed and reported in Figure 6. Both FC and Y201-C showed a significant increase in *SOX9, ACAN* and *COL2A1* gene expression over the 21 days of culture in healthy conditions. *SOX9* and *ACAN* showed an upregulation at 21 days for both cells in Healthy conditions compared to the relative OA-HC and OA-LC conditions ($p < 0.0001$). Similarly, a significant difference in the *COL2A1* expression between the three different conditions at 21 days for both FC and Y201-C can be observed, with a gradual increase of the expression from OA-HC to Healthy. *COL1A2* displayed an upregulation on day 10, followed by a significant decrease in its expression in each condition for both cells from day 10 to day 21. Also, Healthy FC showed a higher expression of *COL1A2* compared to the pathological, while Y201-C showed the highest fold-regulation in the OA-LC condition. *MMP13* catabolic

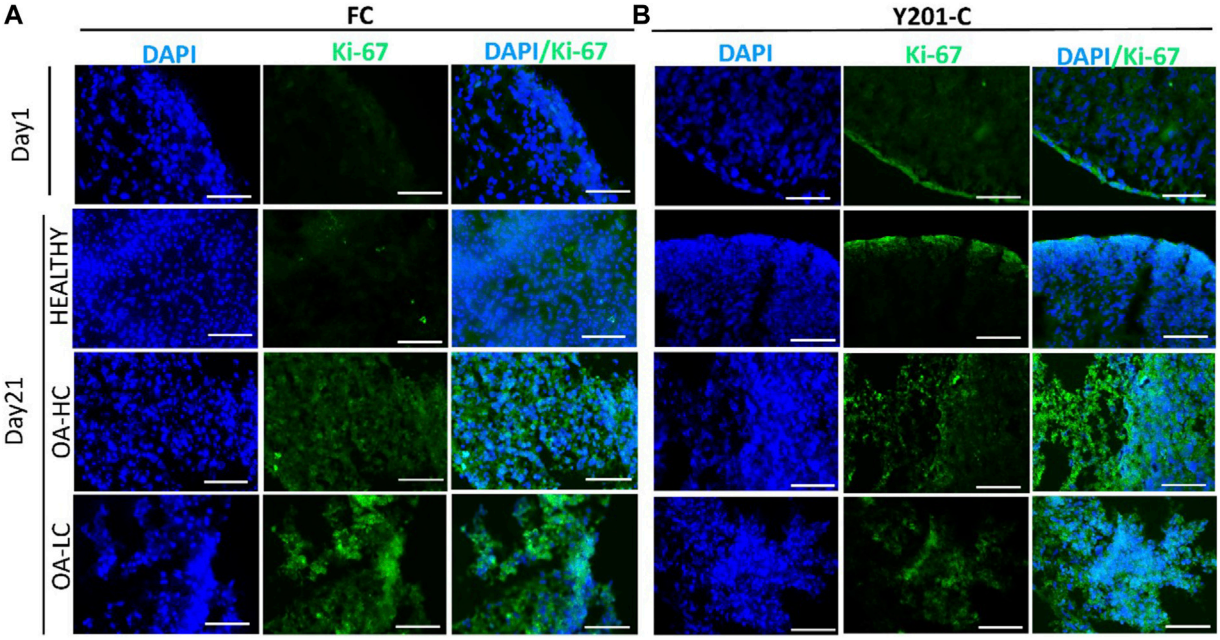

FIGURE 4
Assessment of cellular proliferation on day 1 and day 21 in Healthy, OA-LC and OA-HC conditions with Ki-67 (green) staining and nuclei counterstained with DAPI (blue), for FC **(A)** and Y201-C **(B)**. Scale bars: 150 μm.

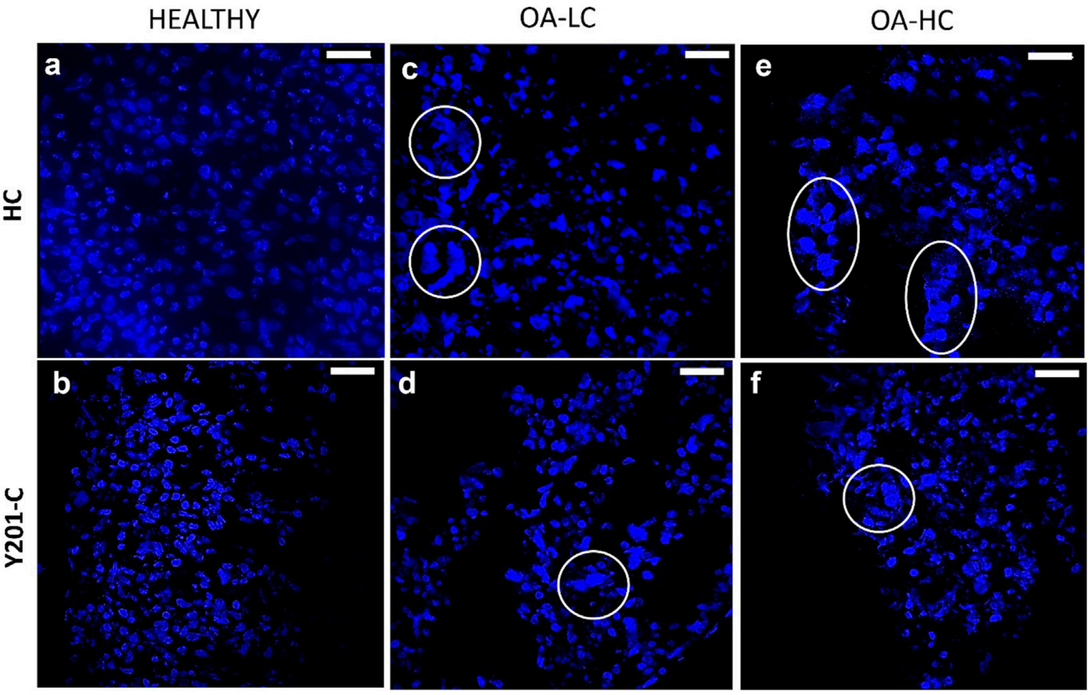

FIGURE 5
Assessment of cells nuclei organisation and morphology at 21 days in Healthy **(A,B)**, OA-LC **(C,D)** and OA-HC **(E,F)** conditions with DAPI (blue) staining at × 63 magnification. Circles are in correspondence with cellular clusters. Scale bars: 20 μm.

marker expression increased from day 1 to day 10 for the FC in all conditions and then, decreased after 21 days (Figure 6E): OA-HC showed a much higher expression on both day 10 and day 21, compared to Healthy and OA-LC. For Y201-C, instead, a similar trend was observed for OA-LC and Healthy condition, with an increase of *MMP13* expression on day 10 and a decrease on day 21,

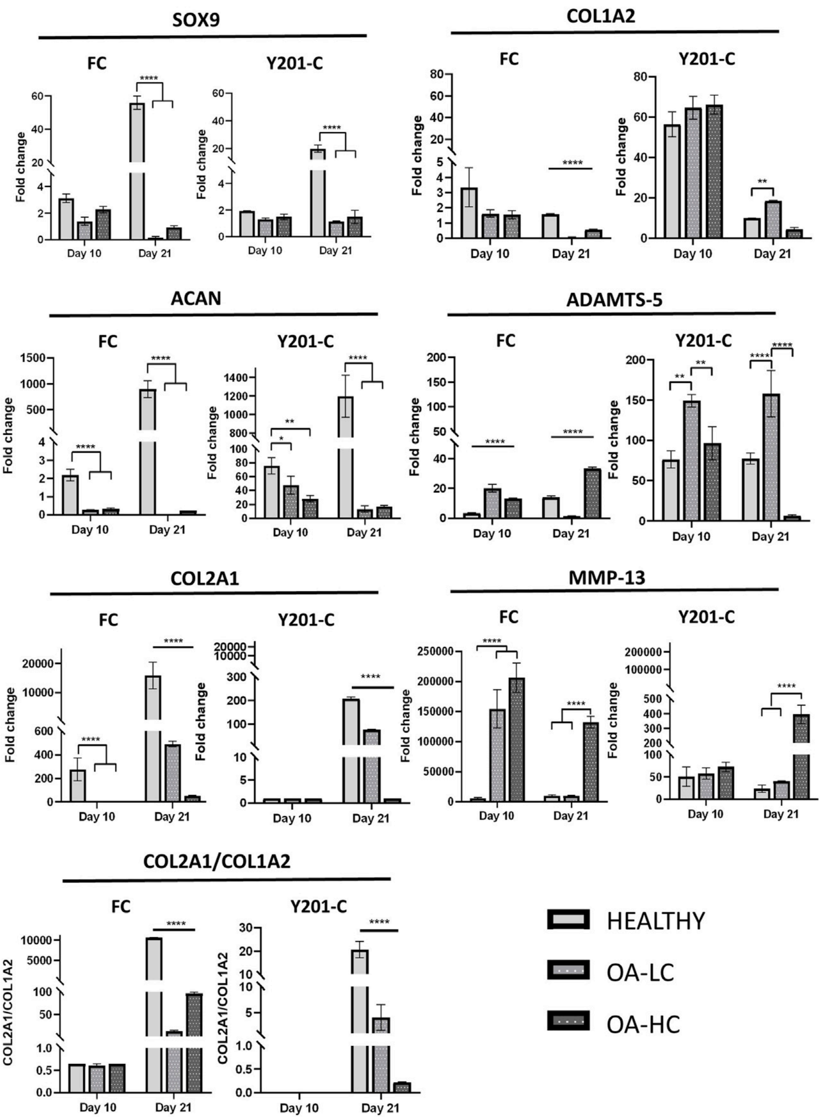

FIGURE 6
Gene expression analysis via RT-qPCR, for both FC and Y201-C in Healthy, OA-LC and OA-HC: SOX-9, COL1A2, ACAN, ADAMTS-5, COL2A1, MMP-13 and report of the col2a1/col1a2 ratio for FC and Y201-C. Statistics: ****$p < 0.0001$, **$p < 0.01$, *$p < 0.05$.

while *MMP13* expression significantly increased over culture in the case of OA-HC, showing values significantly higher compared to Healthy and OA-LC ($p < 0.0001$). Finally, *ADAMTS-5* catabolic marker expression increased on day 10 for both cell types in each condition, with significant differences observed on day 21. FC showed a similar value of OA-LC and Healthy on day 21 compared to day 10, while they presented a decrease in *ADAMTS-5* expression. All values were significantly different ($p < 0.0001$) from each other at 21 days, with OA-LC presenting the highest expression. On the other side, Y201-C showed an increase in *ADAMTS-5* expression on day 21 in healthy and OA-HC conditions and a decrease in OA-LC compared to day 10. All values were significantly different ($p < 0.0001$) from each other at 21 days, with OA-HC presenting the highest expression. In addition, the ratio of *COL2A1/COL1A2* did not differ between the three conditions after 10 days of culture (~0.65 for FC and ~0 for Y201-C), while it showed statistically significant differences at day 21 with values of: 10,614.0 ± 32.7 in healthy condition compared to 12.3 ± 2.5 and 96.4 ± 3.2 in LC-OA and HC-OA for FC, respectively; and 20.66 ± 3.5 in healthy samples compared to. 4.1 ± 2.5 and 0.2 ± 0.1 in LC-OA and HC-OA for Y201-C, respectively.

3.4 Analysis of the quality of tissue in the healthy and pathological state

H&E staining intensity was higher for both FC and Y201-C on day 21 compared to day 1 in Healthy conditions, whereas it was observed a decrease in the staining intensity for OA-LC and OA-HC conditions compared to the healthy control on day 21 (Figures 7A, B). Also, chondrospheres in OA conditions showed a decrease in

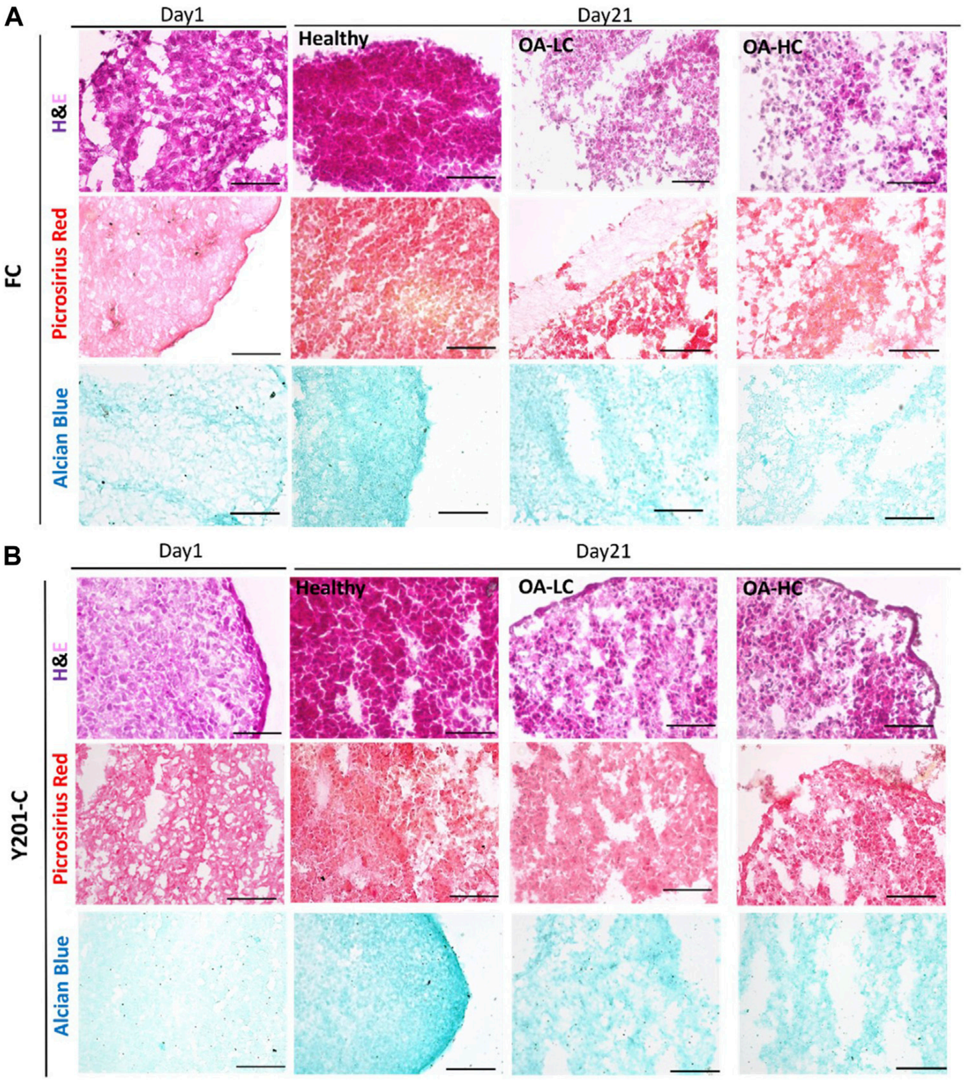

FIGURE 7
Histological analyses on cryosections at day 1 and day 21 in Healthy, OA-LC and OA-HC conditions. H&E, Picrosirius Red and Alcian Blue stainings for FC **(A)** and Y201-C **(B)** Scale bars = 150 µm.

cellularity for both cell types and this feature seemed to be more evident in the middle of the construct, compared to the edges, especially for the Y201-C cells (Figure 7B). In healthy conditions, both FC and Y201-C samples presented higher collagen deposition (detected with Picrosirius Red) and mucopolysaccharides (detected via Alcian Blue) on day 21, compared to day 1 and both OA-HC and OA-LC on day 21. Chondrospheres cultivated in healthy conditions showed a homogenous distribution of Picrosirius Red and Alcian blue staining, whereas those in OA conditions showed a weaker signal in a restricted area, in the zones of the slices where cells' nuclei were aggregated.

From the IHC analyses, chondrospheres showed at 21 days an increase in Coll II and Aggrecan staining in healthy conditions, compared to both the control at day 1 and OA conditions at day 21, for both FC and Y201-C. In OA-HC and OA-LC conditions, samples showed less intense staining of Coll II and Aggrecan (Figure 8).

4 Discussion

The development of a patho-physiologically relevant *in vitro* model for OA should reflect the complexity of the disease, characterised by AC degeneration accompanied by the whole joint inflammation (Goldberg & Kresina, 1987). Herein, we obtained an OA-induced environment by adding to the culture media the main pro-inflammatory cytokines, released from the synovium cells and chondrocytes, during OA progression (IL-1β, TNFα and IL-6) to recreate a naturally diseased environment (Scalzone et al., 2023). Compared to previous literature, the combination of a cocktail of cytokines allowed to obtain OA-like cell and tissue responses that more closely resemble the native disease at an early stage, particularly taking into consideration the importance of synovium-related inflammation effects in the model design, which results in the release of pro-inflammatory mediators (Johnson et al., 2016).

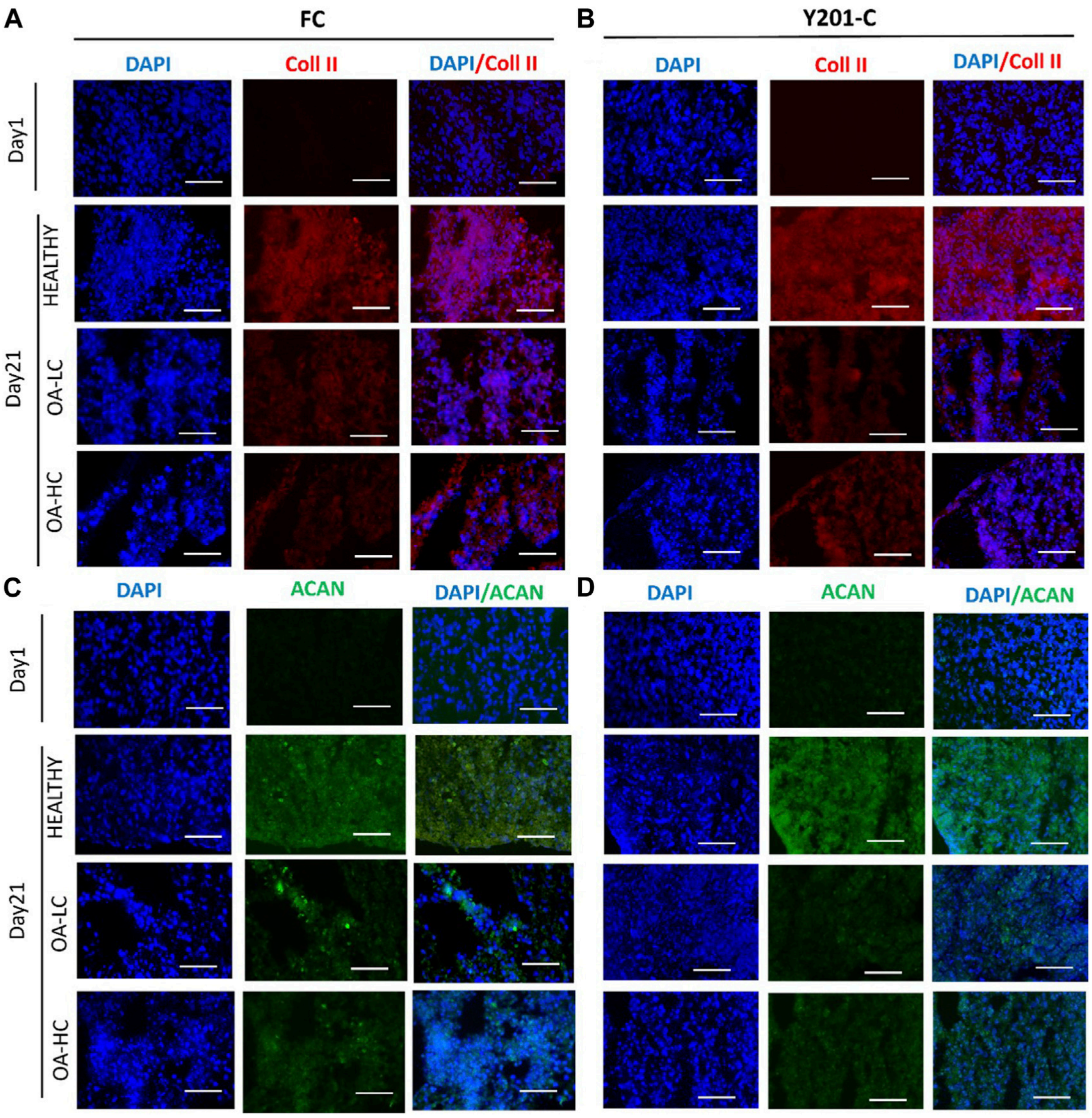

FIGURE 8
Immunohistochemical analyses of cartilage-specific markers: Collagen type II (Coll II, Red) and Aggrecan (ACAN, Green). Nuclei were counterstained with DAPI (blue). Images were reported in Healthy, OA-HC and OA-LC conditions for Coll II and DAPI for FC **(A)** and Y201-C **(B)**; ACAN and DAPI for FC **(C)** and Y201-C **(D)**. Scale bars = 150 μm.

For both FC and Y201-C, the size of healthy spheroids gradually decreased over 10 days of culture, as dispersed cells formed tightly packed aggregates due to cell-cell interaction and condensation. However, spheroids did not reduce in size when exposed to cytokines, possibly due to a cell proliferation effect as a typical feature of early-stage OA chondrocytes and the interference of cytokines on cell-cell interaction (Gao et al., 2014; Wojdasiewicz et al., 2014). Indeed, a significant difference was observed on day 10 between both pathological conditions and healthy for FC and Y201-C.

Also, Y201-C showed an increase in metabolic activity over culture while FC showed a decrease. However, on day 10, both cells showed a similar pattern: increased metabolic activity in presence of cytokines, which may be related to the production of inflammatory and degradative enzymes, as well as an attempt to repair the ECM that had begun to break down, a characteristic of early-stage OA (Goldring & Goldring, 2016).

Three key events that characterize OA in an early-phase are cell hyperproliferation in contrast to well-established increased production and breakdown of ECM components and inflammation (Quinn et al., 2005; Elmore, 2007). Both cell types showed strong staining of Ki-67, which is a cells proliferation marker, in OA-HC and OA-LC conditions compared to the healthy model on day 21, and the control on day 1 (Miller et al., 2018). This result indicates that cells in pathological conditions tend to proliferate; indeed, OA-induced cells represent a cell population with abnormal proliferation, which is the common chondrocyte response to altered joint environments (Sandell & Aigner, 2001; Dreier, 2010).

Then, it was evaluated at high magnification the morphology of cells nuclei stained with DAPI: both cells in OA conditions, compared to the healthy, showed a decrease in the size of nuclei, their clusterisation, and an anomalous shape due to the presence of apoptotic bodies, nuclear condensation, and fragmentation. All these events are related to the shift of cells towards the hypertrophic pathway, which may result in chondrocyte apoptosis and, as a result, AC loss (Blanco et al., 1998; Muldrew et al., 2001; Elmore, 2007). Also, gene expression was altered in OA conditions: anabolic markers (*SOX9, ACAN* and *COL2A1*) were up-regulated at 21 days of culture in the healthy model with FC and Y201-C compared to both pathological, in which their expression decreased over culture, as expected.

To evaluate the gene expression pathways involved into spheroids weakness in OA environment we compared the expression of *MMP13*, which is the main collagenase responsible for the degradation and cleavage of collagen II, with *COL2A1*. *COL2A1* expression was down-regulated in OA conditions respect Heathy environment while *MMP-13* was massively up-regulated especially in OA-HC for both cell types. Moreover, the expression of *ADAMTS-5*, which together with the *ADAMTS-4* constitutes the family of aggrecanases responsible for the *ACAN* cleavage, was compared with *ACAN*. Also in this context the anabolic and the catabolic markers were inversely related and showed a higher *ACAN* expression in Healthy condition and an *ADAMTS-5* upregulation for both OA-LC and OA-HC. *ADAMTS-5* expression even in the Healthy was in according to literature that confirms that this aggrecanase is constitutively expressed by chondrocytes. The analysis of *COL1A2* by itself does not give great information about the OA progression, but the ratio of *COL2A1*/*COL1A2*, which was shown to be considerably greater in healthy conditions compared to pathological for both cells, is a crucial indicator between healthy and OA cartilage. However, *COL2A1*/*COL1A2* ratio decreased mostly due to a change or down-regulation of *COL2A1* expression, whereas *COL1A2* expression altered far less. This characteristic is consistent with earlier literature investigations (Marlovits et al., 2004).

The morphological quality of the spheroid model as the degree of degradation was determined by histology and IHC stainings. H&E staining indicates the presence of nucleated cells with abundant cytoplasmic content in all conditions. The main difference between the healthy and both pathological models is the weaker staining of collagen (stained with Picrosirius Red) and of strongly and weakly sulphated proteoglycans (stained with Alcian Blue) in OA conditions. Also, OA samples showed less compact and more scattered tissue. IHC supported the findings of histology and gene expression: when compared to pathological conditions, FC and Y201-C cells in healthy conditions formed a tissue rich in Coll II and aggrecan, as seen by the stronger staining and the compactness of the tissue slice. This is the result of the inhibition of the biosynthetic activity and matrix degradation by proteinases (Matyas et al., 2002; Roughley & Mort, 2014).

Overall, both cells at 21 days in the pathological state (OA-LC & OA-HC) showed a down-regulation in the expression of anabolic markers, compared to the healthy state and a higher expression of catabolic markers in the pathological model with a high concentration of cytokines.

5 Conclusion

Current OA models often replicate either post-traumatic and/or late-stage OA, leaving a large gap in understanding the spontaneous occurring disease and its early stages, where slowing disease progression would be an attractive treatment strategy. The presented *in vitro* model of AC in healthy and pathological condition allowed the study of the OA progression from early stage by demonstrating: (1) stimulated cell proliferation and apoptotic pathway, (2) decreased expression of anabolic markers and (3) lower biosynthetic activity in the simulated pathological environment when compared to the healthy environment. These functional biological changes in the spheroid models were observed even at low cytokine concentrations (in agreement with values seen in native human synovium during OA progression. Furthermore, Y201-C was shown to be a suitable cell source for easier and reproducible manufacturing of scaffold-free *in vitro* OA models. Given the obtained features, this model can be faithfully be used to (i) study OA molecular evolution from the on-set to its degeneration and (ii) to assess the effect and optimize the therapeutic dose of drugs and molecules, such as micro-RNAs or exosomes, targeting for example, the cellular pathways involved in the OA progression.

Data availability statement

The original contributions presented in the study are included in the article/Supplementary Material, further inquiries can be directed to the corresponding author.

Author contributions

AS, AF-D, PG, XW, and KD conceived and designed the experiments. AS performed the experiments; AS and GC analysed the data. AF-D, XW, MM-B, KD, and PG contributed material preparation; AS wrote the paper and GC, KD, XW, AF-D, MM-B, and PG revised the paper drafts. All authors contributed to the article and approved the submitted version.

Funding

AS acknowledges support from EPSRC for her Ph.D. studentship (EPSRC Grant EP/R51309X/1). XW and KD acknowledge support from Versus Arthritis (Award 21156).

Acknowledgments

The authors thank I. Carmagnola and Prof Chiara Tonda-Turo (Politecnico di Torino, Torino, Italy) for providing the electrospun membranes.

Conflict of interest

The authors declare that the research was conducted in the absence of any commercial or financial relationships that could be construed as a potential conflict of interest.

Publisher's note

References

Bartolotti, I., Roseti, L., Petretta, M., Grigolo, B., and Desando, G. (2021). A roadmap of *in vitro* models in osteoarthritis: A focus on their biological relevance in regenerative medicine. *J. Clin. Med.* 10 (9), 1920. doi:10.3390/jcm10091920

Blanco, F. J., Guitian, R., Vázquez-Martul, E., de Toro, F. J., and Galdo, F. (1998). Osteoarthritis chondrocytes die by apoptosis: A possible pathway for osteoarthritis pathology. *Arthritis & Rheumatism Official J. Am. Coll. Rheumatology* 41 (2), 284–289. doi:10.1002/1529-0131(199802)41:2<284:aid-art12>3.0.co;2-t

Bondeson, J., Blom, A. B., Wainwright, S., Hughes, C., Caterson, B., and van den Berg, W. B. (2010). The role of synovial macrophages and macrophage-produced mediators in driving inflammatory and destructive responses in osteoarthritis. *Arthritis Rheumatism* 62 (3), 647–657. doi:10.1002/art.27290

Calich, A. L. G., Domiciano, D. S., and Fuller, R. (2010). Osteoarthritis: Can anti-cytokine therapy play a role in treatment? *Clin. Rheumatol.* 29 (5), 451–455. doi:10.1007/s10067-009-1352-3

Cross, M., Smith, E., Hoy, D., Nolte, S., Ackerman, I., Fransen, M., et al. (2014). The global burden of hip and knee osteoarthritis: Estimates from the global burden of disease 2010 study. *Ann. Rheumatic Dis.* 73 (7), 1323–1330. doi:10.1136/annrheumdis-2013-204763

Dreier, R. (2010). Hypertrophic differentiation of chondrocytes in osteoarthritis: The developmental aspect of degenerative joint disorders. *Arthritis Res. Ther.* 12 (5), 216. doi:10.1186/ar3117

Elmore, S. (2007). Apoptosis: A review of programmed cell death. *Toxicol. Pathol.* 35 (4), 495–516. doi:10.1080/01926230701320337

Fan, Z., Söder, S., Oehler, S., Fundel, K., and Aigner, T. (2007). Activation of interleukin-1 signaling cascades in normal and osteoarthritic articular cartilage. *Am. J. Pathology* 171 (3), 938–946. doi:10.2353/ajpath.2007.061083

Gabriel, N., Innes, J. F., Caterson, B., and Vaughan-Thomas, A. (2010). Development of an *in vitro* model of feline cartilage degradation. *J. Feline Med. Surg.* 12 (8), 614–620. doi:10.1016/j.jfms.2010.03.007

Gao, Y., Liu, S., Huang, J., Guo, W., Chen, J., Zhang, L., et al. (2014). The ECM-cell interaction of cartilage extracellular matrix on chondrocytes. *BioMed Res. Int.* 2014, 1–8. doi:10.1155/2014/648459

Gikas, P. D., Bayliss, L., Bentley, G., and Briggs, T. W. R. (2009). An overview of autologous chondrocyte implantation. *J. Bone Joint Surg. Br.* 91 (8), 997–1006.

Goldberg, V. M., and Kresina, T. F. (1987). Immunology of articular cartilage. *J. Rheumatology* 14, 73–76.

Goldring, S. R., and Goldring, M. B. (2016). Changes in the osteochondral unit during osteoarthritis: Structure, function and cartilage–bone crosstalk. *Nat. Rev. Rheumatol.* 12 (11), 632–644. doi:10.1038/nrrheum.2016.148

Grenier, S., Bhargava, M. M., and Torzilli, P. A. (2014). An *in vitro* model for the pathological degradation of articular cartilage in osteoarthritis. *J. Biomechanics* 47 (3), 645–652. doi:10.1016/j.jbiomech.2013.11.050

Johnson, C. I., Argyle, D. J., and Clements, D. N. (2016). *In vitro* models for the study of osteoarthritis. *Veterinary J.* 209, 40–49. doi:10.1016/j.tvjl.2015.07.011

Kloppenburg, M., and Berenbaum, F. (2020). Osteoarthritis year in review 2019: Epidemiology and therapy. *Osteoarthr. Cartil.* 28 (3), 242–248. doi:10.1016/j.joca.2020.01.002

Livak, K. J., and Schmittgen, T. D. (2001). Analysis of relative gene expression data using real-time quantitative PCR and the 2-ΔΔCT method. *Methods* 25 (4), 402–408. doi:10.1006/meth.2001.1262

Löfgren, M., Svala, E., Lindahl, A., Skiöldebrand, E., and Ekman, S. (2018). Time-dependent changes in gene expression induced *in vitro* by interleukin-1β in equine articular cartilage. *Res. Veterinary Sci.* 118, 466–476. doi:10.1016/j.rvsc.2018.04.013

Marlovits, S., Hombauer, M., Truppe, M., Vècsei, V., and Schlegel, W. (2004). Changes in the ratio of type-I and type-II collagen expression during monolayer culture of human chondrocytes. *J. Bone Jt. Surg. - Ser. B* 86 (2), 286–295. doi:10.1302/0301-620X.86B2.14918

Matyas, J. R., Huang, D., Chung, M., and Adams, M. E. (2002). Regional quantification of cartilage type II collagen and aggrecan messenger RNA in joints with early experimental osteoarthritis. *Arthritis Rheumatism* 46 (6), 1536–1543. doi:10.1002/art.10331

Meliconi, R., Pulsatelli, L., Addimanda, O., Brusi, V., and Pavloska, B. (2013). New findings in osteoarthritis pathogenesis: Therapeutic implications. *Ther. Adv. Chronic Dis.* 4 (1), 23–43. doi:10.1177/2040622312462734

Miller, I., Min, M., Yang, C., Tian, C., Gookin, S., Carter, D., et al. (2018). Ki67 is a graded rather than a binary marker of proliferation versus quiescence. *Cell Rep.* 24 (5), 1105–1112.e5. doi:10.1016/j.celrep.2018.06.110

Muldrew, K., Chung, M., Novak, K., Schachar, N. S., Zernicke, R. F., Mcgann, L. E., et al. (2001). Evidence of chondrocyte repopulation in adult ovine articular cartilage following cryoinjury and long-term transplantation. *Osteoarthr. Cartil.* 9 432–439. doi:10.1053/joca.2000.0409

Novakofski, K. D., Torre, C. J., and Fortier, L. A. (2012). Interleukin-1α, -6, and -8 decrease Cdc42 activity resulting in loss of articular chondrocyte phenotype: Cdc42 IN ARTICULAR CHONDROCYTES. *J. Orthop. Res.* 30 (2), 246–251. doi:10.1002/jor.21515

Quinn, T. M., Hunziker, E. B., and Häuselmann, H. J. (2005). Variation of cell and matrix morphologies in articular cartilage among locations in the adult human knee. *Osteoarthr. Cartil.* 13 (8), 672–678. doi:10.1016/j.joca.2005.04.011

Rigoglou, S., and Papavassiliou, A. G. (2013). The NF-κB signalling pathway in osteoarthritis. *Int. J. Biochem. Cell Biol.* 45 (11), 2580–2584. doi:10.1016/j.biocel.2013.08.018

Roughley, P. J., and Mort, J. S. (2014). The role of aggrecan in normal and osteoarthritic cartilage. *J. Exp. Orthop.* 1 (1), 8–11. doi:10.1186/s40634-014-0008-7

Sandell, L. J., and Aigner, T. (2001). Articular cartilage and changes in Arthritis Cell biology of osteoarthritis. *Arthritis Res.* 3, 107–113. doi:10.1186/ar148

Scalzone, A., Cerqueni, G., Bonifacio, M. A., Pistillo, M., Cometa, S., Belmonte, M. M., et al. (2022a). Valuable effect of Manuka Honey in increasing the printability and chondrogenic potential of a naturally derived bioink. *Mater. Today Bio* 14, 100287. doi:10.1016/j.mtbio.2022.100287

Scalzone, A., Cerqueni, G., Wang, X. N., Ferreira-Duarte, A., Dalgarno, K., Mattioli-Belmonte, M., et al. (2023). An *in vitro* engineered osteochondral model as tool to study osteoarthritis environment. *Adv. Healthc. Mater.* 12 (2), 2202030. doi:10.1002/adhm.202202030

Scalzone, A., Wang, X. N., Dalgarno, K., Ferreira, A. M., and Gentile, P. (2022b). A chondrosphere-based scaffold free approach to manufacture an *in vitro* articular cartilage model. *Tissue Eng. - Part A* 28 (1–2), 84–93. doi:10.1089/ten.tea.2021.0061

Scanzello, C. R., and Goldring, S. R. (2012). The role of synovitis in osteoarthritis pathogenesis. *Bone* 51 (2), 249–257. doi:10.1016/j.bone.2012.02.012

Sohn, D. H., Sokolove, J., Sharpe, O., Erhart, J. C., Chandra, P. E., Lahey, L. J., et al. (2012). Plasma proteins present in osteoarthritic synovial fluid can stimulate cytokine production via Toll-like receptor 4. *Arthritis Res. Ther.* 14 (1), R7–R13. doi:10.1186/ar3555

Sylvester, J., El Mabrouk, M., Ahmad, R., Chaudry, A., and Zafarullah, M. (2012). Interleukin-1 induction of aggrecanase gene expression in human articular chondrocytes is mediated by mitogen-activated protein kinases. *Cell. Physiology Biochem.* 30 (3), 563–574. doi:10.1159/000341438

Valdes, A. M. (2010). Molecular pathogenesis and genetics of osteoarthritis: Implications for personalized medicine. *Pers. Med.* 7 (1), 49–63. doi:10.2217/pme.09.68

Wojdasiewicz, P., Poniatowski, Ł. A., and Szukiewicz, D. (2014). The role of inflammatory and anti-inflammatory cytokines in the pathogenesis of osteoarthritis. *Mediat. Inflamm.* 2014, 1–19. doi:10.1155/2014/561459

Yuan, G., Masuko-Hongo, K., Kato, T., and Nishioka, K. (2003). Immunologic intervention in the pathogenesis of osteoarthritis. *Arthritis & Rheumatism* 48 (3), 602–611. doi:10.1002/art.10768

frontiers | Frontiers in Bioengineering and Biotechnology

TYPE Original Research
PUBLISHED 23 June 2023
DOI 10.3389/fbioe.2023.1200618

Check for updates

OPEN ACCESS

EDITED BY
Behnam Akhavan,
The University of Newcastle, Australia

REVIEWED BY
Annachiara Scalzone,
Center for Advanced Biomaterials for Healthcare (IIT), Italy
Dana Akilbekova,
Nazarbayev University, Kazakhstan

*CORRESPONDENCE
Mh Busra Fauzi,
fauzibusra@ukm.edu.my

RECEIVED 05 April 2023
ACCEPTED 09 June 2023
PUBLISHED 23 June 2023

CITATION
Tahri S, Maarof M, Masri S, Che Man R, Masmoudi H and Fauzi MB (2023), Human epidermal keratinocytes and human dermal fibroblasts interactions seeded on gelatin hydrogel for future application in skin *in vitro* 3-dimensional model.
Front. Bioeng. Biotechnol. 11:1200618.
doi: 10.3389/fbioe.2023.1200618

Human epidermal keratinocytes and human dermal fibroblasts interactions seeded on gelatin hydrogel for future application in skin *in vitro* 3-dimensional model

Safa Tahri[1,2], Manira Maarof[1], Syafira Masri[1], Rohaina Che Man[3], Hatem Masmoudi[2] and Mh Busra Fauzi[1]*

[1]Centre for Tissue Engineering and Regenerative Medicine, Faculty of Medicine, Universiti Kebangsaan Malaysia, Kuala Lumpur, Malaysia, [2]Research Laboratory LR12SP18 "Autoimmunity, Cancer, and Immunogenetics", University Hospital Habib Bourguiba, Sfax, Tunisia, [3]Pathology Department, Faculty of Medicine, Universiti Kebangsaan Malaysia, Kuala Lumpur, Malaysia

Introduction: Plenty of biomaterials have been studied for their application in skin tissue engineering. Currently, gelatin-hydrogel is used to support three-dimensional (3D) skin *in vitro* models. However, mimicking the human body conditions and properties remains a challenge and gelatin-hydrogels have low mechanical properties and undergo rapid degradation rendering them not suitable for 3D *in vitro* cell culture. Nevertheless, changing the concentration of hydrogels could overcome this issue. Thus, we aim to investigate the potential of gelatin hydrogel with different concentrations crosslinked with genipin to promote human epidermal keratinocytes and human dermal fibroblasts culture to develop a 3D-*in vitro* skin model replacing animal models.

Methods: Briefly, the composite gelatin hydrogels were fabricated using different concentrations as follows 3%, 5%, 8%, and 10% crosslinked with 0.1% genipin or non-crosslinked. Both physical and chemical properties were evaluated.

Results and discussion: The crosslinked scaffolds showed better properties, including porosity and hydrophilicity, and genipin was found to enhance the physical properties. Furthermore, no alteration was prominent in both formulations of CL_GEL 5% and CL_GEL8% after genipin modification. The biocompatibility assays showed that all groups promoted cell attachment, cell viability, and cell migration except for the CL_GEL10% group. The CL_GEL5% and CL_GEL8% groups were selected to develop a bi-layer 3D-*in vitro* skin model. The immunohistochemistry (IHC) and hematoxylin and eosin staining (H&E) were performed on day 7, 14, and 21 to evaluate the reepithelization of the skin constructs. However, despite satisfactory biocompatibility properties, neither of the selected formulations, CL_GEL 5% and CL_GEL 8%, proved adequate for creating a bi-layer 3D *in-vitro* skin model. While this study provides valuable insights into the potential of gelatin hydrogels, further research is needed to address the challenges associated with their use in developing 3D skin models for testing and biomedical applications.

KEYWORDS

gelatin hydrogel, 3D *in vitro* skin model, genipin, keratinocytes, fibroblasts, biomaterial

1 Introduction

Tissue engineering is defined as a new branch of knowledge that combines technologies from different research areas including biology, chemistry, engineering, medicine, pharmacy, and material science (Bas et al., 2021). In addition to the potential to solve the current health issue of organ and tissue failure, this multidisciplinary field can provide advanced *in vitro* model systems. Indeed, the importance of enhancing the physiological relevance of *in vitro* systems and expanding their applications has increased exponentially to replace animal experiments as well as many other applications. Therefore, intensified efforts have been made toward systematic development and evaluation of relevant, reliable and more robust non-animal models.

The first attempts in alternative testing are based on the three Rs (3R principles, i.e., replacement, reduction, and refinement) (Russell and Burch, 1960). The 3Rs philosophy promotes the quest for 1) the replacement of animals with non-living models, 2) the reduction in the use of animals, and 3) the refinement of animal use practices. In this context, the Organization for Economic Cooperation and Development (OECD) allowed *in vitro* procedure that may be used for the hazard identification of irritant chemicals. It is based on reconstructed human epidermis (RhE), which in its overall design closely mimics the histological, morphological, biochemical, and physiological properties of the upper parts of the human skin (Organisation for Economic Co-operation and Development, 2020); (Organisation for Economic Co-operation and Development, 2015). This alternative approach has been thoroughly evaluated, validated and approved as a successful alternative for animal experimentation.

The three-dimensional (3D) *in vitro* models are an advanced approach to develop a full-thickness skin models that shows significant potential to evidently advance the engineering of skin replacements. Indeed, two examples of verified 3D models that are offered for sale commercially are the EpiDerm (MATTEK, 2020) skin model and the EPISKIN (LOREAL, 2020). Thus far, plenty of materials have been studied for their application in skin tissue engineering. Among these materials, a widely employed biomaterial in this field is gelatin, a protein obtained by partially hydrolyzing collagen, the main protein found in the skin, bones and white connective tissues of animals (Imeson, 1992). Besides the fact that gelatin has therapeutic properties for drug research or drug delivery, it also plays an important role in tissue engineering. Specifically, since it has the ability to create 3D porous structures in which cells can grow, this biomaterial can imitate *in vivo* microenvironment conditions. In fact, gelatin has been used to culture different cancer and stromal cells (Nii, 2021), (Ertekin et al., 2022), (Nii et al., 2020).

Currently, gelatin-hydrogel is used to support skin regeneration (Yehkung et al., 2011); (Nicodemus and Bryant, 2008); (Hoffman, 2012). Zhao et al. (2016) and co-workers revealed that the mechanical and degradation properties of a developed gelatin hydrogel can be modified by changing the hydrogel concentration. Furthermore, all concentrations of hydrogel showed excellent cell viability (>90%) with increases in cell adhesion and proliferation that is proportional to the gelatin hydrogel concentration (Zhao et al., 2015). Additionally, the hydrogel is found to support keratinocytes growth, differentiation, and stratification into a reconstructed multilayered epidermis with adequate barrier functions (Zhao et al., 2016). The properties of this hydrogel suggest that the keratinocytes/fibroblasts filled hydrogels can be used as epidermal substitutes, wound dressings, or substrates to construct various *in vitro* skin models. Epidermal keratinocytes and dermal fibroblasts that interact together can actively participate in cutaneous immune responses and are two of the major cell types that respond to the inflammatory phase in the cutaneous repair/regeneration process. Despite the promising results, it is still hard to mimic the human body conditions and properties and the gelatin-hydrogel suffers from poor mechanical properties and high degradation rate that maybe not suitable for 3D *in vitro* keratinocytes and fibroblasts culture and new 3D *in vitro* models need to be validated. To improve mechanical features of our gelatin hydrogels, we used genipin as a natural crosslinker. Genipin is a molecule extracted from the fruit of the gardenia plant that has been used to crosslink a variety of protein and polysaccharide matrices, including gelatin for drug-delivery applications (Liang et al., 2003); (Wei et al., 2007); (Dare et al., 2009); (Ko et al., 2009).

In short, gelatin may serve as an effective platform to support culture systems, which is a step towards the design of more accurate 3D *in vitro* skin models and it paves the way for investigating the performance of a wide range of chemical and pharmaceutical safety assessment in the future on in vivo-like and animal-free approaches. Hence, this study aims to characterize the physical-chemical parameters for gelatin hydrogel crosslinked with genipin and to evaluate the biocompatibility of the engineering 3D keratinocytes and fibroblasts culture seeded on bioscaffold prior to the formation of a matured bilayer co-culture for future application *in vitro* 3D skin model.

2 Materials and methods

2.1 Fabrication of gelatin hydrogel crosslinked with genipin

Gelatin hydrogel was fabricated from Nitta gelatin powder (Nitta Gelatin Inc®, Japan). The gelatin was mixed with distilled water with a magnetic stirrer until homogenized at 250 rpm at 40°C for 30 min to remove air bubbles and to completely blend after adding the genipin (FUJIFILM Wako Pure Chemical Corporation®, Japan). Then, 2 mL of the gelatin mixture was added to each well of a 12-well plate. The mixture was incubated at room temperature to initiate gelation to form the 3D constructs, which were termed gelatin10%-genipin0.1% (CL_GEL10%), gelatin8%-genipin0.1% (CL_GEL8%), gelatin5%-genipin0.1% (CL_GEL5%) and gelatin3%-genipin0.1% (CL_GEL3%) ($n = 3$, $N = 3$). Gelatin non crosslinked was used as control (NC_GEL10%), (NC_GEL8%), (NC_GEL5%), and (NC_GEL3%).

The gross morphology and microstructure of CL_GEL5% and CL_GEL8% constructs were observed via scanning electron microscopy (SEM; Quanta FEG 450, FEI; Eindhoven, North Brabant, Netherlands). The SEM analysis was performed to show the characteristics of the surface and porosity of different groups.

2.2 Physical and chemical characterization

2.2.1 Porosity of gelatin hydrogel

The percentage of porosity of the gelatin hydrogel was measured by the below formula (School of Chemical Engineering, 2019). The measuring cylinder with the ethanol was recorded as V. The initial weight of the lyophilized gelatin hydrogel was recorded as *Wd*. The final weight of the immersed gelatin hydrogel in the 99.5% ethanol after 24 h was recorded as *Ws*.

$$Porosity\ (\%) = \frac{Ws - Wd}{\rho \, x \, V} X\ 100\%$$

Where ρ = density of absolute ethanol.

2.2.2 Swelling ratio

The formula below was used to calculate how much volume of water the gelatin hydrogel can absorb. The bio-scaffold was weighed in a dry condition (*Wd*). After dry weight, the bio-scaffold was immersed into the phosphate buffer saline (PBS 1X, pH 7.4) for 6 h. The wet bio-scaffold (*Ws*) was weighed and recorded at a constant time period (Maji et al., 2016).

$$\text{Swelling ratio (S)} = \frac{Ws - Wd}{Wd} X\ 100\%$$

2.2.3 Biodegradation

To observe the degradation of the gelatin hydrogel, the gelatin hydrogel was weighed first (W_0) after pre-freezing at −80°C for 6 h and freeze-drying. The gelatin hydrogel was immersed in the diluted enzyme 0.0006% collagenase type I (Worthington®, NJ, United States) prepared in phosphate buffer saline (PBS 1X) and recorded in three different times 2, 4, and 24 h (t), which imitated the human body's enzyme. After that, the gelatin hydrogel was washed using distilled water and pre-freeze at −80°C. The gelatin hydrogel underwent the freeze-drying process and its final weight was measured (W_t). The biodegradation rate and the weight loss were calculated by using the following formulas:

$$\text{Degradation rate (mg/h)} = (W_0 - W_t)/t$$
$$\text{Weight Loss (\%)} = [(W_0 - W_t)/W_0] \times 100$$

2.2.4 Degree of crosslinking

The ninhydrin assay (Sigma-Aldrich®, Saint Louis, MO, United States) was used to determine the degree of crosslinking of the sample. 10 mg of the sample and 200 µL of ninhydrin reagent were added into a clean test tube. After the vortex, the sample which was covered by the aluminum foil was boiled for 2 min. The sample was cooled before 200 µL of 95% ethanol was added into the test tube. We used the spectrophotometer reader (Bio-Tek®, Power Wave XS, Boston, United States) at 570 nm to measure the absorbance of the sample and we compared the control sample without crosslinking and the sample with crosslinking by using the ninhydrin assay.

2.2.5 Contact angle

The gelatin hydrogel solutions were put on the glass slide and dried overnight. A water droplet was dropped on the glass slide in order to measure the angle of the gelatin hydrogel in contact with the surface of the glass slide by using ImageJ software (National Institute of Health, V1.5, Bethesda, MA, United States) to determine the surface wettability.

2.2.6 Compression and resilience

The formulas below were used to calculate the compression ratio and the resilience ratio. The gelatin hydrogel was compressed using a tensile testing analyzer (Instron, Norwood, MA, United States) and then released in water for 5 min to observe the resilience. The hydrogel was compressed and released 3 times which needed to take a picture for every time.

$$\text{Compression ratio (C\%)} = (A_i - A_c / A_i)\ x\ 100$$
$$\text{Resilience ratio (R\%)} = (A_f / A_c)\ x\ 100$$

Where, A_i: Area of thickness before compression. A_c: Area of thickness after compression; A_f: Area of thickness after resilience.

2.2.7 Fourier transform infrared spectrometry

The chemical structure of the constructs was characterized using Fourier transform infrared spectrometry (FTIR) (IR Prestige-21, Shimadzu®, Kyoto, Japan) through functional group identification. The CL_GEL5% and CL_GEL8% constructs were prepared as described above, and the FTIR spectra of the constructs (n = 1) was recorded in the frequency range of 600–4,000 cm^{-1}. The data were analyzed using Shimadzu IR Solution FTIR (spectroscopy) software (Shimadzu®).

2.2.8 X-ray diffraction

The crystallographic structure analysis of the CL_GEL5% and CL_GEL8% biomaterials was performed by X-ray diffractometer (Bruker®, D8 Advance, United Kingdom) with diffraction angle (2θ) in the range of 0° to 80°. The obtained diffractogram was evaluated by using the integrated software (Diffrac. Suite EVA, V4.0, Bruker®, Coventry, United Kingdom).

2.3 Biocompatibility characterization

2.3.1 Cell isolation and culture (keratinocytes and fibroblasts)

The six patients underwent abdominal surgery. The redundant skin samples were collected at Hospital Canselor Tuanku Mukhriz (HCTM) (Ethics approval number: UKM 1.5.3.5/244/FF-2015-376). The sample collection based on the inclusion and exclusion criteria listed in Table 1.

After collecting the redundant skin samples from patients who underwent abdominal surgery, the unwanted materials such as hair, fat, and debris were cleaned from the 3 cm^2 of skin samples. The samples were cut into a few small pieces with approximately 2 mm^2. The cut pieces were incubated with 0.6% of collagenase type 1 (Worthington®, NJ, United States) in the 37°C for digestion for 2–4 h. The cells were dissociated or degraded by using 0.05% of Trypsin-EDTA (Gibco®, CA, United States) for 8–10 min. The human epidermal keratinocytes (HEKs) and human dermal fibroblasts (HDFs) contained in the digested skin were resuspended in the co-culture medium at a 1:1 ratio (a mixture

TABLE 1 Inclusive and exclusive criteria.

Inclusive criteria	Exclusive criteria
• The patient needs to do the abdominal surgery	• Severe infections and/or ongoing antibiotic treatment
• Age is between 11 and 60 years old	
• The patient does not suffer from any chronic diseases	

of HEKs growth medium; Epilife® (Gibco®, NY, United States) and HDF growth medium; F-12:Dulbecco's Modified Eagle Medium (Gibco®, United States) supplemented with 10% fetal bovine serum (FBS; Biowest®, MO, United States) (FDC). In the six-well culture plate, we seeded the medium in three wells that the surface area is 9.6 cm^2/well at 37°C in 5% CO_2. By using the differential trypsinization, the fibroblasts were separated from the co-cultured keratinocytes after the waste medium reached 70%–80% confluence. The detached fibroblasts were re-cultured with FDC in a T75 flask. The keratinocytes were propagated in a six-well culture plate and the desired number of cells was obtained by the sub-culture fibroblasts and keratinocytes for further analysis. Three technical replicates were performed for each biological replicate.

2.3.2 Cell attachment

HDFs (5×10^4) and HEKs (15×10^4) were seeded on hydrogels of different formulations, which were presoaked in F12: DMEM (Gibco®, NY, United States) and Epilife® (Gibco®, NY, United States) with supplements, respectively, overnight. The cells were allowed to attach at 37°C with 5% CO_2. The hydrogel was washed gently with Dulbecco's Phosphate Buffer Saline (DPBS) (Sigma®, MO, United States) after 24 h. The remaining (unattached) cells in DPBS were counted using a hemocytometer and 0.4% trypan blue solution (Sigma®, MO, United States). The percentage of cell attachment was calculated as per the equation below:

Cell attachment (%) = [(Initial cell seeding – number of cells in DPBS)/Initial cell seeding] x 100.

2.3.3 Cell toxicity assessment

Cytotoxicity test was performed towards HEKs and HDFs via LIVE/DEAD cytotoxicity assay for mammalian cells (Thermo Fisher Scientific®, MA, United States). The hydrogels were fabricated in a 48-well culture plate by using sterile gelatin and genipin solution. Immediately after polymerization, 5×10^4 HDFs and 15×10^4 HEKs at passage three (P3) were seeded on the top of hydrogel prior to the incubation for 24 h. Cell toxicity was examined by using a fluorescence microscope (Nikon® A1R-A1, Japan) at ×10 magnification after treatment with 500 μL of a mixture of 2 mM acetomethoxy derivative of calcein (calcein-AM) and 4 mM ethidium homodimer-1 (EthD-1) at 37°C for 30 min.

2.3.4 Viability and proliferation evaluation

The viability and proliferation of HEKs and HDFs were evaluated by using 3-(4,5-dimethylthiazol-2-yl)-2,5-diphenyltetrazolium bromide (MTT) (Thermo Fisher Scientific®, MA, United States). Briefly, 5×10^4 HDFs and 15×10^4 HEKs at P3 (Nike et al., 2021); (Xi Loh et al., 2018) were seeded on the top of hydrogel according to the protocol previously described elsewhere (Masri et al., 2023); (Mh Busra et al., 2019) and MTT reagent was added after 1, 3, 5 and 7 days of incubation prior to the dimethyl sulfoxide (DMSO) addition as dissolution reagent. The absorbance was recorded by using a spectrophotometer reader (Bio-Tek®, Power Wave XS, Washington, United States) at 540 nm at specific time intervals. The cellular viability at day 1 was used as an indicator of the efficiency of HDFs and HEKs attachment. The total number of cells was calculated using the standard curve.

2.3.5 Cell migration

The migration ability of the HDFs and HEKs in 3D hydrogels was evaluated by using gelatin-hydrogel models in which cells were seeded. The net migration of the cell population was measured from an upper chamber to a lower chamber through a microporous membrane. Subsequently, a 1 cm^2 of each hydrogel was used for cell seeding in 48 well-plates. The cells were stained with blue cell tracker (Hoescht dye, Invitrogen®, MA, United States) and green cell tracker (Green dye, Invitrogen®, MA, United States) and incubated for 30 min in 37°C. HDFs and HEKs were stabilized for 2 and 24 h, respectively. Next, 5×10^4 HDFs and 15×10^4 HEKs stained with green dye were seeded on the top of the scaffolds of each group and 5×10^4 HDFs and 15×10^4 HEKs stained with blue dye were seeded in 48-well plate. The fluorescent dye retained in the cells allowing for multigenerational tracking of cellular movements. Meanwhile, the gelatin-cells constructs were monitored at day 1, 3, 5 and 7 to observe the cell migration from the transplanted site to the surrounding matrix. Cell migration images were captured using Nikon A1R confocal microscope (Nikon®, Japan), and cell migration distances from the hole edge to the cell outgoing front in all directions were measured via image analysis software (ImageJ) (National Institute of Health, V1.5, MA, United States). Afterward, the average migration distance was calculated for statistical analysis.

2.3.6 Immunocytochemistry staining for proliferative cells

Keratinocytes and fibroblasts were fixed with 4% paraformaldehyde (Sigma-Aldrich®, MO, United States) for at least 15 min, permeabilized with 0.1% Triton X-100 solution (Sigma-Aldrich®, MO, United States) for 20 min, and blocked with 10% goat serum (Sigma-Aldrich®, MO, United States) for 1 h at 37°C. Next, the cells were incubated with mouse collagen type 1 monoclonal antibody (COL-I) (Abcam®, United Kingdom), rabbit alpha-smooth muscle actin antibody (α-SMA) (Abcam®, United Kingdom) and rabbit cytokeratin 14 antibody (CK-14) (Abcam®, United Kingdom) overnight at 4°C. On the next day, the cells were incubated with goat anti-mouse IgG Alexa Fluor 594 (Red-fluorescent dye, Invitrogen®, MO, United States) and goat anti-rabbit IgG Alexa Fluor 488 (Green-fluorescent dye, Invitrogen®, MO, United States) for 2 h at 37°C in dark. The cells then were counterstained with DAPI (Dako®, Denmark) for 20 min at room temperature and observed using Nikon A1R confocal microscope (Nikon®, Japan) for expression of collagen type 1, α-SMA and cytokeratin 14.

2.4 Develop a two-layer skin construct

2.4.1 Preparation of the two-layer skin construct

The ability of the fibroblasts and keratinocytes to migrate into a gelatin hydrogel was compared in four-time intervals (on days 1, 3, 5 and 7 after cell seeding) and the CL_GEL5% and the CL_GEL8% gelatin hydrogels were selected for the preparation of the two-layer skin construct. Thus, a two-layer cell construct was composed of a CL_GEL5% and CL_GEL8% gelatin hydrogel pre-seeded with HDFs. A 1.9 cm^2 of gelatin hydrogel samples were fitting into 12-well cell culture plates and seeded with HDFs. The fibroblasts were seeded on the scaffold at a density of 50,000 cells, (Nike et al., 2021); (Mh Busra et al., 2019) and were cultivated in FD supplemented with 10% of FBS and 1% of antibacterial-antimycotic (Gibco®, China). After 3 days of fibroblast cultivation, the collagen hydrogel was prepared on the fibroblast-seeded membrane, and the fibroblasts started to migrate into the hydrogel. The keratinocytes were seeded at a density of 150,000 cells after 4 days of gelatin hydrogel preparation (already seeded with of fibroblasts). After the keratinocytes had been seeded, the medium was replaced by FD and Epilife with supplements, as mentioned above. The medium was changed every 2 days. After 7, 14 and 21 days of fibroblast cultivation, the immunohistochemistry (IHC) and hematoxylin and eosin staining (H&E) were performed in order to evaluate the reepithelization of the skin constructs.

2.4.2 Hydrogel frozen section technique

The frozen section method is a rapid and efficient technique for soft tissue analysis. Using a cryostat, the portion of hydrogels (1 cm diameter) were immediately frozen. The freezing procedure normally takes a few minutes and preserves the original condition of the tissue. Next, using a microtome, the hydrogels were sliced into thin sections with 4 μm thickness. Sectioned hydrogels were subjected for hematoxylin and eosin (H&E) and immunofluorescent (IF) staining to make them visible under microscope.

2.4.3 Hematoxylin and eosin staining

The H&E staining was used to detect the nucleus and extracellular matrix (ECM) protein, allowing the identification of structural features of the epidermis and dermis layer. The H&E staining was carried out according to standard protocol. The hydrogel samples were first fixed in a solution such as 10% formalin, to preserve the hydrogels. First, the hydrogel samples were embedded in optimal cutting temperature (OCT) compound and snap-frozen in liquid nitrogen or dry ice. The frozen tissue block was then sectioned using a cryostat to a thickness of 4 μm and left for air dried. The hydrogel-sectioned slides were then dipped in H&E solution for 5–10 min. Next, the slides were then rinsed in distilled water and immersed in eosin solution for 30 s. Following that, the slides were rinsed with distilled water again before being dehydrated with graded alcohol solutions (70%, 90%, and 100% ethanol). Lastly, the slides were cleaned using xylene, and mounted with a coverslip using a mounting medium and ready to be observed under light microscope.

2.4.4 Immunofluorescent staining

IHC was carried out using specific markers, cytokeratin 14 and collagen type 1 (Abcam®, MA, United States) to evaluate, respectively, the regenerated skin's maturity for keratinocytes and the fibroblasts maturity. The hydrogels were then sectioned with a cryostat and mounted on glass slides. The fixed tissue sections were then blocked with 10% goat serum (Sigma Aldrich®, MO, United States) to prevent non-specific binding of the primary antibody. The tissue sections were incubated with a primary antibody that specifically binds to the protein of interest. The tissue sections are then incubated with a secondary antibody that recognizes the primary antibody Alexa 488 (Abcam®, MA, United States). The labelled secondary antibody is detected using fluorescence microscopy. Finally, the tissue sections counterstained with DAPI to visualize the nuclei and provide morphological context.

2.5 Statistical analysis

The quantitative results were shown as mean ± standard error mean (SEM). Statistical analyses were performed using GraphPad Prism 7.0 (GraphPad Software, United States) and the results were analyzed using one-way analysis of variance (ANOVA). The difference between groups is significant if $p < 0.05$.

3 Results

3.1 Characterization of hydrogels

3.1.1 Gross appearance

The gelatin hydrogel scaffolds were fabricated with four different concentrations of gelatin crosslinked or non-crosslinked with genipin, respectively (CL_Gel 10%—CL_GEL 8% - CL_GEL 5% and CL_GEL 3%) and (NC_Gel 10% - NC_GEL 8% - NC_GEL 5% and NC_GEL 3%). Figure 1A shows the gross appearance of gelatin hydrogel with or without crosslinking. The scaffold crosslinked with genipin showed a greenish blue color as compared to the non-crosslinked one. In contrast, the non-crosslinked hydrogel showed a transparent structure. The crosslinked hydrogel was semi-solid gel and showed a smooth surface. The structure of the gel appeared to be more solid in the scaffolds with the highest concentration of gelatin. The same observation was observed in the non-crosslinked groups. Despite using the same material, these scaffolds vary in their gross appearance.

3.1.2 Swelling ratio

The swelling ratio was determined as shown in Figure 1B. The NC_GEL 3% hydrogel scaffold demonstrated the best swelling property (2268.63 ± 136.9%) compared to the other experimental groups followed by the NC_GEL 5% (1556.05 ± 120.98%) and the CL_GEL 3% (1079.52 ± 38.42%). Meanwhile, the NC_GEL 10% hydrogel had the poorest swelling property (633.22 ± 27.4%),

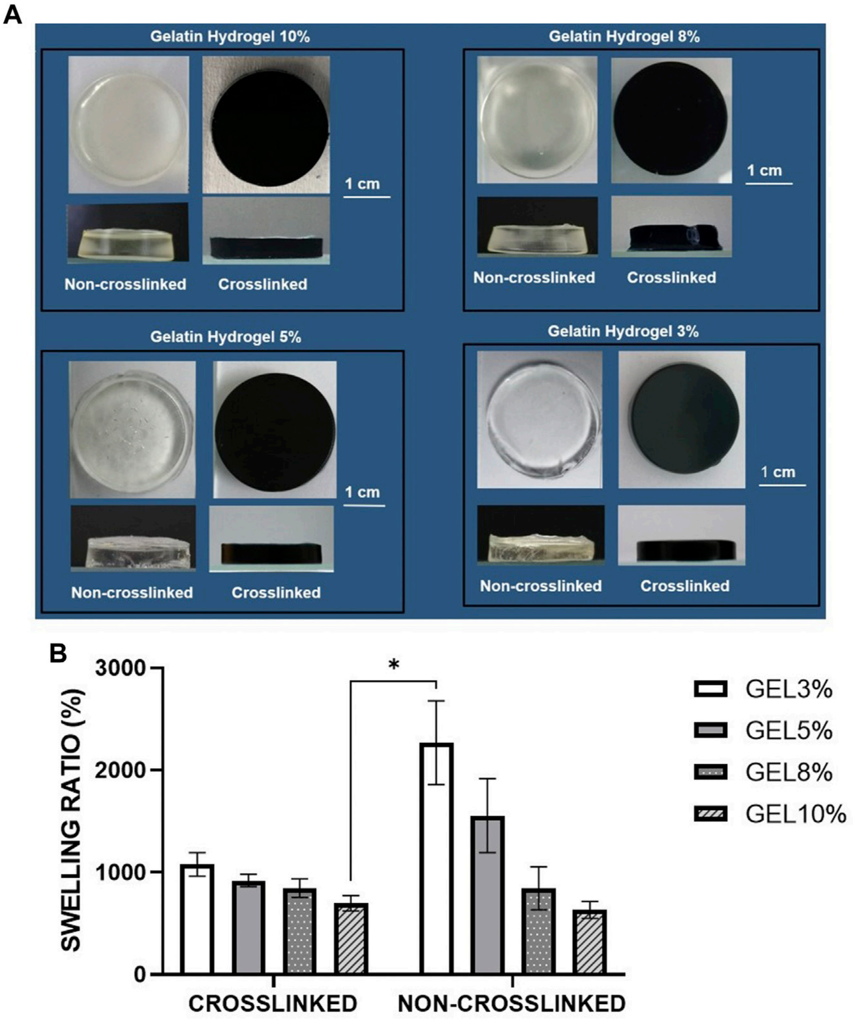

FIGURE 1
(A) Gross appearance of different gelatin hydrogel groups (3%,5%,8%, and 10%) non-crosslinked and crosslinked with 0.1% genipin at room temperature (22°–24°C). The crosslinked groups with 0.1% genipin showed greenish blue color while the non-crosslinked groups showed transparent structure. **(B)** Physical evaluation: swelling ratio of gelatin hydrogel scaffolds, i.e., GEL3%, GEL5%, GEL 8%, and GEL10% with and without genipin crosslinking. The non-crosslinked groups demonstrated higher swelling properties compared to crosslinked groups. *Represents the significant difference between crosslinked and non-crosslinked hydrogel (N = 3, *n* = 3).

followed by CL_GEL 10% (698.52 ± 24.88%) and NC_GEL 8% (844.40 ± 70.52%). As the ratio of the polymers in the hydrogel was changed, keeping the crosslinker constant, swelling is increased. It was also found that the sample was unstable in the aqueous solution and was challenging to handle. It can be easily observed by the large error bars especially in the non-crosslinked groups.

One of the desired properties that plays a crucial role in cell adhesion and development as well as transfer of nutrients and metabolites via the hydrogel (Rodríguez-Vázquez et al., 2015), is water permeability. It was reported that the ability of the bioscaffold to absorb fluid 80 times over its initial weight is adequate for skin tissue engineering (Luangbudnark et al., 2012). The hydrogel concentration in our study caused a growing proportion of swelling in all constructions where the ability of CL_GEL8% to swell was almost 100 times over its initial weight, which is consistent with the gelatin's microporous structure and porosity.

3.1.3 *In vitro* biodegradation

Given that cells seeded in a hydrogel may secrete several proteases, such as collagenase, which could lead to hydrogel degradation, the degradation performance of gelatin hydrogel was evaluated. The degradation test was carried out in all groups. The biodegradation rates of the scaffolds were evaluated using the enzymatic degradation approach, as shown in Figure 2A. The non-crosslinked scaffolds (NC_GEL10%, NC_GEL8%, NC_GEL5%, and NC_GEL3%) together, were able to degrade faster (59.59 ± 1.45 mg/h) than crosslinked gelatin hydrogels (CL_GEL10%, CL_GEL8%, CL_GEL5%, and CL_GEL3%) together (2.58 ± 0.47 mg/h). The addition of genipin was able to decrease the degradation rate in the scaffolds dramatically. The weight loss test was carried out in all groups as shown in Figure 2B. After 2 h, the weight loss of the non-crosslinked groups was (69.85% ± 3.68%), and (83.97% ± 2.3%) in NC_GEL10% and NC_GEL8%, respectively and after 24 h, the weight

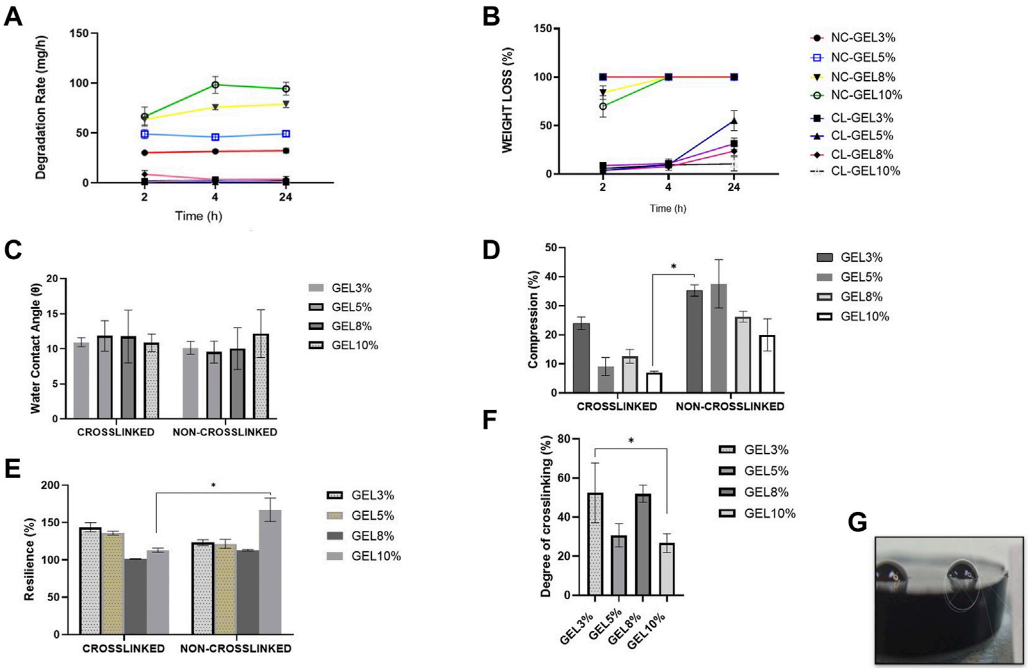

FIGURE 2
(A) Biodegradation rate and **(B)** weight loss at 37°C of the fabricated scaffolds compared to control at various times (2, 4, and 24 h). **(C)** Water contact angle of the fabricated scaffolds at room temperature. **(D)** compression and **(E)** resilience properties of the different hydrogel formulations compared to control. **(F)** Degree of crosslinking of the fabricated scaffolds. **(G)** measurement of water contact angle with ImageJ software * Represents the significant difference between groups.

loss of the non-crosslinked groups was 100%. After 2 h, the highest weight loss percentage in crosslinked group was in CL_GEL3% (8.87% ± 0.53%) and the lowest value was in CL_GEL8% (3.72% ± 0.17%). After 4 h, the CL_GEL3% registered the highest value of weight loss (10.94% ± 0.38%) and CL_GEL8% (7.61% ± 0.29%) registered the lowest value. And after 24 h, the CL_GEL5% showed the highest value (55.15% ± 3.41%) followed by CL_GEL3% (31.27% ± 1.96%) and CL_GEL8% (23.62% ± 1.52%) and CL_GEL10% (10.49% ± 2.39%). It seems that, the gelatin hydrogel concentration significantly helps in decreasing the weight loss. Comparing the crosslinked groups, the increase of gelatin hydrogel concentration helps in slowing down the weight loss process in crosslinked formulation.

Another way to improve the mechanical properties of the hydrogels is by using biodegradable synthetic scaffolds. The biodegradable hydrogel would serve as a substrate for the initial attachment and growth of fibroblasts and keratinocytes (MacNeil, 2007). Our results showed that the gelatin hydrogel concentration was found to significantly help in decreasing the weight loss, which indicates the possibility to control the degradation rate by changing the hydrogel formulation as reported by Zhao et al. (2016) and coworkers. Also, the addition of GNP as a crosslinker was able to decrease dramatically the degradation rate in the scaffolds. The same results were reported by Mh Busra et al. (2019); Ke et al.; Ren et al. (2017). For skin tissue engineering, it follows that the scaffold degradation rate coincides with the generation rate of new skin (Nam et al., 2012); (Branco da Cunha et al., 2014).

3.1.4 Contact angle

The water contact angle (Figure 2G) is important for determining hydrogel hydrophilicity or hydrophobicity, an essential factor in drug delivery, cell proliferation and adherence. The contact angle results of all groups are shown in Figure 2C. The contact angle revealed a range from (12.1° ± 1.2°) to (9.5° ± 0.9°). No significance association was found among the groups. This shows that our scaffolds have very hydrophilic properties.

3.1.5 Compression and resilience

The compression and resilience results of all groups are shown in Figures 2D, E, respectively. The NC_GEL5% showed the highest value in compression, without a significant difference, compared to other groups with (37.5% ± 4.7%). The lowest value was recorded in CL_GEL10% (7.03% ± 0.2%) followed by CL_GEL5%, and CL_GEL8% with (9.1% ± 1.7%) and (12.6% ± 1.3%), respectively. The NC_GEL10% recorded the highest resilience value with (167.3% ± 8.9%) followed by CL_GEL3% (143.7% ± 3.5%) and CL_GEL5% (135.9% ± 1.4%). The lowest resilience value was in CL_GEL8% (101.4% ± 0.2%) followed by NC_GEL8% (113% ± 0.6%). All groups represent a high resilience value superior than 100%.

The appropriate mechanical stability and the ability of the scaffolds to resemble the skin stiffness are crucial to select the appropriate biomaterial (Nam et al., 2012), (Xie et al., 2017). In the current study, the compression tests showed compression values between 7% and 37% in CL_GEL5%, CL_GEL8%, and CL_GEL10%, which suggest that gelatin concentration plays a crucial

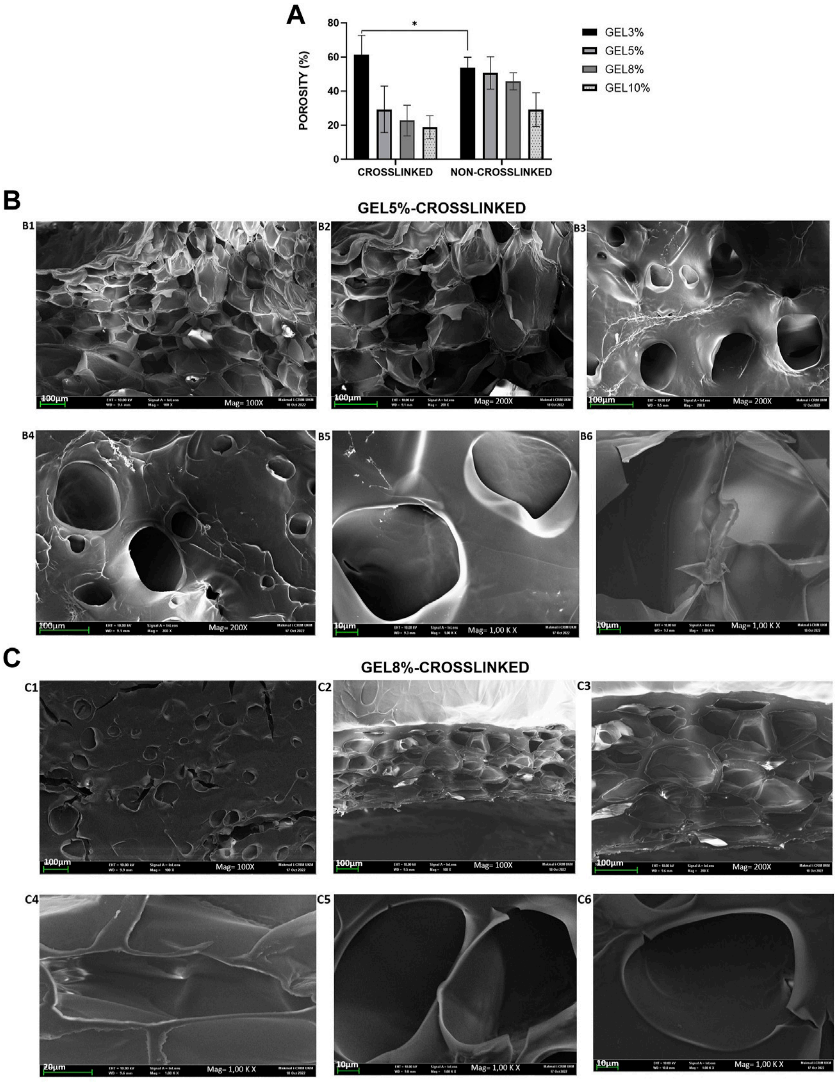

FIGURE 3
(A): Physical evaluation: porosity of gelatin hydrogel scaffolds non-crosslinked and crosslinked, i.e., GEL3%, GEL5%, GEL 8%, and GEL10%. Overall, the non-crosslinked groups demonstrated higher porosity properties compared to crosslinked groups. **(B)** View under scanning electron microscope of **(B)** CL_Gel5% at magnification of ×100, scale 100 µm (B1); magnification of ×200, scale 100 µm (B2–B4); and magnification of 1.00 K X, scale 10 µm (B5-B6). **(C)** View under scanning electron microscope of CL_Gel8% at magnification of ×100, scale 100 µm (C1-C2); magnification of ×200, scale 100 µm (C3); magnification of 1.00 KX, scale 20 µm (C4) and); magnification of 1.00KX, scale 10 µm (C5-C6).

role in improving mechanical strength. It has been reported that fibroblasts show thick stress fibers when cultured on rigid substrate compared to soft scaffolds where the stress fibers are less thick or even absent (Nam et al., 2012), (Xie et al., 2017). All groups had resilience rates more than 100. High resilience shows optimum hydrogel elasticity, which is desired for shape recovery during application to maintain its efficacity (Liu et al., 2016). Resilience and adhesive force properties could be improved with GNP crosslinking by creating an intermolecular bridge between gelatin molecules through the covalent bond (Kirchmajer et al., 2013), (Arif et al., 2020). The crucial contribution of gelatin hydrogels towards strengthening mechanical properties has also been demonstrated in previous studies (Rodríguez-Rodríguez et al., 2019), (Arif et al., 2020).

3.1.6 Degree of crosslinking

The degree of crosslinking results of all groups are shown in Figure 2F. The results show that the CL_GEL3% has the highest degree of crosslinking followed by the CL_GEL8% with (52.49% ± 8.8%) and (52.02% ± 2.5%), respectively. The poorest degree of crosslinking was recorded in the CL_GEL10% followed by CL_GEL5% with (26.76% ± 2.7%) and (30.72% ± 3.4%), respectively.

3.1.7 Porosity and scanning electron microscope

The porosity, which is the percentage of void volume in a material, was determined as shown in Figure 3A. The CL_GEL 3% hydrogel scaffold demonstrated the highest porosity property (66.88% ± 5.76%) compared to the other experimental groups followed by the NC_GEL 3% (53.81% ± 2.03%) and NC_GEL 5%

(50.68% ± 3.18%). Meanwhile, the CL_GEL 10% (18.87% ± 2.22%) had the poorest porosity property, followed by the CL_GEL 8% (27.84% ± 5.54%).

The results of the scanning electron microscope (SEM) of CL_GEL5% and CL_GEL8% are shown in Figures 3B, C, respectively. SEM analysis showed that the CL_GEL 5% scaffold had interconnected pores with size range of 40–183 μm. The SEM analysis showed that the CL_GEL8% scaffold had interconnected pores with size range of 39–170 μm.

The biomaterial properties of the scaffolds are vital in determining the cells behavior and the full reepithelization of the tissue. Therefore, the 3D scaffolds should be highly porous with interconnected pores to enable the diffusion of oxygen, nutrient and the waste removal (Loh and Choong, 2013). According to earlier research, porous materials with a range within 20–125 μm are optimum to reconstruct adult skin (Sisso et al., 2020); (Rodríguez-Rodríguez et al., 2020); (El-Sherbiny and Yacoub, 2013) and pore sizes within 40–600 μm promote capillary ingrowth (Crowley et al., 2016); (de Mel et al., 2009). The SEM results of the CL_GEL5% and the CL_GEL8% show that the range of the pore sizes is within 40–183 μm and 39–170 μm; respectively, which is acceptable for tissue regeneration. However, The porosity of all four hydrogel formulations was between 18% and 60% this is fell short of several other biomaterials studied in the literature, which might approach 80%–90% porosity (Wang et al., 2016), (Mahboudi et al., 2015). The porosity and pore size determine the ultimate mechanical quality of the scaffold, which affects cell behavior (Mahboudi et al., 2015).

3.1.8 Energy dispersive X-Ray (EDX) composition analysis

The results of the energy dispersive X-Ray composition analysis of CL_GEL5% and CL_GEL8% groups are shown in Supplementary Figure S1A. Elemental study of CL_GEL5% and CL_GEL8% treatment groups revealed three main components, including nitrogen (N; 11%), carbon (C; 60%–80%), and oxygen (O; 25%–30%) in CL_GEL5%, and (C; 55%–60%), (N; 25%),(O; 10%–25%) in CL_GEL8%, as shown in Supplementary Figures S1A1, A2, respectively.

3.1.9 Fourier transform infrared spectrometry

The Fourier transform infrared spectrometry (FTIR) results of CL_GEL5% and CL_GEL8% are presented in Supplementary Figures S1B1, B2, respectively. The FTIR revealed 4 regions, the region A, B, C and D. The IR spectra of CL_GEL8% and CL_GEL5% showed similar absorbances resembling the Amide A (3,400–2,300 cm^{-1}), Amide I (1,600–1,650 cm^{-1}), Amide II (1,530–1,200 cm^{-1}), and Amide III (1,230–670 cm^{-1}). No major shift was prominent in FTIR spectra in both formulations after genipin modification as described in a previous study (Nike et al., 2021). Briefly, at the A region, the amine group attack O-H group. CL-GEL8% had highest O-H group (3,285.94 cm^{-1}) and lower crosslinking followed by CL_GEL5% (3,283.59 cm^{-1}). The region B and C showed that CL_GEL5% had the highest Amide I (1,631 cm^{-1}) and Amide II (1,544.78 cm^{-1}) followed by CL_GEL8% (Amide I (1,629.55 $cm^{-1)}$) (Amide II (1,541.58 cm^{-1}). At region D, both CL_GEL5% and CL_GEL8% presented almost the same level of Amide III (1,238.32 cm^{-1} and 1,238.72 cm^{-1}), respectively**.**

3.1.10 X-ray diffraction

The X-ray diffractogram of fabricated hydrogels demonstrated almost similar patterns for both CL_GEL5% and CL_GEL8% treatment groups as shown in Supplementary Figures S1C1, C2, respectively. All diffractograms represented a broad peak at 2θ in between 10° to 50°. The XRD patterns for CL_GEL5% described CL_GEL8% due to similar gelatin initial stock except for its concentration. CL_GEL5% presented the highest percentage of crystallinity with 29.3% and 70.7% of amorphous followed by CL_GEL8% with 15.5% of crystallinity and 84.5% of amorphous. As expected, the EDX, FTIR and the XRD analysis demonstrated that GNP did not affect the native chemical properties of gelatin.

3.2 Biocompatibility characterization

3.2.1 Cell isolation and culture (keratinocytes and fibroblasts)

The primary culture of human epidermal keratinocytes and human dermal fibroblast were successfully established from skin samples (Figure 4).

3.2.2 Cell attachment

HDFs and HEKs were seeded on top of the gelatin hydrogel scaffolds (CL_GEL3%, CL_GEL5%, CL_GEL8%, and CL_GEL10%), and the efficiency of cell attachment was evaluated at 24 h after seeding (Figures 5A1, B1). All groups showed a high attachment property and the CL_GEL 10% (98.75% ± 0.38%) scaffolds demonstrated the highest attachment of HEKs compared to other scaffolds followed by the CL_GEL 8% (98.16% ± 0.72%), CL_GEL 5% (97% ± 0.57%) and CL_GEL 3% (93.83% ± 0.44%). The same observation goes with the HDFs where the CL_GEL 10% showed the highest attachment property with (94.33% ± 4.66%) followed by CL_GEL 8% (89.33% ± 1.7%), CL_GEL 5% (78% ± 4%) and CL_GEL 3% (76.33% ± 4.33%). The attachment properties of the gelatin hydrogel scaffolds increased proportionally with the concentration of gelatin. Additionally, the scaffolds with different formulations presented a higher attachment property for HEKs than HDFs.

Our fabricated 3D gelatin hydrogel showed favorable characteristics in terms of stability and in supporting the attachment of HDFs and HEKs as expected. The properties that may affect cell attachment like hydrophilicity, pore size, surface roughness, were almost similar between the different formulations and were favorable for cell attachment. This suggests that the gelatin hydrogel exhibits rapid cell attachment as more than 90% of HEKs and HDFs are already attached after 24 h. The excellent attachment rate may be explained by the hydrophilicity of the hydrogel and the surface area reasonably available for the cells to attach as the porosity is rather low. This property is very important for cell function including cell spreading, migration and proliferation (Anselme et al., 2010).

3.2.3 Cell toxicity assessment

HEKs and HDFs were seeded on top of the gelatin hydrogel scaffolds, and the efficiency of cell attachment and viability were evaluated at 24 h after seeding as shown in Figures 5A4, B3, respectively. All groups showed a high attachment property and high viability. The CL_GEL 10% scaffolds demonstrated the higher

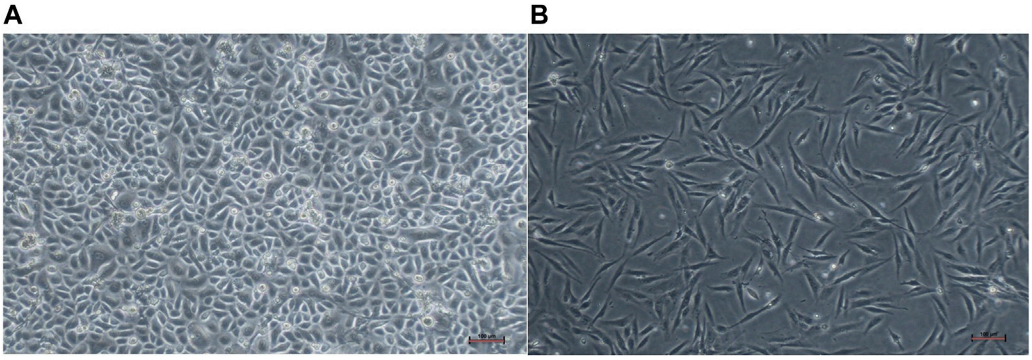

FIGURE 4
Monolayer cells cultured in 6-well plate: **(A)** culture of human epidermal keratinocytes (HEKs), and **(B)** human dermal fibroblasts (HDFs), The cultured cells became confluent in a week's time and fibroblasts were separated by differential trypsinization before seeding into a new flask. Scale bar: 100 μm, magnification ×4.

attachment and viability of HDFs compared to other scaffolds. All scaffolds demonstrated a high attachment and viability of HEK.

The results for the cell viability assay demonstrated a high number of live cells and a very low number of dead cells on all formulations of hydrogel, this confirms that the hydrogel supports cell viability and provides nontoxic 3D scaffolds.

3.2.4 Cell migration

The cell migration results of HEKs and HDFs are shown in Figures 5A2, B2, respectively. Figure 5A3 showed HEKs migrating from an upper chamber to a lower chamber (upper chamber cells stained in blue, migrated cells stained in green). HEKs and HDFs did migrate into the hydrogel as the cells did not and remained at the top surface on day 3, 5 and 7 unlike the first day where the cells seemed to be at the same level with the attached cells in the plate (upper chamber).

At the third day, the highest distance of migration in HEKs (μm) was recorded in CL_GEL3% followed by CL_GEL8% with (119.8 ± 2.01 μm) and (96.23 ± 3.8 μm). The lowest distance of migration was recorded in CL_GEL10% with (55.2 ± 1.7 μm). For HDFs, the CL_GEL3% showed the highest distance of migration with (359.29 ± 2.5 μm) followed by CL_GEL10% with (76.8 ± 1.4 μm) and the lowest migration distance for HDFs was recorded in CL_GEL5% with (72.3 ± 1.5 μm), but no significant difference was observed between CL_GEL5% and CL_GEL8%. The results showed a significant difference between CL_GEL3% and all other groups at the third day.

At the fifth day, HEKs showed the highest distance of migration in the hydrogel CL_GEL3% followed by the CL_GEL5% with (149.96 ± 3.1 μm) and (142 ± 3.7 μm), respectively. The lowest distance was recorded also in CL_GEL10% with (84.22 ± 1.8 μm). The results showed a significant difference among all the groups except for CL_GEL3% and CL_GEL5%. HDFs showed the highest distance of migration in the hydrogel CL_GEL3% followed by the CL_GEL5% with (374.66 ± 1.9 μm) and (206.36 ± 1.2 μm), respectively. The lowest distance was recorded in CL_GEL8% and CL_GEL10% with (79.02 ± 1.2 μm) and (80.58 ± 1.5 μm), respectively with no significant difference. The results show a significant difference among the other groups.

At the seventh day, the HEKs migrated the longest distance in CL_GEL5% followed by CL_GEL3% with (160.01 ± 3.9 μm) and (158.56 ± 2 μm), respectively with no significant difference, while the shortest distance was reported in CL_GEL10% with (99.74 ± 1.5 μm). All others groups showed significant difference. HDFs showed the highest distance of migration in the hydrogel CL_GEL3% followed by the CL_GEL5% and the CL_GEL8% with (390.75 ± 3.5 μm), (303.36 ± 1.6 μm), and (184.8 ± 1.2 μm), respectively. The lowest distance was recorded in CL_GEL10% with (84.34 ± 2.2 μm). The results showed significant difference among all groups.

Cell migration within scaffolds is crucial for skin tissue adaptation. The results of cell migration on different formulations were significantly different among groups. The CL_GEL3%, CL_GEL5%, and CL_GEL8%, showed positive results in cell migration after 7 days with a range of 390 μm, 303 μm and 184 μm in HDF and 158 μm, 160 μm, and 136 μm in HEK; respectively. It has been reported that the optimum pore size for fibroblasts is between 20 and 120 μm which goes along with our results in CL_GEL5% and CL_GEL8%. This suggests that the pore sizes within 39–170 and the pore size within 40–183 μm are suitable for HEKs and HDFs migration on gelatin hydrogel. The scaffolds should promote HEKs and HDFs adhesion and migration and allow the retention of metabolic functions of attached cells. However, The CL_GEL10% did not allowed the migration of HDFs and HEKs which may be due to the small pore sizes caused by the increasing of the gelatin concentration. This indicates that the CL_GEL10% is not suitable for cell migration. Oliveira Barud et al. (2015), reported that even with an average pore size of 102 ± 5.43, no noticeable migration of fibroblasts was observed on bacterial cellulose/50% fibroin scaffold and they suggest that this is due to the dense network that do not generate enough pore size to facilitate cell migration. We suggest also that the CL_GEL10% did not promote the HEKs and the HDFs, perhaps, because of the dense network created by gelatin-genipin hydrogel that does not possess enough pores with the suitable size for the cell migration compared to all other formulations. It is noteworthy that the HDFs migrate better than HEKs which could be due to their capacity to adapt.

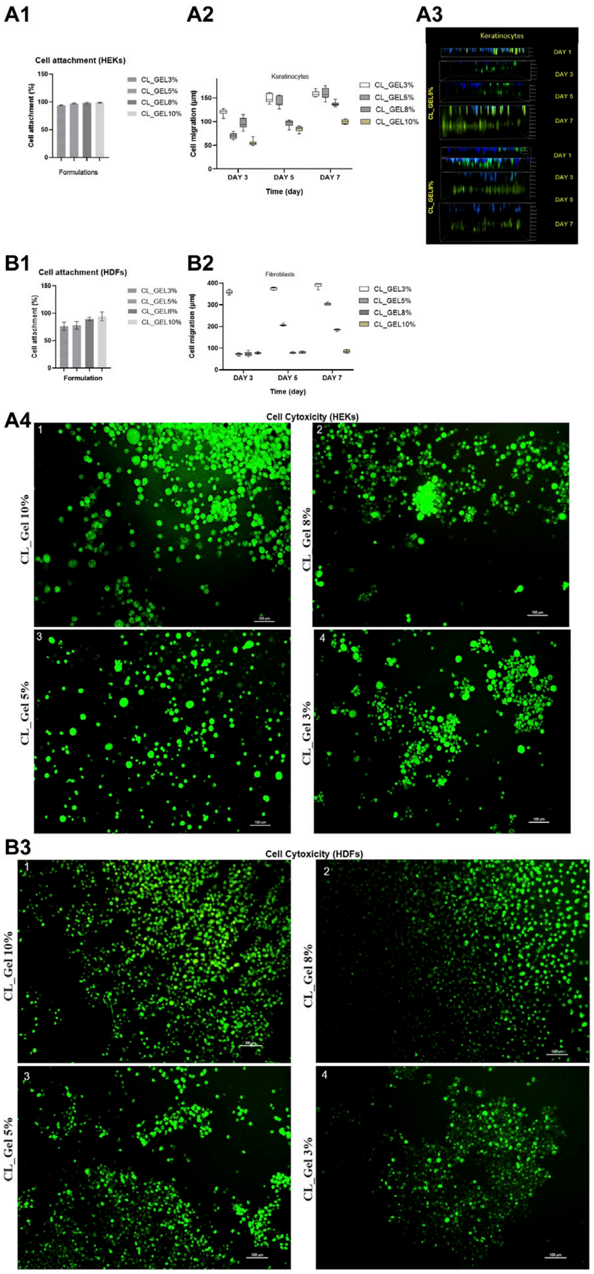

FIGURE 5
Cell attachment (%) of (A1): human epidermal keratinocytes (HEKs) and (B1): human dermal fibroblasts (HDFs) in CL_GEL3%, CL_GEL5%, CL_GEL8%, and CL_GEL10% formulations after 24 h. Cell migration (µm) of (A2) keratinocytes and (B2) fibroblasts of CL_GEL3%, CL_GEL5%, CL_GEL8%, and CL_GEL10% at various interval times (day 3, 5 and 7). (A3) Three-dimensional (3D) confocal image of cell migration (µm) on days 1, 3, 5 and 7 of CL_GEL5% and CL_GEL8% of keratinocytes (Green: cell tracker; Blue: Hoescht dye), the green color demonstrated that the cells are migrating from an upper chamber to a lower chamber through a microporous membrane. Live/dead staining of (A4) human epidermal keratinocytes (HEKs) and (B3) human dermal fibroblasts (HDFs) seeded on (1) CL_GEL10%, CL_GEL8%, CL_GEL5% and CL_GEL3%, after 24 h. The results revealed non-cytotoxic effect of gelatin hydrogel crosslinked with genipin. The green color demonstrated live (HEKs) and (HDFs) cells. Scale bar = 100 µm (10X). (Green: live cells; Red: dead cells).

3.2.5 Immunocytochemistry

HDF on both CL_GEL5% and CL_GEL8% revealed the positive expression of α-SMA (green); and collagen type 1 (red) as shown in Figures 6A2, A3, respectively. However, the number of α-SMA and collagen type 1 positive cells was low compared to that of total cells. In addition, if we compare the cell behavior on the hydrogel and on the 2-dimentional (2-D) cell culture control (Figure 6A1), the number of the adherent cells was significantly higher in the control in both groups. On the other hand, HEK on both scaffolds showed the presence of cytokeratin 14 (green) and the number of cytokeratin 14 positive cells was high (Figures 6B2, B3). Interestingly, the number of the adherent cells in the CL_GEL5% and the CL_GEL8% was higher than the 2D control (Figure 6B1).

In order to investigate the maturation process, the changes in the expression of cytokeratin 14 in HEKs and the expression of α-SMA and collagen type 1 in HDFs were examined. The cytokeratin 14, a type 1 keratin, is mainly located in the basal keratinocytes of the epidermis, stratified epithelia and in the hair follicle's exterior root sheet (Seet et al., 2012). The positive results suggest that CL_GEL5% and CL_GEL8% promote the differentiation of keratinocytes and fibroblasts. The increased expression of this marker of basal keratinocytes proliferating in the CL_GEL5% and CL_GEL8% groups compared to the 2-D control indicated more layers of proliferating keratinocytes, which suggests that HEKs were in an earlier phase of maturation. On the other hand, collagen type 1 was highly expressed in 2-D fibroblasts culture, which suggests that there was no disruption of collagen type 1 level. However, collagen type 1 was scarcely present in the CL_GEL5% and CL_GEL8% groups, which suggests that the HDFs are still in the earlier phase of maturation compared to 2-D controls. The results showed that there was more collagen type 1 in the control compared to the hydrogel groups loaded with cells which does not match the cell viability and cell attachment findings. It is known that during the remodeling and maturation phase of wound healing, collagen type III is remodeled to collagen type 1 (Miedel et al., 2015), which supports the finding that the treatment using hydrogel loaded with cells promote regeneration faster than using the hydrogel alone. However, this our results contradict this observation as the hydrogel does not promote the HDFs maturation.

In addition, The expression of α-SMA is linked to myofibroblasts, which are involved in tissue contraction (Desmouliere et al., 2014). In physiological remodeling, the contractile activity of myofibroblasts is terminated when the tissue is repaired; α-SMA expression subsequently decreases and myofibroblasts are removed by apoptosis (Desmoulière et al., 1995). In our experiments, the expression of α-SMA in the 2D control group was the highest, which suggests that differentiation is much faster compared to the gelatin hydrogel groups.

3.2.6 Cell proliferation

MTT assay confirmed that HDFs and HEKs proliferations were too low compared to the 2D culture control as shown in Figures 7A, B, respectively. At the third day, the CL_GEL5% showed the highest cell viability in HDFs followed by CL_GEL8% with 68.033 ± 5.3 and 53.03 ± 4.9; respectively compared to 164.77 ± 11.5 in 2D HDFs

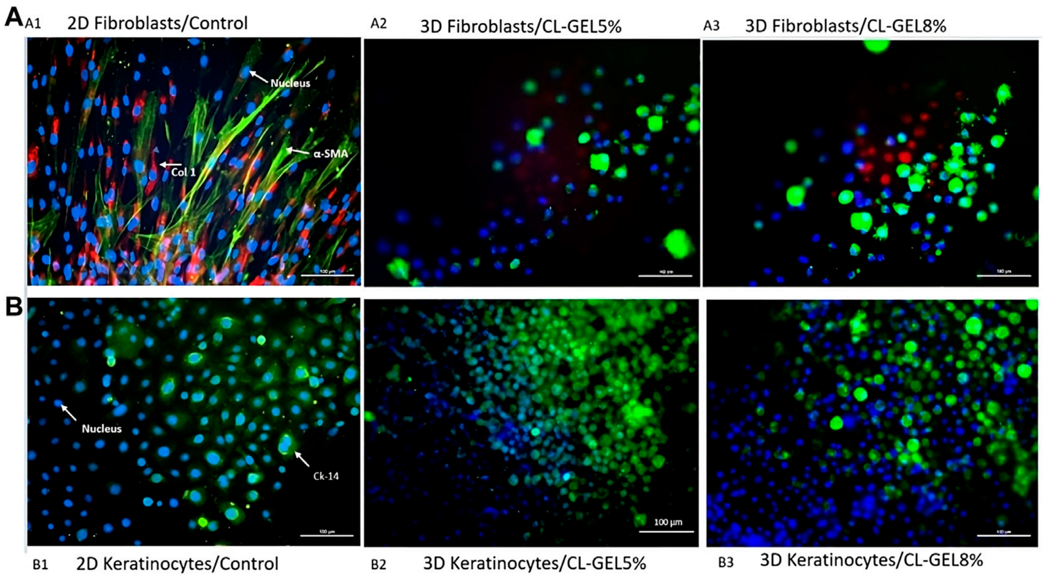

FIGURE 6
Immunocytochemistry staining of collagen type 1, α-SMA, and cytokeratin 14. **(A)** Immunocytochemistry staining of human dermal fibroblasts (HDFs) on (A1) monolayer 2D culture as control; (A2) CL_GEL5% and (A3) CL_GEL8%. The cells were stained with immunofluorescence (Alexa 594, red; COL I), (Alexa 488, green; α-SMA) and with Hoechst (blue; cell nuclei). HDFs on both CL_GEL5% and CL_GEL8% demonstrated the presence of α-SMA (green) positive cells; and collagen type 1 (red) positive cells. **(B)** Immunocytochemistry staining of human epidermal keratinocytes (HEKs) on (B1) monolayer 2D culture as control; (B2) CL_GEL5% and (B3) CL_GEL8%. The cells were stained by immunofluorescence (Alexa 488, green; CK-14) and with Hoechst (blue; cell nuclei). HEKs on both CL_GEL5% and CL_GEL8% demonstrated the presence of cytokeratin 14 (green) positive cells. Scale bar: 100 µm.

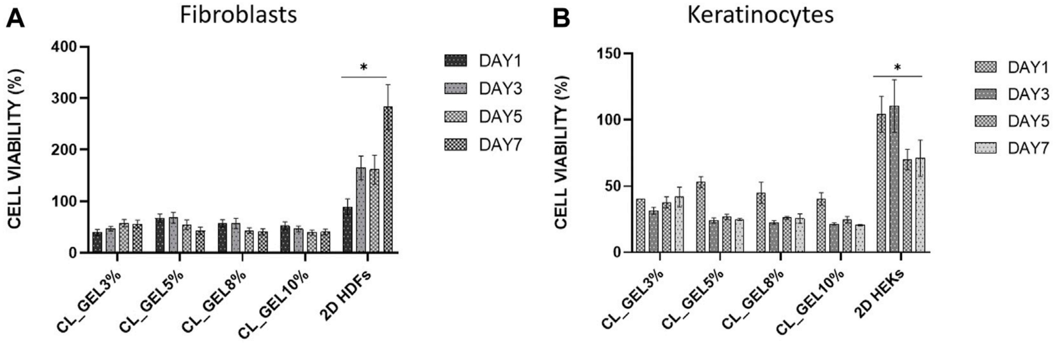

FIGURE 7
Cell proliferation of **(A)** human dermal fibroblasts (HDFs) and **(B)** human epidermal keratinocytes (HEKs) seeded on gelatin hydrogel 3D scaffolds (CL_GEL3%, CL_GEL5%, CL_GEL8%, and CL_GEL10%) and 2D controls after 1,3,5 and 7 days. HDFs and HEKs proliferations were too low compared to the 2D culture controls. *Control group significantly higher compared to other groups for both cell types.

control. This rate decreased to 42.86 ± 3.55 and 40.84 ± 3 in CL_GEL5% and CL_GEL8%; respectively after 7 days. However, the cell viability in control increased to 282.88 ± 21.8. The cell viability in HEKs was lower compared to HDFs. At the third day, the highest cell viability was recorded in CL_GEL3% followed by CL_GEL5% and CL_GEL8% with 31.31 ± 1.5, 23.95 ± 1.1 and 22.6 ± 0.7; respectively. The cell viability was higher in 2D HEKs control with 110.4 ± 11.4. After 7 days, the cells proliferate slightly in CL_GEL3% with 41.67 ± 4.3, in CL_GEL8% with 25.5 ± 2.03 and in CL_GEL5% with 24.77 ± 0.45 which is lower compared to the 2D HEKs control (71.05 ± 7.9). All groups showed low viability and proliferation of HDFs and HEKs compared to 2D controls.

Cellular compatibility is another concern for an ideal bioscaffold for skin tissue engineering to maintain viability and support human skin cells proliferation. Unfortunately, all gelatin hydrogel groups showed a negative proliferative effect on HDFs and HEKs as the proliferation was either too low or decreasing which is not consistent with previous findings from Ilkar Erdagi et al. (2020). Unfortunately, the proliferation of

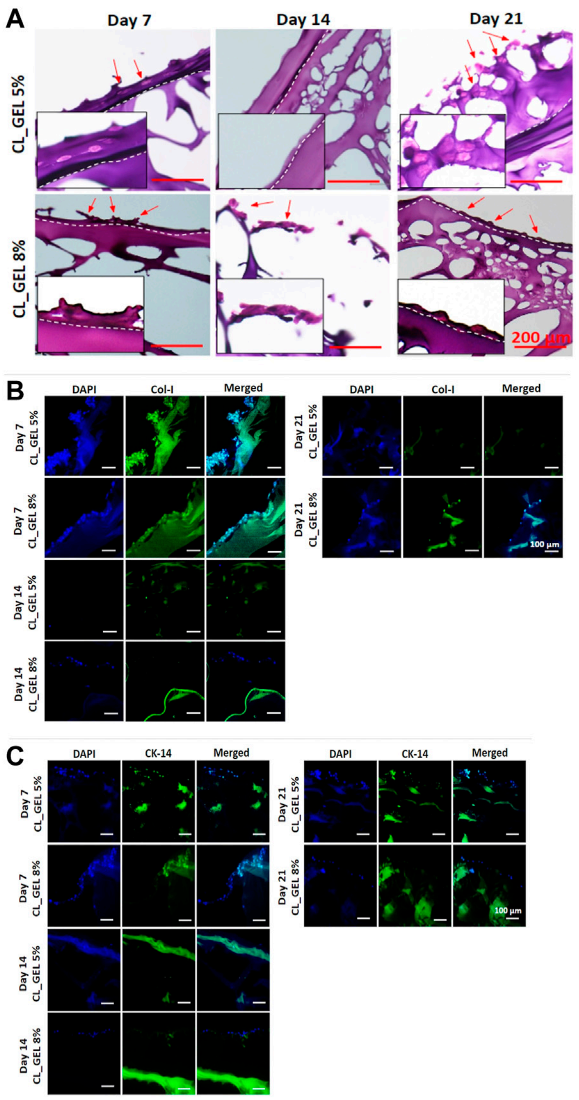

FIGURE 8
Microscopic evaluation of hydrogel model **(A)** H&E-stained images of hydrogels performed on day 7, 14, and 21 (scale bar: 200 μm), **(B)** immunofluorescent images of hydrogels to detect the presence of collagen type 1 on day 7, 14, and 21 (×20 magnification), **(C)** immunofluorescent images of hydrogels to detect the presence of cytokeratin 14 on day 7, 14, and 21 (×20 magnification).

HDF at the top surface of hydrogels was decreased after 7 days incubation and the proliferation of HEKs was slightly increased but still very low compared to the control. This phenomenon is probably related to its mechanical strength, as was reported previously by Lee et al. (2014) who concluded that a limited proliferative effect occurred in the hydrogel with higher stiffness due to slower degradation and lower permeability (Gupta et al., 2019).

3.2.7 Histological and immunohistochemical analysis of skin maturation

The H&E staining was carried out to verify the maturity level of the 3D *in vitro* skin model using hydrogels. For comparison, we used both HEKs and HDFs cells to construct *in vitro* skin models using hydrogels. Figure 8A displays the H&E-stained images of the hydrogels under different incubation periods (7, 14, and 21 days). From day 7 until day 21 incubation, the presence of stratified keratinocytes that are exposed to air was indicated in both CL_GEL 5%, and CL_GEL 8%. It can be seen from the images that about two layers occurred which indicates the separation of epidermis and dermis layer. Nonetheless, due to an insufficient incubation period, both formulations were unable to attain sufficient maturity to form a suprabasal layer or thicken the spinous layer. In addition, there is no presence of fibroblasts cells in the inner layer of the hydrogels.

3.2.8 Immunofluorescent analysis of skin maturation

The skin model was constructed by cultivating mixed skin cells (HEKs and HDFs) onto gelatin hydrogels. Thus, we examined the expression marker of collagen type 1, and cytokeratin 14 using immunofluorescent staining. Figure 8B showed the immunofluorescent stained images of the hydrogels using collagen type 1 marker for day 7, 14, and 21. Results showed that collagen type 1 staining was present in both CL_GEL 5% and CL_GEL 8% microstructure Day 7 only. This indicates that there is no HDFs in both CL_GEL 5% and CL_GEL 8% on day 14 and 21 incubation period. Moreover, Figure 8C shows the IF-stained images of hydrogels using cytokeratin 14 marker for day 7, 14, and 21. Cytokeratin 14 is known as an important marker for epidermal basal cell detection. The results indicate that CL_GEL 5% and CL_GEL 8% expressed higher level of cytokeratin 14 on day 7 while CL_GEL 8% slightly expressed cytokeratin 14 on day 14. This indicates that the 3D *in vitro* models are not fully matured after 21 days of incubation.

Complex biofabricated scaffolds cannot be employed immediately after fabrication as *in vitro* tissue models. The generation of a fully functional skin equivalent that closely resembles the structure and functionality of native skin is required for the maturation of a hydrogel-based 3D *in vitro* skin model. This includes the successfully differentiation of keratinocytes to form epidermis layers, and the development of dermal compartment with fibroblasts and extracellular matrix.

Generally, tissue maturation requires ideal circumstances, including culture environment, time, and medium composition (nutrition) to support cell growth. Based on our findings, the presence of separation layers between epidermis and dermis. This phenomenon have been occurred and explained by Kwak et al. (2018) who mentioned that the epidermis' differentiation was triggered by air exposure. Moreover, our histological findings also found that the 3D *in vitro* model using CL_GEL 5%, and CL_GEL 8% were not fully matured after 21 days incubation period. Longer cultured of HEKs and HDFs in the hydrogels did not increase the expression of collagen type 1 and cytokeratin 14. This finding was similar with a previous study by Kim et al. (2019) who developed a 3D *in vitro* model using hydrogels claimed that it is not sufficient to prove that their skin model recapitulates a more accurate and predictive *in vivo* response given in the milieu of original skin.

4 Conclusion

Our three-dimensional (3D) scaffolds demonstrated good physical and chemical properties (hydrophilic, crosslinked polymeric networks, high swelling rate, biodegradation) while maintaining their 3D structure except for Gel3% that was excluded. All gelatin hydrogel groups were compatible for skin tissue engineering applications in cellular attachment, cell viability but not for cell proliferation. Considering that the intended use of the hydrogel is to serve as a skin substitute, the ability to maintain cell attachment and viability is not sufficient for its function as cell proliferation deemed important to ensure a full regeneration of the HDFs and HEKs. Insufficient incubation time and the absence of additional measures to enhance cell differentiation could represent limitations in our study. We require a longer period of incubation and additional adjustments to further stimulate cell differentiation and regeneration. Future studies could focus on modifying the hydrogel composition to enhance its ability to promote cell proliferation and further investigate the potential of these 3D scaffolds for skin tissue engineering applications. We also suggest exploring the use of different cell concentrations and increasing the initial number of cells to address the limitations of skin maturation in our model.

The 3D *in vitro* skin model made from gelatin hydrogel has several applications, including as an alternative to animal experiments in preclinical studies, for screening for toxicity of various substances, for studying wound healing and disease modeling, and for developing personalized medicine. Overall, this model has the potential to provide a more accurate and reliable testing platform, accelerate the development of new treatments for skin-related conditions, and reduce the need for animal testing.

Data availability statement

The original contributions presented in the study are included in the article/Supplementary Material, further inquiries can be directed to the corresponding author.

Ethics statement

The studies involving human participants were reviewed and approved by the Research Ethic Committee Universiti Kebangsaan Malaysia (UKM), Malaysia. The patients/participants provided their written informed consent to participate in this study.

Author contributions

Conception and design: MF and MM. Analysis and interpretation of the data: ST, MF, MM, and SM. Drafting of the article: ST. Critical revision of the article for important intellectual content: MF, MM, and HM. Final approval of the article: MF, MM, and HM. Provision of study materials or patients: MF, MM, and RC. Statistical expertise: ST. Obtaining of funding: MF and MM. Collection and assembly of data: ST and SM. All authors contributed to the article and approved the submitted version.

Funding

Geran Fundamental Fakulti Perubatan (GFFP), Faculty of Medicine, Universiti Kebangsaan Malaysia, Grant code: FF-2021-491 for research fund. No funding for open access publication under this grant.

Acknowledgments

The authors would like to acknowledge financial support from UKM Medical Centre (Fundamental Grant Code: FF-2021-491).

Conflicts of interest

The authors declare that the research was conducted in the absence of any commercial or financial relationships that could be construed as a potential conflict of interest.

Publisher's note

Supplementary material

The Supplementary Material for this article can be found online at: https://www.frontiersin.org/articles/10.3389/fbioe.2023.1200618/full#supplementary-material

SUPPLEMENTARY FIGURE S1
Chemical characterization. **(A)** Energy dispersive X-Ray (EDX) map and spectra gave information that the presence of the element in the surface of (A1) CL_GEL5% and (A2) CL_GEL8% were similar to NC_GEL5% and NC_GEL8% (data not shown). **(B)** Fourier Transform Infrared Spectrometry (FTIR) spectra of (B1) CL_GEL5% and (b2) CL_GEL8%. **(C)** X-ray diffractogram of (C1) CL_GEL5% and (C2) CL_GEL8% confirmed that genipin modification did not alter the origin functional groups and amorphous nature of gelatin.

References

Anselme, K., Ploux, L., and Ponche, A. (2010). Cell/material interfaces: Influence of surface chemistry and surface topography on cell adhesion. *J. Adhes. Sci. Technol. janv* 24 (5), 831–852. doi:10.1163/016942409x12598231568186

Arif, M. M. A., Fauzi, M. B., Nordin, A., Hiraoka, Y., Tabata, Y., and Yunus, M. H. M. (2020). Fabrication of bio-based gelatin sponge for potential use as A functional acellular skin substitute. *Polymers* 12 (11), 2678. doi:10.3390/polym12112678

Bas, A., Burns, N., Gulotta, A., Junker, J., Drasler, B., Lehner, R., et al. (2021). Understanding the development, standardization, and validation process of alternative *in vitro* test methods for regulatory approval from a researcher perspective. *Small. avr* 17 (15), 2006027. doi:10.1002/smll.202006027

Branco da Cunha, C., Klumpers, D. D., Li, W. A., Koshy, S. T., Weaver, J. C., Chaudhuri, O., et al. (2014). Influence of the stiffness of three-dimensional alginate/collagen-I interpenetrating networks on fibroblast biology. *Biomaterials* 35 (32), 8927–8936. doi:10.1016/j.biomaterials.2014.06.047

Crowley, C., Klanrit, P., Butler, C. R., Varanou, A., Platé, M., Hynds, R. E., et al. (2016). Surface modification of a POSS-nanocomposite material to enhance cellular integration of a synthetic bioscaffold. *Biomater. mars* 83, 283–293. doi:10.1016/j.biomaterials.2016.01.005

Dare, E. V., Griffith, M., Poitras, P., Kaupp, J. A., Waldman, S. D., Carlsson, D. J., et al. (2009). Genipin cross-linked fibrin hydrogels for *in vitro* human articular cartilage tissue-engineered regeneration. *Cells Tissues Organs* 190 (6), 313–325. doi:10.1159/000209230

de Mel, A., Punshon, G., Ramesh, B., Sarkar, S., Darbyshire, A., Hamilton, G., et al. (2009). *In situ* endothelialisation potential of a biofunctionalised nanocomposite biomaterial-based small diameter bypass graft. *Biomed. Mater Eng.* 19 (4-5), 317–331. doi:10.3233/bme-2009-0597

Desmouliere, A., Darby, I. A., Laverdet, B., and Bonté, F. (2014). Fibroblasts and myofibroblasts in wound healing. *Clin. Cosmet. Investig. Dermatol. Nov.* 7, 301–311. doi:10.2147/ccid.s50046

Desmoulière, A., Redard, M., Darby, I., and Gabbiani, G. (1995). Apoptosis mediates the decrease in cellularity during the transition between granulation tissue and scar. *Am. J. Pathol. janv* 146 (1), 56–66.

El-Sherbiny, I. M., and Yacoub, M. H. (2013). Hydrogel scaffolds for tissue engineering: Progress and challenges. *Glob. Cardiol. Sci. Pract. Sept.* 2013 (3), 38. doi:10.5339/gcsp.2013.38

Ertekin, Ö., Monavari, M., Krüger, R., Fuentes-Chandía, M., Parma, B., Letort, G., et al. (2022). 3D hydrogel-based microcapsules as an *in vitro* model to study tumorigenicity, cell migration and drug resistance. *Acta Biomater. avr* 142, 208–220. doi:10.1016/j.actbio.2022.02.010

Gupta, A., Kowalczuk, M., Heaselgrave, W., Britland, S. T., Martin, C., and Radecka, I. (2019). The production and application of hydrogels for wound management: A review. *Eur. Polym. J. févr* 111, 134–151. doi:10.1016/j.eurpolymj.2018.12.019

Hoffman, A. S. (2012). Hydrogels for biomedical applications. *Adv. Drug Deliv. Rev. déc* 64, 18–23. doi:10.1016/j.addr.2012.09.010

Ilkar Erdagi, S., Asabuwa Ngwabebhoh, F., and Yildiz, U. (2020). Genipin crosslinked gelatin-diosgenin-nanocellulose hydrogels for potential wound dressing and healing applications. *Int. J. Biol. Macromol. avr* 149, 651–663. doi:10.1016/j.ijbiomac.2020.01.279

Imeson, A. (1992). *Thickening and gelling agents for food*. Boston, MA: Springer US.

Kim, B. S., Gao, G., Kim, J. Y., and Cho, D. W. (2019). 3D cell printing of perfusable vascularized human skin equivalent composed of epidermis, dermis, and hypodermis for better structural recapitulation of native skin. *Adv. Healthc. Mater* 8 (7), 1801019–1801111. doi:10.1002/adhm.201801019

Kirchmajer, D. M., Watson, C. A., Ranson, M., and Panhuis, M. (2013). Gelapin, a degradable genipin cross-linked gelatin hydrogel. *RSC Adv.* 3 (4), 1073–1081. doi:10.1039/c2ra22859a

Ko, C. S., Huang, J. P., Huang, C. W., and Chu, I. M. (2009). Type II collagen-chondroitin sulfate-hyaluronan scaffold cross-linked by genipin for cartilage tissue engineering. *J. Biosci. Bioeng. févr* 107 (2), 177–182. doi:10.1016/j.jbiosc.2008.09.020

Kwak, B. S., Choi, W., won, Jeon J., Won, J. I., Sung, G. Y., Kim, B., et al. (2018). *In vitro* 3D skin model using gelatin methacrylate hydrogel. *J. Ind. Eng. Chem.* 66, 254–261. doi:10.1016/j.jiec.2018.05.037

Lee, Y., Bae, J. W., Lee, J. W., Suh, W., and Park, K. D. (2014). Enzyme-catalyzed *in situ* forming gelatin hydrogels as bioactive wound dressings: Effects of fibroblast delivery on wound healing efficacy. *J. Mater Chem. B* 2 (44), 7712–7718. doi:10.1039/c4tb01111b

Liang, H. C., Chang, W. H., Lin, K. J., and Sung, H. W. (2003). Genipin-crosslinked gelatin microspheres as a drug carrier for intramuscular administration:*in vitro* and*in vivo* studies. *J. Biomed. Mater Res. 1 mai* 65A (2), 271–282. doi:10.1002/jbm.a.10476

Liu, Y., Xu, K., Chang, Q., Darabi, M. A., Lin, B., Zhong, W., et al. (2016). Highly flexible and resilient elastin hybrid cryogels with shape memory, injectability, conductivity, and magnetic responsive properties. *Adv. Mater. Sept.* 28 (35), 7758–7767. doi:10.1002/adma.201601066

Loh, Q. L., and Choong, C. (2013). Three-dimensional scaffolds for tissue engineering applications: Role of porosity and pore size. *Tissue Eng. Part B Rev. déc* 19 (6), 485–502. doi:10.1089/ten.teb.2012.0437

LOREAL (2020). Celebrating pride month with L'oréal. Available at: www.loreal.com (accessed November, 2020).

Luangbudnark, W., Viyoch, J., Laupattarakasem, W., Surakunprapha, P., and Laupattarakasem, P. (2012). Properties and biocompatibility of chitosan and silk fibroin blend films for application in skin tissue engineering. *Sci. World J.* 2012, 1–10. doi:10.1100/2012/697201

MacNeil, S. (2007). Progress and opportunities for tissue-engineered skin. *Nat. févr* 445 (7130), 874–880. doi:10.1038/nature05664

Mahboudi, S., Pezeshki-Modaress, M., and Noghabi, K. A. (2015). The study of fibroblast cell growth on the porous scaffold of gelatin–starch blend using the salt-leaching and lyophilization method. *Int. J. Polym. Mater Polym. Biomater.* 64 (12), 653–659. doi:10.1080/00914037.2014.1002095

Maji, K., Dasgupta, S., Pramanik, K., and Bissoyi, A. (2016). Preparation and evaluation of gelatin-chitosan-nanobioglass 3D porous scaffold for bone tissue engineering. *Int. J. Biomater.* 2016, 1–14. doi:10.1155/2016/9825659

Masri, S., Maarof, M., Aziz, I. A., Idrus, R., and Fauzi, M. B. (2023). Performance of hybrid gelatin-PVA bioinks integrated with genipin through extrusionbased 3D bioprinting: An *in vitro* evaluation using human dermal fibroblasts. *Int. J. Bioprinting* 9 (3), 677. Disponible sur: Available at:. doi:10.18063/ijb.677

MATTEK (2020). Supporting your science. Available at: www.mattek.com (accessed November, 2020).

Mh Busra, F., Rajab, N. F., Tabata, Y., Saim, A. B., Idrus R, B. H., and Chowdhury, S. R. (2019). Rapid treatment of full-thickness skin loss using ovine tendon collagen type I scaffold with skin cells. *J. Tissue Eng. Regen. Med. mai* 13 (5), 874–891. doi:10.1002/term.2842

Miedel, E. L., Brisson, B. K., Hamilton, T., Gleason, H., Swain, G. P., Lopas, L., et al. (2015). Type III collagen modulates fracture callus bone formation and early remodeling: col3 modulates fracture repair. *J. Orthop. Res. mai* 33 (5), 675–684. doi:10.1002/jor.22838

Nam, K., Sakai, Y., Hashimoto, Y., Kimura, T., and Kishida, A. (2012). Fabrication of a heterostructural fibrillated collagen matrix for the regeneration of soft tissue function. *Soft Matter* 8 (2), 472–480. doi:10.1039/c1sm06543b

Nicodemus, G. D., and Bryant, S. J. (2008). Cell encapsulation in biodegradable hydrogels for tissue engineering applications. *juin* 14 (2), 149–165. doi:10.1089/ten.teb.2007.0332

Nii, T., Makino, K., and Tabata, Y. (2020). Three-dimensional culture system of cancer cells combined with biomaterials for drug screening. *Cancers* 12 (10), 2754. doi:10.3390/cancers12102754

Nii, T. (2021). Strategies using gelatin microparticles for regenerative therapy and drug screening applications. *Molecules* 26 (22), 6795. doi:10.3390/molecules26226795

Nike, D., Katas, H., Mohd, N., Hiraoka, Y., Tabata, Y., Idrus, R., et al. (2021). Characterisation of rapid *in situ* forming gelipin hydrogel for future use in irregular deep cutaneous wound healing. *Polymers* 13 (18), 3152. doi:10.3390/polym13183152

Oliveira Barud, H. G., Barud, H. da S., Cavicchioli, M., do Amaral, T. S., Junior Ob de, O., Santos, D. M., et al. (2015). Preparation and characterization of a bacterial cellulose/silk fibroin sponge scaffold for tissue regeneration. *Carbohydr. Polym. Sept.* 128, 41–51. doi:10.1016/j.carbpol.2015.04.007

Organisation for Economic Co-operation and Development (2015). *Vitro skin irritation: Reconstructed human epidermis test method, OECD guidelines for the testing of chemicals, section 4 test No. 439*. Paris, France: OECD Publishing.

Organisation for Economic Co-operation and Development (2020). *Vitro skin irritation: Reconstructed human epidermis test method, OECD guidelines for the testing of chemicals, section 4 test No. 439*. Paris, France: OECD Publishing.

Ren, K., Wang, Y., Sun, T., Yue, W., and Zhang, H. (2017). Electrospun PCL/gelatin composite nanofiber structures for effective guided bone regeneration membranes. *Mater Sci. Eng. C. Sept.* 78, 324–332. doi:10.1016/j.msec.2017.04.084

Rodríguez-Rodríguez, R., Espinosa-Andrews, H., Velasquillo-Martínez, C., and García-Carvajal, Z. Y. (2020). Composite hydrogels based on gelatin, chitosan and polyvinyl alcohol to biomedical applications: A review. *Int. J. Polym. Mater Polym. Biomater. 2 janv* 69 (1), 1–20. doi:10.1080/00914037.2019.1581780

Rodríguez-Rodríguez, R., García-Carvajal, Z. Y., Jiménez-Palomar, I., Jiménez-Avalos, J. A., and Espinosa-Andrews, H. (2019). Development of gelatin/chitosan/PVA hydrogels: Thermal stability, water state, viscoelasticity, and cytotoxicity assays. *J. Appl. Polym. Sci. 10 mars* 136 (10), 47149. doi:10.1002/app.47149

Rodríguez-Vázquez, M., Vega-Ruiz, B., Ramos-Zúñiga, R., Saldaña-Koppel, D. A., and Quiñones-Olvera, L. F. (2015). Chitosan and its potential use as a scaffold for tissue engineering in regenerative medicine. *Biomed. Res. Int.* 2015, 1–15. doi:10.1155/2015/821279

Russell, W. M. S., and Burch, R. L. (1960). The principles of humane experimental technique. *Med. J. Aust. mars* 1 (13), 500.

School of Chemical Engineering (2019). Universiti Sains Malaysia, George Town, Malaysia, et al. M. Injectable collagen-chitosan hydrogel using ultrasonic pretreated ovine tendon collagen. *Int. J. Adv. Appl. Sci. déc* 3(12), 58–66. doi:10.21833/ijaas.2019.12.006

Seet, W. T., Maarof, M., Khairul Anuar, K., Chua, K. H., Ahmad Irfan, A. W., Ng, M. H., et al. (2012). Shelf-life evaluation of bilayered human skin equivalent, MyDerm™. *MyDerm™. Brand. JM, Éditeur. PLoS ONE. 23 août* 7 (8), e40978. doi:10.1371/journal.pone.0040978

Sisso, A. M., Boit, M. O., and DeForest, C. A. (2020). Self-healing injectable gelatin hydrogels for localized therapeutic cell delivery. *J. Biomed. Mater Res. A. mai* 108 (5), 1112–1121. doi:10.1002/jbm.a.36886

Wang, Y., Wang, X., Shi, J., Zhu, R., Zhang, J., Zhang, Z., et al. (2016). A biomimetic silk fibroin/sodium alginate composite scaffold for soft tissue engineering. *Sci. Rep. déc* 6 (1), 39477. doi:10.1038/srep39477

Wei, H. J., Yang, H. H., Chen, C. H., Lin, W. W., Chen, S. C., Lai, P. H., et al. (2007). Gelatin microspheres encapsulated with a nonpeptide angiogenic agent, ginsenoside Rg1, for intramyocardial injection in a rat model with infarcted myocardium. *J. Control. Release. juill* 120 (1-2), 27–34. doi:10.1016/j.jconrel.2007.04.005

Xi Loh, E. Y., Fauzi, M. B., Ng, M. H., Ng, P. Y., Ng, S. F., Ariffin, H., et al. (2018). Cellular and molecular interaction of human dermal fibroblasts with bacterial nanocellulose composite hydrogel for tissue regeneration. *ACS Appl. Mater Interfaces* 10 (46), 39532–39543. doi:10.1021/acsami.8b16645

Xie, J., Bao, M., Bruekers, S. M. C., and Huck, W. T. S. (2017). Collagen gels with different fibrillar microarchitectures elicit different cellular responses. *ACS Appl. Mater Interfaces. 14 juin* 9 (23), 19630–19637. doi:10.1021/acsami.7b03883

Yehkung, M., Liang, Y. ming, Chengming, K., Dai, N. T., che, Liu C., and Young, J. jong (2011). A novel cell support membrane for skin tissue engineering: Gelatin film cross-linked with 2-chloro-1-methylpyridinium iodide. *Polym. févr* 52 (4), 996–1003. doi:10.1016/j.polymer.2010.10.060

Zhao, X., Lang, Q., Yildirimer, L., Lin, Z. Y., Cui, W., Annabi, N., et al. (2016). Photocrosslinkable gelatin hydrogel for epidermal tissue engineering. *Adv. Healthc. Mater. 7 janv* 5 (1), 108–118. doi:10.1002/adhm.201500005

Zhao, X., Li, P., Guo, B., and Ma, P. X. (2015). Antibacterial and conductive injectable hydrogels based on quaternized chitosan-graft-polyaniline/oxidized dextran for tissue engineering. *Acta Biomater*. 26, 236–248. doi:10.1016/j.actbio.2015.08.006

frontiers | Frontiers in Bioengineering and Biotechnology

TYPE Original Research
PUBLISHED 27 June 2023
DOI 10.3389/fbioe.2023.1184938

OPEN ACCESS

EDITED BY
Zuhao Li,
Jilin University, China

REVIEWED BY
Matjaž Jeras,
University of Ljubljana, Slovenia
Xuan Mei,
Harvard Medical School, United States

*CORRESPONDENCE
Christopher M. Jewell,
✉ cmjewell@umd.edu

RECEIVED 12 March 2023
ACCEPTED 12 June 2023
PUBLISHED 27 June 2023

CITATION
Bridgeman CJ, Shah SA, Oakes RS and Jewell CM (2023), Dissecting regulatory T cell expansion using polymer microparticles presenting defined ratios of self-antigen and regulatory cues. *Front. Bioeng. Biotechnol.* 11:1184938.
doi: 10.3389/fbioe.2023.1184938

Dissecting regulatory T cell expansion using polymer microparticles presenting defined ratios of self-antigen and regulatory cues

Christopher J. Bridgeman[1], Shrey A. Shah[1], Robert S. Oakes[1,2] and Christopher M. Jewell[1,2,3,4,5]*

[1]Fischell Department of Bioengineering, University of Maryland College Park, Baltimore, MD, United states, [2]United States Department of Veterans Affairs, Baltimore, MD, United states, [3]Robert E Fischell Institute of Biomedical Devices, University of Maryland College Park, Baltimore, MD, United states, [4]Department of Microbiology and Immunology, University of Maryland Medical School, Baltimore, MD, United states, [5]Marlene and Stewart Greenebaum Cancer Center, Baltimore, MD, United states

Biomaterials allow for the precision control over the combination and release of cargo needed to engineer cell outcomes. These capabilities are particularly attractive as new candidate therapies to treat autoimmune diseases, conditions where dysfunctional immune cells create pathogenic tissue environments during attack of self-molecules termed self-antigens. Here we extend past studies showing combinations of a small molecule immunomodulator co-delivered with self-antigen induces antigen-specific regulatory T cells. In particular, we sought to elucidate how different ratios of these components loaded in degradable polymer particles shape the antigen presenting cell (APC) -T cell interactions that drive differentiation of T cells toward either inflammatory or regulatory phenotypes. Using rapamycin (rapa) as a modulatory cue and myelin self-peptide (myelin oligodendrocyte glycoprotein- MOG) – self-antigen attacked during multiple sclerosis (MS), we integrate these components into polymer particles over a range of ratios and concentrations without altering the physicochemical properties of the particles. Using primary cell co-cultures, we show that while all ratios of rapa:MOG significantly decreased expression of co-stimulation molecules on dendritic cells (DCs), these levels were insensitive to the specific ratio. During co-culture with primary T cell receptor transgenic T cells, we demonstrate that the ratio of rapa:MOG controls the expansion and differentiation of these cells. In particular, at shorter time points, higher ratios induce regulatory T cells most efficiently, while at longer time points the processes are not sensitive to the specific ratio. We also found corresponding changes in gene expression and inflammatory cytokine secretion during these times. The *in vitro* results in this study contribute to *in vitro* regulatory T cell expansion techniques, as well as provide insight into future studies to explore other modulatory effects of rapa such as induction of maintenance or survival cues.

KEYWORDS

microparticle and nanoparticle, autoimmunity, mTOR, antigen-specificity, tolerance, biomaterial, vaccine, immunotherapy

Introduction

Multiple sclerosis (MS) is an autoimmune disease whereby dysfunctional immune cells attack myelin that insulates neurons in the central nervous system leading to loss of motor control. In MS, innate and adaptive immune cells drive a proinflammatory state that leads to degradation of the myelin protein matrix (MPM) (Dendrou, Fugger and Friese, 2015). Although the pathogenesis of MS is incompletely understood, both the innate and the adaptive immune cell compartments contribute to disease progression. For example, antigen-specific B cells contribute to disease through the generation of myelin recognizing auto-antibodies (Arneth, 2019). Antigen presenting cells (APCs) such as dendritic cells (DCs) also initiate auto-activation of self-reactive T cells through the presentation of MPM-derived peptide antigen to myelin-specific CD4$^+$ and CD8$^+$ T cells (Gandhi, Laroni and Weiner, 2010; Weissert, 2013; Saxena et al., 2019). Once activated, these T cells drive disease through inflammatory cytokine production and targeted killing of host tissue expressing myelin antigens. Although therapies exist for MS, these require lifelong treatment and none are curative (Huang, Chen and Zhang, 2017). Further, even the most advanced therapies – such as monoclonal antibodies – do not distinguish between healthy and dysfunctional immune cells (Torkildsen, Myhr and Bø, 2016; Hauser and Cree, 2020). Thus, there is a need for new treatments that selectively control autoreactive immune cells while leaving the remainder of the immune system intact. Regulatory CD4$^+$ T cells (T_{REG}) are one target of particular interest that attenuate unwanted inflammation through the release of anti-inflammatory cytokines in response to self-antigens (Danikowski, Jayaraman and Prabhakar, 2017; Kimura, 2020). Indeed, *ex vivo* expanded T_{REG} have shown promise in clinical trials for treatment of autoimmune diseases such as type 1 diabetes and Crohn's disease (Mosanya and Isaacs, 2019; Romano et al., 2019). However, these T_{REG} are polyclonal, and not necessarily specific to the disease-causing self-antigen. Alternatively, the expansion of disease specific T_{REG} may improve the potency and efficacy of these engineered cells. One emerging strategy to treat MS relies on the use of biomaterials to control the delivery of the T_{REG} promoting small molecule drug rapamycin (rapa) with MPM peptides to drive the expansion of antigen-specific T_{REG} that would protect against myelin degradation. This strategy fundamentally relies on the use of polymer microparticles (MPs) to control the release of these cues for myelin specific T_{REG} expansion *in vivo* (Tostanoski et al., 2016).

Polymer particle delivery strategies are an exciting area of research due to their ability to control drug delivery parameters, such as controlled release, drug co-localization, and tissue targeting (Andorko, Hess and Jewell, 2015; Tostanoski, 2016; Bookstaver et al., 2018). Poly(lactic-co-glycolic acid) (PLGA), for example, is a biodegradable polymer of particular interest due to its biocompatibility and degradation into non-toxic byproducts (Blasi, 2019; Su et al., 2021). Additionally, these particles are versatile in their ability to encapsulate a variety of immune cargos including proteins, peptides, and nucleic acids (Danhier et al., 2012). We and others have used poly(lactic-co-glycolide) (PLGA) microparticles loaded with myelin self-peptides, including myelin oligodendrocyte glycoprotein (MOG) and the mechanistic target of rapamycin (mTOR) inhibitor rapa to re-condition the microenvironment of lymph nodes (LNs) to promote antigen-specific T_{REG} (Tostanoski et al., 2016; Gammon et al., 2023). However, it is unclear how specific combinations and concentrations of these signals could further shape the response of APCs and T cells.

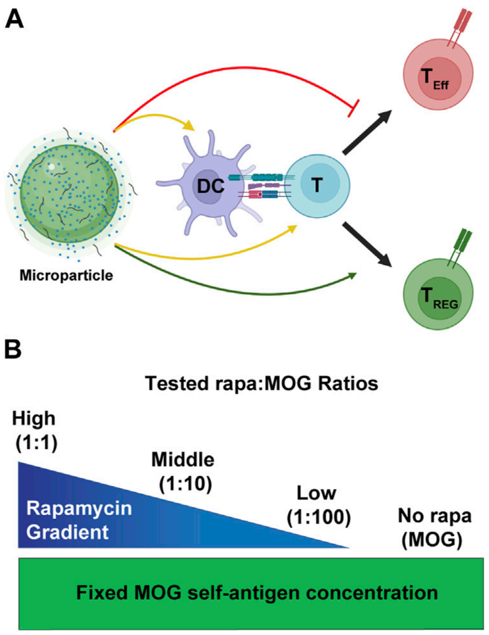

FIGURE 1
Overview schematic of MP treatment strategy. **(A)** MPs release immune cues that act on both DCs and T cells (yellow arrows). These cues modulate the interaction of DCs and T cells to promote generation of T_{REG} (green arrow) and not inflammatory effector T cells (T_{Eff}). **(B)** To test the effect of rapa:MOG ratio, quantity of MOG peptide encapsulated in MPs was kept constant while rapa quantity was titrated. Created with BioRender.

The mTOR metabolic pathway has been shown to critically regulate cell functions such as proliferation, and metabolism (März et al., 2013; Mukhopadhyay et al., 2016; Yoo et al., 2017). While rapa has historically served a role of an important immunosuppressant (Saunders, Metcalfe and Nicholson, 2001; Yellen et al., 2011; Hester et al., 2012), over the last decade its ability to facilitate T_{REG} expansion and survival has been extensively explored (Marín Morales et al., 2019; Sato et al., 2021; Vakrakou et al., 2022). Additionally, rapa encapsulation in microparticle and nanoparticle systems for antigen-specific T_{REG} induction has been studied in multiple pre-clinical models of autoimmune diseases (Maldonado et al., 2015; Tostanoski, 2016; Gammon et al., 2023). However, more mechanistic studies are needed to deconvolute how specific ratios of encapsulated rapa:MOG fundamentally shape the APC-T cell signaling axis to promote antigen-specific T_{REG}. This paper seeks to bridge this knowledge gap by using validated *in vitro* assays to test how specific ratios of rapa and MOG regulate APC activation, and subsequent antigen-specific T_{REG} polarization (Figure 1A). In particular, MPs were synthesized with specific ratios of rapa and MOG (Figure 1B) to test their effect on primary APCs and subsequent polarization of antigen-specific T cells to T_{REG}. Using this library, we show all particles containing rapa reduced the activation of stimulated DCs, but these effects were insensitive to the ratio of rapa:MOG. Interestingly, however, the expansion of MOG-specific T cells could be maximized by tuning the rapa:MOG ratio. These results provide additional insight into design parameters for polarizing T cells toward T_{REG} for antigen-specific autoimmune therapies.

Materials and methods

Materials and reagents

MOG peptide (MOG_{35-55}, MEVGWYRSPFSRVVHLYRNGK) was synthesized by Genscript (Piscataway, NJ, United States) with >98% purity. Rapamycin was purchased from LC Laboratories (Woburn, MA, United States). 50:50 poly(lactic-co-glycolide) (PLGA) was purchased from LACTEL Absorbable Polymers. High molecular weight poly(vinyl alcohol) (PVA) was purchased from Alpha Aesar (Tewksbury, MA, United States). Dichloromethane (DCM) was purchased from Sigma Aldrich (St. Louis, MO, United States). Dimethyl sulfoxide (DMSO), micro-bicinchoninic acid (mBCA) assay, and eBioscience FoxP3 Fixation/Permeation kit were purchased from Thermo Fisher Scientific (Waltham, MA, United States). Antibodies for flow cytometry, including BV605-CD11c, v450-CD25, PE-T-bet, PE-CD40, PE-Cy-7-CD4, PE-Cy-7-CD86, APC-FoxP3, APC-CD80 were purchased from BD Biosciences. Zombie NIR Fixable Viability Kit was purchased from BioLegend.

Synthesis of microparticles

MPs were synthesized as previously described using a water-in-oil-in-water double emulsion technique (Tostanoski et al., 2016). Briefly, 500 μL of aqueous phase was prepared by dissolving 2.2 mg of MOG into water. An organic phase was prepared by first dissolving PLGA at 16 mg/mL in DCM for 1 h (PLGA-DCM). For rapa-loaded MPs, lyophilized rapa was dissolved in a PLGA-DCM aliquot to 0.22 mg/mL, and then titrated 1:10 in PLGA-DCM. Inner emulsion was formed by sonicating the aqueous phase with organic phase at 12 W for 30 s. This emulsion was then homogenized with 40 mL of 2% w/v PVA solution for 3 min at 16,000 RPM to form final emulsions. MP solutions were then stirred overnight to evaporate DCM. MPs were then poured through a 40 μm cell strainer, and centrifuged for 5 min at 5000g. After aspiration of supernatant, MPs were washed 3x with 1 mL of water (resuspend, spin 5 min 5000g). MPs were resuspended in a final volume of 1 mL of water.

Microparticle characterization

MP size and distribution were calculated using dynamic laser scattering (DLS) (Horiba LA-950). Rapa and MOG loading were quantified by dissolving a known mass of dried MPs in DMSO. MOG concentration was determined using a mBCA assay according to the manufacturer's instructions. Rapa concentration was determined by measuring ultraviolet/visible (UV/Vis) spectroscopy values and comparing to a standard curve of known concentrations. Loading efficiency was calculated by comparing measured quantities to initial loading quantities.

Dendritic cell activation assay

All studies involving animals were carried out under the supervision of the University of Maryland Institutional Animal Care and Use Committee (IACUC) in compliance with local, state, and federal guidelines. To test the effect of rapa:MOG in MPs on DC activation, $CD11c^+$ DCs were harvested from the spleens of female C57Bl/6J mice (Jackson Laboratories, United States) using a bead based CD11c positive selection kit according to manufacturer's instructions (Miltenyi, United States). DCs were plated at 100,000 cells per well in a 96 well flat bottom plate in 100 μL of RPMI + L-Glutamine media supplemented with 10% fetal bovine serum, 55 μM β-mercaptoethanol, 1x non-essential amino acid, 10 mM HEPES, and 2 x Pen/Strep. Cells were then immediately treated with MP formulations matched to treat each well with 15 μg of MPs. MOG (no rapa) MPs, and empty MPs were used to control for the effect of MOG and MP effect respectively. To assess the effect of rapa on DC activation, cells were stimulated with 0.25 μg/mL lipopolysaccharide (LPS). DCs were cultured at 37°C for 24 h at 5% CO_2. DCs were then sequentially Fc blocked for 20 min, washed, stained in NIR viability dye, and stained with anti-CD80, anti-CD86, and anti-CD40 antibodies for flow cytometry on a Beckman Coulter CytoFLEX. Median fluorescence intensity of markers was used to determine activation.

T cell and dendritic cell co-culture assay

To test the effect of rapa:MOG on antigen-specific T cell proliferation, transgenic 2D2 mice that express a MOG specific T cell receptor (TCR) were used (Jackson Laboratories). DCs were first harvested as described, and treated with MP formulations. After 24 h, $CD4^+$ T cells were isolated from 2D2 mouse spleens using a bead based negative selection kit (Stem Cell, United States). T cells were added in a 3:1 ratio to wells containing DCs (300,000 T cells per well). At 48 h post T cell addition, T cells were sequentially Fc blocked for 20 min, washed, and then stained in NIR viability dye for 20 min. Cells were then washed and stained with antibodies for anti-CD4 and anti-CD25. After 1 h, cells were washed and placed in fixation buffer. Cells were then intracellularly stained with antibodies for the expression of forkhead box P3 (FoxP3) and T-box 21 (T-bet) transcription factors. Cells were analyzed for the expression of these markers using a Beckman Coulter CytoFLEX.

RT-qPCR analysis of gene expression

To test the effect of rapa:MOG MPs on $CD4^+$ T cell gene expression, real time quantitative polymerase chain reaction (RT-qPCR) was used to look at the expression of pro-inflammatory and regulatory genes. DCs and $CD4^+$ T cells were co-cultured as described. Twenty-four hours following

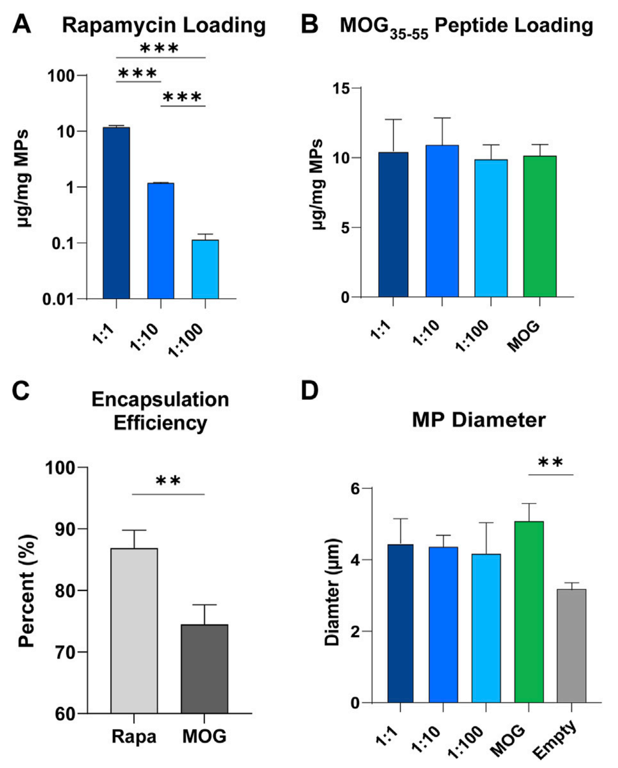

FIGURE 2
Characterization of MPs. **(A)** Quantity of rapa-loaded into MPs as measured through UV/Vis spectroscopy. N = 3 for each group. An ANOVA with a Tukey multiple comparisons post-hoc test was used to compare each group. Statistical significance is indicated by a (*). ***$p < 0.001$. **(B)** Quantity of MOG peptide loaded into MPs as measured through mBCA. **(C)** Loading efficiency of rapa and MOG into PLGA microparticles. An unpaired *t*-test was used to compare groups. Statistical significance is indicated by a (*). **$p < 0.01$. **(D)** MP size quantified through DLS. An ANOVA with a Tukey multiple comparisons post-hoc test was used to compare each group. Statistical significance is indicated by a (*). **$p < 0.01$.

T cell addition to DCs, the non-adherent T cells were removed, pelleted, and lysed using RNA lysis buffer (Zymo Research). After lysis, RNA isolation was performed followed by RNA quantification using a NanoDrop 2000c (Fisher Scientific). Complementary DNA (cDNA) amplification was then performed on 200 ng of RNA from each sample using the SuperScript IV VILO Master Mix kit and following the manufacturer's instructions. cDNA samples were then stored at −80°C until RT-qPCR analysis. For RT-qPCR analysis, 1 µL of probe, 10 µL of Master Mix, 4 µL of cDNA, and 5 µL of molecular grade water were combined in a 96 well RT-qPCR reaction plate. T cell expression of interferon gamma (IFN-ɣ) was tested against control probes for glyceraldehyde 3-phosphate dehydrogenase (GAPDH) and beta-actin (ACTB). RT-qPCR and determination of cycle threshold (Ct) values were performed by a QuantStudio 7 Flex Real Time PCR System (Thermo Fisher Scientific). Delta Ct (ΔCt) was determined as previously described (Schmittgen and Livak, 2008). ΔCt values for cells treated with rapa:MOG were divided by the MOG (no rapa) ΔCt value to determine fold difference. Values are plotted as -$\log_2(\Delta Ct)$.

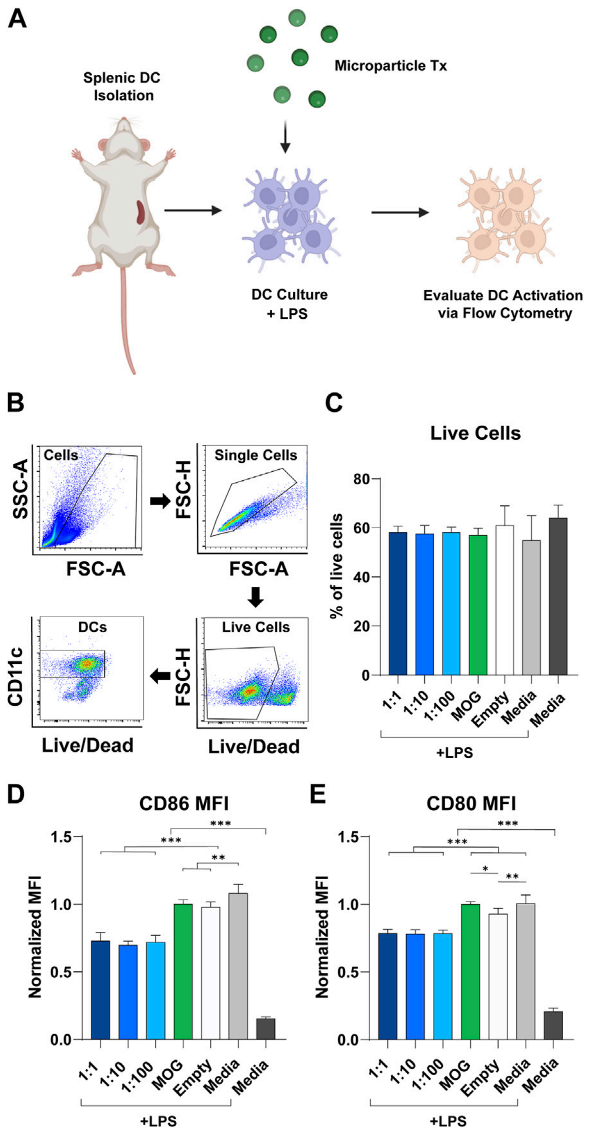

FIGURE 3
Effect of rapa:MOG MP treatment (Tx) on DC expression of activation receptors. **(A)** Overview schematic of experiment design. Primary derived DCs were harvested from mice and cultured with MP treatment for 24 h. DCs were then evaluated via flow cytometry for their expression of surface receptors. **(B)** Representative flow cytometry gating strategy. **(C)** Rapa:MOG MP treatment did not significantly reduce DC viability. **(D)** CD86 and **(E)** CD80 co-stimulation molecule expression on DCs was significantly lower compared to controls, but not within different rapa:MOG treatments. This study was completed in triplicate. For each study, N = 3. An ANOVA with a Tukey multiple comparisons post-hoc test was used to compare each group. Statistical significance is indicated by a (*). *$p < 0.05$, **$p < 0.01$, ***$p < 0.001$. Created with BioRender.

Statistical methods and analysis

Flow cytometry gating and analysis was performed in FlowJo (v 10.8.1). All statistical analyses were performed using GraphPad Prism (v 9.4.1). To test significant difference between two groups, an unpaired *t*-test was used. To test significance between multiple groups, an analysis of variance (ANOVA) was used followed by a

Tukey post-hoc test for multiple comparisons. Significance was defined if p values were less than 0.05. Graphs were made using GraphPad Prism software.

Results

Defined ratios of rapa and MOG peptide can be predictably loaded into microparticles

An established double emulsion synthesis procedure was used to prepare particles with defined ratios of rapa:MOG (Figure 2A; Supplementary Figure S1) (Gammon et al., 2017; Gosselin, Tostanoski and Jewell, 2017). This process resulted in particles with direct control over the quantity of loaded rapa (Figure 2A) and peptide (Figure 2B). We observed a slightly larger standard deviation in the MOG loading into MPs co-loaded with high and middle quantities of rapa which could be attributed to charge interactions between hydrophobic rapa and PLGA, and hydrophilic MOG. This hypothesis is supported by our data showing that rapa had a significantly higher loading efficiency (87%) compared to MOG (74%) (Figure 2C). MP size was determined using dynamic laser scattering. These measurements revealed that MP diameter was not impacted by the specific rapa: MOG composition (Figure 2D). However, MPs compositions containing cargo were modestly larger than empty MPs. There was no significant difference between MPs loaded with rapa: MOG relative to MOG (no rapa) MPs; MP size was consistent with values previously reported from our lab (Tostanoski et al., 2016; Gosselin et al., 2021).

Blunting of dendritic cell activation is not sensitive to the specific rapa:MOG ratio

To study the modulatory effect of rapa:MOG ratio, primary derived wildtype splenic DCs were isolated, activated using LPS, then and treated with MPs (Figure 3A). After 24 h, DC expression of activation markers was characterized using flow cytometry. Live cell population was determined using a fixable viability stain, followed by positive selection of DCs based on their expression of CD11c (Figure 3B). Quantification of live cells showed that rapa: MOG MP treatment did not significantly impact cell viability compared to controls (Figure 3C). CD11c$^+$ DCs were then analyzed for their expression of co-stimulation molecules CD86 (Figure 3D) and CD80 (Figure 3E) which play an important role in DC-T cell engagement. All groups treated with MPs containing both rapa and MOG exhibited reduced expression of CD86 and CD80 relative to control samples pulsed with LPS, including empty MPs. However, these reductions were equivalent irrespective to the specific rapa:MOG ratio in the MPs. This indicates rapa:MOG MP treatment modulates DC CD86 and CD80 signaling under highly inflammatory conditions, as opposed to complete attenuation of cell activity, and that this modulation is relative insensitive to ratio. As this assay was designed to test the effect of rapa:MOG ratio directly on DCs, we next wanted to test the effect of rapa:MOG treatment in the context of both DCs and T cells.

Rapa:MOG microparticle treatments significantly increase T_{REG} frequencies 96 h after treatment

Next, we tested if the ratio of rapa:MOG in MPs differentially expands antigen-specific T_{REG} *in vitro*. DCs were cultured with each MP formulation for 24 h. Transgenic CD4$^+$ T cells expressing a MOG specific TCR were then isolated from 2D2 mice and co-cultured with the DCs (Figure 4A). After 96 h, cells were stained for viability and T cell phenotype markers to characterize their polarization as a function of ratio (Figure 4B). Increasing the ratio of rapa:MOG loaded into MPs did not decrease CD4$^+$ T cell viability (Figure 4C). MOG (no rapa) MP treated cells on average had a higher trend in CD4$^+$ T cell count compared to rapa: MOG treatments, but this was not significant (Figure 4D). This is likely due to the absence of the restraining effect of rapa in the control group, leading to more rapid T cell expansion. However, at this 96-hour expansion timepoint, polarization of T_{REG} (CD4$^+$/CD25$^+$/FoxP3$^+$) percentage was not dependent on the specific ratio of rapa:MOG (Figure 4E). This result was also observed in our analysis of T_{REG} count confirming that rapa:MOG treatment increased polarization of T_{REG} independent of ratio (Figure 4F).

Rapa:MOG promotes T_{REG} expansion and anti-inflammatory gene expression at 48 h post addition

Since T cell polarization and expansion is a dynamic process, we hypothesized that differences in rapa:MOG polarization may be distinguishable at earlier timepoints of T cell-APC engagement. To test this hypothesis, we analyzed T cells after 48 h of co-culture instead of 96 h (Figure 5A). Interestingly, we observed a significant increase in T cell counts of low rapa:MOG treated cells compared to MOG (no rapa) treated cells (Figure 5B). Similar to the 96-h timepoint, rapa:MOG MP treatment significantly expanded T_{REG} across all tested ratios. Excitingly, however, there was a significant dependence on the ratio of rapa:MOG for the polarization of T_{REG} percentage (Figure 5C). Since we observed this ratio dependent trend in T_{REG}, we hypothesized that there would also be a decrease in functional inflammatory profile of T cells. First, we used intra-cellular antibody staining to assess the transcription T-bet which is associated with inflammatory T cell subtypes, and found that rapa: MOG treatment significantly reduced T-bet expression (Figure 5D). We also used RT-qPCR to assess T cell gene expression for a key functional cytokine produced during inflammation, IFN-ɣ, and found that the highest rapa:MOG treatment led to the lowest expression of the IFN-ɣ gene (Figure 5E). Taken together, these results indicate MPs loaded with a high ratio of rapa:MOG MP play an important role in polarizing antigen-specific T cell differentiation to T_{REG} and correspondingly decreasing expression of inflammatory markers.

Discussion

Biomaterial enabled strategies for drug delivery are gaining increasing interest due to their ability to precisely control release

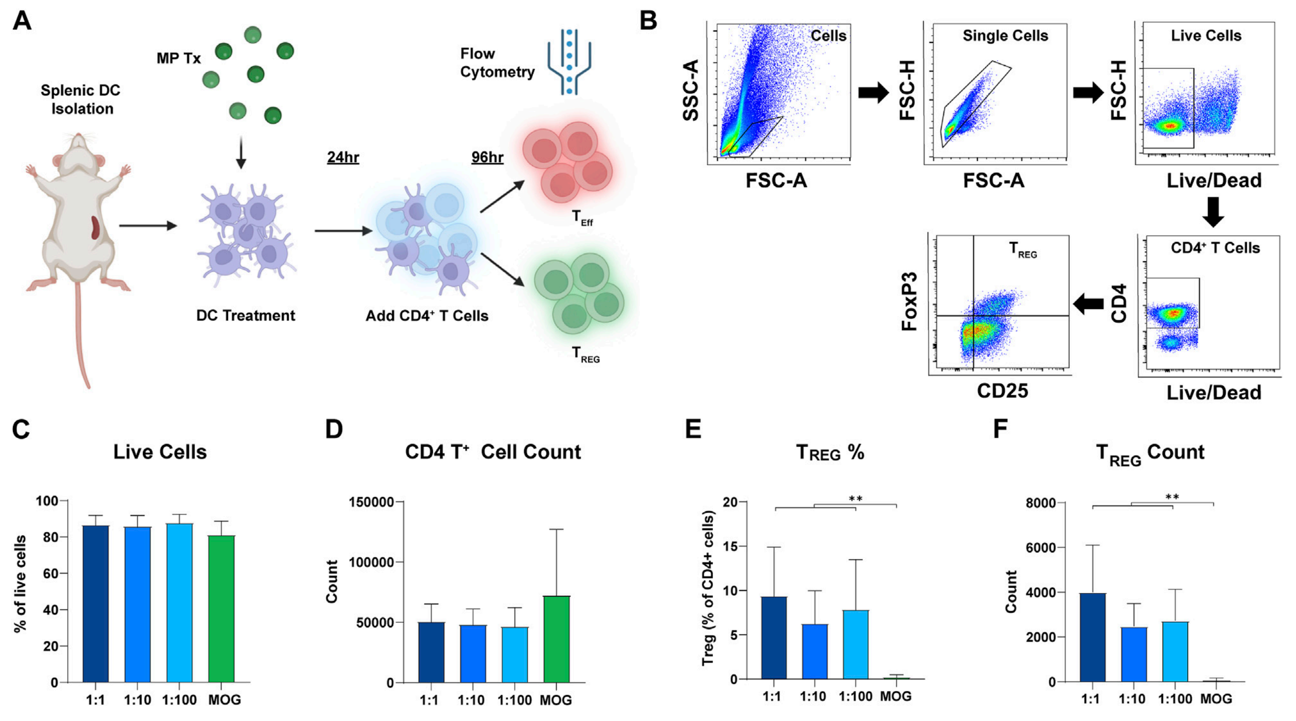

FIGURE 4
Results of DC-CD4 T cell co-culture experiment after 72 h. **(A)** Overview schematic of co-culture assay. **(B)** Representative gating strategy. **(C)** Viability was not significantly different between groups. **(D)** $CD4^+$ T cell count was not significantly different between groups. **(E)** T_{REG} percentage of $CD4^+$ T cells was significantly increased compared to MOG (no rapa) control. **(F)** Similarly, T_{REG} count confirmed that the number of T_{REG} was significantly higher compared to the MOG (no rapa) control. This study was completed in triplicate. For each study, N = 3. An ANOVA with a Tukey multiple comparisons post-hoc test was used to compare each group. Statistical significance is indicated by a (*). $^{**}p < 0.01$. Created with BioRender.

parameters such as time, location, and concentration. Particularly, rapa delivery through both microparticle and nanoparticle formulations *in vivo* has shown significant immune engineering promise across multiple species models in the study of chronic inflammation, transplant rejection, and auto-immune disorders (Fan et al., 2019; Fisher et al., 2019; Nguyen et al., 2022). Although many biomaterial vehicles may be used to facilitate rapa delivery, much work continues to rely on the use of PLGA due to its versatility and extensive use in U.S. Food and Drug Administration (FDA) approved products (E. Emerson et al., 2020). More recently, the addition of specific self-antigens to rapa delivery strategies has shown promise in directing the formation of antigen-specific T_{REG}. The work in this paper builds off of previous studies that have shown that co-encapsulation of self-antigen (MOG) and a modulatory cue (rapa) can promote the polarization of antigen-specific regulatory T cells for treatment of pre-clinical model of MS (experimental autoimmune encephalomyelitis) (Tostanoski et al., 2016). Specifically, this paper studies how the ratio of rapa and MOG co-localized in MPs controls the activation of APCs and the formation of T_{REG} *in vitro*.

Diffusion limited MPs rely on their size for retention within the LN in order to facilitate the direct release of cues to the tissue (Jewell, Bustamante López and Irvine, 2011). Although the quantity of rapa was decreased by over 100-fold, particles retained previously reported engineered diameter that would allow for future *in vivo* testing (Jewell, Bustamante López and Irvine, 2011). Additionally, particle size plays an important role in phagocytic uptake, which could have implications for *in vitro* T_{REG} expansion therapies. Interestingly, both the hydrophilic MOG cargo, and hydrophobic rapa cargo had an influence on MP size. However, our results showed that particles maintained a diameter that would permit phagocytosis.

APC co-stimulation is an important requirement for T cell activation and polarization into either an inflammatory or anti-inflammatory phenotype. However, rapa is a potent mTOR inhibitor that has been previously linked to reduced expression of co-stimulation receptors on APCs (Carey, Gammon and Jewell, 2021; Gosselin et al., 2021). Thus, it is important to understand if high ratios of rapa:MOG have a deleterious effect on DC viability and co-stimulation. Our study focused on the expression of the co-stimulatory molecules CD86 and CD80 which are the main ligands for the T cell activation receptor CD28 which is needed to promote T cell survival. The results of our experiments showed that DC expression of co-stimulation receptors was insensitive to rapa:MOG treatment. This suggests that both the low and high ratio of rapa:MOG exerted similar modulatory effects on DCs after 24 h.

To understand the effect of rapa:MOG ratio on the interaction of DCs and antigen-specific T cells, we co-cultured and treated primary derived DCs and primary derived transgenic MOG recognizing T cells. As the transgenic T cells only express one receptor, groups without MOG antigen had low viability and were excluded from analysis. Rapa is a well-known immunomodulator that drives proliferation of T_{REG}, and our experiment showed that groups treated with MPs containing rapa indeed adopted a $CD25^+$

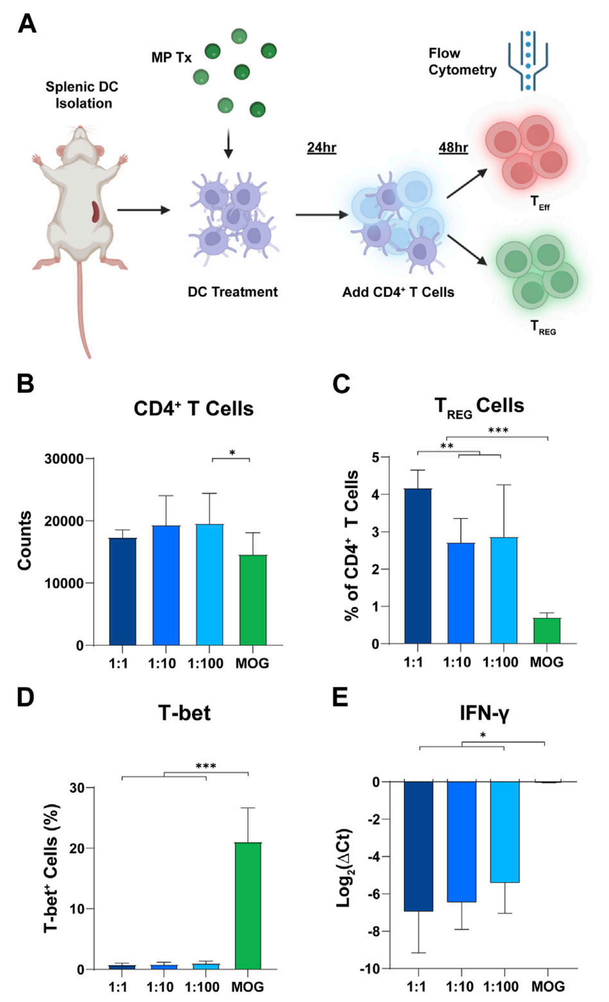

FIGURE 5
High rapa:MOG promotes greater expansion of T_{REG} after 48 h. **(A)** Overview schematic of co-culture assay. **(B)** There was no significant difference in T cell count between rapa:MOG treated groups. **(C)** High ratio of rapa:MOG induced the highest percentage of T_{REG}. All groups induced significant increase in T_{REG} percentage over MOG (no rapa) control. **(D)** Rapa:MOG polarized cells away from expression of the inflammatory transcription factor T-bet. **(E)** RT-qPCR analysis showed rapa:MOG treated cells had significantly lower expression of the gene for the inflammatory cytokine IFN-ɣ. This study was completed in triplicate. An ANOVA with a Tukey multiple comparisons post-hoc test was used to compare each group. Statistical significance is indicated by a (*). *$p < 0.05$, **$p < 0.01$, ***$p < 0.001$. Created with BioRender.

FoxP3⁺ regulatory phenotype. Although the ratio of rapa:MOG did not significantly change the percentage of polarized T_{REG} after 96 h, we did observe significant ratio dependent changes after 48 h. The lack of significant difference between rapa:MOG treatments at later timepoints could potentially be attributed to the aggressive expansion kinetics of transgenic T cells engineered to recognize specific self-antigens. Alternatively, the half-life of rapa is approximately 60 h and may elicit its strongest effect at earlier timepoints. Additionally, T cells would not have undergone as many divisions at earlier timepoints, and thus the concentration of rapa per cell could have a more evident effect-potentially as a function of cell metabolism (Zhang et al., 2019). However, these ratio dependent differences were only observed for the percentage of T_{REG}, and not for T-bet transcription factor expression or IFN-ɣ gene expression. Despite the highly constrained nature of this study, these results lay important groundwork for interrogating the role of rapa and self-antigen in directing anti-inflammatory responses at initial stages of treatment.

Although this study focused on testing how rapa:MOG ratios shape T_{REG} induction, it has been shown that rapa can have modulatory effects beyond T_{REG} induction such as in the generation of "memory" like phenotypes. Future work should seek to understand how the ratio of rapa and self-antigen modulate the adoption of memory cells which could be useful in engineering long lasting tolerizing T cell responses for treatment of auto-immune diseases. Although the concept of regulatory memory is continually evolving, metabolic reprogramming of T cells is known to play a critical role in cell fate. Interestingly, our results showed rapa:MOG led to a trend in lower T cell counts at 96 h, but actually resulted in a significant increase in the low ratio group at 48 h. This suggests that the MOG and rapa work synergistically to modulate cell functions such as metabolism and proliferation. Thus, future studies should attempt to mechanistically differentiate antigen-specific T_{REG} responses from non-antigen-specific responses which potentially carries important implications for *in vitro* T_{REG} expansion applications. Finally, the *in vitro* culture conditions assayed here do not fully recapitulate the complexity of the immune microenvironment. Thus, future studies should test how rapa:MOG ratios can shape efficacy or immune memory under *in vivo* conditions.

Conclusion

Our work here showed that the ratio of rapa:MOG encapsulated in polymer MPs does not differentially alter the engineered properties of MPs for future *in vivo* intra-LN translation. Rapa:MOG ratio did not modulate APC expression of costimulatory receptors involved in T cell activation highlighting DC tolerance to rapa. Interestingly, the ratio of rapa:MOG differentially drives the expansion of T_{REG}, and anti-inflammatory T cell profile of CD4⁺ T cells.

Data availability statement

The raw data supporting the conclusion of this article will be made available by the authors, without undue reservation.

Ethics statement

The animal study was reviewed and approved by University of Maryland Institutional Animal Care and Use Committee (IACUC).

Author contributions

CB, SS, RO, and CJ designed the experiments. CB and CJ wrote the manuscript. CB and SS performed all experiments. CB characterized all MP formulations and performed all *in vitro* cell studies. CB and SS performed RT-qPCR experiments. RO and SS contributed to RT-qPCR experiment design, and data analysis. All authors contributed to the article and approved the submitted version.

Funding

This data was supported in part by NIH R01 AI169686.

Acknowledgments

The authors acknowledge the University of Maryland Department of Laboratory Animal Resources staff for their support with animal husbandry. The authors acknowledge support from University of Maryland Bioworkshop core facility for use of its QuantStudio 7 Flex Real-Time PCR System, and NanoDrop 2000c Spectrophotometer.

Conflict of interest

CJ and RO are employees of the VA Maryland Health Care System. The reviews reported here do not reflect the views of the VA or the United States Government. CJ has an equity position with Cartesian Therapeutics.

The remaining authors declare that the research was conducted in the absence of any commercial or financial relationships that could be construed as a potential conflict of interest.

Publisher's note

Author disclaimer

The view reported here do not reflect those of the United States Government or Department of Veteran Affairs.

Supplementary material

The Supplementary Material for this article can be found online at: https://www.frontiersin.org/articles/10.3389/fbioe.2023.1184938/full#supplementary-material

References

Andorko, J. I., Hess, K. L., and Jewell, C. M. (2015). Harnessing biomaterials to engineer the lymph node microenvironment for immunity or tolerance. *AAPS J.* 17 (2), 323–338. doi:10.1208/s12248-014-9708-2

Arneth, B. M. (2019). Impact of B cells to the pathophysiology of multiple sclerosis. *J. Neuroinflammation* 16 (1), 128. doi:10.1186/s12974-019-1517-1

Blasi, P. (2019). Poly(lactic acid)/poly(lactic-co-glycolic acid)-based microparticles: An overview. *J. Pharm. Investigation* 49 (4), 337–346. doi:10.1007/s40005-019-00453-z

Bookstaver, M. L., Tsai, S. J., Bromberg, J. S., and Jewell, C. M. (2018). Improving vaccine and immunotherapy design using biomaterials. *Trends Immunol.* 39 (2), 135–150. doi:10.1016/j.it.2017.10.002

Carey, S. T., Gammon, J. M., and Jewell, C. M. (2021). Biomaterial-enabled induction of pancreatic-specific regulatory T cells through distinct signal transduction pathways. *Drug Deliv. Transl. Res.* 11 (6), 2468–2481. doi:10.1007/s13346-021-01075-5

Danhier, F., Ansorena, E., Silva, J. M., Coco, R., Le Breton, A., and Préat, V. (2012). PLGA-based nanoparticles: An overview of biomedical applications. *J. Control. Release* 161 (2), 505–522. doi:10.1016/j.jconrel.2012.01.043

Danikowski, K. M., Jayaraman, S., and Prabhakar, B. S. (2017). Regulatory T cells in multiple sclerosis and myasthenia gravis. *J. Neuroinflammation* 14 (1), 117. doi:10.1186/s12974-017-0892-8

Dendrou, C. A., Fugger, L., and Friese, M. A. (2015). Immunopathology of multiple sclerosis. *Nat. Rev. Immunol.* 15 (9), 545–558. doi:10.1038/nri3871

Emerson, E., Hiremath, S. C., and Weaver, J. D. (2020). Biomaterial-based approaches to engineering immune tolerance. *Biomaterials Sci.* 8 (24), 7014–7032. doi:10.1039/D0BM01171A

Fan, Y., Zheng, X., Ali, Y., Berggren, P. O., and Loo, S. C. J. (2019). Local release of rapamycin by microparticles delays islet rejection within the anterior chamber of the eye. *Sci. Rep.* 9 (1), 3918. doi:10.1038/s41598-019-40404-0

Fisher, J. D., Balmert, S. C., Zhang, W., Schweizer, R., Schnider, J. T., Komatsu, C., et al. (2019). Treg-inducing microparticles promote donor-specific tolerance in experimental vascularized composite allotransplantation. *Proc. Natl. Acad. Sci.* 116 (51), 25784–25789. doi:10.1073/pnas.1910701116

Gammon, J. M., Carey, S. T., Saxena, V., Eppler, H. B., Tsai, S. J., Paluskievicz, C., et al. (2023). Engineering the lymph node environment promotes antigen-specific efficacy in type 1 diabetes and islet transplantation. *Nat. Commun.* 14 (1), 681. doi:10.1038/s41467-023-36225-5

Gammon, J. M., Gosselin, E. A., Tostanoski, L. H., Chiu, Y. C., Zeng, X., Zeng, Q., et al. (2017). Low-dose controlled release of mTOR inhibitors maintains T cell plasticity and promotes central memory T cells. *J. Control. Release* 263, 151–161. doi:10.1016/j.jconrel.2017.02.034

Gandhi, R., Laroni, A., and Weiner, H. L. (2010). Role of the innate immune system in the pathogenesis of multiple sclerosis. *J. Neuroimmunol.* 221 (1), 7–14. doi:10.1016/j.jneuroim.2009.10.015

Gosselin, E. A., Noshin, M., Black, S. K., and Jewell, C. M. (2021). Impact of excipients on stability of polymer microparticles for autoimmune therapy. *Front. Bioeng. Biotechnol.* 8, 609577. doi:10.3389/fbioe.2020.609577

Gosselin, E. A., Tostanoski, L. H., and Jewell, C. M. (2017). Controlled release of second generation mTOR inhibitors to restrain inflammation in primary immune cells. *AAPS J.* 19 (4), 1175–1185. doi:10.1208/s12248-017-0089-1

Hauser, S. L., and Cree, B. A. C. (2020) 'Treatment of multiple sclerosis: A review', *Am. J. Med.*, 133(12), pp. 1380–1390. doi:10.1016/j.amjmed.2020.05.049

Hester, J., Schiopu, A., Nadig, S., and Wood, K. (2012). Low-Dose rapamycin treatment increases the ability of human regulatory T cells to inhibit transplant arteriosclerosis *in vivo*. *Am. J. Transplant.* 12 (8), 2008–2016. doi:10.1111/j.1600-6143.2012.04065.x

Huang, W.-J., Chen, W.-W., and Zhang, X. (2017). Multiple sclerosis: Pathology, diagnosis and treatments. *Exp. Ther. Med.* 13 (6), 3163–3166. doi:10.3892/etm.2017.4410

Jewell, C. M., Bustamante López, S. C., and Irvine, D. J. (2011). *In situ* engineering of the lymph node microenvironment via intranodal injection of adjuvant-releasing polymer particles. *Proc. Natl. Acad. Sci.* 108 (38), 15745–15750. doi:10.1073/pnas.1105200108

Kimura, K. (2020). Regulatory T cells in multiple sclerosis. *Clin. Exp. Neuroimmunol.* 11 (3), 148–155. doi:10.1111/cen3.12591

Maldonado, R. A., LaMothe, R. A., Ferrari, J. D., Zhang, A. H., Rossi, R. J., Kolte, P. N., et al. (2015). Polymeric synthetic nanoparticles for the induction of antigen-specific immunological tolerance. *Proc. Natl. Acad. Sci.* 112 (2), E156–E165. doi:10.1073/pnas.1408686111

Marín Morales, J. M., Münch, N., Peter, K., Freund, D., Oelschlägel, U., Hölig, K., et al. (2019). Automated clinical grade expansion of regulatory T cells in a fully closed system. *Front. Immunol.* 10, 38. doi:10.3389/fimmu.2019.00038

März, A. M., Fabian, A. K., Kozany, C., Bracher, A., and Hausch, F. (2013). Large FK506-binding proteins shape the pharmacology of rapamycin. *Mol. Cell. Biol.* 33 (7), 1357–1367. doi:10.1128/MCB.00678-12

Mosanya, C. H., and Isaacs, J. D. (2019). Tolerising cellular therapies: What is their promise for autoimmune disease? *Ann. Rheumatic Dis.* 78 (3), 297–310. doi:10.1136/annrheumdis-2018-214024

Mukhopadhyay, S., Frias, M. A., Chatterjee, A., Yellen, P., and Foster, D. A. (2016). The enigma of rapamycin dosage. *Mol. Cancer Ther.* 15 (3), 347–353. doi:10.1158/1535-7163.MCT-15-0720

Nguyen, T. L., Choi, Y., Im, J., Shin, H., Phan, N. M., Kim, M. K., et al. (2022). Immunosuppressive biomaterial-based therapeutic vaccine to treat multiple sclerosis via re-establishing immune tolerance. *Nat. Commun.* 13 (1), 7449. doi:10.1038/s41467-022-35263-9

Romano, M., Fanelli, G., Albany, C. J., Giganti, G., and Lombardi, G. (2019). Past, present, and future of regulatory T cell therapy in transplantation and autoimmunity. *Front. Immunol.* 10. doi:10.3389/fimmu.2019.00043

Sato, Y., Keino, H., Nakayama, M., Kano, M., and Okada, A. A. (2021). Effect of *in vivo* expansion of regulatory T cells with IL-2/anti-IL-2 antibody complex plus rapamycin on experimental autoimmune uveoretinitis. *Ocular Immunol. Inflamm.* 29 (7–8), 1520–1529. doi:10.1080/09273948.2020.1757119

Saunders, R. N., Metcalfe, M. S., and Nicholson, M. L. (2001). Rapamycin in transplantation: A review of the evidence. *Kidney Int.* 59 (1), 3–16. doi:10.1046/j.1523-1755.2001.00460.x

Saxena, V., Li, L., Paluskievicz, C., Kasinath, V., Bean, A., Abdi, R., et al. (2019). Role of lymph node stroma and microenvironment in T cell tolerance. *Immunol. Rev.* 292 (1), 9–23. doi:10.1111/imr.12799

Schmittgen, T. D., and Livak, K. J. (2008). Analyzing real-time PCR data by the comparative CT method. *Nat. Protoc.* 3 (6), 1101–1108. doi:10.1038/nprot.2008.73

Su, Y., Zhang, B., Sun, R., Liu, W., Zhu, Q., Zhang, X., et al. (2021). PLGA-Based biodegradable microspheres in drug delivery: Recent advances in research and application. *Drug Deliv.* 28 (1), 1397–1418. doi:10.1080/10717544.2021.1938756

Torkildsen, Ø., Myhr, K.-M., and Bø, L. (2016). Disease-modifying treatments for multiple sclerosis – A review of approved medications. *Eur. J. Neurology* 23 (S1), 18–27. doi:10.1111/ene.12883

Tostanoski, L. H., Chiu, Y. C., Gammon, J., Simon, T., Andorko, J., Bromberg, J., et al. (2016). Reprogramming the local lymph node microenvironment promotes tolerance that is systemic and antigen specific. *Cell. Rep.* 16 (11), 2940–2952. doi:10.1016/j.celrep.2016.08.033

Tostanoski, L. H., Gosselin, E. A., and Jewell, C. M. (2016). Engineering tolerance using biomaterials to target and control antigen presenting cells. *Discov. Med.* 21 (117), 403–410.

Vakrakou, A. G., Alexaki, A., Brinia, M. E., Anagnostouli, M., Stefanis, L., and Stathopoulos, P. (2022). The mTOR signaling pathway in multiple sclerosis; from animal models to human data. *Int. J. Mol. Sci.* 23 (15), 8077. doi:10.3390/ijms23158077

Weissert, R. (2013). The immune pathogenesis of multiple sclerosis. *J. Neuroimmune Pharmacol.* 8 (4), 857–866. doi:10.1007/s11481-013-9467-3

Yellen, P., Saqcena, M., Salloum, D., Feng, J., Preda, A., Xu, L., et al. (2011). High-dose rapamycin induces apoptosis in human cancer cells by dissociating mTOR complex 1 and suppressing phosphorylation of 4E-BP1. *Cell. Cycle* 10 (22), 3948–3956. doi:10.4161/cc.10.22.18124

Yoo, Y. J., Kim, H., Park, S. R., and Yoon, Y. J. (2017). An overview of rapamycin: From discovery to future perspectives. *J. Industrial Microbiol. Biotechnol.* 44 (4–5), 537–553. doi:10.1007/s10295-016-1834-7

Zhang, J., Jin, H., Xu, Y., and Shan, J. (2019). Rapamycin modulate treg/Th17 balance via regulating metabolic pathways: A study in mice. *Transplant. Proc.* 51 (6), 2136–2140. doi:10.1016/j.transproceed.2019.04.067

frontiers | Frontiers in Bioengineering and Biotechnology

TYPE Review
PUBLISHED 21 July 2023
DOI 10.3389/fbioe.2023.1187974

OPEN ACCESS

EDITED BY
Behnam Akhavan,
The University of Newcastle, Australia

REVIEWED BY
Monica Mattioli-Belmonte,
Marche Polytechnic University, Italy
Ian James Martins,
University of Western Australia, Australia

*CORRESPONDENCE
Jincheng Wang,
✉ jinchengwang@hotmail.com
Hui Jin,
✉ jinhui0203@jlu.edu.cn

RECEIVED 16 March 2023
ACCEPTED 10 July 2023
PUBLISHED 21 July 2023

CITATION
Lu J, Li H, Zhang Z, Xu R, Wang J and Jin H (2023), Platelet-rich plasma in the pathologic processes of tendinopathy: a review of basic science studies.
Front. Bioeng. Biotechnol. 11:1187974.
doi: 10.3389/fbioe.2023.1187974

Platelet-rich plasma in the pathologic processes of tendinopathy: a review of basic science studies

Jialin Lu[1,2], Han Li[2], Ziyu Zhang[2], Rui Xu[3], Jincheng Wang[4]* and Hui Jin[1,4]*

[1]Department of Pain, The Second Hospital of Jilin University, Changchun, China, [2]Norman Bethune Health Science Center of Jilin University, Changchun, China, [3]Department of Endocrinology and Metabolism, Ruijin Hospital, Shanghai Jiao Tong University, Shanghai, China, [4]Department of Orthopedics, The Second Hospital of Jilin University, Changchun, China

Tendinopathy is a medical condition that includes a spectrum of inflammatory and degenerative tendon changes caused by traumatic or overuse injuries. The pathological mechanism of tendinopathy has not been well defined, and no ideal treatment is currently available. Platelet-rich plasma (PRP) is an autologous whole blood derivative containing a variety of cytokines and other protein components. Various basic studies have found that PRP has the therapeutic potential to promote cell proliferation and differentiation, regulate angiogenesis, increase extracellular matrix synthesis, and modulate inflammation in degenerative tendons. Therefore, PRP has been widely used as a promising therapeutic agent for tendinopathy. However, controversies exist over the optimal treatment regimen and efficacy of PRP for tendinopathy. This review focuses on the specific molecular and cellular mechanisms by which PRP manipulates tendon healing to better understand how PRP affects tendinopathy and explore the reason for the differences in clinical trial outcomes. This article has also pointed out the future direction of basic research and clinical application of PRP in the treatment of tendinopathy, which will play a guiding role in the design of PRP treatment protocols for tendinopathy.

KEYWORDS

platelet-rich plasma, tendinopathy, pathogenesis, healing process, cell proliferation, differentiation

1 Introduction

A tendon is a dense connective tissue that connects muscle to bone. It comprises bundles of parallel collagen fibers that can carry tensile loads. The tendon has the function of stabilizing the joint and realizing the joint motion. Therefore, it is usually subjected to heavy mechanical loads that may lead to injury and dysfunction (Millar et al., 2021). Tendinopathy is a common musculoskeletal disorder that is more likely to occur in professional athletes or the middle-aged and elderly population participating in sports. Tendinopathy is characterized by pain, swelling, and dysfunction of the tendon and peritendinous tissue, with the accumulation of lipids, proteoglycans, and calcium in the tendon (Nourissat et al., 2015a). Eventually, tendinopathy will lead to long-term or permanent deficits in the patient's motor system function. The incidence of tendinopathy has been increasing around the world since the 21st century. About 30% of current clinical consultations for musculoskeletal disorders involve tendinopathy, and about 16.4 million people seek medical intervention each year in orthopedic clinics in the

United States alone (James et al., 2008; Macedo et al., 2019). To date, the pathological mechanism of tendinopathy has not been clarified. Research progress in tendinopathy lags behind that in inflammatory arthritis, osteoarthritis, and other motor system diseases. Current hypotheses on tendinopathy pathogenesis describe tendinopathy as a degenerative or failed healing process (Cook and Purdam, 2009; Cook and Purdam, 2021). Degenerative pathology emphasizes apoptosis and matrix degradation of the affected tendon tissue (Cook and Purdam, 2009). Failed healing pathology is characterized by an excessive amount of non-collagenous extracellular matrix, collagen fiber disruption, chronic inflammation, and disordered arrangement of neovascularization within the tendon (Cook and Purdam, 2009). The scar tissue is formed by the deposition of a large number of interlaced or disordered collagen fibers. This will negatively affect the reconstruction of tendon structure and the recovery of tendon biomechanical characteristics, leading to a higher probability of secondary tendon injury (Katzel et al., 2011). Furthermore, scar tissue can cause adhesion and contraction of the tendon, which will significantly impair the inherent function of the tendon and limit the motion range of the joint (Wong et al., 2009).

Treatment of tendinopathy usually requires clinical intervention. The blood and nutrition supply of tendon is not abundant, and neurotrophin and is always in a high-stress state, which leads to limited self-healing ability. Achilles tendinopathy, patellar tendinopathy, rotator cuff tendinopathy, and lateral elbow tendinopathy are the most common tendinopathy without ideal treatment currently available (Ruan et al., 2021). The clinical treatment strategies of tendinopathy are mainly based on non-surgical treatments, including cold therapy, rest, fixation, non-steroidal anti-inflammatory drug therapy, rehabilitation therapy, and extracorporeal shock wave therapy, to relieve the pain and slow the progress of the degenerative process (Andia et al., 2018). However, most conservative therapies can only be effective in the short term with suboptimal long-term outcomes. Approximately 24%–45.5% of patients eventually require surgical treatment to relieve pain and recover tendon function (Roche and Calder, 2013; Schemitsch et al., 2019). Surgical repair of the tendon can cause complications, such as wound infection, tendon stiffness, adhesions, pain, and swelling. A significant proportion of patients are at risk of re-tearing (Chung et al., 2013; Brockmeyer et al., 2015). Therefore, it is necessary to deeply investigate the pathological process of tendinopathy and the mechanism of tendon healing to update the current treatment therapy. In recent years, platelet-rich plasma (PRP) has emerged as a popular option for the treatment of motor system diseases, including tendinopathy (Zhou and Wang, 2016). The platelet concentration in PRP is usually five times the physiological plasma level ($100–300 \times 10^9$ cells/L), which can form a local cytokine-rich microenvironment for tendon regeneration (Basdelioglu et al., 2020; Lyu et al., 2021). After activation, platelets in PRP release a variety of growth factors, including platelet-derived growth factor (PDGF), transforming growth factor-β (TGF-β), vascular endothelial growth factor (VEGF), epidermal growth factor (EGF), insulin-like growth factor-I (IGF-I), fibroblast growth factor (FGF), and hepatocyte growth factor (HGF) (Alsousou et al., 2013). PRP can improve the microenvironment of the degenerative tendon by inducing cell recruitment, proliferation, and differentiation, promoting collagen fiber formation and angiogenesis, and regulating inflammation

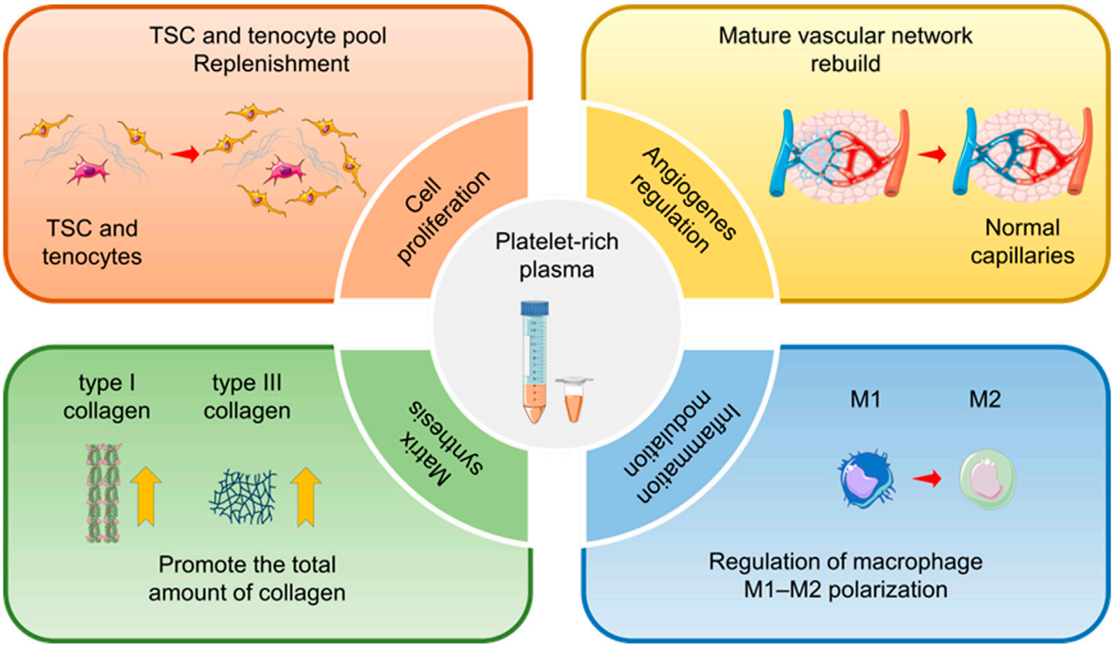

SCHEME 1
Therapeutic effects of platelet-rich plasma (PRP) for tendinopathy. For chronic tendinopathy, PRP has the therapeutic potential to promote cell proliferation and differentiation, regulate angiogenesis, increase extracellular matrix synthesis, and modulate inflammation. Therefore, PRP has been widely used in the clinical practice of tendinopathy treatment.

(Scheme 1). In addition to platelets, PRP contains components such as plasma, leukocytes, and residual erythrocytes, which can synthesize and release some bioactive factors. Neutrophils and monocytes are the most significant leukocytes in PRP. They can release a series of pro-inflammatory mediators, such as peroxidases, matrix metalloproteinases (MMPs), interleukin (IL)-1β, IL-6, and tumor necrosis factor-α (TNF-α), and growth factors, such as platelet-activating factor (PAF), TGF-β, VEGF, and EGF (Lyu et al., 2021; Lin et al., 2022). These cytokines can modulate the inflammation of tendinopathy and positively affect tendon healing. PRP can be further divided into leukocyte-poor PRP (LP-PRP) and leukocyte-rich PRP (LR-PRP) according to its composition. LP-PRP has a low platelet content, only 1.5–3 times the baseline level, and contains few erythrocytes and leukocytes (Le et al., 2018). However, LR-PRP usually has high platelet content, 3–8 times the baseline level, and a high leukocyte count (Le et al., 2018).

PRP is derived from autologous whole blood and does not present a risk of immune rejection. A large number of basic experiments have proven that for tendinopathy, PRP has the therapeutic potential to modulate inflammation, stimulate angiogenesis, promote cell proliferation, and increase extracellular matrix synthesis (de Mos et al., 2008; Kajikawa et al., 2008; Zhang and Wang, 2010b; Zhang et al., 2013). However, the clinical efficacy of PRP for tendinopathy is not always satisfactory. Several clinical trials and meta-analyses have shown that PRP therapy does not improve the prognosis of tendinopathy compared with the control groups (Chahal et al., 2012; Saltzman et al., 2016; Filardo et al., 2018). The pathological mechanisms of tendinopathy and the process of tendon healing were reviewed in this article to better understand how PRP affects tendinopathy and explore the reason for the differences in clinical trial outcomes. On this basis, the specific molecular and cellular mechanisms by which PRP manipulates tendon healing were integrated. Finally, we present a critical analysis of the available basic and clinical trial results. We have also pointed out the future direction of basic research and clinical application of PRP in the treatment of tendinopathy, which will play a guiding role in the design of PRP treatment protocols for tendinopathy.

2 Physiology and pathology of tendon

2.1 Molecular and cellular composition of tendon

Oligovascularity, hypocellularity, and abundant extracellular matrix are unique histological features of the tendon. The tight parallel arrangement of the extracellular matrix within the tendon determines its unique morphology and biomechanical properties. The extracellular matrix mainly includes three types of organic macromolecules: collagen, proteoglycans, and glycoproteins (Citeroni et al., 2020). Collagen is the main substantial component of the tendon extracellular matrix, accounting for 60%–85% of the dry weight of the tendon (Kannus, 2000). Type I collagen is the major component of collagen fibers and accounts for 95% of the total collagen in the tendon (Kannus, 2000). Type I collagen comprises three helical polypeptide chains that initially aggregate to form microfibers. The microfibers further aggregate to form collagen fibers that are considered the basic mechanical transfer unit of the tendon. The collagen fibers eventually aggregate to form a bundle of collagen fibers wrapped by the connective tissue sheaths (i.e., the endotendineum and the epitendineum) (Killian et al., 2012), which form a complete tendon structure. Type III collagen is the second most abundant collagen fibers after type I collagen in the tendon. Type III collagen is small, immature, and unstable; it cannot provide good mechanical support for the tendon (Thorpe and Screen, 2016). Under normal circumstances, type III collagen is mainly found in the endotendineum and epitendineum, but it is present in large amounts in scar tissue formed early in the healing process of the injured tendon (Masuda et al., 2002; Yoshida et al., 2003). The content of type III collagen can be up to 20%–30% in the scar tissue (Masuda et al., 2002; Yoshida et al., 2003). Increased levels of type III collagen relative to type I collagen in the tendon will inhibit collagen fiber growth, causing adhesion and scar tissue formation. This will also reduce the ability of the tendon to transmit stress and increase the risk of tearing. In addition, there are many other types of collagen in the tendon, such as types V, XII, and XIV. They play an important role in forming collagen fibers and linking type I collagen to other extracellular matrices (Riley, 2004; Banos et al., 2008). Furthermore, the tendon contains many kinds of proteoglycans adhering closely to collagen. Decorin is a vital component of proteoglycans, accounting for about 80% of the total amount of proteoglycans in the tendon. Decorin helps collagen fibers adapt to the tensile load and plays an important role in tendon development (Thorpe et al., 2013). Other types of proteoglycans, such as biglycan and fibromodulin, exist in small amounts within the tendon. They are combined with type I collagen to form mature collagen fibrils and enhance the mechanical strength of the tendon (Derwin et al., 2001). Proteoglycans carry a large number of negative charges. They can attract and bind to water molecules to form an aqueous gel, affecting the viscoelasticity of the tendon and helping resist compression. Glycoproteins are formed by the glycosylation of proteins, with a similar structure to proteoglycans but with few branching parts. Glycoproteins play a significant role in linking tendon cells to extracellular matrix molecules (O'Brien, 1997). Among glycoproteins, elastin is more common and is usually combined with type I collagen as the main component of elastic fibers. Elastin assists in the storage of elastic potential energy when the tendon is subjected to stress (Kielty et al., 2002). Glycoproteins also include fibronectin, tenascin C, and cartilage oligomeric matrix protein, which interact with collagen or other matrix components to promote tendon repair and improve tendon mechanical stability after injury (Sharma and Maffulli, 2005).

Tenoblasts and tenocytes are two types of tendon-specific cells, accounting for 90%–95% of all cells in the tendon. They are important for tendon development, extracellular matrix synthesis and turnover, and tendon homeostasis maintenance (Chuen et al., 2004b; Citeroni et al., 2020). Tenoblasts mainly exist in the endotendineum and are in a relatively low differentiation state, with a round appearance and large and oval nucleus. Tenoblasts play a dominant role in tendon development and maturation and can transform into tenocytes (Pennisi, 2002; Chuen et al., 2004a). Tenocytes are derived from the terminal differentiation of tenoblasts and are similar to fibrocytes, with a spindle-shaped appearance, long nucleus, and thin cytoplasm (Russo et al., 2015). Tenocytes are widely distributed within the tendon and colonize among collagen fibers. They precisely regulate the synthesis and breakdown of the extracellular matrix and maintain homeostasis of the tendon. In the case of stress stimulation or tendon injury, tenocytes can mediate tendon repair by increasing the extracellular matrix level through complex signaling pathways (Giordano et al., 2020). In addition, gap junctions between tenocytes enable the exchange of nutrients, signaling molecules, and electrical signals. Thus, tenocytes can coordinate the biological behavior and form a cell communication network within the tendon (McNeilly et al., 1996; Willecke et al., 2002). Bi et al. (2007) discovered the tendon stem cell (TSC), a new type of tendon cell, in the human hamstring tendon. Studies have shown that TSCs have the classic properties of mesenchymal stem cells, such as the presence of specific surface antigens and the ability to self-renew and differentiate into three lineages (i.e., lipogenesis, osteogenesis, and chondrogenesis) (Docheva et al., 2015). Meanwhile, TSCs can express tendon-related genes and form a tendon or tendon-like tissue after *in vivo* implantation (Docheva et al., 2015). The exact role TSC plays in maintaining tendon homeostasis and tendon healing remains uncertain, as well as the exact association among TSCs, tenoblasts, and tenocytes. However, TSCs are still regarded as a potential source of stem cells in tendon healing (Zhang and Wang, 2010a; Zhang et al., 2010; Ruzzini et al., 2014). Additionally, endothelial cells and smooth muscle cells in blood vessels, chondrocytes in insertion sites, and synovial cells in the endotendineum and epitendineum exist within the tendon (Walden et al., 2017) (Figure 1).

2.2 Pathogenesis of tendinopathy

Tendinopathy is an injury to a tendon (as from acute trauma or chronic overuse) that is often accompanied by pain, weakness, inflammation, or stiffness (Wu et al., 2017) (Scheme 2). The affected tendons are gray-brown in color, with the original structure destroyed. The matrix components change pathologically. The mechanical properties are weakened. There are clinical features of stiffness, adhesion, functional impairment, local swelling, and pain (Steinmann et al., 2020). Unlike acute tendon injury, which occurs in bursts of intense pain and loss of function, chronic tendinopathy often results in progressive pain and loss of tendon function (Wu et al., 2017). The slow-onset process of tendinopathy may delay the diagnosis of symptoms and ultimately lead to a poor prognosis. With the development of the etiology of tendinopathy, many risk factors associated with tendinopathy have been identified.

The risk factors are generally divided into external, internal, and environmental factors. Different risk factors may be present in

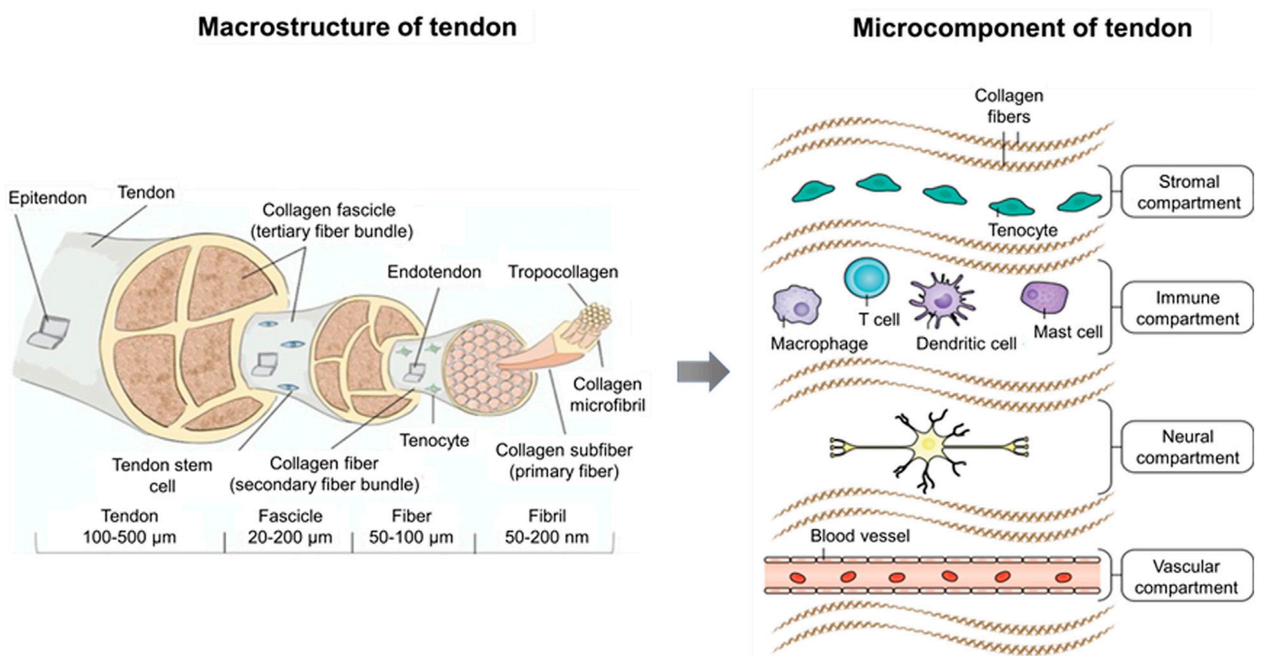
Macrostructure of tendon

Microcomponent of tendon

FIGURE 1
Macrostructure and microcomponent of tendon. The tendon sub-structures (e.g., fascicle, fiber, fibril, and tropocollagen) are illustrated with relative dimensions thereof in a healthy tendon. Microcomponents of the tendon encompass four distinct compartments. The stromal compartment includes tissue-resident tenocytes and matrix components, which are essential for tissue remodeling and repair. The immune compartment involving T cells, dendritic cells, mast cells, and macrophages responds to initial tissue insult through damage-associated molecular patterns (DAMPs) or pathogen-associated molecular patterns (PAMPs). The neural compartment, which in the homeostatic state plays a role in proprioception, interacts with mast cells to modulate adaptive responses in the normal tendon. Although most tendons are poorly vascularized, they respond to hypoxia by secreting angiogenic factors that induce the growth of neovessels, which comprise the vascular compartment (Lipman et al., 2018; Millar et al., 2021).

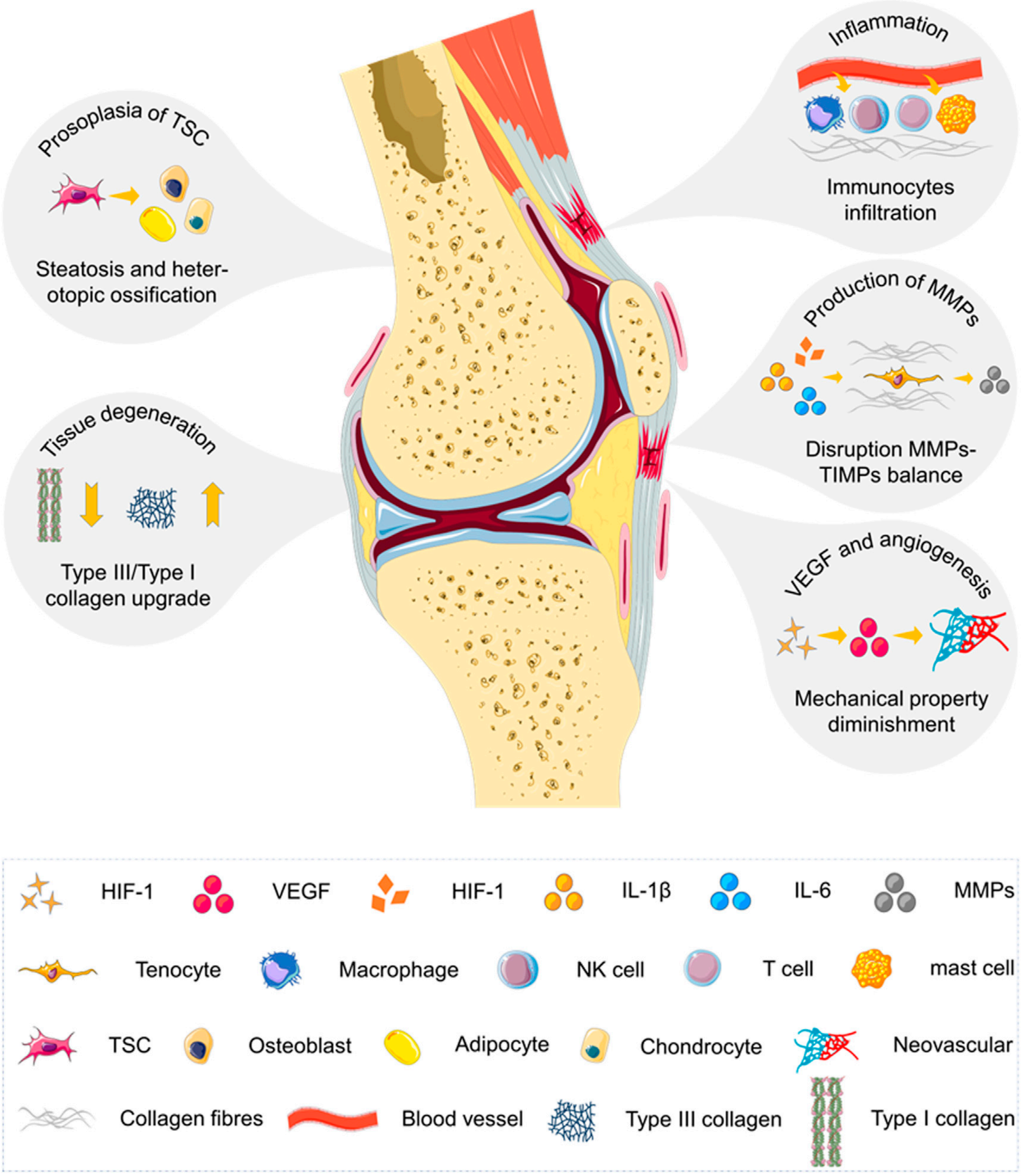

SCHEME 2
Summarization of underlying biological mechanisms involved in the progression of chronic tendinopathy. Tendinopathy is a medical condition including traumatic or overuse injuries and a spectrum of inflammatory and degenerative tendon changes. The process of angiogenesis and neurogenesis is activated, leading to inflammation and pain. Tendon stem cell receives pathological signals and enters the abnormal differentiation pathway. The balance between matrix metalloproteinases (MMPs) and tissue inhibitors of matrix metalloproteinases (TIMPs) within tendons is also disrupted. The loss of matrix integrity by reduction of total collagen content and augmentation of type III/type I collagen ratio is revealed in pathological tendons. The chronic degenerative tendon has a high level of vascular endothelial growth factor (VEGF) and a large amount of disordered neovascularization attributed to hypoxia and excessive mechanical loading.

different patients, either individually or simultaneously. External factors include tendon overloading, short-term changes in the volume or type of the load, and improper training practices (e.g., the use of inferior equipment or short intervals between repeated loads) (Li and Hua, 2016). Acute loading injury, repeated mechanical injury, and overuse of the tendon caused by external factors are considered the key predisposing factors for tendinopathy (Steinmann et al., 2020). Internal factors related to tendinopathy have obvious individual differences, including age, sex, weight, genetic factors, hormone levels, immune function, and previous medical history (e.g., obesity, hypercholesterolemia, diabetes, hyperlipidemia, and arthritis) (Kjaer et al., 2009; Scott et al., 2015; Leblanc et al., 2017). These internal factors can change the mechanical properties, decrease the load tolerance, and regulate the repair response of the injured tendon. Environmental factors associated with tendinopathy include daily living and working environment, malnutrition, smoking, alcohol abuse, temperature (over low ambient temperature), and pharmacological factors (fluoroquinolones and quinolones, corticosteroid, aromatase inhibitors, and statins) (Scott et al., 2015; Knobloch, 2016).

Tendinopathy-related risk factors will initiate tendinopathy, leading to progressive loss of intrinsic cells and matrix components of the tendon through abnormal cell–cell and cell–matrix communication, eventually resulting in tendon rupture. Angiogenesis and neurogenesis are activated during this process, leading to inflammation and pain (Steinmann et al., 2020). The TSC receives pathological signals and enters the abnormal differentiation pathway, resulting in tendon thickening and calcification (Steinmann et al., 2020). Disruption of the balance between MMPs and the tissue inhibitor of matrix metalloproteinases (TIMPs) plays a key role in the process of tendon degeneration (Jones et al., 2006; Del Buono et al., 2013). The loss of matrix integrity (i.e., reduction in total collagen content and augmentation of type III/type I collagen ratio) is revealed in pathological tendons (Riley et al., 1994a; Riley et al., 1996; Tillander et al., 2002). The chronic degenerative tendon exhibits a high level of VEGF and a large number of disordered neovascular attributed to hypoxia and excessive mechanical loading (Lakemeier et al., 2010; Bosch et al., 2011; Andarawis-Puri et al., 2015).

At present, the main hypothesis of tendinopathy includes degenerative and failed healing pathologies. Degenerative pathology emphasizes apoptosis and matrix degradation of the affected tendon tissue. Failed healing pathology is characterized by an excessive amount of non-collagenous extracellular matrix, collagen fiber disruption, chronic inflammation, and disordered arrangement of neovascularization within the tendon. Cook and Purdam (2009) combined the main ideas of the degenerative pathology hypothesis and the failed healing pathology hypothesis. They proposed that tendinopathy is a continuous process and creatively built a continuum model of tendinopathy (Cook and Purdam, 2009). The continuum model divides the pathological process of tendinopathy from normal tendons to ruptured tendons into three consecutive stages: early reactive tendinopathy, tendon disrepair, and degenerative tendinopathy (Cook and Purdam, 2009). Early reactive tendinopathy, occurring after acute stress or trauma, is characterized by a non-inflammatory proliferative response of cells and matrix. During this period, the tendon attempts to reduce the stress effect per unit area through adaptive and relatively uniform thickening. Tendon disrepair, in which the matrix is severely degraded, is accompanied by a massive increase in the number of cells and the production of new proteins (e.g., proteoglycans and collagen). In the later degenerative tendinopathy, the pathological changes in tendon structure and composition are serious and eventually progress to an irreversible stage. As a result of cell apoptosis, tissue disintegration, severe functional impairment, or even complete failure, the degenerative tendon is prone to rupture. It should be noted that the tendon affected by tendinopathy may simultaneously exhibit different stages of pathological processes. The continuum model lays the foundation for clinicians to assess the pathological progression of tendinopathy and provide targeted therapy for the specific pathological stage. In addition, the model can be continuously evaluated and modified in combination with the researchers' clinical, histological, and imaging information.

2.3 Healing mechanism of injured tendon

The current understanding of the cellular and histologic mechanisms of tendon healing is largely based on animal models with experimentally induced tendon injury (Carpenter and Hankenson, 2004; Warden, 2007). The cellular mechanisms of tendon healing include extrinsic and intrinsic healing mechanisms, which are considered to act synergistically in the process of tissue repair (Kajikawa et al., 2007; James et al., 2008). After a tendon injury, inflammatory cells and fibroblasts from the tendon sheath and blood circulation are attracted to the damaged sites by chemokines, causing cell infiltration and adhesion. Subsequently, the intrinsic cells colonizing the tendon are activated. They migrate to the damaged site, proliferate massively, and express a variety of extracellular matrices. They reconstruct the extracellular matrix and form a vascular network during tendon healing. It is noteworthy that compared with the extrinsic repair mechanism, the intrinsic repair mechanism reduces tissue adhesion and, in a sense, preserves the tendon sliding properties within the sheath (Lipman et al., 2018). This could be attributed to the trait differences in extracellular matrix synthesis and proliferation traits of tenocytes or fibroblasts of different origins (Lipman et al., 2018).

In general, the healing process of the injured tendon can be divided into three main stages in terms of histological characteristics: inflammation, proliferation, and remodeling (Voleti et al., 2012; Andarawis-Puri et al., 2015) (Table 1). These

TABLE 1 Tendon repair process in humans.

Phases	Time	Cellular and matrix changes	Cytokines
Inflammatory	48 h	Aggregation of platelets, neutrophils, mononuclear macrophages, erythrocytes, and mesenchymal stem cells, increased pro-inflammatory cytokine production	IL-6, IL-1β, TNF-α, bFGF, TGF-β, PDGF, IGF-I, VEGF
Proliferation (reparative)	6–8 weeks	Increased cellularity and matrix production, activation of local TSCs, promoted type III collagen synthesis	PDGF, TGF-β, VEGF, EGF, IGF-I, HGF
Remodeling (consolidation and maturation)	1–2 years	Reduced cellularity and matrix production, reduced type III collagen, increased type I collagen production, maturation of neovascularization	TGF-β, IGF-I, GDF-5, GDF-6, and GDF-7

(Schultz et al., 2003; Sharma and Maffulli, 2006; Battery and Maffulli, 2011; Del Buono et al., 2011; Voleti et al., 2012; Kaux and Crielaard, 2013; Nourissat et al., 2013; Docheva et al., 2015; Marques et al., 2015; Chisari et al., 2019; Li et al., 2021).

three stages could partially overlap in time and space. The duration of each stage depends on the location and severity of the lesion. Inflammation occurs within 48 h after tendon injury and starts with hematoma formation (Chisari et al., 2021). Activated platelets release clotting factors to initiate the coagulation cascade through degranulation. They also secrete a variety of growth factors and bioactive substances to increase capillary permeability, induce inflammatory cells, and initiate an acute inflammatory response (Kaux and Crielaard, 2013; Marques et al., 2015). Subsequently, the inflammatory cells, including neutrophils, macrophages, and mast cells, migrate to the damaged site, clear the blood clots and necrotic tissue, and further secrete pro-inflammatory cytokines to exacerbate the inflammatory response (Schultz et al., 2003). In addition, platelets and inflammatory cells secrete angiogenic factors that promote angiogenesis and mediate the formation of a disordered neovascular network within the tendon (Tempfer and Traweger, 2015). This is critical for the subsequent healing process and the maintenance of extracellular matrix homeostasis. The damaged tendon enters the proliferation stage after an acute inflammatory response, which is characterized by cellular and extracellular matrix hyperplasia (Nourissat et al., 2013). The proliferation stage lasts for 4–6 weeks. Circulating-derived mesenchymal stem cells, fibroblasts, and TSCs migrate to the affected site and are activated to enter the cell cycle (Chisari et al., 2019). Macrophages convert from type M1 to type M2 and produce large amounts of extracellular matrix together with tenocytes, including collagens and proteoglycans (Li et al., 2021). Much immature and unstable type III collagen is synthesized and forms scar tissue in a disorderly arrangement (Del Buono et al., 2011; Nourissat et al., 2013). Glycosaminoglycan regulates the concentration of water molecules to form local edema within the tendon (Del Buono et al., 2011; Nourissat et al., 2013). At this stage, the tendon exhibits edema, enlargement, a slight increase in mechanical properties, and persistent, intermittent, or activity-related pain (D'Addona et al., 2017). The remodeling stage begins 6–8 weeks after the injury and lasts 1–2 years. This stage is characterized by reduced cell proliferation and extracellular matrix synthesis, replacement of type III collagen with type I collagen, increased cross-linking of collagen fibers and fibrosis, decreased number of capillaries, mature vascular network, and eventual formation of mature tendon tissue (Sharma and Maffulli, 2006). In most patients, especially the middle-aged and elderly, disordered extracellular matrix, impaired collagen fiber integrity, and an increased ratio of type III to type I collagen occur after tendon injury or degeneration. This results in the thickening and hardening of the tendon, with less mechanical strength and mobility than the healthy one.

Tendon healing involves a complex cascade of cytokines. These cytokines originate from platelets, inflammatory cells, endothelium cells, tenocytes, tenoblasts, or TSCs. They are released when stimulated by specific extracellular signals (Citeroni et al., 2020). These cytokines can bind to specific receptors on the target cell membrane and regulate intracellular levels of DNA transcription and translation. Several healing processes, such as cell chemotaxis, proliferation, differentiation, apoptosis, and extracellular matrix turnover, are directly affected (Citeroni et al., 2020). Notably, cytokines play a key role only in the inflammation and proliferation stage. During the inflammation stage, pro-inflammatory cytokines (e.g., IL-6, IL-1β, and TNF-α) and growth factors (e.g., bFGF, TGF-β, PDGF, IGF-I, and VEGF) are mainly released by inflammatory cells and platelets to regulate the early inflammatory response (Battery and Maffulli, 2011; Del Buono et al., 2011). During the reparative stage, growth factors, such as PDGF, TGF-β, VEGF, EGF, IGF-I, and HGF, are mainly secreted by the intrinsic cells of the injured tendon to promote proliferation (Voleti et al., 2012). Considering the critical role of cytokines in tendon healing, the administration of exogenous cytokines, such as PRP, has evolved as one of the potential therapies for the treatment of tendon injury.

3 PRP-induced regeneration of degenerative tendon

3.1 Promotion of tendon cell differentiation and proliferation

After being activated, PRP forms a blood clot that can release a variety of growth factors at high concentrations, including PDGF, TGF-β, HGF, FGF, IGF-I, EGF, and high mobility group protein 1 (HMGB1) (Table 2). Therefore, PRP has the function of inducing tendonogenic differentiation of TSCs, promoting the migration and proliferation of TSCs and tenocytes. The binding of PDGF-BB to PDGF receptors can initiate a series of signaling pathways, including Ras-MAPK, PI3K, PLCγ, and JAK, impacting chemotaxis, mitosis, and angiogenesis during tendon healing (Evrova and Buschmann, 2017). Specifically, neutrophils and macrophages can be induced to converge on the lesion site and degrade tissue debris by PDGF-BB (Evrova and Buschmann, 2017). Furthermore, PDGF-BB can also stimulate tenocyte migration and proliferation, collagen synthesis, and angiogenesis, thereby improving the mechanical properties of the tendon (Evrova and Buschmann, 2017). The activation of the TGF-β signaling pathway can induce the tendonogenic differentiation of TSCs, regulate the metabolism of tenocytes, and stimulate the proliferation of TSCs and tenocytes (Nourissat et al., 2015a). In addition, TGF-β is a crucial growth factor that can regulate the production of collagen and other extracellular matrix, which is closely linked to fibrosis and scar formation in tendinopathy (Katzel et al., 2011). In the classical TGF-β signaling pathway, TGF-β binds to the TGF-β type I or type II receptor on the cell surface to form a ligand–receptor complex, activating the downstream Smad protein and regulating gene transcription and translation (Li et al., 2022). Among them, TGF-β1 can upregulate the levels of Scleraxis (Scx) and Mohawk (Mkx) genes and induce tendonogenic differentiation of TSC, whereas TGF-β2 can stimulate collagen type I alpha 1 (COL1A1) and Scx gene expression (Zhang et al., 2018). Recent studies have shown that TGF-β can also transmit signals through various MAPK pathways, collectively known as non-Smad signaling pathways (Zhang, 2017). HGF can promote the proliferation and migration of TSCs by activating HGF/c-Met, MAPK/ERK1/2, and PI3K/AKT signaling pathways (Han et al., 2019). HGF can also hamper the osteogenic differentiation of TSCs by inhibiting the BMP/Smad1/5/8 signaling pathway (Han et al., 2019). It can also improve the biological activity of the tenocyte, regulate the expression of the extracellular matrix, and enhance the biomechanical properties and migration ability of the degenerative

TABLE 2 Growth factors involved in cell recruitment, proliferation, and differentiation.

Growth factors	Proposed function in tendon healing
PDGF-BB	Chemotaxis, mitogenic, and pro-angiogenic induction
TGF-β	Promoted collagen synthesis, neovascularization, and fibrosis/excessive scar formation, stimulated TSCs, and tenocyte differentiation and proliferation
HGF	Promoted TSC proliferation, migration, and ECM synthesis, prevented osteogenic differentiation of TSCs
bFGF	Induced fibrogenic differentiation of circulating-derived mesenchymal stem cells and proliferation of TSCs, accelerated tendon-to-bone healing
IGF-I and EGF	Induced migration and proliferation of fibroblasts
Platelet-derived HMGB1	Inflammation regulation and stem cell migration induction

(Chan et al., 1997; Wei et al., 2008; Throm et al., 2010; Katzel et al., 2011; Yuan et al., 2013; Nourissat et al., 2015a; Evrova and Buschmann, 2017; Han et al., 2019; Zhang J. et al., 2021; Zhang Z. et al., 2021).

tendon (Zhang Z. et al., 2021). Furthermore, bFGF not only induces fibrotic differentiation of circulating mesenchymal stem cells but also stimulates TSC proliferation and accelerates tendon-to-bone healing (Wei et al., 2008; Yuan et al., 2013). *In vitro* studies have shown that IGF-I and EGF can stimulate fibroblast migration and proliferation (Chan et al., 1997; Throm et al., 2010). Zhang J. et al. (2021) showed that in addition to releasing multiple growth factors, PRP can modulate tendinopathy inflammation and induce stem cell migration to injury sites by releasing platelet-derived HMGB1, thereby promoting the healing process. PRP does not provide a single growth factor but rather a proportional combination of multiple growth factors. Therefore, growth factors released by PRP could amplify their therapeutic effects in promoting cell proliferation and differentiation through synergistic actions, but they also could exert adverse effects through antagonism (Docheva et al., 2015). Furthermore, the plasma component of PRP contains fibrinogen and other coagulation factors. The activated PRP can form a temporary fibrin network as a three-dimensional biomaterial scaffold for cell migration, adhesion, and proliferation (Xie et al., 2014).

TSCs play an important role in tendon healing and tendinopathy. Under physiological conditions, TSCs can differentiate into tenocytes and migrate to the injury site to synthesize extracellular matrix. In degenerative tendinopathy, hazardous factors such as excessive mechanical loading, chronic inflammation, and abnormal tissue microenvironment could induce TSCs to differentiate into chondrocytes, osteoblasts, or adipocytes (Zhang X. et al., 2016). Aberrant differentiation of TSCs not only causes tendons to exhibit steatosis or heterotopic ossification, but also highly depletes the tendinous stem cell pool and indirectly reduces the number of tenocytes at the lesion site (Zhang X. et al., 2016). This view is supported by several basic experiments. Compared with TSCs from the healthy tendon, TSCs from the collagenase-induced tendinopathy site exhibit lower expression of tendonogenic markers and higher expression of osteogenic and chondrogenic markers, with lower proliferation and higher senescence rates (Rui et al., 2013). TSCs of biglycan and fibromodulin double-knockout osteoarthritis model mice rather than wild-type mice exhibit decreased expression of tendonogenic markers Scx and type I collagen, increased expression of chondrocyte markers type II collagen and aggrecan, and a significant change in cellular function (Bi et al., 2007). The self-renewal capacity of TSCs from aged/degenerated human Achilles is significantly reduced, but they still retain the potential for multidirectional differentiation (Kohler et al., 2013). The size and adaptive function of the TSC pool from aged/degenerated tendon tissues are remarkably decreased (Kohler et al., 2013). Therefore, adequate and functional TSC is essential for tendon healing, which is one of the key targets of PRP in the treatment of tendinopathy.

Cell culture experiments have shown that PRP-clot releasate (PRCR) could induce the differentiation of TSCs into tenocytes (Zhang and Wang, 2010b). TSCs cultured with PRCR exhibit a fibroblast phenotype, highly expressing tendonogenic genes rather than fat, cartilage, and bone-related genes (Zhang and Wang, 2010b). PRP also substantially increases the number of tenocytes in the culture mediums. These tenocytes highly express α-SMA and type I and type III collagen with robust proliferation and collagen-producing potential (Zhang and Wang, 2010b; Zhou et al., 2015) (Figure 2). Flow cytometry analysis has shown that for TSCs cultured in isolation, the administration of PRCR increases the number of type I and III collagen-expressing cells in a dose-dependent manner (Chen et al., 2012). Meanwhile, the number of PPARγ-, SOX-9-, and RUNX2-positive cells decreased (Chen et al., 2012). This suggests that PRCR accelerates tendon healing by stimulating the tendonogenic differentiation of TSCs and promoting extracellular matrix synthesis. At the same time, PRCR has the potential to inhibit the differentiation of TSCs into adipocytes, chondrocytes, and osteocytes. Based on this, Zhang and Wang (2014) further explored the condition and mechanism of PRCR in inhibiting the abnormal differentiation of TSCs. They found that the aberrant differentiation of TSCs was significantly inhibited when cultured in 10% (volume/volume) PRCR without any pretreatment. However, for TSCs pretreatment with non-tendonogenic media for 2 days, PRCR could only significantly inhibit the chondrogenic differentiation and slightly inhibit adipogenic and osteogenic differentiation. Finally, PRCR failed to reverse the abnormal differentiation of TSCs pretreated with non-tendonogenic media for 1 week. These results demonstrate that PRP cannot prevent the development of tendinopathy in the later stage, although PRP does not worsen the degenerative process. This might partially explain why PRP is not clinically effective in some patients with refractory tendinopathy. In this case, thorough tissue debridement is necessary to improve the lesion site microenvironment and induce TSCs to re-enter the tendonogenic differentiation pathway (Witt and Hyer,

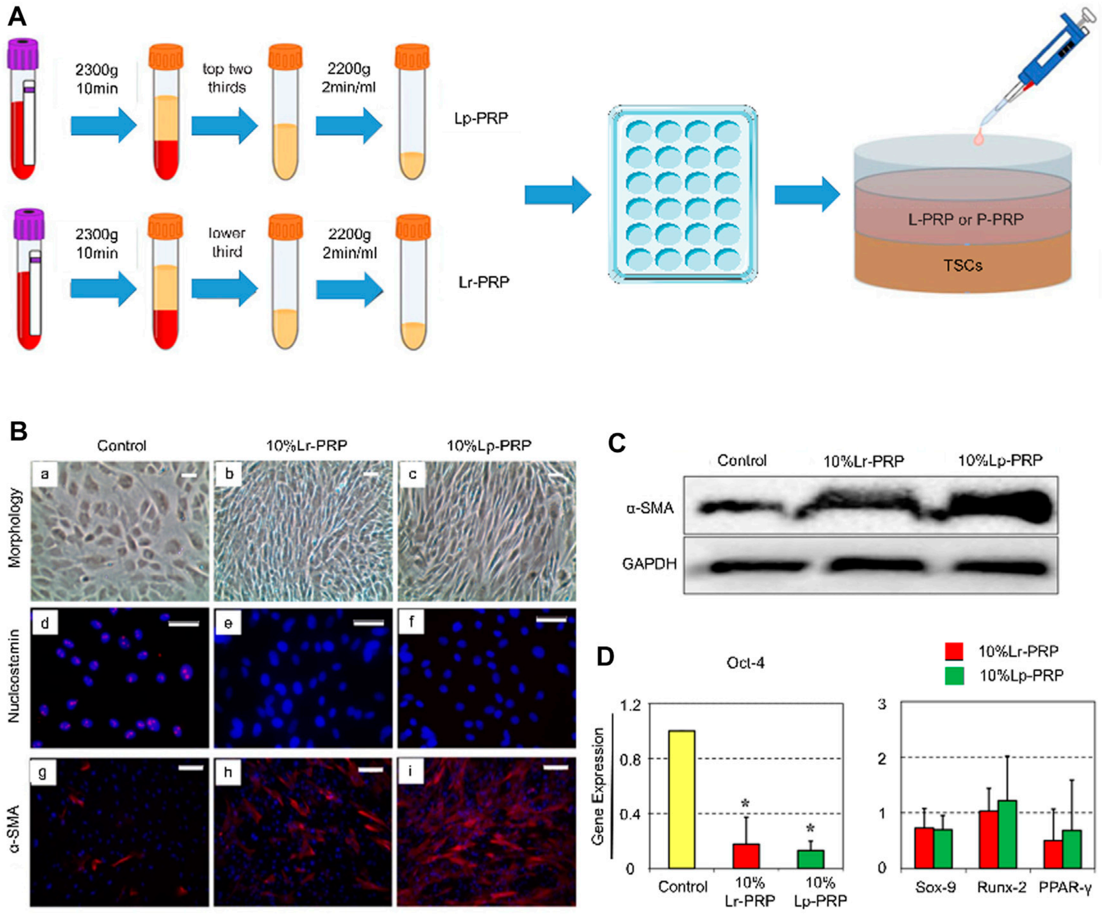

FIGURE 2
Leukocyte-rich platelet-rich plasma (LR-PRP) and leukocyte-poor platelet-rich plasma (LP-PRP) induce tendon stem cell (TSC) differentiation into tenocytes. **(A)** Illustration of the process of two kinds of PRP and study design. **(B)** Morphology of TSCs in the control, Lp-PRP, and Lr-PRP groups after 14 days in culture **(A–C)**. PRP treatment changed TSC morphology into more elongated tenocyte-like cells and increased the cell number. Immunostaining for nucleostemin and α-SMA (d-i). Nucleostemin (a stem cell marker) staining was positive in the control but negative in the PRP-treated cells. PRP treatment increased the expression of α-SMA (a marker of active tenocytes) with higher staining. **(C)** Western blot analysis of cultured cells in the control, Lp-PRP, and Lr-PRP groups. An intensely stained α-SMA protein band after PRP treatment validated increased the α-SMA protein level. **(D)** Expression of the stem cell marker gene Oct-4, Sox-9, Runx-2, and PPARγ of cultured cells in the control, Lp-PRP, and Lr-PRP groups. Oct-4 was reduced in PRP-treated cells. PRP-induced changes in the expression of non-tenocyte genes, Sox-9, Runx-2, and PPARγ, were minimal (Zhou et al., 2015).

2012; Gill et al., 2013). Xu et al. (2017) compared PRP–collagen–TSC constructs (PCTCs) and collagen–TSC constructs (CTCs). They found that the microstructure of PCTCs displayed more obvious microvascular and fibrous tissue characteristics than CTCs after 3 weeks in culture. After *in vivo* transplantation, PCTCs improved the macroscopic structure, histological characteristics, and biomechanical strength of ruptured Achilles in comparison with CTCs, with a better effect on tendon healing. Likewise, Imai et al. (2019) investigated the effects of PRP on peritendinous cells and reported that PRP could promote the migration and proliferation of peritendinous cells and induce the expression of the tendonogenic markers Scx and COL1A1.

Recently, researchers have proposed the combination of PRP and TSCs for the treatment of tendinopathy (Wang and Nirmala, 2016). PRP can provide abundant growth factors and a collagen scaffold, which can be a good biomaterial for TSC delivery. Exogenous TSCs can replenish the TSC pool and accelerate the healing process. For example, Chen et al. (2014) demonstrated that the combination therapy of PRP and TSCs promoted healing quality and improved histological and biomechanical scores in collagenase-induced Achilles tendinopathy. Meanwhile, the mRNA and protein expression levels of tendonogenic genes (type I collagen, Scx, and Tenascin C) increased (Chen et al., 2014). The FAK and ERK1/2 signaling pathway plays a key role (Chen et al., 2014).

Tenocytes are a major cellular component of the tendon and play an important role in maintaining its homeostasis. Meanwhile, they can proliferate and synthesize extracellular matrix to initiate the tendon repair process (Zhou and Wang, 2016). Anitua et al. (2005) reported that 20% PRP (volume/volume) could induce the synthesis of VEGF and HGF in tenocytes and promote tenocyte proliferation. de Mos et al. (2008) found that PRCR, compared with PPCR, further promoted tenocyte proliferation and collagen synthesis and increased the concentration of PDGF-BB, VEGF, and TGF-β1 in the medium. *In vitro* experiments designed by Wang et al. (2012) showed similar results. They reported that tenocytes were activated, proliferated, and collagen synthesis was stimulated by 10% (volume/volume) PRCR. Furthermore, the mRNA expression levels of Scx, type I collagen, type III collagen, and decorin were decreased, whereas the differentiation potential of tenocytes was preserved by PRCR (Wang et al., 2012). However, the tenocyte samples used in these studies were all from healthy tendons and might not fully reflect the effect of PRP on the tenocytes harvested in tendinopathy tendons. On this basis, Jo et al. (2012) investigated the effect of PRP on tenocytes from the diseased rotator cuff. They found that PRP could stimulate the proliferation of tenocytes in a dose-dependent manner; induce the expression of Scx, decorin, and tenascin C; promote the synthesis of type I and type III collagen; and increase the total amount of collagen (Jo et al., 2012). Pauly et al. (2018) also isolated tenocytes from patients with rotator cuff tendinopathy and cultured them in a medium containing autologous PRP. Their results showed that PRP increased the concentration of growth factors, such as IGF-I, TGF-β1, and PDGF-AB, in the medium compared with the control group and promoted cell proliferation and the absolute synthesis of type I collagen. Furthermore, Yoon et al. (2018) evaluated the effect of 10% (volume/volume) PRP on tenocytes from the healthy rotator cuff and the degenerative torn rotator cuff. They reported that PRP could promote the proliferation and extracellular matrix synthesis of tenocytes from both sources. However, tenocytes from the diseased rotator cuff had higher rates of cell proliferation and glycosaminoglycan synthesis, as well as a higher ratio of type I/type III collagen (Yoon et al., 2018). There are few studies on the exact mechanism of PRP in promoting tenocyte proliferation. Yu et al. (2015) reported that PRP, which contains high concentrations of TGF-β1 and PDGF, could modulate the Stat3/p27(Kip1) activity, promote the expression of cyclin–Cdk complexes, and, in turn, stimulate tenocyte proliferation.

In addition to directly promoting cell differentiation and proliferation, PRP can indirectly increase the number of cells in the lesion site by inhibiting the apoptosis of tenocytes. Platelet microparticles are tissue fragments of 0.1–1 μm in diameter, secreted by activated, stressed, or apoptotic platelets. They have been shown to enhance cell viability by activating protein kinase B through phosphorylation to inactivate B-cell lymphoma-2 (Bcl-2) associated death promoter, a member of the Bcl-2 family with pro-apoptotic effects (Burnouf et al., 2014). PRP-releasing substances, including HGF, stromal cell-derived factor-1 alpha (SDF-1α), 5-hydroxytryptamine, ADP, sphingosine-1-phosphate (S1P), IGF-I, brain-derived neurotrophic factor (BDNF), and TIMP-1, can also resist apoptosis (Gawaz and Vogel, 2013). Recently, Yu et al. (2021) evaluated the therapeutic effects of PRP-releasing substance on an injured Achilles model in rats. The results showed that the PRP-releasing substance could reduce the number of apoptotic cells at the edge of injury, promote the synthesis of collagen, and reduce the infiltration of macrophages. Compared with the control group, the rat Achilles treated with PRP could bear further mechanical loading.

The anti-aging gene Sirtuin 1 (Sirt1) is a nicotinamide adenine dinucleotide-dependent class III histone deacetylase that targets transcription factors to adapt gene expression to metabolic activity. Sirt1 is involved in telomerase reverse transcriptase and genomic DNA repair, with its participation in telomere maintenance for chromosome stability and cell proliferation. Sirt1 is also involved in cell cycle regulation, cell differentiation, cell survival, and apoptosis, with effects on nonalcoholic fatty liver disease, inflammation, energy metabolism, cognition, glucose/cholesterol metabolism, and amyloidosis. Metabolic diseases profoundly interfere with tendon health, including type 2 diabetes mellitus, dyslipidemia, chronic kidney disease, and nonalcoholic fatty liver disease (Afifi et al., 2019; Turk et al., 2020; Lin et al., 2023). For instance, chronic liver disease raises the risk of tendon disorder around 1.33-fold higher than usual (Lin et al., 2023). Tendon disorder occurs on average 3 years after being diagnosed with liver disease (Lin et al., 2023). The risk of tendon disorder increases further in this population with concurrent use of certain tendon–toxic medications, such as systemic glucocorticoids and statins (Lin et al., 2023). Therefore, Sirt1 activation is important for reversing metabolic diseases, such as nonalcoholic fatty liver disease, with relevance to tendinopathy. In addition, Simic et al. (2013) showed that Sirt1 deacetylated Runx2 and β-catenin to regulate the differentiation of mesenchymal stem cells. Sirt1 activated by resveratrol was reported to promote the osteogenic differentiation of mesenchymal stem cells by increasing Runx2 expression, facilitating its combination with PPARγ, and inhibiting the activity of PPARγ through its cofactor nuclear receptor, co-repressor 1 (Hata et al., 2003). Overexpressed Sirt1 can be anchored to NCoR1 and NCoR2, the inhibitory co-factors of PPARγ, which in turn suppress the expression of PPARγ and C/EBPα and further reduce the transformation of pre-adipocytes into adipocytes (Hata et al., 2003). In TSCs, Sirt1 is demonstrated to time-dependently promote the osteogenic differentiation by upregulating β-catenin and Runx2 and to inhibit the adipogenic differentiation by inhibiting the PI3K/AKT pathway with the downregulation of CEBPα and PPARγ (Liu et al., 2016). During the repair process of tendon injury, TSCs favor differentiation into cartilage and bone, whereas the accumulation of adipose tissue is not conducive to recovery from tendinopathy (Liu et al., 2016). Therefore, by targeting Sirt1, it may be possible to regulate the osteogenic differentiation of TSCs and adipose accumulation in injured tendons. Furthermore, Sirt1 downregulation leads to similar effects caused by stimulation with IL-1β, such as enhanced inflammatory signaling, reduced cell survival, and activated NF-κB in human tenocytes (Busch et al., 2012). In contrast, Sirt1 activation by resveratrol suppresses IL-1β-induced inflammatory signaling and apoptosis through deacetylation of NF-κB subunit p65 and tumor suppressor p53, thereby inhibiting the activation pathway of NF-κB- and p53-mediated apoptosis of tenocytes (Busch et al., 2012). Prevention of adhesion is associated with Sirt1 signaling. An *in vitro* experiment conducted by Chen et al. (2015) demonstrated a regulatory role of Sirt1 signaling (via NF-κB, a subunit of p53, and p53) in the prevention of adhesion using chitosan. These results suggest that the upregulation of Sirt1 appears to be useful for the treatment of tendinopathy.

PRP has the potential to activate the Sirt1 signaling pathway, promote tenocyte proliferation, regulate TSC differentiation and inflammation, and prevent tendon adhesion (Li et al., 2021). Weng et al. (2021) comprehensively investigated PRP effects on the metabolic reprogramming of fibroblasts and demonstrated that PRP halts the senescence progression of fibroblasts by activating Sirt1 expression. In addition, thrombin-activated PRP can increase the expression of Sirt1 in periodontal ligament stem cells and significantly enhance cell viability, ALP activity, osteogenic-related mRNA levels, and alizarin red-mineralization activity in a dose-dependent manner (Xu et al., 2021). Further studies are needed to confirm the exact role and specific mechanism of PRP in activating the Sirt1 signaling pathway in TSCs and tenocytes of chronic tendinopathy.

3.2 Promotion of tendon matrix synthesis and remodeling

In recent decades, biochemical and molecular biological studies of tendinopathy have deepened our understanding of the process of tendon degeneration. Tendinopathy can be considered an abnormal matrix remodeling process of the tendon. Excessive mechanical loading disrupts the balance between matrix synthesis and catabolism (Steinmann et al., 2020). Several studies have examined the changes in matrix molecules in the tendons affected by chronic tendinopathy (Riley et al., 1994a; b; Riley et al., 1996; Riley, 2005; Yamada et al., 2007). The total amount of collagen in pathological tendon tissue significantly decreases. The levels of type I and type II collagen and the ratio of type III collagen to type I collagen increase (Riley et al., 1994a; Riley et al., 1996; Tillander et al., 2002). For proteoglycans, some studies suggested that the contents of hyaluronic acid, glycosaminoglycan, and aggrecan increased remarkedly, whereas the content of decorin decreased significantly (Riley et al., 1994a; Lo et al., 2005). In addition, glycoproteins, such as tenascin C and fibronectin, generally increase in the degenerative tendon (Riley et al., 1996; Tillander et al., 2002). The activity of various MMPs also changes. There is an increase in the levels of MMP-1, MMP-2, MMP-23, disintegrin metalloproteinase 12 (ADAM-12), and platelet-reactive protein disintegrin metallopeptidase 2 (ADAM-TS2) and -TS3, but a decrease in MMP-3, MMP-10, MMP-12, and MMP-27 levels (Riley, 2008). Disruption of the balance between MMPs and TIMPs plays a key role in the process of tendon degeneration (Jones et al., 2006; Del Buono et al., 2013). Tendons can adapt to mechanical loading by increasing collagen synthesis and the activity of multiple MMPs. This adaptation enhances the mechanical strength and the viscoelastic properties of the tendon and reduces the stress sensitivity of the tendon, generally enhancing its load resistance. However, long-term repeated excessive mechanical loading leads to micro-injury accumulation in the tendon, which promotes the progression of tendinopathy and eventually leads to rupture (Diniz-Fernandes et al., 2018).

PRP contains many growth factors, such as IGF-I, FGF, TGF-β, EGF, HGF, and PDGF, which can prevent the change in the matrix molecule caused by tendinopathy to some extent. IGF-I plays an important regulatory role in collagen synthesis. IGF-I upregulation can stimulate collagen synthesis by activating downstream signal transduction pathways, such as ERK and Akt/mTOR (Hansen et al., 2013; Ren and Anversa, 2015). Local injection of IGF-I can promote collagen synthesis and increase the diameter of collagen fibers in healthy tendon tissues. This can also reduce swelling, promote tenocyte proliferation, and increase the total content of collagen in the degenerative tendon (Olesen et al., 2006; Hansen et al., 2013; Nielsen et al., 2014). bFGF can stimulate the proliferation and migration of tenocytes, upregulate the levels of type I and III collagen, and coordinate the orientation of collagen fibers, thereby improving the mechanical properties of the tendons (Goncalves et al., 2013; Chen et al., 2021). TGF-β is a crucial growth factor that regulates the production of the extracellular matrix. TGF-β2 can stimulate the expression of Col1A1 and Scx genes. A moderate amount of TGF-β2 can promote tendon healing, but excessive TGF-β2 is closely related to fibrosis and scar formation of the injured tendon (Katzel et al., 2011; Zhang et al., 2018). EGF has been shown to accelerate wound healing by promoting the formation of extracellular matrix and granulation tissue and stimulating fibroblast proliferation and tissue regrowth (Throm et al., 2010).

Numerous *in vitro* experiments have proven that PRP can stimulate tenocytes derived from normal or diseased tendons to synthesize non-collagen extracellular matrices and increase the total amount of collagen and the expression of type I and III collagen (Jo et al., 2012; de Vos, 2016; Kelly et al., 2016; Pauly et al., 2018; Yoon et al., 2018). In addition, PRP did not appear to affect the level of type I/III collagen expression in tenocytes (de Mos et al., 2008; Jo et al., 2012). Notably, de Mos et al. (2008) reported that PRP reduced the relative cellular expression of type I and III collagen (i.e., the ability of an individual tenocyte to synthesize type I and III collagen). However, owing to the increase in the number of tenocytes, the total amount of collagen remained higher than that of the control group (de Mos et al., 2008). This conclusion was confirmed by previous studies (Wang et al., 2012; Pauly et al., 2018). In contrast, some studies did not support this view (Jo et al., 2012; Kelly et al., 2016; Yoon et al., 2018). A variety of factors can cause differences in the collagen expression capacity of tenocyte samples in different experiments, including the age of donors, the origin of tenocytes, the pathological changes in the tendon tissue, and the components of PRP.

The therapeutic effect of PRP in promoting matrix synthesis was also validated *in vivo* and manifested macroscopically as an improvement in the biomechanical properties of the tendon and a shorter recovery time. Yu et al. (2021) investigated the therapeutic effect of PRP on rat models of acute Achilles injury. They found that PRP could increase the number of tenocytes in the vicinity of the wound and stimulate collagen synthesis in a short period, thus increasing the maximum load the tendon can bear and shortening the recovery time. Some studies evaluated the long-term therapeutic effect of PRF or PRP on a rabbit model with Achilles injury using imaging and histological analysis (Fukawa et al., 2015; Wong et al., 2020). Meanwhile, the release kinetics of growth factors in PRF was tested *in vitro* (Fukawa et al., 2015; Wong et al., 2020). The results show that PRF has good properties of growth factor delivery, which could store and stably release PDGF, bFGF, TGF-β1, and IGF-I for a long time. Ultrasound images suggest that the area of the hyperechoic zone (consisting of scar tissue formed by a disordered arrangement of cells and matrix) in the rabbit Achilles with PRF implantation is smaller than that in the control group. MRI suggests that the T2 signal of the rabbit Achilles in the PRP treatment group decreases gradually over time, reflecting the normalization of collagen fiber arrangement and the depletion of water concentration. Histological analysis shows that tendons in the PRF group have thicker, denser, and more continuous collagen fibers arranged in the direction of stress

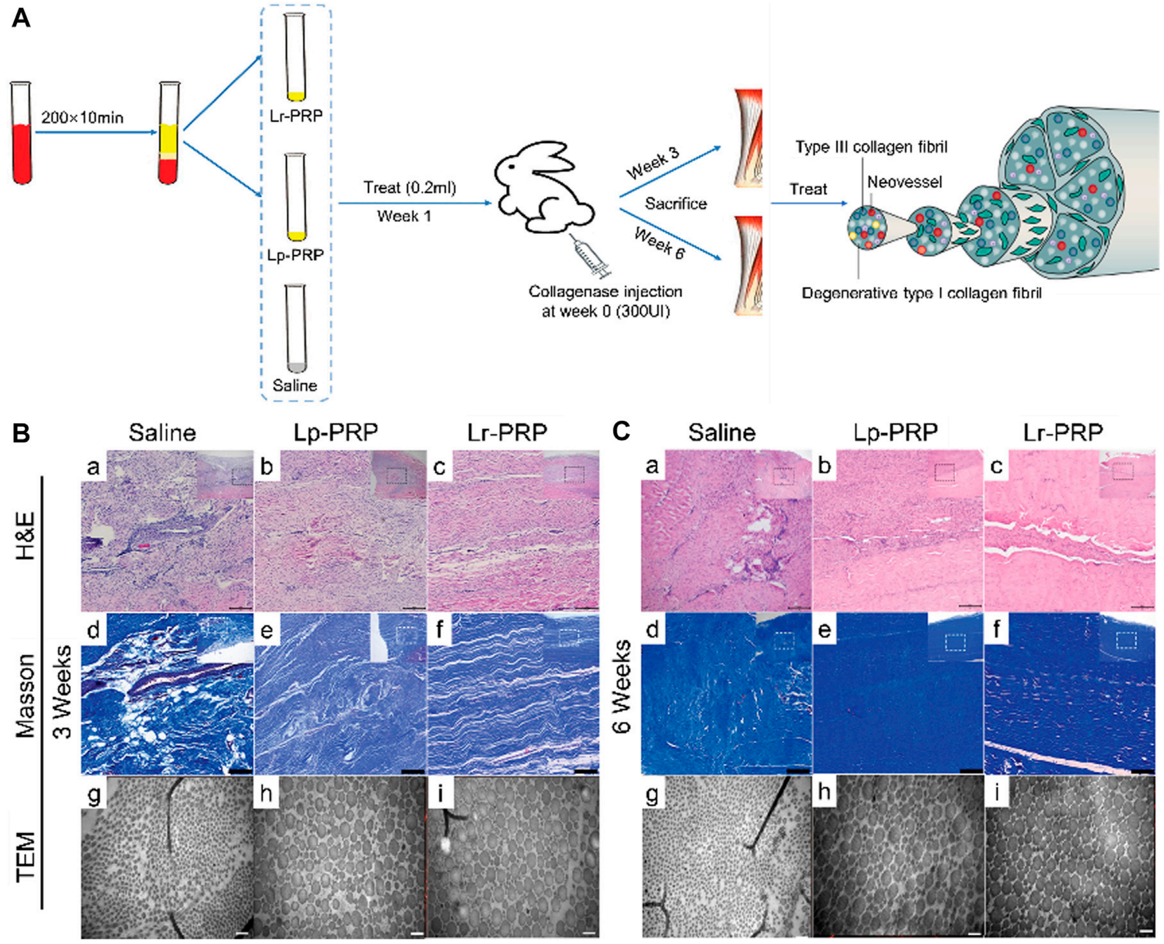

FIGURE 3
Effects of leukocyte-rich platelet-rich plasma (LR-PRP) and leukocyte-poor platelet-rich plasma (LP-PRP) on Achilles tendinopathy when applied at an early stage. **(A)** Illustration of the process of two kinds of PRP and study design. **(B)** Hematoxylin and eosin (H&E) staining, Masson staining, and transmission electron microscopy (TEM) of the saline, Lp-PRP, and Lr-PRP groups at 3 weeks. A better fiber structure and less angiogenesis were observed in the Lr-PRP and Lp-PRP groups. **(C)** H&E staining, Masson staining, and TEM of the saline, Lp-PRP, and Lr-PRP groups at 6 weeks. The tendons in both treated groups had better recovery than the saline group, but they were still worse compared with the healthy tendons (Jiang et al., 2020).

and have a smaller degenerative area with bone and cartilage. A basic experiment using histological analysis to assess the effect of PRP on Achilles injuries in rabbits came to a similar conclusion (Takamura et al., 2017). In the first 2 weeks after surgery, PRP could promote the migration and proliferation of tenocytes and stimulate angiogenesis. In the next 4 weeks, PRP can promote collagen synthesis and tissue maturation, thereby accelerating the healing process of the tendon. In conclusion, PRP can improve the mechanical property and load-bearing capacity of injured Achilles, shorten the healing time, and promote tendon maturity. This is clinically beneficial because PRP not only reduces the risk of secondary rupture of the Achilles, but also promotes the early recovery of motor function. Early moderate weight-bearing and exercise can prevent adhesion, extend the motion range of the affected limb, and accelerate recovery, achieving higher patient satisfaction (Maffulli et al., 2003). On this basis, Alsousou et al. (2015) treated 20 patients with Achilles rupture by PRP and performed histological and immunochemical biopsies 6 weeks after surgery. The results show that local application of PRP can promote the deposition of type I collagen, increase the ratio of type I collagen to type III collagen, and upregulate the content of glycosaminoglycan. It can also promote the recovery and maturity of the injured tendon, reflected in fewer blood vessels, a smaller proportion of cells, and a more consistent and regular arrangement of collagen fibers. For rotator cuff tendinopathy model animals, PRP also has a good therapeutic effect. Some studies have shown that the administration of PRP can increase collagen content, promote tissue maturation, and improve the biomechanical properties of the tendon, including stiffness, tenacity, and mechanical load capacity (Hapa et al., 2012; Dolkart et al., 2014; Ersen et al., 2014). Kobayashi et al. (2020) reported the therapeutic effect of PRP on the patellar tendon injury model in mice. According to the Bonar Score, injured patellar tendons in the PRP group form more neovascularization in the early stage of the healing process and have more aligned collagen fibers in the late stage of the healing process, which indicates that PRP can accelerate the healing of injured patellar tendons (Kobayashi et al., 2020). In addition to treating the animal model with a tendon injury, PRP can also improve the healing of degenerative tendons induced by collagenase, increase the expression of type I collagen protein, inhibit the process of degeneration in a certain sense, and promote tissue remodeling and maturity (Moshiri et al., 2014; Yan et al., 2017; Jiang et al., 2020) (Figure 3).

Recently, several basic studies have reported that PRP might play a role in promoting MMP secretion by tenocytes or TSCs. For example, PRP or PRCR could significantly increase the mRNA and protein levels of type I collagen and MMP-1 in human fibroblasts (Kim et al., 2011; Shin et al., 2014). Pifer et al. (2014) showed that certain concentrations of MMP-2, MMP-3, and MMP-9 could be detected both in low platelet concentration LP-PRP (prepared by ACP) and in high platelet concentration LR-PRP (prepared by GPS). Most of these MMPs are in an active state and can maintain their plasma levels for at least 6 days. Human ligament fibroblasts also release a variety of MMPs after exposure to ACP or GPS-prepared PRP (Pifer et al., 2014). In addition, Zhou et al. (2015) found that tenocytes treated with LR-PRP could express more catabolic genes, including MMP-1, MMP-13, IL-1β, IL-6, and TNF-α. The research implicated that PRP might regulate the tissue remodeling process by controlling the level of MMPs within the tendon. The balance between MMPs and TIMPs plays a key role in tendon remodeling (Jones et al., 2006; Del Buono et al., 2013). A moderate amount of MMPs can reduce hypertrophy and scar tissue formation of the affected tendon and promote matrix remodeling (Fleming et al., 2009; Scollon-Grieve and Malanga, 2011; Thanasas et al., 2011). Excessive MMPs promote catabolism and aggravate the degenerative process in tendinopathy (Marqueti et al., 2006; Arnoczky et al., 2007; Bedi et al., 2010). Currently, only a few studies have explored the efficacy of PRP in combination with MMP inhibitors in the treatment of tendinopathy. For example, Jafari et al. (2019) compared the efficacy of single PRP *versus* PRP plus broad-spectrum or narrow-spectrum MMP inhibitors for tendinopathy. They found that tendons treated with MMP narrow-spectrum inhibitor (specific inhibition of MMP-13) and PRP had the best histological and biomechanical properties.

3.3 Regulation of tendon angiogenesis

The role of VEGF and angiogenesis in tendinopathy or tendon healing has not been fully elucidated. The present studies suggest that VEGF and neovascularization may play different roles in different stages of tendinopathy. After an acute tendon injury, hypoxia, pro-inflammatory cytokines, nerve signals, and mechanical loading can upregulate the VEGF level. Increased metabolism attributed to tendon injury indirectly leads to hypoxia and upregulation of the hypoxia-inducible factor-1 (HIF-1) level (Pufe et al., 2005; Li et al., 2013; Halper, 2014; Rahim et al., 2016). HIF-1 can further induce VEGF gene transcription. The release of pro-inflammatory cytokines, such as IL-1β, IL-6, and IL-8, and the infiltration of inflammatory cells can also promote VEGF synthesis. Upregulated nerve growth factor promotes neuronal growth, leading to an increased level of neurogenic VEGF (Pufe et al., 2005; Li et al., 2013; Halper, 2014; Rahim et al., 2016). Excessive mechanical loading can also promote the release of VEGF from the tendon tissue. The trend of VEGF concentration is similar in various animal models with tendon injury. This increases gradually in the early stage of the proliferative phase and eventually decreases with the relief of symptoms (Liu et al., 2021b). VEGF is a potent angiogenic stimulant. It can promote angiogenesis and increase vascular permeability, mediating the delivery of circulating cells, growth factors, oxygen, and nutrients to the tendon lesions (Molloy et al., 2003). In addition, neurogenic VEGF-mediated neovascularization is surrounded by perivascular cells. This cell type has mesenchymal stem cell properties and is considered a source of TSCs, which can mediate the healing process of the injured tendon (Wu et al., 2017; Li et al., 2019; Lee et al., 2021). Therefore, the changes in VEGF and angiogenesis reflect the early healing process of acute tendon injury in a sense.

Some researchers believe that PRP promotes vascular endothelial cell proliferation and augments vasopermeability in the early stage of tendinopathy, providing a suitable microenvironment for tendon healing. Activated platelets release a range of pro-angiogenic factors, such as VEGF, HGF, TGF-β, PDGF-BB, IL-8, angiopoietin, and chemokine (C-X-C motif) ligand 12 (CXCL12), as well as MMP-1, MMP-2, and MMP-9 (Nurden et al., 2008). Leukocytes further replenish the pro-angiogenic protein pool of PRP by releasing VEGF, angiopoietin, FGF, HGF, PDGF, and MMPs (Kobayashi et al., 2016; Andia and Abate, 2018). As one of the most important angiogenic factors, VEGF can regulate angiogenesis in both healthy and degenerative tendons (Molloy et al., 2003; Pufe et al., 2005). VEGF is a specific mitogen of endothelial cells that promotes the growth and proliferation of endothelial cells and perivascular cells, increases the permeability of capillaries, and promotes angiogenesis within the tendon (Wu et al., 2017; Peach et al., 2018). Meanwhile, VEGF has the function of promoting the proliferation of fibroblasts, stimulating the chemotaxis of macrophages and granulocytes, and initiating the production of other growth factors (Liu et al., 2021a). bFGF has a strong angiogenic effect in synergy with VEGF, which can regulate intratendon inflammation, cell proliferation, angiogenesis, and collagen synthesis (Thomopoulos et al., 2010; Tang et al., 2016). PDGF-BB can indirectly regulate the migration of endothelial cells and vascular smooth muscle cells and participate in the maturation and stabilization of neovascularization by upregulating the levels of VEGF and integrin (Evrova and Buschmann, 2017). Furthermore, MMPs are directly involved in the process of angiogenesis. MMPs can regulate the activity of chemokines, such as IL-8 and CXCL12, as well as growth factors, such as TGF-β and HGF, released by PRP (Moser et al., 2004; Kawase et al., 2015). MMPs can also stimulate the migration of endothelial cells by degrading the extracellular matrix (Andia and Abate, 2018). Moreover, MMP-2 and MMP-9 can activate the wnt/β-catenin signaling pathway, which is beneficial to the survival and proliferation of endothelial cells (Kawase et al., 2015).

Basic research further confirms that PRP has the therapeutic effect of promoting angiogenesis in the initial period of tendon healing. Bosch et al. (2011) used color Doppler ultrasound and Factor VIII immunohistochemical staining to study the effect of PRP on the angiogenesis of acutely injured tendons. They found that PRP significantly increased angiogenesis for at least 23 weeks compared with the placebo (Bosch et al., 2011). The author speculated that a a large number of neovascular vessels within the tendon might be one of the main factors that a single PRP injection can promote the long-term repair of the injured tendon

(Bosch et al., 2011). Kobayashi et al. (2020) explored the specific mechanisms by which PRP affects tendon healing using a patellar tendon injury mouse model. As a result, the Bonar vascular score of the PRP group was significantly higher than that of the control group 2 and 4 weeks after the operation. Kobayashi et al. also reported that PRP not only had a direct effect of stimulating tenocytes to produce an extracellular matrix, but also indirectly facilitated tendon healing by promoting the angiogenesis and the recruitment of circulating repair cells (Kobayashi et al., 2020). These results suggest that the pro-angiogenic proteins of PRP can effectively mediate angiogenesis in the early stage of tendon healing and provide adequate blood supply and a suitable microenvironment for tendon repair. PRP also has a good therapeutic effect on injured Achilles of New Zealand white rabbits (Lyras et al., 2009). The injured Achilles in the PRP group had more neovascularization than the control group in the first 2 weeks (Lyras et al., 2009). Although at the 4th week, in the PRP group, the number of neovascular vessels and the rate of tenocyte metabolism significantly decreased, the consistency of collagen fiber arrangement and the histological characteristics of tendons were improved (Lyras et al., 2009). Additionally, *in vitro* experiments have reported that PRP can temporarily improve cell migration by activating VEGF receptor 2 born on the endothelial cell membrane directly (Kawase et al., 2015). However, this therapeutic effect is dose- and time-dependent and cannot be sustained over the long term, which is attributed to the reduced sensitivity of endothelium to PRP over a long period (Kawase et al., 2015). This is also an important factor to be considered when designing similar experiments.

Under normal circumstances, neovascularization in the injured tendon will gradually subside as the healing process progresses, eventually forming a mature vascular network. However, chronic tendinopathy can lead to the long-term presence of intratendon capillaries and worsen the microenvironment of tendon healing (Liu et al., 2021b). The VEGF-mediated angiogenesis cascade appears to be highly active in the chronic degenerative tendon attributed to prolonged hypoxia and excessive mechanical loading (Lakemeier et al., 2010; Bosch et al., 2011; Andarawis-Puri et al., 2015). However, Jarvinen (2020) reported in a recent study that neovascularization within the chronic degenerative tendon is hyperpermeable, unable to provide oxygen and nutrients to the tissue and transport metabolic waste. This means that neovascularization induced by tendinopathy is weak or even non-functional, without normal blood flow perfusion, and unable to change the hypoxic state of the affected areas. Fibrin-rich exudates constantly leak from the neovascular, leading to fibrin degeneration of the tendon (Jarvinen, 2020). This is a typical histological feature of tendinopathy. The persistent vascularization in tendinopathy might be attributed to low-grade inflammation triggered by chronic irritants and might be considered a symbol of incomplete repair (Bosch et al., 2011). High levels of VEGF in the affected tendon can exacerbate the side effects of vascularization, resulting in constant pain and decreased biomechanical function of the tendon (Sahin et al., 2012; Korntner et al., 2019). Neovascularization and nerve fibers usually form together. The latter can secrete a series of neurotransmitters, such as calcitonin gene-related peptide and substance P, eventually causing long-term pain in the affected tendon (Ackermann et al., 2003). Meanwhile, a high level of VEGF can stimulate the expression of MMPs and inhibit the expression of TIMPs in endothelial cells and tenocytes, disrupting the balance of extracellular matrix remodeling and impairing the mechanical properties of the tendon (Sahin et al., 2012; Halper, 2014). In addition, long-term hypoxia and overexpression of VEGF are considered the key inducers of neovascularization, which is hyperpermeable, immature, and non-perfusionable (Jarvinen, 2020). These anomalous vascular networks cannot alter hypoxia and nutrient deficiencies of the affected tendon (Jarvinen, 2020). High levels of VEGF have also been shown to maintain inflammation in tendinopathy and promote scar tissue formation (Korntner et al., 2019). Therefore, some researchers regard neovascularization as one of the main pathological processes of tendinopathy and believe that the mechanical properties of the tendon are negatively correlated with the level of neovascularization.

PRP can provide not only angiogenic protein but also a variety of angiogenesis inhibitors, including endostatin, fibronectin, platelet factor 4 (PF4), thrombospondin-1 (TSP-1), α2-macroglobulin, plasminogen activator inhibitor-1, angiostatin, and TIMPs (Nurden et al., 2008). The activation of angiogenesis inhibitors acts as a negative feedback mechanism limiting the capillary number and the VEGF level within the tendon. For example, TSP-1 and endostatin can block VEGF signaling pathways and inhibit endothelial cell proliferation (Andia and Maffulli, 2013). PF4 has the strongest ability to inhibit angiogenesis among all chemokines, directly through the binding of CXCR3 receptors and indirectly through blocking VEGF and bFGF to their receptors (Andia et al., 2012). Therefore, PRP might regulate the capillary network in chronic tendinopathy. Finnoff et al. (2011) explored the efficacy of ultrasound-guided PRP injection in the treatment of chronic refractory tendinopathy. They reported that the tendon function improvement rate and the pain relief rate were respectively 68% and 58% in 41 patients (10 with upper-extremity tendinopathy and 31 with lower-extremity tendinopathy), and 84% of patients had an improvement in imaging echo texture (Finnoff et al., 2011). In addition, intratendon calcification was relieved in 64% of patients, and neovascularization was reduced in 82% of patients (Finnoff et al., 2011). For chronic Achilles tendinopathy, a random controlled clinical trial designed by Boesen et al. (2017) demonstrated that PRP in combination with 12-week eccentric exercise rehabilitation therapy was superior to eccentric exercise alone. Combination therapy has advantages in improving tendon function and reducing pain, thickness, and the number of capillaries within the tendon (Boesen et al., 2017). However, a random controlled clinical trial designed by de Vos et al. (2011) showed that PRP could not improve vascularization and the structure of the collagen bundle within diseased Achilles compared with the saline group.

More long-term, high-quality, multi-center, large-scale basic or clinical trials are needed to confirm the exact effect and specific mechanism of PRP in regulating the capillary network of chronic tendinopathy. Bevacizumab is a VEGF-targeted monoclonal antibody agent used to treat many metastatic cancers (Garcia et al., 2020). Basic studies have demonstrated that early injection of bevacizumab in collagenase-induced tendinopathy can modulate the capillary network of the affected area, reduce tendon thickness, and improve the consistency of collagen fiber alignment

(Dallaudiere et al., 2013). On this basis, Dallaudiere et al. (2014) used bevacizumab in combination with PRP to treat tendinopathy and found that the tendon healing effect was better in the combination group than in the single PRP injection group. The authors declaimed that angiogenesis inhibitors can reduce neovascularization and secretion of MMPs and prostaglandins in the early stage of tendinopathy. In the later stage of tendon healing, PRP can provide rich active cytokines that will compensate for the reduced concentrations of growth factors due to the decreased angiogenesis, promote the recruitment of stem cells and fibroblasts, and boost collagen synthesis (Dallaudiere et al., 2014). Although angiogenesis is one of the key steps in the pathogenesis of tendinopathy, few studies have been conducted on inhibiting angiogenesis for tendinopathy treatment. Further studies are needed to determine whether it is necessary to develop a series of therapies aimed at inhibiting tendon angiogenesis.

3.4 Regulation of inflammation

The role of inflammation in the pathogenesis of tendinopathy has not been determined. In the past 20 years, tendinopathy has been described as a non-inflammatory degenerative disease. Similarly, the continuum model did not emphasize the specific role of inflammation in the pathological process of tendinopathy (Cook and Purdam, 2009; D'Addona et al., 2017). However, the development and application of modern cellular and molecular biotechnology have improved the understanding of the inflammatory process in tendinopathy. The relevant roles of various cytokines, immune cells, and non-immune cells (mainly tenocytes) in the inflammation of tendinopathy have been elaborated. This suggests that inflammation may play a key role in the progression of degeneration and may be a key target for the treatment of tendinopathy.

IL-1β is produced by macrophages or tenocytes under pathological conditions and is expressed in the early stage of tendon injury (Yang et al., 2005; Mobasheri and Shakibaei, 2013). IL-1β can induce the expression of inflammatory mediators such as cyclooxygenase (COX-2), prostaglandin E2 (PGE 2), and MMP-1 in tenocytes, which will promote matrix breakdown and negatively affect the mechanical properties of the tendon (Yang et al., 2005; Mobasheri and Shakibaei, 2013). IL-1β can also inhibit the tendonogenic differentiation and tendon-related gene expression (e.g., Scx, tenomodulin, and collagen) of TSC, counteracting the tendon healing process (Zhang et al., 2015). IL-6 is a multifunctional Th2 cytokine induced by IL-1β and TNF-α (Lin et al., 2006; Millar et al., 2010; Tang et al., 2018). It has the function of regulating tendon inflammation and the healing process. IL-6 and IL-1β mediate inflammatory response after tendon injury by activating the NF-κB pathway (Abraham et al., 2019). Animal models showed that the NF-κB pathway was closely related to tendinopathy (Abraham et al., 2019; Best et al., 2019). Knockdown of the key target NFKB1 can enhance the activity of NF-κB and MAPK, which will promote the recruitment of macrophages, the proliferation of tenocytes, and the deposition of collagen at the repair site, thus enhancing the mechanical properties of the tendon (Abraham et al., 2019; Best et al., 2019). Moreover, IL-6 can promote the expression of COL1A1 in the tendon, indicating that IL-6 is involved in the regulation of tendon healing (Millar et al., 2010). Animal models of acute tendon injury showed that the TNF-α gene level increased gradually from 2 h to 9 days after injury and then decreased in roughly the second week (Morita et al., 2017). TNF-α can stimulate tenocytes to express a multitude of pro-inflammatory or anti-inflammatory mediators, such as IL-1β, TNF-α, IL-6, IL-10, and MMPs (John et al., 2010; Tang et al., 2018). TNF-α may even induce apoptosis of the tenocyte, which in turn inhibits the production of extracellular matrix (John et al., 2010; Tang et al., 2018). Han et al. (2017) designed an *in vitro* experiment that demonstrates that TNF-α has the function of inhibiting TSC proliferation and tendonogenic differentiation. However, the combination of TNF-α with TGF-β1 can promote proliferation and tendonogenic differentiation of TSCs. Moreover, IL-10, IL-4, IL-33, IL-18, TGF-β, VEGF, COX-2, PGE 2, and other cytokines have important regulatory effects on inflammatory progression and the tissue repair process in tendinopathy (Tang et al., 2018; Chisari et al., 2019; Arvind and Huang, 2021; Chisari et al., 2021) (Table 3).

Millar et al. (2017) reviewed the role and status of immune cells (resident or infiltrated) and stromal fibroblasts in the inflammatory response in tendinopathy. The inflammatory sites of tendinopathy are creatively divided into three different cell compartments in this review: the stromal compartment, immune-sensing compartment, and infiltrating compartment (Millar et al., 2017). The infiltrating compartment accumulates a variety of circulating immune cells, including macrophages, NK cells, and lymphocytes. These circulating immune cells converge to the lesion by sensing pro-inflammatory cytokines released by resident immune cells and stromal fibroblasts. The immune-sensing compartment has resident immune cells, such as macrophages and mast cells. They can sense the damage/pathogen-related molecular patterns (DAMPs/PAMPs), take the lead in responding to tissue damage, and are activated by pro-inflammatory cytokines. Tenocytes located in the stroma are mainly responsible for tissue remodeling and repair. After sensing extracellular signals, tenocytes initiate downstream pathways and produce cytokines and chemokines in an autocrine or paracrine form, which can adjust tenocytes to an inflammatory phenotype (i.e., an "Activated" state). Consequently, extracellular matrix remodeling is accelerated. The interaction between different cell regions constitutes a complex environment of tendonitis, which affects the homeostasis of matrix degeneration and repair (Figure 4).

Among immune cells, the role of macrophages has been increasingly emphasized in the tendon inflammatory response, early tissue repair, and remodeling process (Lana et al., 2019). Traditionally, tendon macrophages have been classified into two phenotypes, M1 (classically activated macrophage) and M2 (alternatively activated macrophage), according to the surface receptors, functions, and cytokines expression (Mantovani et al., 2002). M1 macrophages promote tendon inflammation by producing cytokines, including CeC motif chemokine ligand 2, monocyte chemoattractant protein 1, inducible nitric oxide synthase, TNF-α, IL-12, IL-1β, and VEGF (Arnold et al., 2007; Ruffell et al., 2009; Ramachandran et al., 2012). M2 macrophages play an anti-inflammatory role, which can produce cytokines such as IL-1 receptor antagonist (IL-1RA), IL-4, IL-10, TGF-β, arginase 1, IGF-I, and PDGF (Arnold et al., 2007; Ruffell et al., 2009; Ramachandran et al., 2012). Therefore, M2 macrophages can

TABLE 3 Cytokines implicated in tendinopathy.

Cytokine	Proposed function in tendinopathy
IL-1β	Pro-inflammatory cytokine induction, ECM remodeling, reduced type I collagen production, and inhibited tendonogenic differentiation of TSCs
IL-6	Increased total collagen synthesis and inflammation regulation
TNF-α	Increased pro-inflammatory cytokine production, reduced type I collagen production, and inhibited proliferation and tendonogenic differentiation of TSCs
IL-4	Promoted acute inflammatory processes and associated with ECM homeostasis
IL-18	ECM remodeling and immune cell recruitment
IL-33	ECM remodeling and increased type III collagen and cytokine production
TGF-β	Promoted collagen synthesis, neovascularization, and fibrosis/excessive scar formation; promoted immune tolerance; and decreased inflammation
VEGF	Induced inflammation, degraded the ECM, and promoted pathogenetic processes of degenerative tendon

(Hershey, 2003; Yang et al., 2005; Lin et al., 2006; Millar et al., 2009; John et al., 2010; Millar et al., 2010; Oliva et al., 2011; Mobasheri and Shakibaei, 2013; Campbell et al., 2014; Millar et al., 2015; Zhang et al., 2015; Han et al., 2017; Tang et al., 2018; Titan et al., 2019).

inhibit tendon inflammation, inducing tenocytes to migrate to the injury site, and can regulate tendon repair and the fibrosis process (Mantovani et al., 2002). M1 macrophages reach the tendon within 24 h after injury and dominate in the subacute stage of tendinopathy (Dakin et al., 2012; Dakin et al., 2014). With the development of chronic tendon degeneration, the function of macrophages changes from pro- to anti-inflammation and tissue repairing (Dakin et al., 2012; Dakin et al., 2014). The number of M2 macrophages increases gradually (Dakin et al., 2012; Dakin et al., 2014). Murray et al. (2014) redefined macrophage types, emphasizing the role of key cytokines and signaling pathways. According to the new definition of macrophages, the interferon (IFN) and NF-κB signaling pathways are activated in the early and middle stages of tendinopathy, whereas the signal transducer and activator of transcription 6 (STAT-6) and glucocorticoid receptor signaling pathways dominate in the later stage (Dakin et al., 2015). Furthermore, CD206 and ALOX15 mRNA pathways of the macrophage are significantly activated in tendinopathy patients with symptomatic relief after treatment compared with those still with symptoms (Dakin et al., 2015). This demonstrates the role of CD206 and ALOX15 pathways in relieving inflammatory pain in tendinopathy patients.

Tendon-resident stromal cells also play an important role in the initiation and maintenance of chronic inflammation. Tenocytes can be transformed from a quiescent state to an activated state by the inflammatory reaction of tendinopathy, being hypertrophic ones and highly expressing molecular markers such as toll-like receptor 4 (TLR4), interferon regulatory factor 1 (IRF1), IRF5, PDPN, CD106, and CD248 (Dakin et al., 2018). Meanwhile, activated tenocytes can synthesize and release cytokines, such as TNF-α, IL-1β, IL-6, IL-10, and VEGF (Serhan et al., 2008). Even when the inflammation of tendinopathy is reduced, the tenocytes remain in an inflammatory-sensitive state to some extent, which undoubtedly increases the risk of inflammation progression or recurrence (Dakin et al., 2018).

Platelets in PRP control the inflammatory response in tendinopathy by coordinating highly complex molecular signaling networks and cell–cell interactions (Andia and Abate, 2018). Platelets can store and release chemokines, including CXCL7 (NAP-2), PF4 (CXCL4), chemokine (C-C motif) ligand 5 (CCL-5), and CCL-2 (Flad and Brandt, 2010). These chemokines can regulate the biological behavior of a range of immune cells, including neutrophils, macrophages, and lymphocytes, maintaining an inflammatory microenvironment within the tendon. For example, CXCL7 has chemotaxis and activation effects on neutrophils (Ghasemzadeh et al., 2013). PF4 can switch macrophages from a pro-inflammation phenotype to a stromal synthesis phenotype, which in turn modulates inflammation in tendinopathy and repair response (Gleissner et al., 2010). CCL-2 and CCL-5 can promote the migration of monocytes and T cells across capillaries by regulating the activity of CCR2, CCR1, and CCR5 (Stalman et al., 2015). Conversely, Zhang et al. (2013) found that HGF in PRP could antagonize the pro-inflammatory effect of IL-1β; inhibit the expression of COX-1, COX-2, and PGE 2 synthase in tenocytes; and reduce the production of PGE 2. Meanwhile, HGF can inhibit the inflammatory reaction by increasing the expression of IκBα (Bendinelli et al., 2010). IκBα is an inhibitor of NFκB; the latter is an inflammatory modulator involved in tendinopathy and is upregulated within tenocytes at the site of tendon inflammation (de Oliveira et al., 2013). Moreover, IGF-1 and PDGF in PRP can inhibit the production of IκB kinase to prevent intratendon inflammation (Zhang and Wang, 2014). TGF-β, an anti-inflammatory cytokine in PRP, has been proven to control local inflammation (Jo et al., 2012). Given that platelets contain both pro- and anti-inflammatory cytokines, LP-PRP might have a complex regulatory mechanism in the inflammatory response of tendinopathy.

Recent data suggest that the microenvironment within the tendon is crucial for the ultimate effect of LP-PRP in regulating inflammation. An *in vitro* experiment designed by Jo et al. (2018) demonstrated that PRP could only exert an anti-inflammatory effect on tenocytes pretreated with IL-1β or derived from degenerative tendons. Conversely, PRP can promote an inflammatory response (Jo et al., 2018). In other words, in the normal, non-inflammatory microenvironment, PRP can upregulate the expression of IL-1β, Cox-2, membrane-bound prostaglandin E2 synthase 1 (mPGES-1), and downstream MMPs; downregulate anti-inflammatory cytokine levels; and thus induce inflammation and pain. However, in the inflammatory microenvironment, PRP can downregulate the expression of pro-inflammatory cytokines and MMPs, upregulate anti-inflammatory cytokine levels, and promote matrix synthesis,

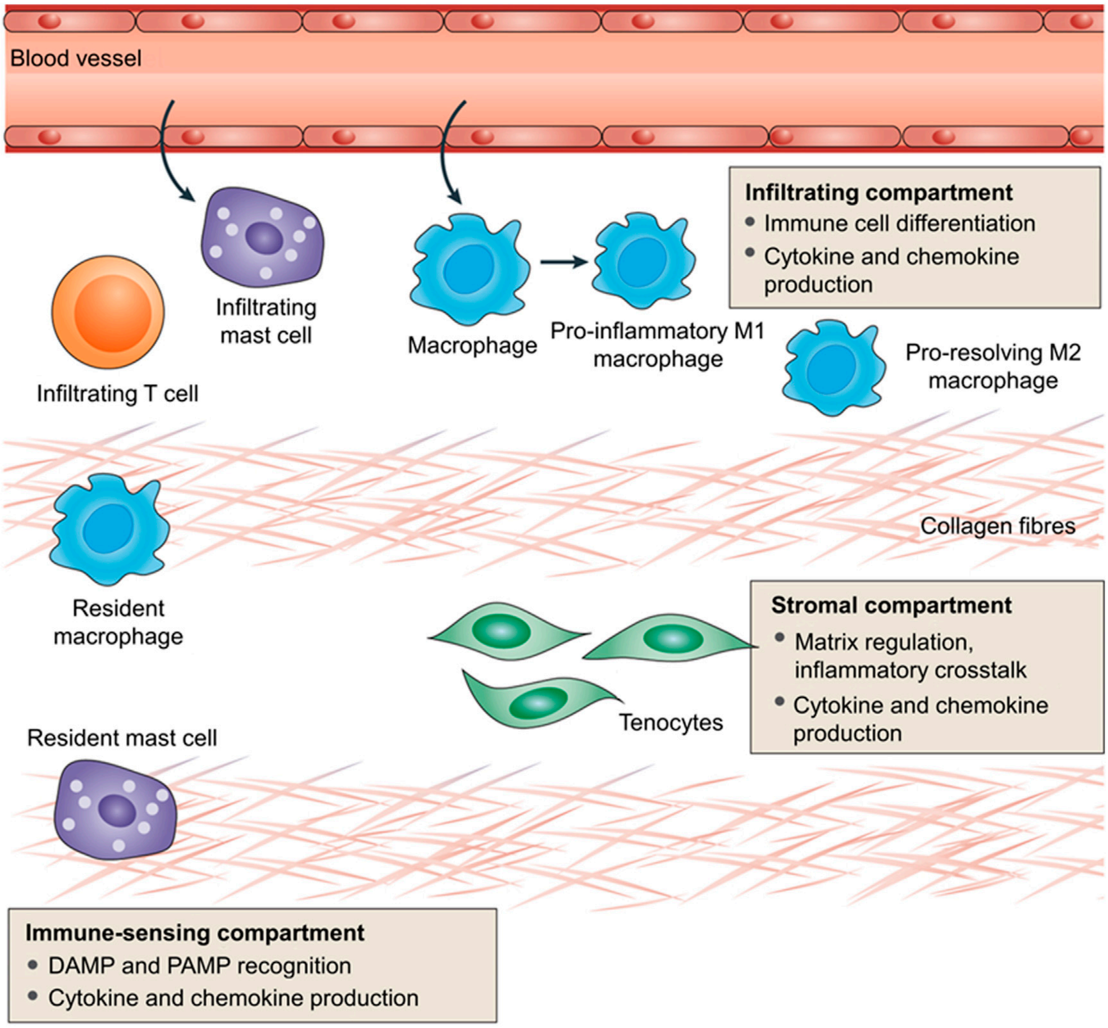

FIGURE 4
Immunobiology of tendinopathy. Inflammation in tendinopathy encompasses three distinct compartments involved in a complex network for tendon homeostasis. The infiltrating compartment includes influxing immune cells, probably recruited through stromal and resident immune cell activation. The infiltration of immune cells represents a homeostatic inflammation in normal circumstances but is aberrant in tendinopathic disease. The immune-sensing compartment comprises tendon-resident innate cells that act as sentinels to respond to initial tissue insult through damage-associated molecular patterns (DAMPs) and pathogen-associated molecular patterns (PAMPs). The centrally placed resident tenocytes sit in the influential stromal compartment, which is responsible for tissue remodeling and repair. Tenocytes can be driven toward an activated inflammatory phenotype and secrete cytokines and chemokines. These three compartments contribute to interactions between the inflammatory response and the extracellular matrix remodeling, which in turn comprise a balance between reparation and further degeneration within the tendon (Millar et al., 2017).

thus inhibiting the inflammatory response and enhancing the repair response. This finding could help explain some of the conflicting claims in previous studies about the anti-inflammatory effect of LP-PRP (El-Sharkawy et al., 2007; Zhang et al., 2013; Andia et al., 2015; Zhang L. et al., 2016; Hudgens et al., 2016). For example, Hudgens et al. (2016) reported that for normal tendon fibroblasts, LP-PRP treatment downregulated the expression of EGR1, EGR2, tenomodulin, and Scx, which are closely correlated to extracellular matrix formation. Furthermore, LP-PRP treatment activated TNF-α and NFκB signaling pathways, inducing an inflammatory response in tendon fibroblasts (Hudgens et al., 2016). LP-PRP also promoted the expression of autophagy-related genes and reactive oxygen species (ROS) genes and activated the oxidative stress pathways (Hudgens et al., 2016). However, Andia et al. (2015) found that for the inflammatory-activated tenocytes induced by IL-1β, PRP treatment downregulated the expression of IL-6/CXCL6, IL-6R, and IL-8/CXCL8 and decreased the secretion of immunomodulatory proteins IL-8/CXCL8, IL-6/CXCL6, and MCP-1/CCL2. Likewise, Li et al. (2020) reported that the injection of LP-PRP into the degenerative Achilles of rabbits could significantly reduce the release of pro-inflammatory cytokine IL-6 and decrease the expression of MMP-1 and MMP-3. In addition, LP-PRP increases the expression of TIMP-1 and maintains the balance of MMPs and TIMPs in the tendon, which is beneficial to the maturation of the extracellular matrix (Li et al., 2020).

In general, M1 macrophages can be stimulated by LPS and IFN-γ, whereas M2 macrophages can be stimulated by Th2 lymphocytes IL-4 and IL-10 (Wynn and Vannella, 2016). Therefore, macrophage activity and functional phenotype might be directly affected by PRP components and their concentration levels, especially leukocytes. The biological basis for this view is that LR-PRP and LP-PRP have different concentrations of pro- and anti-inflammatory mediators. LR-PRP contains higher concentrations of pro-inflammatory mediators, such as TNF-α, IL-6, and IFN-γ (Sundman et al., 2011; Braun et al., 2014). However, LP-PRP can increase the concentrations of anti-inflammatory mediators such as IL-4 and IL-10 in the local tissue (Sundman et al., 2011; Braun et al., 2014). For example, a random controlled trial by Nishio et al. (2020) found that in the injured patellar tendon model, the number of M1 macrophages increased significantly on days 4 and 7 after treatment with LR-PRP or LP-PRP compared with the control group. However, the M1 macrophage count/M2 macrophage count decreased significantly on days 7 and 14 after surgery only in the LP-PRP group (Nishio et al., 2020). This proves that LP-PRP has the function of anti-inflammation and acceleration of the recovery of the degenerative tendon. In summary, LR-PRP might elicit a more severe inflammatory response when considered in terms of macrophage alone. Rapid infiltration of inflammatory cells might stimulate the tissue repair process more rapidly. On the contrary, LP-PRP has a strong potential to induce anabolism, which is beneficial in enhancing tenocyte proliferation and promoting tendon remodeling.

The presence and concentration of leukocytes (mainly neutrophils) in PRP must be considered in the treatment of tendinopathy. The leukocyte number in LP-PRP is reduced by 22-fold compared with baseline, almost eliminating this cellular component (Fitzpatrick et al., 2017b). However, LR-PRP can enrich leukocytes 3–5 times the baseline level (Fitzpatrick et al., 2017b). In addition, PRP produced by different preparation systems has different proportions of neutrophils, lymphocytes, and monocytes (Fitzpatrick et al., 2017b). The role of leukocytes is controversial. Some researchers claim that leukocytes in PRP have some positive and antibacterial effects. They can regulate the local immune microenvironment, which is helpful to prevent or control the infection of the injured tendon (Castillo et al., 2011). Leukocytes can also increase the concentration of growth factors in PRP by directly releasing or indirectly stimulating platelets to release growth factors (Zimmermann et al., 2001). In addition, leukocytes are able to promote angiogenesis and recruit macrophages at the lesion site to transform chronic low-grade inflammation in tendinopathy into regenerative inflammation (Millar et al., 2017; Chisari et al., 2021). However, other researchers believe that leukocyte is not an ideal component of PRP. Leukocytes can not only release multiple MMPs, but also stimulate tenocytes and TSCs to express MMP-1, MMP-3, and MMP-13, which has a negative effect on tendon matrix deposition (McCarrel et al., 2012; Cross et al., 2015; Zhou et al., 2015; Zhang L. et al., 2016; Bonilla-Gutierrez et al., 2018). Meanwhile, leukocyte infiltration can increase the levels of IL-1β, IL-6, TNF-α, and IL-8 in the tendon. It might inactivate growth factors, such as PDGF and TGF-β1, further worsen the microenvironment of the degenerative tendon, and aggravate the inflammatory reaction (McCarrel et al., 2012; Cross et al., 2015; Zhou et al., 2015; Zhang L. et al., 2016; Bonilla-Gutierrez et al., 2018). In addition, macrophages and other inflammatory cells can release a variety of COX, such as COX-1 and COX-2. Under the influence of high concentrations of COX-1 and COX-2, a large amount of PGE2 is produced and enriched in the affected site by mPGES, resulting in vasodilatation and pain (Ferreira et al., 1978; Williams, 1979; Smith, 1989).

Recent studies suggest that whether leukocytes in PRP are beneficial to tendon healing depends on the severity of tendinopathy. LR-PRP can further improve the therapeutic effect on tendinopathy in the early stage, whereas LP-PRP is more effective in the middle and late stages of tendinopathy. Yan et al. (2017) established a rabbit model of Achilles tendinopathy by injection of collagenase (Figure 5). In the 4th week after collagenase injection, LP-PRP, LR-PRP, and saline were utilized respectively to treat the degenerative Achilles (Yan et al., 2017). Yan et al. (2017) found that the LP-PRP group had higher histological scores, better structure and alignment of collagen fibers, and fewer pro-catabolic inflammatory factors than the other two groups. On this basis, Jiang et al. (2020) applied LP-PRP, LR-PRP, and saline, respectively, to treat the degenerative Achilles in rabbits in the 1st week after collagenase injection. They found that the Achilles treated with LR-PRP had more mature collagen fibers and better mechanical properties. Similarly, Li et al. (2020) treated tendinopathy with LR-PRP and saline separately in the 1st and 4th weeks after collagenase injection. The effect was evaluated by cytokine quantification, MRI, histological analysis, and transmission electron microscopy in the 6th week after collagenase injection (Li et al., 2020). The results show that LR-PRP can achieve the best therapeutic effect in the early stage of tendinopathy. The LR-PRP group in the 1st week had the smallest lesion area, the lowest MRI signal intensity, the largest mean diameter of collagen fibers, the highest expression level of type I and III collagen genes, and the best histological score (Li et al., 2020). However, the injection of LR-PRP in the late stage of tendinopathy can induce excessive catabolism and inflammation, which is not beneficial for the repair of tendinopathy (Li et al., 2020).

4 The use of PRP in clinical practice or clinical trials

Over the past few years, many studies have been conducted to evaluate the effectiveness of PRP in treating musculoskeletal conditions. A large number of basic research and clinical trials have proven the curative efficacy and safety of PRP for tendinopathy, although some of the results show that PRP is not so effective (de Vos et al., 2010b; Kearney et al., 2021; Dai et al., 2023). Consequently, there is controversy about the benefits of PRP for patients with tendinopathy. Currently, according to the mainstream view, such controversy is attributed to a lack of unified standards for the preparation process and the way of activation and administration of PRP in the research, as well as the pathological process of tendinopathy. Therefore, some researchers suggest recording the characterization details in clinical trials. These characterization details include the preparation methods (parameters of centrifugation and activation status/activator used); composition (concentration of platelets, leukocytes, and relative growth factors); and dosing methods

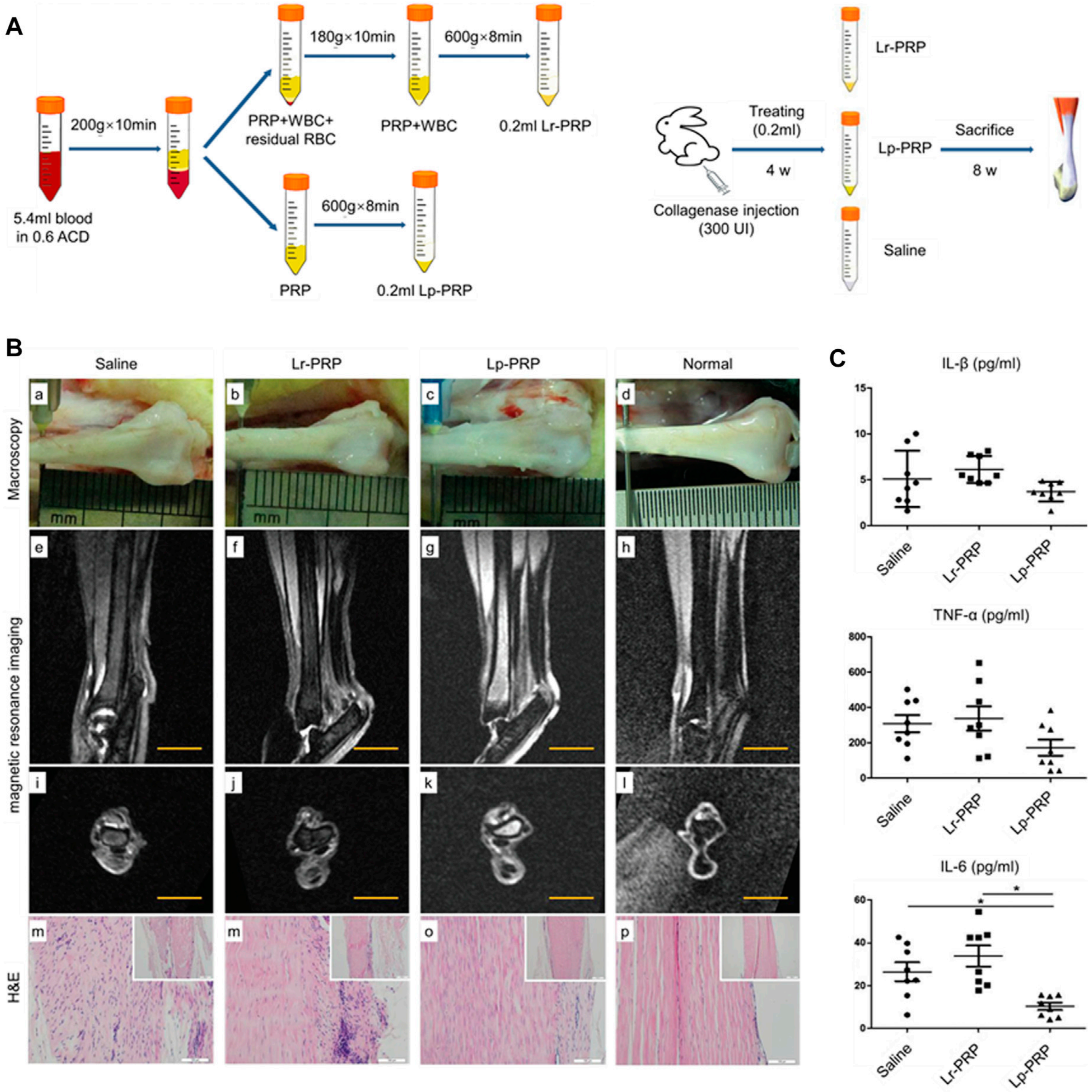

FIGURE 5
Anti-inflammatory effect of the intratendon delivery of leukocyte-poor PRP (LP-PRP) and leukocyte-rich PRP (LR-PRP) in a rabbit Achilles chronic tendinopathy model *in vivo*. **(A)** Flowchart of the preparation process of two kinds of PRP and the study design. **(B)** Gross view of the tendon in the saline, Lr-PRP, Lp-PRP, and normal groups (a–d). The Achilles tendons of the Lr-PRP group appeared to be pallid and displayed more swelling compared with the Lp-PRP group. Sagittal and transverse magnetic resonance imaging (MRI) T2-weighted images of the Achilles tendon in the saline, Lr-PRP, Lp-PRP, and normal groups (e–l). MRI revealed that the Lr-PRP and saline groups displayed higher signal intensities compared with the Lp-PRP group with T2 mapping, representing inflammatory edema at the lesion site. **(C)** Detection of IL-1b, TNF-a, and IL-6 by enzyme-linked immunosorbent assay, indicating Lr-PRP elicited more catabolic cytokine release than Lp-PRP at the local lesion site of the tendon (Yan et al., 2017).

(volume of therapeutic dose and number of doses administered) of PRP (Fitzpatrick et al., 2017a; Chahla et al., 2017; Murray et al., 2017; Rodeo, 2019). Meanwhile, researchers should identify the onset site and properly evaluate the current pathological process (early reactive tendinopathy, tendon disrepair, or degenerative tendinopathy) (Nourissat et al., 2015b; Filardo et al., 2018). This section discusses and analyzes the topics above, with the aim of establishing norms in clinical studies to allow comparison among studies and provide reproducibility.

The difference in the composition of PRP may be one of the main reasons for the controversy. The final ingredients of PRP are affected by two interrelated factors. The first is the concentration of platelets, leukocytes, and cytokines in the whole blood of patients (Mazzocca et al., 2012). The second is the anticoagulation methods, speed, rounds, and duration of the centrifugation process for different PRP preparation systems (DeLong et al., 2012; Chahla et al., 2017). For example, significant differences exist in the platelet capture efficiency; leukocyte concentration; and PDGF-AB, PDGF-

BB, and VEGF concentrations in the PRP prepared by three different systems (Cascade, Magellan, and Biomet GPS III) (Castillo et al., 2011). However, there is a general lack of detailed recording of PRP preparation schemes and composition in the current clinical trials, making it impossible to reproduce the trial or compare the efficiency of PRP prepared by different systems (Abate et al., 2012). A systematic review of PRP application in orthopedic practice shows that among the 105 clinical studies included, only 11 (10%) submitted comprehensive PRP preparation reports, and 17 (16%) reported PRP composition (Chahla et al., 2017). Another recent study found that only a third of studies among all specialties, including musculoskeletal specialties, provided details on the PRP processing and characteristics, with only half of those studies performing leukocyte analysis (Nazaroff et al., 2021). Classification systems that can evaluate PRP are available now. The platelet, activation, white blood cell (PAW) classification system designed by DeLong et al. (2012) is regarded as a feasible PRP classification system. The PAW system evaluates the platelet count, activation methods, and leukocyte and neutrophil concentrations of PRP. Therefore, it can accurately compare the efficacies of PRP with different compositions and facilitate further exploration of optimal PRP ingredients. The concentration level for some other important growth factors, such as PDGF, TGF-β, and VEGF, should also be considered (Chen et al., 2022).

PRP can maintain an anticoagulation state for up to 8 h. However, PRP must be activated to release platelet granule content to exert treatment effects. The activated RPR will form a growth factor-rich blood clot that can release high-concentration growth factors and play a positive role in promoting the proliferation and migration of tenocytes and the formation of a tendon matrix. The choice of PRP activators and the activation duration will affect the release rate of growth factors, causing differences in the overall efficacy (Chen et al., 2018). Bovine thrombin and calcium chloride are the two most widely used PRP activators. Bovine thrombin is not recommended because it causes faster release of the growth factors from the platelet and has toxicity on human bodies. Marx (2004) showed that bovine thrombin caused 70% of the growth factors from platelet to release in 10 min and nearly 100% of the growth factors to release in 1 h. Furthermore, the use of bovine thrombin as the clotting initiator could put patients at risk of coagulopathy (Alsousou et al., 2013). Calcium chloride is safe but with a longer activation time (at least 20 min). Preparing and using calcium chloride solution to activate PRP will not expose patients to viruses or prions. The addition of calcium chloride results in the formation of a dense fibrin matrix, and intact platelets are subsequently trapped within (Abate et al., 2012). This system minimizes platelet activation, and the result is a slow release of growth factors over a 7-day period. Endogenous type I collage is also considered to be able to activate platelets within PRP to release growth factors (DeLong et al., 2012). An *in vitro* experiment compared the differences in activation effects on human PRP between type I collagen and bovine thrombin (Fufa et al., 2008; DeLong et al., 2012). This experiment found that from day 1 to day 10, the release volumes of PDGF-AB and VEGF for the two groups were approximately equal. However, from day 1 to day 5, the release volume of TGF-β for the type I collagen group was higher, and the shrinkage of the blood clot was significantly inhibited. This proved that type I collagen is effective in activating PRP. Photoactivation is considered an alternative to platelet activation. A recent study has compared the light-activated PRP with the chloride-activated PRP (Irmak et al., 2020). Studies have shown that the activation of platelets using a polychromatic light source (wavelengths in the range of 600–1,200 nm, near-infrared region) for 10 min will cause a sustainable release of growth factors for 28 days. Compared with the calcium-chloride-activated PRP, the light-activated PRP maximizes the release time of growth factors, such as PDGF, FGF, and TGF-β1, with a higher release volume.

During the treatment of tendinopathy, how to concentrate PRP at the lesion site efficiently and safely is one of the key factors that affect treatment outcomes. PRP injection to the osteotendinous junction, tendon, or myotendinous junction, respectively, will produce diverse outcomes, indicating the efficacy varies by administration positions (Anitua et al., 2009). Ultrasound-guided musculoskeletal procedures have become an effective administration therapy and are more widely used for the treatment of musculoskeletal diseases (Barile et al., 2016). Ultrasound-guided PRP injection technique allows the surgeons to control the depth of needle insertion and accurately deliver PRP to the lesion site of tendons (de Vos et al., 2010a). Some researchers use a peppering injection technique to eliminate the range of inflammation and stimulate the self-healing process of the tendon (Edwards and Calandruccio, 2003). In recent years, various PRP delivery systems have been successfully developed, including injectable biodegradable gelatin hydrogel microspheres and biological macromolecule hybrid hydrogels (Nagae et al., 2007; Saito et al., 2009; Lu et al., 2019). Choi et al. (2020) used microfluidics to fabricate biodegradable PRP-loaded polyethylene glycol microspheres. This system dramatically slowed the degradation of polyethylene glycol, achieved the sustained release of growth factors within PRP, and to some extent, resolved the fast-release problem of growth factors with a single injection.

The number of PRP administrations is also a key factor. Research shows that a single injection and multiple injections bring different outcomes in the treatment of tendinopathy (Zayni et al., 2015). A meta-analysis discussing the efficacy of PRP on patellar tendinopathy has shown that a single injection of PRP delivers better outcomes in the short term, whereas multiple PRP injections demonstrate more obvious benefits in the long term (Andriolo et al., 2019). Therefore, personalized PRP administration protocols should be given to patients based on their tolerance and the severity of symptoms. For chronic tendinopathy with severe symptoms, it is suggested to combine multiple PRP injections with rehabilitation training (Kon et al., 2009).

PRP application may offer different outcomes according to the tendon disorders considered. The specific anatomical areas of the tendon and tendinopathy pathological progress could be potential factors that affect the efficacy of PRP. Patellar tendons seem to benefit from PRP injections. A systematic review, including 70 studies with 2,350 patients, has shown that multiple PRP injections are an appropriate option for patients with chronic patellar tendinopathy (Andriolo et al., 2019). Dragoo et al. (2014) compared clinical outcomes in patellar tendinopathy after a single ultrasound-guided LR-PRP injection *versus* dry needling. At 12 weeks after treatment, the PRP group showed a better Victorian Institute of Sports Assessment score for patellar tendinopathy than the dry needling group. No significant difference was observed in the scores of the two groups at 26 weeks. This indicates that patellar tendinopathy can benefit from PRP in the early stage of the treatment. However, results in the Achilles tendon do not justify the application of the evaluated platelet concentrates, neither conservatively nor surgically. A meta-analysis, including five randomized control trials with 189 patients, has reported that PRP injection therapy for chronic Achilles tendinopathy is not better than placebo treatment (Liu et al., 2019). The first double-blind, randomized control trial was authored by the group of de Vos et al., who compared a single non-activated intratendinous injection of PRP in patients with chronic midportion Achilles tendinopathy against a single injection of saline (de Vos et al., 2010b; de Jonge et al., 2011). Although an overall improvement was described in both groups, the authors failed to show any significant inter-group differences. Similar results were also reported by Krogh et al. (2016), who found no difference between PRP and saline solution 3 months after the injective treatment. Lateral elbow tendinopathy showed improvement with the application of PRP in most of the high-level studies. A meta-analysis, including seven randomized control trials with 515 patients, showed that 6 months after treatment, the PRP group was better than the local corticosteroid injection group in relieving pain and improving elbow function (Xu et al., 2019). Another systematic review, including nine meta-analyses with 8,656 patients, revealed that corticosteroid injection can improve the function and relieve the pain for patients with lateral epicondylitis in the short term, and PRP injection is the most effective therapy in the middle term (Houck et al., 2019). The findings on the PRP conservative treatment of rotator cuff are still too limited to provide viable indications. A systematic review, including five randomized control trials, showed that for patients with chronic rotator cuff injury, PRP injections may not be beneficial in the short term. When directly compared with exercise therapy, PRP does not result in superior functional outcomes, pain scores, or range of motion (Hurley et al., 2019). With respect to the surgical application, PRP has been widely used as a biological enhancer during or immediately after arthroscopic rotator cuff repair. There is more consistent literature with an overall agreement on the benefit of PRP surgical augmentation (Jo et al., 2013; Malavolta et al., 2014; Pandey et al., 2016).

From a clinical viewpoint, an important consideration is the considerable pathogenetic heterogeneity of tendinopathy. The pathological characteristics of treated tendinopathy are not always described in detail in the published work, which limits the validity of study conclusions and hinders comparisons across studies (Nourissat et al., 2015b). Distinct injury–repair reactions will occur in different pathological stages of tendinopathy. An appropriate description of the patient's medical history and an accurate evaluation of the tendinopathy pathological stage based on the continuum model is necessary in the manuscripts. Useful information could no doubt be obtained by performing studies in narrower indications, probably at an early stage of the tendon disease. Currently, the available scientific evidence does not warrant the use of PRP for the first-line treatment of tendinopathy. PRP therapy may deserve consideration in specific tendinopathy subtypes after the failure of ultrasound-guided corticosteroid injections. Nevertheless, further studies are needed to define these potential indications and the optimal treatment protocols.

Moreover, considering tendinopathy in competitive athletes and the possible use of PRP for tissue recovery, the world anti-doping agency (WADA) position on this treatment is particularly important. According to the 2023 list of prohibited substances and methods, growth factors and growth factor modulators affecting muscle, tendon, or ligament protein synthesis/degradation, vascularization, energy utilization, and regenerative capacity of fiber type switching are prohibited at all times (in- and out-of-competition). Activated PRP contains a variety of growth factors, including PDGF, HGF, VEGF, and FGF, which should be prohibited in principle. For competitive athletes with tendinopathy, using PRP for treatment is required to be in compliance with the appropriate international standards for therapeutic use exemptions and to obtain the legal right for PRP therapy. Notably, the latest international standard for therapeutic use exemption stipulates that athletes may be granted a therapeutic use exemption if (and only if) they can show on the balance of probabilities that each of the following conditions is met. a) The prohibited substance or method in question is needed to treat a diagnosed medical condition supported by relevant clinical evidence. b) The therapeutic use of the prohibited substance or prohibited method will not, on the balance of probabilities, produce any additional enhancement of performance beyond what might be anticipated by a return to the athlete's normal state of health following the treatment of the medical condition. c) The prohibited substance or method is an indicated treatment for the medical condition, and there is no reasonably permitted therapeutic alternative. d) The necessity for the use of the prohibited substance or method is not a consequence, wholly or in part, of the prior use of a substance or method which was prohibited at the time of such use. Competitive athletes with tendinopathy and their coaches should decide whether to use PRP for tendinopathy after giving full consideration to the regulations above and are required to submit a request to the competent authority to obtain the legal right to apply PRP therapy.

5 Conclusion

PRP is self-derived and easily accessible without risk of immune rejection or disease transmission. PRP has been gradually applied in the treatment of many diseases, especially in the field of musculoskeletal, and has shown certain curative effects. Researchers have conducted several trials over the past decade to assess the efficacy of PRP for tendinopathy. However, some experimental results are conflicting, and there is no consensus regarding the efficacy of PRP for tendinopathy. The controversy over the results can be attributed to differences among studies, known as "4D," which means differences in PRP ingredient, mode of administration, donor (patient), and disease (type, stage). This article focuses on the pathogenesis of tendinopathy and attempts to combine the PRP mechanism with the pathological process of tendinopathy, thereby better understanding how PRP treats tendinopathy and the reasons for the differences in the clinical outcomes. Moreover, based on fundamental research, this article integrates the specific molecular and cellular mechanisms by which PRP manipulates tendon healing, including promoting tendon regeneration and modulating inflammation in tendinopathy. Future studies should further elucidate PRP and tendinopathy/tendon regeneration interaction, as well as the optimal PRP component and application mode, depending on the type and stage of tendinopathy. Finally, although the safety of this biological approach obtains overall support, reports about adverse consequences still exist. Therefore, the prognosis of PRP in all studies needs to be documented to clearly identify possible contraindications. Based on current literature, PRP should not be used indiscriminately in clinical practice for tendinopathy but rather as a second-line treatment until further evidence provides a clear indication. Clinicians should be aware of the different therapeutic potentials of PRP for different types or stages of tendinopathy and should provide suitable treatment for patients with tendinopathy.

Author contributions

JL: writing—original draft. HL: conceptualization. ZZ: conceptualization. RX: supervision. JW: investigation and methodology. HJ: investigation and methodology. All authors contributed to the article and approved the submitted version.

Conflict of interest

The authors declare that the research was conducted in the absence of any commercial or financial relationships that could be construed as a potential conflict of interest.

Publisher's note

All claims expressed in this article are solely those of the authors and do not necessarily represent those of their affiliated organizations or those of the publisher, the editors, and the reviewers. Any product that may be evaluated in this article, or claim that may be made by its manufacturer, is not guaranteed or endorsed by the publisher.

References

Abate, M., Di Gregorio, P., Schiavone, C., Salini, V., Tosi, U., and Muttini, A. (2012). Platelet rich plasma in tendinopathies: How to explain the failure. *Int. J. Immunopathol. Pharmacol.* 25 (2), 325–334. doi:10.1177/039463201202500202

Abraham, A. C., Shah, S. A., Golman, M., Song, L., Li, X., Kurtaliaj, I., et al. (2019). Targeting the NF-κB signaling pathway in chronic tendon disease. *Sci. Transl. Med.* 11 (481), eaav4319. doi:10.1126/scitranslmed.aav4319

Ackermann, P. W., Li, J., Lundeberg, T., and Kreicbergs, A. (2003). Neuronal plasticity in relation to nociception and healing of rat achilles tendon. *J. Orthop. Res.* 21 (3), 432–441. doi:10.1016/S0736-0266(02)00207-3

Afifi, W. M., Abo Elsaoud, A. M., Elgawish, M. H., and Ghorab, A. M. (2019). Musculoskeletal manifestations in end-stage renal disease patients on hemodialysis and relation to parathyroid dysfunction. *Saudi J. Kidney Dis. Transpl.* 30 (1), 68–82. doi:10.4103/1319-2442.252935

Alsousou, J., Ali, A., Willett, K., and Harrison, P. (2013). The role of platelet-rich plasma in tissue regeneration. *Platelets* 24 (3), 173–182. doi:10.3109/09537104.2012.684730

Alsousou, J., Thompson, M., Harrison, P., Willett, K., and Franklin, S. (2015). Effect of platelet-rich plasma on healing tissues in acute ruptured achilles tendon: A human immunohistochemistry study. *Lancet* 385 (1), S19. doi:10.1016/S0140-6736(15)60334-8

Andarawis-Puri, N., Flatow, E. L., and Soslowsky, L. J. (2015). Tendon basic science: Development, repair, regeneration, and healing. *J. Orthop. Res.* 33 (6), 780–784. doi:10.1002/jor.22869

Andia, I., and Abate, M. (2018). Platelet-rich plasma: Combinational treatment modalities for musculoskeletal conditions. *Front. Med.* 12 (2), 139–152. doi:10.1007/s11684-017-0551-6

Andia, I., and Maffulli, N. (2013). Platelet-rich plasma for managing pain and inflammation in osteoarthritis. *Nat. Rev. Rheumatol.* 9 (12), 721–730. doi:10.1038/nrrheum.2013.141

Andia, I., Martin, J. I., and Maffulli, N. (2018). Advances with platelet rich plasma therapies for tendon regeneration. *Expert Opin. Biol. Ther.* 18 (4), 389–398. doi:10.1080/14712598.2018.1424626

Andia, I., Rubio-Azpeitia, E., and Maffulli, N. (2015). Platelet-rich plasma modulates the secretion of inflammatory/angiogenic proteins by inflamed tenocytes. *Clin. Orthop. Relat. Res.* 473 (5), 1624–1634. doi:10.1007/s11999-015-4179-z

Andia, I., Sanchez, M., and Maffulli, N. (2012). Joint pathology and platelet-rich plasma therapies. *Expert Opin. Biol. Ther.* 12 (1), 7–22. doi:10.1517/14712598.2012.632765

Andriolo, L., Altamura, S. A., Reale, D., Candrian, C., Zaffagnini, S., and Filardo, G. (2019). Nonsurgical treatments of patellar tendinopathy: Multiple injections of platelet-rich plasma are a suitable option: A systematic review and meta-analysis. *Am. J. Sports Med.* 47 (4), 1001–1018. doi:10.1177/0363546518759674

Anitua, E., Andia, I., Sanchez, M., Azofra, J., del Mar Zalduendo, M., de la Fuente, M., et al. (2005). Autologous preparations rich in growth factors promote proliferation and induce VEGF and HGF production by human tendon cells in culture. *J. Orthop. Res.* 23 (2), 281–286. doi:10.1016/j.orthres.2004.08.015

Anitua, E., Sanchez, M., Zalduendo, M. M., de la Fuente, M., Prado, R., Orive, G., et al. (2009). Fibroblastic response to treatment with different preparations rich in growth factors. *Cell Prolif.* 42 (2), 162–170. doi:10.1111/j.1365-2184.2009.00583.x

Arnoczky, S. P., Lavagnino, M., Egerbacher, M., Caballero, O., and Gardner, K. (2007). Matrix metalloproteinase inhibitors prevent a decrease in the mechanical properties of stress-deprived tendons: An *in vitro* experimental study. *Am. J. Sports Med.* 35 (5), 763–769. doi:10.1177/0363546506296043

Arnold, L., Henry, A., Poron, F., Baba-Amer, Y., van Rooijen, N., Plonquet, A., et al. (2007). Inflammatory monocytes recruited after skeletal muscle injury switch into antiinflammatory macrophages to support myogenesis. *J. Exp. Med.* 204 (5), 1057–1069. doi:10.1084/jem.20070075

Arvind, V., and Huang, A. H. (2021). Reparative and maladaptive inflammation in tendon healing. *Front. Bioeng. Biotechnol.* 9, 719047. doi:10.3389/fbioe.2021.719047

Banos, C. C., Thomas, A. H., and Kuo, C. K. (2008). Collagen fibrillogenesis in tendon development: Current models and regulation of fibril assembly. *Birth Defects Res. C Embryo Today* 84 (3), 228–244. doi:10.1002/bdrc.20130

Barile, A., La Marra, A., Arrigoni, F., Mariani, S., Zugaro, L., Splendiani, A., et al. (2016). Anaesthetics, steroids and platelet-rich plasma (PRP) in ultrasound-guided musculoskeletal procedures. *Br. J. Radiol.* 89 (1065), 20150355. doi:10.1259/bjr.20150355

Basdelioglu, K., Meric, G., Sargin, S., Atik, A., Ulusal, A. E., and Akseki, D. (2020). The effect of platelet-rich plasma on fracture healing in long-bone pseudoarthrosis. *Eur. J. Orthop. Surg. Traumatol.* 30 (8), 1481–1486. doi:10.1007/s00590-020-02730-2

Battery, L., and Maffulli, N. (2011). Inflammation in overuse tendon injuries. *Sports Med. Arthrosc. Rev.* 19 (3), 213–217. doi:10.1097/JSA.0b013e31820e6a92

Bedi, A., Fox, A. J., Kovacevic, D., Deng, X. H., Warren, R. F., and Rodeo, S. A. (2010). Doxycycline-mediated inhibition of matrix metalloproteinases improves healing after rotator cuff repair. *Am. J. Sports Med.* 38 (2), 308–317. doi:10.1177/0363546509347366

Bendinelli, P., Matteucci, E., Dogliotti, G., Corsi, M. M., Banfi, G., Maroni, P., et al. (2010). Molecular basis of anti-inflammatory action of platelet-rich plasma on human chondrocytes: Mechanisms of NF-κB inhibition via HGF. *J. Cell Physiol.* 225 (3), 757–766. doi:10.1002/jcp.22274

Best, K. T., Lee, F. K., Knapp, E., Awad, H. A., and Loiselle, A. E. (2019). Deletion of NFKB1 enhances canonical NF-κB signaling and increases macrophage and myofibroblast content during tendon healing. *Sci. Rep.* 9 (1), 10926. doi:10.1038/s41598-019-47461-5

Bi, Y., Ehirchiou, D., Kilts, T. M., Inkson, C. A., Embree, M. C., Sonoyama, W., et al. (2007). Identification of tendon stem/progenitor cells and the role of the extracellular matrix in their niche. *Nat. Med.* 13 (10), 1219–1227. doi:10.1038/nm1630

Boesen, A. P., Hansen, R., Boesen, M. I., Malliaras, P., and Langberg, H. (2017). Effect of high-volume injection, platelet-rich plasma, and sham treatment in chronic midportion achilles tendinopathy: A randomized double-blinded prospective study. *Am. J. Sports Med.* 45 (9), 2034–2043. doi:10.1177/0363546517702862

Bonilla-Gutierrez, A. F., Castillo-Franz, C., Lopez, C., Alvarez, M. E., Giraldo, C. E., and Carmona, J. U. (2018). Equine suspensory ligament and tendon explants cultured with platelet-rich gel supernatants release different anti-inflammatory and anabolic mediators. *Biomed. Pharmacother.* 108, 476–485. doi:10.1016/j.biopha.2018.09.065

Bosch, G., Moleman, M., Barneveld, A., van Weeren, P. R., and van Schie, H. T. (2011). The effect of platelet-rich plasma on the neovascularization of surgically created equine superficial digital flexor tendon lesions. *Scand. J. Med. Sci. Sports* 21 (4), 554–561. doi:10.1111/j.1600-0838.2009.01070.x

Braun, H. J., Kim, H. J., Chu, C. R., and Dragoo, J. L. (2014). The effect of platelet-rich plasma formulations and blood products on human synoviocytes: Implications for intra-articular injury and therapy. *Am. J. Sports Med.* 42 (5), 1204–1210. doi:10.1177/0363546514525593

Brockmeyer, M., Diehl, N., Schmitt, C., Kohn, D. M., and Lorbach, O. (2015). Results of surgical treatment of chronic patellar tendinosis (Jumper's Knee): A Systematic

Review of the Literature. *Arthroscopy* 31 (12), 2424–2429.e3. doi:10.1016/j.arthro.2015.06.010

Burnouf, T., Goubran, H. A., Chou, M. L., Devos, D., and Radosevic, M. (2014). Platelet microparticles: detection and assessment of their paradoxical functional roles in disease and regenerative medicine. *Blood Rev.* 28 (4), 155–166. doi:10.1016/j.blre.2014.04.002

Busch, F., Mobasheri, A., Shayan, P., Stahlmann, R., and Shakibaei, M. (2012). Sirt-1 is required for the inhibition of apoptosis and inflammatory responses in human tenocytes. *J. Biol. Chem.* 287 (31), 25770–25781. doi:10.1074/jbc.M112.355420

Campbell, A. L., Smith, N. C., Reilly, J. H., Kerr, S. C., Leach, W. J., Fazzi, U. G., et al. (2014). IL-21 receptor expression in human tendinopathy. *Mediat. Inflamm.* 2014, 1–7. doi:10.1155/2014/481206

Carpenter, J. E., and Hankenson, K. D. (2004). Animal models of tendon and ligament injuries for tissue engineering applications. *Biomaterials* 25 (9), 1715–1722. doi:10.1016/S0142-9612(03)00507-6

Castillo, T. N., Pouliot, M. A., Kim, H. J., and Dragoo, J. L. (2011). Comparison of growth factor and platelet concentration from commercial platelet-rich plasma separation systems. *Am. J. Sports Med.* 39 (2), 266–271. doi:10.1177/0363546510387517

Chahal, J., Van Thiel, G. S., Mall, N., Heard, W., Bach, B. R., Cole, B. J., et al. (2012). The role of platelet-rich plasma in arthroscopic rotator cuff repair: a systematic review with quantitative synthesis. *Arthroscopy* 28 (11), 1718–1727. doi:10.1016/j.arthro.2012.03.007

Chahla, J., Cinque, M. E., Piuzzi, N. S., Mannava, S., Geeslin, A. G., Murray, I. R., et al. (2017). A Call for Standardization in Platelet-Rich Plasma Preparation Protocols and Composition Reporting: A Systematic Review of the Clinical Orthopaedic Literature. *J. Bone Jt. Surg. Am.* 99 (20), 1769–1779. doi:10.2106/JBJS.16.01374

Chan, B. P., Chan, K. M., Maffulli, N., Webb, S., and Lee, K. K. (1997). Effect of basic fibroblast growth factor. An *in vitro* study of tendon healing. *Clin. Orthop. Relat. Res.* 342, 239–247. doi:10.1097/00003086-199709000-00031

Chen, J., Svensson, J., Sundberg, C. J., Ahmed, A. S., and Ackermann, P. W. (2021). FGF gene expression in injured tendons as a prognostic biomarker of 1-year patient outcome after Achilles tendon repair. *J. Exp. Orthop.* 8 (1), 20. doi:10.1186/s40634-021-00335-0

Chen, J., Wan, Y., and Jiang, H. (2022). The effect of platelet-rich plasma injection on chronic Achilles tendinopathy and acute Achilles tendon rupture. *Platelets* 33 (3), 339–349. doi:10.1080/09537104.2021.1961712

Chen, L., Dong, S. W., Tao, X., Liu, J. P., Tang, K. L., and Xu, J. Z. (2012). Autologous platelet-rich clot releasate stimulates proliferation and inhibits differentiation of adult rat tendon stem cells towards nontenocyte lineages. *J. Int. Med. Res.* 40 (4), 1399–1409. doi:10.1177/147323001204000418

Chen, L., Liu, J. P., Tang, K. L., Wang, Q., Wang, G. D., Cai, X. H., et al. (2014). Tendon derived stem cells promote platelet-rich plasma healing in collagenase-induced rat achilles tendinopathy. *Cell Physiol. Biochem.* 34 (6), 2153–2168. doi:10.1159/000369659

Chen, Q., Lu, H., and Yang, H. (2015). Chitosan prevents adhesion during rabbit flexor tendon repair via the sirtuin 1 signaling pathway. *Mol. Med. Rep.* 12 (3), 4598–4603. doi:10.3892/mmr.2015.4007

Chen, X., Jones, I. A., Park, C., and Vangsness, C. T., Jr. (2018). The Efficacy of Platelet-Rich Plasma on Tendon and Ligament Healing: A Systematic Review and Meta-analysis With Bias Assessment. *Am. J. Sports Med.* 46 (8), 2020–2032. doi:10.1177/0363546517743746

Chisari, E., Rehak, L., Khan, W. S., and Maffulli, N. (2019). Tendon healing in presence of chronic low-level inflammation: a systematic review. *Br. Med. Bull.* 132 (1), 97–116. doi:10.1093/bmb/ldz035

Chisari, E., Rehak, L., Khan, W. S., and Maffulli, N. (2021). Tendon healing is adversely affected by low-grade inflammation. *J. Orthop. Surg. Res.* 16 (1), 700. doi:10.1186/s13018-021-02811-w

Choi, M. H., Blanco, A., Stealey, S., Duan, X., Case, N., Sell, S. A., et al. (2020). Micro-Clotting of Platelet-Rich Plasma Upon Loading in Hydrogel Microspheres Leads to Prolonged Protein Release and Slower Microsphere Degradation. *Polym. (Basel)* 12 (8), 1712. doi:10.3390/polym12081712

Chuen, F. S., Chuk, C. Y., Ping, W. Y., Nar, W. W., Kim, H. L., and Ming, C. K. (2004a). Immunohistochemical characterization of cells in adult human patellar tendons. *J. Histochem Cytochem* 52 (9), 1151–1157. doi:10.1369/jhc.3A6232.2004

Chuen, F. S., Chuk, C. Y., Ping, W. Y., Nar, W. W., Kim, H. L., and Ming, C. K. (2004b). Immunohistochemical characterization of cells in adult human patellar tendons. *J. Histochem. Cytochem.* 52 (9), 1151–1157. doi:10.1369/jhc.3A6232.2004

Chung, S. W., Huong, C. B., Kim, S. H., and Oh, J. H. (2013). Shoulder stiffness after rotator cuff repair: risk factors and influence on outcome. *Arthroscopy* 29 (2), 290–300. doi:10.1016/j.arthro.2012.08.023

Citeroni, M. R., Ciardulli, M. C., Russo, V., Della Porta, G., Mauro, A., El Khatib, M., et al. (2020). *In vitro* Innovation of Tendon Tissue Engineering Strategies. *Int. J. Mol. Sci.* 21 (18), 6726. doi:10.3390/ijms21186726

Cook, J. L., and Purdam, C. R. (2009). Is tendon pathology a continuum? A pathology model to explain the clinical presentation of load-induced tendinopathy. *Br. J. Sports Med.* 43 (6), 409–416. doi:10.1136/bjsm.2008.051193

Cross, J. A., Cole, B. J., Spatny, K. P., Sundman, E., Romeo, A. A., Nicholson, G. P., et al. (2015). Leukocyte-Reduced Platelet-Rich Plasma Normalizes Matrix Metabolism in Torn Human Rotator Cuff Tendons. *Am. J. Sports Med.* 43 (12), 2898–2906. doi:10.1177/0363546515608157

D'Addona, A., Maffulli, N., Formisano, S., and Rosa, D. (2017). Inflammation in tendinopathy. *Surgeon* 15 (5), 297–302. doi:10.1016/j.surge.2017.04.004

Dai, W., Yan, W., Leng, X., Wang, J., Hu, X., Cheng, J., et al. (2023). Efficacy of Platelet-Rich Plasma Versus Placebo in the Treatment of Tendinopathy: A Meta-analysis of Randomized Controlled Trials. *Clin. J. Sport Med.* 33 (1), 69–77. doi:10.1097/JSM.0000000000000961

Dakin, S. G., Dudhia, J., and Smith, R. K. (2014). Resolving an inflammatory concept: the importance of inflammation and resolution in tendinopathy. *Vet. Immunol. Immunopathol.* 158 (3-4), 121–127. doi:10.1016/j.vetimm.2014.01.007

Dakin, S. G., Martinez, F. O., Yapp, C., Wells, G., Oppermann, U., Dean, B. J., et al. (2015). Inflammation activation and resolution in human tendon disease. *Sci. Transl. Med.* 7 (311), 311ra173. doi:10.1126/scitranslmed.aac4269

Dakin, S. G., Newton, J., Martinez, F. O., Hedley, R., Gwilym, S., Jones, N., et al. (2018). Chronic inflammation is a feature of Achilles tendinopathy and rupture. *Br. J. Sports Med.* 52 (6), 359–367. doi:10.1136/bjsports-2017-098161

Dakin, S. G., Werling, D., Hibbert, A., Abayasekara, D. R., Young, N. J., Smith, R. K., et al. (2012). Macrophage sub-populations and the lipoxin A4 receptor implicate active inflammation during equine tendon repair. *PLoS One* 7 (2), e32333. doi:10.1371/journal.pone.0032333

Dallaudiere, B., Lempicki, M., Pesquer, L., Louedec, L., Preux, P. M., Meyer, P., et al. (2013). Acceleration of tendon healing using US guided intratendinous injection of bevacizumab: first pre-clinical study on a murine model. *Eur. J. Radiol.* 82 (12), e823–e828. doi:10.1016/j.ejrad.2013.06.012

Dallaudiere, B., Zurlinden, O., Perozziello, A., Deschamps, L., Larbi, A., Louedec, L., et al. (2014). Combined intra-tendinous injection of Platelet Rich Plasma and bevacizumab accelerates and improves healing compared to Platelet Rich Plasma in tendinosis: comprehensive assessment on a rat model. *Muscles Ligaments Tendons J.* 4 (3), 351–356.

de Jonge, S., de Vos, R. J., Weir, A., van Schie, H. T., Bierma-Zeinstra, S. M., Verhaar, J. A., et al. (2011). One-year follow-up of platelet-rich plasma treatment in chronic Achilles tendinopathy: a double-blind randomized placebo-controlled trial. *Am. J. Sports Med.* 39 (8), 1623–1630. doi:10.1177/0363546511404877

de Mos, M., van der Windt, A. E., Jahr, H., van Schie, H. T., Weinans, H., Verhaar, J. A., et al. (2008). Can platelet-rich plasma enhance tendon repair? A cell culture study. *Am. J. Sports Med.* 36 (6), 1171–1178. doi:10.1177/0363546508314430

de Oliveira, R. R., Martins, C. S., Rocha, Y. R., Braga, A. B., Mattos, R. M., Hecht, F., et al. (2013). Experimental diabetes induces structural, inflammatory and vascular changes of Achilles tendons. *PLoS One* 8 (10), e74942. doi:10.1371/journal.pone.0074942

de Vos, R. J. (2016). Does Platelet-Rich Plasma Increase Tendon Metabolism? *Adv. Exp. Med. Biol.* 920, 263–273. doi:10.1007/978-3-319-33943-6_25

de Vos, R. J., van Veldhoven, P. L., Moen, M. H., Weir, A., Tol, J. L., and Maffulli, N. (2010a). Autologous growth factor injections in chronic tendinopathy: a systematic review. *Br. Med. Bull.* 95, 63–77. doi:10.1093/bmb/ldq006

de Vos, R. J., Weir, A., Tol, J. L., Verhaar, J. A., Weinans, H., and van Schie, H. T. (2011). No effects of PRP on ultrasonographic tendon structure and neovascularisation in chronic midportion Achilles tendinopathy. *Br. J. Sports Med.* 45 (5), 387–392. doi:10.1136/bjsm.2010.076398

de Vos, R. J., Weir, A., van Schie, H. T., Bierma-Zeinstra, S. M., Verhaar, J. A., Weinans, H., et al. (2010b). Platelet-rich plasma injection for chronic Achilles tendinopathy: a randomized controlled trial. *JAMA* 303 (2), 144–149. doi:10.1001/jama.2009.1986

Del Buono, A., Battery, L., Denaro, V., Maccauro, G., and Maffulli, N. (2011). Tendinopathy and inflammation: some truths. *Int. J. Immunopathol. Pharmacol.* 24, 45–50. doi:10.1177/03946320110241S209

Del Buono, A., Oliva, F., Osti, L., and Maffulli, N. (2013). Metalloproteases and tendinopathy. *Muscles Ligaments Tendons J.* 3 (1), 51–57. doi:10.32098/mltj.01.2013.08

DeLong, J. M., Russell, R. P., and Mazzocca, A. D. (2012). Platelet-rich plasma: the PAW classification system. *Arthroscopy* 28 (7), 998–1009. doi:10.1016/j.arthro.2012.04.148

Derwin, K. A., Soslowsky, L. J., Kimura, J. H., and Plaas, A. H. (2001). Proteoglycans and glycosaminoglycan fine structure in the mouse tail tendon fascicle. *J. Orthop. Res.* 19(2), 269–277. doi:10.1016/S0736-0266(00)00032-2

Diniz-Fernandes, T., Godoy-Santos, A. L., Santos, M. C., Pontin, P., Pereira, C. A. A., Jardim, Y. J., et al. (2018). Matrix metalloproteinase-1 (MMP-1) and (MMP-8) gene polymorphisms promote increase and remodeling of the collagen III and V in posterior tibial tendinopathy. *Histol. Histopathol.* 33 (9), 929–936. doi:10.14670/HH-11-982

Docheva, D., Muller, S. A., Majewski, M., and Evans, C. H. (2015). Biologics for tendon repair. *Adv. Drug Deliv. Rev.* 84, 222–239. doi:10.1016/j.addr.2014.11.015

Dolkart, O., Chechik, O., Zarfati, Y., Brosh, T., Alhajajra, F., and Maman, E. (2014). A single dose of platelet-rich plasma improves the organization and strength of a surgically repaired rotator cuff tendon in rats. *Arch. Orthop. Trauma Surg.* 134 (9), 1271–1277. doi:10.1007/s00402-014-2026-4

Dragoo, J. L., Wasterlain, A. S., Braun, H. J., and Nead, K. T. (2014). Platelet-rich plasma as a treatment for patellar tendinopathy: a double-blind, randomized controlled trial. *Am. J. Sports Med.* 42 (3), 610–618. doi:10.1177/0363546513518416

Edwards, S. G., and Calandruccio, J. H. (2003). Autologous blood injections for refractory lateral epicondylitis. *J. Hand Surg. Am.* 28 (2), 272–278. doi:10.1053/jhsu.2003.50041

El-Sharkawy, H., Kantarci, A., Deady, J., Hasturk, H., Liu, H., Alshahat, M., et al. (2007). Platelet-rich plasma: growth factors and pro- and anti-inflammatory properties. *J. Periodontol.* 78 (4), 661–669. doi:10.1902/jop.2007.060302

Ersen, A., Demirhan, M., Atalar, A. C., Kapicioglu, M., and Baysal, G. (2014). Platelet-rich plasma for enhancing surgical rotator cuff repair: evaluation and comparison of two application methods in a rat model. *Arch. Orthop. Trauma Surg.* 134 (3), 405–411. doi:10.1007/s00402-013-1914-3

Evrova, O., and Buschmann, J. (2017). *In vitro* and *in vivo* effects of PDGF-BB delivery strategies on tendon healing: a review. *Eur. Cell Mater* 34, 15–39. doi:10.22203/eCM.v034a02

Ferreira, S. H., Nakamura, M., and de Abreu Castro, M. S. (1978). The hyperalgesic effects of prostacyclin and prostaglandin E2. *Prostaglandins* 16 (1), 31–37. doi:10.1016/0090-6980(78)90199-5

Filardo, G., Di Matteo, B., Kon, E., Merli, G., and Marcacci, M. (2018). Platelet-rich plasma in tendon-related disorders: results and indications. *Knee Surg. Sports Traumatol. Arthrosc.* 26 (7), 1984–1999. doi:10.1007/s00167-016-4261-4

Finnoff, J. T., Fowler, S. P., Lai, J. K., Santrach, P. J., Willis, E. A., Sayeed, Y. A., et al. (2011). Treatment of chronic tendinopathy with ultrasound-guided needle tenotomy and platelet-rich plasma injection. *PM R.* 3 (10), 900–911. doi:10.1016/j.pmrj.2011.05.015

Fitzpatrick, J., Bulsara, M. K., McCrory, P. R., Richardson, M. D., and Zheng, M. H. (2017b). Analysis of Platelet-Rich Plasma Extraction: Variations in Platelet and Blood Components Between 4 Common Commercial Kits. *Orthop. J. Sports Med.* 5 (1), 232596711667527. doi:10.1177/2325967116675272

Fitzpatrick, J., Bulsara, M., and Zheng, M. H. (2017a). The Effectiveness of Platelet-Rich Plasma in the Treatment of Tendinopathy: A Meta-analysis of Randomized Controlled Clinical Trials. *Am. J. Sports Med.* 45 (1), 226–233. doi:10.1177/0363546516643716

Flad, H. D., and Brandt, E. (2010). Platelet-derived chemokines: pathophysiology and therapeutic aspects. *Cell Mol. Life Sci.* 67 (14), 2363–2386. doi:10.1007/s00018-010-0306-x

Fleming, B. C., Spindler, K. P., Palmer, M. P., Magarian, E. M., and Murray, M. M. (2009). Collagen-platelet composites improve the biomechanical properties of healing anterior cruciate ligament grafts in a porcine model. *Am. J. Sports Med.* 37 (8), 1554–1563. doi:10.1177/0363546509332257

Fufa, D., Shealy, B., Jacobson, M., Kevy, S., and Murray, M. M. (2008). Activation of platelet-rich plasma using soluble type I collagen. *J. Oral Maxillofac. Surg.* 66 (4), 684–690. doi:10.1016/j.joms.2007.06.635

Fukawa, T., Yamaguchi, S., Watanabe, A., Sasho, T., Akagi, R., Muramatsu, Y., et al. (2015). Quantitative Assessment of Tendon Healing by Using MR T2 Mapping in a Rabbit Achilles Tendon Transection Model Treated with Platelet-rich Plasma. *Radiology* 276 (3), 748–755. doi:10.1148/radiol.2015141544

Garcia, J., Hurwitz, H. I., Sandler, A. B., Miles, D., Coleman, R. L., Deurloo, R., et al. (2020). Bevacizumab (Avastin®) in cancer treatment: A review of 15 years of clinical experience and future outlook. *Cancer Treat. Rev.* 86, 102017. doi:10.1016/j.ctrv.2020.102017

Gawaz, M., and Vogel, S. (2013). Platelets in tissue repair: control of apoptosis and interactions with regenerative cells. *Blood* 122 (15), 2550–2554. doi:10.1182/blood-2013-05-468694

Ghasemzadeh, M., Kaplan, Z. S., Alwis, I., Schoenwaelder, S. M., Ashworth, K. J., Westein, E., et al. (2013). The CXCR1/2 ligand NAP-2 promotes directed intravascular leukocyte migration through platelet thrombi. *Blood* 121 (22), 4555–4566. doi:10.1182/blood-2012-09-459636

Gill, T. J. t., Carroll, K. M., and Hariri, S. (2013). Open Patellar Tendon Debridement for Treatment of Recalcitrant Patellar Tendinopathy: Indications, Technique, and Clinical Outcomes After a 2-Year Minimum Follow-up. *Sports Health* 5 (3), 276–280. doi:10.1177/1941738112467950

Giordano, L., Porta, G. D., Peretti, G. M., and Maffulli, N. (2020). Therapeutic potential of microRNA in tendon injuries. *Br. Med. Bull.* 133 (1), 79–94. doi:10.1093/bmb/ldaa002

Gleissner, C. A., Shaked, I., Little, K. M., and Ley, K. (2010). CXC chemokine ligand 4 induces a unique transcriptome in monocyte-derived macrophages. *J. Immunol.* 184 (9), 4810–4818. doi:10.4049/jimmunol.0901368

Goncalves, A. I., Rodrigues, M. T., Lee, S. J., Atala, A., Yoo, J. J., Reis, R. L., et al. (2013). Understanding the role of growth factors in modulating stem cell tenogenesis. *PLoS One* 8 (12), e83734. doi:10.1371/journal.pone.0083734

Halper, J. (2014). Advances in the use of growth factors for treatment of disorders of soft tissues. *Adv. Exp. Med. Biol.* 802, 59–76. doi:10.1007/978-94-007-7893-1_5

Han, P., Cui, Q., Lu, W., Yang, S., Shi, M., Li, Z., et al. (2019). Hepatocyte growth factor plays a dual role in tendon-derived stem cell proliferation, migration, and differentiation. *J. Cell Physiol.* 234 (10), 17382–17391. doi:10.1002/jcp.28360

Han, P., Cui, Q., Yang, S., Wang, H., Gao, P., and Li, Z. (2017). Tumor necrosis factor-α and transforming growth factor-β1 facilitate differentiation and proliferation of tendon-derived stem cells *in vitro*. *Biotechnol. Lett.* 39 (5), 711–719. doi:10.1007/s10529-017-2296-3

Hansen, M., Boesen, A., Holm, L., Flyvbjerg, A., Langberg, H., and Kjaer, M. (2013). Local administration of insulin-like growth factor-I (IGF-I) stimulates tendon collagen synthesis in humans. *Scand. J. Med. Sci. Sports* 23 (5), 614–619. doi:10.1111/j.1600-0838.2011.01431.x

Hapa, O., Cakici, H., Kukner, A., Aygun, H., Sarkalan, N., and Baysal, G. (2012). Effect of platelet-rich plasma on tendon-to-bone healing after rotator cuff repair in rats: an *in vivo* experimental study. *Acta Orthop. Traumatol. Turc* 46 (4), 301–307. doi:10.3944/aott.2012.2664

Hata, K., Nishimura, R., Ikeda, F., Yamashita, K., Matsubara, T., Nokubi, T., et al. (2003). Differential roles of Smad1 and p38 kinase in regulation of peroxisome proliferator-activating receptor gamma during bone morphogenetic protein 2-induced adipogenesis. *Mol. Biol. Cell* 14 (2), 545–555. doi:10.1091/mbc.e02-06-0356

Hershey, G. K. (2003). IL-13 receptors and signaling pathways: an evolving web. *J. Allergy Clin. Immunol.* 111 (4), 677–690. doi:10.1067/mai.2003.1333

Houck, D. A., Kraeutler, M. J., Thornton, L. B., McCarty, E. C., and Bravman, J. T. (2019). Treatment of Lateral Epicondylitis With Autologous Blood, Platelet-Rich Plasma, or Corticosteroid Injections: A Systematic Review of Overlapping Meta-analyses. *Orthop. J. Sports Med.* 7 (3), 232596711983105. doi:10.1177/2325967119831052

Hudgens, J. L., Sugg, K. B., Grekin, J. A., Gumucio, J. P., Bedi, A., and Mendias, C. L. (2016). Platelet-Rich Plasma Activates Proinflammatory Signaling Pathways and Induces Oxidative Stress in Tendon Fibroblasts. *Am. J. Sports Med.* 44 (8), 1931–1940. doi:10.1177/0363546516637176

Hurley, E. T., Hannon, C. P., Pauzenberger, L., Fat, D. L., Moran, C. J., and Mullett, H. (2019). Nonoperative Treatment of Rotator Cuff Disease With Platelet-Rich Plasma: A Systematic Review of Randomized Controlled Trials. *Arthroscopy* 35 (5), 1584–1591. doi:10.1016/j.arthro.2018.10.115

Imai, S., Kumagai, K., Yamaguchi, Y., Miyatake, K., and Saito, T. (2019). Platelet-Rich Plasma Promotes Migration, Proliferation, and the Gene Expression of Scleraxis and Vascular Endothelial Growth Factor in Paratenon-Derived Cells *in vitro*. *Sports Health* 11 (2), 142–148. doi:10.1177/1941738118807479

Irmak, G., Demirtas, T. T., and Gumusderelioglu, M. (2020). Sustained release of growth factors from photoactivated platelet rich plasma (PRP). *Eur. J. Pharm. Biopharm.* 148, 67–76. doi:10.1016/j.ejpb.2019.11.011

Jafari, L., Hassanisaber, H., Savard, M., Gobeil, F., Jr., and Langelier, E. (2019). Efficacy of Combining PRP and MMP Inhibitors in Treating Moderately Damaged Tendons *ex vivo*. *J. Orthop. Res.* 37 (8), 1838–1847. doi:10.1002/jor.24319

James, R., Kesturu, G., Balian, G., and Chhabra, A. B. (2008). Tendon: biology, biomechanics, repair, growth factors, and evolving treatment options. *J. Hand Surg. Am.* 33 (1), 102–112. doi:10.1016/j.jhsa.2007.09.007

Jarvinen, T. A. (2020). Neovascularisation in tendinopathy: from eradication to stabilisation? *Br. J. Sports Med.* 54 (1), 1–2. doi:10.1136/bjsports-2019-100608

Jiang, G., Wu, Y., Meng, J., Wu, F., Li, S., Lin, M., et al. (2020). Comparison of Leukocyte-Rich Platelet-Rich Plasma and Leukocyte-Poor Platelet-Rich Plasma on Achilles Tendinopathy at an Early Stage in a Rabbit Model. *Am. J. Sports Med.* 48 (5), 1189–1199. doi:10.1177/0363546520906142

Jo, C. H., Kim, J. E., Yoon, K. S., and Shin, S. (2012). Platelet-rich plasma stimulates cell proliferation and enhances matrix gene expression and synthesis in tenocytes from human rotator cuff tendons with degenerative tears. *Am. J. Sports Med.* 40 (5), 1035–1045. doi:10.1177/0363546512437525

Jo, C. H., Lee, S. Y., Yoon, K. S., Oh, S., and Shin, S. (2018). Allogenic Pure Platelet-Rich Plasma Therapy for Rotator Cuff Disease: A Bench and Bed Study. *Am. J. Sports Med.* 46 (13), 3142–3154. doi:10.1177/0363546518800268

Jo, C. H., Shin, J. S., Lee, Y. G., Shin, W. H., Kim, H., Lee, S. Y., et al. (2013). Platelet-rich plasma for arthroscopic repair of large to massive rotator cuff tears: a randomized, single-blind, parallel-group trial. *Am. J. Sports Med.* 41 (10), 2240–2248. doi:10.1177/0363546513497925

John, T., Lodka, D., Kohl, B., Ertel, W., Jammrath, J., Conrad, C., et al. (2010). Effect of pro-inflammatory and immunoregulatory cytokines on human tenocytes. *J. Orthop. Res.* 28 (8), 1071–1077. doi:10.1002/jor.21079

Jones, G. C., Corps, A. N., Pennington, C. J., Clark, I. M., Edwards, D. R., Bradley, M. M., et al. (2006). Expression profiling of metalloproteinases and tissue inhibitors of metalloproteinases in normal and degenerate human achilles tendon. *Arthritis Rheum.* 54 (3), 832–842. doi:10.1002/art.21672

Kajikawa, Y., Morihara, T., Sakamoto, H., Matsuda, K., Oshima, Y., Yoshida, A., et al. (2008). Platelet-rich plasma enhances the initial mobilization of circulation-derived cells for tendon healing. *J. Cell Physiol.* 215 (3), 837–845. doi:10.1002/jcp.21368

Kajikawa, Y., Morihara, T., Watanabe, N., Sakamoto, H., Matsuda, K., Kobayashi, M., et al. (2007). GFP chimeric models exhibited a biphasic pattern of mesenchymal cell invasion in tendon healing. *J. Cell Physiol.* 210 (3), 684–691. doi:10.1002/jcp.20876

Kannus, P. (2000). Structure of the tendon connective tissue. *Scand. J. Med. Sci. Sports* 10 (6), 312–320. doi:10.1034/j.1600-0838.2000.010006312.x

Katzel, E. B., Wolenski, M., Loiselle, A. E., Basile, P., Flick, L. M., Langstein, H. N., et al. (2011). Impact of Smad3 loss of function on scarring and adhesion formation during tendon healing. *J. Orthop. Res.* 29 (5), 684–693. doi:10.1002/jor.21235

Kaux, J. F., and Crielaard, J. M. (2013). Platelet-rich plasma application in the management of chronic tendinopathies. *Acta Orthop. Belg* 79 (1), 10–15.

Kawase, T., Tanaka, T., Okuda, K., Tsuchimochi, M., Oda, M., and Hara, T. (2015). Quantitative single-cell motility analysis of platelet-rich plasma-treated endothelial cells *in vitro*. *Cytoskelet. Hob.* 72 (5), 246–255. doi:10.1002/cm.21221

Kearney, R. S., Ji, C., Warwick, J., Parsons, N., Brown, J., Harrison, P., et al. (2021). Effect of Platelet-Rich Plasma Injection vs Sham Injection on Tendon Dysfunction in Patients With Chronic Midportion Achilles Tendinopathy: A Randomized Clinical Trial. *JAMA* 326 (2), 137–144. doi:10.1001/jama.2021.6986

Kelly, B. A., Proffen, B. L., Haslauer, C. M., and Murray, M. M. (2016). Platelets and plasma stimulate sheep rotator cuff tendon tenocytes when cultured in an extracellular matrix scaffold. *J. Orthop. Res.* 34 (4), 623–629. doi:10.1002/jor.23058

Kielty, C. M., Sherratt, M. J., and Shuttleworth, C. A. (2002). Elastic fibres. *J. Cell Sci.* 115 (Pt 14), 2817–2828. doi:10.1242/jcs.115.14.2817

Killian, M. L., Cavinatto, L., Galatz, L. M., and Thomopoulos, S. (2012). The role of mechanobiology in tendon healing. *J. Shoulder Elb. Surg.* 21 (2), 228–237. doi:10.1016/j.jse.2011.11.002

Kim, D. H., Je, Y. J., Kim, C. D., Lee, Y. H., Seo, Y. J., Lee, J. H., et al. (2011). Can Platelet-rich Plasma Be Used for Skin Rejuvenation? Evaluation of Effects of Platelet-rich Plasma on Human Dermal Fibroblast. *Ann. Dermatol* 23 (4), 424–431. doi:10.5021/ad.2011.23.4.424

Kjaer, M., Langberg, H., Heinemeier, K., Bayer, M. L., Hansen, M., Holm, L., et al. (2009). From mechanical loading to collagen synthesis, structural changes and function in human tendon. *Scand. J. Med. Sci. Sports* 19 (4), 500–510. doi:10.1111/j.1600-0838.2009.00986.x

Knobloch, K. (2016). Drug-Induced Tendon Disorders. *Adv. Exp. Med. Biol.* 920, 229–238. doi:10.1007/978-3-319-33943-6_22

Kobayashi, Y., Saita, Y., Nishio, H., Ikeda, H., Takazawa, Y., Nagao, M., et al. (2016). Leukocyte concentration and composition in platelet-rich plasma (PRP) influences the growth factor and protease concentrations. *J. Orthop. Sci.* 21 (5), 683–689. doi:10.1016/j.jos.2016.07.009

Kobayashi, Y., Saita, Y., Takaku, T., Yokomizo, T., Nishio, H., Ikeda, H., et al. (2020). Platelet-rich plasma (PRP) accelerates murine patellar tendon healing through enhancement of angiogenesis and collagen synthesis. *J. Exp. Orthop.* 7 (1), 49. doi:10.1186/s40634-020-00267-1

Kohler, J., Popov, C., Klotz, B., Alberton, P., Prall, W. C., Haasters, F., et al. (2013). Uncovering the cellular and molecular changes in tendon stem/progenitor cells attributed to tendon aging and degeneration. *Aging Cell* 12 (6), 988–999. doi:10.1111/acel.12124

Kon, E., Filardo, G., Delcogliano, M., Presti, M. L., Russo, A., Bondi, A., et al. (2009). Platelet-rich plasma: New clinical application. *Injury* 40 (6), 598–603. doi:10.1016/j.injury.2008.11.026

Korntner, S., Lehner, C., Gehwolf, R., Wagner, A., Grutz, M., Kunkel, N., et al. (2019). Limiting angiogenesis to modulate scar formation. *Adv. Drug Deliv. Rev.* 146, 170–189. doi:10.1016/j.addr.2018.02.010

Krogh, T. P., Ellingsen, T., Christensen, R., Jensen, P., and Fredberg, U. (2016). Ultrasound-Guided Injection Therapy of Achilles Tendinopathy With Platelet-Rich Plasma or Saline: A Randomized, Blinded, Placebo-Controlled Trial. *Am. J. Sports Med.* 44 (8), 1990–1997. doi:10.1177/0363546516647958

Lakemeier, S., Reichelt, J. J., Patzer, T., Fuchs-Winkelmann, S., Paletta, J. R., and Schofer, M. D. (2010). The association between retraction of the torn rotator cuff and increasing expression of hypoxia inducible factor 1α and vascular endothelial growth factor expression: an immunohistological study. *BMC Musculoskelet. Disord.* 11, 230. doi:10.1186/1471-2474-11-230

Lana, J. F., Huber, S. C., Purita, J., Tambeli, C. H., Santos, G. S., Paulus, C., et al. (2019). Leukocyte-rich PRP versus leukocyte-poor PRP - The role of monocyte/macrophage function in the healing cascade. *J. Clin. Orthop. Trauma* 10 (Suppl. 1), S7–S12. doi:10.1016/j.jcot.2019.05.008

Le, A. D. K., Enweze, L., DeBaun, M. R., and Dragoo, J. L. (2018). Current Clinical Recommendations for Use of Platelet-Rich Plasma. *Curr. Rev. Musculoskelet. Med.* 11 (4), 624–634. doi:10.1007/s12178-018-9527-7

Leblanc, D. R., Schneider, M., Angele, P., Vollmer, G., and Docheva, D. (2017). The effect of estrogen on tendon and ligament metabolism and function. *J. Steroid Biochem. Mol. Biol.* 172, 106–116. doi:10.1016/j.jsbmb.2017.06.008

Lee, S., Hwang, C., Marini, S., Tower, R. J., Qin, Q., Negri, S., et al. (2021). NGF-TrkA signaling dictates neural ingrowth and aberrant osteochondral differentiation after soft tissue trauma. *Nat. Commun.* 12 (1), 4939. doi:10.1038/s41467-021-25143-z

Li, H. Y., and Hua, Y. H. (2016). Achilles Tendinopathy: Current Concepts about the Basic Science and Clinical Treatments. *Biomed. Res. Int.* 2016, 1–9. doi:10.1155/2016/6492597

Li, S., Wu, Y., Jiang, G., Tian, X., Hong, J., Chen, S., et al. (2020). Intratendon delivery of leukocyte-rich platelet-rich plasma at early stage promotes tendon repair in a rabbit Achilles tendinopathy model. *J. Tissue Eng. Regen. Med.* 14 (3), 452–463. doi:10.1002/term.3006

Li, W., Kohara, H., Uchida, Y., James, J. M., Soneji, K., Cronshaw, D. G., et al. (2013). Peripheral nerve-derived CXCL12 and VEGF-A regulate the patterning of arterial vessel branching in developing limb skin. *Dev. Cell* 24 (4), 359–371. doi:10.1016/j.devcel.2013.01.009

Li, Y., Liu, X., Liu, X., Peng, Y., Zhu, B., Guo, S., et al. (2022). Transforming growth factor-beta signalling pathway in tendon healing. *Growth factors.* 40, 98–107. doi:10.1080/08977194.2022.2082294

Li, Z. J., Yang, Q. Q., and Zhou, Y. L. (2021). Basic Research on Tendon Repair: Strategies, Evaluation, and Development. *Front. Med. (Lausanne)* 8, 664909. doi:10.3389/fmed.2021.664909

Li, Z., Meyers, C. A., Chang, L., Lee, S., Li, Z., Tomlinson, R., et al. (2019). Fracture repair requires TrkA signaling by skeletal sensory nerves. *J. Clin. Invest.* 129 (12), 5137–5150. doi:10.1172/JCI128428

Lin, C. Y., Huang, S. C., Tzou, S. J., Yin, C. H., Chen, J. S., Chen, Y. S., et al. (2023). Tendon Disorders in Chronic Liver Disease: A Retrospective Cohort Study in Taiwan. *Int. J. Environ. Res. Public Health* 20 (6), 4983. doi:10.3390/ijerph20064983

Lin, K. Y., Chen, P., Chen, A. C., Chan, Y. S., Lei, K. F., and Chiu, C. H. (2022). Leukocyte-Rich Platelet-Rich Plasma Has Better Stimulating Effects on Tenocyte Proliferation Compared With Leukocyte-Poor Platelet-Rich Plasma. *Orthop. J. Sports Med.* 10 (3), 232596712210847. doi:10.1177/23259671221084706

Lin, T. W., Cardenas, L., Glaser, D. L., and Soslowsky, L. J. (2006). Tendon healing in interleukin-4 and interleukin-6 knockout mice. *J. Biomech.* 39 (1), 61–69. doi:10.1016/j.jbiomech.2004.11.009

Lipman, K., Wang, C., Ting, K., Soo, C., and Zheng, Z. (2018). Tendinopathy: injury, repair, and current exploration. *Drug Des. Devel Ther.* 12, 591–603. doi:10.2147/DDDT.S154660

Liu, C. J., Yu, K. L., Bai, J. B., Tian, D. H., and Liu, G. L. (2019). Platelet-rich plasma injection for the treatment of chronic Achilles tendinopathy: A meta-analysis. *Med. Baltim.* 98 (16), e15278. doi:10.1097/MD.0000000000015278

Liu, J., Han, W., Chen, L., and Tang, K. (2016). Mechanism of osteogenic and adipogenic differentiation of tendon stem cells induced by sirtuin 1. *Mol. Med. Rep.* 14 (2), 1643–1648. doi:10.3892/mmr.2016.5417

Liu, X., Zhang, R., Zhu, B., Li, Y., Liu, X., Guo, S., et al. (2021a). Effects of leukocyte- and platelet-rich plasma on tendon disorders based on *in vitro* and *in vivo* studies (Review). *Exp. Ther. Med.* 21 (6), 639. doi:10.3892/etm.2021.10071

Liu, X., Zhu, B., Li, Y., Liu, X., Guo, S., Wang, C., et al. (2021b). The Role of Vascular Endothelial Growth Factor in Tendon Healing. *Front. Physiol.* 12, 766080. doi:10.3389/fphys.2021.766080

Lo, I. K., Boorman, R., Marchuk, L., Hollinshead, R., Hart, D. A., and Frank, C. B. (2005). Matrix molecule mRNA levels in the bursa and rotator cuff of patients with full-thickness rotator cuff tears. *Arthroscopy* 21 (6), 645–651. doi:10.1016/j.arthro.2005.03.008

Lu, H. T., Chang, W. T., Tsai, M. L., Chen, C. H., Chen, W. Y., and Mi, F. L. (2019). Development of Injectable Fucoidan and Biological Macromolecules Hybrid Hydrogels for Intra-Articular Delivery of Platelet-Rich Plasma. *Mar. Drugs* 17 (4), 236. doi:10.3390/md17040236

Lyras, D. N., Kazakos, K., Verettas, D., Polychronidis, A., Tryfonidis, M., Botaitis, S., et al. (2009). The influence of platelet-rich plasma on angiogenesis during the early phase of tendon healing. *Foot Ankle Int.* 30 (11), 1101–1106. doi:10.3113/FAI.2009.1101

Lyu, F. J., Cui, H., Pan, H., Mc Cheung, K., Cao, X., Iatridis, J. C., et al. (2021). Painful intervertebral disc degeneration and inflammation: from laboratory evidence to clinical interventions. *Bone Res.* 9 (1), 7. doi:10.1038/s41413-020-00125-x

Macedo, C. S. G., Tadiello, F. F., Medeiros, L. T., Antonelo, M. C., Alves, M. A. F., and Mendonca, L. D. (2019). Physical Therapy Service delivered in the Polyclinic During the Rio 2016 Paralympic Games. *Phys. Ther. Sport* 36, 62–67. doi:10.1016/j.ptsp.2019.01.003

Maffulli, N., Tallon, C., Wong, J., Lim, K. P., and Bleakney, R. (2003). Early weightbearing and ankle mobilization after open repair of acute midsubstance tears of the achilles tendon. *Am. J. Sports Med.* 31 (5), 692–700. doi:10.1177/03635465030310051001

Malavolta, E. A., Gracitelli, M. E., Ferreira Neto, A. A., Assuncao, J. H., Bordalo-Rodrigues, M., and de Camargo, O. P. (2014). Platelet-rich plasma in rotator cuff repair: a prospective randomized study. *Am. J. Sports Med.* 42 (10), 2446–2454. doi:10.1177/0363546514541777

Mantovani, A., Sozzani, S., Locati, M., Allavena, P., and Sica, A. (2002). Macrophage polarization: tumor-associated macrophages as a paradigm for polarized M2 mononuclear phagocytes. *Trends Immunol.* 23 (11), 549–555. doi:10.1016/s1471-4906(02)02302-5

Marques, L. F., Stessuk, T., Camargo, I. C., Sabeh Junior, N., dos Santos, L., and Ribeiro-Paes, J. T. (2015). Platelet-rich plasma (PRP): methodological aspects and clinical applications. *Platelets* 26 (2), 101–113. doi:10.3109/09537104.2014.881991

Marqueti, R. C., Parizotto, N. A., Chriguer, R. S., Perez, S. E., and Selistre-de-Araujo, H. S. (2006). Androgenic-anabolic steroids associated with mechanical loading inhibit matrix metallopeptidase activity and affect the remodeling of the achilles tendon in rats. *Am. J. Sports Med.* 34 (8), 1274–1280. doi:10.1177/0363546506286867

Marx, R. E. (2004). Platelet-rich plasma: evidence to support its use. *J. Oral Maxillofac. Surg.* 62 (4), 489–496. doi:10.1016/j.joms.2003.12.003

Masuda, K., Ishii, S., Ito, K., and Kuboki, Y. (2002). Biochemical analysis of collagen in adhesive tissues formed after digital flexor tendon injuries. *J. Orthop. Sci.* 7 (6), 665–671. doi:10.1007/s007760200118

Mazzocca, A. D., McCarthy, M. B., Chowaniec, D. M., Cote, M. P., Romeo, A. A., Bradley, J. P., et al. (2012). Platelet-rich plasma differs according to preparation method and human variability. *J. Bone Jt. Surg. Am.* 94 (4), 308–316. doi:10.2106/JBJS.K.00430

McCarrel, T. M., Minas, T., and Fortier, L. A. (2012). Optimization of leukocyte concentration in platelet-rich plasma for the treatment of tendinopathy. *J. Bone Jt. Surg. Am.* 94 (19), e143. doi:10.2106/JBJS.L.00019

McNeilly, C. M., Banes, A. J., Benjamin, M., and Ralphs, J. R. (1996). Tendon cells *in vivo* form a three dimensional network of cell processes linked by gap junctions. *J. Anat.* 189 (Pt 3), 593–600.

Millar, N. L., Gilchrist, D. S., Akbar, M., Reilly, J. H., Kerr, S. C., Campbell, A. L., et al. (2015). MicroRNA29a regulates IL-33-mediated tissue remodelling in tendon disease. *Nat. Commun.* 6, 6774. doi:10.1038/ncomms7774

Millar, N. L., Hueber, A. J., Reilly, J. H., Xu, Y., Fazzi, U. G., Murrell, G. A., et al. (2010). Inflammation is present in early human tendinopathy. *Am. J. Sports Med.* 38 (10), 2085–2091. doi:10.1177/0363546510372613

Millar, N. L., Murrell, G. A., and McInnes, I. B. (2017). Inflammatory mechanisms in tendinopathy - towards translation. *Nat. Rev. Rheumatol.* 13 (2), 110–122. doi:10.1038/nrrheum.2016.213

Millar, N. L., Silbernagel, K. G., Thorborg, K., Kirwan, P. D., Galatz, L. M., Abrams, G. D., et al. (2021). Tendinopathy. *Nat. Rev. Dis. Prim.* 7 (1), 1. doi:10.1038/s41572-020-00234-1

Millar, N. L., Wei, A. Q., Molloy, T. J., Bonar, F., and Murrell, G. A. (2009). Cytokines and apoptosis in supraspinatus tendinopathy. *J. Bone Jt. Surg. Br.* 91 (3), 417–424. doi:10.1302/0301-620X.91B3.21652

Mobasheri, A., and Shakibaei, M. (2013). Is tendinitis an inflammatory disease initiated and driven by pro-inflammatory cytokines such as interleukin 1beta? *Histol. Histopathol.* 28 (8), 955–964. doi:10.14670/HH-28.955

Molloy, T., Wang, Y., and Murrell, G. (2003). The roles of growth factors in tendon and ligament healing. *Sports Med.* 33 (5), 381–394. doi:10.2165/00007256-200333050-00004

Morita, W., Dakin, S. G., Snelling, S. J. B., and Carr, A. J. (2017). Cytokines in tendon disease: A Systematic Review. *Bone Jt. Res.* 6 (12), 656–664. doi:10.1302/2046-3758.612.BJR-2017-0112.R1

Moser, B., Wolf, M., Walz, A., and Loetscher, P. (2004). Chemokines: multiple levels of leukocyte migration control. *Trends Immunol.* 25 (2), 75–84. doi:10.1016/j.it.2003.12.005

Moshiri, A., Oryan, A., Meimandi-Parizi, A., and Koohi-Hosseinabadi, O. (2014). Effectiveness of xenogenous-based bovine-derived platelet gel embedded within a three-dimensional collagen implant on the healing and regeneration of the Achilles tendon defect in rabbits. *Expert Opin. Biol. Ther.* 14 (8), 1065–1089. doi:10.1517/14712598.2014.915305

Murray, I. R., Geeslin, A. G., Goudie, E. B., Petrigliano, F. A., and LaPrade, R. F. (2017). Minimum Information for Studies Evaluating Biologics in Orthopaedics (MIBO): Platelet-Rich Plasma and Mesenchymal Stem Cells. *J. Bone Jt. Surg. Am.* 99 (10), 809–819. doi:10.2106/JBJS.16.00793

Murray, P. J., Allen, J. E., Biswas, S. K., Fisher, E. A., Gilroy, D. W., Goerdt, S., et al. (2014). Macrophage activation and polarization: nomenclature and experimental guidelines. *Immunity* 41 (1), 14–20. doi:10.1016/j.immuni.2014.06.008

Nagae, M., Ikeda, T., Mikami, Y., Hase, H., Ozawa, H., Matsuda, K., et al. (2007). Intervertebral disc regeneration using platelet-rich plasma and biodegradable gelatin hydrogel microspheres. *Tissue Eng.* 13 (1), 147–158. doi:10.1089/ten.2006.0042

Nazaroff, J., Oyadomari, S., Brown, N., and Wang, D. (2021). Reporting in clinical studies on platelet-rich plasma therapy among all medical specialties: A systematic review of Level I and II studies. *PLoS One* 16 (4), e0250007. doi:10.1371/journal.pone.0250007

Nielsen, R. H., Holm, L., Malmgaard-Clausen, N. M., Reitelseder, S., Heinemeier, K. M., and Kjaer, M. (2014). Increase in tendon protein synthesis in response to insulin-like growth factor-I is preserved in elderly men. *J. Appl. Physiol. (1985)* 116 (1), 42–46. doi:10.1152/japplphysiol.01084.2013

Nishio, H., Saita, Y., Kobayashi, Y., Takaku, T., Fukusato, S., Uchino, S., et al. (2020). Platelet-rich plasma promotes recruitment of macrophages in the process of tendon healing. *Regen. Ther.* 14, 262–270. doi:10.1016/j.reth.2020.03.009

Nourissat, G., Berenbaum, F., and Duprez, D. (2015a). Tendon injury: from biology to tendon repair. *Nat. Rev. Rheumatol.* 11 (4), 223–233. doi:10.1038/nrrheum.2015.26

Nourissat, G., Houard, X., Sellam, J., Duprez, D., and Berenbaum, F. (2013). Use of autologous growth factors in aging tendon and chronic tendinopathy. *Front. Biosci. (Elite Ed.* 5 (3), 911–921. doi:10.2741/e670

Nourissat, G., Ornetti, P., Berenbaum, F., Sellam, J., Richette, P., and Chevalier, X. (2015b). Does platelet-rich plasma deserve a role in the treatment of tendinopathy? *Jt. Bone Spine* 82 (4), 230–234. doi:10.1016/j.jbspin.2015.02.004

Nurden, A. T., Nurden, P., Sanchez, M., Andia, I., and Anitua, E. (2008). Platelets and wound healing. *Front. Biosci.* 13, 3532–3548. doi:10.2741/2947

O'Brien, M. (1997). Structure and metabolism of tendons. *Scand. J. Med. Sci. Sports* 7 (2), 55–61. doi:10.1111/j.1600-0838.1997.tb00119.x

Olesen, J. L., Heinemeier, K. M., Haddad, F., Langberg, H., Flyvbjerg, A., Kjaer, M., et al. (2006). Expression of insulin-like growth factor I, insulin-like growth factor binding proteins, and collagen mRNA in mechanically loaded plantaris tendon. *J. Appl. Physiol. (1985)* 101 (1), 183–188. doi:10.1152/japplphysiol.00636.2005

Oliva, F., Barisani, D., Grasso, A., and Maffulli, N. (2011). Gene expression analysis in calcific tendinopathy of the rotator cuff. *Eur. Cell Mater* 21, 548–557. doi:10.22203/ecm.v021a41

Pandey, V., Bandi, A., Madi, S., Agarwal, L., Acharya, K. K., Maddukuri, S., et al. (2016). Does application of moderately concentrated platelet-rich plasma improve clinical and structural outcome after arthroscopic repair of medium-sized to large rotator cuff tear? A randomized controlled trial. *J. Shoulder Elb. Surg.* 25 (8), 1312–1322. doi:10.1016/j.jse.2016.01.036

Pauly, S., Klatte-Schulz, F., Stahnke, K., Scheibel, M., and Wildemann, B. (2018). The effect of autologous platelet rich plasma on tenocytes of the human rotator cuff. *BMC Musculoskelet. Disord.* 19 (1), 422. doi:10.1186/s12891-018-2339-5

Peach, C. J., Mignone, V. W., Arruda, M. A., Alcobia, D. C., Hill, S. J., Kilpatrick, L. E., et al. (2018). Molecular Pharmacology of VEGF-A Isoforms: Binding and Signalling at VEGFR2. *Int. J. Mol. Sci.* 19 (4), 1264. doi:10.3390/ijms19041264

Pennisi, E. (2002). Tending tender tendons. *Science* 295 (5557), 1011–1011. doi:10.1126/science.295.5557.1011

Pifer, M. A., Maerz, T., Baker, K. C., and Anderson, K. (2014). Matrix metalloproteinase content and activity in low-platelet, low-leukocyte and high-platelet, high-leukocyte platelet rich plasma (PRP) and the biologic response to PRP by human ligament fibroblasts. *Am. J. Sports Med.* 42 (5), 1211–1218. doi:10.1177/0363546514524710

Pufe, T., Petersen, W. J., Mentlein, R., and Tillmann, B. N. (2005). The role of vasculature and angiogenesis for the pathogenesis of degenerative tendons disease. *Scand. J. Med. Sci. Sports* 15 (4), 211–222. doi:10.1111/j.1600-0838.2005.00465.x

Rahim, M., El Khoury, L. Y., Raleigh, S. M., Ribbans, W. J., Posthumus, M., Collins, M., et al. (2016). Human Genetic Variation, Sport and Exercise Medicine, and Achilles Tendinopathy: Role for Angiogenesis-Associated Genes. *OMICS* 20 (9), 520–527. doi:10.1089/omi.2016.0116

Ramachandran, P., Pellicoro, A., Vernon, M. A., Boulter, L., Aucott, R. L., Ali, A., et al. (2012). Differential Ly-6C expression identifies the recruited macrophage phenotype, which orchestrates the regression of murine liver fibrosis. *Proc. Natl. Acad. Sci. U. S. A.* 109 (46), E3186–E3195. doi:10.1073/pnas.1119964109

Ren, J., and Anversa, P. (2015). The insulin-like growth factor I system: physiological and pathophysiological implication in cardiovascular diseases associated with metabolic syndrome. *Biochem. Pharmacol.* 93 (4), 409–417. doi:10.1016/j.bcp.2014.12.006

Riley, G. (2005). Chronic tendon pathology: molecular basis and therapeutic implications. *Expert Rev. Mol. Med.* 7 (5), 1–25. doi:10.1017/S1462399405008963

Riley, G. P., Harrall, R. L., Cawston, T. E., Hazleman, B. L., and Mackie, E. J. (1996). Tenascin-C and human tendon degeneration. *Am. J. Pathol.* 149 (3), 933–943.

Riley, G. P., Harrall, R. L., Constant, C. R., Chard, M. D., Cawston, T. E., and Hazleman, B. L. (1994a). Glycosaminoglycans of human rotator cuff tendons: changes with age and in chronic rotator cuff tendinitis. *Ann. Rheum. Dis.* 53 (6), 367–376. doi:10.1136/ard.53.6.367

Riley, G. P., Harrall, R. L., Constant, C. R., Chard, M. D., Cawston, T. E., and Hazleman, B. L. (1994b). Tendon degeneration and chronic shoulder pain: changes in the collagen composition of the human rotator cuff tendons in rotator cuff tendinitis. *Ann. Rheum. Dis.* 53 (6), 359–366. doi:10.1136/ard.53.6.359

Riley, G. (2008). Tendinopathy-from basic science to treatment. *Nat. Clin. Pract. Rheumatol.* 4 (2), 82–89. doi:10.1038/ncprheum0700

Riley, G. (2004). The pathogenesis of tendinopathy. A molecular perspective. *Rheumatol. Oxf.* 43 (2), 131–142. doi:10.1093/rheumatology/keg448

Roche, A. J., and Calder, J. D. (2013). Achilles tendinopathy: A review of the current concepts of treatment. *Bone Jt. J.* 95-B (10), 1299–1307. doi:10.1302/0301-620X.95B10.31881

Rodeo, S. (2019). The Need for Minimum Reporting Standards for Studies of "Biologics" in Sports Medicine. *Am. J. Sports Med.* 47 (11), 2531–2532. doi:10.1177/0363546519872219

Ruan, D., Fei, Y., Qian, S., Huang, Z., Chen, W., Tang, C., et al. (2021). Early-Stage Primary Anti-inflammatory Therapy Enhances the Regenerative Efficacy of Platelet-Rich Plasma in a Rabbit Achilles Tendinopathy Model. *Am. J. Sports Med.* 49 (12), 3357–3371. doi:10.1177/03635465211037354

Ruffell, D., Mourkioti, F., Gambardella, A., Kirstetter, P., Lopez, R. G., Rosenthal, N., et al. (2009). A CREB-C/EBPβ cascade induces M2 macrophage-specific gene expression and promotes muscle injury repair. *Proc. Natl. Acad. Sci. U. S. A.* 106 (41), 17475–17480. doi:10.1073/pnas.0908641106

Rui, Y. F., Lui, P. P., Wong, Y. M., Tan, Q., and Chan, K. M. (2013). Altered fate of tendon-derived stem cells isolated from a failed tendon-healing animal model of tendinopathy. *Stem Cells Dev.* 22 (7), 1076–1085. doi:10.1089/scd.2012.0555

Russo, V., Mauro, A., Martelli, A., Di Giacinto, O., Di Marcantonio, L., Nardinocchi, D., et al. (2015). Cellular and molecular maturation in fetal and adult ovine calcaneal tendons. *J. Anat.* 226 (2), 126–142. doi:10.1111/joa.12269

Ruzzini, L., Abbruzzese, F., Rainer, A., Longo, U. G., Trombetta, M., Maffulli, N., et al. (2014). Characterization of age-related changes of tendon stem cells from adult human tendons. *Knee Surg. Sports Traumatol. Arthrosc.* 22 (11), 2856–2866. doi:10.1007/s00167-013-2457-4

Sahin, H., Tholema, N., Petersen, W., Raschke, M. J., and Stange, R. (2012). Impaired biomechanical properties correlate with neoangiogenesis as well as VEGF and MMP-3 expression during rat patellar tendon healing. *J. Orthop. Res.* 30 (12), 1952–1957. doi:10.1002/jor.22147

Saito, M., Takahashi, K. A., Arai, Y., Inoue, A., Sakao, K., Tonomura, H., et al. (2009). Intraarticular administration of platelet-rich plasma with biodegradable gelatin hydrogel microspheres prevents osteoarthritis progression in the rabbit knee. *Clin. Exp. Rheumatol.* 27 (2), 201–207.

Saltzman, B. M., Jain, A., Campbell, K. A., Mascarenhas, R., Romeo, A. A., Verma, N. N., et al. (2016). Does the Use of Platelet-Rich Plasma at the Time of Surgery Improve Clinical Outcomes in Arthroscopic Rotator Cuff Repair When Compared With Control Cohorts? A Systematic Review of Meta-analyses. *Arthroscopy* 32 (5), 906–918. doi:10.1016/j.arthro.2015.10.007

Schemitsch, C., Chahal, J., Vicente, M., Nowak, L., Flurin, P. H., Lambers Heerspink, F., et al. (2019). Surgical repair versus conservative treatment and subacromial decompression for the treatment of rotator cuff tears: a meta-analysis of randomized trials. *Bone Jt. J.* 101-B (9), 1100–1106. doi:10.1302/0301-620X.101B9.BJJ-2018-1591.R1

Schultz, G. S., Sibbald, R. G., Falanga, V., Ayello, E. A., Dowsett, C., Harding, K., et al. (2003). Wound bed preparation: a systematic approach to wound management. *Wound Repair Regen.* 11 (Suppl. 1), S1–S28. doi:10.1046/j.1524-475x.11.s2.1.x

Scollon-Grieve, K. L., and Malanga, G. A. (2011). Platelet-rich plasma injection for partial patellar tendon tear in a high school athlete: a case presentation. *PM R.* 3 (4), 391–395. doi:10.1016/j.pmrj.2010.11.008

Scott, A., Backman, L. J., and Speed, C. (2015). Tendinopathy: Update on Pathophysiology. *J. Orthop. Sports Phys. Ther.* 45 (11), 833–841. doi:10.2519/jospt.2015.5884

Serhan, C. N., Chiang, N., and Van Dyke, T. E. (2008). Resolving inflammation: dual anti-inflammatory and pro-resolution lipid mediators. *Nat. Rev. Immunol.* 8 (5), 349–361. doi:10.1038/nri2294

Sharma, P., and Maffulli, N. (2005). Basic biology of tendon injury and healing. *Surgeon-Journal R. Coll. Surg. Edinb. Irel.* 3 (5), 309–316. doi:10.1016/S1479-666x(05)80109-X

Sharma, P., and Maffulli, N. (2006). Biology of tendon injury: healing, modeling and remodeling. *J. Musculoskelet. Neuronal Interact.* 6 (2), 181–190.

Shin, M. K., Lee, J. W., Kim, Y. I., Kim, Y. O., Seok, H., and Kim, N. I. (2014). The effects of platelet-rich clot releasate on the expression of MMP-1 and type I collagen in human adult dermal fibroblasts: PRP is a stronger MMP-1 stimulator. *Mol. Biol. Rep.* 41 (1), 3–8. doi:10.1007/s11033-013-2718-9

Simic, P., Zainabadi, K., Bell, E., Sykes, D. B., Saez, B., Lotinun, S., et al. (2013). SIRT1 regulates differentiation of mesenchymal stem cells by deacetylating beta-catenin. *EMBO Mol. Med.* 5 (3), 430–440. doi:10.1002/emmm.201201606

Smith, W. L. (1989). The eicosanoids and their biochemical mechanisms of action. *Biochem. J.* 259 (2), 315–324. doi:10.1042/bj2590315

Stalman, A., Bring, D., and Ackermann, P. W. (2015). Chemokine expression of CCL2, CCL3, CCL5 and CXCL10 during early inflammatory tendon healing precedes nerve regeneration: an immunohistochemical study in the rat. *Knee Surg. Sports Traumatol. Arthrosc.* 23 (9), 2682–2689. doi:10.1007/s00167-014-3010-9

Steinmann, S., Pfeifer, C. G., Brochhausen, C., and Docheva, D. (2020). Spectrum of Tendon Pathologies: Triggers, Trails and End-State. *Int. J. Mol. Sci.* 21 (3), 844. doi:10.3390/ijms21030844

Sundman, E. A., Cole, B. J., and Fortier, L. A. (2011). Growth factor and catabolic cytokine concentrations are influenced by the cellular composition of platelet-rich plasma. *Am. J. Sports Med.* 39 (10), 2135–2140. doi:10.1177/0363546511417792

Takamura, M., Yasuda, T., Nakano, A., Shima, H., and Neo, M. (2017). The effect of platelet-rich plasma on Achilles tendon healing in a rabbit model. *Acta Orthop. Traumatol. Turc* 51 (1), 65–72. doi:10.1016/j.aott.2016.12.001

Tang, C., Chen, Y., Huang, J., Zhao, K., Chen, X., Yin, Z., et al. (2018). The roles of inflammatory mediators and immunocytes in tendinopathy. *J. Orthop. Transl.* 14, 23–33. doi:10.1016/j.jot.2018.03.003

Tang, J. B., Wu, Y. F., Cao, Y., Chen, C. H., Zhou, Y. L., Avanessian, B., et al. (2016). Basic FGF or VEGF gene therapy corrects insufficiency in the intrinsic healing capacity of tendons. *Sci. Rep.* 6, 20643. doi:10.1038/srep20643

Tempfer, H., and Traweger, A. (2015). Tendon Vasculature in Health and Disease. *Front. Physiol.* 6, 330. doi:10.3389/fphys.2015.00330

Thanasas, C., Papadimitriou, G., Charalambidis, C., Paraskevopoulos, I., and Papanikolaou, A. (2011). Platelet-rich plasma versus autologous whole blood for the treatment of chronic lateral elbow epicondylitis: a randomized controlled clinical trial. *Am. J. Sports Med.* 39 (10), 2130–2134. doi:10.1177/0363546511417113

Thomopoulos, S., Das, R., Sakiyama-Elbert, S., Silva, M. J., Charlton, N., and Gelberman, R. H. (2010). bFGF and PDGF-BB for tendon repair: controlled release and biologic activity by tendon fibroblasts *in vitro*. *Ann. Biomed. Eng.* 38 (2), 225–234. doi:10.1007/s10439-009-9844-5

Thorpe, C. T., Birch, H. L., Clegg, P. D., and Screen, H. R. (2013). The role of the non-collagenous matrix in tendon function. *Int. J. Exp. Pathol.* 94 (4), 248–259. doi:10.1111/iep.12027

Thorpe, C. T., and Screen, H. R. (2016). Tendon Structure and Composition. *Adv. Exp. Med. Biol.* 920, 3–10. doi:10.1007/978-3-319-33943-6_1

Throm, A. M., Liu, W. C., Lock, C. H., and Billiar, K. L. (2010). Development of a cell-derived matrix: effects of epidermal growth factor in chemically defined culture. *J. Biomed. Mater Res. A* 92 (2), 533–541. doi:10.1002/jbm.a.32369

Tillander, B., Franzen, L., and Norlin, R. (2002). Fibronectin, MMP-1 and histologic changes in rotator cuff disease. *J. Orthop. Res.* 20 (6), 1358–1364. doi:10.1016/S0736-0266(02)00057-8

Titan, A. L., Foster, D. S., Chang, J., and Longaker, M. T. (2019). Flexor Tendon: Development, Healing, Adhesion Formation, and Contributing Growth Factors. *Plast. Reconstr. Surg.* 144 (4), 639e–647e. doi:10.1097/PRS.0000000000006048

Turk, A. C., Fidan, N., Ozcan, O., Ozkurt, S., Musmul, A., and Sahin, F. (2020). Comparison of shoulder Magnetic Resonance Imaging findings between patients with stage 4 chronic kidney disease and hemodialysis patients with healthy controls. *J. Back Musculoskelet. Rehabil.* 33 (2), 179–184. doi:10.3233/BMR-170896

Voleti, P. B., Buckley, M. R., and Soslowsky, L. J. (2012). Tendon healing: repair and regeneration. *Annu. Rev. Biomed. Eng.* 14, 47–71. doi:10.1146/annurev-bioeng-071811-150122

Walden, G., Liao, X., Donell, S., Raxworthy, M. J., Riley, G. P., and Saeed, A. (2017). A Clinical, Biological, and Biomaterials Perspective into Tendon Injuries and Regeneration. *Tissue Eng. Part B Rev.* 23 (1), 44–58. doi:10.1089/ten.TEB.2016.0181

Wang, J. H., and Nirmala, X. (2016). Application of Tendon Stem/Progenitor Cells and Platelet-Rich Plasma to Treat Tendon Injuries. *Oper. Tech. Orthop.* 26 (2), 68–72. doi:10.1053/j.oto.2015.12.008

Wang, X., Qiu, Y., Triffitt, J., Carr, A., Xia, Z., and Sabokbar, A. (2012). Proliferation and differentiation of human tenocytes in response to platelet rich plasma: an *in vitro* and *in vivo* study. *J. Orthop. Res.* 30 (6), 982–990. doi:10.1002/jor.22016

Warden, S. J. (2007). Animal models for the study of tendinopathy. *Br. J. Sports Med.* 41 (4), 232–240. doi:10.1136/bjsm.2006.032342

Wei, X. L., Lin, L., Hou, Y., Fu, X., Zhang, J. Y., Mao, Z. B., et al. (2008). Construction of recombinant adenovirus co-expression vector carrying the human transforming growth factor-β1 and vascular endothelial growth factor genes and its effect on anterior cruciate ligament fibroblasts. *Chin. Med. J. Engl.* 121 (15), 1426–1432. doi:10.1097/00029330-200808010-00017

Weng, H. P., Cheng, Y. Y., Lee, H. L., Hsu, T. Y., Chang, Y. T., and Shen, Y. A. (2021). Enhanced Platelet-Rich Plasma (ePRP) Stimulates Wound Healing through Effects on Metabolic Reprogramming in Fibroblasts. *Int. J. Mol. Sci.* 22 (23), 12623. doi:10.3390/ijms222312623

Willecke, K., Eiberger, J., Degen, J., Eckardt, D., Romualdi, A., Guldenagel, M., et al. (2002). Structural and functional diversity of connexin genes in the mouse and human genome. *Biol. Chem.* 383 (5), 725–737. doi:10.1515/BC.2002.076

Williams, T. J. (1979). Prostaglandin E2, prostaglandin I2 and the vascular changes of inflammation. *Br. J. Pharmacol.* 65 (3), 517–524. doi:10.1111/j.1476-5381.1979.tb07860.x

Witt, B. L., and Hyer, C. F. (2012). Achilles tendon reattachment after surgical treatment of insertional tendinosis using the suture bridge technique: a case series. *J. Foot Ankle Surg.* 51 (4), 487–493. doi:10.1053/j.jfas.2012.03.006

Wong, C. C., Huang, Y. M., Chen, C. H., Lin, F. H., Yeh, Y. Y., and Bai, M. Y. (2020). Cytokine and Growth Factor Delivery from Implanted Platelet-Rich Fibrin Enhances Rabbit Achilles Tendon Healing. *Int. J. Mol. Sci.* 21 (9), 3221. doi:10.3390/ijms21093221

Wong, J. K., Lui, Y. H., Kapacee, Z., Kadler, K. E., Ferguson, M. W., and McGrouther, D. A. (2009). The cellular biology of flexor tendon adhesion formation: an old problem in a new paradigm. *Am. J. Pathol.* 175 (5), 1938–1951. doi:10.2353/ajpath.2009.090380

Wu, F., Nerlich, M., and Docheva, D. (2017). Tendon injuries: Basic science and new repair proposals. *EFORT Open Rev.* 2 (7), 332–342. doi:10.1302/2058-5241.2.160075

Wynn, T. A., and Vannella, K. M. (2016). Macrophages in Tissue Repair, Regeneration, and Fibrosis. *Immunity* 44 (3), 450–462. doi:10.1016/j.immuni.2016.02.015

Xie, X., Zhang, C., and Tuan, R. S. (2014). Biology of platelet-rich plasma and its clinical application in cartilage repair. *Arthritis Res. Ther.* 16 (1), 204. doi:10.1186/ar4493

Xu, K., Al-Ani, M. K., Sun, Y., Xu, W., Pan, L., Song, Y., et al. (2017). Platelet-rich plasma activates tendon-derived stem cells to promote regeneration of Achilles tendon rupture in rats. *J. Tissue Eng. Regen. Med.* 11 (4), 1173–1184. doi:10.1002/term.2020

Xu, Q., Chen, J., and Cheng, L. (2019). Comparison of platelet rich plasma and corticosteroids in the management of lateral epicondylitis: A meta-analysis of randomized controlled trials. *Int. J. Surg.* 67, 37–46. doi:10.1016/j.ijsu.2019.05.003

Xu, Y., Wang, X., Liu, W., and Lu, W. (2021). Thrombin-activated platelet-rich plasma enhances osteogenic differentiation of human periodontal ligament stem cells by activating SIRT1-mediated autophagy. *Eur. J. Med. Res.* 26 (1), 105. doi:10.1186/s40001-021-00575-x

Yamada, T., Gotoh, M., Nakama, K., Mitsui, Y., Higuchi, F., and Nagata, K. (2007). Effects of hyaluronan on cell proliferation and mRNA expression of procollagens alpha 1 (I) and alpha 1 (III) in tendon-derived fibroblasts from patients with rotator cuff disease: an *in vitro* study. *Am. J. Sports Med.* 35 (11), 1870–1876. doi:10.1177/0363546507305015

Yan, R., Gu, Y., Ran, J., Hu, Y., Zheng, Z., Zeng, M., et al. (2017). Intratendon Delivery of Leukocyte-Poor Platelet-Rich Plasma Improves Healing Compared With Leukocyte-Rich Platelet-Rich Plasma in a Rabbit Achilles Tendinopathy Model. *Am. J. Sports Med.* 45 (8), 1909–1920. doi:10.1177/0363546517694357

Yang, G., Im, H. J., and Wang, J. H. (2005). Repetitive mechanical stretching modulates IL-1β induced COX-2, MMP-1 expression, and PGE2 production in human patellar tendon fibroblasts. *Gene* 363, 166–172. doi:10.1016/j.gene.2005.08.006

Yoon, J. Y., Lee, S. Y., Shin, S., Yoon, K. S., and Jo, C. H. (2018). Comparative Analysis of Platelet-rich Plasma Effect on Tenocytes from Normal Human Rotator Cuff Tendon and Human Rotator Cuff Tendon with Degenerative Tears. *Clin. Shoulder Elb.* 21 (1), 3–14. doi:10.5397/cise.2018.21.1.3

Yoshida, M., Funasaki, H., Saito, M., Kajitani, K., and Fujii, K. (2003). Pathologic gene expression in adhesive subacromial bursae of human shoulder. *Clin. Orthop. Relat. Res.* 412, 57–64. doi:10.1097/01.blo.0000071757.07450.3f

Yu, T. Y., Pang, J. H., Wu, K. P., Lin, L. P., Tseng, W. C., and Tsai, W. C. (2015). Platelet-rich plasma increases proliferation of tendon cells by modulating Stat3 and p27 to up-regulate expression of cyclins and cyclin-dependent kinases. *Cell Prolif.* 48 (4), 413–420. doi:10.1111/cpr.12189

Yu, T. Y., Pang, J. S., Lin, L. P., Cheng, J. W., Liu, S. J., and Tsai, W. C. (2021). Platelet-Rich Plasma Releasate Promotes Early Healing in Tendon After Acute Injury. *Orthop. J. Sports Med.* 9 (4), 232596712199037. doi:10.1177/2325967121990377

Yuan, T., Zhang, C. Q., and Wang, J. H. (2013). Augmenting tendon and ligament repair with platelet-rich plasma (PRP). *Muscles Ligaments Tendons J.* 3 (3), 139–149. doi:10.32098/mltj.03.2013.05

Zayni, R., Thaunat, M., Fayard, J. M., Hager, J. P., Carrillon, Y., Clechet, J., et al. (2015). Platelet-rich plasma as a treatment for chronic patellar tendinopathy: comparison of a single versus two consecutive injections. *Muscles Ligaments Tendons J.* 5 (2), 92–98. doi:10.32098/mltj.02.2015.07

Zhang, J., Li, F., Augi, T., Williamson, K. M., Onishi, K., Hogan, M. V., et al. (2021a). Platelet HMGB1 in Platelet-Rich Plasma (PRP) promotes tendon wound healing. *PLoS One* 16 (9), e0251166. doi:10.1371/journal.pone.0251166

Zhang, J., Middleton, K. K., Fu, F. H., Im, H. J., and Wang, J. H. (2013). HGF mediates the anti-inflammatory effects of PRP on injured tendons. *PLoS One* 8 (6), e67303. doi:10.1371/journal.pone.0067303

Zhang, J., Pan, T., Liu, Y., and Wang, J. H. (2010). Mouse treadmill running enhances tendons by expanding the pool of tendon stem cells (TSCs) and TSC-related cellular production of collagen. *J. Orthop. Res.* 28 (9), 1178–1183. doi:10.1002/jor.21123

Zhang, J., and Wang, J. H. (2010a). Mechanobiological response of tendon stem cells: implications of tendon homeostasis and pathogenesis of tendinopathy. *J. Orthop. Res.* 28 (5), 639–643. doi:10.1002/jor.21046

Zhang, J., and Wang, J. H. (2010b). Platelet-rich plasma releasate promotes differentiation of tendon stem cells into active tenocytes. *Am. J. Sports Med.* 38 (12), 2477–2486. doi:10.1177/0363546510376750

Zhang, J., and Wang, J. H. (2014). PRP treatment effects on degenerative tendinopathy - an *in vitro* model study. *Muscles Ligaments Tendons J.* 4 (1), 10–17. doi:10.32098/mltj.01.2014.03

Zhang, K., Asai, S., Yu, B., and Enomoto-Iwamoto, M. (2015). IL-1β irreversibly inhibits tenogenic differentiation and alters metabolism in injured tendon-derived progenitor cells *in vitro*. *Biochem. Biophys. Res. Commun.* 463 (4), 667–672. doi:10.1016/j.bbrc.2015.05.122

Zhang, L., Chen, S., Chang, P., Bao, N., Yang, C., Ti, Y., et al. (2016a). Harmful Effects of Leukocyte-Rich Platelet-Rich Plasma on Rabbit Tendon Stem Cells *in vitro*. *Am. J. Sports Med.* 44 (8), 1941–1951. doi:10.1177/0363546516644718

Zhang, X., Lin, Y. C., Rui, Y. F., Xu, H. L., Chen, H., Wang, C., et al. (2016b). Therapeutic Roles of Tendon Stem/Progenitor Cells in Tendinopathy. *Stem Cells Int.* 2016, 1–14. doi:10.1155/2016/4076578

Zhang, Y. E. (2017). Non-Smad Signaling Pathways of the TGF-beta Family. *Cold Spring Harb. Perspect. Biol.* 9 (2), a022129. doi:10.1101/cshperspect.a022129

Zhang, Y. J., Chen, X., Li, G., Chan, K. M., Heng, B. C., Yin, Z., et al. (2018). Concise Review: Stem Cell Fate Guided By Bioactive Molecules for Tendon Regeneration. *Stem Cells Transl. Med.* 7 (5), 404–414. doi:10.1002/sctm.17-0206

Zhang, Z., Li, Y., Zhang, T., Shi, M., Song, X., Yang, S., et al. (2021b). Hepatocyte Growth Factor-Induced Tendon Stem Cell Conditioned Medium Promotes Healing of Injured Achilles Tendon. *Front. Cell Dev. Biol.* 9, 654084. doi:10.3389/fcell.2021.654084

Zhou, Y., and Wang, J. H. (2016). PRP Treatment Efficacy for Tendinopathy: A Review of Basic Science Studies. *Biomed. Res. Int.* 2016, 1–8. doi:10.1155/2016/9103792

Zhou, Y., Zhang, J., Wu, H., Hogan, M. V., and Wang, J. H. (2015). The differential effects of leukocyte-containing and pure platelet-rich plasma (PRP) on tendon stem/progenitor cells - implications of PRP application for the clinical treatment of tendon injuries. *Stem Cell Res. Ther.* 6, 173. doi:10.1186/s13287-015-0172-4

Zimmermann, R., Jakubietz, R., Jakubietz, M., Strasser, E., Schlegel, A., Wiltfang, J., et al. (2001). Different preparation methods to obtain platelet components as a source of growth factors for local application. *Transfusion* 41 (10), 1217–1224. doi:10.1046/j.1537-2995.2001.41101217.x

Frontiers in Bioengineering and Biotechnology

TYPE Original Research
PUBLISHED 30 August 2023
DOI 10.3389/fbioe.2023.1178938

Chemonucleolysis combined with dynamic loading for inducing degeneration in bovine caudal intervertebral discs

Andrea Vernengo[1], Helen Bumann[1], Nadine Kluser[1], Astrid Soubrier[1], Amra Šećerović[1], Jan Gewiess[1], Jan Ulrich Jansen[2], Cornelia Neidlinger-Wilke[2], Hans-Joachim Wilke[2] and Sibylle Grad[1,3]*

[1]AO Research Institute Davos, Davos, Switzerland, [2]Institute of Orthopaedic Research and Biomechanics, Ulm University, Ulm, Germany, [3]Department of Health Sciences and Technology, ETH Zürich, Zurich, Switzerland

OPEN ACCESS

EDITED BY
Zuhao Li,
Jilin University, China

REVIEWED BY
Guus van den Akker,
Maastricht University, Netherlands
Xuan Mei,
Harvard Medical School, United States

*CORRESPONDENCE
Sibylle Grad,
sibylle.grad@aofoundation.org

RECEIVED 03 March 2023
ACCEPTED 01 August 2023
PUBLISHED 30 August 2023

CITATION
Vernengo A, Bumann H, Kluser N, Soubrier A, Šećerović A, Gewiess J, Jansen JU, Neidlinger-Wilke C, Wilke H-J and Grad S (2023), Chemonucleolysis combined with dynamic loading for inducing degeneration in bovine caudal intervertebral discs.
Front. Bioeng. Biotechnol. 11:1178938.
doi: 10.3389/fbioe.2023.1178938

Chemonucleolysis has become an established method of producing whole organ culture models of intervertebral disc (IVD) degeneration. However, the field needs more side-by-side comparisons of the degenerative effects of the major enzymes used in chemonucleolysis towards gaining a greater understanding of how these organ culture models mimic the wide spectrum of characteristics observed in human degeneration. In the current work we induced chemonucleolysis in bovine coccygeal IVDs with 100 μL of papain (65 U/mL), chondroitinase ABC (chABC, 5 U/mL), or collagenase II (col'ase, 0.5 U/mL). Each enzyme was applied in a concentration projected to produce moderate levels of degeneration. After 7 days of culture with daily dynamic physiological loading (0.02–0.2 MPa, 0.2 Hz, 2 h), the cellular, biochemical and histological properties of the IVDs were evaluated in comparison to a PBS-injected control. Papain and collagenase, but not chABC, produced macroscopic voids in the tissues. Compared to day 0 intact IVDs, papain induced the greatest magnitude glycosaminoglycan (GAG) loss compared to chABC and col'ase. Papain also induced the greatest height loss (3%), compared to 0.7%, 1.2% and 0.4% for chABC, col'ase, and PBS, respectively. Cell viability in the region adjacent to papain and PBS-injection remained at nearly 100% over the 7-day culture period, whereas it was reduced to 60%–70% by chABC and col'ase. Generally, enzyme treatment tended to downregulate gene expression for major ECM markers, type I collagen (COL1), type II collagen (COL2), and aggrecan (ACAN) in the tissue adjacent to injection. However, chABC treatment induced an increase in COL2 gene expression, which was significant compared to the papain treated group. In general, papain and col'ase treatment tended to recapitulate aspects of advanced IVD degeneration, whereas chABC treatment captured aspects of early-stage degeneration. Chemonucleolysis of whole bovine IVDs is a useful tool providing researchers with a robust spectrum of degenerative changes and can be utilized for examination of therapeutic interventions.

KEYWORDS

organ culture, chemonucleolysis (CN), intervertebral disc, degeneration, extracellular matrix

Introduction

Degeneration of the lumbar intervertebral disc (IVD) is a frequent medical occurrence. Its clinical presentation is diverse, varying from asymptomatic patients whose lumbar spines show radiological degenerative changes up to severe chronic pain (Brinjikji et al., 2015). Multiple studies have shown a close association between degeneration of the IVD and low back pain (LBP) (Paajanen et al., 1997; de Schepper et al., 2010; Rahyussalim et al., 2020). To date, LBP caused by IVD degeneration is mainly treated by the administration of pain medication, physiotherapy, or surgery. These treatment options target the reduction of pain without directly addressing the root cause, and thus have not been proven effective for reversing disease progression. There is an urgent clinical need for improved treatments which are aimed at restoring the structure and function of IVD tissue.

The IVD consists of connective tissue bridging two vertebrae with each other, therefore allowing motion between the osseous parts of the spine (Bogduk, 2016). The IVD is a composite structure comprised of a nucleus pulposus (NP), annulus fibrosus (AF), and cartilaginous endplates (CEP) (Dowdell et al., 2017). It has been proposed that degeneration is initiated in the NP region (Barcellona et al., 2022), due to numerous possible factors such as calcification, microvascular disease, or smoking (Daly et al., 2016). The reported activity of IVD cells during degeneration has been variable, marked by cell death (Liao et al., 2019; Yang et al., 2022), increased proliferation and cluster formation (Lama et al., 2019; Bonnaire et al., 2021), or senescence (Zhang et al., 2020a; Song et al., 2023). The tissue matrix content in degenerative IVDs is characterized by a continuous loss of proteoglycans (PGs) and water content from NP and inner AF (iAF) tissue (Urban and Roberts, 2003; Freemont, 2009). In the early stages of degeneration, COL2 content increases in the NP, possibly as a salvage attempt by the cells (Takaishi et al., 1997; Cs-Szabo et al., 2002; Uei et al., 2006; Zhou et al., 2021). However, as degeneration advances, COL2 is replaced by COL1, and concomitantly increased levels of COL2 are observed in the outer AF (oAF) (Le Maitre et al., 2007a). Degeneration is further characterized by the elevated expression of proinflammatory cytokines such as IL-1β (Le Maitre et al., 2007b) and IL-8 (Ahn et al., 2002), as well as catabolic enzymes such as matrix metalloproteinases (MMPs) (Roberts et al., 2000; Liu et al., 2018) and the A Disintegrin and Metalloproteinase with Thrombospondin motifs (ADAMTS) family of enzymes (Wang et al., 2015; Wang et al., 2017). Taken together, these alterations lead to a shift in the ECM composition at the center of the IVD, driving abnormal biomechanics and leading to the appearance of fissures in the AF, NP herniation, and overall disc height loss (Boos et al., 2002). However, the transcriptomic and proteomic profiles of an IVD during degeneration can depend on anatomical location (Panebianco et al., 2021; van den Akker et al., 2017), age (Nerlich et al., 2007), genetics (Miller et al., 1988), inflammatory signals (Zhang et al., 2021), and mechanical stress/loading patterns (Wang et al., 2020; Fu et al., 2021). Collectively, research indicates that there will be no “one size fits all” cure for reversing IVD degeneration, and that discerning effective therapeutic interventions will require testing platforms that can mimic the wide spectrum of characteristics observed in degenerating IVDs.

To date, various interventions such as growth factors (Zhu et al., 2019; Kim et al., 2020), cell-based therapies (Panebianco et al., 2020; Barcellona et al., 2021), and injectable biomaterials (Pennicooke et al., 2018; Fujii et al., 2020) have been explored towards achieving tissue reparation. For evaluating the efficacy of these approaches, several *in vitro*, *ex vivo* and *in vivo* models of IVD degeneration have been developed, each with its own set of limitations. *In vitro* models generally require isolation of IVD cells from their native tissues, making the outcomes less predictive of the clinical situation (Teixeira et al., 2020). Meanwhile, *in vivo* models are more predictive, but they are costly, time-intensive and have ethical disadvantages. *Ex vivo* organ models serve as cost-effective testing platforms bridging *in vitro* and *in vivo* studies (Alini et al., 2008). In recent years, a number of whole IVD explant organ culture systems have been developed, mainly focused on bovine coccygeal discs due to their similarity to human lumbar vertebrae in terms of cellular activity, tissue composition and geometry (Oshima et al., 1993; Alini et al., 2008). In such models, fresh tissue explants are derived from recently slaughtered animals and degeneration can be induced by a variety of methods, such as mechanical overload (Christiani et al., 2021; Fu et al., 2021), proinflammatory cytokines (Du et al., 2020), structural injury (Korecki et al., 2008), or chemonucleolysis (Roberts et al., 2008; Gullbrand et al., 2017; Rustenburg et al., 2020).

Chemonucleolysis involves the intradiscal delivery of enzymes to induce cleavage and release of native ECM components, thus initiating a degenerative cascade. At present, a variety of *in vivo* and *ex vivo* IVD degeneration models using chemonucleolysis have been established. For instance, chondroitinase ABC (chABC) has been used to induce degradation of glycosaminoglycans (GAG) side chains of PGs, leading to decreased disc height, loss of structural integrity, and increased expression of inflammatory mediators (Imai et al., 2007; Gullbrand et al., 2017; Zhang et al., 2020b). Other studies with IVD chemonucleolysis have utilized papain, a plant proteolytic enzyme that cleaves peptide bonds in basic amino acids (Mamboya, 2012). Papain was initially used as a therapy in IVD herniation (Javid, 1980), but was later studied *ex vivo*, inducing losses of GAG, disrupted structure of the tissue, and degenerative biomechanical properties (Uei et al., 2006; Roberts et al., 2008; Chan et al., 2013). Collagenase enzymes have the ability to degrade triple-helical native collagen fibrils, (Van Wart and Steinbrink, 1985), leading to significant IVD height loss *in vivo* 2–7 days post-injection (Kalaf et al., 2014) and osteophyte formation at 3 months (Stern and Coulson, 1976). *Ex vivo,* collagenase treatment increased expression of inflammatory cytokines, such as IL-1β, and matrix changes consistent with moderate human IVD degeneration (Rustenburg et al., 2020). Importantly, multiple studies show that injecting higher concentrations of matrix-degrading enzymes produces more aggressive degenerative changes (Chan et al., 2013; Gullbrand et al., 2017; Rustenburg et al., 2020). However, due to the aforementioned complexities of human IVD degeneration, it is unlikely that any single model can effectively recapitulate the disease. In fact, to increase the quality of new reparative technologies, the field needs to continue exploring models of IVD degeneration in order to effectively capture the wide breadth of phenotypic and molecular changes associated with the disease. While chemonucleolysis models have potential to be very useful in this respect, to date there has been no side-by-side comparisons of the commonly used enzymes to elucidate similarities and differences in their degenerative signatures across the NP and AF of an IVD.

To this end, in the current work we induced chemonucleolysis in bovine coccygeal IVDs with injection of three different enzymes, papain, chABC, and collagenase. It was hypothesized that each of the enzymes, having a unique substrate in the IVD ECM, would induce a distinct subset of degenerative characteristics in the tissues. Comprising this study, the enzymes were applied in a concentration projected to produce moderate levels of degeneration based on earlier observations (Chan et al., 2013; Gullbrand et al., 2017; Rustenburg et al., 2020). The resulting cellular, biochemical and histological properties of the IVDs were evaluated adjacent to the site of enzyme injection (the iAF) and in the oAF. From a broader perspective, we posited the varied spectrum of degenerative responses would provide multiple viable platforms mimicking known degenerative responses in IVD tissues and allowing for more thorough evaluation of pre-clinical therapeutics.

Materials and methods

Dissection of bovine IVD

Caudal IVDs from bovine tails were collected fresh from a local slaughterhouse (all male, age less than 24 months, and a minimum of five IVDs were isolated per tail). IVDs were isolated from the tails with endplates (EP) and a minimum amount of bone from their surrounding tissue as described previously (Lang et al., 2018). The IVDs were cleaned via a Pulsavac wound debridement irrigation system (Zimmer, Inc., Winterthur, Switzerland). After isolation, except for IVDs set aside as day 0 intact samples, the remainder of the samples were cultured in a 6-well-plate with 8 mL of complete IVD culture medium containing high glucose Dulbecco's modified Eagle's medium (HG DMEM) supplemented with 2.5% HEPES buffer (Gibco), 1% Penicillin/Streptomycin (Gibco), ascorbate 2 phosphate (50 ug/mL, Sigma Aldrich), 1% ITS+ (Corning), 2% fetal calf serum, 1% non-essential amino acid (Gibco) and 50 ug/mL primocin (Invitrogen). The IVD specimens were cultured at 37°C and 5% CO_2 for a total of 7 days. Cultured samples were transferred daily to a bioreactor for dynamic axial loading applied between 0.02 and 0.2 MPa at a frequency of 0.2 Hz for 2 h, a regime established in previous work to be optimal for maintenance of cell metabolic activity (Maclean et al., 2004; Gantenbein et al., 2006; Paul et al., 2012; Lang et al., 2018). Each experimental group consisted of $n = 4$ replicates isolated from two to four donors.

Enzyme treatment

Papain (from *Carica papaya*, Roche) was diluted to a concentration of 65 U/mL (Chan et al., 2013) in phosphate buffered saline (PBS) containing 0.8 mM cysteine HCl and 0.4 mM Ethylenediaminetetraacetic acid (EDTA). The chondroitinase ABC suspension (chABC, from *proteus* vulgaris, Sigma Aldrich) was delivered at a concentration of 5 U/mL in PBS containing 0.1% bovine serum albumin (BSA) (Gullbrand et al., 2017). Collagenase II (col'ase, Gibco) was prepared at a concentration of 0.5 U/mL (Rustenburg et al., 2020) in Hank's salt balanced solution. On day 1 immediately after the first application of loading, the isolated IVDs were randomly assigned to receive either PBS ($n = 4$) or enzyme injection ($n = 4$ per enzyme). Enzyme suspensions (100 µL) were manually injected into the center of each IVD using an insulin syringe (29G). All results were compared to the intact tissue samples from the respective tail (day 0) that were never cultured. The general study design is summarized in Figure 1.

Disc height measurement

Disc height was measured immediately after dissection (day 0) and daily for 7 days immediately prior to loading. Each disc was measured with calipers at two positions and the average value was used to calculate disc height change at day 7 normalized to the initial height after dissection.

Histological analysis

At day 7 of culture the IVDs were harvested and cut into two equal halves along the sagittal plane. One half was taken for histological and cell viability analyses, where the bony and cartilaginous end plates were removed prior to snap freezing in cryocompound. Sagittal sections (10 µm thick) were made with a cryotome (NX70 model; Thermo Fisher Scientific, Waltham, MA, United States). Representative sections from each group were stained with lactate dehydrogenase (LDH) and ethidium homodimer as previously described (Stoddart et al., 2006) to determine cell viability. For cell viability analyses, four random regions of interest (ROI) were analyzed in each the inner or outer annulus fibrosus (AF) regions across three representative sections per replicate and per group. Cells stained blue and blue/red were assigned to living cells, and cells that stained red were assigned to dead cells. The numbers of alive and dead cells were counted using ImageJ and expressed as a measure of cell viability per ROI. The cell viability in each region at day 7 was normalized to day 0 for the same donor.

Remaining histological sections were fixed in methanol and stained with 0.1% Safranin-O and 0.02% Fast Green and Weigert's Haematoxylin to highlight proteoglycan, collagen, and cell nuclei, respectively. All sections were imaged with light microscope (Zeiss, Oberkochen, Germany and Olympus, Tokio, Japan) under transmitted and/or fluorescent light.

A semi-quantitative scoring scheme (Table 1) adapted from Lee et al. (2021) was used to evaluate the Safranin O/Fast Green staining. NP and AF structure and matrix characteristics were summed up by two blinded observers to assess the degree of IVD degeneration observed for day 0 intact, PBS, and enzyme-injected groups ($n = 3$ sections per group).

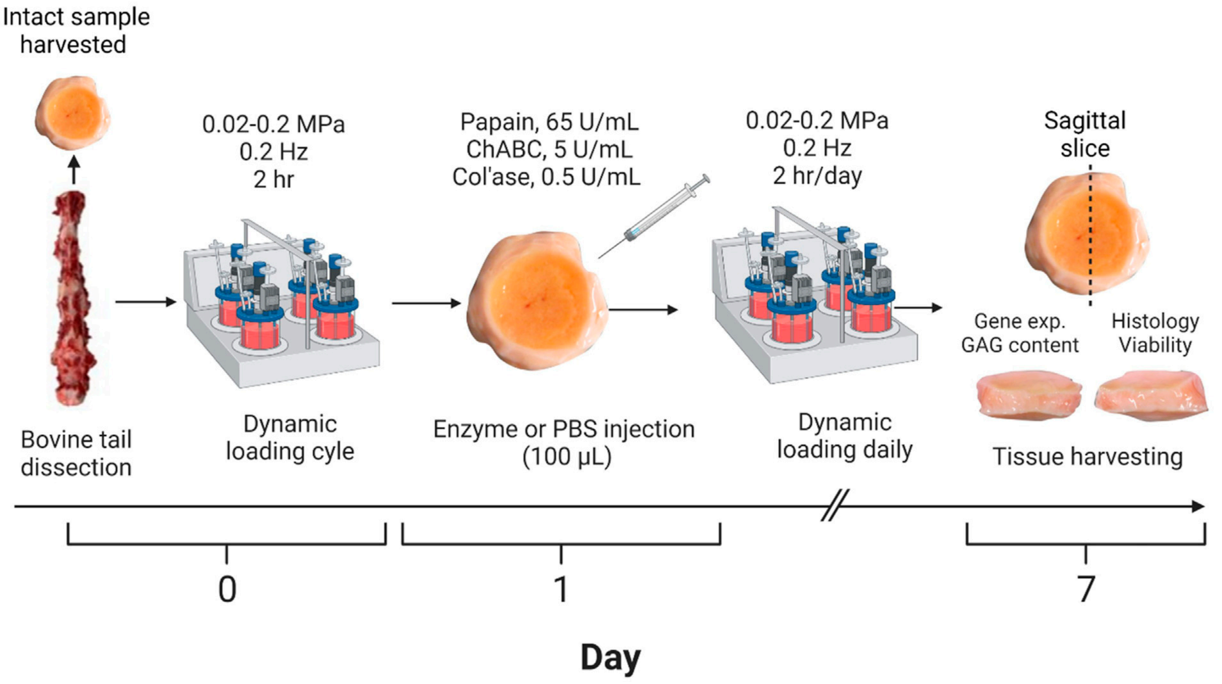

FIGURE 1
Workflow for developing the enzyme-induced model of IVD degeneration. Bovine coccygeal IVDs were isolated. An intact IVD from each tail was set aside as the day 0 control, and the remaining samples subjected to dynamic axial loading. The IVDs were subsequently injected with 100 µL of PBS (control), papain (65 U/mL), chABC (5 U/mL) or col'ase (0.5 U/mL) and cultured for 7 days with daily physiological loading applied. IVD height was measured daily prior to each loading cycle. At the end of the study period, the specimens were sliced along the sagittal plane and evaluated for gene expression, GAG content, histological staining, and cell viability analyses. A total of *n* = 4 replicates were used per enzyme/control group, isolated from two to four donors.

TABLE 1 Histological grading criteria, based on Lee et al. (2021).

Grade	Histological characteristics
NP matrix staining	
0	Proteoglycan staining dominates
1	Slight reduction in proteoglycan (fading)
2	Severe reduction in proteoglycan
3	Loss of proteoglycan staining
AF Morphology	
0	Well-organized, well-defined, uniform collagen lamellae form concentric half-ring arcs throughout entire AF
1	Mild disorganization/delamination of collagen fiber lamellae with some disruption or loss of concentric layers (<25%)
2	Moderately disorganization/delamination of collagen fiber lamellae with progressive disruption or loss of concentric layer (25%–75%)
3	Complete disorganization/delamination/collapse of AF; almost all concentric collagen lamellae are severely disrupted or lost (>75%)
Distinction between NP and AF	
0	Clear distinction between AF and NP tissue with intense purple proteoglycan ECM staining in NP
1	Distinction less clear: loss of annular-nuclear demarcation
2	Distinction poor: loss of annular-nuclear demarcation
3	No discernable annular-nuclear demarcation

TABLE 2 Oligonucleotide primers (900 nM final concentration), probes (250 nM final concentration) (bovine) and gene expression assays (Applied Biosystems) used for quantitative real-time PCR.

Gene	Primer/Probe type sequence or assay ID	
ACAN	Primer forward (5′-3′)	5′-CCA ACG AAA CCT ATG ACG TGT ACT-3′
	Primer reverse (5′-3′)	5′-GCA CTC GTT GGC TGC CTC-3′
	Probe (5′FAM/3′TAMRA)	5′-ATG TTG CAT AGA AGA CCT CGC CCT CCA T-3′
COL1 A2	Primer forward (5′-3′)	5′-TGC AGT AAC TTC GTG CCT AGC A-3′
	Primer reverse (5′-3′)	5′-CGC GTG GTC CTC TAT CTC CA-3′
	Probe (5′FAM/3′TAMRA)	5′-CAT GCC AAT CCT TAC AAG AGG CAA CTG C-3′
COL2 A1	Primer forward (5′-3′)	5′-AAG AAA CAC ATC TGG TTT GGA GAA A-3′
	Primer reverse (5′-3′)	5′-TGG GAG CCA GGT TGT CAT C-3′
	Probe (5′FAM/3′TAMRA)	5′-CAA CGG TGG CTT CCA CTT CAG CTA TGG-3′
IL-1β	Primer forward (5′-3′)	5′-TTA CTA CAG TGA CGA GAA TGA GCT GTT-3′
	Primer reverse (5′-3′)	5′-GGT CCA GGT GTT GGA TGC A-3′
	Probe (5′FAM/3′TAMRA)	5′-CTC TTC ATC TGT TTA GGG TCA TCA GCC TCA A-3′
RPLP0		Bt03218086_m1
ELN		Bt03216594_m1
IL-8		Bt03211906_m1
MCAM		Bt03258894_m1
MKX		Bt04292311_m1
MMP3		Bt04259490_m1
TAGLN		Bt03234600_m1
ADAMTS5		Bt04230789_m1

GAG content

The second half of the harvested IVDs was designated for quantitative analyses. Because the NP was digested by enzymes in many samples, the region closest to the enzyme-induced void was taken for analyses and designated as inner annulus fibrosus (iAF). In addition, tissue was sampled from the periphery of the IVDs, designated as outer annulus fibrosus (oAF). For GAG analysis, tissue samples from each IVD region (30–50 mg) were lyophilized and digested in 2 mL of 0.5 mg/mL proteinase K solution (Roche, Mannheim, Germany) per 10 mg of dry tissue until complete breakdown. Sulfated GAG content was measured by using 1,9-Dimethyl-methylene blue (Aldrich). Absorbance was read at 535 mm with a Victor3 Micro Plate Reader. GAG concentrations were calculated from a standard curve obtained with chondroitin 4-sulfate sodium salt from bovine trachea (Fluka Bio Chemika). GAG contents were normalized to initial wet tissue mass and to the GAG content of the day 0 tissue sample from the same donor.

Gene expression

Tissue samples (100–200 mg) were cut from the iAF and oAF of the specimens. The oAF was defined in this study as the outermost fibrous ring of tissue on the specimens. Tissues were digested in 2 mg/mL pronase (Roche), snap frozen in liquid nitrogen and pulverized into powder pellets using a hammering device (Caprez et al., 2018). Pulverized samples were homogenized in 1.5 mL TRI reagent containing 7.5 μL polyacryl carrier (Molecular Research Centre Inc., Cincinnati, OH, United States) using a tissue-lyser (Retsch GmbH & Co., Haan, Germany). RNA was extracted with RNeasy columns (Qiagen) according to the manufacturer’s protocol. Reverse transcription was performed using SuperScript® VILO™ cDNA Synthesis Kit (Invitrogen) with 400 ng total RNA according to the manufacturer’s protocol. QPCR was performed using TAQMAN™ Universal MasterMix (Applied Biosysems). The forward primer, reverse primer, probe (or Gene Expression Assay mixture, Applied Biosystems), and cDNA were combined to make a reaction volume of 10 μL. Gene expression for the following bovine transcripts were analyzed: RPLP0 (Ribosomal Protein Lateral Stalk Subunit P0, endogenous reference gene), TAGLN (transgelin), ELN (elastin), MKX (mohawk homeobox), MCAM (Melanoma Cell Adhesion Molecule), COL1 (collagen1α2), COL2 (collagen2α1), MMP3 (matrix metalloproteinase-3), ADAMTS5 (ADAM Metallopeptidase With Thrombospondin Type 1 Motif 5), ACAN (aggrecan), IL-1β (Interleukin-1beta), and IL-8 (CXCL8 Gene—C-X-C Motif Chemokine Ligand 8). All primer sequences or IDs of Gene Expression Assays are listed in Table 2. The qPCR was performed using QuantStudio 7 Flex (Applied Biosystems,

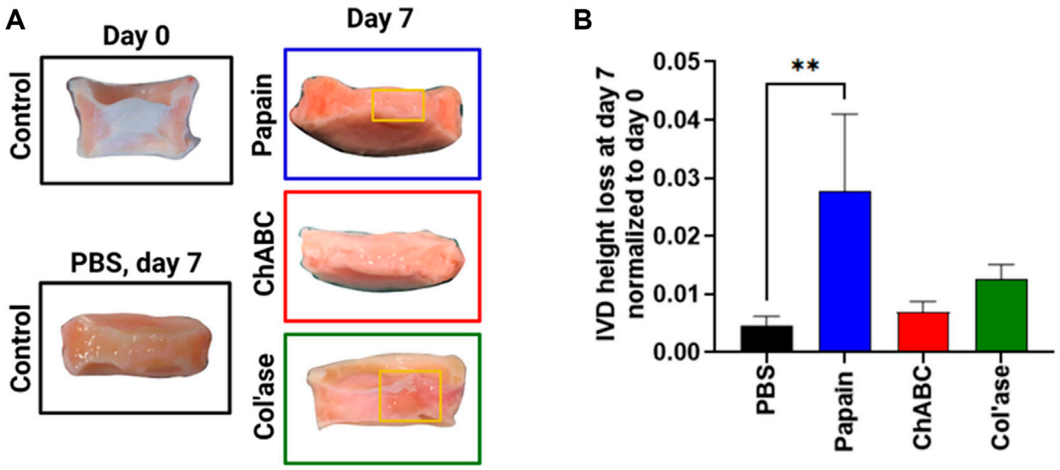

FIGURE 2
(A) Gross morphology of the IVD study groups. At day 7 post-enzyme treatment, macroscopic voids were observed in the papain and col'ase-injected specimens, indicated by the yellow boxes, but not in chABC-injected specimens. **(B)** Height loss during 7 days of IVD culture with daily loading in the bioreactor, calculated relative to the initial IVD height after dissection. Papain produced the highest magnitude height loss in the IVD specimens compared to the PBS control. Data are shown as the mean and standard deviation of $n = 4$ replicates, where ** indicates $p = 0.0065$.

Thermo Fisher Scientific) for 40 cycles with the following protocol: heating of 1.9°C per second until 95°C followed by 15 s at 95°C and cooling of 1.6°C/s to 60°C and continuing for 60 s at 60°C. The relative expression of analyzed genes was identified using $2^{-\Delta\Delta Ct}$ method with RPLP0 and day 0 expression from the same tissue donor used for normalization.

Statistics

GraphPad Prism 9 (version 9.3.1, GraphPad Software, LLC, San Diego, United States) was used for statistical analysis of the data. Data were not normally distributed as defined by Shapiro-wilk normality test. Kruskal Wallis with Dunn's post-hoc test was used to determine differences among experimental groups. Values of $p < 0.05$ (*), $p < 0.01$ (**), $p < 0.001$ (***), and $p < 0.0001$ (****) were considered statistically significant.

Results

Macroscopic IVD changes with chemonucleolysis

Differences between the enzyme treatments were evident in the gross morphology of the IVD specimens shown in Figure 2A. Papain and col'ase produced macroscopic tissue voids at the center of the IVDs in the region local to enzyme injection (yellow boxes), but no macroscopic voids were observed in the chABC samples.

The IVD height change at day 7 of culture period was calculated and normalized to initial height after dissection (day 0) (Figure 2B). Papain digestion induced the greatest height loss compared to day 0 (nearly 3%), whereas chABC and col'ase induced approximately 0.6% and 1.2% height loss. All three enzyme treatments induced greater height loss than the PBS control, with difference between papain and PBS ($p = 0.0065$) being statistically significant.

GAG content changes with chemonucleolysis

The GAG content of the tissues relative to day 0 is shown in Figure 3. In the iAF, the PBS control samples retained approximately 100% of the GAG content compared to day 0. In contrast, papain digested tissue was measured to retain less than 10% of the GAG content relative to day 0. ChABC and col'ase each exhibited approximately 35% retention of GAG content relative to day 0. The change in iAF GAG content measured over the culture period compared to the PBS-injected control was only significant for papain ($p = 0.0143$, Figure 3A). In the oAF (Figure 3B), papain and chABC digestion tended to decrease GAG content of the tissues, although the shifts were not statistically significant compared to the PBS control ($p > 0.05$). The col'ase group tended to increase GAG content, but the differences among the groups and in comparison to the PBS control were not statistically significant ($p > 0.05$).

Cell viability after chemonucleolysis

In the iAF, adjacent to tissue void, papain digestion produced no changes in cell viability relative to day 0 (Figure 3C). For all papain samples, cell viability remained at nearly 100% at day 7 of culture. Compared to papain, chABC and Col'ase treatment produced decreasing trends in cell viability in the iAF to approximately 60%–70% at day 7 culture, though the shifts were not statistically significant compared to PBS ($p > 0.05$). Cell viability in the oAF was maintained at nearly 100% for the duration of the culture period for

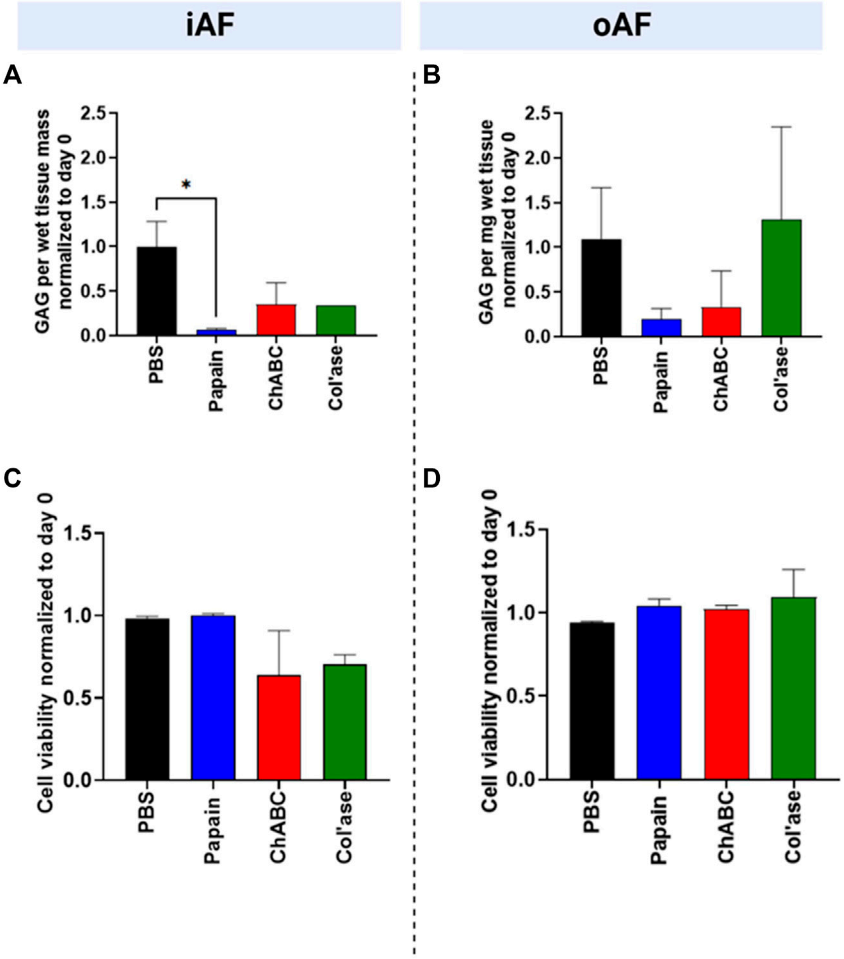

FIGURE 3
Biochemical and cellular changes in the IVDs at day 7 after enzyme treatment. GAG content/wet tissue mass of **(A)** iAF and **(B)** oAF tissue samples at day 7 normalized to day 0 of the respective donor. Papain produced the largest drop in GAG content of the iAF and oAF compared to the PBS control, the drop being statistically significant for the iAF ($p = 0.0143$.) **(C)** Cell viability (%) at day 7 normalized to day 0 of the respective donor for the iAF and **(D)** oAF of the IVDs quantified from LDH staining images. No significant changes in cell viability were measured compared to the PBS control in the iAF or oAF, although cell viability in the iAF for the papain-treated samples trended highest (close to 100%) compared to the chABC and col'ase (60%–70%). Results are shown as the mean and standard deviation of four replicates, except for **(A)** col'ase, where one replicate could only be recovered due to digestion.

all sample groups, with no statistical differences detected between PBS-injected and any of the enzyme-injected groups ($p > 0.05$, Figure 3D).

Histological changes with chemonucleolysis

Shown in Figure 4 are representative overview histological images of safranin-O and fast green staining to highlight the distributions of GAG and collagens, respectively. PBS-injected controls exhibited preservation of GAG staining in the NP region at day 7 of culture (Figure 4B) compared to day 0 (Figure 4A). Papain digestion resulted in complete obliteration of the GAG staining across the sagittal cross-sectional area of the IVDs (Figure 4C), but left behind collagenous tissues, evidenced by fast green staining. Papain also induced the formation of millimeter-scale voids containing small tissue fragments (Figure 4C, yellow box). Conversely, no voids of similar scale were observed after chABC treatment (Figure 4D). Col'ase produced voids similar in size to papain (Figures 4E, F, yellow box). One of the specimens in the collagenase group exhibited a region of highly concentrated GAG staining in the oAF (Figure 4E, red arrow).

A modified histological scoring standard was used based on literature (Lee et al., 2021) to assess degeneration from the histological overviews. The scoring standard allowed for an assessment of proteoglycan staining in the NP (Figure 4G), morphological organization of the AF (Figure 4H), and the structural distinction between the NP and AF (Figure 4I) at day 7 for the PBS and enzyme-treated groups compared to day 0 intact. Across all grading criteria, no significant differences in degeneration scores between PBS and day 0 intact were measured ($p > 0.05$). Additionally, chABC treatment induced no significant changes in degeneration score at day 7 ($p > 0.05$). In contrast, papain and col'ase enzyme-treated samples exhibited similar grades of degeneration ($p > 0.05$). Also, papain and col'ase

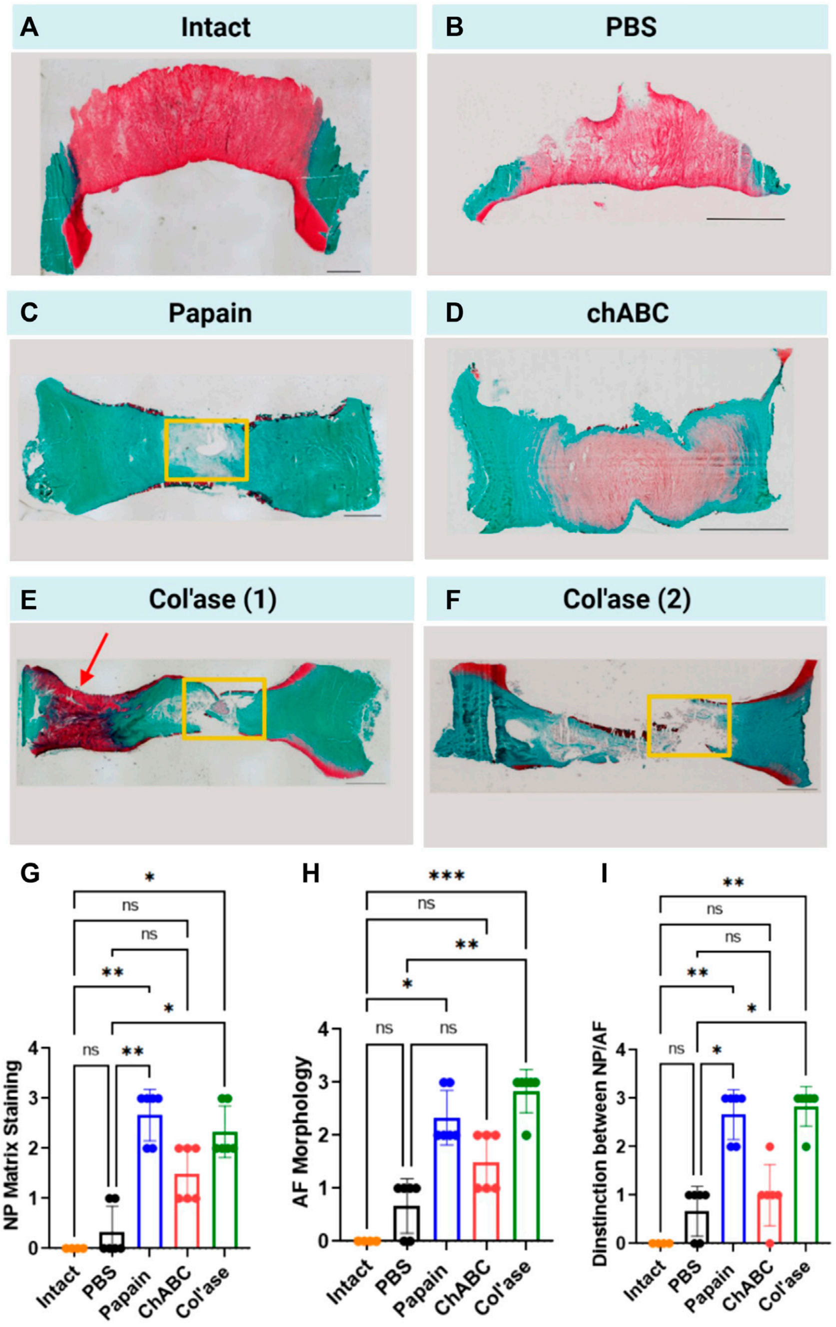

FIGURE 4
Safranin-O and fast green staining across whole sagittal cross-sectional areas of the IVD sample groups highlighting the morphology of GAG (red) and collagens (green) in the matrix for **(A)** Day 0 intact control, and at day 7 for **(B)** PBS control, **(C)** papain, **(D)** chABC, **(E)** col'ase, specimen 1, and **(F)** col'ase, specimen 2. While voids and significant GAG loss could be identified at day 7 in papain and col'ase treated specimens, chABC produced the mildest changes, with no void produced and some GAG staining remaining. Two representative specimens are shown for the col'ase group to demonstrate a region of concentrated GAG staining observed in the oAF of one of the samples (red arrow). Yellow boxes highlight macroscopic voids produced by enzyme digestion. Scale bars = 2 mm. **(G,H,I)** Histological scoring values based on criteria detailed in Table 1 for Safranin O/Fast green staining of whole sagittal cross-sections. Overall, papain and col'ase produced higher degeneration scores than chABC, PBS and day 0 intact controls. Grading was assessed by two blinded observers on three sections per group, where $^{*}p < 0.05$, $^{**}p < 0.01$, and $^{***}p < 0.001$.

treatment produced statistically significant increases in degeneration grade compared to the PBS-inject controls at day 7 and day 0 intact samples ($p < 0.05$).

High magnification images of the NP, iAF and oAF regions of each of these specimens are shown in Figure 5.

Phenotypic characterization after chemonucleolysis

Gene expression for the major disc ECM markers, COL1, COL2 and ACAN, in the iAF and oAF of the treatment groups

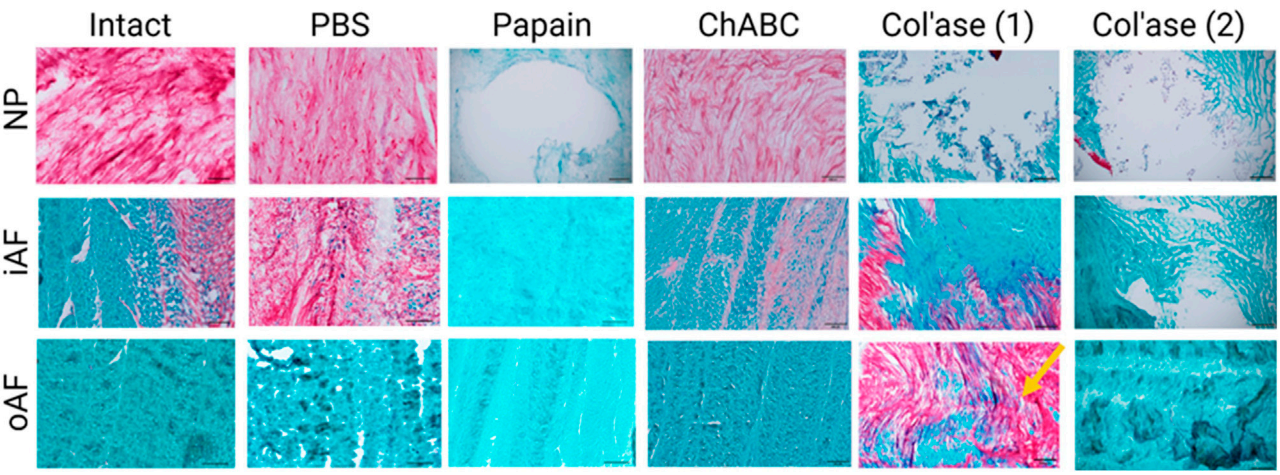

FIGURE 5
High magnification images of Safranin-O and fast green staining highlighting the morphology of GAG (red) and collagens (green) in the nucleus pulposus (NP), inner annulus fibrosus (iAF) and outer annulus fibrosus (oAF) of the intact (day 0), PBS-treated (day 7), and enzyme-treated (day 7) groups. Overall, papain and col'ase digestion resulted in complete loss of GAG staining in the NP region. GAG staining could still be identified in the NP and iAF of chABC treated specimens. Two representative specimens are shown for the col'ase group to demonstrate a region of concentrated GAG staining observed in the oAF of one of the samples (yellow arrow). Scale bars = 200 μm.

is shown in Figure 6. ChABC digestion resulted in increased trends in gene expression for both COL1 and COL2 in the iAF of loaded specimens compared to PBS controls, though the differences were not statistically significant ($p > 0.05$). An upregulation in COL2 gene expression was measured for the chABC group that was significantly higher than that of the papain group ($p = 0.0286$). ACAN expression tended to be downregulated with all enzyme treatments compared to PBS ($p > 0.05$). In the oAF, col'ase digestion produced increasing trends in gene expression for COL1, COL2 and ACAN ($p > 0.05$). ChABC injection tended to increase COL2 and aggrecan expression ($p > 0.05$).

Gene expression for catabolic enzymes MMP3 and ADAMTS5 are shown in Figure 7. In the iAF, col'ase treatment produced a small increase in gene expression for MMP3 relative to PBS control ($p > 0.05$). Papain and chABC produced small increasing trends in ADAMTS5 expression compared to the PBS control ($p > 0.05$). In the oAF, general trends of decreasing MMP3 expression were observed, though the shifts were not significant ($p > 0.05$). ADAMTS5 expression was largely unchanged in oAF with enzyme or PBS injection ($p > 0.05$)

Expression of oAF-specific markers (MCAM, ELN, TAGLN and MKX) are shown in Figure 8. In the iAF, col'ase treatment tended to downregulate expression of oAF markers, TAGLN, ELN, MCAM and MKX, compared to the PBS control ($p > 0.05$). Relative gene expression for TAGLN was significantly higher in the chABC group compared to col'ase ($p = 0.0360$). Papain and chABC tended to upregulate TAGLN and MKX relative to the PBS control ($p > 0.05$). In the oAF, no significant shifts in gene expression for MCAM, ELN, TAGLN or MKX were measured relative the PBS controls ($p > 0.05$). However, the expression of ELN, TAGLN and MKX tended to increase with col'ase injection relative to the PBS control.

Expression of pro-inflammatory markers (IL-1β and IL-8) is shown in Figure 9. In the iAF, there were no significant shifts in IL-1β expression compared to the PBS control ($p > 0.05$). Relative gene expression for IL-8 tended towards upregulation with papain, yet the change was not statistically significant compared to the PBS control ($p > 0.05$). In the oAF, no significant shifts in gene expression for IL-1β or IL-8 were measured relative to PBS controls ($p > 0.05$). However, compared to PBS controls, chABC tended to increase the expression of IL-1β, and both papain and chABC tended to decrease the expression of IL-8 ($p > 0.05$).

Discussion

The aim of this study was to develop and compare three different *ex vivo* bovine organ culture models of chemonucleolysis-induced IVD degeneration. *Ex vivo* models, which bridge *in vitro* and *in vivo* studies, are essential tools for evaluating therapeutic interventions for IVD degeneration by providing a cost-effective route for recapitulating the multifactorial 3D microenvironment of the IVD. With increasing relevance of bioreactor-loaded whole organ cultures (Pfannkuche et al., 2020), the field of IVD repair needs more *ex vivo* models, providing researchers with a robust set of pre-clinical evaluation tools to utilize for thorough examination of therapeutic efficacy. To this end, we aimed to deepen the understanding of IVD chemonucleolysis by targeting moderate levels of degeneration with three different enzymes, papain, chABC and col'ase and comparing the effects side-by-side. It was hypothesized that the distinct mechanisms of ECM digestion from each of the enzymes would produce differing degenerative effects on the explanted tissues, helping to capture more aspects of human pathogenesis.

Notably, in prior *ex vivo* studies with papain and trypsin, enzymatic digestion alone was not sufficient to induce dimensional changes in the IVDs (Chan et al., 2013). In this study, application of enzymes combined with daily dynamic loading resulted in IVD height loss compared to the PBS treated samples. Height loss was most pronounced for the papain-treated samples. IVD height loss can be

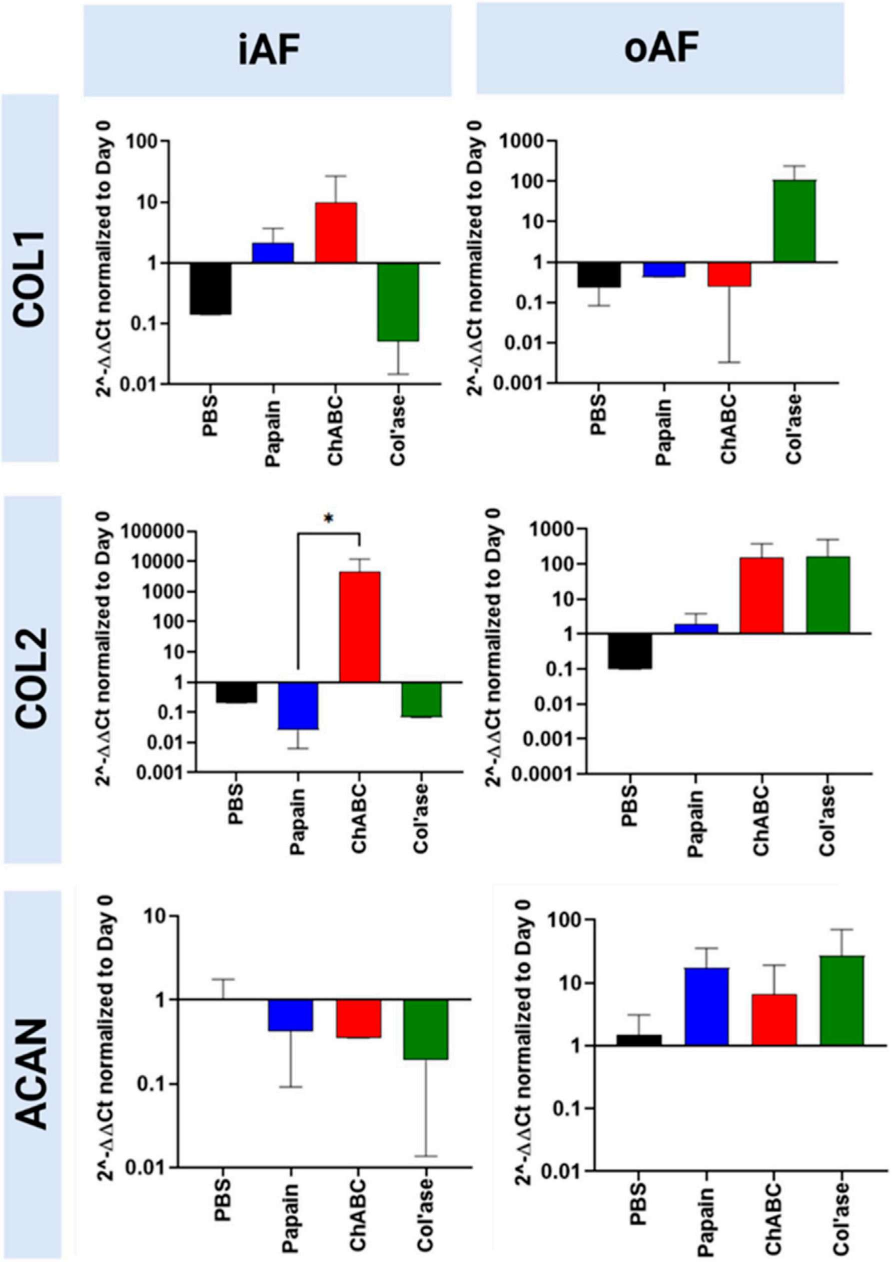

FIGURE 6
Bovine mRNA expression at day 7 for the major IVD ECM components, COL1, COL2 and ACAN, relative to day 0 and RPLP0 for the PBS-injected and enzyme-treated sample groups. In the iAF, papain and col'ase resulted in mild downregulation in the major disc NP matrix markers, ACAN and COL2. ChABC treatment resulted in a statistically significant upregulation of a major ECM marker, COL2, within the iAF compared to papain (*p = 0.0286), suggesting chABC could be inducing the mildest degenerative response. Results are shown as the mean and standard deviation of four replicates.

regarded as the result of decreased mechanical integrity of the ECM (Balkovec et al., 2013; Yoganandan et al., 2017). Aggrecan molecules are known to confer mechanical properties, like compressibility and elasticity, to the ECM through stabilizing intermolecular interactions (Pratta et al., 2003). In the decreased presence of proteoglycan, which was most extensive after papain treatment, extrinsic loading allowed mechanical fatigue of the remaining tissues, resulting in dimensional changes such as height loss.

The differences in substrate specificity among the three enzymes used in the study made it impractical to target a single concentration for their application as chemonucleolytic agents. Rather, each enzyme was applied in a concentration shown to induce moderate degeneration in prior *in vivo* and *ex vivo* IVD studies (Chan et al., 2013; Gullbrand et al., 2017; Rustenburg et al., 2020). All enzymes induced an overall loss of GAG in the iAF region, with papain having the most pronounced effect and producing voids around the site of injection. With its known proteolytic activity towards polypeptides (Mamboya, 2012), papain does not directly degrade GAG side chains. However, GAG loss is associated with the enzyme in this and prior studies (Roberts et al., 2008; Chan et al., 2013), suggesting papain

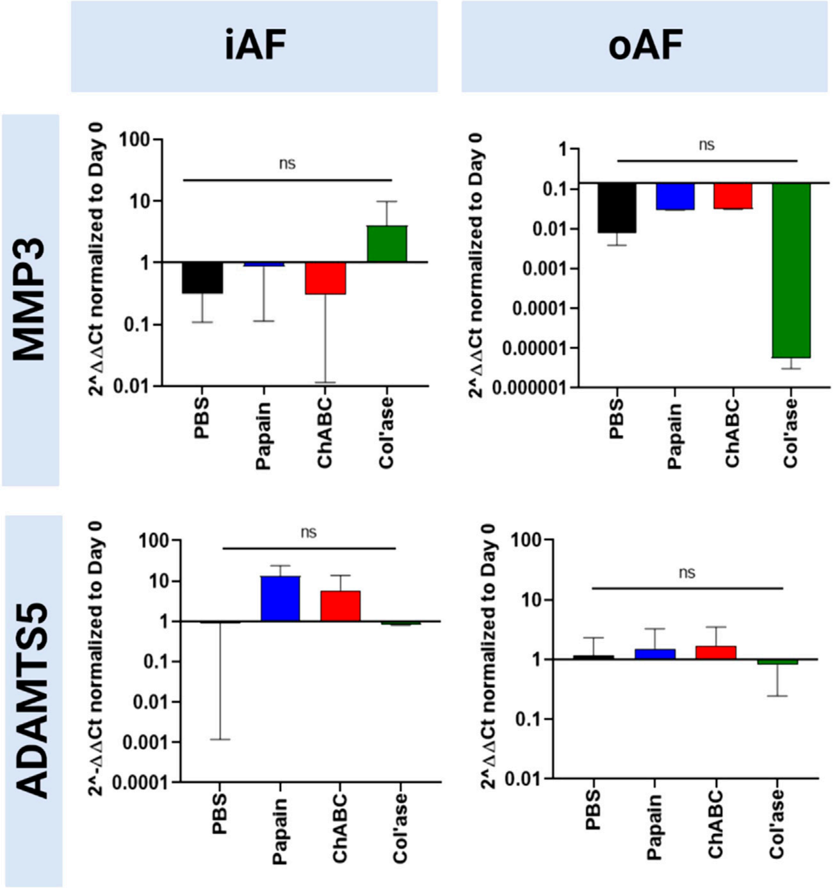

FIGURE 7
Bovine mRNA expression at day 7 for catabolic enzymes, ADAMTS5 and MMP3, relative to day 0 and RPLP0 for the PBS-injected and enzyme-treated sample groups. The highest magnitude shift was observed for MMP3 in the oAF, although no statistically significant shifts were detected ($p > 0.05$). Results are shown as the mean and standard deviation of four replicates.

activity for cleaving the link protein or core protein on aggrecan. Conversely, chABC cleaves chondroitin 4-sulfate, dermatan sulfate, and chondroitin 6-sulfate side chains on aggrecan molecules (Takagaki and Kakizaki, 2007). In our study, this enzyme produced milder losses of GAG in the NP and iAF compared to papain and no major voids. The col'ase class II enzyme, with broad specificity to multiple types of native collagen fibrils (Van Wart and Steinbrink, 1985), produced tissue voids similar in size to papain. The formation of a void, which implies loss of both GAG and collagen induced by col'ase, can be explained by the fact that aggrecan molecules interact with the collagen network (Adams et al., 1977; Zhou et al., 2021). Thus, release of GAG from the tissues may occur concomitantly with collagen. Generally, matrix degradation and void formation are important considerations for evaluating NP replacement or repair materials. Biomaterial implantation may require ECM removal to relieve intradiscal pressures and provide physical space for accommodation (Roberts et al., 2008). Also, void-producing chemonucleolytic models provide proximity to the current clinical practice of discectomy. Within this context, the papain and col'ase models provide more functionality than chABC. Conversely, the chABC model may represent structural similarity with early stages of degeneration.

A goal of this study was to compare gene expression changes after chemonucleolysis to understand the extent to which the models mimic the phenotypical changes in natural human IVD degeneration. Generally, none of the enzymes used in our study induced gene expression changes exactly following reported degenerative patterns for iAF tissue, which generally involves concomitant upregulation of type I collagen (Le Maitre et al., 2007a; Markova et al., 2013), downregulation of collagen II and proteoglycan (Le Maitre et al., 2007a; Lian et al., 2017; Silagi et al., 2018), and upregulation of matrix degrading enzymes like MMP3 (Roberts et al., 2000; Le Maitre et al., 2004) and ADAMTS5 (Gruber et al., 2007; Pockert et al., 2009). Interestingly, chABC significantly upregulated COL2 expression in the iAF, which could be indicative of a compensatory behavior by the IVD cells, making it a potential model for early-stage degeneration (Cs-Szabo et al., 2002; Uei et al., 2006; Markova et al., 2013; Malonzo et al., 2015). Whereas, papain and col'ase provided no such upregulation, and thus in this respect, more closely following advanced degeneration. Interestingly, enzyme digestion did not induce a profound proinflammatory effect, as indicated by no significant shifts measured in IL-1β or IL-8 gene expression, an outcome also reported in a previous organ culture model of degeneration induced by one strike loading (Zhou et al., 2021).

Throughout the 7-day culture period, no major cracks or fissures were formed in the oAF with chemonucleolysis. It is possible that more prolonged culture conditions, especially in combination with loading, would lead to formation of severe structural abnormalities in the oAF region. Worth noting is the effect of enzyme digestion on GAG content in the oAF. Tissue histology detected an area of concentrated GAG staining for one of the col'ase -digested specimens. Possibly, this was a rescue effect by oAF cells, which in prior reports have been shown to retain capacity for repair during IVD degeneration resulting in an upregulation of proteoglycan (Cs-Szabo et al., 2002). Further indicative of a "rescue" capacity of the host IVD cells in the oAF, anabolic trends in mRNA expression were detected for COL2, ACAN and COL1 with col'ase injection.

Taking a further look at cell scale responses, viability remained largely unaffected in the oAF after enzyme treatment. In the iAF, on the other hand, cell viability depended on enzyme treatment, with the papain-digested specimens retaining higher cell viability than chABC and col'ase-injected groups. A recent study used attenuated total reflectance Fourier-transform infrared spectroscopy to demonstrate the structural soundness of collagen networks following papain digestion (Silva et al., 2016). Differences in nanoscale tissue organization and conformational properties of adhesion domains on collagens and aggrecan post-chemonucleolysis is a possible factor that could account for the higher cell viability observed with papain versus the other enzymes, and is an area requiring further study. Human IVD degeneration and acute tissue injury have been reported to be associated with decreases in cell viability and metabolic activity (Iatridis et al., 2009; Alkhatib et al., 2014). It stands to reason that the papain model, which leaves cell viability unaffected, may yield regenerative responses more predictive of clinical outcomes more representative for trauma or nucleotomy cases. IVD degeneration has also been marked by increased clustering and proliferation (Johnson et al., 2001), effects which were not observed by histology. Thus, the enzyme models presented in this study may replicate some, but not all, instances of abnormal cellular activity occurring during degeneration.

This study aimed to enhance our understanding of chemonucleolytic *ex vivo* models of IVD degeneration. Our results demonstrate that all three enzymes induced distinct changes in the major categories associated with clinical disc degeneration, including histology, IVD height loss, cell viability, and gene expression. Analyzing the outcomes of each enzyme, as summarized in Table 3, we can generally conclude that chABC most closely resembles the early stages of degeneration compared to the other enzymes. Yet, it is important to note that a single chemonucleolysis model is unlikely to replicate all the complex pathological features present in *in vivo* lumbar IVD degeneration. This work significantly contributes to the understanding of *ex vivo* bovine models of chemonucleolysis by comparing outcomes of three enzymes side by side, and we posit that all three models have potential to serve as viable models for evaluating the efficacy of therapeutic approaches under development. Furthermore, we propose that studying therapeutic outcomes with all three models can aid in providing a comprehensive evaluation of regenerative outcomes.

However, limitations of this study are to be noted. Morphology of tissue voids may be produced more uniform with an automated, rather than manual, enzyme injection process, making the

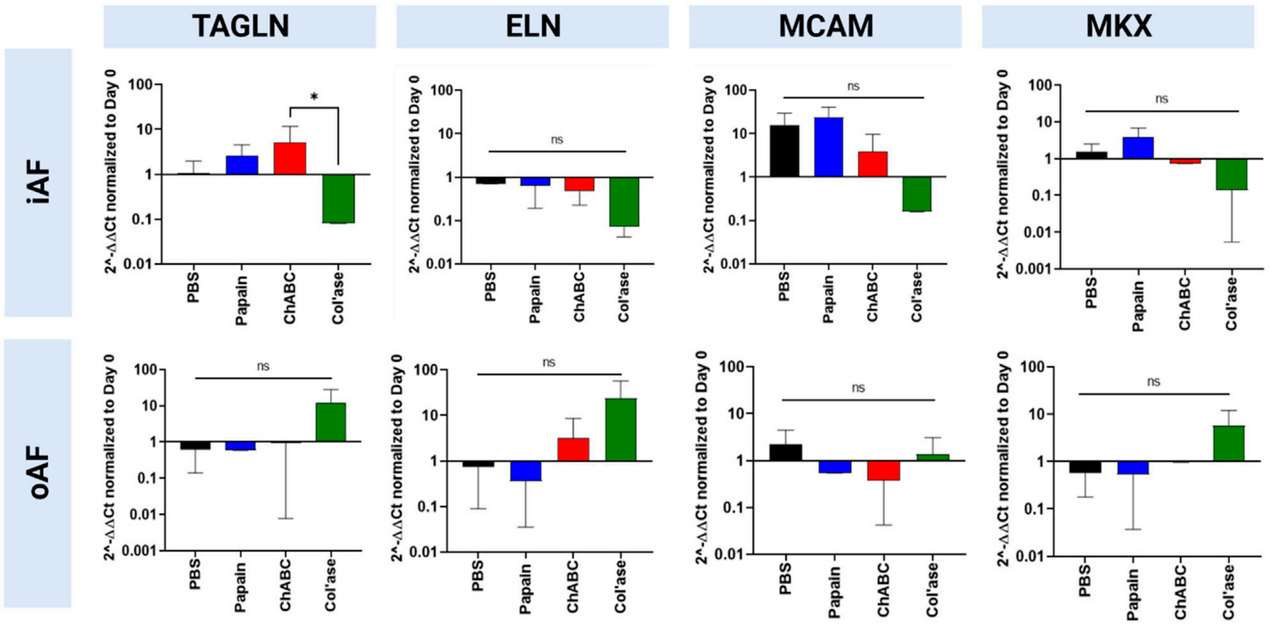

FIGURE 8
Bovine mRNA expression at day 7 for oAF markers, TAGLN, ELN, MCAM, and MKX, relative to day 0 and RPLP0 for the PBS-injected and enzyme-treated sample groups. Notably, in the iAF, col'ase treatment tended to downregulate expression of all oAF markers compared to the PBS control, although the shifts were not statistically significant ($p > 0.05$). In the oAF, col'ase treatment tended to upregulate oAF markers compared to PBS ($p > 0.05$). Results are shown as the mean and standard deviation of four replicates with $*p = 0.0360$.

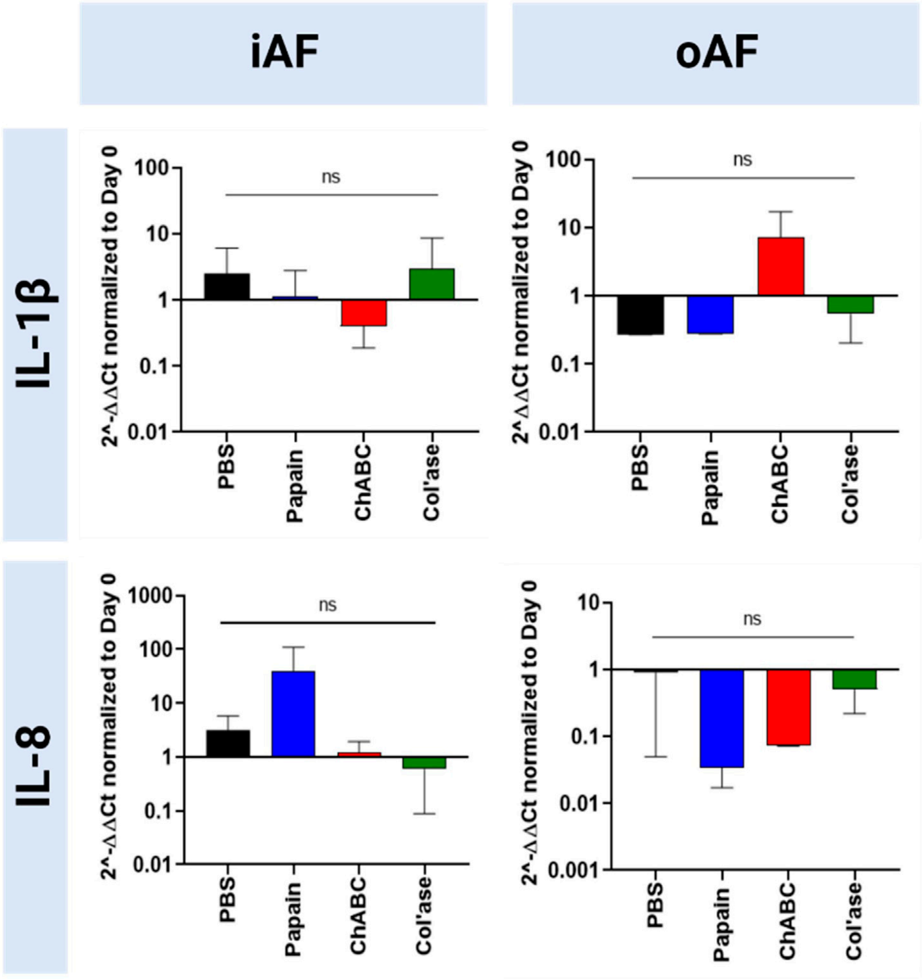

FIGURE 9
Bovine mRNA expression at day 7 for proinflammatory markers relative to day 0 and RPLP0 for the PBS-injected and enzyme-treated sample groups. Papain treatment produced the highest upregulation in the expression of a proinflammatory marker, 1L-1β, although the none of the shifts were statistically significant relative to each other or the PBS control ($p > 0.05$). Results are shown as the mean and standard deviation of four replicates.

TABLE 3 Summary of the major changes observed in bovine caudal intervertebral discs induced by chemonucleolysis combined with daily dynamic loading.

Enzyme	Dose (U/mL)	Void?	Height loss (%)	Histology	Cell viability	Gene expression adjacent to injection site
Papain	65	Yes	Highest (2.77% ± 1.3%)	Complete loss of GAG staining in NP, high degeneration scores	100% ± 1.1% in iAF, 100% ± 3.7% in oAF	Mild downregulation in matrix markers (COL2, ACAN), mild upregulation ADAMTS5 and IL-1β
chABC	5	No	Lowest (0.69% ± .2%)	Some GAG staining remaining in NP, lower degeneration scores	64% ± 27.0% in iAF, 100% ± 2.1% oAF	Moderate upregulation in COL2, mild upregulation in COL1 and ADAMTS5
Col'ase	0.5	Yes	Intermediate (1.25% ± .2%)	Complete loss of GAG staining in NP; concentrated region observed in oAF for one sample, high degeneration scores	70.3% ± 5.9% in iAF, 100% ± 16.4% in oAF	Mild downregulation in matrix markers (COL1, COL2, ACAN) and mild upregulation MMP3

degenerative changes potentially more reproducible. Gene expression of neurotropic factors, such as brain derived neurotropic factor (BDNF), and angiogenic factors, such as VEGF, are important to evaluate the models' predictive capacity for pain response *in vivo* and should be evaluated in future studies. Finally, spatiotemporal transcriptomic and proteomic profiling should be applied in the tissue models, towards developing a more comprehensive understanding of tissue response to enzymatic degradation and the extent to which it mimics human degeneration.

Conclusion

We did a side-by-side comparison of the effects of chemonucleolysis on bovine coccygeal IVDs by three different enzymes, papain, chABC, and col'ase after 7 days of loaded culture. Generally, all three enzymes were useful for recapitulating certain clinically and biologically relevant aspects of human IVD degeneration. Papain produced macroscopic tissue voids and the most aggressive GAG and height loss, although cell viability in the remaining tissues was largely preserved. In contrast to this, ChABC and col'ase digestion caused greater losses in cell viability. Compared to papain, col'ase produced similar size tissue voids. Because chABC did not produce macroscopic tissue voids, but the mildest height loss and an anabolic shift in iAF COL2 expression, it is concluded that chABC recapitulates early-stage degeneration more so than papain and col'ase. This work significantly contributes to the understanding of *ex vivo* bovine models of chemonucleolysis by comparing outcomes of three enzymes side by side. Overall, the results of our study show that chemonucleolysis is a useful tool providing researchers with a robust spectrum of degenerative changes in IVD tissues and the models have potential as tools for assessment of therapeutic interventions.

Data availability statement

The original contributions presented in the study are included in the article/Supplementary Material, further inquiries can be directed to the corresponding author.

Author contributions

AV, HB, NK, AŠe, ASo, and JG carried out the studies. AV and HB conducted the data analysis and drafted the manuscript. AV conceived of the study. JJ, CN-W, H-JW, and SG participated in the study design and helped draft the manuscript. All authors contributed to the article and approved the submitted version.

Funding

The work described is part of the iPSpine project, which has received funding from the European Union's Horizon 2020 Research and Innovation Programme (Grant No. 825925). Open access funding by ETH Zurich.

Acknowledgments

The authors would like to acknowledge Dr. Christoph Sprecher for assistance with imaging and Nadja Vonlanthen for assistance with RT-PCR.

Conflict of interest

The authors declare that the research was conducted in the absence of any commercial or financial relationships that could be construed as a potential conflict of interest.

Publisher's note

References

Adams, P., Eyre, D. R., and Muir, H. (1977). Biochemical aspects of development and ageing of human lumbar intervertebral discs. *Rheumatol. Rehabil.* 16 (1), 22–29. doi:10.1093/rheumatology/16.1.22

Ahn, S. H., Cho, Y. W., Ahn, M. W., Jang, S. H., Sohn, Y. K., and Kim, H. S. (2002). mRNA expression of cytokines and chemokines in herniated lumbar intervertebral discs. *Spine (Phila Pa 1976)* 27 (9), 911–917. doi:10.1097/00007632-200205010-00005

Alini, M., Eisenstein, S. M., Ito, K., Little, C., Kettler, A. A., Masuda, K., et al. (2008). Are animal models useful for studying human disc disorders/degeneration? *Eur. Spine J.* 17 (1), 2–19. doi:10.1007/s00586-007-0414-y

Alkhatib, B., Rosenzweig, D., Krock, E., Roughley, P., Beckman, L., Steffen, T., et al. (2014). Acute mechanical injury of the human intervertebral disc: link to degeneration and pain. *Eur. Cell Mater* 28, 98–111. discussion 110-1. doi:10.22203/ecm.v028a08

Balkovec, C., Vernengo, J., and McGill, S. M. (2013). The use of a novel injectable hydrogel nucleus pulposus replacement in restoring the mechanical properties of cyclically fatigued porcine intervertebral discs. *J. biomechanical Eng.* 135 (6), 061004–061005. doi:10.1115/1.4024285

Barcellona, M. N., McDonnell, E. E., Samuel, S., and Buckley, C. T. (2022). Rat tail models for the assessment of injectable nucleus pulposus regeneration strategies. *JOR Spine* 5, e1216. doi:10.1002/jsp2.1216

Barcellona, M. N., Speer, J. E., Jing, L., Patil, D. S., Gupta, M. C., Buchowski, J. M., et al. (2021). Bioactive *in situ* crosslinkable polymer-peptide hydrogel for cell delivery to the intervertebral disc in a rat model. *Acta biomater.* 131, 117–127. doi:10.1016/j.actbio.2021.06.045

Bogduk, N. (2016). "Functional anatomy of the spine," in *Handbook of clinical neurology*, 675–688.

Bonnaire, F. C., Danalache, M., Sigwart, V. A., Breuer, W., Rolauffs, B., and Hofmann, U. K. (2021). The intervertebral disc from embryonic development to disc degeneration: insights into spatial cellular organization. *Spine J.* 21 (8), 1387–1398. doi:10.1016/j.spinee.2021.04.015

Boos, N., Weissbach, S., Rohrbach, H., Weiler, C., Spratt, K. F., and Nerlich, A. G. (2002). Classification of age-related changes in lumbar intervertebral discs: 2002 volvo award in basic science. *Spine* 27 (23), 2631–2644. doi:10.1097/00007632-200212010-00002

Brinjikji, W., Diehn, F., Jarvik, J., Carr, C., Kallmes, D., Murad, M., et al. (2015). MRI findings of disc degeneration are more prevalent in adults with low back pain than in asymptomatic controls: a systematic review and meta-analysis. *Am. J. Neuroradiol.* 36 (12), 2394–2399. doi:10.3174/ajnr.a4498

Caprez, S., Menzel, U., Li, Z., Grad, S., Alini, M., and Peroglio, M. (2018). Isolation of high-quality RNA from intervertebral disc tissue via pronase predigestion and tissue pulverization. *JOR Spine* 1 (2), e1017. doi:10.1002/jsp2.1017

Chan, S. C., Bürki, A., Bonél, H. M., Benneker, L. M., and Gantenbein-Ritter, B. (2013). Papain-induced *in vitro* disc degeneration model for the study of injectable nucleus pulposus therapy. *Spine J.* 13 (3), 273–283. doi:10.1016/j.spinee.2012.12.007

Christiani, T., Mys, K., Dyer, K., Kadlowec, J., Iftode, C., and Vernengo, A. J. (2021). Using embedded alginate microparticles to tune the properties of *in situ* forming poly (N-isopropylacrylamide)-graft-chondroitin sulfate bioadhesive hydrogels for replacement and repair of the nucleus pulposus of the intervertebral disc. *JOR spine* 4 (3), e1161. doi:10.1002/jsp2.1161

Cs-Szabo, G., Ragasa-San Juan, D., Turumella, V., Masuda, K., and Thonar, E. J. M. (2002). Changes in mRNA and protein levels of proteoglycans of the anulus fibrosus and nucleus pulposus during intervertebral disc degeneration. *Spine (Phila Pa 1976)* 27 (20), 2212–2219. doi:10.1097/00007632-200210150-00006

Daly, C., Ghosh, P., Jenkin, G., Oehme, D., and Goldschlager, T. (2016). A review of animal models of intervertebral disc degeneration: pathophysiology, regeneration, and translation to the clinic. *BioMed Res. Int.* 2016, 1–14. doi:10.1155/2016/5952165

de Schepper, E. I., Damen, J., van Meurs, J. B. J., Ginai, A. Z., Popham, M., Hofman, A., et al. (2010). The association between lumbar disc degeneration and low back pain: the influence of age, gender, and individual radiographic features. *Spine* 35 (5), 531–536. doi:10.1097/brs.0b013e3181aa5b33

Dowdell, J., Erwin, M., Choma, T., Vaccaro, A., Iatridis, J., and Cho, S. K. (2017). Intervertebral disk degeneration and repair. *Neurosurgery* 80 (30S), S46–S54. doi:10.1093/neuros/nyw078

Du, J., Pfannkuche, J., Lang, G., Häckel, S., Creemers, L. B., Alini, M., et al. (2020). Proinflammatory intervertebral disc cell and organ culture models induced by tumor necrosis factor alpha. *Jor Spine* 3 (3), e1104. doi:10.1002/jsp2.1104

Freemont, A. J. (2009). The cellular pathobiology of the degenerate intervertebral disc and discogenic back pain. *Rheumatology* 48 (1), 5–10. doi:10.1093/rheumatology/ken396

Fu, F., Bao, R., Yao, S., Zhou, C., Luo, H., Zhang, Z., et al. (2021). Aberrant spinal mechanical loading stress triggers intervertebral disc degeneration by inducing pyroptosis and nerve ingrowth. *Sci. Rep.* 11 (1), 772–815. doi:10.1038/s41598-020-80756-6

Fujii, K., Lai, A., Korda, N., Hom, W. W., Evashwick-Rogler, T. W., Nasser, P., et al. (2020). *Ex-vivo* biomechanics of repaired rat intervertebral discs using genipin crosslinked fibrin adhesive hydrogel. *J. biomechanics* 113, 110100. doi:10.1016/j.jbiomech.2020.110100

Gantenbein, B., Grünhagen, T., Lee, C. R., van Donkelaar, C. C., Alini, M., and Ito, K. (2006). An *in vitro* organ culturing system for intervertebral disc explants with vertebral endplates: a feasibility study with ovine caudal discs. *Spine (Phila Pa 1976)* 31 (23), 2665–2673. doi:10.1097/01.brs.0000244620.15386.df

Gruber, H. E., Mougeot, J. L., Hoelscher, G., Ingram, J. A., and Hanley, E. N. (2007). Microarray analysis of laser capture microdissected-anulus cells from the human intervertebral disc. *Spine (Phila Pa 1976)* 32 (11), 1181–1187. doi:10.1097/brs.0b013e318053ec89

Gullbrand, S. E., Malhotra, N., Schaer, T., Zawacki, Z., Martin, J., Bendigo, J., et al. (2017). A large animal model that recapitulates the spectrum of human intervertebral disc degeneration. *Osteoarthr. Cartil.* 25 (1), 146–156. doi:10.1016/j.joca.2016.08.006

Iatridis, J. C., Michalek, A. J., Purmessur, D., and Korecki, C. L. (2009). Localized intervertebral disc injury leads to organ level changes in structure, cellularity, and biosynthesis. *Cell Mol. Bioeng.* 2 (3), 437–447. doi:10.1007/s12195-009-0072-8

Imai, Y., Okuma, M., Nakagawa, K., Yamada, M., Muehleman, C., et al. (2007). Restoration of disc height loss by recombinant human osteogenic protein-1 injection into intervertebral discs undergoing degeneration induced by an intradiscal injection of chondroitinase ABC. *Spine (Phila Pa 1976)* 32 (11), 1197–1205. doi:10.1097/brs.0b013e3180574d26

Javid, M. J. (1980). Treatment of herniated lumbar disk syndrome with chymopapain. *Jama* 243 (20), 2043–2204. doi:10.1001/jama.1980.03300460025019

Johnson, W. E., Eisenstein, S. M., and Roberts, S. (2001). Cell cluster formation in degenerate lumbar intervertebral discs is associated with increased disc cell proliferation. *Connect. Tissue Res.* 42 (3), 197–207. doi:10.3109/03008200109005650

Kalaf, E. A. G., Sell, S. A., and Bledsoe, J. G. (2014). Developing a mechanical and chemical model of degeneration in young bovine lumbar intervertebral disks and reversing loss in mechanical function. *Clin. Spine Surg.* 27 (5), E168–E175. doi:10.1097/bsd.0000000000000085

Kim, M. J., Lee, J. H., Kim, J. S., Kim, H. Y., Lee, H. C., Byun, J. H., et al. (2020). Intervertebral disc regeneration using stem cell/growth factor-loaded porous particles with a leaf-stacked structure. *Biomacromolecules* 20 (12), 4795–4805. doi:10.1021/acs.biomac.0c00992

Korecki, C. L., Costi, J. J., and Iatridis, J. C. (2008). Needle puncture injury affects intervertebral disc mechanics and biology in an organ culture model. *Spine* 33 (3), 235–241. doi:10.1097/brs.0b013e3181624504

Lama, P., Claireaux, H., Flower, L., Harding, I. J., Dolan, T., Le Maitre, C. L., et al. (2019). Physical disruption of intervertebral disc promotes cell clustering and a degenerative phenotype. *Cell Death Discov.* 5, 154. doi:10.1038/s41420-019-0233-z

Lang, G., Liu, Y., Geries, J., Zhou, Z., Kubosch, D., Südkamp, N., et al. (2018). An intervertebral disc whole organ culture system to investigate proinflammatory and degenerative disc disease condition. *J. Tissue Eng. Regen. Med.* 12 (4), e2051–e2061. doi:10.1002/term.2636

Le Maitre, C. L., Freemont, A. J., and Hoyland, J. A. (2007a). Accelerated cellular senescence in degenerate intervertebral discs: a possible role in the pathogenesis of intervertebral disc degeneration. *Arthritis Res. Ther.* 9 (3), R45–R12. doi:10.1186/ar2198

Le Maitre, C. L., Freemont, A. J., and Hoyland, J. A. (2004). Localization of degradative enzymes and their inhibitors in the degenerate human intervertebral disc. *J. Pathol.* 204 (1), 47–54. doi:10.1002/path.1608

Le Maitre, C. L., Pockert, A., Buttle, D., Freemont, A., and Hoyland, J. (2007b). Matrix synthesis and degradation in human intervertebral disc degeneration. *Biochem. Soc. Trans.* 35 (4), 652–655. doi:10.1042/bst0350652

Lee, N. N., Salzer, E., Bach, F. C., Bonilla, A. F., Cook, J. L., Gazit, Z., et al. (2021). A comprehensive tool box for large animal studies of intervertebral disc degeneration. *JOR Spine* 4 (2), e1162. doi:10.1002/jsp2.1162

Lian, C., Gao, B., Wu, Z., Qiu, X., Peng, Y., Liang, A., et al. (2017). Collagen type II is downregulated in the degenerative nucleus pulposus and contributes to the degeneration and apoptosis of human nucleus pulposus cells. *Mol. Med. Rep.* 16 (4), 4730–4736. doi:10.3892/mmr.2017.7178

Liao, Z., Luo, R., Li, G., Song, Y., Zhan, S., Zhao, K., et al. (2019). Exosomes from mesenchymal stem cells modulate endoplasmic reticulum stress to protect against nucleus pulposus cell death and ameliorate intervertebral disc degeneration *in vivo*. *Theranostics* 9 (14), 4084–4100. doi:10.7150/thno.33638

Liu, S., Yang, S. D., Huo, X. W., Yang, D. L., Ma, L., and Ding, W. Y. (2018). 17β-Estradiol inhibits intervertebral disc degeneration by down-regulating MMP-3 and MMP-13 and up-regulating type II collagen in a rat model. *Artif. cells, nanomedicine, Biotechnol.* 46 (2), 182–191. doi:10.1080/21691401.2018.1453826

Maclean, J. J., Lee, C. R., Alini, M., and Iatridis, J. C. (2004). Anabolic and catabolic mRNA levels of the intervertebral disc vary with the magnitude and frequency of *in vivo* dynamic compression. *J. Orthop. Res.* 22 (6), 1193–1200. doi:10.1016/j.orthres.2004.04.004

Malonzo, C., Chan, S. C. W., Kabiri, A., Eglin, D., Grad, S., Bonél, H. M., et al. (2015). A papain-induced disc degeneration model for the assessment of thermo-reversible hydrogel-cells therapeutic approach. *J. Tissue Eng. Regen. Med.* 9 (12), E167–E176. doi:10.1002/term.1667

Mamboya, E. A. F. (2012). Papain, a plant enzyme of biological importance: A review. *Am. J. Biochem. Biotechnol.* 8 (2), 99–104. doi:10.3844/ajbbsp.2012.99.104

Markova, D. Z., Kepler, C. K., Addya, S., Murray, H. B., Vaccaro, A. R., Shapiro, I. M., et al. (2013). An organ culture system to model early degenerative changes of the intervertebral disc II: profiling global gene expression changes. *Arthritis Res. Ther.* 15 (5), R121. doi:10.1186/ar4301

Miller, J. A., Schmatz, C., and Schultz, A. B. (1988). Lumbar disc degeneration: correlation with age, sex, and spine level in 600 autopsy specimens. *Spine* 13 (2), 173–178. doi:10.1097/00007632-198802000-00008

Nerlich, A. G., Bachmeier, B. E., Schleicher, E., Rohrbach, H., Paesold, G., and Boos, N. (2007). Immunomorphological analysis of RAGE receptor expression and NF-κB activation in tissue samples from normal and degenerated intervertebral discs of various ages. *Ann. N. Y. Acad. Sci.* 1096 (1), 239–248. doi:10.1196/annals.1397.090

Oshima, H., Ishihara, H., Urban, J. P. G., and Tsuji, H. (1993). The use of coccygeal discs to study intervertebral disc metabolism. *J. Orthop. Res.* 11 (3), 332–338. doi:10.1002/jor.1100110304

Paajanen, H., Erkintalo, M., Parkkola, R., Salminen, J., and Kormano, M. (1997). Age-dependent correlation of low-back pain and lumbar disc degeneration. *Archives Orthop. trauma Surg.* 116 (1), 106–107. doi:10.1007/bf00434112

Panebianco, C. J., Dave, A., Charytonowicz, D., Sebra, R., and Iatridis, J. C. (2021). Single-cell RNA-sequencing atlas of bovine caudal intervertebral discs: discovery of heterogeneous cell populations with distinct roles in homeostasis. *FASEB J.* 35 (11), e21919. doi:10.1096/fj.202101149r

Panebianco, C. J., Meyers, J., Gansau, J., Hom, W., and Iatridis, J. (2020). Balancing biological and biomechanical performance in intervertebral disc repair: a systematic review of injectable cell delivery biomaterials. *Eur. cells Mater.* 40, 239–258. doi:10.22203/ecm.v040a15

Paul, C. P., Zuiderbaan, H. A., Zandieh Doulabi, B., van der Veen, A. J., van de Ven, P. M., Smit, T. H., et al. (2012). Simulated-physiological loading conditions preserve biological and mechanical properties of caprine lumbar intervertebral discs in *ex vivo* culture. *PLoS One* 7 (3), e33147. doi:10.1371/journal.pone.0033147

Pennicooke, B., Hussain, I., Berlin, C., Sloan, S. R., Borde, B., Moriguchi, Y., et al. (2018). Annular repair using high-density collagen gel: *in vivo* ovine model. *Spine* 43 (4), E208–E215. doi:10.1097/brs.0000000000002334

Pfannkuche, J. J., Guo, W., Cui, S., Ma, J., Lang, G., Peroglio, M., et al. (2020). Intervertebral disc organ culture for the investigation of disc pathology and regeneration - benefits, limitations, and future directions of bioreactors. *Connect. Tissue Res.* 61 (3-4), 304–321. doi:10.1080/03008207.2019.1665652

Pockert, A. J., Richardson, S. M., Le Maitre, C. L., Lyon, M., Deakin, J. A., Buttle, D. J., et al. (2009). Modified expression of the ADAMTS enzymes and tissue inhibitor of metalloproteinases 3 during human intervertebral disc degeneration. *Arthritis Rheum.* 60 (2), 482–491. doi:10.1002/art.24291

Pratta, M. A., Yao, W., Decicco, C., Tortorella, M. D., Liu, R. Q., Copeland, R. A., et al. (2003). Aggrecan protects cartilage collagen from proteolytic cleavage. *J. Biol. Chem.* 278 (46), 45539–45545. doi:10.1074/jbc.m303737200

Rahyussalim, A. J., Zufar, M. L. L., and Kurniawati, T. (2020). Significance of the association between disc degeneration changes on imaging and low back pain: A review article. *Asian spine J.* 14 (2), 245–257. doi:10.31616/asj.2019.0046

Roberts, S., Caterson, B., Menage, J., Evans, E. H., Jaffray, D. C., and Eisenstein, S. M. (2000). Matrix metalloproteinases and aggrecanase: their role in disorders of the human intervertebral disc. *Spine* 25 (23), 3005–3013. doi:10.1097/00007632-200012010-00007

Roberts, S., Menage, J., Sivan, S., and Urban, J. P. (2008). Bovine explant model of degeneration of the intervertebral disc. *BMC Musculoskelet. Disord.* 9, 24. doi:10.1186/1471-2474-9-24

Rustenburg, C. M. E., Snuggs, J., Emanuel, K., Thorpe, A., Sammon, C., Le Maitre, C., et al. (2020). Modelling the catabolic environment of the moderately degenerated disc with a caprine *ex vivo* loaded disc culture system. *Eur. cells Mater.* 40, 21–37. doi:10.22203/ecm.v040a02

Silagi, E. S., Shapiro, I. M., and Risbud, M. V. (2018). Glycosaminoglycan synthesis in the nucleus pulposus: dysregulation and the pathogenesis of disc degeneration. *Matrix Biol.* 71-72, 368–379. doi:10.1016/j.matbio.2018.02.025

Silva, Z. S., Jr., Huang, Y. Y., de Freitas, L. F., França, C. M., Botta, S. B., Ana, P. A., et al. (2016). Papain gel containing methylene blue for simultaneous caries removal and antimicrobial photoinactivation against Streptococcus mutans biofilms. *Sci. Rep.* 6, 33270. doi:10.1038/srep33270

Song, C., Zhou, Y., Cheng, K., Liu, F., Cai, W., Zhou, D., et al. (2023). Cellular senescence - molecular mechanisms of intervertebral disc degeneration from an immune perspective. *Biomed. Pharmacother.* 162, 114711. doi:10.1016/j.biopha.2023.114711

Stern, W. E., and Coulson, W. F. (1976). Effects of collagenase upon the intervertebral disc in monkeys. *J. Neurosurg.* 44 (1), 32–44. doi:10.3171/jns.1976.44.1.0032

Stoddart, M. J., Furlong, P., Simpson, A., Davies, C., and Richards, R. (2006). A comparison of non-radioactive methods for assessing viability in *ex vivo* cultured cancellous bone: technical note. *Eur. Cell Mater* 12, 16–25. doi:10.22203/ecm.v012a02

Takagaki, K., and Kakizaki, I. (2007). "Degradation of glycosaminoglycans," in *Comprehensive glycoscience: From chemistry to systems biology* (Amsterdam: Elsevier Science BV).

Takaishi, H., Nemoto, O., Shiota, M., Kikuchi, T., Yamada, H., Yamagishi, M., et al. (1997). Type-II collagen gene expression is transiently upregulated in experimentally induced degeneration of rabbit intervertebral disc. *J. Orthop. Res.* 15 (4), 528–538. doi:10.1002/jor.1100150408

Teixeira, J. H., Pereira, C. L., Almeida, M. I., Teixeira, G. Q., Gonçalves, R. M., Barbosa, M. A., et al. (2020). Articular repair/regeneration in healthy and inflammatory conditions: from advanced *In vitro* to *in vivo* models. *Adv. Funct. Mater.* 30 (44), 1909523. doi:10.1002/adfm.201909523

Uei, H., Matsuzaki, H., Oda, H., Nakajima, S., Tokuhashi, Y., and Esumi, M. (2006). Gene expression changes in an early stage of intervertebral disc degeneration induced by passive cigarette smoking. *Spine* 31, 510–514. doi:10.1097/01.brs.0000201304.81875.cc

Urban, J. P., and Roberts, S. (2003). Degeneration of the intervertebral disc. *Arthritis Res. Ther.* 5 (3), 120–130. doi:10.1186/ar629

van den Akker, G. G., Koenders, M. I., van de Loo, F. A. J., van Lent, P. L. E. M., Blaney Davidson, E., and van der Kraan, P. M. (2017). Transcriptional profiling distinguishes inner and outer annulus fibrosus from nucleus pulposus in the bovine intervertebral disc. *Eur. Spine J.* 26 (8), 2053–2062. doi:10.1007/s00586-017-5150-3

Van Wart, H. E., and Steinbrink, D. R. (1985). Complementary substrate specificities of class I and class II collagenases from Clostridium histolyticum. *Biochemistry* 24 (23), 6520–6526. doi:10.1021/bi00344a032

Wang, K., Song, Y., Liu, W., Wu, X., Zhang, Y., Li, S., et al. (2017). The noncoding RNA linc-ADAMTS5 cooperates with RREB1 to protect from intervertebral disc degeneration through inhibiting ADAMTS5 expression. *Clin. Sci.* 131 (10), 965–979. doi:10.1042/cs20160918

Wang, W. J., Yu, X. H., Wang, C., Yang, W., He, W. S., Zhang, S. J., et al. (2015). MMPs and ADAMTSs in intervertebral disc degeneration. *Clin. Chim. Acta* 448 (448), 238–246. doi:10.1016/j.cca.2015.06.023

Wang, W., Pei, B., Pei, Y., Li, H., Lu, S., Wu, X., et al. (2020). Biomechanical effects of over lordotic curvature after spinal fusion on adjacent intervertebral discs under continuous compressive load. *Clin. Biomech.* 73, 149–156. doi:10.1016/j.clinbiomech.2020.01.002

Yang, F., Liu, W., Huang, Y., Yang, S., Shao, Z., Cai, X., et al. (2022). Regulated cell death: implications for intervertebral disc degeneration and therapy. *J. Orthop. Transl.* 37, 163–172. doi:10.1016/j.jot.2022.10.009

Yoganandan, N., Umale, S., Stemper, B., and Snyder, B. (2017). Fatigue responses of the human cervical spine intervertebral discs. *J. Mech. Behav. Biomed. Mater.* 69, 30–38. doi:10.1016/j.jmbbm.2016.11.026

Zhang, C., Gullbrand, S. E., Schaer, T. P., Lau, Y. K., Jiang, Z., Dodge, G. R., et al. (2020b). Inflammatory cytokine and catabolic enzyme expression in a goat model of intervertebral disc degeneration. *J. Orthop. Res.* 38 (11), 2521–2531. doi:10.1002/jor.24639

Zhang, J., Hao, X., Chi, R., Qi, J., and Xu, T. (2021). Moderate mechanical stress suppresses the IL-1β-induced chondrocyte apoptosis by regulating mitochondrial dynamics. *J. Cell Physiol.* 236 (11), 7504–7515. doi:10.1002/jcp.30386

Zhang, Y., Yang, B., Wang, J., Cheng, F., Shi, K., Ying, L., et al. (2020a). Cell senescence: a nonnegligible cell state under survival stress in pathology of intervertebral disc degeneration. *Oxid. Med. Cell Longev.* 2020, 1–12. doi:10.1155/2020/9503562

Zhou, Z., Cui, S., Du, J., Richards, R. G., Alini, M., Grad, S., et al. (2021). One strike loading organ culture model to investigate the post-traumatic disc degenerative condition. *J. Orthop. Transl.* 26, 141–150. doi:10.1016/j.jot.2020.08.003

Zhu, J., Xia, K., Yu, W., Wang, Y., Hua, J., Liu, B., et al. (2019). Sustained release of GDF5 from a designed coacervate attenuates disc degeneration in a rat model. *Acta Biomater.* 86, 300–311. doi:10.1016/j.actbio.2019.01.028

Frontiers in Bioengineering and Biotechnology

TYPE Original Research
PUBLISHED 03 November 2023
DOI 10.3389/fbioe.2023.1283526

OPEN ACCESS

EDITED BY
Antonella Motta,
University of Trento, Italy

REVIEWED BY
Kui Xu,
Anhui University of Chinese Medicine, China
Zhuocheng Lyu,
Shanghai Jiao Tong University, China

*CORRESPONDENCE
Dongsong Li,
✉ lidongsong@jlu.edu.cn
Peibiao Zhang,
✉ zhangpb@ciac.ac.cn
Jianguo Liu,
✉ liujg6@126.com

RECEIVED 26 August 2023
ACCEPTED 23 October 2023
PUBLISHED 03 November 2023

CITATION
Shi X, Wang Z, Guo M, Wang Y, Bi Z, Li D, Zhang P and Liu J (2023), PRP coating on different modified surfaces promoting the osteointegration of polyetheretherketone implant. *Front. Bioeng. Biotechnol.* 11:1283526. doi: 10.3389/fbioe.2023.1283526

PRP coating on different modified surfaces promoting the osteointegration of polyetheretherketone implant

Xiaotong Shi[1], Zongliang Wang[2], Min Guo[2], Yu Wang[2], Zhiguo Bi[1], Dongsong Li[1]*, Peibiao Zhang[2]* and Jianguo Liu[1]*

[1]Department of Orthopedic Surgery, The First Hospital of Jilin Uniersity, Changchun, China, [2]Key Laboratory of Polymer Ecomaterials, Changchun Institute of Applied Chemistry, Chinese Academy of Sciences, Changchun, China

Introduction: Polyetheretherketone (PEEK) material implants have been applied more and more clinically recently. In order to increase the osteogenic activity of PEEK material, the microstructure change of the material surface and the construction of functional microcoatings have become a hot research topic. This study investigated the ability of PEEK surfaces modified by different methods to carry Platelet-rich plasma (PRP) and the osteogenic ability of different PEEK microstructures after carrying PRP *in vivo*/*in vitro*.

Methods: In this study, PEEK surfaces were modified by sulfuric acid, gaseous sulfur trioxide and sandpaper. Next, PRP from SD rats was prepared and incubated on PEEK material with different surface microstructures. Lactate dehydrogenase test, scanning electron microscope and Elisa assay was used to evaluate adhesion efficiency of PRP. Then *in vitro* tests such as CCK-8, ALP staining, ARS staining and RT-qPCR et al were used to further evaluate osteogenesis ability of the PRP coating on PEEK surface. Finally, The tibia defects of SD rats were established, and the new bone was evaluated by Micro-CT, HE staining, and immunofluorescence staining.

Results: The sandpaper-polished PEEK with the strongest PRP carrying capacity showed the best osteogenesis. Our study found that the modified PEEK surface with PRP coating has excellent osteogenic ability and provided the basis for the interface selection of PRP for the further application of PEEK materials.

Discussion: Among the three PEEK modified surfaces, due to the most PRP carrying and the strongest osteogenic ability *in vitro/vivo*, the frosted surface was considered to be the most suitable surface for the preparation of PRP coating.

KEYWORDS

polyetheretherketone, surface treatment, platelet-rich plasma, growth factor, osteointegration

1 Introduction

Bone defects caused by various reasons, such as tumor surgery and trauma, are common worldwide. Therefore, bone defect repair and osseointegration of bone replacement materials have been a hot topic worldwide (Quarto and Giannoni, 2016). At present, titanium and its alloy are the most used bone implant materials in clinical due to their good mechanical properties, chemical stability, and biocompatibility. However, the persistent release of metal ions, anaphylaxis, and stress shielding are its side effects difficult to solve (HuiskesWeinans and Van, 1992; Niki et al., 2001).

Therefore, in recent years, in order to overcome the shortcomings of titanium alloys, PEEK with an elastic modulus closer to human bone tissue has become a powerful alternative to titanium (Lee et al., 2012; Ruiter et al., 2021; Vogel et al., 2021). However, the biological inertness of PEEK materials has hindered its clinical application. There are three kind methods to improve the biological activity of PEEK material: First, change the surface morphology of PEEK material to facilitate cell adhesion, growth and differentiation; Second, the PEEK material is blended with other bioactive materials; Third, bioactive factors were grafted on the PEEK surface by chemical and physical methods (Vogel et al., 2021). Previous studies have shown that there are a variety of ways to change the surface shape of PEEK materials. The surface morphology of PEEK with different roughnesses can be obtained by grinding the PEEK surface with sandpaper of different roughnesses (Sunarso et al., 2018). Concentrated sulfuric acid can create a three-dimensional pore structure on the surface of PEEK, enhance the osteogenesis of PEEK, and give PEEK material a certain drug loading ability (Wu et al., 2018; Zhu et al., 2019; Ma et al., 2020). In previous studies in our laboratory, gaseous sulfur trioxide was used to fabricate hydrophilic PEEK surfaces with the 3D pore structure. This PEEK modified surface was also proved to have good mineralization and osteogenesis ability *in vitro* (Wan et al., 2020).

Platelet-rich plasma (PRP) is a plasma rich in high concentrations of platelets obtained from animal or human whole blood by centrifugation (Ehrenfest et al., 2009). The number of platelets in PRP is usually more than three times higher than that in whole blood. Platelets in PRP can secrete a variety of growth factors such as transforming growth factor (TGF), vascular endothelial growth factor (VEGF), and platelet-derived growth factor (PDGF) after activation (Ehrenfest et al., 2009). At present, PRP has been widely used to enhance the biological activity of biomaterials such as hydrogels and gelatin. The study showed that the 3D-printed PRP-GelMA hydrogel prepared by Jiang et al. could promote cartilage regeneration through macrophage immunomodulation (Jiang et al., 2021). Naga et al. demonstrated that perfusion of PRP into 3D microvasculature promoted endothelial cell maturation and improved cell function within 24 h (Nagao et al., 2019). In addition, injectable PRP has been widely used in orthopedic surgeries such as spinal fusion and joint replacement due to its excellent osteopromoting ability (Zavadil et al., 2007; Imagama et al., 2017). However, few studies have reported PRP as a bioactive factor to improve the osteogenic activity of PEEK materials. Therefore, we intend to develop a new method using PRP to improve the biological activity of PEEK materials. At the same time, we believe that morphology is an important factor affecting the biological activity of PRP on PEEK surface.

Therefore, in this study, we fabricated PEEK surfaces with different microstructures using sandpaper, sulfuric acid, and

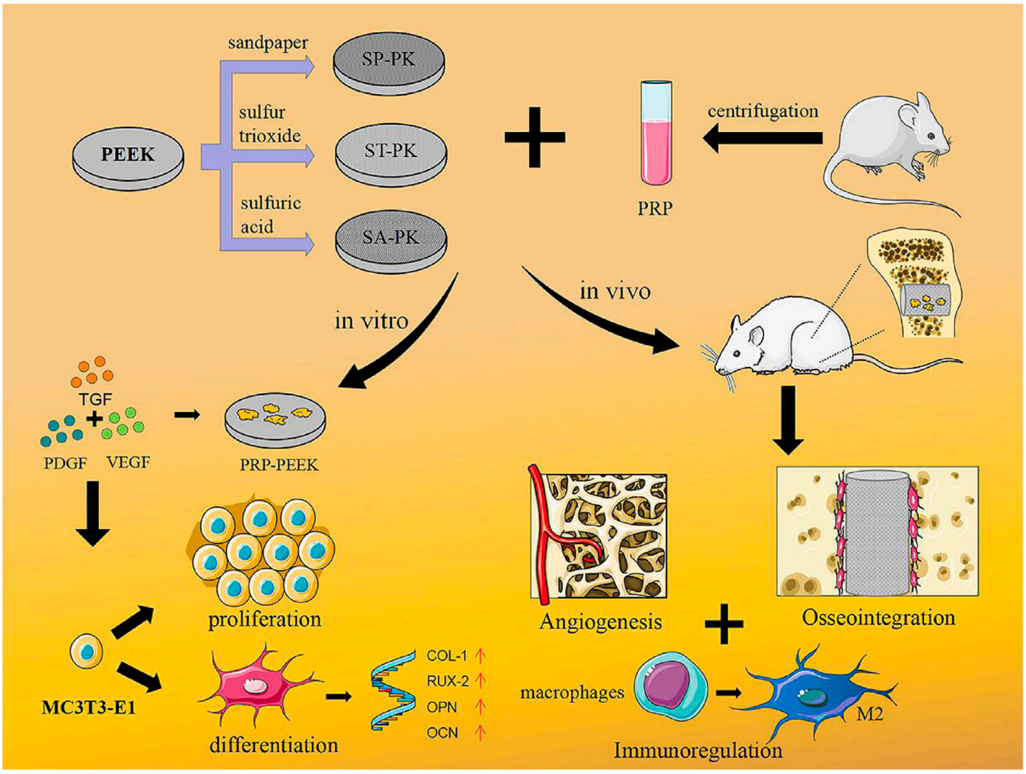

SCHEME 1
Concept illustration. PEEK samples with three different modified surfaces were fabricated and PRP coatings were prepared. This combination treatment promoted osteoblast proliferation and differentiation *in vitro*, while *in vivo* it could regulate immunity, promote angiogenesis, and ultimately promote osseointegration.

gaseous sulfur trioxide. Firstly, we used SEM, EDS, AFM, and universal testing machines to compare and analyze the different morphologies and material characteristics of PEEK. Secondly, we used SEM, LDH test and Elisa to analyze the adhesion characteristics and growth factor release of PRP on PEEK surfaces with different morphologies. Finally, *in vivo* and *in vitro* experiments, we compared and analyzed the osteogenic ability of PEEK materials with different morphologies equipped with PRP (Scheme 1).

2 Materials and methods

2.1 Preparation of PEEK surface

Biograde PEEK (Victrex, United Kingdom) was fabricated as disks (diameter 15 mm, thickness 0.5 mm) for physicochemical characterization and *in vitro* cell experiments, and cylinders (diameter 2 mm, height 3 mm) for mechanical tests and *in vivo* studies. These samples were ultrasonically rinsed in acetone, absolute ethanol, and deionized water for 30 min and then dried under vacuum to give the original PEEK (named PK).

The original PEEK was fully polished with 220-mesh sandpaper to obtain the frosted PEEK (named SP-PK). The sanding direction was in a single direction and the sanding time was 1 min.

According to the previous research of our research group, the reaction of H_2SO_4 and P_2O_5 was used to produce gaseous sulfur trioxide (SO_3), and the SO_3 modified PEEK surface was obtained (named ST-PK) (Wan et al., 2020). Briefly, PEEK disks were placed on the bracket of refitted glassware and P_2O_5 was placed at the bottom. H_2SO_4 was then titrated into glassware through a constant voltage funnel. The whole apparatus was maintained in a 75°C thermostatic water bath to maintain the gaseous state of SO_3, and the exposure time of the PEEK disks to SO_3 was set to 60 min. Finally, these samples were also ultrasonically rinsed in acetone, absolute ethanol, and deionized water for 30 min and then dried under vacuum.

According to previous studies, PEEK disks were placed in concentrated sulfuric acid to obtain sulfonated PEEK surface (named SA-PK). In brief, the PEEK disks were immersed in concentrated sulfuric acid (95–98 wt%) with ultrasonic stirring for 1 min at room temperature. Finally these samples were ultrasonically cleaned and vacuum dried as described above.

2.2 Characterization of PEEK surface

To observe the morphological attributes of the PEEK surface, dried PEEK disks were evaluated with a scanning electron microscope (XL-30 ESEM FEG Scanning Electron Microscope; FEI Company, Hillsboro, OR, United States) after being sprayed with gold. The surface elemental distribution of the PEEK disks was analyzed using energy-dispersive X-ray spectroscopy (EDS). The hydrophilicity/hydrophobicity of these sample surfaces were evaluated by water contact angle measurements (VCA 2000; AST Products Inc., United States): 2 lL DI water droplets were dropped onto the PEEK sample surfaces at room temperature; pictures were taken by a camera after stabilization. Atomic force microscopy (AFM, Veeco, United States) was used to detect the surface structure of modified PEEK surface. Fourier transform infrared spectroscopy (FT-IR; PerkinElmer, FT-IR-2000) was used to measure the chemical structure in the wavenumber region from 400 to 3,500 cm^{-1}.

Since PEEK material implants mainly bear compressive stress *in vivo*, we tested the effects of three different surface modification methods on the compressive mechanical properties of PEEK material according to the National Standard of China (GB/T1039). At room temperature, the compressive mechanical properties of PEEK cylinders (diameter 2 mm, height 3 mm) with various modified surfaces were measured by a universal mechanical testing machine (Instron 1121, United Kingdom) with a speed of 2 mm/min.

2.3 Fabrication of PRP-PEEK surface

According to previous reports, SD rat-derived PRP was prepared (Zavadil et al., 2007). First, 1 mL of anticoagulant was added to 5 mL of whole blood extracted from SD rats. Then, erythrocytes were removed after centrifugation at 2,000 g for 3 min. Finally, the mixture was centrifuged at 5,000 g for 5 min to obtain the supernatant and platelet precipitate. PRP was obtained by resuspension of the platelet precipitate. An automated counter (Sysmex, XS-800i, Kobe, Japan) was used to analyze platelet concentrations in whole blood and PRP.

Sterile PEEK disks (diameter 15 mm, thickness 0.5 mm) were placed in 24-well plates, and 200 μL of PRP solution was added to each well and incubated in a 37°C incubator for 2 h. At the end of the incubation, each PEEK sheet was washed three times with sterile PBS to obtain PEEK disks with PRP coating (named PRP-PK, PRP-SP-PK, PRP-ST-PEEK and PRP-SA-PEEK respectively).

2.4 Evaluation of PRP carrying capacity of PEEK surface

2.4.1 Platelet adhesion observation

Platelet adhesion on various modified PEEK surfaces was observed by SEM after incubation with PRP. Before performing SEM observations, PEEK disks with PRP incubated on the surface were transferred to new 24-well plates and fixed with 2.5% glutaraldehyde(in PBS buffer) for 8 h at 4°C. Then they were dehydrated in 30%, 50%, 70%, 90%, and 100% ethanol solution for 30 min and dried under vacuum.

2.4.2 Quantitative analysis of platelet adhesion

The LDH cytotoxicity kit (Beyotime; Shanghai, China) was used to quantitatively analyze the number of platelets adhered to the surface of different modified PEEK discs. The test procedure was carried out according to the instructions and references (Tamada et al., 1995; Grunkemeier et al., 1998). The number of platelets in PRP solution was recorded as A after determination with an automatic hematology analyzer, and the OD value was recorded as B after LDH detection of PRP solution. The OD value of platelets adhered to the PEEK surface after LDH detection was recorded as C, thus the number of platelets adhered to the PEEK surface $n = A \times C/B$. LDH assays were performed at least three times for each surface, and the number of adhered platelets obtained was then averaged.

2.4.3 Assessment of PDGF release

An enzyme-linked immunosorbent assay (ELISA) was used to evaluate PDGF-BB release from different PEEK surfaces modified with PRP. PRP-modified PEEK disks were placed into 24-well plates, and after 1 mL sterile PBS solution was added to each well, the plates were incubated at 37°C. The PBS solution was collected and stored at 20°C at preset time points (0, 2, 4, 8, 12, 24 h) and an equal volume of new PBS solution was added to the wells. An ELISA kit (Solarbio; Beijing, China) was used to measure the release of PDGF-BB from modified PEEK discs, and the absorbance was measured at 450 nm (Infifinite M200, Tecan, Switzerland). A standard curve was also plotted to calculate cumulative release of PDGF.

2.5 *In vitro* cell-material interactions assay

2.5.1 Cell culture

In this study, MC3T3-E1 cells were used to evaluate the cytocompatibility and osteogenic activity of different PEEK surfaces before and after PRP incubation. In a humidified atmosphere (37°C, 5% CO_2), the cells were incubated in Dulbecco's Modified Eagle Medium (DMEM; Gibco, Thermo Fisher Scientific, United States) containing 10% fetal bovine serum (Gibco, Thermo Fisher Scientific, United States) and 1% penicillin/streptomycin (Sigma-Aldrich, United States). When the cells were >90% confluent, cell culture medium was aspirated and the cells were then trypsinized, centrifuged and resuspended for cell passage. When the cells were passed to the 3 to 5 passages, they were digested down for cell experiments. 2×10^4 cells were seeded onto the PEEK surfaces in a 24-well plate and DMEM was changed every other day.

2.5.2 Cell adhesion

When 2×10^4 cells on the PEEK surfaces were cultured for 24 h, they were rinsed twice with PBS and fixed with 4% Paraformaldehyde (PFA). Nuclei were stained with 4',6-diamidino-2-phenylindole (DAPI; Sigma-Aldrich, United States) and visualized under fluorescence microscopy (TE 2000U, Nikon, Japan). Nuclei from at least three independent areas of each type of PEEK surface were counted for quantitative analysis.

The cell morphology of MC3T3-E1 grown on PEEK surfaces was visualized by SEM. Briefly, after cells were incubated on the PEEK surface for 24 h, PEEK samples were washed with PBS and fixed with 4% PFA at room temperature. This was followed by dehydration with gradient concentration of ethanol (50%, 60%, 70%, 80%, 90%, and 100%) for 30 min. Finally, SEM observations were performed after gold spraying on dry PEEK surface.

2.5.3 Cell proliferation

Cell proliferation ability on the surface of PEEK was detected by The Cell Counting Kit-8 (CCK-8; Beyotime Institute of Biotechnology, Shanghai, China). After the cells were seeded onto the PEEK surface at predetermined time points, the original cell culture medium in the 24-well plate was discarded and 1 mL of fresh DMEM containing 10%CCK-8 reagent was added. After 4 h of co-culture, the absorbance value was measured at 450 nm (Infifinite M200, Tecan, Switzerland).

2.5.4 Alkaline phosphatase (ALP) staining and quantitative analysis

Cells on the PEEK surfaces were cultured for 7 and 14 days, then ALP staining and quantitative analysis were performed to evaluate early osteogenesis ability. After washing the PEEK disks twice with PBS, they were fixed with 4% PFA for 15 min at room temperature, then washed again and stained with BCIP/NBT (Beyotime; Shanghai, China). Finally, the PEEK surface was observed under microscope and photographed.

The quantitative analysis of ALP was performed using ALP quantification kit (Beyotime; Shanghai, China). After cells were cultured on PEEK surfaces for 7 and 14 days, they were washed three times with PBS, lysis buffer was added and cell lysate supernatants were collected. The supernatant was co-cultured with p-nitrophenyl phosphate at 37°C for 30 min, and the 405 nm absorbance was measured. Meanwhile, the standard curve was drawn according to the instructions of ALP kit, and the ALP activity was calculated according to the standard curve.

2.5.5 Alizarin red S (ARS) staining and quantitative analysis

Alizarin red S (ARS) staining and quantitative analysis were used to assess extracellular matrix calcium deposition at late stages of osteogenic differentiation. Briefly, cells on the PEEK surface were cultured for 21 days, rinsed and fixed as described in 2.5.4. The PEEK surface was then immersed in ARS solution for staining for 30 min 37°C. Finally, the PEEK surfaces were observed under microscope after washing off excess ARS with PBS.

After the observation, the ARS-stained PEEK surface was immersed in a 10% cetylpyridinium chloride (CPC) solution at 37°C for 2 h, and the absorbance was measured at 540 nm at the end.

2.5.6 Real-time quantitative polymerase chain reaction (RT-qPCR) for osteogenesis

RT-qPCR was used to detect the expression of collagen type I (Col-I), runt-related transcription factor 2 (Rux-2), osteopontin (OPN), and osteocalcin (OCN) genes to examine the effect of the PEEK surface on osteogenic differentiation. The primers are listed in Table 1. After 14 days of culture of cells seeded on the PEEK surface, total RNA was extracted with TRIzol reagent (Invitrogen, Carlsbad, CA, United States of America). It was then reverse transcribed into cDNA with an All-In-One 5X RT MasterMix (abm; Vancouver, Canada), and mRNA expression levels were assessed by RT-qPCR with a BlasTaqTM 2X qPCR MasterMix (abm; Vancouver, Canada).

TABLE 1 Primers used in RT-qPCR.

Gene	Forward primer	Reverse primer
Col-I	CGCTGGC AA GA ATOGCGATC	ATGCCTCTGTC A CCTTGTTCG
RUNX2	GCCGGGAATGATGAG AACTA	GGACCGTCCACTGTCACTIT
OPN-F	TCAGGACAACAACGG AAAGGG	TCAGGACAACAACGG AAAGGG
OCN-F	AAGCAGGAGGGCAAT AAGGT	TTTGTAGGCGGTCTTCAAGC

Finally, the comparative Ct method ($2^{-\Delta\Delta CT}$) was used to calculate the relative gene expression and normalization was done based on the expression of the endogenous mouse GAPDH gene.

2.6 *In vivo* bone repair studies

2.6.1 Animals and surgery

In this study, animal experiments were approved by the Laboratory Animal Welfare and Ethics Committee at the Changchun Institute of Applied Chemistry, Chinese Academy of Sciences and were performed in compliance with the National Institutes of Health's Guide for the Care and Use of Laboratory Animals (NIH Publications No. 8023, revised 1978). A rat model of unilateral proximal tibial defect was used to observe the induction of osteogenesis after the implantation of each component (PK,SP-PK,ST-PK,SA-PK, P-PK,P-SP-PK,P-ST-PK,P-SA-PK). In total, 48 male Sprague-Dawley (SD) rats (10 weeks, 250 ± 15 g) were used for *in vivo* osteogenic experiments, 6 for each group. The rats were operated under general anesthesia with 3% pentobarbital (0.1 mL/100 g), and all procedures were performed under aseptic conditions. First, a hole of 3 mm depth was drilled perpendicular to the long axis of the tibia with a sterile drill bit of 2 mm diameter. Next, the cylindrical PEEK materials of each group were carefully implanted into the bone defect site. Finally, saline was used to clean the surgical site and suture the wound layer by layer. After surgery, rats were injected with penicillin for 3 consecutive days to prevent infection. The rats were euthanized at 4 and 8 weeks after surgery, and tibial specimens were collected and fixed in 4% paraformaldehyde solution for subsequent experiments.

2.6.2 Microcomputed tomography (Micro-CT) evaluation

In this study, micro-CT was used to assess bone regeneration. Collected tibial specimens were scanned with the Skyscan 1172 Micro-CT system (14 mm resolution, 80 kV, nofilter; Bruker Kontich, Belgium) and reconstructed in 3D using multimodal 3D visualization software (Skyscan 1,076 Scanner, Bruker Micro-CT, NV, Kontich, Belgium). Bone volume fraction (BV/TV), trabecular thickness (Tb. Th), trabecular number (Tb. N), and trabecular separation (Tb. Sp) were used as quantitative analysis indicators of bone regeneration, and these indicators were analyzed by the CTAn software (SkyScan, Belgium).

2.6.3 Histological evaluation

Rat tibial specimens obtained at 4 and 8 weeks were fixed in 4% paraformaldehyde, and the PEEK implant was removed after decalcification for 45 days. Then, bone tissue was sectioned by an electric slicer after being embedded in paraffin. Hematoxylin and eosin (HE) stain and Sirius red stain were used for general analysis of the new bone and collagen evaluation, respectively. Finally, an imaging system (NIKON DS-U3, Japan) was used to observe these sections.

Immunofluorescence staining of OPN and OCN was performed to analyze osteogenesis. Briefly, tibial specimen sections were blocked in serum and incubated with antibodies against the osteogenic marker antibody Col-I at 4°C overnight. Then, the sections were treated with a secondary antibody with immunofluorescence label. Finally, the sections were observed under a fluorescence microscope.

2.7 Statistical analysis

All data are presented as mean ± standard deviation (SD). Each experimental condition was independently tested a minimum of three times. SPSS software (IBM, Chicago, United States) was used for all statistical analyses. Differences between experimental groups were statistically analyzed by one-way analysis of variance (ANOVA) and Tukey's multiple comparison test A p-value of <0.05 was considered statistically significant.

3 Results

3.1 Characterization of PEEK surface

The SEM results revealed the microstructure of four different PEEK surfaces including original PEEK. As shown in Figure 1A, the original PEEK surface is relatively flat; a gully like microstructure was constructed on the surface of the frosted PEEK. The sulfur trioxide treatment formed potholes and surface micropores on PEEK surface. The concentrated sulfuric acid treatment formed a 3D pore structure on the PEEK surface. The nanoscale microstructure and roughness of four PEEK surfaces were measured by AFM (Figure 2A). Consistent with the SEM results, the PK surface was flat and SP-PK surface had gully shape. However, a fine pore structure was observed on the ST-PK surface; coarse and deep crater-like structures were observed on the SA-PK surface. The roughness of different PEEK surfaces was analyzed (Figure 2B). The results showed that there was no significant difference in surface roughness between SP-PK (7.16 ± 1.28 nm) and PK (7.30 ± 1.30 nm) surfaces. The surface roughness of ST-PK group (22.54 ± 4.05 nm) was significantly higher than that of PK and SP groups, and the surface roughness of SA-PK group (33.10 ± 1.33 nm) was significantly higher than that of the other three groups.

The chemical characteristics of the PEEK surfaces of each group were evaluated using FT-IR in the range of 1,700 cm^{-1} to 900 cm^{-1} wavenumber (Figure 1D). In the spectrogram, all characteristic peaks can be identified. The diketobenzene band at positions 1650 cm^{-1},1490 cm^{-1}, and 926 cm^{-1};C-O-C stretching vibration of diaryl groups at position 1188 cm^{-1} and 1158 cm^{-1}, C = C of the benzene ring in PEEK position at 1600 cm^{-1}. According to the results of FT-IR, the waveforms of the SP-PK and SA-PK groups had the same trend as that of the PK group. In the waveform of ST-PK, a peak related to O= S=O at 1255 cm^{-1} and a peak related to S= O at 1050 cm^{-1} could be found. This indicates that the sulfur trioxide gas sufficiently introduces $-SO_3H$ group to the PEEK surface. The EDS analysis results show the elemental composition of PEEK surface of each group (Figure 1B). Both the ST-PK and SA-PK groups contained S elements-PK group was significantly higher than that in the SA-PK group. Thus, it is also proved that both sulfur trioxide and sulfuric acid introduce $-SO_3H$ group to the PEEK surface, and the amount of $-SO_3H$ group introduced by sulfur trioxide is more.

The water contact angle of each PEEK surface was evaluated and the results are shown in Figure 1C. The water contact angle in the PK group was 92.98 ± 2.92°. Among the four groups, the water contact angle of the SP-PK group was significantly higher than that of the other three groups (121.52 ± 5.29°, $p < 0.05$). The water contact angle in the ST-PK group was significantly lower than that in the other

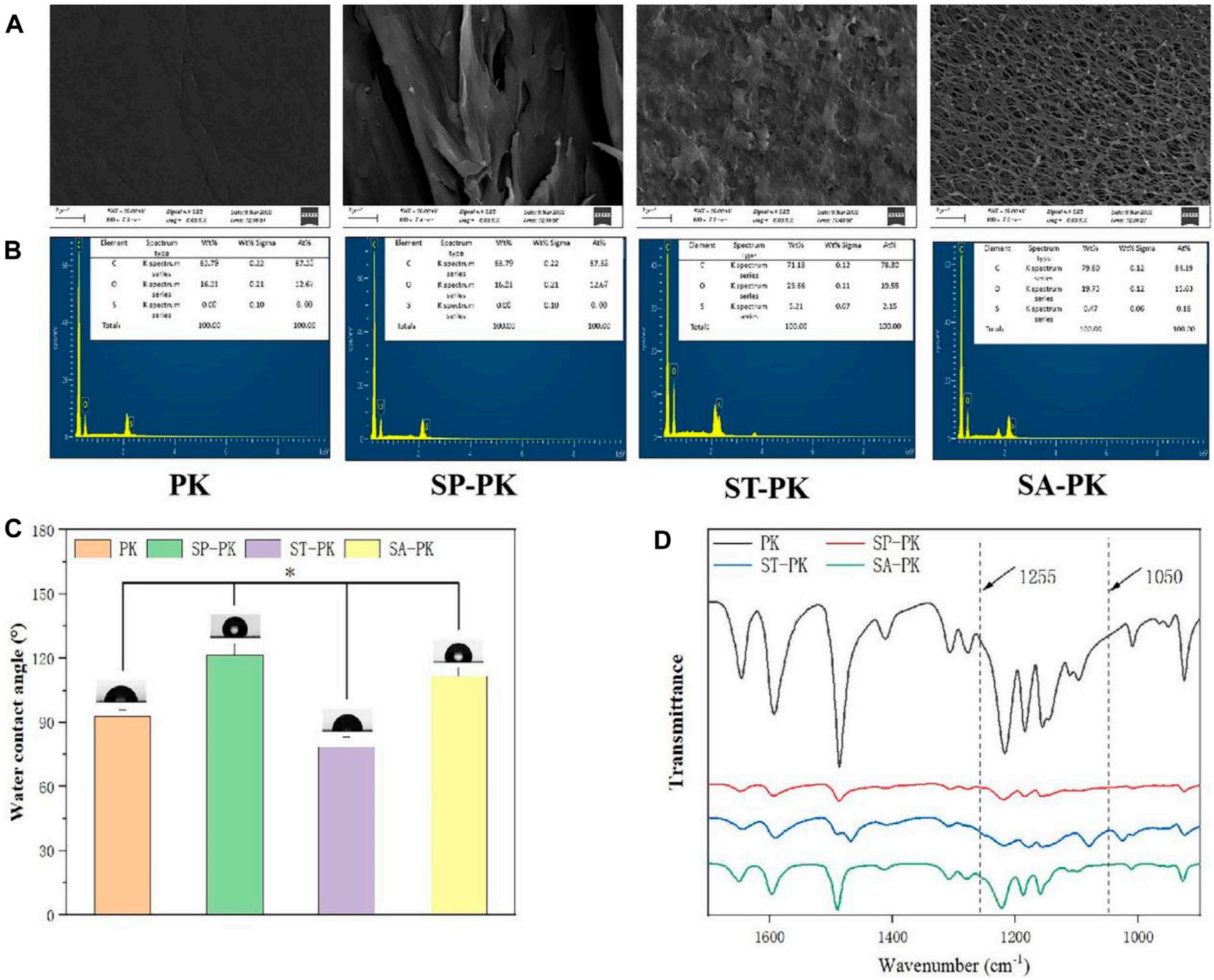

Element	Spectrum type	Wt%	Wt% Sigma	At%
C	K spectrum series	83.79	0.22	87.33
O	K spectrum series	16.21	0.21	12.67
S	K spectrum series	0.00	0.10	0.00
Total:		100.00		100.00

Element	Spectrum type	Wt%	Wt% Sigma	At%
C	K spectrum series	83.79	0.22	87.33
O	K spectrum series	16.21	0.21	12.67
S	K spectrum series	0.00	0.10	0.00
Total:		100.00		100.00

Element	Spectrum type	Wt%	Wt% Sigma	At%
C	K spectrum series	71.13	0.12	78.30
O	K spectrum series	23.66	0.11	19.55
S	K spectrum series	5.21	0.07	2.15
Total:		100.00		100.00

Element	Spectrum type	Wt%	Wt% Sigma	At%
C	K spectrum series	79.80	0.12	84.19
O	K spectrum series	19.73	0.12	15.63
S	K spectrum series	0.47	0.06	0.18
Total:		100.00		100.00

FIGURE 1
(A) The SEM morphology of the surface of PEEK samples from each group. **(B)** EDS results of elemental composition on the surface of PEEK samples in each group. **(C)** Results of water contact angles on PEEK surfaces in each group. **(D)** FT-IR spectral characteristics of PEEK surfaces in each group, *n* = 5.* indicate *p* < 0.05.

three groups (78.64 ± 4.45°, $p < 0.05$). The water contact angle of the SA-PK group (111.72 ± 3.96°) was significantly higher than that of the PK group and significantly lower than that of the SP-PK group.

The compressive mechanical data of the PEEK samples in each group are shown in Figures 2C, D. The compressive strength of the PK group was 777.63 ± 148.63MPa, and that of the other three groups was lower than that of the PK group (558.10 ± 27.19, 700.39 ± 124.20 and 509.40 ± 6.21 respectively). Only the compressive strength of the SA-PK group was significantly lower than that of the PK group. The maximum compressive loads of the PK and ST-PK groups was 1961.67 ± 34.27N and 1857.33 ± 139.15N, and there was no significant difference between them, however, both of them were significantly higher than those of the SP-PK and SA-PK groups. The maximum compressive load of the SP-PK group was 1555.67 ± 61.08, which was significantly lower than that of the PK and the ST groups, but significantly higher than that of the SA-PK group. The maximum compression load in the SA group was1280.33 ± 102.55, which was significantly lower than the other three groups.

3.2 Evaluation of PRP carrying capacity of PEEK surface

The number of platelets in whole blood was 6.74 ± 0.17 × 10^{11}, and that in PRP was 34.12 ± 0.21 × 10^{11}. The concentration of platelets in PRP was 5.06 times that in whole blood. After incubation of PRP onto the PEEK surfaces of each group, the adhesion of platelets to different PEEK surfaces was observed using SEM (Figure 3A). Platelets that ruptured after full activation are shown by yellow arrows in the Figure 3A and are flat disc-shaped. Non-activated ruptured platelets are shown by red arrows and are spherical. Therefore, we can observe that there are more activated platelets on the surface of PK group, while the surface of other three groups is mostly non-activated platelets. As shown in Figure 3A, platelets can adhere to almost any spot on the frosted PEEK surface, including ridges and gullies. However, on the surface of ST-PK and SA-PK groups, the platelet volume was much larger than the inner diameter of micropore and could not enter the inside of microstructure.

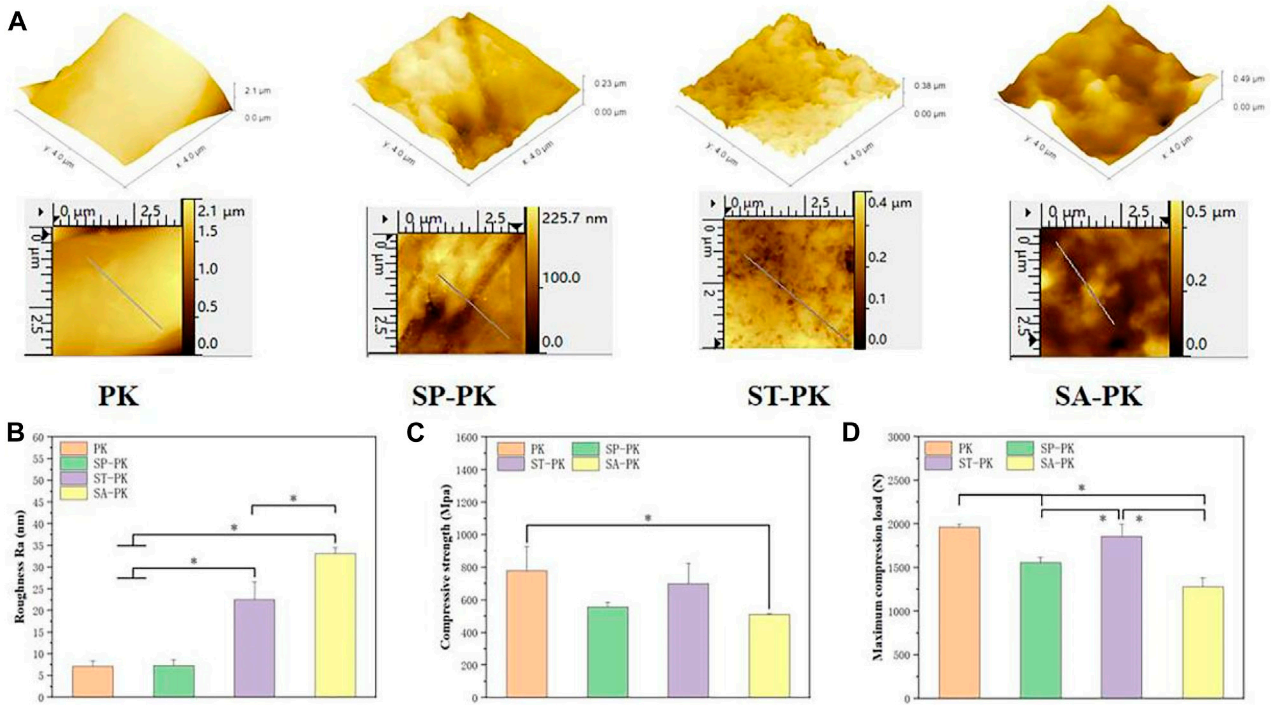

FIGURE 2
(A) AFM images of the surfaces of PEEK samples from each group. Yellow arrows: fully activated platelets; Red arrows: non-activated platelets. **(B)** Surface roughness of each group of PEEK samples analyzed based on AFM images, $n = 3$. **(C)** Compressive strength of PEEK samples in each group, $n = 5$. **(D)** Maximum compression load of PEEK samples in each group, $n = 5$.* indicate $p < 0.05$.

The amount of platelet adhesion on a single PEEK surface of each group was quantified using the LDH assay and the results are shown in Figure 3B. The number of platelets adhered to the surface of each PK group was 122.60 ± 32.50, which was the least of the four groups. The number of surface adherent platelets in each SP-PK group was 270.50 ± 70.75, which was significantly higher than that in the other three groups. The number of platelet adhesions on the surface of each ST-PK group and SA-PK group was 205.33 ± 20.66 and 201.13 ± 17.59, respectively, which was higher than that of the PK group and lower than that of the SP-PK group.

The results of PDGF-BB release from PRP coatings on different PEEK surfaces evaluated using Elisa kits are shown in Figure 3C. The release trend of PDGF-BB in the four groups was basically the same, and the release gradually decreased with the increase in time. At each time point accumulated from 0 h, the amount of PDGF-BB released was higher in the SP-PK group than in the other three groups. The amount of PDGF-BB released in the PK group was lower than that in the other three groups. Cumulative PDGF-BB release was consistently higher in the ST-PK group than in the SA-PK group until 4 h after which the cumulative release was reversed in both groups. In addition, as shown in Figure 1, the cumulative release of PDGF-BB at the beginning (0 h) and the end (24 h) were analyzed separately (Figures 3D, E). It can be found that the release of PDGF-BB in the SP-PK group was significantly higher than that in the other three groups at both time points, while no statistical difference was found among the other three groups.

3.3 *In vitro* cell-material interactions assay

3.3.1 Cell adherence

After MC3T3-E1 cells were cultured on the surface of each PEEK sample for 24 h, nuclei were stained with DAPI and counted, as shown in Figure 4A. It was evident that the nuclei on the surface of SP-PK group were the densest either before or after the incubation of PRP. It can be clearly seen that for the PEEK surface treated in the same way, the density of nuclei on the PEEK surface after PRP incubation was significantly higher than that before incubation. The nuclei on the surface of the SP-PK group were the densest either before or after PRP incubation. The number of nuclei in the ST-PK and SA-PK groups was significantly higher than that in the PK group, but there was no significant difference between the two groups. The above results were confirmed by the cell counts on the PEEK surface of each group shown in Figure 4B.

The cells were cultured on the PEEK surface of each group for 24 h, and the cell adhesion morphology was observed using SEM (Figure 4C). The cells on the surface of the PK group without PRP incubation tended to be undifferentiated and round with few cell pseudopodia. The cells on the surface of the PK group incubated with PRP and the other three groups without PRP showed mild differentiation and obvious pseudopodia. The cells on the surface of the SP-PK group, especially after the surface was incubated with PRP, appeared more stereoscopic and formed more connections between cells. The cells and their synapses are too large to enter the microstructures of ST-PK (P-ST-PK) and SA-PK(P-SA-PK) groups,

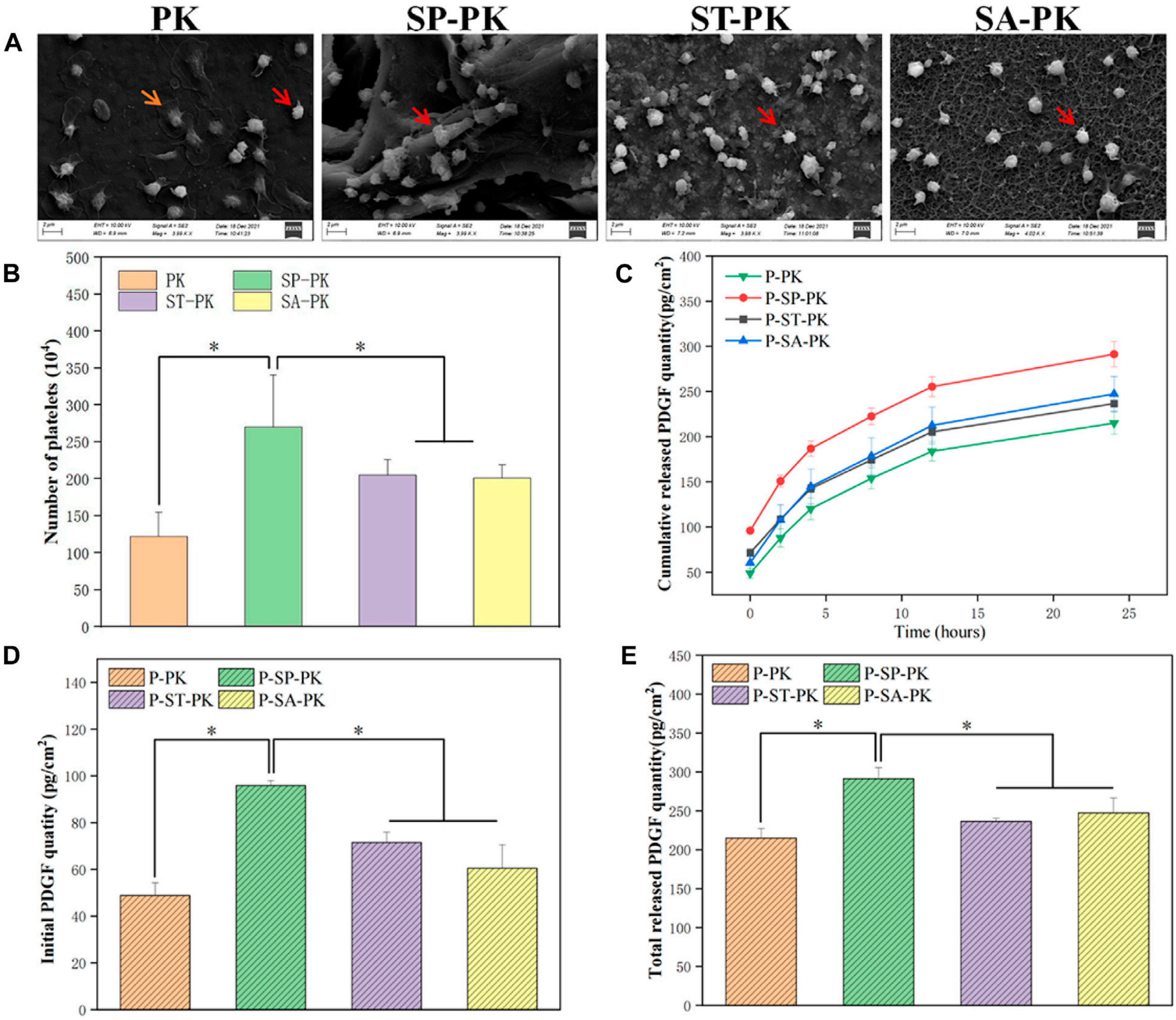

FIGURE 3
(A) SEM results of PEEK samples from each group after incubation with PRP. **(B)** Results of LDH assay for the number of platelets adhered to the surface of PEEK samples in each group, *n* = 3. **(C)** PDGF-BB release curves in each group, n = 3. **(D)** The initial release of PDGF-BB from the surface of each PEEK sample was measured, *n* = 3. **(E)** Final cumulative release of PDGF-BB from the surface of various PEEK samples, *n* = 3.* indicate $p < 0.05$.

but the cells can "climb" along the microstructures of SP-PK(P-SP-PK) group.

3.3.2 Cell proliferation

Figure 4D shows the results of cell proliferation using CCK-8 assay after culturing the cells on the surface of different samples in each group for 1,3, and 7 days. On the first day, the OD values of P-ST-PK and P-ST-PEEK groups were significantly higher than those of ST-PK and ST-PEEK groups, respectively. The OD values of cells on the surface of frosted PEEK were significantly higher than those in the other three groups, regardless of whether PRP was incubated or not. Meanwhile, the OD value of the P-ST-PK group was significantly higher than that of the P-SA-PK group. On the third day, the OD values of the P-SP-PK,P-ST-PK, and P-SA-PK groups were significantly higher than those of the SP-PK,ST-PK, and SA-PK groups. The P-PK group had a significantly lower OD value than the P-SP-PK,P-ST-PK, and P-SA-PK groups. On the seventh day, the P-SP-PK,P-ST-PK, and P-SA-PK groups showed significantly higher OD values than the SP-PK,ST-PK and SA-PK groups. The OD values of the P-SP-PK group were significantly higher than those of the other three groups after PRP incubation. These results indicated that surface incubation of PRP could improve cell proliferation ability of the modified PEEK surface. In this study, the frosted PEEK surface with PRP coating had the strongest ability to promote cell proliferation.

3.3.3 Cell differentiation

The ALP activity is one of the commonly used indicators to evaluate osteogenic differentiation ability of cells. Therefore, we performed ALP staining and quantitative evaluation of cells on the surface of different groups of samples at specific time points, and the results are shown in Figures 5A, B. ALP staining results at the same time point showed that before PRP incubation, the color of PK group was the lightest, and the color of SP-PK group was the darkest.

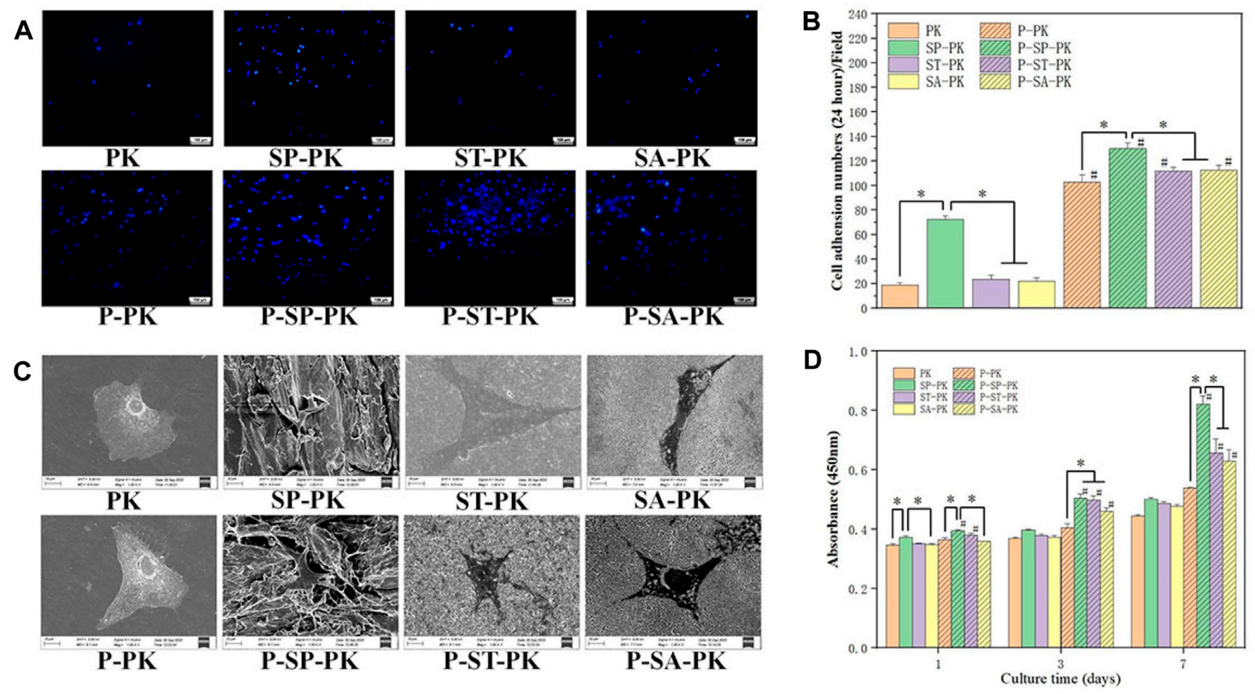

FIGURE 4
(A) DAPI staining of nuclei of adherent cells on the surface of PEEK samples from each group. **(B)** Quantitative analysis of the nuclei of adherent cells on the surface of each PEEK sample, $n = 3$. **(C)** SEM images of adherent cells on the surface of PEEK samples from each group. **(D)** CCK-8 results of the proliferation of MC-3T3-E1 cells on the PEEK surface of each group for 1,3, and 7 days, $n = 3$.* indicate $p < 0.05$, $^{\#}$ represents that compared with the same treatment method, the group incubated with PRP was significantly higher than the group not incubated, $p < 0.05$.

After incubation with PRP, the P-PK group showed the lightest staining and the P-SP-PK group showed the darkest staining. The staining of P-PK, P-SP-PK,P-ST-PK, and P-SA-PK groups was darker than that of PK, SP-PK,ST-PK, and SA-PK groups, respectively. These results tend to be consistent with the results of the quantitative analysis in Figure 2. The quantitative results on days 7 and 14 showed that the OD values of P-PK,P-SP-PK,P-ST-PK and P-SA-PK groups were higher than those of PK, SP and SA-PK groups without PRP incubation, respectively. The P-SP-PK group had a significantly higher OD value than the P-PK,P-ST-PK, and P-SA-PK groups. The OD values of the P-ST-PK and P-SA-PK groups were significantly higher than those of the P-PK group at 7 days. At 14 days, the P-ST-PK group had higher OD values than the P-PK group.

ARS staining and quantification represent an extracellular matrix calcium deposition in the late stages of osteogenic differentiation and the results are shown in Figures 5C, D. For APS staining, the trend between the groups was the same as for ALP staining described above. The P-SP-PK group had the most calcium deposition, which was bright red with large calcium nodules. The ARS quantitative analysis showed that the OD value of the SP-PK group was significantly higher than that of the PK group. The P-SP-PK group had significantly higher OD values than the other three groups incubated with PRP. The OD values of P-PK,P-SP-PK, and P-ST-PK groups were significantly higher than those of PK, SP and ST-PK groups, respectively.

Figures 5E–H show the expression levels of four osteogenic genes (Col-1,Rux-2,OPN,OCN) in surface cells of each group of samples. The results showed that the incubation of PRP significantly increased the expression level of osteogenic genes on different modified PEEK surfaces. The expression levels of osteogenic genes in the P-SP-PK group were significantly higher than those in the P-PK,P-ST-PK, and P-SA-PK groups. The expression levels of most osteogenic genes (Col-1,OPN,OCN) in P-ST-PK and P-SA-PK groups were significantly higher than those in P-PK group. There was no significant difference in the expression levels of most osteogenic genes between ST-PK and SA-PK groups, but the expression levels of half of the osteogenic genes in the P-ST-PK group were significantly higher than those in the P-SA-PK group. In the group without PRP incubation, the expression level of osteogenic genes in SP-PK group was the highest, and the expression level of osteogenic genes in SP-PK,ST-PK and SA-PK groups was significantly higher than that in PK group.

The above results indicate that PRP greatly enhances the ability of various PEEK surfaces to promote cell osteogenic differentiation. In this study, P-SP-PK was found to have the strongest ability to promote the osteogenic differentiation.

3.4 *In vivo* bone repair

3.4.1 Microcomputed tomography (Micro-CT) evaluation

The SD rat tibial defect model is a commonly used animal model to evaluate the osteogenic ability of implants. At 4 and 6 weeks after operation, the fixed tibial specimens described in 2.6.1 were scanned

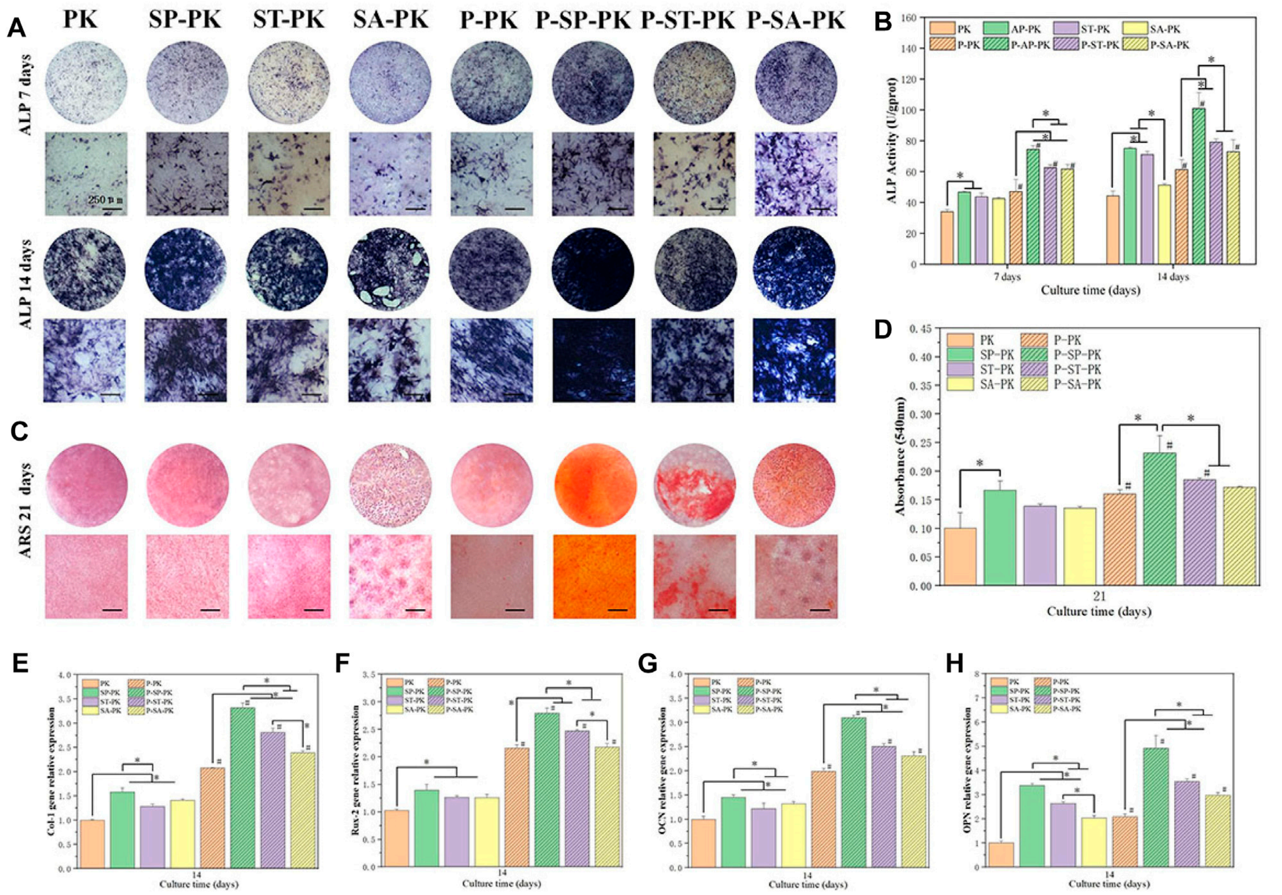

FIGURE 5

(A) ALP staining results of MC3T3-E1 cultured on PEEK surface for 7 days and 14 days in each group. **(B)** ALP quantitative analysis results of cells cultured on PEEK surface for 7 days and 14 days, *n* = 3. **(C)** ARS staining of cells cultured on PEEK surfaces for 21 days in each group. **(D)** Quantitative ARS analysis of cells cultured on PEEK surfaces for 21 days in each group, *n* = 3. **(E–H)** Osteogenesis-related gene (Col-1, Rux-2, OPN, OCN) expressions of MC3T3-E1 were evaluated by RT-qPCR (*n* = 3) 14 days after cultured on the surface of PEEK surface of each group, *n* = 3.* indicate $p < 0.05$, # represents that compared with the same treatment method, the group incubated with PRP was significantly higher than the group not incubated, $p < 0.05$.

by CT, three-dimensional reconstruction was performed, and the microstructure parameters of bone tissue were calculated. Using DATA Viewer processing, two-dimensional images were obtained, as shown in Figure 6A. The black rectangle where the orange triangle is located is the implanted PEEK material, and the white line shown by the red arrow is the new bone tissue around the material. At 4 weeks, new bone formation around the implants in the PK group was less and punctuated. In the ST-PK and SA-PK groups, the new bone formed a short continuous in the local area. The SP-PK group showed longer continuous new bone around the implant, and the new bone was thicker than the other three groups. At 4 weeks, the new bone around the implants in each PRP group roughly wrapped the implants in a U-shape, and the new bone in the P-SP-PK and P-ST-PK groups was significantly thicker than that in the other two groups. In the P-SP-PK group, the continuous new bone was also formed at the open end of the implant (green arrow). Meanwhile, the new bone formation around the implants in P-PK, P-SP-PK, P-ST-PK and P-SA-PK groups was more continuous and thicker than that in PK, SP-PK, ST-PK and SA-PK groups, respectively. At 8 weeks, the new bone mass around the implants in each group was consistent with that at 4 weeks: P-PK > PK, P-SP-PK > SP-PK, P-ST-PK > ST-PK, P-SA-PK > SA-PK, and at the same time: PK < ST-PK/SA-PK < SP-PK. P-PK < P-ST-PK/P-SA-PK < P-SP-PK.

Figure 6F shows the 3D reconstruction results of 4-week and 8-week tibial specimens from each group. The gray columns are the reconstructed PEEK implants of each group, and the new bone on the surface is blue-purple. The volume of new bone attached to the prosthesis surface in each group incubated with PRP was significantly higher than that in each group without incubated PRP. With the extension of time, the volume of new bone on the implant surface of each group at 8 weeks was significantly higher than that at 4 weeks. The volume of new bone around the implants was the largest in the P-SP-PK group at either 4 or 8 weeks.

The results of CT were further evaluated by quantitative analysis, including bone volume fraction (BV/TV), trabecular bone number (Tb. N), trabecular bone thickness (Tb. Th), and trabecular bone separation (Tb. Sp) (Figures 6B–E). The BV/TV, Tb. N and Tb. Th of each group incubated with PRP was significantly higher than that of each group incubated without PRP Among all the groups BV/TV, Tb. N and Tb. Th in the P-SP-PK group was

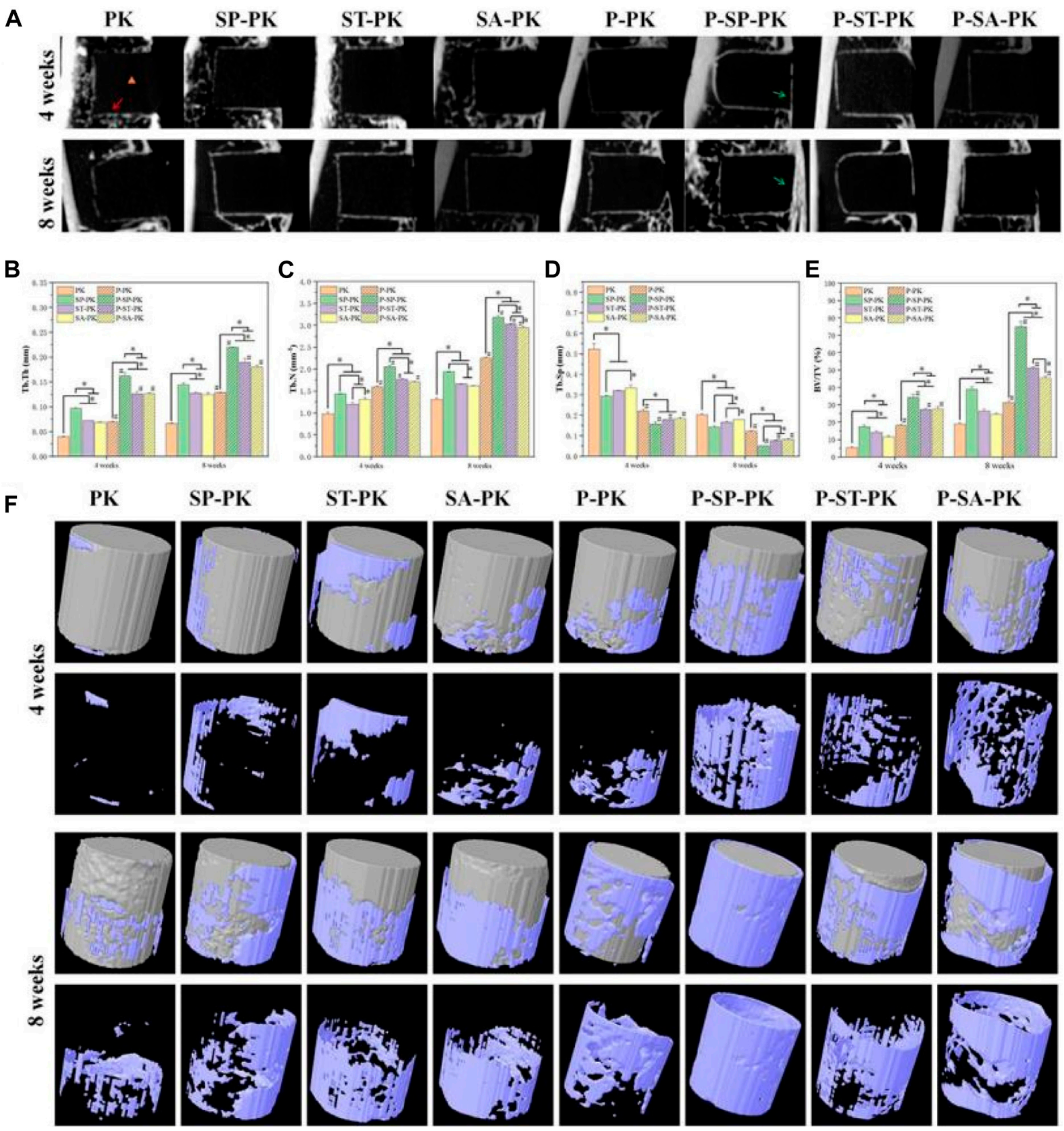

FIGURE 6
(A) 2D images of *in vivo* osteogenesis in each group of samples. Yellow triangle: PEEK material location; Red arrow: new bone; Green arrow: new bone at the tibial burr site. **(B–E)** Quantitative analysis of *in vivo* samples of each group for bone volume fraction (BV/TV), trabecular bone number (Tb. N), trabecular bone thickness (Tb. Th) and trabecular bone separation (Tb. Sp), $n = 3$. **(F)** 3D reconstruction of PEEK samples and surrounding new bone in each group. PEEK samples are shown in gray, and new bone is shown in blue. * indicate $p < 0.05$, # represents that compared with the same treatment method, the group incubated with PRP was significantly higher than the group not incubated, $p < 0.05$.

significantly higher than that in the other groups. At the same time, the trend of the results of Tb. Sp is opposite to that described above.

3.4.2 Histological evaluation

The HE staining results of the tibial specimens at 8 weeks are shown in Figure 7A. The position of the black triangle is the space left after the removal of the implant, the red arrow shows the new bone, and the yellow triangle shows the medullary cavity and bone marrow tissue. It can be clearly seen that the pink ring formed by the bone tissue around the implant in the HE staining results of each group incubated with PRP was more complete and the wall was thicker than that of each group without incubation with PRP. The new bone around the modified PEEK implant was significantly more than that around the original PEEK. Meanwhile, the P-SP-PK group had the most new bone formation among all groups.

Figure 7B shows the Sirius staining results of tibial specimens from each group at 8 weeks, showing the distribution of different types of collagen. The groups without PRP incubation were

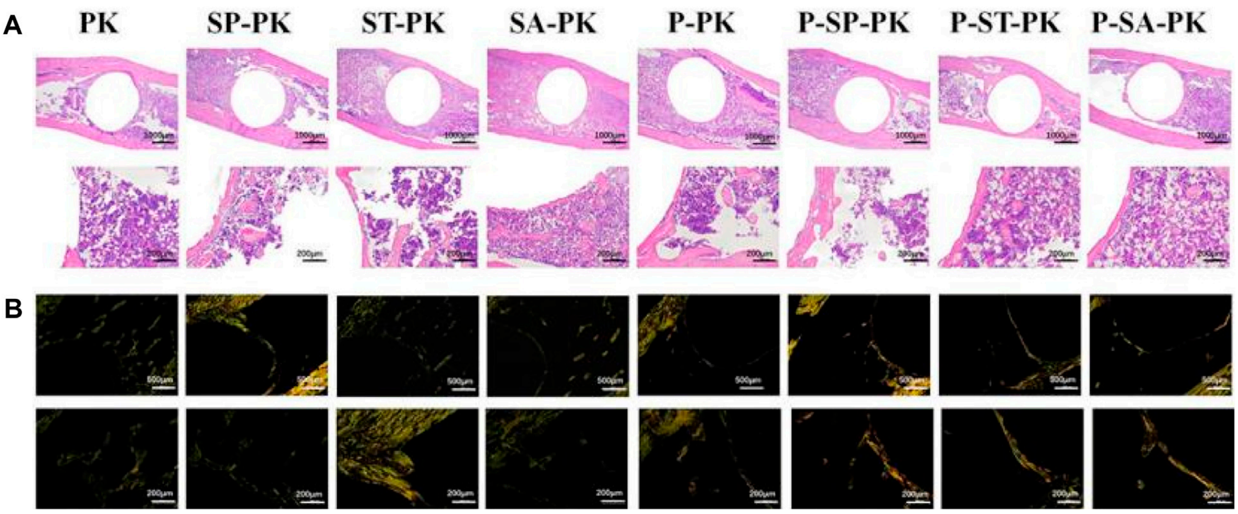

FIGURE 7
(A) The HE staining results of the tibial specimens of each group. **(B)** Sirius staining results of tibial specimens from each group; Orange represented typeIcollagen, green represented type III collagen.

dominated by green immature type III collagen. The green immature type III collagen was predominant in the groups without PRP incubation, whereas the mature orange type I collagen was predominant in the groups with PRP incubation. The P-SP-PK group showed the darkest orange among all groups.

Figure 8 show the immunofluorescence staining results of CON and OPN in tibial sample sections of each group at 8 weeks, respectively. In Figure 8A, the dark red represents the expression of OCN and the blue is the nucleus. In Figure 8B, the bright red represents OPN expression and the blue represents the nucleus. It could be seen that the expressions of OCN and OPN in the PRP incubated group were obviously higher than those in the non-incubated group, respectively:the red ring expression band was more complete and the wall was wider. The expression of OCN/OPN in each PEEK surface modification group was significantly higher than that in the original PEEK group, and the P-SP-PK group had the highest expression.

4 Discussion

In the process of bone defect repair, it is important to find suitable bone replacement materials. At present, bone replacement materials used in clinical practice mainly include metal, ceramic, and autologous (allogeneic) bone grafts. However, they all have limitations, such as high elastic modulus, large brittleness, and are difficult to obtain (HuiskesWeinans and Van, 1992).At present, bone replacement materials used in clinical practice mainly include metal, ceramic, and autologous (allogeneic) bone grafts. However, they all have limitations such as high elastic modulus, large brittleness, and difficulty in obtaining them (Kokubo et al., 2003). In recent years, PEEK has become one of the most promising bone replacement materials due to its mechanical strength and elastic modulus close to bone, chemical inertance, and radiation permeability. However, the high hydrophobicity and biological inertness of raw PEEK materials are not conducive to the adhesion, proliferation and differentiation of bone cells on its surface, which hinders its clinical application. Therefore, modification of PEEK materials to improve their biological activity has become a hot research topic (Gu et al., 2021; Dondani et al., 2023).

In this study, three methods were selected to modify the surface structure of PEEK, including sandpaper grinding, concentrated sulfuric acid sulfonation and sulfur trioxide gas fumigation. The three modification methods have their own characteristics. Sandpaper polishing is one of the simplest ways of PEEK surface modification, which can significantly improve the surface roughness of PEEK. Previous studies have shown that exfoliated PEEK surfaces can promote the proliferation and differentiation of rat bone marrow mesenchymal stem cells *in vitro*. In orthopedic clinics, hydroxyapatite coating that alters the surface roughness of metals is also one of the mature methods to improve the ability of joint prosthesis surface to integrate with the host bone (Søballe, 1993). Sulfuric acid can form 3-dimensional connected pore structure on PEEK surface through sulfation, thereby improving the bioactivity of PEEK surface. At the same time, these pore structures increase the ability of the PEEK surface to carry drugs and bioactive molecules, providing a basis for further improving the biological activity of PEEK. In our previous study, gaseous sulfur trioxide was used to fabricate a hydrophilic and porous PEEK surface. The study has shown that the surface has good mineralization ability and is conducive to cell adhesion, proliferation and differentiation (Wan et al., 2020).

According to the SEM picture results, it can be seen that the size of the microstructure produced by sandpaper polishing on the PEEK surface is much larger than that of the other two methods. We believe that this difference in microstructure size is one of the reasons why the polished sandpaper surface can carry PRP much more than the other two. EDS results showed that the content of S element on the surface of the ST-PK group was much higher than

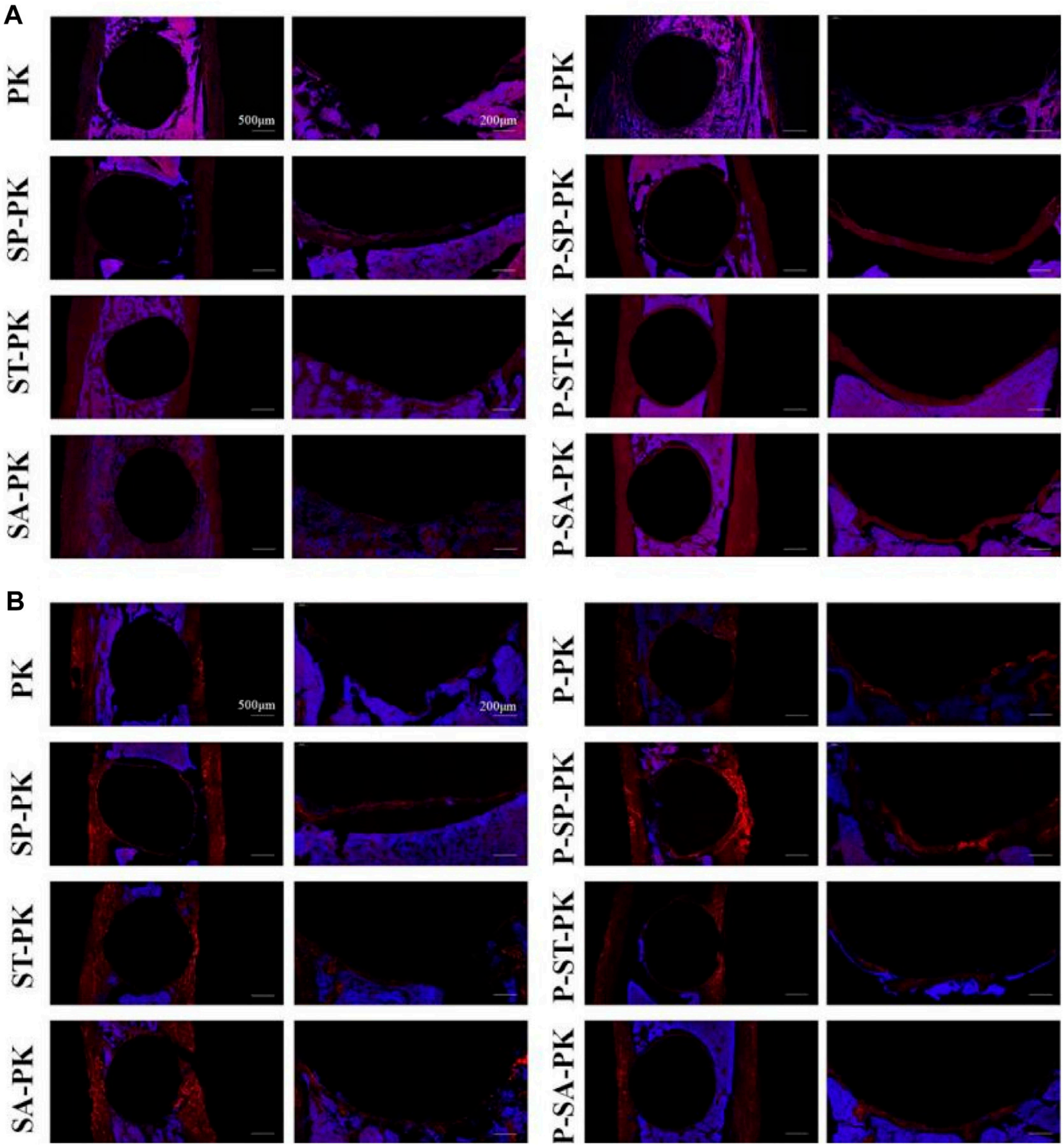

FIGURE 8
(A) OCN immunofluorescence staining of tibial samples from each group. Red represents the expression of OCN, and blue is the nucleus. **(B)** OPN immunofluorescence staining of tibial samples from each group. Red represents the expression of OPN, and blue is the nucleus.

that of the other three groups. Combined with the FTIR results, we speculate that the S element is in the form of -SO$_3$H on the surface of PEEK materials in ST-PK group. Previous studies have shown that sulfonation of PEEK in concentrated sulfuric acid is accompanied by mild dissolution of PEEK materials (Ma et al., 2020). However, according to our observation, in the reaction between gaseous sulfur trioxide and PEEK, a darker and darker yellow coating will be formed on PEEK surface over time. We believe that this coating protects PEEK to some extent from further corrosion by gaseous sulfur trioxide while also ensuring adequate reaction of the same layer of PEEK surface with sulfur trioxide. Thus, the micropores on the PEEK surface of the ST-PK group were less dense than those of the SA-PK group, as observed in the SEM images. At the same time, the more adequate reaction of the PEEK surface with gaseous sulfur trioxide made the PEEK surface of the ST-PK group contain more -SO$_3$H than that of the SA-PK group, and therefore have more S elements. The abrasive surface of PEEK material reduces the hydrophilicity of PEEK material, which is consistent with the results of previous studies (Mahjoubi et al., 2017). There are many factors affecting the hydrophilicity of materials, including surface structure and surface group properties Even though the ST-PK group sample has increased roughness compared with the original PEEK material, the introduction of large amount of -SO3H still increases its hydrophilicity (Wang et al., 2016). However, for SA-PK group, the surface microstructure was still the main reason for the weakening of hydrophilicity because the amount of -SO3H introduced into the surface was too small.

Whether used as bone or dental implants, sufficient mechanical strength is a prerequisite for implant materials, especially compressive resistance (Koh et al., 2019). Therefore, we examined the compression resistance of different samples. Not surprisingly, the sulfur trioxe treated PEEK exhibits the closest compressive resistance to the original PEEK. This may be related to the protective ability of yellow colloidal coating formed on the PEEK surface during the reaction of PEEK with gaseous sulfur trioxide as we mentioned above. It is this yellow coating that prevents excessive dissolution of PEEK material. However, unexpectedly, the SP-PK group, which had a significantly larger surface microstructure under electron microscopy, performed better in the compressive stress test than the SA-PK group. This may be due to the rapid dissolution of PEEK in concentrated sulfuric acid. On the other hand, we used AFM to observe the finer structure of different groups of sample surfaces. The nanoscale surface roughness of SA-PK group was significantly higher than that of the other three groups, which also confirmed that the corrosion of PEEK material by concentrated sulfuric acid was significantly higher than that of the other groups, which was also the reason for the worst compressive resistance of SA-PK group.

PRP is rich in various growth factors which can promote the proliferation and differentiation of various cells. It has been widely used in orthopedics, cardiothoracic surgery, plastic surgery, dermatology, dentistry, and diabetic wound healing (Everts et al., 2021; Mijiritsky et al., 2021; Oneto and Etulain, 2021). In addition, several studies have reported that PRP has an immunomodulatory effect, which can promote the polarization of macrophages to anti-inflammatory M2, while inhibiting the polarization of macrophages to pro-inflammatory M1 (Jiang et al., 2021). Studies have shown that implants can trigger an inflammatory response after being implanted in the body, and excessive inflammatory response is not conducive to the integration of implants with the host (Brown and Badylak, 2013; Klopfleisch and Jung, 2017). At the same time, wear particles produced after joint prosthesis implantation will trigger macrophage M1 polarization, which will lead to osteolysis and ultimately implant failure (Gao et al., 2018; Guo et al., 2022; Lu et al., 2023). All these results indicate that PRP is a potentially ideal bioactive coating on PEEK surface. However, most of the existing studies are on doping of PRP with other degradable materials. Therefore, this study can be regarded as a preliminary attempt to apply PRP on a PEEK surface alone. Although previous studies have shown that exogenous growth factors on the surface of PEEK have a good osteopromoting effect, PRP still has two major advantages: autologous and relatively low cost. In other words, the autologous PRP coating on the PEEK surface will not cause immune rejection; the mature PRP preparation technology reduces the threshold for promotion.

The electron microscope images of PRP adhered to the PEEK surface of each group showed that the platelets on the surface of the samples in P-SP-PK,P-ST-PK and P-SA-PK groups were mostly inactive and spherical (Goodman, 1999), which was beneficial to the preservation of platelets and the release of more growth factors after implantation *in vivo*. Although PRP can be activated in many ways, such as repeated freezing and thawing, the use of activators, etc. In this study, we did not use any activation method to activate PRP *in vitro*. The main reasons are as follows: 1. The use of *in vitro* activation can produce a strong platelet activation effect, which may affect our judgment on the effect of PEEK morphology on platelet status and growth factor release; 2. Activated platelets release a large amount of growth factors in a short period of time, and exposure of growth factors to PEEK surface for too long may affect their biological activity; 3. There is a large amount of collagen in the extracellular matrix and the body, and studies have shown that collagen itself is a good activator of PRP (Hechtman et al., 2011; Zhang et al., 2019). At the same time, the large surface microstructure of SP-PK is most conducive to the capture of platelets. This is also the reason why the samples in PRP-SP-PK group released the most PDGF-BB. It should be noted that the amount of PDGF-BB released at 0 was not zero in each group. This indicated that the PRP solution itself contained PDGF-BB and was adsorbed on the surface of samples in each group. At the same time, we believe that the large size of the microstructure on the surface of SP-PK expanded the adsorption area and was conducive to the adsorption of PDGF-BB, which was the reason why the samples in SP-PK group adsorbed the most PDGF-BB at 0 h. Hydrophilicity is one of the factors affecting cell adhesion on the surface of materials, and hydrophilic materials are more conducive to cell adhesion. It is obvious that the three PEEK surface modification methods in this study all changed the water contact Angle of PEEK material to varying degrees. However, the most hydrophobic group of SP-PK samples had the most platelets adhering to their surfaces. We speculated that in this study, the surface structure of PEEK was still the main influencing factor in the process of PRP incubation.

We used DAPI to stain the nuclei of MC3T3-E1 on the surface of each group; platelets did not have nuclei and could not be stained. The number of nuclei on the surface of the samples in each group incubated with PRP was significantly higher than that in the non-incubated groups. This indicates that PRP coating significantly improves the cell affinity of PEEK surface and facilitates cell adhesion. At the same time, electron microscope images showed that the number of cell pseudopodia on the surface of each group of samples incubated with PRP was more, which also confirmed that PRP coating improved the cell adhesion ability of PEEK material (Liu et al., 2018; Wan et al., 2019). In the SEM images, the cells were embedded in the surface microstructure of the sanded PEEK, indicating that the larger microstructure can be beneficial to the capture of cells, which is also the reason why the number of cell adhesion in the SP-PK group is much more than that in the PK, ST-PK and SA-PK groups. For each group incubated with PRP, the number of platelets and growth factors incubated on the surface was the determinant of the number of adherent MC3T3-E1 cells. In addition, SEM images showed that the cells in PK, ST-PK and SA-PK groups spread better than those in SP-PK group, indicating that the flat surface of the material was more conducive to cell spreading. However, in practical clinical applications, the surface of materials such as SP-PK group that can incorporate cells can better achieve bone ingrosis, thereby enhancing the bonding force between the material and bone (Kuboki et al., 2001).

PRP is enriched with various growth factors, including VEGF, TGF, and PDGF. Previous studies have shown that these growth factors promote osteocyte proliferation (Wu et al., 2016; Hu and Olsen, 2017; Wang et al., 2023). Therefore, in the CCK-8 test, cell proliferation on the surface of the samples in each group incubated with PRP was significantly higher than that in the non-incubated group. Because growth factors promoted cell proliferation in a dose-dependent manner, the P-SP-PK group samples loaded with the most PRP had the strongest ability to promote cell proliferation. ALP is an important mineralization enzyme in the process of bone formation, metabolism, and regeneration. ALP activity is a marker activity in the early differentiation stage of osteoblasts, and it is a characteristic index to evaluate the differentiation of osteoblasts (Bai et al., 2020). Calcified nodules are another important indicator for osteoblast identification under *in vitro* culture conditions. When cultured *in vitro*, osteoblasts can not only show cell proliferation, differentiation, and matrix secretion but also form mineralized nodules similar to embryonic bone or woven bone *in vivo*, which is the last stage of osteoblast differentiation. Alizarin red staining is a specific staining for calcified nodules, which can directly reflect the mineralization ability of osteoblasts. In the ALP and ARS tests in this study, the groups incubated with PRP showed better ability to promote osteogenic differentiation than the groups without PRP. Numerous studies have confirmed that PRP can promote bone defects and has been widely used in clinical practice. However, the specific mechanism by which PRP promotes bone defect repair is still not fully understood. Although PDGF is a recombinant growth factor approved by the FDA for clinical use to promote bone regeneration, recent studies have shown that PDGF-BB alone does not significantly directly promote bone defect repair (Luvizuto et al., 2016; de Oliveira et al., 2017; Bai et al., 2020). However, studies have shown that PDGF-BB contributes to osteocyte proliferation and intraosseous angiogenesis (Wang et al., 2023). Studies have shown that TGF-β can promote the proliferation, chemotaxis, and early differentiation of osteoprogenitor cells through the Smad pathway and inhibit osteoclast differentiation by downregulating the RANKL/OPG secretion ratio (Wu et al., 2016). VEGF also plays an important role in bone defect repair. When the bone defect appears, blood vessels first invade the defect site, and then osteoprogenitor cells migrate to the defect to start the process of bone defect repair. The main role of VEGF is to promote angiogenesis and the integration of bone and neovascularization (Hu and Olsen, 2017; Grosso et al., 2023). Finally, in the RT-PCR assay, we confirmed that PRP coating on the PEEK surface significantly increased the expression of osteogenesis-related genes.

Next, to verify the osteogenic ability of the samples in each group *in vivo*, we established an SD rat tibial defect model. Tibia samples were collected at 4 and 8 weeks. In the 2D and 3D reconstructed CT images, it was obvious that the amount of new bone formation in the samples with PRP coating was significantly higher than that in the samples without PRP coating. The P-SP-PK group incubated with the most PRP had the most new bone formation. Subsequent quantitative analysis confirmed the above results. To further confirm the molecular mechanism of osteogenesis promoted by PRP coating on the PEEK surface, we performed HE, Sirius red, and immunofluorescence staining on tibial specimens. HE stain confirmed the formation of more complete and wider new bone around PEEK samples with PRP coating in each group. Sirius staining is a method to distinguish the type of collagen. Bone contains up to 90% type I collagen, while bone containing more type III collagen represents the immature state (Adel-Khattab et al., 2020; Metwally et al., 2020). Therefore, in this study, the newly formed bone on the surface of the samples in each group with PRP coating, especially in the P-SP-PK group, was more mature than that in the groups without PRP coating. Osteopontin (OPN) is secreted by osteoblasts and stored in the bone matrix. It can induce the maturation of mineralized bone matrix, regulate the formation of hydroxyapatite and bone salt deposition (Hou et al., 2022). Osteocalcin (OCN) appears in the late stage of osteoblast differentiation and has the function of regulating calcium homeostasis (Karsenty and Ferron, 2012). Compared with the groups without PRP coating, the expressions of OPN and OCN in the groups with PRP coating were significantly increased, which confirmed the osteogenic ability of PRP coating. Similarly, the P-SP-PK group expressed the most OPN and OCN.

However, this study still has some limitations. Firstly the release time of growth factors in PRP coating in this study was short. Second, although the PRP extraction procedure is mature, the loading efficiency of PRP is low when preparing native PRP layer on the PEEK surface. Finally, the immunoregulation and angiogenesis ability of the PRP coating on PEEK were not investigated in this study. In the future study, we plan to develop a PRP gel coating on PEEK surface to enable the sustained release of growth factors. The immunomodulatory and angiogenic effects of PRP coating on PEEK were also investigated.

5 Conclusion

In summary, three modifications were carried out on PEEK, including sandpaper grinding, gaseous sulfur trioxide fumigation and sulfuric acid sulfonation, and PRP coating was incubated on the PEEK surfaces. Among the three PEEK modified surfaces, the frosted surface was considered to be the most suitable surface for the preparation of PRP coating due to the most PRP carrying. *In vitro* and *in vivo* experiments, the PRP coating on the PEEK surface significantly improved its cell affinity, greatly promoted cell proliferation and differentiation, and finally achieved the ability to promote bone defect repair. All three modified surfaces enhanced the ability of PEEK to carry PRP, thereby further enhancing osteogenesis. Among them, the sandpaper surface was equipped with the most PRP and had the strongest osteogenic ability.

Data availability statement

The raw data supporting the conclusions of this article will be made available by the authors, without undue reservation.

Ethics statement

The animal study was approved by the Laboratory Animal Welfare and Ethics Committee at the Changchun Institute of Applied Chemistry, Chinese Academy of Sciences. The study was conducted in accordance with the local legislation and institutional requirements.

Author contributions

XS: Data curation, Investigation, Methodology, Software, Visualization, Writing–original draft, Writing–review and editing. ZW: Investigation, Methodology, Software, Writing–original draft, Writing–review and editing. MG: Data curation, Formal Analysis, Investigation, Writing–original draft, Writing–review and editing. YW: Methodology, Software, Writing–original draft, Writing–review and editing. ZB: Formal Analysis, Investigation, Software, Writing–original draft, Writing–review and editing. DL: Methodology, Project administration, Visualization, Writing–original draft, Writing–review and editing. PZ: Conceptualization, Methodology, Resources, Supervision, Writing–original draft, Writing–review and editing. JL: Conceptualization, Funding acquisition, Project administration, Supervision, Writing–original draft, Writing–review and editing.

Funding

The authors declare financial support was received for the research, authorship, and/or publication of this article. This work was financially supported by Jilin Province Development and Reform Commission (2020C030-2).

Conflict of interest

The authors declare that the research was conducted in the absence of any commercial or financial relationships that could be construed as a potential conflict of interest.

Publisher's note

References

Adel-Khattab, D., Abu el Sadat, S. M., Aboul-Fotouh, M. N., Tarek, K., and Horowitz, R. A. (2020). Bone regeneration and graft material resorption in extraction sockets grafted with bioactive silica-calcium phosphate composite (SCPC) versus non-grafted sockets: clinical, radiographic, and histological findings. *J. periodontal and implant Sci.* 50 (6), 418–434. doi:10.5051/jpis.2000040002

Bai, H., Cui, Y., Wang, C., Wang, Z., Luo, W., Liu, Y., et al. (2020). 3D printed porous biomimetic composition sustained release zoledronate to promote osteointegration of osteoporotic defects. *Mater. Des.* 189, 108513. doi:10.1016/j.matdes.2020.108513

Brown, B. N., and Badylak, S. F. (2013). Expanded applications, shifting paradigms and an improved understanding of host-biomaterial interactions. *Acta biomater.* 9 (2), 4948–4955. doi:10.1016/j.actbio.2012.10.025

de Oliveira, S., César, J., Sonoda, C. K., Poi, W. R., Garcia Júnior, I. R., and Luvizuto, E. R. (2017). Evaluation of the osteoinductive effect of PDGF-BB associated with different carriers in bone regeneration in bone surgical defects in rats. *Implant Dent.* 26 (4), 559–566. doi:10.1097/ID.0000000000000580

Dondani, Jay, R., and Tran, S. D. (2023). Surface treatments of PEEK for osseointegration to bone. *Biomolecules* 13 (3), 464. doi:10.3390/biom13030464

Ehrenfest, D., David, M., and Albrektsson, T. (2009). Classification of platelet concentrates: from pure platelet-rich plasma (P-PRP) to leucocyte- and platelet-rich fibrin (L-PRF). *Trends Biotechnol.* 27 (3), 158–167. doi:10.1016/j.tibtech.2008.11.009

Everts, P. A., van Erp, A., DeSimone, A., Cohen, D. S., and Gardner, R. D. (2021). Platelet rich plasma in orthopedic surgical medicine. *Platelets* 32 (2), 163–174. doi:10.1080/09537104.2020.1869717

Gao, X.-R., Ge, J., Li, W. y., Zhou, W. c., Xu, L., and Geng, D. q. (2018). NF-κB/let-7f-5p/IL-10 pathway involves in wear particle-induced osteolysis by inducing M1 macrophage polarization. *Cell cycleGeorget. Tex.)* 17 (17), 2134–2145. doi:10.1080/15384101.2018.1515549

Goodman, S. L. (1999). Sheep, pig, and human platelet-material interactions with model cardiovascular biomaterials. *J. Biomed. Mater. Res.* 45 (3), 240–250. doi:10.1002/(sici)1097-4636(19990605)45:3<240::aid-jbm12>3.0.co;2-c

Grosso, A., Lunger, A., Burger, M. G., Briquez, P. S., Mai, F., Hubbell, J. A., et al. (2023). VEGF dose controls the coupling of angiogenesis and osteogenesis in engineered bone. *NPJ Regen. Med.* 8 (1 15), 15. doi:10.1038/s41536-023-00288-1

Grunkemeier, J. M., Tsai, W. B., and Horbett, T. A. (1998). Hemocompatibility of treated polystyrene substrates: contact activation, platelet adhesion, and procoagulant activity of adherent platelets. *J. Biomed. Mater. Res.* 41 (4), 657–670. doi:10.1002/(sici)1097-4636(19980915)41:4<657::aid-jbm18>3.0.co;2-b

Gu, X., Sun, X., Sun, Y., Wang, J., Liu, Y., Yu, K., et al. (2021). Bioinspired modifications of PEEK implants for bone tissue engineering. *Front. Bioeng. Biotechnol.* 8 631616. doi:10.3389/fbioe.2020.631616

Guo, X., Bai, J., Ge, G., Wang, Z., Wang, Q., Zheng, K., et al. (2022). Bioinspired peptide adhesion on Ti implants alleviates wear particle-induced inflammation and improves interfacial osteogenesis. *J. colloid interface Sci.* 605, 410–424. doi:10.1016/j.jcis.2021.07.079

Hechtman, K. S., Uribe, J. W., Botto-vanDemden, A., and Kiebzak, G. M. (2011). Platelet-rich plasma injection reduces pain in patients with recalcitrant epicondylitis. *Orthopedics* 34 (2), 92. doi:10.3928/01477447-20101221-05

Hou, P., Sun, Y., Yang, W., Wu, H., Sun, L., Xiu, X., et al. (2022). Magnesium promotes osteogenesis via increasing OPN expression and activating CaM/CaMKIV/CREB1 pathway. *J. Biomed. Mater. Res. Part B, Appl. biomaterials* 110 (7), 1594–1603. doi:10.1002/jbm.b.35020

Hu, K., and Olsen, B. R. (2017). Vascular endothelial growth factor control mechanisms in skeletal growth and repair. *Dev. Dyn.* 246 (4), 227–234. an official publication of the American Association of Anatomists. doi:10.1002/dvdy.24463

HuiskesWeinans, R. H., and Van, R. B. (1992). The relationship between stress shielding and bone resorption around total hip stems and the effects of flexible materials. *Clin. Orthop. Relat. Res.* 274, 124–134. doi:10.1097/00003086-199201000-00014

Imagama, S., Ando, K., Kobayashi, K., Ishikawa, Y., Nakamura, H., Hida, T., et al. (2017). Efficacy of early fusion with local bone graft and platelet-rich plasma in lumbar spinal fusion surgery followed over 10 years. *Glob. spine J.* 7 (8), 749–755. doi:10.1177/2192568217696690

Jiang, G., Li, S., Yu, K., He, B., Hong, J., Xu, T., et al. (2021). A 3D-printed PRP-GelMA hydrogel promotes osteochondral regeneration through M2 macrophage polarization in a rabbit model. *Acta biomater.* 128, 150–162. doi:10.1016/j.actbio.2021.04.010

Karsenty, G., and Ferron, M. (2012). The contribution of bone to whole-organism physiology. *Nature* 481, 7381 314–320. doi:10.1038/nature10763

Kim, H. J., Kim, K. H., Lee, Y. M., Ku, Y., Rhyu, I. C., and Seol, Y. J. (2021). In ovariectomy-induced osteoporotic rat models, BMP-2 substantially reversed an impaired alveolar bone regeneration whereas PDGF-BB failed. *Clin. oral Investig.* 25 (11), 6159–6170. doi:10.1007/s00784-021-03915-7

Klopfleisch, R., and Jung, F. (2017). The pathology of the foreign body reaction against biomaterials. *J. Biomed. Mater. Res. Part A* 105 (3), 927–940. doi:10.1002/jbm.a.35958

Koh, Y.-G., Park, K. M., Lee, J. A., Nam, J. H., Lee, H. Y., and Kang, K. T. (2019). Total knee arthroplasty application of polyetheretherketone and carbon-fiber-reinforced polyetheretherketone: a review. *Mater. Sci. Eng. C, Mater. Biol. Appl.* 100, 70–81. doi:10.1016/j.msec.2019.02.082

Kokubo, T., Kim, H. M., and Kawashita, M. (2003). Novel bioactive materials with different mechanical properties. *Biomaterials* 24 (13), 2161–2175. doi:10.1016/s0142-9612(03)00044-9

Kuboki, Y., Jin, Q., and Takita, H. (2001). Geometry of carriers controlling phenotypic expression in BMP-induced osteogenesis and chondrogenesis. *American* 83, S105–S115.

Lee, W.-T., Koak, J., Lim, Y., Kim, S., Kwon, H., and Kim, M. (2012). Stress shielding and fatigue limits of poly-ether-ether-ketone dental implants. *J. Biomed. Mater. Res. Part B, Appl. biomaterials* 100 (4), 1044–1052. doi:10.1002/jbm.b.32669

Liu, W., Li, J., Cheng, M., Wang, Q., Yeung, K. W. K., Chu, P. K., et al. (2018). Zinc-modified sulfonated polyetheretherketone surface with immunomodulatory function for guiding cell fate and bone regeneration. *Adv. Sci. (Weinheim, Baden-Wurttemberg, Ger.* 5 (10), 1800749. doi:10.1002/advs.201800749

Lu, Y., Xu, X., Yang, C., Hosseinkhani, S., Zhang, C., Luo, K., et al. (2023). Copper modified cobalt-chromium particles for attenuating wear particle induced-inflammation and osteoclastogenesis. *Biomater. Adv.* 147, 213315. doi:10.1016/j.bioadv.2023.213315

Luvizuto, Eloá, R., Dobsak, T., Reich, K., Gruber, R., Sonoda, C. K., et al. (2016). Effect of recombinant PDGF-BB on bone formation in the presence of β-tricalcium phosphate and bovine bone mineral matrix: a pilot study in rat calvarial defects. *BMC oral health* 16 (1 52), 52. doi:10.1186/s12903-016-0210-3

Ma, R., Wang, J., Ma, K., Wei, J., Yang, P., et al. (2020). Effects of different sulfonation times and post-treatment methods on the characterization and cytocompatibility of sulfonated PEEK. *J. biomaterials Appl.* 35 (3), 342–352. doi:10.1177/0885328220935008

Mahjoubi, H., Buck, E., Manimunda, P., Farivar, R., Chromik, R., Murshed, M., et al. (2017). Surface phosphonation enhances hydroxyapatite coating adhesion on polyetheretherketone and its osseointegration potential. *Acta biomater.* 47, 149–158. doi:10.1016/j.actbio.2016.10.004

Metwally, S., Ferraris, S., Spriano, S., Krysiak, Z. J., Kaniuk, Ł., Marzec, M. M., et al. (2020). Surface potential and roughness controlled cell adhesion and collagen formation in electrospun PCL fibers for bone regeneration. *Mater. Des.* 194, 108915. doi:10.1016/j.matdes.2020.108915

Mijiritsky, E., Assaf, H. D., Peleg, O., Shacham, M., Cerroni, L., and Mangani, L. (2021). Use of PRP, PRF and CGF in periodontal regeneration and facial rejuvenation-A narrative review. *Biology* 10, 317. doi:10.3390/biology10040317

Miroshnychenko, O., Chalkley, R. J., Leib, R. D., Everts, P. A., and Dragoo, J. L. (2020). Proteomic analysis of platelet-rich and platelet-poor plasma. *Regen. Ther.* 15 226, 226–235. doi:10.1016/j.reth.2020.09.004

Nagao, Ryan, J., Wang, Y., Wang, L., Arakawa, C., DeForest, C., et al. (2019). Transforming endothelium with platelet-rich plasma in engineered microvessels. *Adv. Sci. (Weinheim, Baden-Wurttemberg, Ger.* 6 (24), 1901725. doi:10.1002/advs.201901725

Niki, Y., Matsumoto, H., Otani, T., Suda, Y., and Toyama, Y. (2001). Metal ion concentrations in the joint fluid immediately after total knee arthroplasty. *Mod. Rheumatol.* 11 (3), 192–196. doi:10.1007/s101650170003

Oneto, P., and Etulain, J. (2021). PRP in wound healing applications. *Platelets* 32 (2), 189–199. doi:10.1080/09537104.2020.1849605

Pan, W., Dai, C., Li, Y., Yin, Y., Gong, L., Machuki, J. O., et al. (2020). PRP-chitosan thermoresponsive hydrogel combined with black phosphorus nanosheets as injectable biomaterial for biotherapy and phototherapy treatment of rheumatoid arthritis. *Biomaterials* 239, 119851. doi:10.1016/j.biomaterials.2020.119851

Quarto, R., and Giannoni, P. (2016). Bone tissue engineering: past-present-future. *Methods Mol. Biol.* 1416, 21–33. doi:10.1007/978-1-4939-3584-0_2

Ruiter, L. D., Rankin, K., Browne, M., Briscoe, A., Janssen, D., and Verdonschot, N. (2021). Decreased stress shielding with a PEEK femoral total knee prosthesis measured in validated computational models. *J. biomechanics* 118 (2021), 110270. doi:10.1016/j.jbiomech.2021.110270

Søballe, K. (1993). Hydroxyapatite ceramic coating for bone implant fixation. Mechanical and histological studies in dogs. *Acta Orthop. Scand. Suppl.* 255, 1–58. doi:10.3109/17453679309155636

Sunarso, Tsuchiya, A., Fukuda, N., Toita, R., Tsuru, K., and Ishikawa, K. (2018). Effect of micro-roughening of poly(ether ether ketone) on bone marrow derived stem cell and macrophage responses, and osseointegration. *J. biomaterials Sci.* 29, 1375–1388. doi:10.1080/09205063.2018.1461448

Tamada, Y., Kulik, E. A., and Ikada, Y. (1995). Simple method for platelet counting. *Biomaterials* 16 (3), 259–261. doi:10.1016/0142-9612(95)92126-q

Vogel, D., Wehmeyer, M., Kebbach, M., Heyer, H., and Bader, R. (2021). Stress and strain distribution in femoral heads for hip resurfacing arthroplasty with different materials: a finite element analysis. *J. Mech. Behav. Biomed. Mater.* 113 (2021), 104115. doi:10.1016/j.jmbbm.2020.104115

Wan, T., Jiao, Z., Guo, M., Wang, Z., Wan, Y., Lin, K., et al. (2020). Gaseous sulfur trioxide induced controllable sulfonation promoting biomineralization and osseointegration of polyetheretherketone implants. *Bioact. Mater.* 5 (4), 1004–1017. doi:10.1016/j.bioactmat.2020.06.011

Wan, T., Li, L., Guo, M., Jiao, Z., Wang, Z., Ito, Y., et al. (2019). Immobilization via polydopamine of dual growth factors on polyetheretherketone: improvement of cell adhesion, proliferation, and osteo-differentiation. *J. Mater. Sci.* 54, 11179–11196. doi:10.1007/s10853-018-03264-z

Wang, F., Ye, Y., Zhang, Z., Teng, W., Sun, H., Chai, X., et al. (2023). PDGFR in PDGF-BB/PDGFR signaling pathway does orchestrates osteogenesis in a temporal manner. *Res. Wash. D.C.)* 6, 0086. doi:10.34133/research.0086

Wang, Z., Chen, L., Wang, Y., Chen, X., and Zhang, P. (2016). Improved cell adhesion and osteogenesis of op-HA/PLGA composite by poly(dopamine)-assisted immobilization of collagen mimetic peptide and osteogenic growth peptide. *ACS Appl. Mater. interfaces* 8 (40), 26559–26569. doi:10.1021/acsami.6b08733

Wu, Y., Huo, S., Liu, S., Hong, Q., Wang, Y., and Lyu, Z. (2023). Cu–Sr bilayer bioactive glass nanoparticles/polydopamine functionalized polyetheretherketone enhances osteogenic activity and prevents implant-associated infections through spatiotemporal immunomodulation. *Adv. Healthc. Mater*, e2301772. undefined. doi:10.1002/adhm.202301772

Wu, J., Li, L., Fu, C., Yang, F., Jiao, Z., Shi, X., et al. (2018). Micro-porous polyetheretherketone implants decorated with BMP-2 via phosphorylated gelatin coating for enhancing cell adhesion and osteogenic differentiation. *Colloids surfaces. B, Biointerfaces* 169, 233–241. doi:10.1016/j.colsurfb.2018.05.027

Wu, M., Chen, G., and Li, Y. P. (2016). TGF-β and BMP signaling in osteoblast, skeletal development, and bone formation, homeostasis and disease. *Bone Res.* 4 (26), 16009. doi:10.1038/boneres.2016.9

Zavadil, Douglas, P., Costigan, J. M., Holt, D. W., and Shostrom, V. K. (2007). Autologous platelet gel and platelet-poor plasma reduce pain with total shoulder arthroplasty. *J. extra-corporeal Technol.* 39 (3), 177–182. doi:10.1051/ject/200739177

Zhang, N., Wang, K., Li, Z., and Luo, T. (2019). Comparative study of different anticoagulants and coagulants in the evaluation of clinical application of platelet-rich plasma (PRP) standardization. *Cell Tissue Bank.* 20 (1), 61–75. Epub 2019 Feb 6. PMID: 30729369. doi:10.1007/s10561-019-09753-y

Zhu, Y., Cao, Z., Peng, Y., Hu, L., Guney, T., and Tang, B. (2019). Facile surface modification method for synergistically enhancing the biocompatibility and bioactivity of poly(ether ether ketone) that induced osteodifferentiation. *ACS Appl. Mater. interfaces* 11 (31), 27503–27511. doi:10.1021/acsami.9b03030

Frontiers in Bioengineering and Biotechnology

TYPE Review
PUBLISHED 20 November 2023
DOI 10.3389/fbioe.2023.1271762

EDITED BY
Antonella Motta,
University of Trento, Italy

REVIEWED BY
Xuan Mei,
Harvard Medical School, United States
Jianxun Ding,
Chinese Academy of Sciences, China

*CORRESPONDENCE
Changjun Zheng,
✉ zhengchangjun9616@126.com
Fei Chang,
✉ ccfei_cn@hotmail.com

RECEIVED 02 August 2023
ACCEPTED 11 October 2023
PUBLISHED 20 November 2023

CITATION
Jia Y, Le H, Wang X, Zhang J, Liu Y, Ding J, Zheng C and Chang F (2023), Double-edged role of mechanical stimuli and underlying mechanisms in cartilage tissue engineering.
Front. Bioeng. Biotechnol. 11:1271762.
doi: 10.3389/fbioe.2023.1271762

Double-edged role of mechanical stimuli and underlying mechanisms in cartilage tissue engineering

Yao Jia[1,2], Hanxiang Le[1,3], Xianggang Wang[1], Jiaxin Zhang[1], Yan Liu[2], Jiacheng Ding[2], Changjun Zheng[1]* and Fei Chang[1]*

[1]Department of Orthopedics, The Second Hospital of Jilin University, Jilin, China, [2]The Second Bethune Clinical Medical College of Jilin University, Jilin, China, [3]The Fourth Treatment Area of Trauma Hip Joint Surgery Department, Tianjin Hospital, Tianjin, China

Mechanical stimuli regulate the chondrogenic differentiation of mesenchymal stem cells and the homeostasis of chondrocytes, thus affecting implant success in cartilage tissue engineering. The mechanical microenvironment plays fundamental roles in the maturation and maintenance of natural articular cartilage, and the progression of osteoarthritis Hence, cartilage tissue engineering attempts to mimic this environment *in vivo* to obtain implants that enable a superior regeneration process. However, the specific type of mechanical loading, its optimal regime, and the underlying molecular mechanisms are still under investigation. First, this review delineates the composition and structure of articular cartilage, indicating that the morphology of chondrocytes and components of the extracellular matrix differ from each other to resist forces in three top-to-bottom overlapping zones. Moreover, results from research experiments and clinical trials focusing on the effect of compression, fluid shear stress, hydrostatic pressure, and osmotic pressure are presented and critically evaluated. As a key direction, the latest advances in mechanisms involved in the transduction of external mechanical signals into biological signals are discussed. These mechanical signals are sensed by receptors in the cell membrane, such as primary cilia, integrins, and ion channels, which next activate downstream pathways. Finally, biomaterials with various modifications to mimic the mechanical properties of natural cartilage and the self-designed bioreactors for experiment *in vitro* are outlined. An improved understanding of biomechanically driven cartilage tissue engineering and the underlying mechanisms is expected to lead to efficient articular cartilage repair for cartilage degeneration and disease.

KEYWORDS

mechanical stimuli, cartilage tissue engineering, mechanoreceptor, downstream pathway, biomaterials

1 Introduction

Articular cartilage is a hyaline cartilage tissue consisting of chondrocytes and a rich extracellular matrix (ECM), mainly composed of proteoglycans, collagen type II, and water (Uzieliene et al., 2021). It serves as a shock absorber and covers the joint surface to create a low friction and load-bearing environment for joint motion (Bernhard and Vunjak-Novakovic, 2016). The articular cartilage is incredibly sensitive to mechanical stimuli.

Articular cartilage's mechanical characteristics are influenced by the microstructure of ECM, which is defined mainly by the mechanical environment. Three overlapping zones that extend from the surface to the subchondral bone can be found in the adult articular cartilage (Hodgkinson et al., 2022). Within these zones, the morphology of chondrocytes, as well as the content and architecture of ECM, reflect the forces experienced during joint motion. For example, type II collagen fibers are oriented perpendicular to the joint surface to resist compressive loads and parallel to the joint surface to disperse shear pressures (Wang Z. H. et al., 2022).

The development, pathology, and regeneration of articular cartilage tissue are fundamentally influenced by biomechanics. Atrophy and acinetatropbia are frequently caused by super-reduced biomechanical loading, although irreparable damage can sometimes be caused by mechanical overload (Le et al., 2020). A 2022 study showed that excessive mechanical load affects the progression of OA by regulating cartilage degradation. Mouse and human cartilage experiments both revealed that high-strain mechanical stress induces GPX4-associated ferroptosis in chondrocytes from OA patients. Piezo1-mediated calcium ion inflow plays a major role in this process, which can be blocked by GsMTx4, an inhibitor of Piezo1 (Wang S. et al., 2022). Additionally, the chondrocytes' physical microenvironment significantly affects the homeostasis and functionality of cartilage. Our previous research showed that biomechanical stimuli can improve cartilage regeneration. Bone marrow-derived cells extracted from patients during orthopedic surgery were divided into two groups, cultured in a rotating wall vessel (RWV) bioreactor or pellet culture as controls. The mechanical stimuli created by RWV significantly promote the formation of hyaline cartilage chondrogenic medium without scaffold. The content of glycosaminoglycan in the experimental group was significantly higher than that in the control group. This study suggests that stress stimulation may promote cells to form 3D structures autonomously, which can be used to construct scaffold-free 3D tissue-engineered cartilage *in vitro* (Sakai et al., 2009). In addition, our *in vivo* experiment demonstrated that appropriate mechanical stimulation can promote cartilage regeneration by enhancing the production of type II collagen. In the experimental group, gradual weight bearing was exerted 6 weeks after a full-thickness defect. The staining area of type II collagen antibody in the experimental group was significantly higher than that in the control group (Nishino et al., 2010b). In another experiment, we explored the long-term effects of mechanical stimuli on cartilage repair after a full-thickness defect. We first applied a hinged external fixation device in rabbits for 6 months. Then, we removed the device and let the rabbits roam free for 6 months. This technique promoted cartilage repair in the long term by increasing the content of type II collagen (Nishino et al., 2010a).

Incorporating the use of mechanical stimuli can fortify neotissue to impart the properties of actual articular cartilage. Through the development of bioreactors, the effect of various complex mechanical stimuli in MSCs, including compression, hydrostatic pressure, fluid shear stress, and osmotic pressure, can be achieved. Moreover, the content and architecture of the ECM structure might be recreated using a variety of modified biomaterials, to mimic the natural articular cartilage as intended for a mechanically competent replacement (Armiento et al., 2018).

Increasing attention is paid to the effect of mechanical stimuli on articular cartilage. However, the precise methods by which mechanical stimulation causes changes in chondrocytes as well as the proper magnitude have not yet been fully understood. To this end, this article provides an overview of the effect of several mechanical stimuli and these processes at the molecular level. A summary of the most well-understood biomaterials is also presented. By doing so, we provide a timely answer to the questions of what the effects of mechanical stimuli on articular cartilage are, which proteins play a crucial role in regulating this process, and how they transduce the mechanical stimuli into signals to the cell (Figure 1).

2 The composition and structure of articular cartilage

The articular surfaces of the bone are covered in hyaline cartilage, which provides a low-friction surface. Articular cartilage works to absorb and distribute stress in the mechanically demanding environment of the joint in addition to providing a low-friction surface (Fahy et al., 2018). These exceptional functional qualities are a result of the articular cartilage's highly specialized composition and structure.

Molecular layers at the sliding cartilage surfaces reduce friction. Three main molecular species are implicated in forming such boundary layers: hyaluronic acid (HA), lubricin, and phosphatidylcholine liposomes (LPs), which, at the high physiological pressures (of order 100 atm), typical of the major joints, appear to produce reduced friction (values down to 10–3) (Lin and Klein, 2021).

Chondrocytes integrated in a rich extracellular matrix (ECM) make up the highly specialized tissue known as articular cartilage (Choi et al., 2018). Two phases can be distinguished within the articular cartilage from a material perspective. First, a framework of collagen fibers that primarily consists of type II, type IX, and type XI collagen is a solid phase that gives the tissue its general structure. Glycosaminoglycans (GAGs), proteoglycans, and glycoproteins make up a small portion of this network. The second phase is a liquid made up of water and electrolytes (Ca^{2+}, K^{+}, Na^{+}, and Cl^{-}), which contains all of the solid components. The ECM is made up of these two stages (Armiento et al., 2018). While collagen fibers provide tensile strength, the tissue is resistant to large compressive pressures due to the significant attraction of water to the negatively charged proteoglycans (Hua and Jiang, 2021). The porous matrix prevents interstitial fluid from escaping during mechanical compression, providing internal pressure to withstand the imposed load and protect the cells within the solid matrix (Schätti et al., 2015). The composition and structure of ECM determine its physical properties, which are highly specialized for weight bearing.

The cartilage in the joints is incredibly sensitive to mechanical strain. The mechanical environment primarily determines the structure of cartilage, which may play a role in cartilage mechanoadaptation (Vincent and Wann, 2019). Three overlapping zones that move from the surface to the subchondral bone make up adult AC: the superficial zone (SZ), the intermediate zone (IZ), and the deep zone (Figure 2) (Armiento et al., 2018;

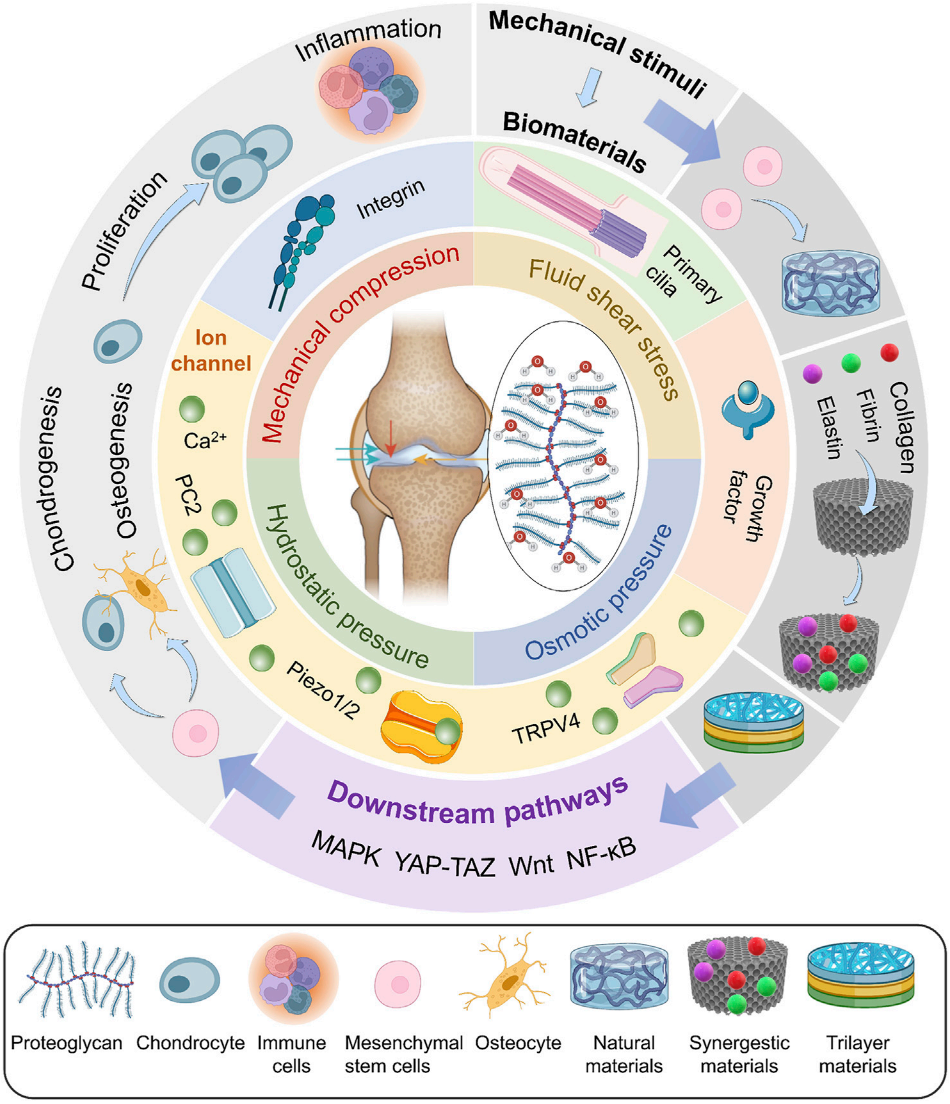

FIGURE 1
Bioreactors exert mechanical stimuli, including mechanical compression, fluid shear stress, osmotic pressure, and hydrostatic pressure, on various biomaterials. These signals are sensed by mechanosensors and regulate the differentiation of MSCs, proliferation of chondrocytes, and inflammation through downstream pathways.

Hodgkinson et al., 2022). Within these zones, the morphology of chondrocytes, as well as the content and architecture of ECM, reflect the forces experienced during movement. In the superficial zone, chondrocytes are immature, have an oblate form, and are scattered singly on the cartilage surface. To distribute shear pressures during articulation, type II collagen fibers are oriented transversely. In the intermediate zones, chondrocytes show a somewhat rounded shape, hypertrophy, and cluster together. Type II collagen fibers are distributed randomly to withstand the pressure coming from various directions since this zone is subject to compressive and shear stresses. In contrast, the pericellular matrix consisting of collagen VI, which surrounds the chondrocytes in the deep zone, is collectively referred to as a chondron. To resist compressive pressures, collagen II fibers are thick and parallel to the joint surface (Figure 2) (Yu et al., 2023), and high proteoglycan concentrations encourage water retention (Wang Z. et al., 2022; Hodgkinson et al., 2022). Col II, PRG4, and FGF content decrease as cartilage sites become deeper; the opposite is true for Col X and glycosaminoglycan (GAG) content (Wang Z. et al., 2022). Structural heterogeneity is more conducive to chondrogenesis. The calcified cartilage zone (CCZ), the transition area between cartilage and subchondral bone, also plays a major role in the repair process after osteochondral defects. At 24 weeks after surgery, the cartilage layer of the CCZ group was primarily repaired by hyaline cartilage, in contrast to the defects in the blank control and non-CCZ groups, which were filled with fibrous tissue. The experiment explored the feasibility of using trilayer scaffold containing natural CCZ as an intervention in osteochondral tissue engineering (Huang Y. et al., 2021). A study determined that spatial distributions of heterogeneous mechanical stimuli might affect the cell behavior. Cell viability is low close to the porous

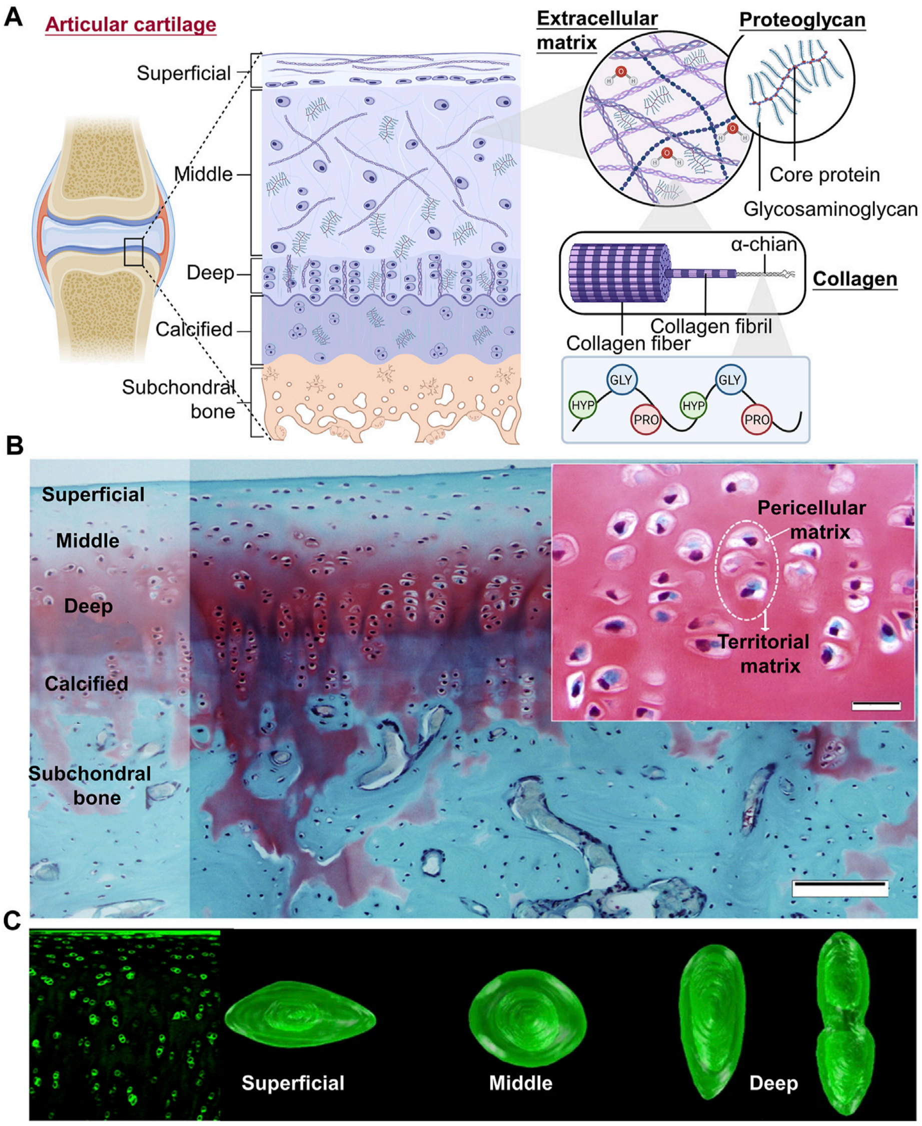

FIGURE 2
Three overlapping zones of articular cartilage **(A)** Three overlapping zones from the surface to the subchondral bone can be found in adult AC: the superficial zone (SZ), the intermediate zone (IZ), and the deep zone. Within these zones, the morphology of chondrocytes, as well as the content and architecture of ECM, reflect the forces exposed during movement (Figure created using BioRender.com). **(B)** Knee joint cartilage structure in rabbits. Articular cartilage is organized into zones in this representative Safranin O/Fast Green-stained tissue segment from the rabbit knee joint. Scale bar: 100 μm. The cartilage ECM regions are highlighted in the little image. Scale bar: 20 μm (Armiento et al., 2018). **(C)** (Left) Blocks of cartilage tissue immunolabeled for type-VI collagen are shown in fluorescence confocal pictures. (Right) In each zone, chondrons showed noticeable variations in height, shape, and volume (Choi et al., 2007).

compression-platen interface, although it rises with depth, according to cross-sectional investigations (Kisiday et al., 2009).

3 Classification and the influence of mechanical stimuli

The expression of MSC chondrogenic genes and the formation of cartilage are both influenced by mechanical stimulation. The maintenance of the homeostasis of articular cartilage is aided by the chondrocyte's responses to suitable mechanical stimulation (Le et al., 2020). However, inappropriate mechanical stimulation causes cell death (Healy et al., 2008). Mechanical stimuli are mainly categorized into four groups: mechanical compression, fluid shear stress, hydrostatic pressure, and osmotic pressure; these are applied singularly or in combination with others.

3.1 Mechanical compression

For cartilage remodeling, mechanical compression has both advantages and disadvantages. Similar metabolic response to compression can be seen in animal research and *in vitro*. While dynamic compression can considerably increase matrix production,

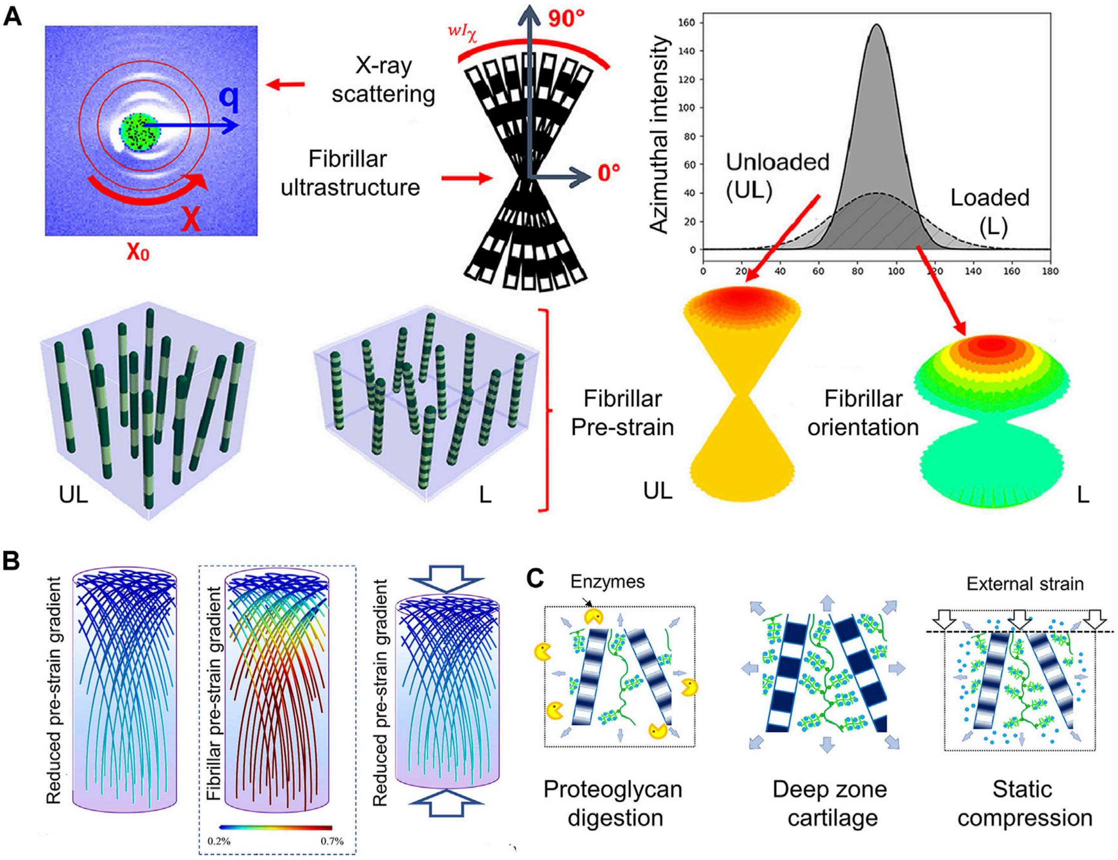

FIGURE 3
The structure of collagen fibrils reflecting the mechanical microenvironment **(A)** Utilizing X-ray scattering and fibrillar ultrastructure explores structural response of the Type II collagen fibrils in cartilage to cyclic loading. Axially symmetric broadening of the fibril orientation distribution and reduction of fibril pre-strain (at a fixed orientation) are shown. The fibril angle with respect to the sample (and loading) axis is shown using color-coding: Green fibrils are off-axis in relation to the joint surface, and red fibrils are close to vertically oriented fibrils at 90° to the joint surface (Inamdar et al., 2021). **(B)** (Centre): Based on scanning SAXS measurements, it has been determined that the articular cartilage exhibits a new gradient of rising fibrillar pre-strain from the surface/transitional (upper) zone to the deep (lower) zone. Pre-strain levels are indicated via a color scale on the fibrils, with blue denoting low pre-strain and red denoting high pre-strain (color online). In a way similar to (Left): treatment with chondroitinase sulphate to remove some of the PG phase, compression (Right) lowers the fibrillar pre-strain gradient (color gradient lowers) (Inamdar et al., 2019). **(C)** Ultrastructural mechanism enabling these fibrillar gradients: enzymatic (left) and load-induced (right) changes to the original fibrillar nanostructure (center) result in loss of water molecules originally bound to PGs, thus reducing the internal pre-stress exerted on the fibrillar network by the PG phase (Inamdar et al., 2019).

static compression significantly reduces the synthesis of collagen and PGs (Alizadeh Sardroud et al., 2021).

Temporal cues controlled by the cell-autonomous circadian clock are one of the many external elements that influence chondrogenesis. A recent study, for the first time, demonstrated that optimal mechanical compression directly enhances cartilage matrix production by entraining the molecular clockwork in chondroprogenitor cells. The chondrogenic markers SOX9 and ACAN, in addition to the several core clock genes and proteins, also exhibited a consistent sinusoidal rhythmic expression pattern. The results showed that the synchronized, rhythmic expression of the chondrogenic transcription factors and main circadian clock genes, at least partially facilitated increased chondrogenesis brought on by mechanical compression (Vágó et al., 2022). This experiment combines mechanical factors with biological cycle factors and proves their correlation.

It is thought that articular cartilage's collagen fibrillar architecture undergoes biomechanical modifications that are essential for facilitating appropriate joint function. The mechanisms behind cartilage's capacity to endure prolonged repetitive compression as well as the structural response of Type II collagen fibrils to cyclic stress *in situ* have been highlighted. The fibrillar response including inter-fibrillar variability orientation, and fibrillar strain were measured by synchrotron small-angle X-ray scattering (SAXS), and 3D reconstruction techniques. The study showed that the fibrils reversibly alter the width of the fibrillar orientation distribution and reduce fibrillar pre-strain under repeated cyclic loading (Figure 3A) (Inamdar et al., 2021).

The functionality of biological tissues and the prevention of harmful interfacial stress concentrations depend on the biomechanical gradients, which means a depth-dependent variation in some mechanical parameters. Periodic fibrillar banding (D-period), a sensitive indicator of zonal structure to the mechanical environment at the nanoscale, is one of the main parameters. This experiment also explored the relationship between proteoglycans and the microstructure of collagen. The removal of extrafibrillar proteoglycans causes fibrillar alterations that are similar to static compression (Figures 3B,C) (Inamdar et al., 2019).

However, the response to dynamic compression relies on the frequency, amplitude (Xie et al., 2006; Uzieliene et al., 2023), zone (Jeon et al., 2012), time-point (Ge et al., 2021; McDermott et al., 2021), and occurs in combination with biochemical cues (Sani et al., 2022; Li et al., 2023).

Xie et al. (2006) showed that when chondrocytes were seeded in the biodegradable elastomeric scaffold poly (L-lactide-co-caprolactone) (PLCL) at 10% compressive strain and 0.1 Hz, the level of type II collagen mRNA expression was elevated (Xie et al., 2006). The molecular mechanism underlying this process was also investigated. The area between −509 and −109 base pairs, where the transcription factor Sp1 is found, is where the short promoter responds to continuous dynamic compression most actively, according to a mutant deletion investigation. Additionally, it was demonstrated that mechanical compression activates transcription, possibly via the Sp1 binding sites in the proximal area of the *COL2A1* gene promoter, to raise the level of type II mRNA expression (Xie et al., 2006). In contrast, a different study demonstrated that compressed OA cartilage under strong mechanical pressure had lower overall levels of glycosaminoglycans and proteoglycans (Uzieliene et al., 2023).

Patients with osteoarthritis (OA) who have zonal chondrocytes can benefit from tailored compressive stimulation since different zones of articular cartilage react differently to compressive loading: Only superficial constructs displayed greater PRG4 staining, retained more GAG (P 0.01), and developed higher compressive moduli than unloaded controls (Jeon et al., 2012).

A 2021 study explored how mechanical dynamic compression affected the chondrogenic development of mesenchymal stem cells (SMSCs) generated from human synovium. The scientists discovered that, in comparison to the unloaded control, dynamic compression that was started at an early time point decreased the expression of markers unique to chondrocytes and hypertrophy. In contrast, dynamic compression applied at a later time point improved the cartilage matrix's levels of gene expression while suppressing SMSCs' hypertrophic growth when compared to unloaded controls (Ge et al., 2021). The results imply that dynamic mechanical compression loading at optimal time-point is essential for maintaining the cartilage phenotype and for promoting SMSCs' chondrogenic development. A different study, investigated the effect of the chondrogenic priming duration, showing that dynamic compression for certain duration enhanced the engineered tissue's equilibrium and dynamic modulus. Dynamic compression improved the expression of *COL2A1* and *ACAN* mRNA at the conclusion of the loading phase for priming durations of 2 weeks or longer. According to the authors, loads start at priming durations of 4 weeks or fewer suppressed transient osteogenic signaling (*RUNX2, OPN*), as well as the expression of *CYR61*, a gene that is a target of the YAP/TAZ-TEAD pathway (McDermott et al., 2021).

According to one study, mechanical stimulation showed no negative effects on the viability and growth of cells. It decreased the expression of matrix metalloproteinase-3 (MMP-3) and increased the expression of chondrogenic markers such as aggrecan, proteoglycan-4, and collagen type II. Despite showing modest increase in neocartilage development, IGF-1 was not as effective as mechanical stimulation (Sani et al., 2022).

Different biological factors may have opposite effects on endochondral ossification and cartilage regeneration. For the dual regulation of endochondral ossification, a coordinated dynamic mechanical stimulation is paired with various biochemical cues, such as parathyroid hormone and hydroxyapatite in the outer and inner region, respectively. In particular, dynamic mechanical stimuli combined with parathyroid hormone in the outer region prevent endochondral ossification and lead to cartilage regeneration, while dynamic mechanical stimulus combined with hydroxyapatite in the inner region encourages endochondral ossification and produces effective subchondral bone regeneration (Li et al., 2023).

3.2 Fluid shear stress

Shear stress is a contentious technique since it can sometimes cause cell death (Healy et al., 2008), but other times it can encourage tissue regeneration (Gemmiti and Guldberg, 2006; Valonen et al., 2010; Gonçalves et al., 2011).

When tissue is compressed, about 70% of the water is released, which could cause fluid shear stress at or near the cellular membrane. When the tissue is unloaded, osmotically, the water is sucked back.

Cartilage is a highly aquiferous connective tissue. When the tissue is compressed, about 70% of the water is released, which could cause fluid shear stress at or near the cellular membrane. When the tissue is unloaded, osmotically, the water is sucked back (Sharifi and Gharravi, 2019). Therefore, when water is relocated during mechanical compression, the chondrocytes may undergo fluid shear stress.

Static cultures are not widely used because shear stress has been associated with the activation of pro-inflammatory and pro-apoptotic proteins in chondrocytes. Shear stress has been associated to matrix degradation in cartilage tissue. When chondrocytes experience shear stress from mechanical loading, an important proinflammatory enzyme called cyclooxygenase-2 (COX-2) is produced (Healy et al., 2008). However, certain shear stress magnitudes have been found to be advantageous (Gemmiti and Guldberg, 2006; Valonen et al., 2010; Gonçalves et al., 2011). In comparison to static culture, dynamic fluid flow culture has a number of benefits, including improved mass transport and a more regulated biochemical environment.

To establish the ideal shear stress levels for the development of new tissues, an adjustable device was created. The mechanical characteristics of neocartilage *in vitro* were subsequently improved up to 3.6-fold as a result of the discovery of a favorable window of fluid-induced shear (FIS) stress. It was discovered that stress of 0.05–0.21 Pa considerably improved build properties. A mechanistic investigation was conducted to better understand the positive effects of FIS stress, and the results showed that the primary cilia of chondrocytes are mechanically gated complexes that are triggered by FIS stress (Salinas et al., 2020). The advantages of FIS stress are not restricted to the neocartilage's surface. Top to bottom cross-sections were stained histologically. The findings demonstrated that the fiber density seen on the

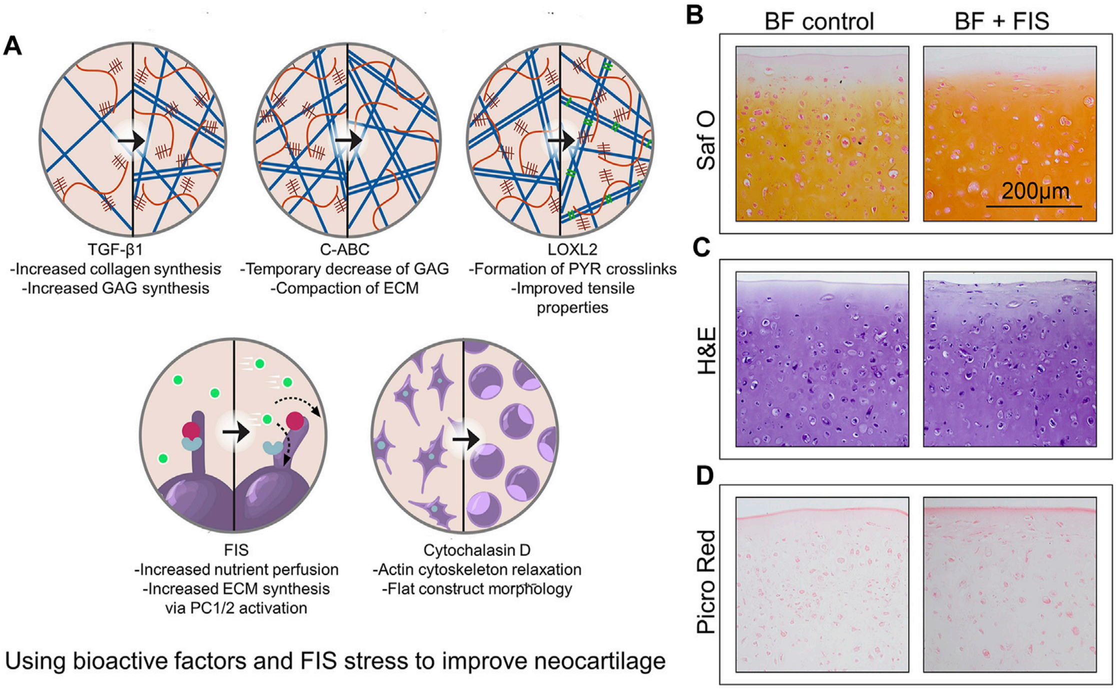

FIGURE 4
Using bioactive factors and FIS stress to improve neocartilage **(A)** Exogenous TGF-1 and FIS stress may enhance ECM content in a comparable way. Further research and combination with other mechanical stimulation regimens are encouraged in the hopes of further improving the functional properties of neocartilage by studies about additional bioactive factors, such as transforming growth factor beta 1 (TGF-β1), chondroitinase ABC (C-ABC), lysyl oxidase-like 2 (LOXL2), polycystin 1/2(PC1/2), and cytochalasin D (Salinas et al., 2022). **(B–D)** The intensity of glycosaminoglycan staining is increased when bioactive substances and FIS stress are combined. The examples show representative images of glycosaminoglycan content **(B)**, general cellular and tissue morphology **(C)**, and general collagen content **(D)**. Bioactive factors (BF), fluid-induced shear (FIS), hematoxylin and eosin (H, E), Picrosirius Red (Picro Red), and safranin O(Saf O) are among the abbreviations used (Zhang J. et al., 2021).

neocartilage constructs' surfaces was constant inside the construct (Salinas et al., 2020).

Abnormal mechanical stimuli are related to the pathophysiology of articular joints and aberrant fluid shear stress (FSS) greatly reduces chondrocyte survival and causes widespread disruption of cell shape. High quantities of inflammatory mediators are produced when FSS is abnormal, which causes cartilage to degeneration and deteriorate (Jin et al., 2021). Gene expression profiles related to osteoarthritis are recapitulated by prolonged application of high FSS to chondrocytes. The information points to a possible connection between the pathophysiology and development of OA and the exposure of chondrocytes and cartilage to aberrant mechanical loading (Zhu et al., 2010). Another study measured the FSS in the interstices surrounding the chondrocytes in growth plate cartilage, demonstrating that the FSS, which is caused by fluid flow over the cell surface, may have the ability to stimulate chondrocytes in the reserve zone close to the subchondral bone plate interface (Kazemi and Williams, 2021).

It has been demonstrated that the primary cilia, which can react to the FIS stress (Salinas et al., 2020), regulate TGF-signaling (Moore and Jacobs, 2018). One work showed that the species origin of chondrocytes and the addition of bioactive factors all affect the aggregate modulus of neocartilage stimulated by FIS stress. The research demonstrated the effect of FIS stress stimulation across sources of bovine and minipig cells. In addition, when FIS stress was added to bioactive factors, advancement in mechanical and biochemical properties was evident, with increased shear modulus by 115% compared to bioactive factor-only controls (Figure 4A) (Salinas et al., 2022). Histologically, samples treated with bioactive substances and FIS stress showed stronger Saf O staining, which is a sign that the neocartilage structures contain more glycosaminoglycans (Figure 4B), and similar staining intensities using H&E (Figure 4C). The spatial arrangement of collagens within the matrix is visible by Picro-Sirius red staining. FIS stress elevated peripheral staining, indicating higher collagen deposition on the outside margins of the neocartilage constructs, despite the groups appearing to have equal overall intensities (Figure 4D). Cells are typically not exposed to fluid mechanical signals after bioprinting, such as FSS, which are essential for tissue formation and function in both health and illness. The bioreactor acts as a simulator to help with the *in vitro* maturation of 3D cell-laden scaffolds for the creation of synthetic human tissues (Zhang J. et al., 2021).

Increased nutritional perfusion and waste transfer may be the cause of FIS stress-induced benefits, but they may also be the result of intricate cellular signaling processes and mechanotransduction-driven matrix remodeling (Salinas et al., 2020). The hydrodynamic environment of the new bioreactor, which is subject to FIS stresses and improved mass movement, may be a successful functional tissue-engineering approach for enhancing matrix composition and mechanical characteristics *in vitro*.

3.3 Hydrostatic pressure

The choice of HP experimental variables can have a big impact on how manufactured cartilage develops. Based on the following variables: static or dynamic, pressure magnitude, and experiment time, the different effects of various HP regimes on proteoglycan synthesis were examined. Analysis showed that the use of the static HP, a magnitude within the mid-high physiological range of cartilage (5–10 MPa), and a research duration of 2 weeks or longer most likely resulted in a strong anabolic response (Hodder et al., 2020). However, excessive HP is a major factor in the development of articular cartilage disease, such as OA. After HP loading, high levels of Gremlin-1, a mechanical loading-inducible factor in chondrocytes, are found in the middle and deep layers of cartilage tissue (Chang et al., 2019).

Although there is not a single best practice that can be applied to all culture systems, hydrostatic pressure (HP) is arguably one of the most important mechanical stimuli for cartilage. Mechanobiology, a vast field of study, is where the effects of HP on cartilage development reside. Interstitial fluid is pressured during cartilage loading, and the surrounding matrix prevents pressure loss by slowing the fluid flow rate from pressurized areas. HP is the term for this type of fluid pressurization, which results in homogenous stress all around the cell without cellular deformation (Pattappa et al., 2019). HP has been extensively used as an agent for promoting the differentiation of MSCs (Wagner et al., 2008), cartilage formation (Chen et al., 2017), and integration between the host cartilage milieu and the regenerated cartilage (Cheng et al., 2019) in tissue engineering.

With the hydrostatic pressure loading regime, chondrogenic genes such as *ACAN, COLIIA1*, and *Sox9* exhibit a substantial increase in mRNA expression. An earlier work showed that HP promoted MSC differentiation when multipotent differentiation factors were present *in vitro*. This finding raises the possibility that the HP regime may be crucial for cartilage growth and regeneration *in vivo* (Wagner et al., 2008). A cartilage regeneration model-based 3D tissue culture *in vitro* was used in one investigation. It was discovered that HP from the newly created bioreactor effectively increased the development of 3D cartilage by enhancing its mechanical strength, thickness, and uniformity (Chen et al., 2017). The study therefore provides an essential approach for improving cartilage regeneration *in vitro*.

In rabbit temporomandibular joints, it was discovered that BMSCs sheet fragments and platelet-rich fibrin granules transplanted into feasible HP-pretreated constructs improved the integration between the regenerated cartilage and host cartilage milieu, and achieved boundary-less repair between the residual host cartilage and the neocartilage (Cheng et al., 2019).

Using 3D bioprinting, it is possible to create constructions that mimic the mechanical characteristics of the natural articular cartilage by adjusting the HP in cartilage tissue. According to Finite Element (FE) modeling, the reinforcement of interpenetrating polymer network (IPN) hydrogels with particular polycaprolactone networks reduced radial expansion and increased the HP produced within the IPN when compressive loading was applied (Schipani et al., 2020).

No effective reports of *in vitro* cartilage regeneration based on photocrosslinkable hydrogels have been made due to nutrient absorption barriers brought on by dense networks and static culture conditions. To address this issue, a hybrid photocrosslinkable hydrogel was controlled using HP given by the bioreactor (Zhao et al., 2022). According to a 2022 study, HP completely counteracted the negative effects of hybrid photocrosslinkable (HPC) hydrogels at 3% weight percentage; significantly increased cell viability, proliferation, and ECM deposition by improving nutrient transportation and up-regulating the expression of genes specific to cartilage; and successfully regenerated homogeneous cartilage with a thickness of over 3 mm. While few living chondrocytes were seen in the center of the control group, chondrocyte-laden HPC hydrogels (CHPC) in the HP group had many live cells throughout, according to phalloidine fluorescence labeling. The distribution of type II collagen in the HP group was clearly denser at both 4 and 8 weeks than in the control group, whose center areas were nearly empty (Figure 5) (Zhao et al., 2022).

3.4 Osmotic pressure

Osmotic pressure sometimes causes chondrocytes to burst (Hara et al., 2018) and, also be used to enhance the mechanical properties of cartilage tissue engineering grafts (Schuiringa et al., 2023).

Osmotic pressure was cited in another study as an external component that could cause chondrocytes burst. It has been demonstrated that osmotic pressure can influence chondrocyte morphology. Mechanical stress and hypotonic solutions both greatly lead to chondrocyte burst. Hara et al. additionally proposed that chondrocyte burst can be connected to the creation of space for mineral expansion (Hara et al., 2018).

Osteoarthritis results from cartilage abnormalities. Due to their capacity to imitate the natural ECM, hydrogels offer a viable regenerative approach for addressing such abnormalities. Hydrogels that are frequently utilized for tissue regeneration, however, are too supple to withstand load-bearing in the joint. To address this problem, researchers have created an implant in which the osmotic pressure created by a charged hydrogel's swelling potential, which is constrained from swelling by a textile spacer fabric, serves as the mechanical load-bearing function (Schuiringa et al., 2023).

Joint-loading and weight-bearing strains compress articular cartilage, which is then followed by a tissue bulge during off-loading. Osmotic pressure is affected by changes in water content, which are brought on by this loading and unloading. Water is expelled from the tissue during compressive loading, which raises the concentration of local proteoglycan and puts chondrocytes under hyperosmotic stress. Surface, middle, and deep zones make up the longitudinal depth of articular cartilage. Each zone has a varied amount of osmotic pressure since each one is made up of distinct extremely negative ions. Previous researches have demonstrated the sensitivity of chondrocytes to both hyper- and hypo-osmotic alteration, which affects cell shape (Erickson et al., 2003; Turunen et al., 2012; Wang et al., 2015), metabolism (Hopewell and Urban, 2003; Tew et al., 2009) and biomechanics (Erickson et al., 2003; Wang et al., 2015). The rate of the osmotic challenge determines how the chondrocytes react to osmotic pressure (Wang et al., 2015), the integrity of the cartilage

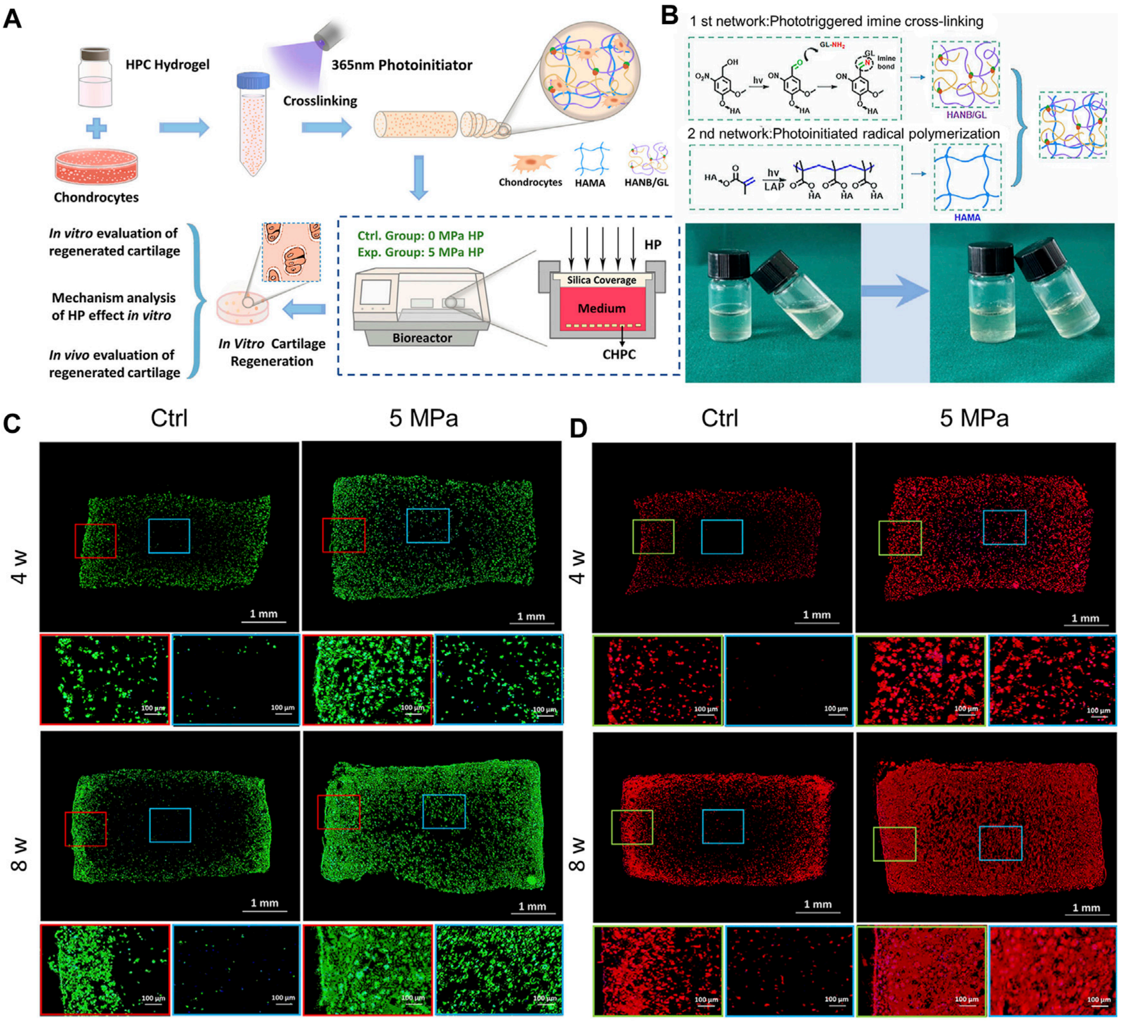

FIGURE 5
A hybrid photocrosslinkable hydrogel-based hydrostatic pressure (HP) bioreactor that controls cartilage regeneration **(A)** Diagrammatic representation of chondrocyte laden HPC hydrogels (CHPC)-based *in vitro* cartilage regeneration in an HP bioreactor. **(B)** (Top): Diagram of hybrid photocrosslinkable (HPC) hydrogel building process and double-network construction. (Bottom): Pre- and post-cross-linking images of the HPC hydrogels using light irradiation technique. **(C, D)** Phalloidine and Collagen II of CHPC produced *in vitro* were stained using immunofluorescence. Blue frames represent the inner regions, while red and green frames represent the periphery (Zhao et al., 2022).

(Turunen et al., 2012) and the phenotype of the chondrocytes (Tew et al., 2009). Osmolarity also determines *in vitro* chondrogenic differentiation (Liang et al., 2012; Caron et al., 2013).

Spheroidal cartilage organoids produced by particular chondrocytes from the longitudinal depth zone were cultured at various osmotic pressures. Takada et al. discovered that all zone-derived chondrocytes significantly enhanced the transient expression of ACAN and collagen type-II (Takada and Mizuno, 2018).

In another investigation, the morphology and biomechanics of chondrocytes were evaluated in response to abrupt and progressive hypo-osmotic pressure (Wang et al., 2015). The 66% of chondrocytes showed an increase in diameter followed by a regulatory volume decline (RVD) in response to abrupt hypo-osmotic stress, while 25% showed no RVD. On the other hand, cells that had gradually experienced hypo-osmotic stress showed decreased cell enlargement without a subsequent RVD. For cells exposed to abrupt hypo-osmotic stress, the equilibrium modulus increased. The gradual hypoosmotic challenge, however, had no effect on the mechanical characteristics of the chondrocytes (Wang et al., 2015). It is demonstrated that the rate of the hypo-osmotic challenge has a significant impact on the morphology and biomechanics of chondrocytes.

Composite materials based on a polyelectrolyte hydrogel embedded in a collagen scaffold mimic the specific molecular interactions of cartilage (Figure 6A). These composites have a mechanical structure similar to articular cartilage that is influenced by osmotic and electrostatic function. Positive counterions between the material and the ambient solution are uneven as a result of the charged matrix's restriction. The resulting imbalance creates an osmotic swelling pressure (Figure 6B). Collagen or poly (vinyl alcohol)-poly (acrylic acid) hydrogels were used to create 2D films that were cross-linked in the same way and to the same degree as the 3D scaffolds in order, to

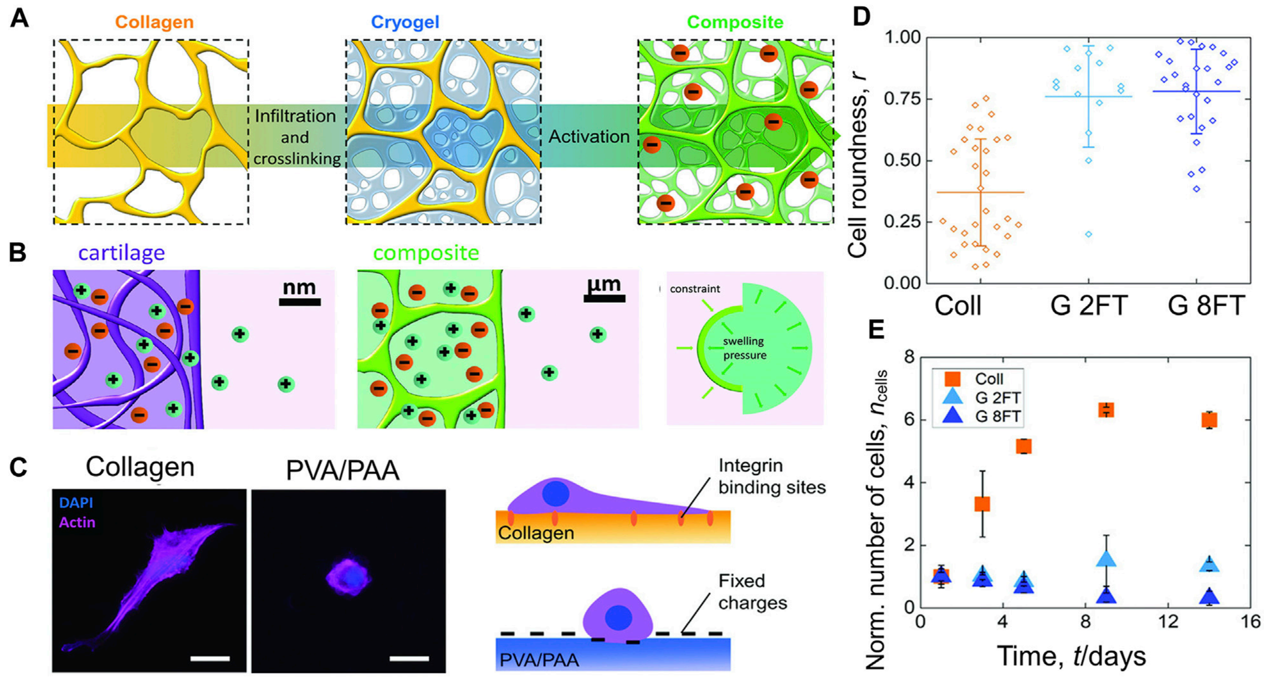

FIGURE 6
The composites' mechanical behavior is influenced by electrostatic and osmotic forces **(A)** A freeze-dried collagen scaffold is infiltrated with a PVA and PAA solution and then cross-linked by freezing and thawing. The created composite is then activated at a high pH. **(B)** (Left and middle): The composite materials replicate the ionic environment seen in genuine articular cartilage. Due to the existence of negative fixed charges, the concentration of positive counter-ions is higher than in the surrounding solution. (Right): Ionic imbalance induces osmotic swelling pressure. **(C)** (Left): Fluorescence microscopy was used to examine the interactions between materials and cells, which were planted on top of in 2D components. (Right): Cell-materials interaction and consequent morphology are shown schematically. **(D)** The ratio of the cell's roundness ranges from 0 (linear shape) to 1 (circular shape). **(E)** Over the course of 14 days of culture, the number of cells on the 2D components has stabilized relative to day 1 and error bars show the standard deviation (Offeddu et al., 2018).

better view and understand the interaction between cells and the components of the composites. After two and eight freeze-thaw cycles, the materials for the composites (C) and cryogel (G) components, respectively, were evaluated (Figures 6C–E) (Offeddu et al., 2018). The biomimetic materials described here represent a completely new technique of composites that are osmotically stiffened.

4 Mechanisms involved in the transduction of macroscopic mechanical forces into intracellular events

Articular cartilage is one of the most important weight-bearing parts of the human body. Therefore, the chondrogenic differentiation of stem cells is influenced by many intracellular and extracellular mechanical signals. Stem cells and chondrocytes can sense and respond to various mechanical signals through a series of mechanisms. Mechanoreceptors, which are the first responders to mechanical forces, include primary cilia, integrins, ion channels, etc. These mechanoreceptors convert macroscopic mechanical signals into specific chemical signals, which are transmitted through a variety of complex downstream pathways to affect the expression of related transcription factors, and ultimately produce biological effects to affect cell behavior.

4.1 Mechanoreceptors

Chondrocytes react to mechanical stimuli "directly" via PCM deformation, cell-ECM adhesions (primary cilia, integrin), and cell sensory structures (ion channels), or "indirectly" as a result of the release of sequestered growth factors and their interactions with cell receptors.

4.1.1 Primary cilia

The axon section and the basal body make up primary cilia, which are organelles that project from the cell surface into the ECM. The basal body of the primary cilia anchors to the inner cell membrane, while the axon section of the cilia protrudes from the membrane's surface. The basal body, a modified version of the centriole, is the source of primary cilia, which are microtubule-based organelles (Tao et al., 2020). The primary cilium's roles in the articular cartilage are as an antenna to sense the biomechanical environment, control the secretion of ECM components, and store cellular positioning information. Numerous ion channels and signaling receptors are found in primary cilia (McGlashan et al., 2006; Lee et al., 2015).

Using immunofluorescence and confocal imaging, the ECM receptors on chondrocyte plasma membranes and the main cilia have been examined. On the plasma membrane, every receptor that was tested showed a punctate distribution. On the primary cilia, integrins α2, α3, β1, and NG2 were also visible (McGlashan et al.,

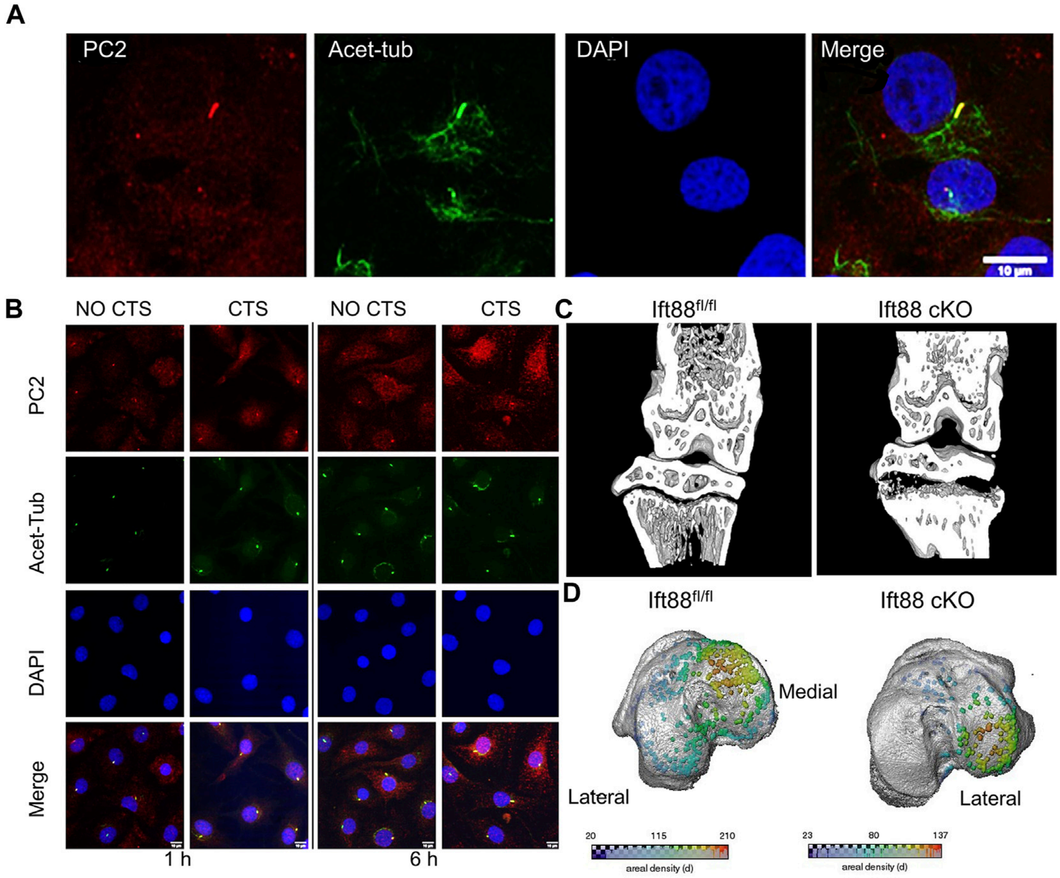

FIGURE 7
Different expression of primary cilia mediated by mechanical stimulation **(A)** Primary cilia were immunolabeled for acetylated tubulin (acet-tub, green), bovine chondrocytes were labeled for polycystin-2 (PC2, red), and primary DAPI was used to counterstain the nuclei. Scale bar: 10 μm (Thompson et al., 2021). **(B)** To explore the effect of cyclic tensile strain (CTS), chondrocytes were stained with DAPI (blue), primary cilia were stained with acetylated -tubulin (green), and polycystin-2 (PC2) was used to mark chondrocytes. Scale bar:10 μm (Thompson et al., 2021). **(C)** Micro-CT partial 3D construction of 10 weeks mice to explore the effect of the deletion of intraflagellar transport protein 88. The effects of IFT88 deletion are only felt in the growth plate's periphery, just below the knee's load-bearing articular surfaces (Coveney et al., 2022a). **(D)** Growth plate bridges across the knee's tibial articular surfaces are mapped using three dimensions representation. The density of the bridges is shown by the color scale (Coveney et al., 2022a).

2006). This study is the first to show that integrins and NG2 are expressed on primary cilia in chondrocyte. Using a FRET-based biosensor fused to ARL13B, Lee et al. report the first observations of Ca^{2+} signaling within primary cilia in osteocyte. They demonstrated that fluid shear stress causes Ca^{2+} increases in primary cilia of osteocytes, which are dependent on both intracellular Ca^{2+} release and external Ca^{2+} entry (Lee et al., 2015).

As one of the transient receptor potential polycystic of ion channels, polycystin-2 (PC2) and polycystin-1 (PC1) have been linked to cilia-mediated mechanotransduction in epithelial cells. Uniaxial cyclic tensile strain (CTS) was used to mechanically stimulate isolated chondrocytes in order to study the impact on PC2 ciliary location and matrix gene expression. The cilium was discovered to have a higher level of PC2 localisation, which co-localized with the ciliary marker acetylated -tubulin (Figure 7A). Response to mechanical stimulation results in an increase in PC2 ciliary localisation (Figure 7B) (Thompson et al., 2021). Furthermore, mechanical stimulation from the ECM can change the degree of deflection (Jensen et al., 2004), length (Fu et al., 2019; Zhao et al., 2020), and orientation (Farnum and Wilsman, 2011) of primary cilia, indicating that primary cilia can sense mechanical signals in bone formation and growth.

The ciliary axoneme was visible interdigitating between collagen fibers and condensed proteoglycans using tomography and TEM. The primary cilium is bent as a result of mechanical stimuli conveyed through matrix macromolecules, suggesting that it may function as a mechanosensor for skeletal patterning and growth (Jensen et al., 2004). Primary cilia in chondrocytes are sensitive to mechanical forces, and when subjected to cyclic tensile strain or hyperosmotic stresses, their length decreases dramatically. The principal cilial length in healthy cartilage is 1.5 mm in the deep layer and 1.1 mm in the superficial layer (Zhao et al., 2020). Treatment with IL-1β at 1 ng/mL produced a statistically significant increase (of 14%) in cilia length. However, this effect was completely inhibited under mechanical loading (Fu et al., 2019). Additionally, there were differences between load-bearing and non-load-bearing zone in the direction of the chondrocyte primary cilia. The axoneme extends from the cellular surface towards the subchondral bone in load-bearing areas of the superficial zone. This uniformity disappears in areas not supporting loads (Farnum and Wilsman, 2011).

During skeletal development, primary cilia proteins, which are involved in the transduction of biological and physiochemical signals, regulate the maturation of cartilage. Researchers tested the effects of the ciliary protein intraflagellar transport protein 88 (IFT88) on postnatal cartilage in mice with the Ift88 gene conditionally knocked out (Ift88-KO). The findings show that IFT88 acts as a chondroprotector in articular cartilage by preventing cartilage from calcifying by maintaining a Hh signaling threshold under physiological loading (Coveney et al., 2022b).

Coveney et al. used a cartilage-specific, inducible Cre (AggrecanCreERT2 Ift88fl/fl) to conditionally target the ciliary gene intraflagellar transport protein 88 (Ift88fl/fl) in the juvenile and adolescent skeleton, in order to investigate the role of primary cilia (Coveney et al., 2022a). IFT88 deletion in cartilage altered chondrocyte differentiation and mineralization by reducing ciliation in the growth plate. These effects were mostly limited to the peripheral tibial regions under the knee's load-bearing chambers (Figure 7C). AggrecanCreER T2; Ift88 fl/fl mice had fewer and lower density bone bridges than controls. This decrease in bridging was notably noticeable on the medial side of the leg (Figure 7D). The authors argue that ciliary IFT88 protects coordinated ossification of the growth plate from an disruptive heterogeneity of physiological mechanical stimuli during this critical stage in adolescent skeletal maturation.

Primary cilia are essential for the formation of mammalian tissues. Although primary cilia are important for chondrocyte function, their specific roles in postnatal articular cartilage morphogenesis are unknown. Rux et al. used a mouse conditional loss-of-function method (Ift88-flox) targeting joint-lineage progenitors (Gdf5Cre) to investigate the mechanisms. They discovered that tidemark patterning and hedgehog signaling were substantially disturbed, and that specificity was demonstrated based on regional load-bearing functions of articular cartilage (Rux et al., 2022).

4.1.2 Integrins

Integrins consisting of α and β subunits, translocate across the cell membrane. Numerous experiments have established that chondrocytes express a number of integrins, including integrins α5β1, αVβ3, αVβ5, α6β1, α1β1, α2β1, α10β1, and α3β1 (Loeser et al., 2000; Lahiji et al., 2004; Shattil et al., 2010; Tian et al., 2015). The protein complex is given the name "integrin" to signify its function as an integral complex involved in the transmembrane interaction between the cytoskeleton and ECM (Tamkun et al., 1986). Integrins are well-known as ECM receptors and cell adhesion molecules. They are also thought to affect intracellular signaling pathways physically and chemically as mechanoreceptors. Through integrin-mediated adhesion, cells detect and react to the elastic properties of ECM. Integrins are a class of well-known mechanosensors in cells that alternate between the inactive, bound, and dissociated states based on the various forces acting on them (Xu et al., 2014). When osteoarthritic chondrocytes and normal chondrocytes are mechanically stimulated, there are obvious differences in the cellular responses. These differences could be connected to variations in integrin expression and function [61].

The traction force between the αV integrin and its ligand is increased by mechanical force, suggesting that the αV integrin-RGD link may survive molecular tensions of up to 54 pN in chondrocytes under mechanical stress. When αV integrin bonds with its RGD-containing ligands, such as latent TGF, in chondrocytes under mechanical stress or not, Zhen et al. used a double-stranded deoxyribonucleic acid (dsDNA) tether as a tension gauge to test the tolerance to tension (Figures 8A,B) (Zhen et al., 2021). Mechanical stimulation of healthy chondrocytes resulted in enhanced GAG production, which was prevented by antibodies to α5 and αVβ5 integrins, as well as CD47 (Holledge et al., 2008). These findings show that αVβ5 integrin plays a significant roles in influencing chondrocytes responses to biomechanical stimuli. The subunits of integrins β1 and 3 are both necessary for osteocyte mechanotransduction. In osteocytes, inhibition of these integrin subunits resulted in poorer responses to fluid shear stress (Geoghegan et al., 2019). Integrin α1β1 has been identified within the integrin family as a critical participant in transducing hypo-osmotic stress. It has been demonstrated that deleting the integrin α1 subunit inhibits chondrocytes' *ex vivo* and *in vitro* production of Ca^{2+} transients in response to hypo-osmotic stress (Jablonski et al., 2014).

The constant external stimulation that chondrocytes experience controls remodeling. The maintenance of chondrocyte homeostasis requires an ideal degree of mechanical stimulation, but excessive mechanical stress results in the production of inflammatory cytokines and proteases such as matrix metalloproteinases (MMPs). Using an integrin receptor antagonist (cilengitide), Hirose et al. investigated the relation between integrins (αVβ3 and αVβ5) and the production of inflammatory markers in chondrocytes under mechanical loading. Interleukin-1 (IL-1), tumor necrosis factor (TNF), matrix metalloproteinase-3 (MMP-3), and MMP-13 gene expression that was increased by severe mechanical stress was inhibited by cilengitide (Hirose et al., 2020). Through the activation of the TGF-1/CCN2/integrin-5 pathway, high mechanical stress also causes chondrocyte fibrosis, and halting the expression of TGF-1, CCN2, or integrin-5 can reduce the fibrous development (Huang Y. Z. et al., 2021).

Recent study evidence indicates that excessive mechanical stress (eMS) is an important contributor in the development of OA. In a rat instability of the medial meniscus model, histologic and proteomic analysis of osteoarthritic cartilage revealed increased expression of integrin αVβ3 as well as more severe cartilage degeneration in the medial weight-bearing region (Figure 8C) (Song et al., 2023).

4.1.3 Ion channels

Based on their gating methods, ion channels can be divided into a number of groups, including voltage-gated, ligand-gated, and mechanically-gated. The chondrocyte has different types of channels, but mechanically gated ion channels are particularly intriguing since they can trigger rapid mechanosensory signal transduction. Mechanosensitive ion channels control ECM generation and matrix protein synthesis in articular chondrocytes. This mechanism involves intracellular cation efflux, extracellular cation influx, and mobilization of Ca^{2+} as a result of large Ca^{2+} release from storage (Zhang K. et al., 2021). The initial responses of chondrocyte mechanotransduction involve

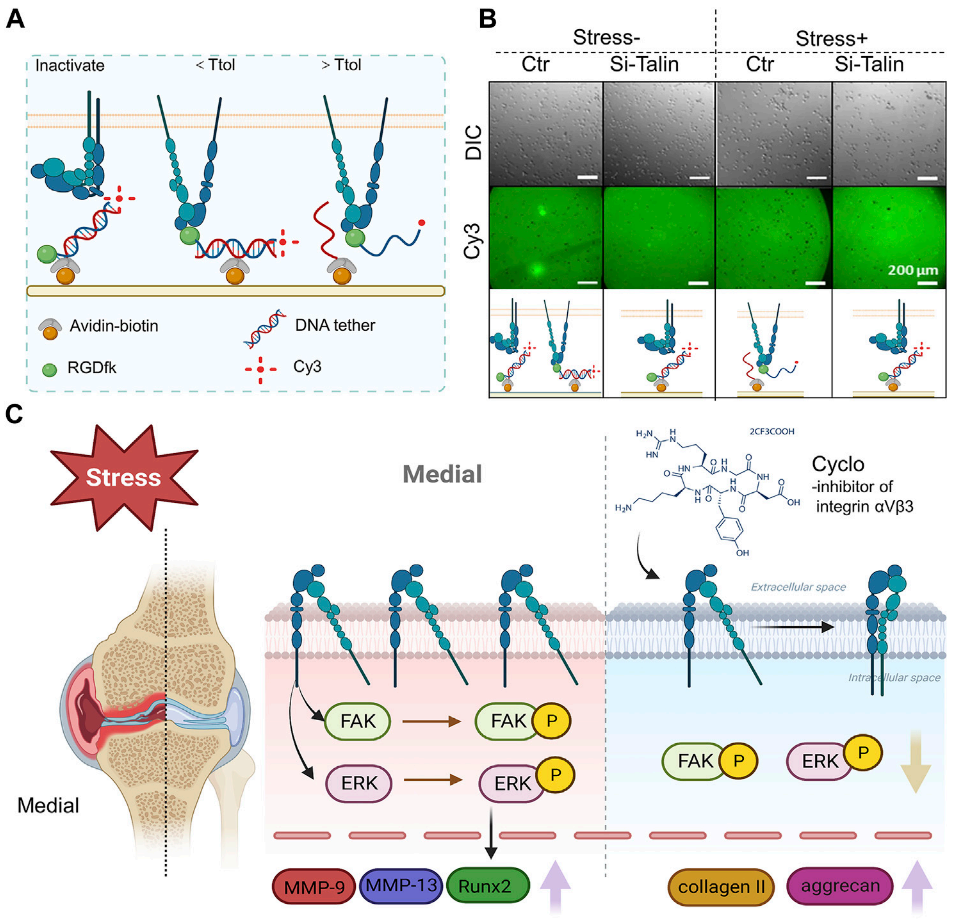

FIGURE 8
The role of integrin αVβ3 signaling in the development of osteoarthritis brought on by high levels of mechanical stress **(A)** An avidin-biotin linker is used to immobilize a dsDNA tether on the PEG surface. The tension tolerance (Ttol) of the dsDNA is determined by the position of the biotin. The cell-expressed integrins attach to the RGDfk coupled with dsDNA at one end. If the tension applied by the cell through the integrin-RGD link is greater than its Ttol, the dsDNA ruptures. If the tension applied by the cell through the integrin-RGD connection is less than its Ttol, the Cy3 fluorescence signals and cell attachment on the PEG surface are maintained (figure created using BioRender.com). **(B)** Direct imaging of RGDfK-dsDNA-Cy3 removal on the PEG surface (bottom row) and representative differential interference contrast images of SV40 cells on the PEG surface (top row). The cells were subjected to a prechallenge with or without fluid shear stress (Zhen et al., 2021). **(C)** Integrin αVβ3 is overexpressed in the area of the OA knee joint that bears weight. In rat chondrocytes, phosphorylation of FAK and ERK encouraged the production of inflammatory and degradative mediators associated with osteoarthritis. Upregulation of collagen II and aggrecan expression was caused by integrin αVβ3 inhibition (Song et al., 2023) (figure created using BioRender.com).

changes in mitochondrial activity and calcium influx, which take place in seconds to minutes (Delco and Bonassar, 2021). The levels of calcium, an universal messenger, regulate a number of critical cellular functions, such as exocytosis, apoptosis, motility, gene transcription, and differentiation (Uzieliene et al., 2018).

TRPV4 and Piezo 1/2 are arguably the most significant calcium channels. TRPV4 was initially identified in articular chondrocytes as an osmotically sensitive Ca^{2+} ion channel, and it was later demonstrated to be sensitive to physiological dynamic compression (Delco and Bonassar, 2021). Additionally, it was found that the mechanically gated Ca^{2+} channels Piezo 1/2 in articular chondrocytes respond to high (supraphysiologic) strain and are in charge of mechanically inducing chondrocyte death (Zhang M. et al., 2022). The potential roles of TRPV4, Piezo1/2 in translating different magnitudes of repetitive mechanical stimuli in chondrocytes were identified in a study. To investigate this, TRPV4, and Piezo1/2 specific siRNAs were transfected into cultured primary chondrocytes to inhibit the expression of TRPV4, Piezo1, or Piezo2, respectively. These cells were then referred to as TRPV4-KD (knock down), Piezo1-KD, or Piezo2-KD cells. Stretch-evoked Ca^{2+} fluctuations were markedly reduced in TRPV4-KD, Piezo1-KD, or Piezo2-KD cells as compared to control siRNA-treated cells, demonstrating the necessity of these channels for Ca^{2+} signaling in chondrocytes generated by stretch stimulation. Notably, these channels responded differently to the calcium oscillation brought on by different stretch stimulation intensities. More specifically, Piezo2-mediated Ca^{2+} signaling was critical for chondrocyte response to damaging levels of strain (18% of strain), whereas TRPV4-mediated Ca2+ signaling was critical for chondrocyte response to normal levels of strain (3% and 8% of strain) (Du et al., 2020). The idea of therapeutically targeting Piezo2-mediated mechanotransduction for the therapy of cartilage disease is prompted by the results, which serve as a foundation for further research into mechanotransduction in cartilage.

GsMTx4, a PIEZO-blocking peptide, and Piezo1/2-specific siRNA blocked mechanically induced Ca^{2+} transients produced by atomic force microscopy in primary articular chondrocytes (Lee et al., 2014), proposing a potential therapeutic approach to attenuate Piezo-mediated cartilage mechanotransduction of damaging stresses to reduce cartilage injury and posttraumatic osteoarthritis. Interleukin-1 (IL-1) was discovered to upregulate Piezo1 in porcine chondrocytes. The enhanced Piezo1 function caused excess intracellular Ca^{2+} both at rest and in response to mechanical deformation. High resting state Ca^{2+} enhanced mechanically generated deformation microtrauma via rarefying the F-actin cytoskeleton (Lee et al., 2021).

Osteoarthritis and joint arthropathy are linked to the loss of TRPV4 function, which is a Ca^{2+}-permeable osmomechano-TRP channel that is extensively expressed in articular chondrocytes. The acute, mechanically mediated regulation of proanabolic and anticatabolic genes has been demonstrated to be prevented by TRPV4 inhibition during dynamic loading. It has also been shown to impede the loading-induced augmentation of matrix accumulation and mechanical characteristics. Additionally, in the absence of mechanical loading, pharmacological stimulation of TRPV4 by the agonist GSK1016790A promoted anabolic and inhibited catabolic gene expression, potently increased matrix production, and improved the mechanical characteristics of the construct (O'Conor et al., 2014). These results lend credence to the idea that mechanical cues that maintain joint health and cartilage extracellular matrix preservation are primarily transmitted by TRPV4-mediated Ca^{2+} signaling.

A study shows that loss of TRPV4-mediated cartilage mechanotransduction in adulthood lessens the severity of aging-associated OA by using tissue-specific, inducible TRPV4 gene-targeted mice. These findings point to a unique disease-modifying strategy for the treatment of OA associated with aging by therapeutically targeting the TRPV4-mediated mechanotransduction pathway (O'Conor et al., 2016). However, blocking TRPV4-mediated calcium ion transmission was insufficient to stop the progression of OA on its own. Ion channels belonging to the Piezo family have recently been found to regulate chondrocyte damage response and cell death, as well as giving chondrocytes mechanosensitivity to high stresses (Lee et al., 2014). Therefore, multimodal therapy strategies may be required.

4.1.4 Growth factors

The growth factor is produced as the inactive latent complex that cannot attach to membrane receptors cause a cellular biological response. Recent research has shown that mechanical stresses may activate dormant growth factors. Growth factors are trapped within the pericellular matrix. Increased bioavailability of these upon mechanical stimulation leads to chondrocyte activation. The PCM and territorial matrix's composition and structure affect the bioavailability of sequestered growth factors like fibroblast growth factor (FGF) (Vincent et al., 2007; Vincent, 2011), transforming growth factor-β (TGFβ) (Albro et al., 2012; Li et al., 2012) and insulin-like growth factor (IGF) (Martin et al., 2002). ECM-sequestered factors are released during deformation or destruction to interact with cell membrane receptors, thus activating downstream intracellular signaling cascades.

The pericellular matrix of articular chondrocytes contains a highly abundant growth factor called FGF2. The location of FGF-2 storage in articular cartilage, the proteoglycan to which it was linked, and its function in chondrocyte mechanotransduction were all uncovered by a study. In articular cartilage, heparan sulphate proteoglycan traps FGF-2. In the type VI collagen-rich pericellular matrix of pig and human articular cartilage, perlecan and FGF-2 co-localize. Chondrocytes enclosed with alginate had the capacity to build up pericellular perlecan and FGF-2 in culture and to activate ERK in a FGF-dependent manner when loaded (Vincent et al., 2007). Studies exploring the function of FGF-2 have shown inconsistent results. The two main articular cartilage FGF receptors, FGFR1 and FGFR3, may have changed in balance, which could explain variations in responses to FGF-2. The majority of FGF2's catabolic and anti-anabolic actions are mediated by FGFR1, whereas the positive effects are handled by FGFR3 (Vincent, 2011).

It has been discovered that delayed compressive stress induces endogenous TGF-1 gene transcription, protein expression, and subsequent activation even when exogenous TGF-1 stimulation is stopped (Li et al., 2012). Shearing synovial fluid may have extra metabolic effects on diarthrodial joints. It was also shown that TGF-β could be activated in cell-free scaffolds, proving that mechanical stress alone is, at least in part, responsible for the observed activation (Albro et al., 2012). Further, an investigation revealed the functions of TGF-β/SMAD and integrin signaling, indicating cross-talk between these two signaling pathways in controlling the development of compression-driven hypertrophy (Zhang et al., 2015).

A number of lines of research indicate that the anabolic cytokine IGF-I is important for maintaining articular cartilage and may even be involved in cartilage repair. IGF-I increases chondrocyte synthesis of matrix macromolecules. The high co-localization of the pure IGFBP-3 and fibronectintwo in the cartilage matrix and the direct binding between them provide evidence in favor of the theory that these two proteins work together to control local IGF-I levels (Martin et al., 2002).

4.2 Downstream pathways

The expression of genes linked to either anabolic or catabolic chondrocyte processes occurs from the activation of certain downstream pathways (Figure 9; Table 1).

4.2.1 MAPK pathway

A number of cell signaling pathways involved in cellular proliferation, the production of the extracellular matrix (ECM), cell survival, and the mediation of pain are controlled by the mitogen-activated protein kinase (MAPK). The MAPK pathway, which is involved in mechanotransduction and is controlled by mechanosensory stimuli, is essential for chondrocyte differentiation. TRPV4, p38, and primary cilia are all necessary to activate ERK.

According to one study, *ex vivo* cartilage compression increases the activation of the JNK pathway enzymes SEK1, p38 MAPK, and ERK1/2. This work also indicates unique temporal patterns of MAPK signaling in response to mechanical stress and that mechanical compression alone can activate MAPK signaling in healthy cartilage (Fanning et al., 2003). Various clinical studies

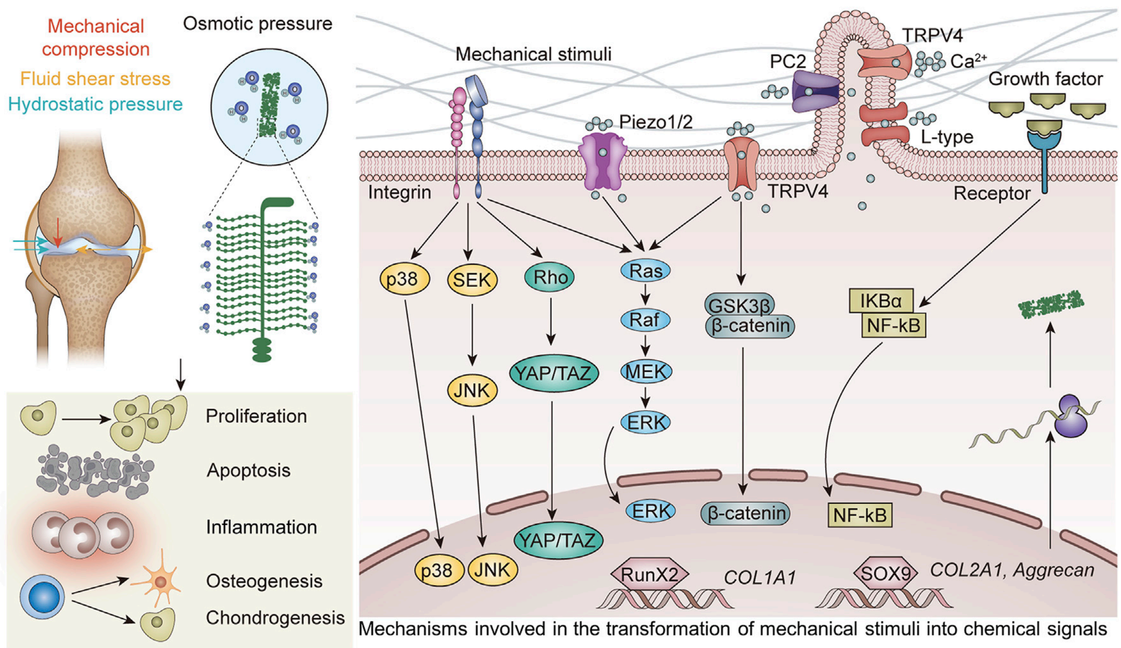

FIGURE 9
Mechanosensors transform mechanical stimuli into chemical signals, and the genes linked to anabolic or catabolic chondrocyte processes are expressed in a context-dependent manner as a result of the activation of downstream pathways.

have found that the MAPK pathway plays an essential role in the cartilage development (Xiang et al., 2019), cartilage catabolism (Zhang H. et al., 2022), expression of inflammation-related factors (Yanoshita et al., 2018), and enhancement of chondrogenesis (Xie et al., 2021).

Magnitude-dependent effects of mechanical stress on chondrocyte survival, phenotypic, and proliferation have been observed. The expression of autophagy and mechanical stress-regulated ERK/mTOR signaling in chondrocytes depend on the structural integrity of primary cilia (Xiang et al., 2019). In mice articular cartilage and cultured chondrocytes, mechanical overloading speeds up senescence. Mechanical overloading reduces the transcription of the F-box and WD repeat domain containing 7 (FBXW7) mRNA and the MKK7 degradation caused by FBXW7, which in turn stimulates JNK signaling. As evidenced by the overexpression of p16INK4A, p21, and Colx and the downregulation of Col2a1 and ACAN, FBXW7 deletion in chondrocytes has been found to cause chondrocyte senescence and accelerate cartilage catabolism in mice, which led to the worsening of OA (Zhang H. et al., 2022).

The non-receptor tyrosine kinase focal adhesion kinase (FAK) is connected to numerous signaling proteins. The phosphorylation of FAK, p-38, ERK, and JNK was triggered by cyclic tensile strain, which also elevated the expression of the genes encoding COX-2, IL-1, and TNF-α. Through MAPK pathways, FAK seems to control inflammation in chondrocytes exposed to cyclic tensile strain (Yanoshita et al., 2018). Dynamic compression raised the compressive moduli of manufactured cartilage tissues and encouraged the formation of cartilage matrix. ACAN and COL2 levels were increased in constructs cultivated under dynamic loading conditions, confirming the function of dynamic loading with 5% strain as a chondro-supportive agent (Xie et al., 2021).

Under high-strain activation, downstream signaling molecules MAPK/ERK1/2 and MAPK/ERK5 cause late excessive death of chondrocytes through the action of Piezo1 channels. Through the traditional MAPK/ERK1/2 signaling pathway, Piezo1 plays a crucial role in the apoptosis of the human chondrocytes (Li et al., 2016). Following apoptosis, the chondrocyte stimulates the joint's surroundings and releases a lot of oxygen free radicals and inflammatory mediators (including IL-1, TNF, and PE) that harm the newly formed cartilage tissue and blood vessels (Liu et al., 2022). After pre-incubation at 380 mOsmol, it was discovered that exposure to hyperosmotic conditions (550 mOsmol) initially reduced the rate of 35S-sulphate incorporation. However, after 24 h of culture, rates bounced back and even exceeded their pre-exposure values. This reaction was eliminated by MAP kinase inhibitors, which suggests that they are involved in the adaption mechanism (Hopewell and Urban, 2003). Therefore, it is believed that a number of mechanosensory stimuli have the MAPKERK pathway as a downstream target.

4.2.2 YAP-TAZ pathway

Chondrogenesis, chondrocyte maturation, and hypertrophy are all controlled by the transcriptional cofactors Yes-associated protein (YAP) and transcriptional coactivator with PDZ-binding motif (TAZ), which together make up a crucial mechanosignaling complex. The roles of YAP and TAZ as nuclear relays of mechanical stimuli exerted by ECM stiffness and cell shape were identified (Dupont et al., 2011).

The transcriptional cofactors YAP and TAZ form an important mechanosignaling complex and are involved in regulating

TABLE 1 Studies from the last 5 years focusing on mechanotransduction mechanisms.

Mechanical stimuli	Magnitude	Cell type	Downstream pathway	Most important contributions	Ref
Dynamic compression	15 V and 2 Hz (sinusoidal waveform)	Chondrocyte (rat)	Integrin αVβ3/FAK/ERK	Expression of inflammatory and degradative mediators as MMP-13, MMP-9, ADAMTS-5, and Runx2 was upregulated	Song et al. (2023)
Dynamic compression	20 kPa (2 s on, 1 s off)	Chondrocyte (mouse)	AT1R/JNK	Col X and Runx2 mRNA expression was increased, which promoted hypertrophic differentiation	Nakamura et al. (2018)
	20 kPa (static offset)				
Elongation strain	20%, 24 h	Chondrocyte (mouse)	FBXW7/MKK7/JNK	Increased *p16INK4A*, *p21*, and *COlX* and downregulated *COLIIA1* and *ACAN*, caused chondrocyte senescence and accelerated cartilage catabolism, exacerbating OA.	Zhang et al. (2022a)
Dynamic compression	5%, 0.2 Hz	Chondrocyte (human)	p-ERK/p38 kinases	ACAN and COLII levels that are increased show that dynamic loading with 5% strain has chondrosupportive effects	Xie et al. (2021)
			RhoA/YAP		
Cyclic tensile strain	20%, 6 cycles/min	Chondrocyte (OA patient)	GPER/YAP	Actin polymerization and the RhoA/LIMK/cofilin pathway were inhibited by mechanical stress	Sun et al. (2021)
Cyclic mechanical tension	10%, 0.5 Hz	Chondrocyte (patient with lumbar disease)	Nuclear localization of p-YAP	Mechanical stimuli enhanced the activity of the ACAN or COL2A1 promoter and postponed the degradation of endplate cartilage	Ding et al. (2022)
Biomaterial stiffness	Slower-degrading, stiff	BM-MSCs (human)	Nuclear localization of p-YAP	Mechanical stimuli promoted the development of cells into hypertrophic chondrocytes and showed greater levels of Runx2, a typical hypertrophy marker	Lee et al. (2020)
Biomaterial stiffness	NX-MC(0.34 ± 0.11 kPa)	MSCs (human)	Nuclear localization of p-YAP	*COL1A1* and *RUNX2* expression was increased, along with the expression of osteogenic markers and mineralization	Zhou et al. (2021)
	MC(3.90 ± 0.36 kPa)				
Dynamic compression	25% cyclic (10 min)	Chondrocyte (human)	Wnt/β-catenin	Decreasing the ECM content and suppressed the upregulation of SOX9	Praxenthaler et al. (2018)
	10% static (10 min)				
	9 times				
Hydrostatic pressure	10 Mpa	Chondrocyte (OA patient)	Wnt/β-catenin	The expression of Col2a1, proteoglycan, and aggrecan was shown to be downregulated, whereas MMPs and ADAMTS were upregulated. Apoptosis signaling was also enhanced	Cheleschi et al. (2020)
	3 h				
Hydrostatic pressure	0.9 Mpa	Meniscus fibrochondrocyte (female)	Wnt/β-catenin	Upregulated the average COL2A1 expression level 215.9-fold was shown in the CHP group for the female cohort	Ma et al. (2022)
	1 Hz				
Mechanical stretch	20%, 1 Hz	Osteoblast and Chondrocyte (rat)	Wnt/β-catenin	Collagen 1a and alkaline phosphatase reduced, and MMP 13, IL-6, and PGE2 increased in osteoblasts. In chondrocytes, there was a decrease in collagen 2a and an increase in MMP-13, the disintegrin, and metalloproteinase 5 with thrombospondin-like motifs	Song et al. (2021)
Hydrostatic pressure	20 MPa	Chondrocyte (mouse)	Gremlin-1/NF-κB	Sox9 and the cartilage matrix genes Col2a1 and Acan were expressed less, whereas catabolic marker genes including MMP-13 and ADAMTS-5 were expressed more	Chang et al. (2019)
	1 Hz				
Mechanical stretch	20%	Nucleus pulposus cell (human)	Ca2+/NF-κB	Promoted NLRP3 inflammasome assembly and upregulated caspase-1 activation and IL-1β production	Sun et al. (2020)
	6 cycles/min				
Dynamic compression	25% cyclic (10 min)	BM-MSC (human)	Nuclear localization of NF-κB	The expression of COX2 and BMP2 was higher, PGE2 synthesis was more than 100 times higher, and SOX9 stimulation was less than the control group	Lückgen et al. (2022)
	10% static (10 min)				
	9 times				

(Continued on following page)

TABLE 1 (***Continued***) **Studies from the last 5 years focusing on mechanotransduction mechanisms.**

Mechanical stimuli	Magnitude	Cell type	Downstream pathway	Most important contributions	Ref
Biomaterial stiffness	PC (4.3 MPa)	BM-MSCs (rat)	Blocking the NF-kappa B signaling pathway	Lowered the expression of Ltb, Traf1, Vcam1, and Mmp13 and elevated that of cartilage-specific genes Col2a1, Acan, and Sox9 in PC.	Jiang et al. (2018)
	P (6.8 MPa)				

mechanical stress-mediated apoptosis of chondrocytes (Sun et al., 2021), the degeneration of chondrocytes (Ding et al., 2022), chondrocyte hypertrophy (Lee et al., 2020) and cartilage degradation (Gong et al., 2019).

The expression of the G protein coupled estrogen receptor (GPER) is negatively linked with the pathophysiology of OA cartilage degradation. By encouraging the expression of YAP and ARHGAP29 as well as YAP nuclear localization, GPER suppresses Piezo1 and the mechanical-stress-mediated RhoA/LIMK/cofilin pathway as well as actin polymerization (Sun et al., 2021).

In mechanical-tension-mediated degenerative discs, YAP1 is a crucial regulator. In degenerative human endplate cartilage tissue, YAP1 expression has been shown to be dramatically reduced with higher mechanical stimulation intensity and duration. Additionally, it has been demonstrated in the cartilage endplate tissue *in vitro* that increasing the expression level of YAP1 can postpone the degeneration of endplate cartilage (Ding et al., 2022).

Although biomaterial design solutions for repairing injured articular cartilage have advanced significantly, preventing stem-cell-derived chondrocyte hypertrophy and the subsequent creation of inferior tissue remains a significant difficulty (Lee et al., 2020).

Furthermore, it has been discovered that OA cartilage tissue expresses higher levels of YAP1, and that YAP1 that is overexpressed interacts with Beclin 1 to advance OA. In a mouse model of mechano-induced OA, researchers attempted to employ siRNA to block YAP1, and they discovered that doing so avoided cartilage breakdown and improved OA development (Gong et al., 2019).

Both in MSCs and chondrocytes, the amount of fluid flow stress controls the expression of YAP. An increase in the stimulation magnitude enhanced the expression of YAP, increasing osteogenesis and initiating dedifferentiation for chondrocytes (Zhong et al., 2013). According to Karystinou et al., YAP is a negative regulator of MSCs' chondrogenic development. Through the derepression of chondrogenic signaling, YAP must be downregulated for chondrogenesis (Karystinou et al., 2015). A promising future in rheumatology involves therapeutic targeting of YAP to promote cartilage repair and avoid subsequent osteoarthritis. These findings demonstrate the importance of YAP/TAZ as effectors that may transmit mechanical stress into the nucleus and support healthy chondrocyte formation, maturation, and homeostasis.

4.2.3 Wnt pathway

Wnt signaling has established roles in the expression of hypertrophic markers (Lee et al., 2020), in decreasing the ECM content of cartilage (Praxenthaler et al., 2018), chondrocyte metabolism and oxidative stress (Cheleschi et al., 2020), pro-chondrogenic effects (Ma et al., 2022), and osteoblast osteogenic differentiation (Song et al., 2021). The Wnt signaling pathways that support increased expression of hypertrophic markers in cartilage can affect how transplanted articular or hypertrophic phenotypes behave. Encapsulated hMSCs were pretreated with Wnt inhibitors for 21 days in order to stop them from developing along hypertrophic pathways. Wnt inhibitor supplementation reduced the expression of indicators linked to hypertrophic chondrogenesis in comparison to controls without the addition of inhibitors, which showed an increase in the expression of hypertrophic markers (Lee et al., 2020).

WNT/-catenin and pSmad1/5/9 levels decreased as cartilage's ECM content rose. In mature constructs, the Wnt agonist CHIR reduced load-induced SOX9-and GAG activation by increasing -catenin levels. IWP-2, a WNT antagonist, on the other hand, had the ability to lessen the GAG-suppression caused by load in developing constructs. In conclusion, a stronger anabolic response of chondrocytes to physiological loading was enabled by either ECM accumulation-associated or chemically induced silencing of WNT-levels (Praxenthaler et al., 2018).

According to one study, hydrostatic pressure (HP) controls chondrocyte metabolism and oxidative stress via the Wnt/-catenin pathway in part by silencing certain miRNAs. Low cyclical HP substantially lowered the amounts of apoptosis, MMP-13, ADAMTS5, miRNA, superoxide anion generation, and mRNA for antioxidant enzymes. On the other hand, Col2a1 and BCL2 genes showed greater expression. The application of continuous static HP produced opposite consequences. Finally, miRNA silencing improved low HP and blocked effects of ongoing HP (Cheleschi et al., 2020). In a different study, mechanical loading by cyclic hydrostatic pressure (CHP) had a pro-chondrogenic impact, whereas mechanical unloading by simulated microgravity (SMG) produced OA-like gene expression in manufactured cartilage. Each sex group displayed a unique gene profile. For instance, the NOTUM gene, which is a part of the Wnt signaling pathway, was considerably elevated in the CHP for the female cohort by 6.7-fold but only by 1.8-fold in the CHP for the male cohort. However, SMG had a negligible impact on NOTUM regulation, and it revealed the opposite direction between male and female cohorts (Ma et al., 2022).

In addition to inhibiting osteoblast osteogenic development, severe mechanical stretching of osteoblasts also caused chondrocyte catabolism and apoptosis. This was accomplished by the Wnt/catenin signaling pathway (Song et al., 2021).

Suppressing canonical Wnt signaling may enhance the chondrogenesis of MSCs and attenuate the progression of OA. In comparison to control hydrogels, encapsulating hMSCs in these self-assembled N-cadherin mimic peptide hydrogels resulted in increased expression of chondrogenic marker genes and deposition of extracellular matrix specific to cartilage that is rich in proteoglycan and Type II collagen. Western blot assessment revealed a substantially reduced level of -catenin and a significantly higher expression of active glycogen synthase kinase-3 (GSK-3), which phosphorylates catenin and promotes ubiquitin-mediated destruction. In N-cadherin mimicking peptide hydrogels, immunofluorescence labeling showed much less nucleus localization of catenin. According to the results, N-cadherin peptide hydrogels increase the chondrogenesis of hMSCs by increasing catenin nuclear translocation and the transcriptional activity of the catenin/LEF-1/TCF complex and suppressing canonical Wnt signaling in hMSCs (Li et al., 2017).

GSK3β is also a downstream protein of TRPV4. In order to regulate GSK3 activation, normal chondrocytes' intracellular calcium levels, which are controlled by TRPV4 ion channels, fluctuate in response to the viscoelasticity of the ECM. Additionally, osteoarthritic chondrocytes' TRPV4-GSK3 molecular axis has been damaged, which prevents OA patients' cells from sensing and reacting to the changed viscoelasticity of the surrounding matrix (Agarwal et al., 2021).

4.2.4 NF-κB pathway

The development of osteoarthritis is heavily influenced by the excessive forces that the articular cartilage is exposed to. Under cyclic strain or hydrostatic pressure loading, Gremlin-1 is found to be a mechanical loading-inducible factor in chondrocytes and is strongly expressed in the middle and deep layers of cartilage. Nuclear factor-B signaling is activated by Gremlin-1, which causes the production of catabolic enzymes (Chang et al., 2019). Osteoarthritis progression is slowed in mice by intra-articular infusion of Gremlin-1 antibody or chondrocyte-specific Gremlin-1 deletion, but this progression is sped up by intra-articular administration of recombinant Gremlin-1 (Chang et al., 2019). These findings point to NF-B's pivotal function in mechanoinflammation as OA progresses, but perhaps more significantly, they point to several intriguing treatment targets.

In addition to being triggered by cytokine signaling, the physical pressures within chondrocytes can also regulate NF-B. NF-κB activation can activate inflammation (Sun et al., 2020), mimic the negative loading effects (Lückgen et al., 2022), and lead to the induction of catabolic enzymes (Chang et al., 2019). A study found evidence connecting the development of NLRP3 inflammasome with Piezo1-mediated inflammation in nucleus pulposus cells. A unique pathogenic mechanism driving the development of intervertebral disc degeneration is the activation of NLRP3 inflammasome in nucleus pulposus cells via Piezo1 through the Ca^{2+}/NF-B pathway (Sun et al., 2020). While catabolic NF-B signaling prevents load-induced deleterious effects on ECM synthesis in MSC-derived neocartilage, NF-B activation mimics negative loading effects and increases PGE2 production (Lückgen et al., 2022). The mechanical characteristic of neocartilage generated from mesenchymal stromal cells is increased by the NF-B suppression.

The new PCL-PTHF urethane electrospun nanofibers with collagen I from calf skin were found to be more effective at inducing chondrogenic differentiation *in vitro* and cartilage regeneration *in vivo* than the stiffer P PCL-PTHF urethane nanofibers. This was true even in the absence of additional chondrogenesis inducers. The researchers discovered that the PC worked better than P at initiating chondrogenesis by specifically blocking the NF-B signaling pathway to reduce inflammation (Jiang et al., 2018). Another study found that the AMPK/NF-B signaling pathway might be used to regulate the sensitivity of articular cartilage and chondrocytes to the inflammatory response. By promoting AMP-activated protein kinase (AMPK) activation and inhibiting nuclear factor (NF)-B translocation, cyclic tensile strain (CTS) may reduce the chondrocyte damage brought on by IL-1 (Yang et al., 2019).

5 Application of mechanical stimuli to chondrocytes

Regenerative cartilage biology involves imitation of *in vivo* cartilage formation and maintenance processes. Current developments in the field of biomaterials engineering center on the use of different alterations and biophysical stimulation of scaffolds to create implants that support cartilage regeneration.

5.1 Biomaterials for cartilage engineering mimic the mechanical properties of natural cartilage

Using cartilage tissue engineering (TE) for healing sick or damaged tissue is a promising new method. Biomaterial engineering aims to fabricate implantable biocompatible scaffolds that accelerate tissue regeneration (Przekora, 2019). It should be noted that the incapacity of biomaterials to accurately mimic the mechanical properties and resist the load of the original cartilage must be overcome in order for them to be successfully used for cartilage TE. The anisotropy of the tissue, which enables the liquid phase of the cartilage to migrate across the solid tissue during loading, is crucial to the complicated mechanical properties of articular cartilage. Body tissues' mechanical qualities decrease in various disease conditions, making them more prone to additional material failure. The ultimate objective is to create materials with mechanical resistance that produce the proper form of cartilage (Dieterle et al., 2021).

Scaffolds imitating the natural mechanical environment for chondrocyte growth have been made from a variety of organic and synthetic materials. In this context, 3D woven fiber scaffolds were used to imitate the mechanical characteristics of the native cartilage. 3D woven poly (epsilon-caprolactone) (PCL) scaffolds seeded with MSCs in MatrigelTM were shown to have aggregate and Young's moduli that were relatively similar to that of healthy articular cartilage (0.1–2.0 MPa and 0.4–0.8 MPa, respectively) (Valonen et al., 2010). Similar to this, biomechanical testing revealed that fiber-reinforced PCL-based constructs had initial compressive and shear properties that were comparable to those of native cartilage. These constructs also maintained these properties over the course of the culture period while promoting the synthesis of a collagen-rich ECM (Moutos and Guilak, 2010).

5.1.1 Natural materials scaffold

Autologous chondrocyte implantation (ACI) on a collagen type I/III scaffold was investigated by Nixon and coworkers, and it appeared to promote cartilage regeneration in a critical-sized lesion in the equine model over the course of 6 months (Nixon et al., 2015). The chondro-inductive effects of 3D collagen and hyaluronic acid hydrogels—self-assembled collagen hydrogel (Col), self-assembled collagen hydrogel cross-linked with genipin (Cgp), and methacrylated hyaluronic acid hydrogel (HA)—on the encapsulated BMSCs were assessed in a different study. In the subsequent stage, there was not enough room in the hydrogels for cell proliferation due to the extreme shrinkage of Col and Cgp. In contrast, the relatively stable mechanical environment of HA supported the maintenance of the ongoing synthesis of the cartilage matrix in the final stage (Yang et al., 2021).

Agarose-based biomaterials are crucial in cartilage tissue healing because of their special qualities, including reversible thermogelling behavior and tissue-like mechanical properties (Salati et al., 2020). Induction, gelation, and quasi-equilibrium are the three phases of the agarose gelation process. The initial phase involves the formation of a number of agarose nuclei, which are then grown into networks (Figure 10A).

5.1.2 Synergistic materials scaffold

Scaffolds were made from elastin, collagen, fibrin, and electrospun polycaprolactone (PCL) with varying ratios to overcome the drawbacks of natural and synthetic polymers by combining them to create a synergistic relationship (Figure 10B). As a result, it was possible to modify the physical and biological characteristics of PCL-based composites, in order to create a beneficial connection for a variety of applications in tissue regeneration (Sawadkar et al., 2020).

Polymeric hydrogels hold promise as potential replacement materials for the cartilage that has been injured. As a matrix for autologous chondrocyte implantation, an injectable polyethylene glycol-crosslinked albumin gel (AG) supplemented with hyaluronic acid holds promise as a beneficial implant for cartilage tissue while also exhibiting non-permissive properties for pathological blood vessel formation (Scholz et al., 2010).

5.1.3 Interpenetrating polymer scaffold

The mechanical properties of the original substrate can be increased by incorporating an interpenetrating polymer network into a single polymer network. By transferring this idea from purely synthetic materials to natural-synthetic hybrid systems, the mechanical properties of bulk biological substrates can also be strengthened (Cooper et al., 2016). This procedure improves the osteoarthritic cartilage's inferior compressive capabilities to those of healthy cartilage. An effective treatment method for the regeneration of posttraumatic or osteoarthritic lesions of the knee, according to a clinical follow-up, is implanting BioSeed-C, which is based on a bioresorbable two-component gel-polymer scaffold (Ossendorf et al., 2007).

Healthy articular cartilage has a complex structure that helps the joint bear external forces, maintain interstitial fluid to reduce strains on its soft tissue, and reduce friction between the cartilages. When

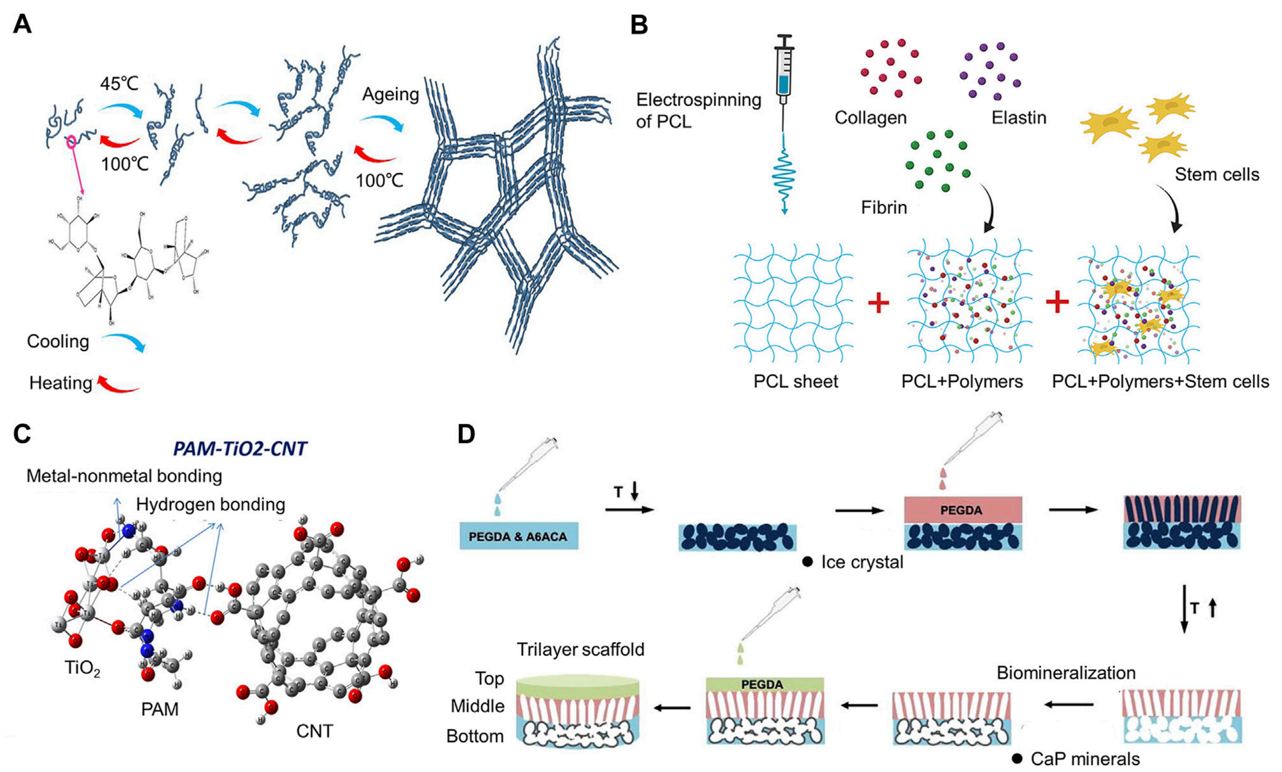

FIGURE 10
Biomaterials for cartilage engineering mimic the mechanical properties of natural cartilage **(A)** Agarose's molecular make-up and a diagram of how it gels are shown (Salati et al., 2020). **(B)** Schematic representation of the fabrication of PCL-based composites and addition of human adipose-derived stem cells (Sawadkar et al., 2020). **(C)** The chemical structure of PAM-TiO2-CNT. It has increased mechanical strength and bioactivity due to strong interfacial bonding by TiO2 and CNT with PAM(Awasthi et al., 2021). **(D)** Schematic for stepwise synthesis of the trilayer scaffold (Kang et al., 2018).

the cartilage is under loading, the surrounding matrix reduces the fluid outflow velocity to provide hydrostatic pressure. Early signs of osteoarthritis include the decrease of glycosaminoglycans and the destruction of the collagen network. An innovative polymeric cartilage supplement that recreates the extracellular matrix's hydrophilic characteristics by forming a charged interpenetrating polymer network (IPN) has been developed (Mäkelä et al., 2018). The hydrophilic ECM is principally strengthened by the IPN in order to recreate the material characteristics of cartilage. The reestablishment of the fluid phase is also impacted by this strengthening of the solid phase.

Hydrogels made of polyacrylamide are frequently used as potential substitutes for cartilage. Their application, however, is severely limited by their low mechanical durability and puncture resistance. The strength of polyacrylamide (PAM) hydrogels was increased by using titanium oxide (TiO2) and carbon nanotubes (CNTs) independently or in combination in a PAM matrix, which was interconnected by bonding between nanoparticles and polymers using a density functional theory (DFT) approach. The PAM-TiO2-CNT hydrogel's outstanding compressive strength, elastic modulus (>0.43 and 2.340 MPa, respectively), and puncture resistance (estimated using the needle insertion test) are attributed to the synergistic effect and solid interfacial bonding, making it potentially a remarkable nanocomposite hydrogel for cartilage repair applications (Figure 10C) (Awasthi et al., 2021).

5.1.4 Multilayer scaffold

The researchers devised and manufactured a strong bilayer nanocomposite acrylamide-acrylic acid hydrogel reinforced with silica nanoparticles (SNPs). By using only 0.6 wt% SNPs, the mechanical properties revealed a considerable improvement in compressive strength up to 1.4 MPa and a doubled elastic modulus (240 kPa) compared to the non-reinforced hydrogel. With appropriate ratios of monomers and SNPs, samples could be compressed without damage until reaching 85% strain (Mostakhdemin et al., 2021). Bilayer silica-reinforced nanocomposite hydrogels are possible choices for synthetic cartilage due to their mechanical properties.

A biomineralized bottom layer that mimics the calcium phosphate (CaP)-rich bone microenvironment is attached to a cryogel middle layer with an anisotropic pore architecture, and a hydrogel top layer is attached to the trilayer scaffold that is depicted in Figure 10D. The macroporous middle layer and hydrogel top layer were intended to support the production of cartilage tissue, whilst the mineralized bottom layer was intended to support the formation of bones. The transplanted cells continuously differentiated to form cartilage tissue, while endogenous cells were recruited through the mineralized bottom layer to build bone tissue, resulting in the creation of osteochondral tissue (Kang et al., 2018).

5.1.5 Piezoelectric materials scaffold

The capacity of some materials to produce electric signals in response to mechanical stress is known as the piezoelectric effect (Zhang et al., 2018). When cartilage tissue is rebuilding naturally, the extracellular matrix (ECM) creates an electric signal that is reminiscent to that produced by piezoelectric biomaterials. In a physiological environment, the compressive strain on collagen fibers in the ECM causes the dipole moment to reorganize, generating negative charges. As a result, an electrical signal enters the cell membrane, causing voltage-gated calcium channels to open.

According to a study, flexible, 3D fibrous scaffolds made of piezoelectric materials can promote ECM development and human mesenchymal stem cell differentiation under physiological loading circumstances. Piezoelectric scaffolds with a high voltage output encourage osteogenic differentiation while those with a low voltage output or streaming potential encourage chondrogenic differentiation. More considerable differentiation was discovered to be induced by electromechanical stimuli than by mechanical loading alone (Damaraju et al., 2017). Using poly (3-hydroxybutyrate-co-3-hydroxyvalerate) (PHBV) and barium titanate (BaTiO3), a clever piezoelectric nanohybrid was created. Comparatively to the control (pure PHBV) and unpolarized scaffolds, the polarized scaffolds greatly enhance cell adhesion, proliferation, and *COLIIA1* gene expression (Jacob et al., 2019).

5.1.6 Novel materials scaffold

For cartilage tissue engineering, the ideal adaptable scaffolds should evolve dynamically and spatiotemporally in response to the physiological microenvironments at each stage of cartilage repair. ECMs' mechanical strength changes as a result of growing tissue adjusting to the body's requirements (Peng et al., 2023b). Therefore, adaptive tissue engineering scaffolds should change their mechanical strength to meet the needs of cells as they grow and mature. In addition, osteochondral tissue is a gradient construct with a seamless transition from cartilage to subchondral bone, involving changes in collagen type and orientation, chondrocyte morphologies, ECM components, and cytokines. To meet the anisotropic properties of osteochondral matrices, bioinspired scaffolds have been created by replicating gradient characteristics in heterogeneous tissues, such as the pores, components, and osteochondrogenesis-inducing substances (Peng et al., 2023a). Bioinspired gradient scaffolds can restore osteochondral defects by modifying the microenvironments of cell development to promote osteochondrogenesis.

Rheumatoid arthritis (RA), is an autoimmune illness brought on by both external (hostile environment and virus invasion) and endogenous (cellular, genic, and neurological issues) components. Today, oral or injectable medications are typically used to treat RA. However, there is an urgent need to create a new method of medication delivery because of the adverse effects such as poor patient compliance, gastrointestinal disturbances, and other toxicity hazards connected with current administrations (Conforti et al., 2021). Hence, transdermal drug delivery systems, represented by microneedles, are becoming popular in the treatments of RA (Zhang et al., 2023). The melittin-loaded MeHA microneedles in the Adjuvant-Induced Arthritis (AIA) animal model prevented the rat's paw from swelling (Ye et al., 2016). TNF and IL-17 levels also decreased as regulatory CD4+T cells increased, which had a suppressive effect on RA and a protective effect on articular cartilage.

In addition, some new drug-delivery scaffolds can promote angiogenesis and subchondral bone formation, indirectly promoting joint repair (Xu et al., 2023a; Xu et al., 2023b). For the best bone regeneration, designing a multifunctional scaffold with osteogenic and angiogenic capabilities offers promise. Exosomes from human bone mesenchymal stem cells (hBMSCs) were immobilized on porous polymer meshes created by PLGA and Cu-based MOF (PLGA/CuBDC@Exo) in one study to create an innovative scaffold. The manufactured exosome-laden scaffold can deliver a dual cooperative controlled release of bioactive copper ions and exosomes that encourage osteogenesis and angiogenesis, resulting in cell-free bone repair (Xu et al., 2023a). A pro-angiogenic small molecule medication (dimethyloxallyl glycine, or DMOG) was loaded onto an iron-based metal-organic framework (MIL-88) and subsequently embedded into PLGA nanofibrous scaffolds to repair cranial lesions in rats in another study (Xu et al., 2023b). Co-delivery system considerably aided angiogenesis by enhancing endothelial cell migration, tube formation, and osteogenesis by enhancing the production of proteins associated with osteoblasts, according to an *in vitro* study.

If we can combine mechanical stimuli with these state-of-the-art biomaterial scaffolds in cartilage tissue engineering, it is expected to construct grafts that are more consistent with natural cartilage and promote joint repair.

5.2 Experimental application to model actual physiological conditions *in vitro*

In vivo, the formation and maintenance of articular cartilage depend on mechanical loading, which is a significant component of the articular cartilage environment. Therefore, efforts have been undertaken to incorporate these stresses as additional elements into cartilage engineering by building a number of bioreactors (Uzieliene et al., 2021).

Compression, tensile, and shear deformations combine to build articular motion, thus it is important to identify the precise combination of various mechanical stimuli and create regimens that have the best chondrogenic outcomes. Numerous mechanical stimulation methods have been developed in an effort to mimic the stresses that articular cartilage tissue experiences *in vivo* since it has proven difficult to manufacture cartilaginous tissue with qualities equal to those of native articular cartilage. The sorts of forces, whether they are static or dynamic, constantly applied or intermittently, applied alone or in combination with other types of forces at the same time, and how they are applied all have a significant impact on the outcomes of such systems.

The most often researched mechanical stimulation technique in cartilage tissue engineering is uniaxial static compression on the tissue surface. Designing the matching bioreactor is straightforward and merely calls for basic weights to be applied to structures made of cartilage (Salinas et al., 2018). The dynamic compression bioreactor has a favorable impact on biomechanical moduli and chondrogenic gene expression (Anderson and Johnstone, 2017). In constructs incorporating MSCs, uniaxial compression causes heterogeneous collagen deposition, with surface deposition being the highest. A cartilage-like tissue cannot likely be produced *in vitro* by compression alone as a mechanical signal. Collagen and proteoglycan production were observed to be increased when mechanical loading (5% compression and 5% shear strain amplitudes) was added compared to static (unstimulated) controls (76±8% and 73±5%, respectively) (Waldman et al., 2007).

Human MSCs have been employed in the multifunctional bioreactor. The cell-seeded scaffold was pressed onto a 32 mm ceramic hip ball. The oscillation of the ball about an axis perpendicular to the tissue axis produced the interface shear motion. Along the scaffold's cylindrical axis, the superimposed compressive strain was applied. Dynamic compression and surface shear were applied for 1 h each day for 7 days after preculture, and this increased hMSC chondrogenesis in comparison to unloaded control samples (Li et al., 2010).

Another study found that the application of shear overlaid atop dynamic compression resulted in much higher levels of chondrogenic gene expression even though no exogenous growth agents were introduced to the culture medium (Schätti et al., 2011).

Cell survival and metachromatic staining were low in TGF-free loaded samples close to the porous compression platen interface, but increased with depth, reaching levels in the deeper part of the hydrogel that were comparable to those of unloaded TGF cultures. According to these findings, low hydrostatic pressure combined with high dynamic strain and fluid flow had a more negative impact on chondrogenesis than high hydrostatic pressure combined with low dynamic strain and fluid flow (Kisiday et al., 2009). The findings might be helpful in guiding the development of enhanced multifunctional bioreactors for chondrogenic differentiation.

Regarding protocols for cartilage engineering that include mechanical stimulation, several aspects should be taken into consideration. The majority of investigations employ bioreactors that were self-designed, which has limited method replication and inconsistent confirmation of the applied forces. Additionally, only certain culture models can be used with mechanical bioreactors. The choice of materials utilized for the scaffolding affects how mechanical stimuli behave. These make data comparisons challenging and ineffective (Grad et al., 2011).

6 Conclusion

The development of MSCs into a chondrogenic phenotype and cartilage homeostasis both depend heavily on mechanical stimuli. Advanced bioreactors capable of exerting mechanical compression, fluid shear, hydrostatic pressure, and osmotic pressure or incorporating them enable the *in vivo* environment to be mimicked and enhance the chondrogenic response. Various experiments have proved that only mechanical load in a specific range of magnitude and time is conducive to cartilage regeneration, while maximal and supramaximal mechanical load is detrimental to articular cartilage. Given these advances, our goal is to provide future researchers with the optimal mechanical stimuli parameters (duration, magnitude, frequency, etc.) to promote extracellular matrix production, maintain cell viability, and promote cartilage repair. In addition, we found that different types of mechanical stimuli play different roles, for example, dynamic compression can increase the content of type II collagen and glycosaminoglycan, and fluid shear stress can promote the transport of nutrients. This suggests that we can combine different types of mechanical stimuli and utilize multiple repair mechanisms to build better cartilage tissue-engineered grafts.

However, we also found that the current research has certain limitations. First, there is no unified standard when exploring some parameters of mechanical stimuli. For example, when exploring the effect of dynamic compression, KPa is used as the unit of measurement in some experiments, while the deformation percentage of the structure generated by the compression is used as the unit of measurement in other experiments. Second, most studies have focused on the biological effects of mechanical stimuli, such as collagen content, cell viability, and inflammation. However, less attention is paid to the properties of tissue engineering construct, such as organization, compression, tensile properties, degradability, etc. Therefore, more research is needed to refine the relevant information and help draw a complete conclusion.

Chondrocytes can effectively respond to mechanical stresses either “directly” by detecting PCM deformation through cell-ECM adhesions (primary cilia, integrins) and cell sensors (ion channels), or “indirectly” by causing the release of growth factors and their interaction with cell receptors. Genes linked to anabolic or catabolic chondrocyte processes are expressed in response to context when downstream pathways are activated. Molecular biological mechanisms are elucidated, and moderate or excessive mechanical stimuli conduct biological signals by activating ion channels on the cell membrane, ultimately producing beneficial or adverse biological effects. This suggests that we may be able to use some mechanical receptor agonists or inhibitors to promote beneficial effects and avoid adverse effects, guiding the application of drug therapy in tissue-engineered constructs. Hopefully, deeper comprehension of these mechanisms in chondrocytes and chondrogenic differentiation of MSCs will result in the creation of cell-based therapies for the disease of cartilage degeneration, as well as manageable preconditioning methods for anatomically shaped MSC-based cartilage replacements.

We believe that the application of various modifications and mechanical stimuli of scaffolds can significantly advance tissue engineering by simulating the natural mechanical environment.

Author contributions

YJ: Visualization, Writing–original draft. HL: Writing–review and editing. XW: Supervision, Writing–review and editing. JZ: Validation, Writing–review and editing. YL: Data curation, Writing–original draft. JD: Data curation, Writing–original draft. FC: Funding acquisition, Writing–review and editing. CZ: Writing–review and editing.

Funding

The author(s) declare financial support was received for the research, authorship, and/or publication of this article. This work was supported by the National Key R&D Program of China (grant number 2022YFE0107700); Science and Technology Department Program of Jilin Province (grant number 20210402006GH); Science and Technology Department Program of Jilin Province (grant number 20190304121YY); and Finance Department of Jilin Province (grant number 2020SC2T001).

Acknowledgments

We would like to acknowledge the reviewers for their helpful comments on this paper.

Conflict of interest

The authors declare that the research was conducted in the absence of any commercial or financial relationships that could be construed as a potential conflict of interest.

The reviewer JD declared a past co-authorship with the author FC to the handling editor.

Publisher’s note

References

Agarwal, P., Lee, H. P., Smeriglio, P., Grandi, F., Goodman, S., Chaudhuri, O., et al. (2021). A dysfunctional TRPV4-GSK3β pathway prevents osteoarthritic chondrocytes from sensing changes in extracellular matrix viscoelasticity. *Nat. Biomed. Eng.* 5 (12), 1472–1484. doi:10.1038/s41551-021-00691-3

Albro, M. B., Cigan, A. D., Nims, R. J., Yeroushalmi, K. J., Oungoulian, S. R., Hung, C. T., et al. (2012). Shearing of synovial fluid activates latent TGF-β. *Osteoarthr. Cartil.* 20 (11), 1374–1382. doi:10.1016/j.joca.2012.07.006

Alizadeh Sardroud, H., Wanlin, T., Chen, X., and Eames, B. F. (2021). Cartilage tissue engineering approaches need to assess fibrocartilage when hydrogel constructs are mechanically loaded. *Front. Bioeng. Biotechnol.* 9, 787538. doi:10.3389/fbioe.2021.787538

Anderson, D. E., and Johnstone, B. (2017). Dynamic mechanical compression of chondrocytes for tissue engineering: a critical review. *Front. Bioeng. Biotechnol.* 5, 76. doi:10.3389/fbioe.2017.00076

Armiento, A. R., Stoddart, M. J., Alini, M., and Eglin, D. (2018). Biomaterials for articular cartilage tissue engineering: learning from biology. *Acta Biomater.* 65, 1–20. doi:10.1016/j.actbio.2017.11.021

Awasthi, S., Gaur, J. K., Pandey, S. K., Bobji, M. S., and Srivastava, C. (2021). High-strength, strongly bonded nanocomposite hydrogels for cartilage repair. *ACS Appl. Mater Interfaces* 13 (21), 24505–24523. doi:10.1021/acsami.1c05394

Bernhard, J. C., and Vunjak-Novakovic, G. (2016). Should we use cells, biomaterials, or tissue engineering for cartilage regeneration? *Stem Cell Res. Ther.* 7 (1), 56. doi:10.1186/s13287-016-0314-3

Caron, M. M., van der Windt, A. E., Emans, P. J., van Rhijn, L. W., Jahr, H., and Welting, T. J. (2013). Osmolarity determines the *in vitro* chondrogenic differentiation capacity of progenitor cells via nuclear factor of activated T-cells 5. *Bone* 53 (1), 94–102. doi:10.1016/j.bone.2012.11.032

Chang, S. H., Mori, D., Kobayashi, H., Mori, Y., Nakamoto, H., Okada, K., et al. (2019). Excessive mechanical loading promotes osteoarthritis through the gremlin-1-NF-κB pathway. *Nat. Commun.* 10 (1), 1442. doi:10.1038/s41467-019-09491-5

Cheleschi, S., Barbarino, M., Gallo, I., Tenti, S., Bottaro, M., Frati, E., et al. (2020). Hydrostatic pressure regulates oxidative stress through microRNA in human osteoarthritic chondrocytes. *Int. J. Mol. Sci.* 21 (10), 3653. doi:10.3390/ijms21103653

Chen, J., Yuan, Z., Liu, Y., Zheng, R., Dai, Y., Tao, R., et al. (2017). Improvement of *in vitro* three-dimensional cartilage regeneration by a novel hydrostatic pressure bioreactor. *Stem Cells Transl. Med.* 6 (3), 982–991. doi:10.5966/sctm.2016-0118

Cheng, B., Tu, T., Shi, X., Liu, Y., Zhao, Y., Zhao, Y., et al. (2019). A novel construct with biomechanical flexibility for articular cartilage regeneration. *Stem Cell Res. Ther.* 10 (1), 298. doi:10.1186/s13287-019-1399-2

Choi, J. B., Youn, I., Cao, L., Leddy, H. A., Gilchrist, C. L., Setton, L. A., et al. (2007). Zonal changes in the three-dimensional morphology of the chondron under compression: the relationship among cellular, pericellular, and extracellular deformation in articular cartilage. *J. Biomech.* 40 (12), 2596–2603. doi:10.1016/j.jbiomech.2007.01.009

Choi, J. R., Yong, K. W., and Choi, J. Y. (2018). Effects of mechanical loading on human mesenchymal stem cells for cartilage tissue engineering. *J. Cell Physiol.* 233 (3), 1913–1928. doi:10.1002/jcp.26018

Conforti, A., Di Cola, I., Pavlych, V., Ruscitti, P., Berardicurti, O., Ursini, F., et al. (2021). Beyond the joints, the extra-articular manifestations in rheumatoid arthritis. *Autoimmun. Rev.* 20 (2), 102735. doi:10.1016/j.autrev.2020.102735

Cooper, B. G., Stewart, R. C., Burstein, D., Snyder, B. D., and Grinstaff, M. W. (2016). A tissue-penetrating double network restores the mechanical properties of degenerated articular cartilage. *Angew. Chem. Int. Ed. Engl.* 55 (13), 4226–4230. doi:10.1002/anie.201511767

Coveney, C. R., Samvelyan, H. J., Miotla-Zarebska, J., Carnegie, J., Chang, E., Corrin, C. J., et al. (2022a). Ciliary IFT88 protects coordinated adolescent Growth Plate ossification from disruptive physiological mechanical forces. *J. Bone Min. Res.* 37 (6), 1081–1096. doi:10.1002/jbmr.4502

Coveney, C. R., Zhu, L., Miotla-Zarebska, J., Stott, B., Parisi, I., Batchelor, V., et al. (2022b). Role of ciliary protein intraflagellar transport protein 88 in the regulation of cartilage thickness and osteoarthritis development in mice. *Arthritis Rheumatol.* 74 (1), 49–59. doi:10.1002/art.41894

Damaraju, S. M., Shen, Y., Elele, E., Khusid, B., Eshghinejad, A., Li, J., et al. (2017). Three-dimensional piezoelectric fibrous scaffolds selectively promote mesenchymal stem cell differentiation. *Biomaterials* 149, 51–62. doi:10.1016/j.biomaterials.2017.09.024

Delco, M. L., and Bonassar, L. J. (2021). Targeting calcium-related mechanotransduction in early OA. *Nat. Rev. Rheumatol.* 17 (8), 445–446. doi:10.1038/s41584-021-00649-4

Dieterle, M. P., Husari, A., Rolauffs, B., Steinberg, T., and Tomakidi, P. (2021). Integrins, cadherins and channels in cartilage mechanotransduction: perspectives for future regeneration strategies. *Expert Rev. Mol. Med.* 23, e14. doi:10.1017/erm.2021.16

Ding, B., Xiao, L., and Xu, H. (2022). YAP1 controls degeneration of human cartilage chondrocytes in response to mechanical tension. *Cell Biol. Int.* 46 (10), 1637–1648. doi:10.1002/cbin.11851

Du, G., Li, L., Zhang, X., Liu, J., Hao, J., Zhu, J., et al. (2020). Roles of TRPV4 and piezo channels in stretch-evoked Ca(2+) response in chondrocytes. *Exp. Biol. Med. (Maywood)* 245 (3), 180–189. doi:10.1177/1535370219892601

Dupont, S., Morsut, L., Aragona, M., Enzo, E., Giulitti, S., Cordenonsi, M., et al. (2011). Role of YAP/TAZ in mechanotransduction. *Nature* 474 (7350), 179–183. doi:10.1038/nature10137

Erickson, G. R., Northrup, D. L., and Guilak, F. (2003). Hypo-osmotic stress induces calcium-dependent actin reorganization in articular chondrocytes. *Osteoarthr. Cartil.* 11 (3), 187–197. doi:10.1053/s1063-4584(02)00347-3

Fahy, N., Alini, M., and Stoddart, M. J. (2018). Mechanical stimulation of mesenchymal stem cells: implications for cartilage tissue engineering. *J. Orthop. Res.* 36 (1), 52–63. doi:10.1002/jor.23670

Fanning, P. J., Emkey, G., Smith, R. J., Grodzinsky, A. J., Szasz, N., and Trippel, S. B. (2003). Mechanical regulation of mitogen-activated protein kinase signaling in articular cartilage. *J. Biol. Chem.* 278 (51), 50940–50948. doi:10.1074/jbc.M305107200

Farnum, C. E., and Wilsman, N. J. (2011). Orientation of primary cilia of articular chondrocytes in three-dimensional space. *Anat. Rec. Hob.* 294 (3), 533–549. doi:10.1002/ar.21330

Fu, S., Thompson, C. L., Ali, A., Wang, W., Chapple, J. P., Mitchison, H. M., et al. (2019). Mechanical loading inhibits cartilage inflammatory signalling via an HDAC6 and IFT-dependent mechanism regulating primary cilia elongation. *Osteoarthr. Cartil.* 27 (7), 1064–1074. doi:10.1016/j.joca.2019.03.003

Ge, Y., Li, Y., Wang, Z., Li, L., Teng, H., and Jiang, Q. (2021). Effects of mechanical compression on chondrogenesis of human synovium-derived mesenchymal stem cells in agarose hydrogel. *Front. Bioeng. Biotechnol.* 9, 697281. doi:10.3389/fbioe.2021.697281

Gemmiti, C. V., and Guldberg, R. E. (2006). Fluid flow increases type II collagen deposition and tensile mechanical properties in bioreactor-grown tissue-engineered cartilage. *Tissue Eng.* 12 (3), 469–479. doi:10.1089/ten.2006.12.469

Geoghegan, I. P., Hoey, D. A., and McNamara, L. M. (2019). Integrins in osteocyte biology and mechanotransduction. *Curr. Osteoporos. Rep.* 17 (4), 195–206. doi:10.1007/s11914-019-00520-2

Gonçalves, A., Costa, P., Rodrigues, M. T., Dias, I. R., Reis, R. L., and Gomes, M. E. (2011). Effect of flow perfusion conditions in the chondrogenic differentiation of bone marrow stromal cells cultured onto starch based biodegradable scaffolds. *Acta Biomater.* 7 (4), 1644–1652. doi:10.1016/j.actbio.2010.11.044

Gong, Y., Li, S. J., Liu, R., Zhan, J. F., Tan, C., Fang, Y. F., et al. (2019). Inhibition of YAP with siRNA prevents cartilage degradation and ameliorates osteoarthritis development. *J. Mol. Med. Berl.* 97 (1), 103–114. doi:10.1007/s00109-018-1705-y

Grad, S., Eglin, D., Alini, M., and Stoddart, M. J. (2011). Physical stimulation of chondrogenic cells *in vitro*: a review. *Clin. Orthop. Relat. Res.* 469 (10), 2764–2772. doi:10.1007/s11999-011-1819-9

Hara, E. S., Okada, M., Nagaoka, N., Hattori, T., Iida, L. M., Kuboki, T., et al. (2018). Chondrocyte burst promotes space for mineral expansion. *Integr. Biol. (Camb)* 10 (1), 57–66. doi:10.1039/c7ib00130d

Healy, Z. R., Zhu, F., Stull, J. D., and Konstantopoulos, K. (2008). Elucidation of the signaling network of COX-2 induction in sheared chondrocytes: COX-2 is induced via a Rac/MEKK1/MKK7/JNK2/c-Jun-C/EBPβ-dependent pathway. *Am. J. Physiol. Cell Physiol.* 294 (5), C1146–C1157. doi:10.1152/ajpcell.00542.2007

Hirose, N., Okamoto, Y., Yanoshita, M., Asakawa, Y., Sumi, C., Takano, M., et al. (2020). Protective effects of cilengitide on inflammation in chondrocytes under excessive mechanical stress. *Cell Biol. Int.* 44 (4), 966–974. doi:10.1002/cbin.11293

Hodder, E., Guppy, F., Covill, D., and Bush, P. (2020). The effect of hydrostatic pressure on proteoglycan production in articular cartilage *in vitro*: a meta-analysis. *Osteoarthr. Cartil.* 28 (8), 1007–1019. doi:10.1016/j.joca.2020.03.021

Hodgkinson, T., Kelly, D. C., Curtin, C. M., and O'Brien, F. J. (2022). Mechanosignalling in cartilage: an emerging target for the treatment of osteoarthritis. *Nat. Rev. Rheumatol.* 18 (2), 67–84. doi:10.1038/s41584-021-00724-w

Holledge, M. M., Millward-Sadler, S. J., Nuki, G., and Salter, D. M. (2008). Mechanical regulation of proteoglycan synthesis in normal and osteoarthritic human articular chondrocytes – roles for α5 and αVβ5 integrins. *Biorheology* 45 (3-4), 275–288. doi:10.3233/bir-2008-0476

Hopewell, B., and Urban, J. P. (2003). Adaptation of articular chondrocytes to changes in osmolality. *Biorheology* 40 (1-3), 73–77.

Hua, R., and Jiang, J. X. (2021). Small leucine-rich proteoglycans in physiological and biomechanical function of bone. *Matrix Biol. Plus* 11, 100063. doi:10.1016/j.mbplus.2021.100063

Huang, Y., Fan, H., Gong, X., Yang, L., and Wang, F. (2021a). Scaffold with natural calcified cartilage zone for osteochondral defect repair in minipigs. *Am. J. Sports Med.* 49 (7), 1883–1891. doi:10.1177/03635465211007139

Huang, Y. Z., Zhao, L., Zhu, Y., Tian, S. J., Zhang, W., Liu, S., et al. (2021b). Interrupting TGF-β1/CCN2/integrin-α5β1 signaling alleviates high mechanical-stress caused chondrocyte fibrosis. *Eur. Rev. Med. Pharmacol. Sci.* 25 (3), 1233–1241. doi:10.26355/eurrev_202102_24827

Inamdar, S. R., Barbieri, E., Terrill, N. J., Knight, M. M., and Gupta, H. S. (2019). Proteoglycan degradation mimics static compression by altering the natural gradients in fibrillar organisation in cartilage. *Acta Biomater.* 97, 437–450. doi:10.1016/j.actbio.2019.07.055

Inamdar, S. R., Prévost, S., Terrill, N. J., Knight, M. M., and Gupta, H. S. (2021). Reversible changes in the 3D collagen fibril architecture during cyclic loading of healthy and degraded cartilage. *Acta Biomater.* 136, 314–326. doi:10.1016/j.actbio.2021.09.037

Jablonski, C. L., Ferguson, S., Pozzi, A., and Clark, A. L. (2014). Integrin α1β1 participates in chondrocyte transduction of osmotic stress. *Biochem. Biophys. Res. Commun.* 445 (1), 184–190. doi:10.1016/j.bbrc.2014.01.157

Jacob, J., More, N., Mounika, C., Gondaliya, P., Kalia, K., and Kapusetti, G. (2019). Smart piezoelectric nanohybrid of poly(3-hydroxybutyrate-co-3-hydroxyvalerate) and barium titanate for stimulated cartilage regeneration. *Acs Appl. Bio Mater.* 2 (11), 4922–4931. doi:10.1021/acsabm.9b00667

Jensen, C. G., Poole, C. A., McGlashan, S. R., Marko, M., Issa, Z. I., Vujcich, K. V., et al. (2004). Ultrastructural, tomographic and confocal imaging of the chondrocyte primary cilium *in situ*. *Cell Biol. Int.* 28 (2), 101–110. doi:10.1016/j.cellbi.2003.11.007

Jeon, J. E., Schrobback, K., Hutmacher, D. W., and Klein, T. J. (2012). Dynamic compression improves biosynthesis of human zonal chondrocytes from osteoarthritis patients. *Osteoarthr. Cartil.* 20 (8), 906–915. doi:10.1016/j.joca.2012.04.019

Jiang, T., Kai, D., Liu, S., Huang, X., Heng, S., Zhao, J., et al. (2018). Mechanically cartilage-mimicking poly(PCL-PTHF urethane)/collagen nanofibers induce chondrogenesis by blocking NF-kappa B signaling pathway. *Biomaterials* 178, 281–292. doi:10.1016/j.biomaterials.2018.06.023

Jin, Y., Li, Z., Wu, Y., Li, H., Liu, Z., Liu, L., et al. (2021). Aberrant fluid shear stress contributes to articular cartilage pathogenesis via epigenetic regulation of ZBTB20 by H3K4me3. *J. Inflamm. Res.* 14, 6067–6083. doi:10.2147/jir.S339382

Kang, H., Zeng, Y., and Varghese, S. (2018). Functionally graded multilayer scaffolds for *in vivo* osteochondral tissue engineering. *Acta Biomater.* 78, 365–377. doi:10.1016/j.actbio.2018.07.039

Karystinou, A., Roelofs, A. J., Neve, A., Cantatore, F. P., Wackerhage, H., and De Bari, C. (2015). Yes-associated protein (YAP) is a negative regulator of chondrogenesis in mesenchymal stem cells. *Arthritis Res. Ther.* 17 (1), 147. doi:10.1186/s13075-015-0639-9

Kazemi, M., and Williams, J. L. (2021). Depth and strain rate-dependent mechanical response of chondrocytes in reserve zone cartilage subjected to compressive loading. *Biomech. Model Mechanobiol.* 20 (4), 1477–1493. doi:10.1007/s10237-021-01457-1

Kisiday, J. D., Frisbie, D. D., McIlwraith, C. W., and Grodzinsky, A. J. (2009). Dynamic compression stimulates proteoglycan synthesis by mesenchymal stem cells in the absence of chondrogenic cytokines. *Tissue Eng. Part A* 15 (10), 2817–2824. doi:10.1089/ten.TEA.2008.0357

Lahiji, K., Polotsky, A., Hungerford, D. S., and Frondoza, C. G. (2004). cyclic strain stimulates proliferative capacity, α2 and α5 integrin, gene marker expression by human articular chondrocytes propagated on flexible silicone membranes. *Vitro Cell Dev. Biol. Anim.* 40 (5-6), 138–142. doi:10.1290/1543-706x(2004)40<138:Csspca>2.0.Co;2

Le, H., Xu, W., Zhuang, X., Chang, F., Wang, Y., and Ding, J. (2020). Mesenchymal stem cells for cartilage regeneration. *J. Tissue Eng.* 11, 204173142094383. doi:10.1177/2041731420943839

Lee, J., Jeon, O., Kong, M., Abdeen, A. A., Shin, J. Y., Lee, H. N., et al. (2020). Combinatorial screening of biochemical and physical signals for phenotypic regulation of stem cell-based cartilage tissue engineering. *Sci. Adv.* 6 (21), eaaz5913. doi:10.1126/sciadv.aaz5913

Lee, K. L., Guevarra, M. D., Nguyen, A. M., Chua, M. C., Wang, Y., and Jacobs, C. R. (2015). The primary cilium functions as a mechanical and calcium signaling nexus. *Cilia* 4, 7. doi:10.1186/s13630-015-0016-y

Lee, W., Leddy, H. A., Chen, Y., Lee, S. H., Zelenski, N. A., McNulty, A. L., et al. (2014). Synergy between Piezo1 and Piezo2 channels confers high-strain mechanosensitivity to articular cartilage. *Proc. Natl. Acad. Sci. U. S. A.* 111 (47), E5114–E5122. doi:10.1073/pnas.1414298111

Lee, W., Nims, R. J., Savadipour, A., Zhang, Q., Leddy, H. A., Liu, F., et al. (2021). Inflammatory signaling sensitizes Piezo1 mechanotransduction in articular chondrocytes as a pathogenic feed-forward mechanism in osteoarthritis. *Proc. Natl. Acad. Sci. U. S. A.* 118 (13), e2001611118. doi:10.1073/pnas.2001611118

Li, J., Wang, J., Zou, Y., Zhang, Y., Long, D., Lei, L., et al. (2012). The influence of delayed compressive stress on TGF-β1-induced chondrogenic differentiation of rat BMSCs through Smad-dependent and Smad-independent pathways. *Biomaterials* 33 (33), 8395–8405. doi:10.1016/j.biomaterials.2012.08.019

Li, R., Xu, J., Wong, D. S. H., Li, J., Zhao, P., and Bian, L. (2017). Self-assembled N-cadherin mimetic peptide hydrogels promote the chondrogenesis of mesenchymal stem cells through inhibition of canonical Wnt/β-catenin signaling. *Biomaterials* 145, 33–43. doi:10.1016/j.biomaterials.2017.08.031

Li, T., Ma, Z., Zhang, Y., Yang, Z., Li, W., Lu, D., et al. (2023). Regeneration of humeral head using a 3D bioprinted anisotropic scaffold with dual modulation of endochondral ossification. *Adv. Sci. (Weinh)* 10, e2205059. doi:10.1002/advs.202205059

Li, X. F., Zhang, Z., Li, X. D., Wang, T. B., and Zhang, H. N. (2016). Mechanism of the Piezo1 protein-induced apoptosis of the chondrocytes through the MAPK/ERK1/2 signal pathway. *Zhonghua Yi Xue Za Zhi* 96 (31), 2472–2477. doi:10.3760/cma.j.issn.0376-2491.2016.31.007

Li, Z., Yao, S. J., Alini, M., and Stoddart, M. J. (2010). Chondrogenesis of human bone marrow mesenchymal stem cells in fibrin-polyurethane composites is modulated by frequency and amplitude of dynamic compression and shear stress. *Tissue Eng. Part A* 16 (2), 575–584. doi:10.1089/ten.TEA.2009.0262

Liang, C., Li, H., Tao, Y., Zhou, X., Li, F., Chen, G., et al. (2012). Responses of human adipose-derived mesenchymal stem cells to chemical microenvironment of the intervertebral disc. *J. Transl. Med.* 10, 49. doi:10.1186/1479-5876-10-49

Lin, W., and Klein, J. (2021). Recent progress in cartilage lubrication. *Adv. Mater* 33 (18), e2005513. doi:10.1002/adma.202005513

Liu, H., Hu, J., Zheng, Q., Feng, X., Zhan, F., Wang, X., et al. (2022). Piezo1 channels as force sensors in mechanical force-related chronic inflammation. *Front. Immunol.* 13, 816149. doi:10.3389/fimmu.2022.816149

Loeser, R. F., Sadiev, S., Tan, L., and Goldring, M. B. (2000). Integrin expression by primary and immortalized human chondrocytes: evidence of a differential role for α1β1 and α2β1 integrins in mediating chondrocyte adhesion to types II and VI collagen. *Osteoarthr. Cartil.* 8 (2), 96–105. doi:10.1053/joca.1999.0277

Lückgen, J., Raqué, E., Reiner, T., Diederichs, S., and Richter, W. (2022). NFκB inhibition to lift the mechano-competence of mesenchymal stromal cell-derived neocartilage toward articular chondrocyte levels. *Stem Cell Res. Ther.* 13 (1), 168. doi:10.1186/s13287-022-02843-x

Ma, Z., Li, D. X., Kunze, M., Mulet-Sierra, A., Westover, L., and Adesida, A. B. (2022). Engineered human meniscus in modeling sex differences of knee osteoarthritis *in vitro*. *Front. Bioeng. Biotechnol.* 10, 823679. doi:10.3389/fbioe.2022.823679

Mäkelä, J. T. A., Cooper, B. G., Korhonen, R. K., Grinstaff, M. W., and Snyder, B. D. (2018). Functional effects of an interpenetrating polymer network on articular cartilage mechanical properties. *Osteoarthr. Cartil.* 26 (3), 414–421. doi:10.1016/j.joca.2018.01.001

Martin, J. A., Miller, B. A., Scherb, M. B., Lembke, L. A., and Buckwalter, J. A. (2002). Co-localization of insulin-like growth factor binding protein 3 and fibronectin in human articular cartilage. *Osteoarthr. Cartil.* 10 (7), 556–563. doi:10.1053/joca.2002.0791

McDermott, A. M., Eastburn, E. A., Kelly, D. J., and Boerckel, J. D. (2021). Effects of chondrogenic priming duration on mechanoregulation of engineered cartilage. *J. Biomech.* 125, 110580. doi:10.1016/j.jbiomech.2021.110580

McGlashan, S. R., Jensen, C. G., and Poole, C. A. (2006). Localization of extracellular matrix receptors on the chondrocyte primary cilium. *J. Histochem Cytochem* 54 (9), 1005–1014. doi:10.1369/jhc.5A6866.2006

Moore, E. R., and Jacobs, C. R. (2018). The primary cilium as a signaling nexus for growth plate function and subsequent skeletal development. *J. Orthop. Res.* 36 (2), 533–545. doi:10.1002/jor.23732

Mostakhdemin, M., Nand, A., and Ramezani, M. (2021). A novel assessment of microstructural and mechanical behaviour of bilayer silica-reinforced nanocomposite hydrogels as a candidate for artificial cartilage. *J. Mech. Behav. Biomed. Mater* 116, 104333. doi:10.1016/j.jmbbm.2021.104333

Moutos, F. T., and Guilak, F. (2010). Functional properties of cell-seeded three-dimensionally woven poly(ε-caprolactone) scaffolds for cartilage tissue engineering. *Tissue Eng. Part A* 16 (4), 1291–1301. doi:10.1089/ten.TEA.2009.0480

Nakamura, F., Tsukamoto, I., Inoue, S., Hashimoto, K., and Akagi, M. (2018). Cyclic compressive loading activates angiotensin II type 1 receptor in articular chondrocytes and stimulates hypertrophic differentiation through a G-protein-dependent pathway. *FEBS Open Bio* 8 (6), 962–973. doi:10.1002/2211-5463.12438

Nishino, T., Chang, F., Ishii, T., Yanai, T., Mishima, H., and Ochiai, N. (2010a). Joint distraction and movement for repair of articular cartilage in a rabbit model with subsequent weight-bearing. *J. Bone Jt. Surg. Br.* 92 (7), 1033–1040. doi:10.1302/0301-620x.92b7.23200

Nishino, T., Ishii, T., Chang, F., Yanai, T., Watanabe, A., Ogawa, T., et al. (2010b). Effect of gradual weight-bearing on regenerated articular cartilage after joint distraction and motion in a rabbit model. *J. Orthop. Res.* 28 (5), 600–606. doi:10.1002/jor.21016

Nixon, A. J., Rickey, E., Butler, T. J., Scimeca, M. S., Moran, N., and Matthews, G. L. (2015). A chondrocyte infiltrated collagen type I/III membrane (MACI® implant) improves cartilage healing in the equine patellofemoral joint model. *Osteoarthr. Cartil.* 23 (4), 648–660. doi:10.1016/j.joca.2014.12.021

O'Conor, C. J., Leddy, H. A., Benefield, H. C., Liedtke, W. B., and Guilak, F. (2014). TRPV4-mediated mechanotransduction regulates the metabolic response of chondrocytes to dynamic loading. *Proc. Natl. Acad. Sci. U. S. A.* 111 (4), 1316–1321. doi:10.1073/pnas.1319569111

O'Conor, C. J., Ramalingam, S., Zelenski, N. A., Benefield, H. C., Rigo, I., Little, D., et al. (2016). Cartilage-specific knockout of the mechanosensory ion channel TRPV4 decreases age-related osteoarthritis. *Sci. Rep.* 6, 29053. doi:10.1038/srep29053

Offeddu, G. S., Tanase, C. E., Toumpaniari, S., Oyen, M. L., and Cameron, R. E. (2018). Stiffening by osmotic swelling constraint in cartilage-like cell culture scaffolds. *Macromol. Biosci.* 18 (11), e1800247. doi:10.1002/mabi.201800247

Ossendorf, C., Kaps, C., Kreuz, P. C., Burmester, G. R., Sittinger, M., and Erggelet, C. (2007). Treatment of posttraumatic and focal osteoarthritic cartilage defects of the knee with autologous polymer-based three-dimensional chondrocyte grafts: 2-year clinical results. *Arthritis Res. Ther.* 9 (2), R41. doi:10.1186/ar2180

Pattappa, G., Zellner, J., Johnstone, B., Docheva, D., and Angele, P. (2019). Cells under pressure - the relationship between hydrostatic pressure and mesenchymal stem cell chondrogenesis. *Eur. Cell Mater* 37, 360–381. doi:10.22203/eCM.v037a22

Peng, Y., Zhuang, Y., Liu, Y., Le, H., Li, D., Zhang, M., et al. (2023a). Bioinspired gradient scaffolds for osteochondral tissue engineering. *J. Biomed. Mater. Res. Part A* 3 (4), 20210043. doi:10.1002/EXP.20210043

Peng, Y., Zhuang, Y., Zhang, Y., Zuo, J., and Ding, J. (2023b). Dynamically adaptive scaffolds for cartilage tissue engineering. *J. Biomed. Mater. Res. Part B Appl. Biomaterials* 2 (3), e49. doi:10.1002/mba2.49

Praxenthaler, H., Krämer, E., Weisser, M., Hecht, N., Fischer, J., Grossner, T., et al. (2018). Extracellular matrix content and WNT/β-catenin levels of cartilage determine the chondrocyte response to compressive load. *Biochim. Biophys. Acta Mol. Basis Dis.* 1864 (3), 851–859. doi:10.1016/j.bbadis.2017.12.024

Przekora, A. (2019). Current trends in fabrication of biomaterials for bone and cartilage regeneration: materials modifications and biophysical stimulations. *Int. J. Mol. Sci.* 20 (2), 435. doi:10.3390/ijms20020435

Rux, D., Helbig, K., Han, B., Cortese, C., Koyama, E., Han, L., et al. (2022). Primary cilia direct murine articular cartilage tidemark patterning through hedgehog signaling and ambulatory load. *J. Bone Min. Res.* 37 (6), 1097–1116. doi:10.1002/jbmr.4506

Sakai, S., Mishima, H., Ishii, T., Akaogi, H., Yoshioka, T., Ohyabu, Y., et al. (2009). Rotating three-dimensional dynamic culture of adult human bone marrow-derived cells for tissue engineering of hyaline cartilage. *J. Orthop. Res.* 27 (4), 517–521. doi:10.1002/jor.20566

Salati, M. A., Khazai, J., Tahmuri, A. M., Samadi, A., Taghizadeh, A., Taghizadeh, M., et al. (2020). Agarose-based biomaterials: opportunities and challenges in cartilage tissue engineering. *Polymers* 12 (5), 1150. doi:10.3390/polym12051150

Salinas, E. Y., Aryaei, A., Paschos, N., Berson, E., Kwon, H., Hu, J. C., et al. (2020). Shear stress induced by fluid flow produces improvements in tissue-engineered cartilage. *Biofabrication* 12 (4), 045010. doi:10.1088/1758-5090/aba412

Salinas, E. Y., Donahue, R. P., Herrera, J. M., Hu, J. C., and Athanasiou, K. A. (2022). The functionality and translatability of neocartilage constructs are improved with the combination of fluid-induced shear stress and bioactive factors. *Faseb J.* 36 (4), e22225. doi:10.1096/fj.202101699R

Salinas, E. Y., Hu, J. C., and Athanasiou, K. (2018). A guide for using mechanical stimulation to enhance tissue-engineered articular cartilage properties. *Tissue Eng. Part B Rev.* 24 (5), 345–358. doi:10.1089/ten.TEB.2018.0006

Sani, M., Hosseinie, R., Latifi, M., Shadi, M., Razmkhah, M., Salmannejad, M., et al. (2022). Engineered artificial articular cartilage made of decellularized extracellular matrix by mechanical and IGF-1 stimulation. *Biomater. Adv.* 139, 213019. doi:10.1016/j.bioadv.2022.213019

Sawadkar, P., Mohanakrishnan, J., Rajasekar, P., Rahmani, B., Kohli, N., Bozec, L., et al. (2020). A synergistic relationship between polycaprolactone and natural polymers enhances the physical properties and biological activity of scaffolds. *ACS Appl. Mater Interfaces* 12 (12), 13587–13597. doi:10.1021/acsami.9b19715

Schätti, O., Grad, S., Goldhahn, J., Salzmann, G., Li, Z., Alini, M., et al. (2011). A combination of shear and dynamic compression leads to mechanically induced chondrogenesis of human mesenchymal stem cells. *Eur. Cell Mater* 22, 214–225. doi:10.22203/ecm.v022a17

Schätti, O. R., Marková, M., Torzilli, P. A., and Gallo, L. M. (2015). Mechanical loading of cartilage explants with compression and sliding motion modulates gene expression of lubricin and catabolic enzymes. *Cartilage* 6 (3), 185–193. doi:10.1177/1947603515581680

Schipani, R., Scheurer, S., Florentin, R., Critchley, S. E., and Kelly, D. J. (2020). Reinforcing interpenetrating network hydrogels with 3D printed polymer networks to engineer cartilage mimetic composites. *Biofabrication* 12 (3), 035011. doi:10.1088/1758-5090/ab8708

Scholz, B., Kinzelmann, C., Benz, K., Mollenhauer, J., Wurst, H., and Schlosshauer, B. (2010). Suppression of adverse angiogenesis in an albumin-based hydrogel for articular cartilage and intervertebral disc regeneration. *Eur. Cell Mater* 20, 24–37. discussion 36-27. doi:10.22203/ecm.v020a03

Schuiringa, G. H., Pastrama, M., Ito, K., and van Donkelaar, C. C. (2023). Towards a load bearing hydrogel: a proof of principle in the use of osmotic pressure for biomimetic cartilage constructs. *J. Mech. Behav. Biomed. Mater* 137, 105552. doi:10.1016/j.jmbbm.2022.105552

Sharifi, N., and Gharravi, A. M. (2019). Shear bioreactors stimulating chondrocyte regeneration, a systematic review. *Inflamm. Regen.* 39, 16. doi:10.1186/s41232-019-0105-1

Shattil, S. J., Kim, C., and Ginsberg, M. H. (2010). The final steps of integrin activation: the end game. *Nat. Rev. Mol. Cell Biol.* 11 (4), 288–300. doi:10.1038/nrm2871

Song, C. X., Liu, S. Y., Zhu, W. T., Xu, S. Y., and Ni, G. X. (2021). Excessive mechanical stretch-mediated osteoblasts promote the catabolism and apoptosis of chondrocytes via the Wnt/β-catenin signaling pathway. *Mol. Med. Rep.* 24 (2), 593. doi:10.3892/mmr.2021.12232

Song, F., Mao, X., Dai, J., Shan, B., Zhou, Z., and Kang, Y. (2023). Integrin αVβ3 signaling in the progression of osteoarthritis induced by excessive mechanical stress. *Inflammation* 46 (2), 739–751. doi:10.1007/s10753-022-01770-6

Sun, Y., Leng, P., Guo, P., Gao, H., Liu, Y., Li, C., et al. (2021). G protein coupled estrogen receptor attenuates mechanical stress-mediated apoptosis of chondrocyte in osteoarthritis via suppression of Piezo1. *Mol. Med.* 27 (1), 96. doi:10.1186/s10020-021-00360-w

Sun, Y., Leng, P., Song, M., Li, D., Guo, P., Xu, X., et al. (2020). Piezo1 activates the NLRP3 inflammasome in nucleus pulposus cell-mediated by Ca(2+)/NF-κB pathway. *Int. Immunopharmacol.* 85, 106681. doi:10.1016/j.intimp.2020.106681

Takada, E., and Mizuno, S. (2018). Reproduction of characteristics of extracellular matrices in specific longitudinal depth zone cartilage within spherical organoids in response to changes in osmotic pressure. *Int. J. Mol. Sci.* 19 (5), 1507. doi:10.3390/ijms19051507

Tamkun, J. W., DeSimone, D. W., Fonda, D., Patel, R. S., Buck, C., Horwitz, A. F., et al. (1986). Structure of integrin, a glycoprotein involved in the transmembrane linkage between fibronectin and actin. *Cell* 46 (2), 271–282. doi:10.1016/0092-8674(86)90744-0

Tao, F., Jiang, T., Tao, H., Cao, H., and Xiang, W. (2020). Primary cilia: versatile regulator in cartilage development. *Cell Prolif.* 53 (3), e12765. doi:10.1111/cpr.12765

Tew, S. R., Peffers, M. J., McKay, T. R., Lowe, E. T., Khan, W. S., Hardingham, T. E., et al. (2009). Hyperosmolarity regulates SOX9 mRNA posttranscriptionally in human articular chondrocytes. *Am. J. Physiol. Cell Physiol.* 297 (4), C898–C906. doi:10.1152/ajpcell.00571.2008

Thompson, C. L., McFie, M., Chapple, J. P., Beales, P., and Knight, M. M. (2021). Polycystin-2 is required for chondrocyte mechanotransduction and traffics to the primary cilium in response to mechanical stimulation. *Int. J. Mol. Sci.* 22 (9), 4313. doi:10.3390/ijms22094313

Tian, J., Zhang, F. J., and Lei, G. H. (2015). Role of integrins and their ligands in osteoarthritic cartilage. *Rheumatol. Int.* 35 (5), 787–798. doi:10.1007/s00296-014-3137-5

Turunen, S. M., Lammi, M. J., Saarakkala, S., Koistinen, A., and Korhonen, R. K. (2012). Hypotonic challenge modulates cell volumes differently in the superficial zone of intact articular cartilage and cartilage explant. *Biomech. Model Mechanobiol.* 11 (5), 665–675. doi:10.1007/s10237-011-0341-z

Uzieliene, I., Bironaite, D., Pachaleva, J., Bagdonas, E., Sobolev, A., Tsai, W. B., et al. (2023). Chondroitin sulfate-tyramine-based hydrogels for cartilage tissue repair. *Int. J. Mol. Sci.* 24 (4), 3451. doi:10.3390/ijms24043451

Uzieliene, I., Bernotas, P., Mobasheri, A., and Bernotiene, E. (2018). The role of physical stimuli on calcium channels in chondrogenic differentiation of mesenchymal stem cells. *Int. J. Mol. Sci.* 19 (10), 2998. doi:10.3390/ijms19102998

Uzieliene, I., Bironaite, D., Bernotas, P., Sobolev, A., and Bernotiene, E. (2021). Mechanotransducive biomimetic systems for chondrogenic differentiation *in vitro*. *Int. J. Mol. Sci.* 22 (18), 9690. doi:10.3390/ijms22189690

Vágó, J., Katona, É., Takács, R., Dócs, K., Hajdú, T., Kovács, P., et al. (2022). Cyclic uniaxial mechanical load enhances chondrogenesis through entraining the molecular circadian clock. *J. Pineal Res.* 73 (4), e12827. doi:10.1111/jpi.12827

Valonen, P. K., Moutos, F. T., Kusanagi, A., Moretti, M. G., Diekman, B. O., Welter, J. F., et al. (2010). *In vitro* generation of mechanically functional cartilage grafts based on adult human stem cells and 3D-woven poly(ε-caprolactone) scaffolds. *Biomaterials* 31 (8), 2193–2200. doi:10.1016/j.biomaterials.2009.11.092

Vincent, T. L. (2011). Fibroblast growth factor 2: good or bad guy in the joint? *Arthritis Res. Ther.* 13 (5), 127. doi:10.1186/ar3447

Vincent, T. L., McLean, C. J., Full, L. E., Peston, D., and Saklatvala, J. (2007). FGF-2 is bound to perlecan in the pericellular matrix of articular cartilage, where it acts as a chondrocyte mechanotransducer. *Osteoarthr. Cartil.* 15 (7), 752–763. doi:10.1016/j.joca.2007.01.021

Vincent, T. L., and Wann, A. K. T. (2019). Mechanoadaptation: articular cartilage through thick and thin. *J. Physiol.* 597 (5), 1271–1281. doi:10.1113/jp275451

Wagner, D. R., Lindsey, D. P., Li, K. W., Tummala, P., Chandran, S. E., Smith, R. L., et al. (2008). Hydrostatic pressure enhances chondrogenic differentiation of human bone marrow stromal cells in osteochondrogenic medium. *Ann. Biomed. Eng.* 36 (5), 813–820. doi:10.1007/s10439-008-9448-5

Waldman, S. D., Couto, D. C., Grynpas, M. D., Pilliar, R. M., and Kandel, R. A. (2007). Multi-axial mechanical stimulation of tissue engineered cartilage: review. *Eur. Cell Mater* 13, 66–75. discussion 73-64. doi:10.22203/ecm.v013a07

Wang, S., Li, W., Zhang, P., Wang, Z., Ma, X., Liu, C., et al. (2022a). Mechanical overloading induces GPX4-regulated chondrocyte ferroptosis in osteoarthritis via Piezo1 channel facilitated calcium influx. *J. Adv. Res.* 41, 63–75. doi:10.1016/j.jare.2022.01.004

Wang, Z. H., Le, H. X., Wang, Y. B., Liu, H., Li, Z. H., Yang, X. Y., et al. (2022c). Instructive cartilage regeneration modalities with advanced therapeutic implantations under abnormal conditions. *Bioact. Mater.* 11, 317–338. doi:10.1016/j.bioactmat.2021.10.002

Wang, Z., Irianto, J., Kazun, S., Wang, W., and Knight, M. M. (2015). The rate of hypo-osmotic challenge influences regulatory volume decrease (RVD) and mechanical properties of articular chondrocytes. *Osteoarthr. Cartil.* 23 (2), 289–299. doi:10.1016/j.joca.2014.11.003

Wang, Z., Le, H., Wang, Y., Liu, H., Li, Z., Yang, X., et al. (2022b). Instructive cartilage regeneration modalities with advanced therapeutic implantations under abnormal conditions. *Bioact. Mater* 11, 317–338. doi:10.1016/j.bioactmat.2021.10.002

Xiang, W., Jiang, T., Hao, X., Wang, R., Yao, X., Sun, K., et al. (2019). Primary cilia and autophagy interaction is involved in mechanical stress mediated cartilage development via ERK/mTOR axis. *Life Sci.* 218, 308–313. doi:10.1016/j.lfs.2019.01.001

Xie, J., Han, Z. Y., and Matsuda, T. (2006). Mechanical compressive loading stimulates the activity of proximal region of human COL2A1 gene promoter in transfected chondrocytes. *Biochem. Biophys. Res. Commun.* 344 (4), 1192–1199. doi:10.1016/j.bbrc.2006.03.243

Xie, M., Fritch, M., He, Y., Fu, H., Hong, Y., and Lin, H. (2021). Dynamic loading enhances chondrogenesis of human chondrocytes within a biodegradable resilient hydrogel. *Biomater. Sci.* 9 (14), 5011–5024. doi:10.1039/d1bm00413a

Xu, C., Kang, Y., Dong, X., Jiang, D., and Qi, M. (2023a). Integration exosomes with MOF-modified multifunctional scaffold for accelerating vascularized bone regeneration. *Chin. Chem. Lett.* 34 (2), 107528. doi:10.1016/j.cclet.2022.05.042

Xu, C., Kang, Y., Guan, S., Dong, X., Jiang, D., and Qi, M. (2023b). Iron-based metal–organic framework as a dual cooperative release system for enhanced vascularization and bone regeneration. *Chin. Chem. Lett.* 34 (5), 107825. doi:10.1016/j.cclet.2022.107825

Xu, G. K., Yang, C., Du, J., and Feng, X. Q. (2014). Integrin activation and internalization mediated by extracellular matrix elasticity: a biomechanical model. *J. Biomech.* 47 (6), 1479–1484. doi:10.1016/j.jbiomech.2014.01.022

Yang, J., Tang, Z., Liu, Y., Luo, Z., Xiao, Y., and Zhang, X. (2021). Comparison of chondro-inductivity between collagen and hyaluronic acid hydrogel based on chemical/physical microenvironment. *Int. J. Biol. Macromol.* 182, 1941–1952. doi:10.1016/j.ijbiomac.2021.05.188

Yang, Y., Wang, Y., Kong, Y., Zhang, X., Zhang, H., Gang, Y., et al. (2019). Mechanical stress protects against osteoarthritis via regulation of the AMPK/NF-κB signaling pathway. *J. Cell Physiol.* 234 (6), 9156–9167. doi:10.1002/jcp.27592

Yanoshita, M., Hirose, N., Okamoto, Y., Sumi, C., Takano, M., Nishiyama, S., et al. (2018). Cyclic tensile strain upregulates pro-inflammatory cytokine expression via FAK-MAPK signaling in chondrocytes. *Inflammation* 41 (5), 1621–1630. doi:10.1007/s10753-018-0805-8

Ye, Y., Yu, J., Wang, C., Nguyen, N. Y., Walker, G. M., Buse, J. B., et al. (2016). Microneedles integrated with pancreatic cells and synthetic glucose-signal amplifiers for smart insulin delivery. *Adv. Mater* 28 (16), 3115–3121. doi:10.1002/adma.201506025

Yu, L., Cavelier, S., Hannon, B., and Wei, M. (2023). Recent development in multizonal scaffolds for osteochondral regeneration. *Bioact. Mater* 25, 122–159. doi:10.1016/j.bioactmat.2023.01.012

Zhang, H., Shao, Y., Yao, Z., Liu, L., Zhang, H., Yin, J., et al. (2022a). Mechanical overloading promotes chondrocyte senescence and osteoarthritis development through downregulating FBXW7. *Ann. Rheum. Dis.* 81 (5), 676–686. doi:10.1136/annrheumdis-2021-221513

Zhang, J., Wehrle, E., Rubert, M., and Müller, R. (2021a). 3D bioprinting of human tissues: biofabrication, bioinks, and bioreactors. *Int. J. Mol. Sci.* 22 (8), 3971. doi:10.3390/ijms22083971

Zhang, K., Wang, L., Liu, Z., Geng, B., Teng, Y., Liu, X., et al. (2021b). Mechanosensory and mechanotransductive processes mediated by ion channels in articular chondrocytes: potential therapeutic targets for osteoarthritis. *Channels (Austin)* 15 (1), 339–359. doi:10.1080/19336950.2021.1903184

Zhang, K., Wang, S., Zhou, C., Cheng, L., Gao, X., Xie, X., et al. (2018). Advanced smart biomaterials and constructs for hard tissue engineering and regeneration. *Bone Res.* 6, 31. doi:10.1038/s41413-018-0032-9

Zhang, M., Meng, N., Wang, X., Chen, W., and Zhang, Q. (2022b). TRPV4 and PIEZO channels mediate the mechanosensing of chondrocytes to the biomechanical microenvironment. *Membr. (Basel)* 12 (2), 237. doi:10.3390/membranes12020237

Zhang, T., Wen, F., Wu, Y., Goh, G. S., Ge, Z., Tan, L. P., et al. (2015). Cross-talk between TGF-beta/SMAD and integrin signaling pathways in regulating hypertrophy of mesenchymal stem cell chondrogenesis under deferral dynamic compression. *Biomaterials* 38, 72–85. doi:10.1016/j.biomaterials.2014.10.010

Zhang, Y., Xu, Y., Kong, H., Zhang, J., Chan, H. F., Wang, J., et al. (2023). Microneedle system for tissue engineering and regenerative medicine. *Explor. (Beijing)* 3 (1), 20210170. doi:10.1002/exp.20210170

Zhao, X., Hua, Y., Wang, T., Ci, Z., Zhang, Y., Wang, X., et al. (2022). *In vitro* cartilage regeneration regulated by a hydrostatic pressure bioreactor based on hybrid photocrosslinkable hydrogels. *Front. Bioeng. Biotechnol.* 10, 916146. doi:10.3389/fbioe.2022.916146

Zhao, Z., Li, Y., Wang, M., Zhao, S., Zhao, Z., and Fang, J. (2020). Mechanotransduction pathways in the regulation of cartilage chondrocyte homoeostasis. *J. Cell Mol. Med.* 24 (10), 5408–5419. doi:10.1111/jcmm.15204

Zhen, G., Guo, Q., Li, Y., Wu, C., Zhu, S., Wang, R., et al. (2021). Mechanical stress determines the configuration of TGFβ activation in articular cartilage. *Nat. Commun.* 12 (1), 1706. doi:10.1038/s41467-021-21948-0

Zhong, W., Tian, K., Zheng, X., Li, L., Zhang, W., Wang, S., et al. (2013). Mesenchymal stem cell and chondrocyte fates in a multishear microdevice are regulated by Yes-associated protein. *Stem Cells Dev.* 22 (14), 2083–2093. doi:10.1089/scd.2012.0685

Zhou, Q., Lyu, S., Bertrand, A. A., Hu, A. C., Chan, C. H., Ren, X., et al. (2021). Stiffness of nanoparticulate mineralized collagen scaffolds triggers osteogenesis via mechanotransduction and canonical Wnt signaling. *Macromol. Biosci.* 21 (3), e2000370. doi:10.1002/mabi.202000370

Zhu, F., Wang, P., Lee, N. H., Goldring, M. B., and Konstantopoulos, K. (2010). Prolonged application of high fluid shear to chondrocytes recapitulates gene expression profiles associated with osteoarthritis. *PLoS One* 5 (12), e15174. doi:10.1371/journal.pone.0015174

frontiers | Frontiers in Bioengineering and Biotechnology

TYPE Original Research
PUBLISHED 23 November 2023
DOI 10.3389/fbioe.2023.1295626

OPEN ACCESS

EDITED BY
Behnam Akhavan,
The University of Newcastle, Australia

REVIEWED BY
Vinod Reddy Lekkala,
University of North Texas, United States
Xuan Mei,
Harvard Medical School, United States

*CORRESPONDENCE
Nohra E. Beltran-Vargas,
✉ nbeltran@cua.uam.mx

RECEIVED 16 September 2023
ACCEPTED 14 November 2023
PUBLISHED 23 November 2023

CITATION
Viveros-Moreno NG, Garcia-Lorenzana M, Peña-Mercado E, García-Sanmartín J, Narro-Íñiguez J, Salazar-García M, Huerta-Yepez S, Sanchez-Gomez C, Martínez A and Beltran-Vargas NE (2023), *In vivo* biocompatibility testing of nanoparticle-functionalized alginate–chitosan scaffolds for tissue engineering applications. *Front. Bioeng. Biotechnol.* 11:1295626. doi: 10.3389/fbioe.2023.1295626

In vivo biocompatibility testing of nanoparticle-functionalized alginate–chitosan scaffolds for tissue engineering applications

Nancy G. Viveros-Moreno[1], Mario Garcia-Lorenzana[2], Eduardo Peña-Mercado[3], Josune García-Sanmartín[4], Judit Narro-Íñiguez[4], Marcela Salazar-García[5], Sara Huerta-Yepez[6], Concepción Sanchez-Gomez[5], Alfredo Martínez[4] and Nohra E. Beltran-Vargas[3]*

[1]Doctorado en Ciencias Biológicas y de la Salud, Universidad Autonoma Metropolitana, Ciudad de Mexico, Mexico, [2]Department of Reproduction Biology, Division of Biological and Health Sciences, Universidad Autonoma Metropolitana, Iztapalapa, Mexico, [3]Department of Processes and Technology, Division of Natural Sciences and Engineering, Universidad Autonoma Metropolitana, Cuajimalpa, Mexico, [4]Angiogenesis Group, Center for Biomedical Research of La Rioja (CIBIR), Logroño, Spain, [5]Research Laboratory of Developmental Biology and Experimental Teratogenesis, Children's Hospital of Mexico Federico Gomez, Mexico City, Mexico, [6]Research Laboratory of Hematooncology, Children's Hospital of Mexico Federico Gomez, Mexico City, Mexico

Background: There is a strong interest in designing new scaffolds for their potential application in tissue engineering and regenerative medicine. The incorporation of functionalization molecules can lead to the enhancement of scaffold properties, resulting in variations in scaffold compatibility. Therefore, the efficacy of the therapy could be compromised by the foreign body reaction triggered after implantation.

Methods: In this study, the biocompatibilities of three scaffolds made from an alginate–chitosan combination and functionalized with gold nanoparticles (AuNp) and alginate-coated gold nanoparticles (AuNp + Alg) were evaluated in a subcutaneous implantation model in Wistar rats. Scaffolds and surrounding tissue were collected at 4-, 7- and 25-day postimplantation and processed for histological analysis and quantification of the expression of genes involved in angiogenesis, macrophage profile, and proinflammatory (IL-1β and TNFα) and anti-inflammatory (IL-4 and IL-10) cytokines.

Results: Histological analysis showed a characteristic foreign body response that resolved 25 days postimplantation. The intensity of the reaction assessed through capsule thickness was similar among groups. Functionalizing the device with AuNp and AuNp + Alg decreased the expression of markers associated with cell death by apoptosis and polymorphonuclear leukocyte recruitment, suggesting increased compatibility with the host tissue. Similarly, the formation of many foreign body giant cells was prevented. Finally, an increased detection of alpha smooth muscle actin was observed, showing the angiogenic properties of the elaborated scaffolds.

Conclusion: Our results show that the proposed scaffolds have improved biocompatibility and exhibit promising potential as biomaterials for elaborating tissue engineering constructs.

KEYWORDS

alginate, chitosan, biocompatibility, foreign body reaction, subcutaneous implantation

1 Introduction

There is a great interest in developing novel scaffolds in tissue engineering (TE) (Goldenberg et al., 2021; Bertsch et al., 2023; Han et al., 2023). To maintain cell viability and functionality, biomaterials used as scaffolds must satisfy biophysical and biochemical requirements associated with mechanical strength, porosity, biodegradability, and biocompatibility (Dzobo et al., 2018). Implant devices often have compromised efficacy due to host recognition problems and subsequent responses, resulting in acute inflammation, chronic inflammation, granulation tissue, foreign body reaction (FBR), chronic encapsulation, or dissolution of the implanted biomaterial (Veiseh et al., 2015; Chung et al., 2017; Ibrahim et al., 2017; Carnicer-Lombarte et al., 2021; Wei et al., 2021).

Immune recognition of a biomaterial initiates a cascade of cellular processes leading to FBR. The response to the materials occurs in four phases: hemostatic, inflammatory, proliferative, and remodeling. Degradation or even complete phagocytosis of the biomaterial resolves the FBR. A failed transition from the inflammatory to the proliferative phase leads to a failed resolution, characterized by fibrous encapsulation rather than tissue regeneration. During this transition, immune cells, such as macrophages and neutrophils, play a crucial role by altering their phenotype and recruiting cells that will follow in the proliferative phase (Anderson et al., 2008; Major et al., 2015; Chung et al., 2017; Martin and García, 2021).

The intensity of the inflammatory response is mainly determined by the composition of the biomaterial and by the porosity, hydrophobicity, topography, and biodegradability of the scaffold, which lead to the recruitment and reactivity of cellular mediators after implantation (Abaricia et al., 2021; Martin and García, 2021; Kyriakides et al., 2022).

Biomaterials of natural origin have been documented to cause mild FBR relative to those of synthetic origin (Ibrahim et al., 2017). Porosity has been shown to impact FBR positively. Porous scaffolds (>40 μm) elicit less severe inflammatory responses (Veiseh et al., 2015), by polarizing macrophages towards the M2 phenotype. Also, porosity contributes to increased vascularization, cellular infiltration, and reduced fibrosis (Kyriakides et al., 2022; Li et al., 2022). Hydrophobicity plays an important role in the degradation of biomaterials and in the adsorption of proteins on the biomaterial. Depending on the hydrophobicity, proteins will have different affinities for the biomaterial, resulting in different inflammatory responses (Jeong et al., 2017). Scaffolds with hydrophilic ends have been documented to result in increased expression of anti-inflammatory cytokines, M2 macrophage recruitment, optimal tissue infiltration (Flaig et al., 2020), and increased material-cell interaction (Patil et al., 2022). The topography of the biomaterial may also affect the FBR, specifically regarding macrophage behavior (Witherel et al., 2019). Finally, it has been observed that biomaterials with prolonged tissue residence develop a relatively avascular collagen-rich capsule around the implant, which sequesters it from the surrounding tissue (Ibrahim et al., 2017).

Strategies aimed at interfering with cellular events driving FBR have been proposed in the design of bioactive scaffolds (Abaricia et al., 2021), including immunomodulatory biomaterials (Whitaker et al., 2021; Chen et al., 2022), functionalization of the scaffold with anti-inflammatory molecules, or with optimization and conservation of bioactive components that maximize the bioactive potential of the biomaterial (Joyce et al., 2021). Thus, the scaffold design should support cellular activity without hindering the post implantation signaling cascade.

Natural biomaterials possess bioactive properties so that biological activity can be imparted to a material using natural polymers (Joyce et al., 2021). Chitosan and alginate stand out among the vast array of natural biomaterials. Chitosan (Cs)—a natural polysaccharide made from glucosamine and an N-acetyl-glucosamine moiety—is extracted from crustacean shells through deacetylation. Cs has the highest chelating capacity of all natural polymers and promotes cell adhesion, proliferation, and differentiation (Muxika et al., 2017; Joyce et al., 2021). Alginate (Alg) is a natural polysaccharide found in marine algae, which contains linked blocks of β-D-mannuronic acid (M) and α-L-guluronic acid (G) monomers (1–4). Alg exhibits poor cell adhesion but combined with peptides or other polymers, such as Cs, it enhances cell adhesion and proliferation *in vitro*. Alg is a biomaterial capable of incorporating and retaining cells and proteins (Sun and Tan, 2013; Joyce et al., 2021) and promotes angiogenesis (Sondermeijer et al., 2018).

Since the search for strategies to improve the electrical properties of biomaterials began, using metallic nanostructures, such as gold (Au), has become relevant in TE (Yadid et al., 2019). It has been reported that the incorporation of Au nanoparticles (Np) reduces apoptosis and inflammation (Shevach et al., 2014; Sridhar et al., 2015; Somasuntharam et al., 2016), which is conducive to cell proliferation (Maharjan et al., 2019), in addition to improving the physical properties of the scaffold (Yadid et al., 2019).

Our working group has designed scaffolds for applications in TE using sodium Alg and Cs, functionalized with alginate-coated gold nanoparticles (AuNp + Alg). The resulting scaffolds are highly porous (>90%) and hydrophilic, with swelling percentages of approximately 3,000% and permeability in the order of 1×10^{-8} m^2 (Beltran-Vargas et al., 2022). Although a physicochemical characterization of the proposed scaffolds was carried out and cell growth tests were reported, with better results using AuNp + Alg, it is important to study how this novel scaffold affect host response, such as inflammation and immune modulation *in vivo*.

This work aimed to analyze the biocompatibility of three types of Alg/Cs scaffolds with and without AuNp functionalization by subdermal implantation in Wistar rats.

2 Materials and methods

2.1 Scaffolding

Sodium alginate (Sigma Aldrich, Mannheim, Germany, #9005-38-3) and chitosan (medium molecular weight, Sigma Aldrich, Mannheim, Germany, #448877) (0.75%–1.25% w/v) powder were mixed and dissolved in ultrapure water and acetic acid (1% w/v, Sigma Aldrich). pH was adjusted between 5 and 6. The solution was placed into 24-well plates. After freezing and freeze-drying, cross-linking was performed with 1% calcium gluconate for 30 min. Subsequently, washings were performed with ultrapure water, and the mixture was dried and freeze-dried for 8 h. Functionalization of Alg/Cs scaffolds with gold nanoparticles (AuNp) was performed as previously reported (Beltran-Vargas et al., 2022).

The scaffolds have 1.4 cm in diameter, 12 mg in weight, and 0.3 cm wide, with 93% swelling, referred to the maximum swelling of the scaffolds, after 40 min of contact with aqueous medium, more than 90% porosity, and degrades less than 20% after 7 days. The average diameter of AuNp was 74.5 and 91 nm for AuNp + Alg. The surface charge values were in average −25.5 and −37 mV for AuNp and AuNp + Alg respectively. AuNp presented a spheroidal structure whereas AuNp + Alg showed cylindrical particle characteristics (Beltran-Vargas et al., 2022).

Unfunctionalized Alg/Cs scaffolds (without Np), Alg/Cs scaffolds functionalized with gold nanoparticles (AuNp), and Alg/Cs scaffolds functionalized with alginate-coated gold nanoparticles (AuNp + Alg) were obtained.

2.2 *In vivo* subcutaneous model

The experiments were performed with female (250–300 g) and male (300–350 g) Wistar rats ($n = 4$ per group), which were provided by the biotherium of the Federico Gomez Children's Hospital of Mexico. The rats were kept in a controlled environment (22°C ± 2°C) with 50%–60% relative humidity and 12–12 h light–dark cycles, with access to food and water *ad libitum* until surgery. All animal procedures follow protocols strictly conformed by Mexican Official Guidelines (NOM-062-ZOO-1999) and were approved by the research, ethics, and biosafety committees of the Children's Hospital of Mexico Federico Gomez (HIM/2020/059).

Subcutaneous implantation of the scaffolds was performed through three 1-cm incisions in the dorsum of the rat under aseptic conditions (70% ethanol) and anesthesia (xylazine and ketamine (10–90 mg/kg) administered intraperitoneally. Each specimen received a scaffold without Np in the interscapular area and functionalized with AuNp and AuNp + Alg on the sides. Prior to implantation, the scaffolds were hydrated for 24 h in phosphate-buffered saline under sterile conditions, and their final dimensions were 6 mm diameter × 0.1 mm thick. A subcutaneous pocket was formed between the skin and muscle tissue, and the corresponding scaffold was placed. After implantation, the incisions were closed with surgical glue (Vetbond Tissue Adhesive 1469Sb) (Figures 1A, B).

The animals were sacrificed on days 4, 7, and 25 after implantation, and the implants were obtained with the surrounding tissue (Figures 1C, D). Four animals were used for each trial. At the end of the experiments, the animals were sacrificed according to NOM-062-ZOO-1999.

2.3 Histological procedure

Tissue samples were fixed in 4% neutral formalin (pH 7.4). The tissue was then processed with standard histological technique and embedded in Paraplast Plus. Finally, 3-µm thick serial transverse sections were made with a rotating microtome and premounted to apply different staining techniques. The overall architecture and infiltration of cells in the connective tissue were observed with hematoxylin-eosin (H–E) staining, and fibrotic tissue development was observed with Masson's trichrome (MT) stain.

2.4 Cell infiltrate and identification of foreign body giant cells

Cell infiltration was determined with H–E staining to quantify cell migration into the scaffold for 4, 7, and 25 days. Six fields per scaffold were scanned and digitized (×20 objective) with Aperio CS2 equipment (Leica Biosystems, Deer Park, IL, United States). Quantitative analysis of the nuclei of infiltrating cells was performed with ImageJ software (National Institutes of Health [NIH]). Photomicrographs were separated into layers via Split Channels. Nuclei within the scaffold were isolated via "color thresholding." The tool "analyze particles" was used to quantify nuclei within the scaffold boundaries. To ensure that the analysis was objective, all samples were quantified with the same thresholding conditions as reported by (Dulany et al., 2020). Subsequently, the average number of infiltrating cell nuclei was obtained for each scaffold type.

For quantification of foreign body giant cells (FBGCs), six fields per scaffold were used. Sections were photographed with ×20 objective, and the total number of cells identified per field was recorded for analysis.

2.5 Fibrotic capsule identification

MT stain was used to identify fibrotic capsule formation around the perimeter of the implanted scaffolds. The fibrotic capsule was determined by the presence of dense collagen bands positive for aniline blue at 4- and 7-day postimplantation. Fibrotic tissue thickness was recorded in 500 µm fields using the Aperio software "pencil" tool to quantify capsule thickness. On average, 25 measurements were obtained per specimen, which were averaged to determine the thickness of the fibrotic capsule.

2.6 Evaluation of collagen deposits internal to the scaffold

Photomicrographs with MT stain of the general field obtained at 25 days were taken with Aperio Software and analyzed using Fiji-

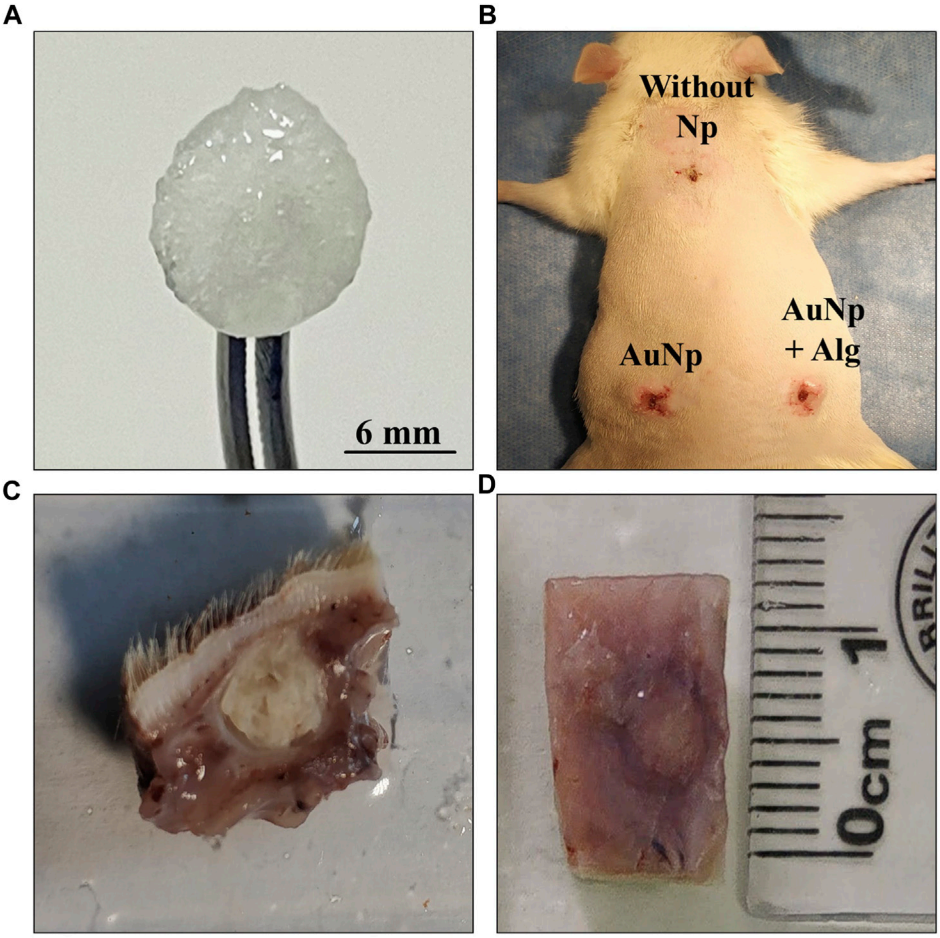

FIGURE 1
(A) Macroscopic appearance of a hydrated chitosan–alginate scaffold. **(B)** Subdermal implantation sites in the dorsal region, no signs of infection or rejection are appreciated. **(C, D)** General view of tissues collected after sacrifice.

ImageJ. With the "Color Deconvolution" tool, the "vectors = Brilliant_Blue" was obtained. The scaffold was delimited with this layer, and the remnants of the capsule and surrounding tissue were excluded. Finally, the "analyze particles" tool was used to quantify the area occupied by the collagen deposits in this region.

2.7 RNA extraction, reverse transcription, and real-time polymerase chain reaction (PCR)

Total RNA was isolated from paraffin tissues section (15 μm-thick) and purified with the High Pure FFPE RNA Isolation kit (Roche Diagnostics, Indianapolis, IN), according to manufacturer's instructions. Resulting RNA (1.0 μg) was reverse transcribed using the NZY First-Strand cDNA Synthesis kit (Nzytech, Lisboa, Portugal), and the synthesized cDNA was amplified using NZY Supreme qPCR Green Master Mix (Nzytech). Transcripts were amplified by real-time PCR (QuantStudio 5, Applied Biosystems, Waltham, MA, United States) as described (García-Sanmartín et al., 2022). A specific cDNA calibration curve was included. GAPDH was used as a housekeeping gene (Table 1).

Healthy skin was used as a control of the experiment.

2.8 Immunohistochemistry

Tissue sections (3 μm-thick) were dewaxed in xylene, and endogenous peroxidase was blocked with 3% H_2O_2 in methanol for 15 min. Samples were rehydrated and subjected to antigen retrieval (10 mM Sodium Citrate, 0.5% Tween 20, pH 6.0, 20 min at 95°C). Nonspecific binding was blocked by exposure to the protein block buffer (Novocastra Leica Biosystems, Newcastle, UK) for 30 min. Then tissue sections were incubated with rabbit polyclonal antibody against Iba1 (019-19741, FUJIFILM Wako Chemicals United States corporation), at 1:500 dilution or with mouse monoclonal antibody against α-SMA (a2547, Sigma-Aldrich), at 1:5,000 dilution at 4°C, overnight.

The following day, sections were incubated with post-primary solution and Novolink polymer (Novocastra Leica Biosystems, Wetzlar, Germany), followed by exposure to 3,3′-diaminobenzidine (Dako, Carpinteria, CA, United States). Slides were lightly counterstained with hematoxylin and analyzed with an

TABLE 1 Sequence of the primers used for quantitative Reverse Transcription—Polymerase Chain Reaction (qRT-PCR) and their annealing temperature.

Gene of interest	Sense primer	Antisense primer	Annealing temp.
TNFalpha	CCACCACGCTCTTCTGTCTA	CACTTGGTGGTTTGCTACGA	60°C
CD11c	AGAAGGGGACAGGTTGGACT	GCCTGGACTGTGCTTGGTAA	60°C
Tlr4	TCTCACAACTTCAGTGGCTGG	AGTACCAAGGTTGAGAGCTGG	60°C
iNOS	AGGCCACCTCGGATATCTCT	GCTTGTCTCTGGGTCCTCTG	60°C
CD86	CTTACGGAAGCACCCACGAT	TGTAAATGGGCACGGCAGAT	60°C
IL-4	TCCACGGATGTAACGACAGC	TGGTGTTCCTTGTTGCCGTA	60°C
IL10	AGGCGCTGTCATCGATTTCT	CTCTTCACCTGCTCCACTGC	60°C
VEGFa	CCAGGCTGCACCCACGACAG	CGCACACCGCATTAGGGGCA	60°C
L1b	AGGCTGACAGACCCCAAAAG	CTCCACGGGCAAGACATAGG	60°C
Arg1	CTCCAAGCCAAAGCCCATAG	GCTGCGGGACCTTTCTCTAC	60°C
Mrc1/CD206	CAAGGAAGGTTGGCATTTGT	GGAACGTGTGCTCTGAGTTG	60°C
Pecam1	AGCACACAGAGAGCTTCGTC	TTTGTCCACGGTCACCTCAG	60°C
Gapdh	ATGGTGAAGGTCGGTGTGAAC	TCTCAGCCTTGACTGTGCC	60°C

Eclipse 50i microscope (Nikon, Tokyo, Japan) equipped with a DXM 1200c digital camera (Nikon).

Quantification of immunohistochemical signals. At least six images from each stained section of each sample were analyzed. Immunoreactivity was evaluated using the ImageJ free software (NIH, Bethesda, MD), following published guidelines (Crowe and Yue, 2019). The procedure included the selection of the region of interest, color deconvolution, threshold setting, and measurement of fraction area (percentage of pixels highlighted in red from the selected area).

2.9 Statistical analysis

Normality of the dataset distribution was assessed using the one-sample Kolmogorov–Smirnov test. Infiltrated cell area, cell density, and capsule thickness analysis were performed with one-way analysis of variance test followed by a Tukey *post hoc* T3 (Six fields per scaffold were scanned and digitized for those analysis). Since the number of animals were small and the distribution was not normal in the other variables analysed, those datasets were compared with the Kruskal–Wallis test. A p-value<0.05 was considered statistically significant. Data are presented as the mean ± standard error of the mean (SEM). Analyses were performed using Prism, version 9 (GraphPad Software, San Diego, CA, United States).

3 Results

3.1 Postimplantation macroscopic observations

All scaffolds remained at the original implantation site with no apparent signs of infection, rejection, tissue necrosis, or abscess formation around the scaffolds. Detailed identification shows a lack of calcifications in the connective tissue (Figures 1B–D).

3.2 Biocompatibility and cellular infiltration in alginate–chitosan scaffolds

Scaffold biocompatibility and cellular infiltration were examined using H–E staining 4, 7, and 25 days after implantation. The overall fields of the longitudinal section of representative scaffolds per group are shown in Figure 2. The host tissue reaction to implantation is consistent with FBR, characterized by the formation of a capsule surrounding the material and the recruitment of immune cells (Figure 2). Within the global view, it was observed that the scaffolds maintain their overall shape throughout the study. The pores of the scaffold are occupied by leukocyte infiltrate, which, over time, gets homogeneously distributed in the center of the scaffold. Resolution of the event at 25 days includes dissolution of the capsule without completely degrading the scaffold. A granulation tissue remains in place in the capsule.

To understand the progression of the FBR, the cell types present in the implanted tissue were monitored over time. Figure 3A shows a magnified section (×20) of the perimeter of the scaffold showing histological changes consistent with an acute immune response at 4 days post-implantation. The initial response of the material included the recruitment of many neutrophils, observable on the periphery of the scaffold. Cell density is reported as the total number of cells per field at 20× analyzed with ImageJ software (Figure 3B). At 7 days, there was a significant increase (p < 0.05) in the number of infiltrated cells in the AuNp + Alg scaffold (3136 ± 2003) compared to the without Np scaffold (1593 ± 772.8). At this time of implantation, increased metabolic activity was observed within the scaffold, characterized by regions with a population of dead cells, apparent cellular debris, and areas of myxoid degeneration, both close to the remnants of the biomaterial. Significant numbers of neutrophils remain on the periphery of the scaffold. The Alg–Cs scaffold shows a larger area

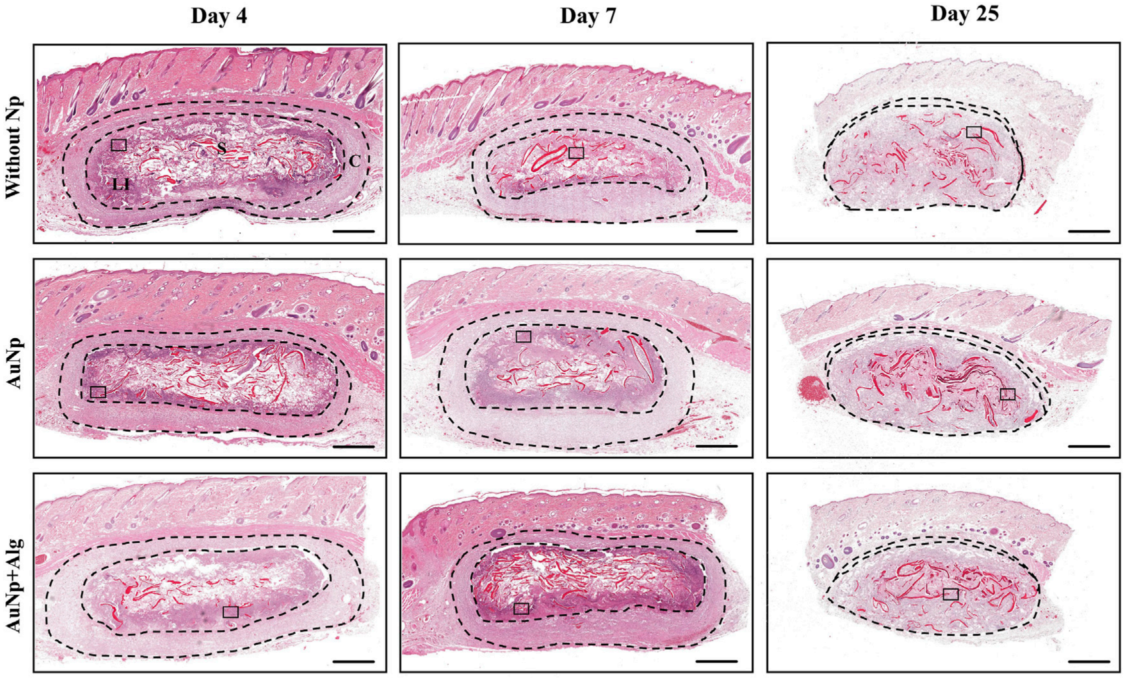

FIGURE 2
Representative photomicrographs of subcutaneously implanted chitosan-alginate scaffolds showing FBR and the development and evolution of the capsule over time, (H−E; bar = 1 mm). Identifiers: C: capsule, LI: leukocyte infiltrate, S: scaffold. The thickness of the capsule is shown between the dashed lines. After 25 days, the capsule decreases. Framed regions were enlarged in Figure 3 to show the details of the cellular infiltrates.

referring to areas of cell necrosis; thus, a significant decrease in the cellular area occupied by the leukocyte infiltrate compared to the functionalized groups (Without Np: 12.54% ± 8.306%, AuNp: 25.82% ± 18.50%, AuNp + Alg: 42.25% ± 31.26%, $p < 0.01$) was observed (Figure 3C). At 25 days after implantation, macrophages represent the predominant cell type. FBGCs are observed located throughout the scaffold. There is a decrease in the number of FBGCs in the AuNp + Alg scaffold (Without Np: 9.8 ± 4.3, AuNp: 7.1 ± 2.6, AuNp + Alg: 5.8 ± 2.6, $p < 0.05$) (Figure 3D). Only a small number of neutrophils are observed around the remnant scaffold fibers. Finally, the epidermis tissue in contact with the scaffold contains the same structures as normal epidermal tissue.

The real-time expression of genes for proinflammatory (IL-1β and TNFα) and anti-inflammatory (IL-4 and IL-10) cytokines was quantified (Figure 4A) from total RNA isolated from the implanted scaffolds. The expression of IL-1β tends to decrease over time in the groups without Np and AuNp + Alg. Despite not registering significant differences between groups, the expression of IL-1β in the AuNp + Alg group is apparently lower compared to that recorded in the experiment for 25 days. TNFα expression tends to increase in the without Np group at 4 and 25 and 7 days in the AuNp group. The low expression in the AuNp + Alg group remained unchanged throughout the study. In the case of anti-inflammatory cytokines, IL-4 expression was only recorded in the groups without Np and AuNp at 4 and 7 days. IL-10 expression tended to increase at 4 and 25 days in the without Np group and to decrease in the AuNp + Alg group at 25 days. No apparent changes were observed in the AuNp group.

In parallel, Iba1 expression was assessed with immunohistochemistry. Iba1 evidenced the level of inflammation in the entire scaffold and surrounding dermis tissue (Figure 4B). Iba1 expression was observed in all groups. The percentage of the positive area presented a tendency to increase in the presence of the scaffold in relation to the control group at 4 days postimplantation (control: 0.55% ± 0.33%, Without Np: 38.14% ± 23.76%, AuNp: 46.04% ± 24.22%, AuNp + Alg: 32.52% ± 16.48%). At 25 days, Iba1 expression was significantly higher in the NpAu scaffold compared to without Np (Without Np: 19.65% ± 8.96%, AuNp: 46.80% ± 25.85%, $p < 0.05$).

These results demonstrate that the FBR had resolved 25 days after implantation. The expression of anti-inflammatory cytokines and markers related to macrophage activation suggests a decrease in inflammation in Alg-coated and functionalized scaffolds.

3.3 Identification of fibrous capsule and collagen areas

MT-stained sections revealed the fibrous capsule formed around the implants. The response is similar among groups. The capsule thickness and internal collagen content are shown in Figure 5A. At 4 days, a capsule formed by lax connective tissue was observed, which subsequently became dense connective tissue at 7 days. The capsule thickness (Figure 5B) is similar among groups (440 ± 23 μm) at 4 days and tends to increase at 7 days (502 ± 14 μm). The capsule decreases at day 25 (Without Np: 150 ± 51 μm, AuNp: 169 ± 99 μm, AuNp + Alg: 58 ± 22 μm). Once the capsule has shrunk towards the ventral and dorsal region of the implant, granulation tissue is identified, characterized by a large number of blood vessels containing erythrocytes, which constitutes a vascularized interface.

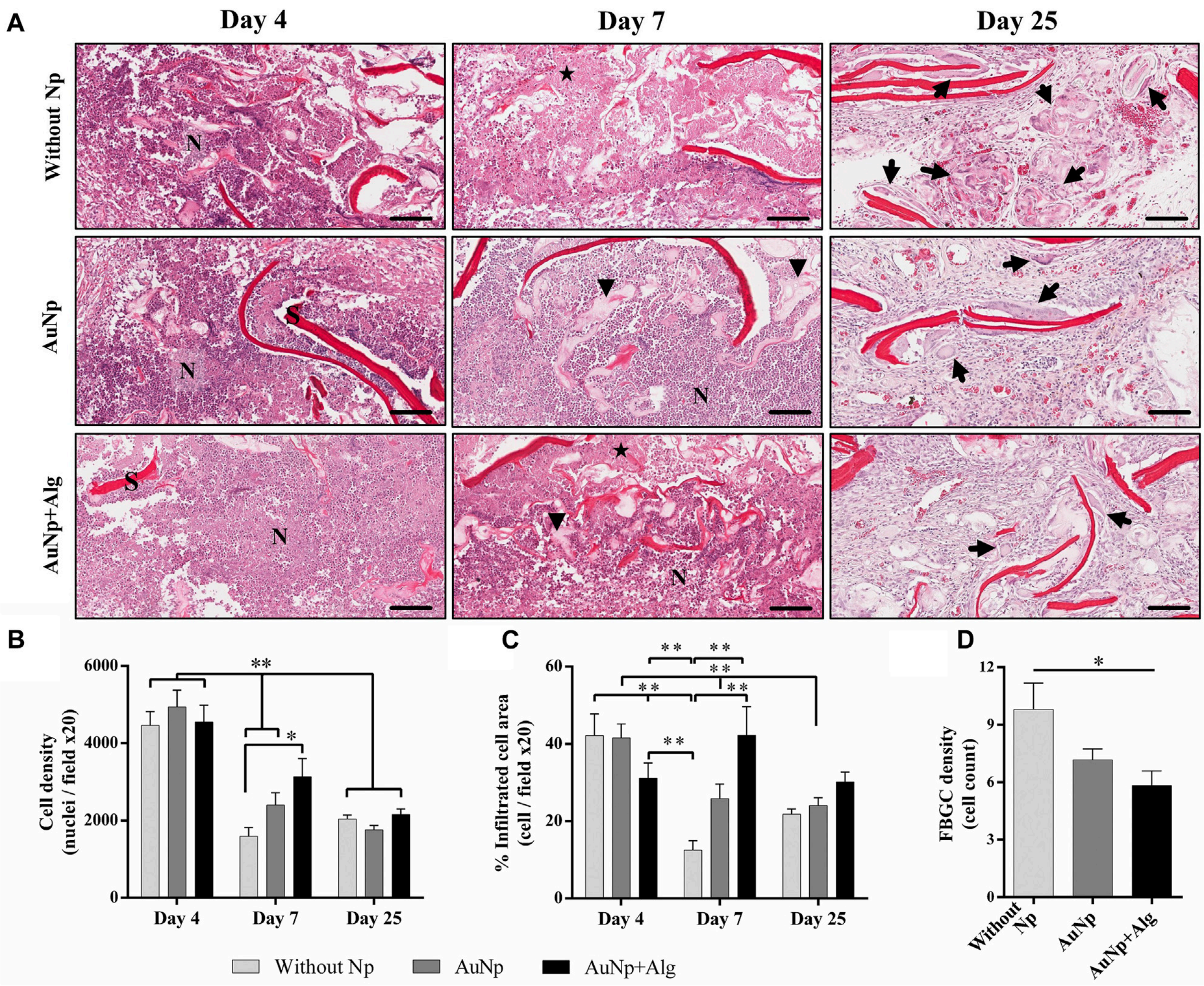

FIGURE 3
(A) Characterization of the response to a foreign body, (H-E; bar = 100 μm). Identifiers: Arrow: foreign body giant cells; arrowhead: myxoid areas; N: neutrophils; star: necrosis; S: scaffold. Graphical representation of **(B)** cell density, **(C)** percentage of area occupied by the cellular infiltrate, and **(D)** density of foreign body giant cells. $*p < 0.01$, $**p < 0.001$. Data are presented as mean ± SEM.

At 25 days, collagen deposits were observed inside the scaffold, suggesting the presence of fibroblasts inside the material (framed regions in day 25, Figure 5A). The quantitative analysis did not show significant differences among groups, but there is a trend in the reduction of collagen content in the functionalized groups (Figure 5C) (Without Np: 15.11% ± 3.146%, AuNp: 10.19% ± 1.143%, AuNp + Alg: 7.309% ± 6.036%).

3.4 Macrophage polarization

Real-time expression of M1 macrophage markers (TNFα, CD11, TLR4, INOS, and CD86) was quantified in the study groups (Figure 6). A trend towards a higher expression of TNFα was present in the NpAu group on day 7 and decreased on day 25. CD11 expression remained constant between groups at 4 and 7 days of the experiment, and a trend towards increased expression was observed at 25 days in the group without Np. TLR4 expression showed a trend to decrease with respect to the reference tissue (healthy skin) and remains constant over time. The expression of iNOS had a tendency to decrease over time and tended to be higher in the groups without the Np scaffold than in the functionalized groups at 25 days. During the analysis of the samples, a tendency to a decreasing expression of CD86 was observed within subjects.

The real-time expression of M2 macrophage markers (IL-4, IL-10, VEGF, Mrc1, and Arg1) is shown in Figure 6. Arg1 tends to decrease at day 4 in the without Np group, remains constant in the NpAu group, and tends to decrease as a function of time in NpAu + Alg.

3.5 Blood vessel formation

As shown in Figure 7A, real-time expression was analyzed for PECAM-1 and VEGFa expression. No significant differences were observed among groups for eitther marker. PECAM-1 expression showed a tendency to increase at 4 days postimplantation and to

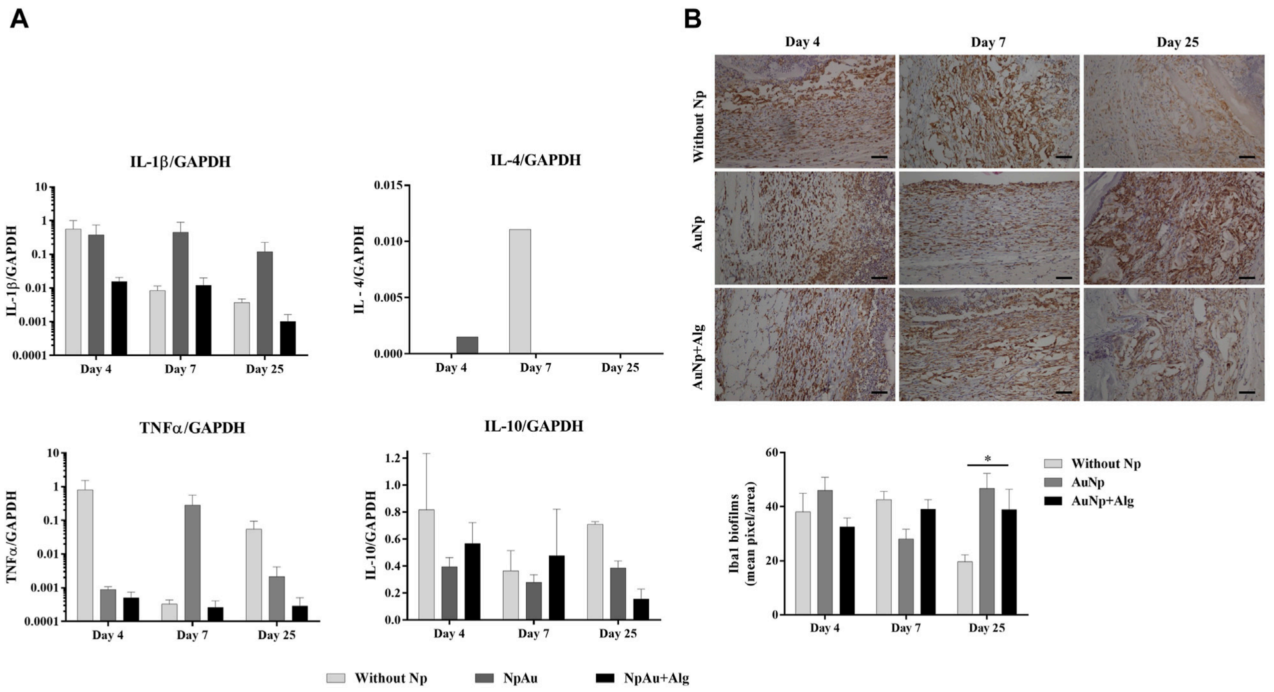

FIGURE 4
Inflammatory response. **(A)** qRT-PCR showing the levels of proinflammatory (IL-1β and TNFα) and anti-inflammatory (IL-4 and IL-10) cytokines. GAPDH was used as a housekeeping gene. **(B)** Representative immunohistochemical images and quantification of anti-Iba1 on the scaffolds at different points of time, (bar = 50 μm). Data are presented as mean ± SEM. (*) $p < 0.05$.

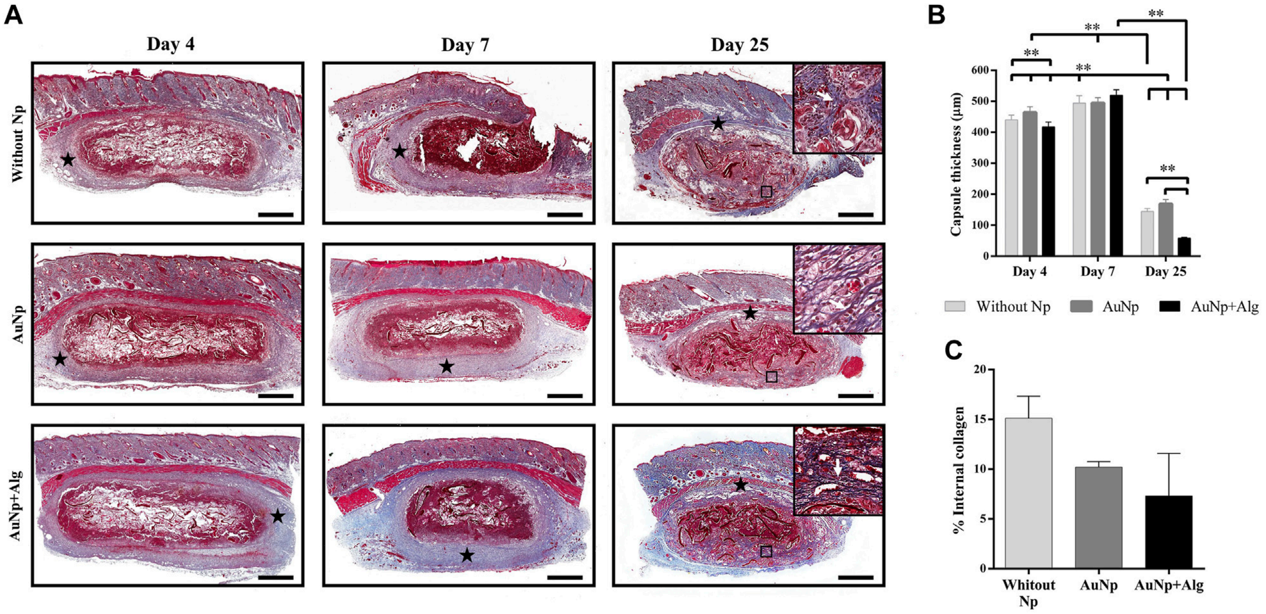

FIGURE 5
Representative photomicrographs of capsule thickness and internal collagen between groups over time **(A)**, (Masson; bar = 1 mm). Framed regions were enlarged (Masson; x 200) to show collagen fibers. Identifiers: star: capsule; white arrow: collagen fibers. **(B)** Graphical representation of capsule thickness. **(C)** Graphical representation of collagen deposits inside the scaffolds. Data are presented as mean ± SEM. **$p < 0.001$.

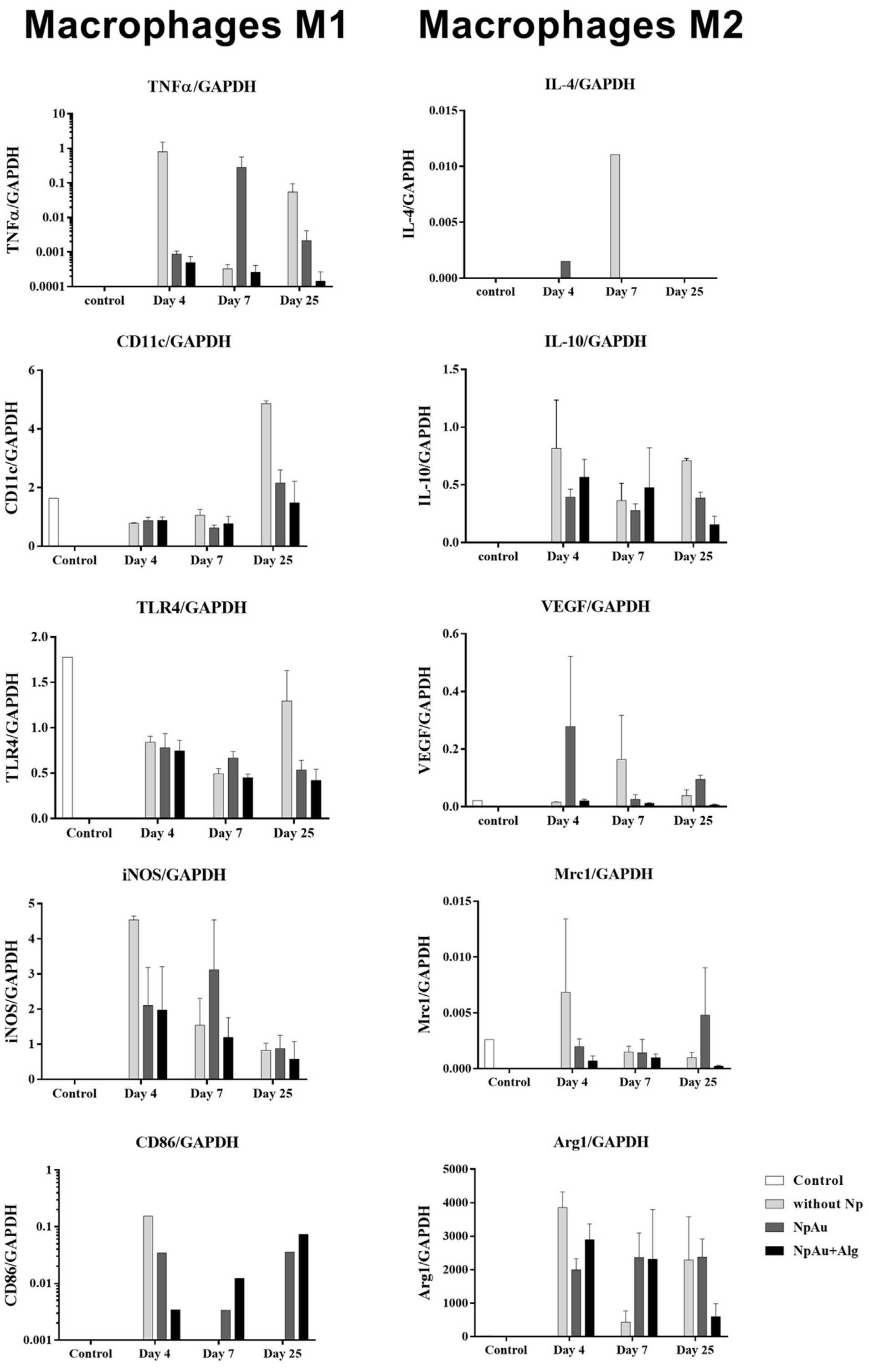

FIGURE 6
Macrophage profile. qRT-PCR values showing the expression of markers for the M1 (TNFα, CD11, TLR4, INOS, and CD86) and M2 phenotype (IL4, IL10, VEGF, Mrc1, and ARG1) in all scaffolds. Data are presented as mean ± SEM.

decrease toward the end of the experiment. VEGFa expression tended to be higher in the without Np scaffold at 4 and 25 days. At 7 days, an increasing trend in VEGFa expression was identified in the NpAu group.

The expression of α-SMA (smooth muscle actin, vascular marker) using immunohistochemistry was observed in blood vessels in all three groups (Figure 7B). Quantitative analysis indicated that α-SMA expression was significantly higher in the

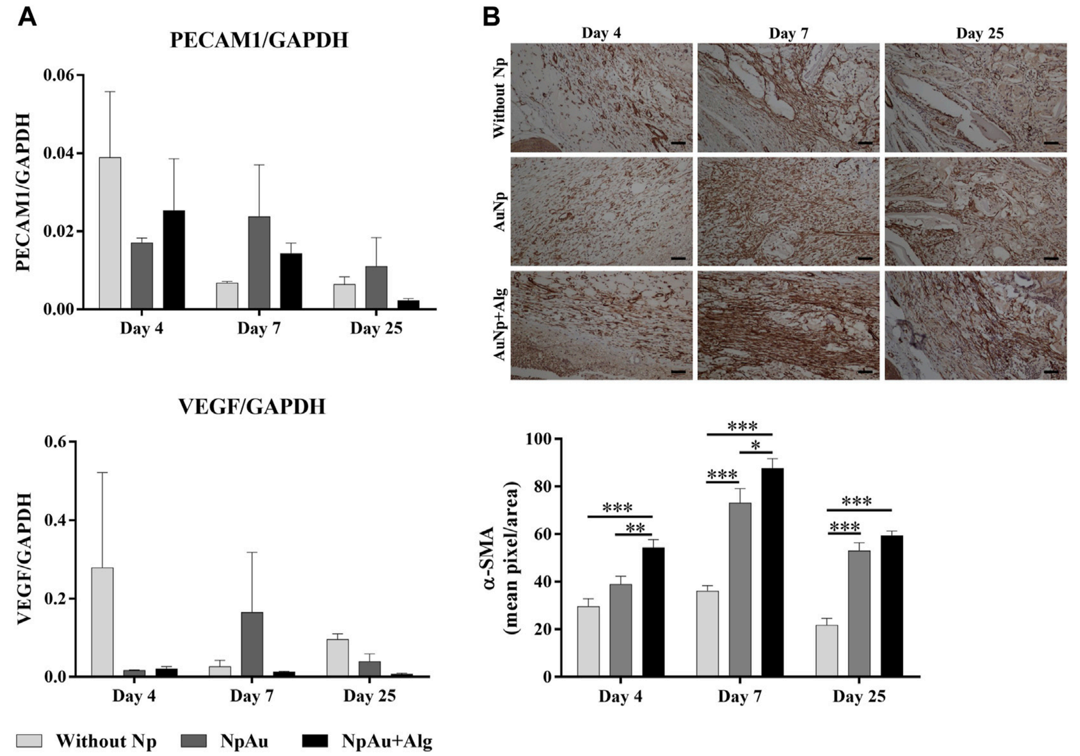

FIGURE 7
Angiogenic response. **(A)** qRT-PCR showing the levels of PECAM1 and VEGF, **(B)** Representative immunohistochemical images and quantification analysis of anti-αSMA on the scaffolds at different points of time, (bar = 50 μm). (*) $p < 0.05$, (**) $p < 0.01$, (***) $p < 0.001$. Data are presented as mean ± SEM.

functionalized groups compared to the without Np scaffold, at 4 days. A significant increase ($p < 0.05$) of α-SMA was identified at 7 and 25 days in the AuNp and AuNp + Alg groups with respect to the Without Np group (D7, Without Np: 36% ± 8.23%, AuNp: 73.03% ± 29.86%, AuNp + Alg: 87.57% ± 17%; D25 Without Np: 21.71% ± 9.53%, AuNp: 52.97% ± 16.76%, AuNp + Alg: 59.28% ± 7.01%).

4 Discussion

The novelty of our scaffold is related to its composition (alginate 0.75% and chitosan 1.25% w/v) and its manufacturing process, which includes the synthesis and incorporation of metallic gold nanoparticles, without and with an alginate cover, which was previously reported by our group (Beltran-Vargas et al., 2022). Additionally, it is important to evaluate the effect of adding an alginate coating to gold nanoparticles on an alginate -chitosan scaffold, to generate a highly vascularized platform. In the area of tissue engineering, it has been documented that the efficiency of therapy increases in strategies that have been functionalized with organic or inorganic molecules. However, the number of functionalized proposals is low in relation to non-functionalized proposals. Therefore, our scaffold meets the current needs in tissue engineering. Limited studies have focused on how biomaterials affect host response, such as inflammation and immune modulation. Given that the functionalization of biomaterials results in an improved representation of the microenvironment for cell culture, the study of biocompatibility in *in vivo* models is of interest to research groups related to the use of non-cytotoxic conductive natural biomaterials.

The success of using biomaterials in TE depends on their ability to not generating an adverse effect on the host organism, such as cytotoxicity, mutagenicity, carcinogenicity, and immunogenicity (Raut et al., 2020). According to macroscopic observations (Figure 1) and histological analysis, our scaffolds showed adequate biocompatibility through integration with host tissue, cell recruitment and release of anti-inflammatory cytokines, blood vessel enlargement, and granulation tissue development within 25 days.

The use of Alg and Cs scaffolds, individually and in combination, has been reported in TE (Farshidfar et al., 2023; Kim et al., 2023). The combination of these biomaterials results in the formation of a complex that can swell in the presence of body fluids (e.g., exudates) (Hao et al., 2021), in addition to modulating the inflammatory phase (Zhu et al., 2020; Soriente et al., 2022), stimulating fibroblast proliferation and accelerating wound healing (Caetano et al., 2015), as well as improving scar tissue quality (Breder et al., 2020). However, the null electrical properties of these scaffolds represent a limitation to replicating the characteristics of various conductive tissues. Conductive scaffolds are often used in TE to create an electrical interface with cells and enable tissue stimulation. This is important during the development of electrically active tissues such as cardiac muscle and nerve tissue.

Natural and synthetic scaffolds with Au incorporation exhibit improved cell viability, binding, and proliferation (Shevach et al., 2014; Baranes et al., 2016; Ghaziof et al., 2022). When evaluating *in vivo* models, Au incorporation in scaffolds promotes proper communication of the graft with the host tissue (Dong et al., 2020).

The incorporation of coated nanoparticles into TEs has been recently explored. Coating Nps with natural materials has been reported to result in improved stability (Sood et al., 2017) and interaction with biological systems *in vitro* (Shen et al., 2019). However, little evidence points to mechanisms associated with their application in animal models. In this work, we evaluated the biocompatibility of alginate-coated AuNp-functionalized scaffolds (AuNp + Alg). Our scaffolds generated the typical FBR (Figure 2), reported by (Bushkalova et al., 2019) and by (Ribeiro et al., 2021); with an increase in cellular infiltrates, reduction in capsule size, and the time to resolution of the inflammatory reaction. The scaffolds used in this work are highly porous (Beltran-Vargas et al., 2022), and it has been reported that scaffolds with these characteristics show less fibrous encapsulation and greater integration of the implant compared to biomaterials with less porosity; in addition to promoting high levels of cellular infiltration and angiogenesis (Whitaker et al., 2021).

Cell infiltration allows for examining the ability of cells to migrate and grow within the scaffold over time. It has been reported that high values of porosity and pore size between 30 and 40 μm can induce increased cell adhesion and promote, in macrophages, an M2 phenotype (Whitaker et al., 2021; Hernandez and Woodrow, 2022). *In vitro*, our scaffolds present high permeability, porosity, and swelling (Beltran-Vargas et al., 2022), which promotes cell recruitment of up to twice the number of cells recorded in non-functionalized scaffolds at 7 days postimplantation (Figure 3B). Similar results were observed in a previous investigation (Dulany et al., 2020), where functionalization with cerium oxide nanoparticles in a synthetic scaffold increased cellular infiltration by 33% with respect to its reference group. In addition, increased cellular infiltrates and decreased duration of acute inflammatory response are associated with early resolution of FBR (Barone et al., 2022). Our results show a decrease of about half the number of infiltrating cells at 25 days compared to their initial values (Figure 3B). Resolution of the inflammatory response in our scaffolds occurs at about 4 weeks. This is a clear improvement over nonfunctionalized chitosan scaffolds, which show a longer resolution of up to 8 weeks (Modulevsky et al., 2016). The distribution of nuclei along the biomaterial, in relation to the tissue events present within the scaffold, may indicate the degree of inflammatory response. In our study, incorporating AuNp + Alg increases the percentage of occupied area within the scaffold, thus reducing the areas of necrosis (Figures 3A, C). Similar results were reported in previous studies (Snider et al., 2022; Cheng et al., 2023). *In vitro*, reduction of cell death by apoptosis in chondrocytes was observed when a decellularized matrix functionalized with 20 nm AuNp was used (Snider et al., 2022). Moreover, the presence of FBGC on and around implanted biomaterials is considered evidence of a chronic inflammatory response of the host tissue to these materials (McNally and Anderson, 2015). In our study, the NpAu + Alg group presented a decrease in FBGC density (Figure 3D), indicating increased biocompatibility in functionalized scaffolds.

Cytokine induction can be used to assess the intensity of immune reactions of biomaterials since biocompatibility is reduced when biomaterials induce very high amounts of cytokine expression (Ding et al., 2007). Thus, the low detection of TNFα and IL-4, shown in Figure 4, suggests that subdermal implantation of Alg/Cs scaffolds without/with NpAu elicits a mild immune reaction. Previous studies have reported that the use of NpAu in combination with other materials decreases the infiltration of inflammatory cells and the level of proinflammatory mediators such as iNOS, COX-2 and cytokines such as TNF-α, IL-1β, IFN-γ and IL- 6; In addition, it increases the expression of anti-inflammatory cytokines such as TGF-β, IL-10 and IL-4 (Park et al., 2019; Mahmoudi et al., 2022).

The design and functionalization of the scaffold impact the expression of the immune response produced after implantation, resulting in variations in the size of the capsule surrounding the biomaterial. The capsule size recorded in our investigation, as shown in Figure 5B, is smaller than that reported by other studies (Divakar et al., 2020), where a capsule thickness of 3 mm was observed around scaffolds made from unfunctionalized collagen. Results similar to those obtained in our investigation were also reported (Dulany et al., 2020; Camarero-Espinosa et al., 2022). The significant reduction in capsule size is usually associated with an increase in pore size (Barone et al., 2022) and modifications in the functional groups of the biomaterial (Jeong et al., 2017). Pore morphology, including size, shape, and microstructure also affect the balance between fibrous encapsulation and tissue integration (Whitaker et al., 2021).

Together with granulation tissue, fibrosis represents a regeneration phase during the reduction of inflammation, with the deposition of extracellular matrix and collagen fibers by fibroblasts within the scaffold (Hernandez and Woodrow, 2022). Our investigation showed increased collagen deposition within the biomaterial in unfunctionalized scaffolds (without Np) (Figure 5C). However, adding Np did not interfere with the resolution of FBR in our scaffolds.

The activity of macrophages and fibroblasts is closely related (Witherel et al., 2019). Macrophages are responsible for releasing proinflammatory cytokines related to NF-κB activation and matrix metalloproteinase production, whereas fibroblasts are responsible for stimulating FGF synthesis. Cs has been described to be analogous to glycosaminoglycans, which stimulate the FGF-2 signaling pathway, chemically bind to it, and facilitate interaction with its cellular receptors on endothelial cells of various tissues (Muzzarelli, 2009). Recently, it has been shown that Cs can stimulate the production of anti-inflammatory cytokines and growth factors in macrophages, which induce fibroblast activity, thus favoring the resolution of inflammation and tissue repair (Muxika et al., 2017; Ribeiro et al., 2021).

During FBR, macrophages initially assume an M1 phenotype that promotes inflammation by releasing inflammatory cytokines (IL-6, IL-12, and TNFα), reactive oxygen species, and antimicrobial peptides. After the acute inflammatory phase subsides, the macrophage population shifts to an M2 phenotype. M2 macrophages are characterized by the secretion of anti-inflammatory mediators (IL-10) and growth factors (PDGF and TGF-β) that aid in tissue healing by stabilizing angiogenesis (Karkanitsa et al., 2021; Martin and García, 2021). In our study, we observed the coexpression of M1 and M2 markers (Figure 6), which has usually been reported in FBR induced by scaffolds (Witherel et al., 2019).

The M1 phenotype is generally identified by the expression of surface markers and co-stimulatory molecules such as CD86 and intracellular molecules such as iNOS (Martin and García, 2021; Wei et al., 2021). In our work, markers such as TNFα and CD86 used to characterize M1 macrophages are expressed in small amounts (see scale of TNFα and CD68 in Figure 6). iNOS had a tendency to decrease throughout the experiment in all study groups, suggesting a resolution of the immune response (Figure 6). It has been documented that chitosan inhibits TNFα production and induces IL-8 expression, which promotes angiogenesis and neutrophil migration (Mori et al., 1997).

The M2 phenotype is characterized by the expression of surface markers and intracellular arginase 1. In our study, markers such as IL-10, Mrc1, and Arg1 are present on the without Np scaffolds and the functionalized scaffolds, thus indicating the presence of the M2 phenotype (Figure 6). Natural biomaterials promote the positive regulation of IL-4, which is released to limit the degree of injury (Karkanitsa et al., 2021). However, in our study, IL-4 expression was not observed in all groups over time. Similar results have been also reported (Vasconcelos et al., 2015; Soriente et al., 2022).

In addition to capsule formation, cell infiltration, and FBGC formation, the protrusion of neovascular sprouts into the biomaterial and surrounding tissue is a significant feature of FBR. Fibroblasts form a fibrous capsule around the biomaterial, which insulates it from the rest of the body and produces extracellular matrix components. In the early stages of FBR, the cells of the cellular infiltrate are likely to encounter locally compromised oxygen pressure (Capuani et al., 2022). Hypoxia activates macrophages to induce hypoxia-inducible transcriptionally active factors, which induce the expression of angiogenic factors such as VEGF, PDGF, adrenomedullin, angiopoietin 2, and others (Boomker et al., 2005). On the other hand, at later stages in FBR, the formation of new blood vessels facilitates the arrival of more inflammatory cells, which may aggravate the inflammatory response. Thus, early angiogenesis is beneficial to ameliorate the response and allow for cell migration within the scaffold (Parlani et al., 2022). Our results show a trend in increased VEGF and PECAM1 expression at the onset of the inflammatory response in all three groups (Figure 7A), while vessel detection by αSMA increases at week 7 and is higher in the functionalized groups (Figure 7B). Porous scaffolds have been documented to promote blood vessel formation. It has been described that the number and diameter of blood vessels are enhanced in the presence of scaffolds made with pores larger than 150 μm (Walthers et al., 2014; Eichholz et al., 2022). On the other hand, in bone tissue engineering, *in vivo* studies showed that the use of various biomaterials functionalized with AuNPs induced angiogenesis at the defect site (Samadian et al., 2021).

In sum, the absence of exacerbated reactions in the host tissue allows us to confirm that the implanted scaffolds are biocompatible. Therefore, AuNp-functionalized scaffolds offer several benefits for TE use while maintaining communication with the host tissue. Should be interesting to test our scaffolds in other organs and tissues. An evaluate other pro- and anti-inflammatory markers with a larger sample.

5 Conclusion

In this study, we evaluated *in vivo* the biocompatibility of scaffolds made from alginate and chitosan (Alg/Cs), functionalized with AuNp and AuNp + Alg. The results suggest that the combination of Alg/Cs with gold nanoparticles forms a scaffold that can swell in the presence of body fluids, modulate the inflammatory process, stimulate fibroblast proliferation and collagen fiber production, promote blood vessel development, and improve scar tissue quality. These scaffolds have the potential to be used for the incorporation of a cellular component for use as regenerative therapy.

Data availability statement

The original contributions presented in the study are included in the article/supplementary material, further inquiries can be directed to the corresponding author.

Ethics statement

The animal study was approved by research, ethics, and biosafety committees of the Children's Hospital of Mexico Federico Gomez (HIM/2020/059). The study was conducted in accordance with the local legislation and institutional requirements.

Author contributions

NV-M: Conceptualization, Data curation, Formal Analysis, Investigation, Methodology, Writing–original draft. MG-L: Conceptualization, Formal Analysis, Investigation, Methodology, Writing–review and editing. EP-M: Data curation, Formal Analysis, Writing–review and editing. JG-S: Data curation, Formal Analysis, Writing–review and editing. JN-Í: Data curation, Formal Analysis, Writing–review and editing. MS-G: Funding acquisition, Resources, Supervision, Validation, Writing–review and editing. SH-Y: Data curation, Formal Analysis, Writing–review and editing. CS-G: Funding acquisition, Investigation, Methodology, Project administration, Resources, Supervision, Writing–review and editing. AM: Data curation, Formal Analysis, Methodology, Resources, Validation, Writing–review and editing. NB-V: Conceptualization, Data curation, Formal Analysis, Funding acquisition, Methodology, Project administration, Resources, Supervision, Writing–review and editing.

Funding

The authors declare financial support was received for the research, authorship, and/or publication of this article. Children's Hospital of Mexico Federico Gomez (protocols HIM/2020/059 and HIM/2022/040).

Acknowledgments

This work was conducted as part of the doctoral studies of NV-M, with funding from CONAHCYT. The authors would like to thank the support of Federico Gomez Children's Hospital of Mexico. The authors thank Crimson Interactive Pvt. Ltd. (Enago)–https://www.enago.com/es/ for their assistance in manuscript translation and editing.

Conflict of interest

The authors declare that the research was conducted in the absence of any commercial or financial relationships that could be construed as a potential conflict of interest.

Publisher's note

References

Abaricia, J. O., Farzad, N., Heath, T. J., Simmons, J., Morandini, L., and Olivares-Navarrete, R. (2021). Control of innate immune response by biomaterial surface topography, energy, and stiffness. *Acta Biomater.* 133, 58–73. doi:10.1016/j.actbio.2021.04.021

Anderson, J. M., Rodriguez, A., and Chang, D. T. (2008). Foreign body reaction to biomaterials. *Semin. Immunol.* 20 (2), 86–100. doi:10.1016/j.smim.2007.11.004

Baranes, K., Shevach, M., Shefi, O., and Dvir, T. (2016). Gold nanoparticle-decorated scaffolds promote neuronal differentiation and maturation. *Nano Lett.* 16 (5), 2916–2920. doi:10.1021/acs.nanolett.5b04033

Barone, D. G., Carnicer-Lombarte, A., Tourlomousis, P., Hamilton, R. S., Prater, M., Rutz, A. L., et al. (2022). Prevention of the foreign body response to implantable medical devices by inflammasome inhibition. *Proc. Natl. Acad. Sci. U. S. A.* 119 (12), e2115857119. doi:10.1073/pnas.2115857119

Beltran-Vargas, N. E., Peña-Mercado, E., Sánchez-Gómez, C., Garcia-Lorenzana, M., Ruiz, J. C., Arroyo-Maya, I., et al. (2022). Sodium alginate/chitosan scaffolds for cardiac tissue engineering: the influence of its three-dimensional material preparation and the use of gold nanoparticles. *Polym. (Basel)* 14 (16), 3233. doi:10.3390/polym14163233

Bertsch, P., Diba, M., Mooney, D. J., and Leeuwenburgh, S. C. G. (2023). Self-healing injectable hydrogels for tissue regeneration. *Chem. Rev.* 123 (2), 834–873. doi:10.1021/acs.chemrev.2c00179

Boomker, J. M., Luttikhuizen, D. T., Veninga, H., de Leij, L. F., The, T. H., de Haan, A., et al. (2005). The modulation of angiogenesis in the foreign body response by the poxviral protein M-T7. *Biomaterials* 26 (23), 4874–4881. doi:10.1016/j.biomaterials.2004.11.059

Breder, J. S. C., Pires, A. L. R., Azevedo, F. F., Apolinário, P. P., Cantaruti, T., Jiwani, S. I., et al. (2020). Enhancement of cellular activity in hyperglycemic mice dermal wounds dressed with chitosan-alginate membranes. *Braz J. Med. Biol. Res.* 53 (1), e8621. doi:10.1590/1414-431X20198621

Bushkalova, R., Farno, M., Tenailleau, C., Duployer, B., Cussac, D., Parini, A., et al. (2019). Alginate-chitosan PEC scaffolds: a useful tool for soft tissues cell therapy. *Int. J. Pharm.* 571, 118692. doi:10.1016/j.ijpharm.2019.118692

Caetano, G. F., Frade, M. A., Andrade, T. A., Leite, M. N., Bueno, C. Z., Moraes Â, M., et al. (2015). Chitosan-alginate membranes accelerate wound healing. *J. Biomed. Mater Res. B Appl. Biomater.* 103 (5), 1013–1022. doi:10.1002/jbm.b.33277

Camarero-Espinosa, S., Carlos-Oliveira, M., Liu, H., Mano, J. F., Bouvy, N., and Moroni, L. (2022). 3D printed dual-porosity scaffolds: the combined effect of stiffness and porosity in the modulation of macrophage polarization. *Adv. Healthc. Mater* 11 (1), e2101415. doi:10.1002/adhm.202101415

Capuani, S., Malgir, G., Chua, C. Y. X., and Grattoni, A. (2022). Advanced strategies to thwart foreign body response to implantable devices. *Bioeng. Transl. Med.* 7 (3), e10300. doi:10.1002/btm2.10300

Carnicer-Lombarte, A., Chen, S. T., Malliaras, G. G., and Barone, D. G. (2021). Foreign body reaction to implanted biomaterials and its impact in nerve neuroprosthetics. *Front. Bioeng. Biotechnol.* 9, 622524. doi:10.3389/fbioe.2021.622524

Chen, Y., Sun, W., Tang, H., Li, Y., Li, C., Wang, L., et al. (2022). Interactions between immunomodulatory biomaterials and immune microenvironment: cues for immunomodulation strategies in tissue repair. *Front. Bioeng. Biotechnol.* 10, 820940. doi:10.3389/fbioe.2022.820940

Cheng, W. Y., Yang, M. Y., Yeh, C. A., Yang, Y. C., Chang, K. B., Chen, K. Y., et al. (2023). Therapeutic applications of mesenchymal stem cell loaded with gold nanoparticles for regenerative medicine. *Pharmaceutics* 15 (5), 1385. doi:10.3390/pharmaceutics15051385

Chung, L., Maestas, D. R., Jr., Housseau, F., and Elisseeff, J. H. (2017). Key players in the immune response to biomaterial scaffolds for regenerative medicine. *Adv. Drug Deliv. Rev.* 114, 184–192. doi:10.1016/j.addr.2017.07.006

Crowe, A. R., and Yue, W. (2019). Semi-quantitative determination of protein expression using immunohistochemistry staining and analysis: an integrated protocol. *Bio Protoc.* 9 (24), e3465. doi:10.21769/BioProtoc.3465

Ding, T., Sun, J., and Zhang, P. (2007). Immune evaluation of biomaterials in TNF-α and IL-1β at mRNA level. *J. Mater Sci. Mater Med.* 18 (11), 2233–2236. doi:10.1007/s10856-007-3014-9

Divakar, P., Moodie, K. L., Demidenko, E., Jack Hoopes, P., and Wegst, U. G. K. (2020). Quantitative evaluation of the *in vivo* biocompatibility and performance of freeze-cast tissue scaffolds. *Biomed. Mater* 15 (5), 055003. doi:10.1088/1748-605X/ab316a

Dong, Y., Hong, M., Dai, R., Wu, H., and Zhu, P. (2020). Engineered bioactive nanoparticles incorporated biofunctionalized ECM/silk proteins based cardiac patches combined with MSCs for the repair of myocardial infarction: *in vitro* and *in vivo* evaluations. *Sci. Total Environ.* 707, 135976. doi:10.1016/j.scitotenv.2019.135976

Dulany, K., Hepburn, K., Goins, A., and Allen, J. B. (2020). *In vitro* and *in vivo* biocompatibility assessment of free radical scavenging nanocomposite scaffolds for bone tissue regeneration. *J. Biomed. Mater Res. A* 108 (2), 301–315. doi:10.1002/jbm.a.36816

Dzobo, K., Thomford, N. E., Senthebane, D. A., Shipanga, H., Rowe, A., Dandara, C., et al. (2018). Advances in regenerative medicine and tissue engineering: innovation and transformation of medicine. *Stem Cells Int.* 2018, 1–24. doi:10.1155/2018/2495848

Eichholz, K. F., Freeman, F. E., Pitacco, P., Nulty, J., Ahern, D., Burdis, R., et al. (2022). Scaffold microarchitecture regulates angiogenesis and the regeneration of large bone defects. *Biofabrication* 14 (4), 045013. doi:10.1088/1758-5090/ac88a1

Farshidfar, N., Iravani, S., and Varma, R. S. (2023). Alginate-Based biomaterials in tissue engineering and regenerative medicine. *Mar. Drugs* 21 (3), 189. doi:10.3390/md21030189

Flaig, F., Ragot, H., Simon, A., Revet, G., Kitsara, M., Kitasato, L., et al. (2020). Design of functional electrospun scaffolds based on poly(glycerol sebacate) elastomer and poly(lactic acid) for cardiac tissue engineering. *ACS Biomater. Sci. Eng.* 6 (4), 2388–2400. doi:10.1021/acsbiomaterials.0c00243

García-Sanmartín, J., Narro-Íñiguez, J., Rodríguez-Barbero, A., and Martínez, A. (2022). Endoglin and activin receptor-like kinase 1 (Alk1) modify adrenomedullin expression in an organ-specific manner in mice. *Biol. (Basel)* 11 (3), 358. doi:10.3390/biology11030358

Ghaziof, S., Shojaei, S., Mehdikhani, M., Khodaei, M., and Jafari Nodoushan, M. (2022). Electro-conductive 3D printed polycaprolactone/gold nanoparticles nanocomposite scaffolds for myocardial tissue engineering. *J. Mech. Behav. Biomed. Mater.* 132, 105271. doi:10.1016/j.jmbbm.2022.105271

Goldenberg, D., McLaughlin, C., Koduru, S. V., and Ravnic, D. J. (2021). Regenerative engineering: current applications and future perspectives. *Front. Surg.* 8, 731031. doi:10.3389/fsurg.2021.731031

Han, F., Meng, Q., Xie, E., Li, K., Hu, J., Chen, Q., et al. (2023). Engineered biomimetic micro/nano-materials for tissue regeneration. *Front. Bioeng. Biotechnol.* 11, 1205792. doi:10.3389/fbioe.2023.1205792

Hao, Y., Zheng, W., Sun, Z., Zhang, D., Sui, K., Shen, P., et al. (2021). Marine polysaccharide-based composite hydrogels containing fucoidan: preparation, physicochemical characterization, and biocompatible evaluation. *Int. J. Biol. Macromol.* 183, 1978–1986. doi:10.1016/j.ijbiomac.2021.05.190

Hernandez, J. L., and Woodrow, K. A. (2022). Medical applications of porous biomaterials: features of porosity and tissue-specific implications for biocompatibility. *Adv. Healthc. Mater* 11 (9), e2102087. doi:10.1002/adhm.202102087

Ibrahim, M., Bond, J., Medina, M. A., Chen, L., Quiles, C., Kokosis, G., et al. (2017). Characterization of the foreign body response to common surgical biomaterials in a murine model. *Eur. J. Plast. Surg.* 40 (5), 383–392. doi:10.1007/s00238-017-1308-9

Jeong, K. J., Song, Y., Shin, H. R., Kim, J. E., Kim, J., Sun, F., et al. (2017). *In vivo* study on the biocompatibility of chitosan-hydroxyapatite film depending on degree of deacetylation. *J. Biomed. Mater Res. A* 105 (6), 1637–1645. doi:10.1002/jbm.a.35993

Joyce, K., Fabra, G. T., Bozkurt, Y., and Pandit, A. (2021). Correction to: bioactive potential of natural biomaterials: identification, retention and assessment of biological properties. *Signal Transduct. Target Ther.* 6 (1), 175. doi:10.1038/s41392-021-00593-5

Karkanitsa, M., Fathi, P., Ngo, T., and Sadtler, K. (2021). Mobilizing endogenous repair through understanding immune reaction with biomaterials. *Front. Bioeng. Biotechnol.* 9, 730938. doi:10.3389/fbioe.2021.730938

Kim, Y., Zharkinbekov, Z., Raziyeva, K., Tabyldiyeva, L., Berikova, K., Zhumagul, D., et al. (2023). Chitosan-Based biomaterials for tissue regeneration. Pharm. *[Online]* 15 (3), 807. doi:10.3390/pharmaceutics15030807

Kyriakides, T. R., Kim, H. J., Zheng, C., Harkins, L., Tao, W., and Deschenes, E. (2022). Foreign body response to synthetic polymer biomaterials and the role of adaptive immunity. *Biomed. Mater* 17 (2), 022007. doi:10.1088/1748-605X/ac5574

Li, W., Dai, F., Zhang, S., Xu, F., Xu, Z., Liao, S., et al. (2022). Pore size of 3D-printed polycaprolactone/polyethylene glycol/hydroxyapatite scaffolds affects bone regeneration by modulating macrophage polarization and the foreign body response. *ACS Appl. Mater Interfaces* 14 (18), 20693–20707. doi:10.1021/acsami.2c02001

Maharjan, B., Kumar, D., Awasthi, G. P., Bhattarai, D. P., Kim, J. Y., Park, C. H., et al. (2019). Synthesis and characterization of gold/silica hybrid nanoparticles incorporated gelatin methacrylate conductive hydrogels for H9C2 cardiac cell compatibility study. *Compos. Part B Eng.* 177, 107415. doi:10.1016/j.compositesb.2019.107415

Mahmoudi, M., Rastin, M., Kazemi Arababadi, M., Anaeigoudari, A., and Nosratabadi, R. (2022). Enhancing the efficacy of *Hypericum perforatum* in the treatment of an experimental model of multiple sclerosis using gold nanoparticles: an *in vivo* study. *Avicenna J. Phytomed* 12 (3), 325–336. doi:10.22038/ajp.2022.19574

Major, M. R., Wong, V. W., Nelson, E. R., Longaker, M. T., and Gurtner, G. C. (2015). The foreign body response: at the interface of surgery and bioengineering. *Plast. Reconstr. Surg.* 135 (5), 1489–1498. doi:10.1097/PRS.0000000000001193

Martin, K. E., and García, A. J. (2021). Macrophage phenotypes in tissue repair and the foreign body response: implications for biomaterial-based regenerative medicine strategies. *Acta Biomater.* 133, 4–16. doi:10.1016/j.actbio.2021.03.038

McNally, A. K., and Anderson, J. M. (2015). Phenotypic expression in human monocyte-derived interleukin-4-induced foreign body giant cells and macrophages *in vitro*: dependence on material surface properties. *J. Biomed. Mater Res. A* 103 (4), 1380–1390. doi:10.1002/jbm.a.35280

Modulevsky, D. J., Cuerrier, C. M., and Pelling, A. E. (2016). Biocompatibility of subcutaneously implanted plant-derived cellulose biomaterials. *PLoS One* 11 (6), e0157894. doi:10.1371/journal.pone.0157894

Mori, T., Okumura, M., Matsuura, M., Ueno, K., Tokura, S., Okamoto, Y., et al. (1997). Effects of chitin and its derivatives on the proliferation and cytokine production of fibroblasts *in vitro*. *Biomaterials* 18 (13), 947–951. doi:10.1016/s0142-9612(97)00017-3

Muxika, A., Etxabide, A., Uranga, J., Guerrero, P., and de la Caba, K. (2017). Chitosan as a bioactive polymer: processing, properties and applications. *Int. J. Biol. Macromol.* 105 (Pt 2), 1358–1368. doi:10.1016/j.ijbiomac.2017.07.087

Muzzarelli, R. A. A. (2009). Chitins and chitosans for the repair of wounded skin, nerve, cartilage and bone. *Carbohydr. Polym.* 76 (2), 167–182. doi:10.1016/j.carbpol.2008.11.002

Park, S. Y., Yi, E. H., Kim, Y., and Park, G. (2019). <p>Anti-neuroinflammatory effects of Ephedra sinica Stapf extract-capped gold nanoparticles in microglia</p>. *Int. J. Nanomedicine* 14, 2861–2877. doi:10.2147/ijn.S195218

Parlani, M., Bedell, M. L., Mikos, A. G., Friedl, P., and Dondossola, E. (2022). Dissecting the recruitment and self-organization of αSMA-positive fibroblasts in the foreign body response. *Sci. Adv.* 8 (51), eadd0014. doi:10.1126/sciadv.add0014

Patil, P., Russo, K. A., McCune, J. T., Pollins, A. C., Cottam, M. A., Dollinger, B. R., et al. (2022). Reactive oxygen species-degradable polythioketal urethane foam dressings to promote porcine skin wound repair. *Sci. Transl. Med.* 14 (641), eabm6586. doi:10.1126/scitranslmed.abm6586

Raut, H. K., Das, R., Liu, Z., Liu, X., and Ramakrishna, S. (2020). Biocompatibility of biomaterials for tissue regeneration or replacement. *Biotechnol. J.* 15 (12), e2000160. doi:10.1002/biot.202000160

Ribeiro, J. C. V., Forte, T. C. M., Tavares, S. J. S., Andrade, F. K., Vieira, R. S., and Lima, V. (2021). The effects of the molecular weight of chitosan on the tissue inflammatory response. *J. Biomed. Mater Res. A* 109 (12), 2556–2569. doi:10.1002/jbm.a.37250

Samadian, H., Khastar, H., Ehterami, A., and Salehi, M. (2021). Bioengineered 3D nanocomposite based on gold nanoparticles and gelatin nanofibers for bone regeneration: *in vitro* and *in vivo* study. *Sci. Rep.* 11 (1), 13877. doi:10.1038/s41598-021-93367-6

Shen, K., Huang, Y., Li, Q., Chen, M., and Wu, L. (2019). Self-assembled polysaccharide-diphenylalanine/Au nanospheres for photothermal therapy and photoacoustic imaging. *ACS Omega* 4 (19), 18118–18125. doi:10.1021/acsomega.9b02009

Shevach, M., Fleischer, S., Shapira, A., and Dvir, T. (2014). Gold nanoparticle-decellularized matrix hybrids for cardiac tissue engineering. *Nano Lett.* 14 (10), 5792–5796. doi:10.1021/nl502673m

Snider, C., Grant, D., and Grant, S. A. (2022). Investigation of an injectable gold nanoparticle extracellular matrix. *J. Biomaterials Appl.* 36 (7), 1289–1300. doi:10.1177/08853282211051586

Somasuntharam, I., Yehl, K., Carroll, S. L., Maxwell, J. T., Martinez, M. D., Che, P.-L., et al. (2016). Knockdown of TNF-α by DNAzyme gold nanoparticles as an anti-inflammatory therapy for myocardial infarction. *Biomaterials* 83, 12–22. doi:10.1016/j.biomaterials.2015.12.022

Sondermeijer, H. P., Witkowski, P., Seki, T., van der Laarse, A., Itescu, S., and Hardy, M. A. (2018). RGDfK-peptide modified alginate scaffold for cell transplantation and cardiac neovascularization. *Tissue Eng. Part A* 24 (9-10), 740–751. doi:10.1089/ten.TEA.2017.0221

Sood, A., Arora, V., Shah, J., Kotnala, R. K., and Jain, T. K. (2017). Multifunctional gold coated iron oxide core-shell nanoparticles stabilized using thiolated sodium alginate for biomedical applications. *Mater Sci. Eng. C Mater Biol. Appl.* 80, 274–281. doi:10.1016/j.msec.2017.05.079

Soriente, A., Fasolino, I., Gomez-Sánchez, A., Prokhorov, E., Buonocore, G. G., Luna-Barcenas, G., et al. (2022). Chitosan/hydroxyapatite nanocomposite scaffolds to modulate osteogenic and inflammatory response. *J. Biomed. Mater. Res. Part A* 110 (2), 266–272. doi:10.1002/jbm.a.37283

Sridhar, S., Venugopal, J. R., Sridhar, R., and Ramakrishna, S. (2015). Cardiogenic differentiation of mesenchymal stem cells with gold nanoparticle loaded functionalized nanofibers. *Colloids Surfaces B Biointerfaces* 134, 346–354. doi:10.1016/j.colsurfb.2015.07.019

Sun, J., and Tan, H. (2013). Alginate-Based biomaterials for regenerative medicine applications. *Mater. (Basel)* 6 (4), 1285–1309. doi:10.3390/ma6041285

Vasconcelos, D. P., Costa, M., Amaral, I. F., Barbosa, M. A., Águas, A. P., and Barbosa, J. N. (2015). Modulation of the inflammatory response to chitosan through M2 macrophage polarization using pro-resolution mediators. *Biomaterials* 37, 116–123. doi:10.1016/j.biomaterials.2014.10.035

Veiseh, O., Doloff, J. C., Ma, M., Vegas, A. J., Tam, H. H., Bader, A. R., et al. (2015). Size- and shape-dependent foreign body immune response to materials implanted in rodents and non-human primates. *Nat. Mater* 14 (6), 643–651. doi:10.1038/nmat4290

Walthers, C. M., Nazemi, A. K., Patel, S. L., Wu, B. M., and Dunn, J. C. (2014). The effect of scaffold macroporosity on angiogenesis and cell survival in tissue-engineered smooth muscle. *Biomaterials* 35 (19), 5129–5137. doi:10.1016/j.biomaterials.2014.03.025

Wei, F., Liu, S., Chen, M., Tian, G., Zha, K., Yang, Z., et al. (2021). Host response to biomaterials for cartilage tissue engineering: key to remodeling. *Front. Bioeng. Biotechnol.* 9, 664592. doi:10.3389/fbioe.2021.664592

Whitaker, R., Hernaez-Estrada, B., Hernandez, R. M., Santos-Vizcaino, E., and Spiller, K. L. (2021). Immunomodulatory biomaterials for tissue repair. *Chem. Rev.* 121 (18), 11305–11335. doi:10.1021/acs.chemrev.0c00895

Witherel, C. E., Abebayehu, D., Barker, T. H., and Spiller, K. L. (2019). Macrophage and fibroblast interactions in biomaterial-mediated fibrosis. *Adv. Healthc. Mater* 8 (4), e1801451. doi:10.1002/adhm.201801451

Yadid, M., Feiner, R., and Dvir, T. (2019). Gold nanoparticle-integrated scaffolds for tissue engineering and regenerative medicine. *Nano Lett.* 19 (4), 2198–2206. doi:10.1021/acs.nanolett.9b00472

Zhu, Y., Ma, Z., Kong, L., He, Y., Chan, H. F., and Li, H. (2020). Modulation of macrophages by bioactive glass/sodium alginate hydrogel is crucial in skin regeneration enhancement. *Biomaterials* 256, 120216. doi:10.1016/j.biomaterials.2020.120216

Frontiers in Bioengineering and Biotechnology

TYPE Original Research
PUBLISHED 06 December 2023
DOI 10.3389/fbioe.2023.1267912

OPEN ACCESS

EDITED BY
Mona Kamal Marei,
Alexandria University, Egypt

REVIEWED BY
Marley Dewey,
University of Pittsburgh, United States
Xuan Mei,
Harvard Medical School, United States

*CORRESPONDENCE
Jincheng Wang,
✉ wangjinc@jlu.edu.cn

RECEIVED 27 July 2023
ACCEPTED 27 November 2023
PUBLISHED 06 December 2023

CITATION
Zhu X, Bai H, Liu H, Wang Z, Wang Y, Zhang J, Liu J, Wang H and Wang J (2023), A variable mineralization time and solution concentration intervene in the microstructure of biomimetic mineralized collagen and potential osteogenic microenvironment.
Front. Bioeng. Biotechnol. 11:1267912.
doi: 10.3389/fbioe.2023.1267912

A variable mineralization time and solution concentration intervene in the microstructure of biomimetic mineralized collagen and potential osteogenic microenvironment

Xiujie Zhu[1,2], Haotian Bai[1,2], He Liu[1,2], Zhonghan Wang[1,2], Yao Wang[1], Jiaxin Zhang[1,2], Jiaqi Liu[1,2], Hui Wang[1,2] and Jincheng Wang[1,2]*

[1]Department of Orthopedics, The Second Hospital of Jilin University, Changchun, China, [2]Orthopaedic Research Institute of Jilin Province, Changchun, China

The absence of a conducive bone formation microenvironment between fractured ends poses a significant challenge in repairing large bone defects. A promising solution is to construct a bone formation microenvironment that mimics natural bone tissue. Biomimetic mineralized collagen possesses a chemical composition and microstructure highly similar to the natural bone matrix, making it an ideal biomimetic bone substitute material. The microstructure of biomimetic mineralized collagen is influenced by various factors, and its biomineralization and microstructure, in turn, affect its physicochemical properties and biological activity. We aimed to utilize mineralization time and solution concentration as variables and employed the polymer-induced liquid precursor strategy to fabricate mineralized collagen with diverse microstructures, to shed light on how mineralization parameters impact the material microstructure and physicochemical properties. We also investigated the influence of microstructure and physicochemical properties on cell biocompatibility and the bone-forming microenvironment. Through comprehensive characterization, we examined the physical and chemical properties of I-EMC under various mineralization conditions and assessed the *in vitro* and *in vivo* biocompatibility and osteogenic performance. By investigating the relationship between mineralization parameters, material physicochemical properties, and osteogenic performance, we revealed how microstructures influence cellular behaviors like biocompatibility and osteogenic microenvironment. Encouragingly, mineralization solutions with varying concentrations, stabilized by polyacrylic acid, successfully produced intrafibrillar and extrafibrillar mineralized collagen. Compared to non-mineralized collagen, all mineralized samples demonstrated improved bone-forming performance. Notably, samples prepared with a 1× mineralization solution exhibited relatively smooth surfaces with even mineralization. Extending the mineralization time enhanced the degree of mineralization and osteogenic performance. Conversely, samples prepared with a 2× mineralization solution had rough surfaces with large calcium phosphate particles, indicating non-uniform mineralization. Overall, our research advances the potential for commercial production of mineralized collagen protein products, characterized by dual biomimetic properties, and their application in treating various types of bone defects.

KEYWORDS

mineralized collagen, mineralization time, mineralization solution concentration, osteogenic microenvironment, microstructure, physicochemical properties

1 Introduction

Fractures, various pathological elements, and other factors can result in bone defects, especially larger ones, which pose a significant clinical challenge in the field of orthopedics due to the disruption of the osteogenic microenvironment between fracture ends (Li et al., 2018). Currently, effective repair methods for these bone defects include bone transport, bone grafting, and biomaterial implantation (Huang et al., 2016). The shared objective of these methods is to establish a favorable osteogenic microenvironment to facilitate bone regeneration and repair the defects. Such a conducive osteogenic microenvironment is vital for the successful treatment of bone defects. However, both autologous and allogeneic bone grafts have limitations in their clinical applications, such as limited availability of suitable donors, higher failure rates, and the risk of host rejection (Agarwal and García, 2015). Consequently, the implantation of bone biomaterials is considered a promising approach to address bone defects.

Excellent bone repair materials must create an optimal microenvironment for bone regeneration. Natural bone is a complex hierarchical composite material, consisting of organic collagen proteins and inorganic minerals. Mineral crystals are found within and between collagen fibers, and on the fiber surfaces, resulting in intrafibrillar and extrafibrillar mineralized collagen (I-EMC) (Reznikov et al., 2014a; Yu and Wei, 2021). Mineralized collagen represents the second level in the nine hierarchical levels of natural bone (Reznikov et al., 2014b), forming the nanoscale foundation responsible for the exceptional mechanical and biological properties of bone (Oosterlaken et al., 2021). Guided by progress in biomimetics and insights from *in vivo* biomineralization, researchers have become proficient at crafting various forms of *in vitro* mineralized collagen, especially extrafibrillar (EMC) and intrafibrillar mineralized collagen (IMC). These synthesized counterparts closely resemble the chemical makeup and microstructure of natural bone matrices. The differences between EMC and IMC lie in their *ex-vivo* biomimetic preparation methods and nanostructural attributes. For instance, EMC preparation largely adopts the traditional ion-mediated crystallization method (Liu S. et al., 2016). This method typically uses metastable solutions, enriched in calcium and phosphate ions or various simulated body fluids, as the reaction medium. Within this process, calcium ions accumulate, aggregate, and, post-nucleation, foster the emergence of hydroxyapatite crystals on collagen fiber surfaces. In contrast, the preparation of IMC predominantly utilizes the Polymer-Induced Liquid-Precursor (PILP) pathway (Zhu et al., 2023). This approach builds upon the conventional ion-mediated crystallization strategy by incorporating acidic polymers such as polyacrylic acid (PAA) and polyaspartic acid (PAsP). These polymers, which act as analogs to non-collagen proteins, excel in binding and isolating calcium ions, effectively delaying the onset of crystallization. This interplay results in a stable and well-hydrated amorphous precursor, preventing the amorphous calcium phosphate (ACP) from clustering and converting into hydroxyapatite before integrating with the collagen fibers (Olszta et al., 2003). Such an intricate procedure facilitates the creation of continuous apatite structures inside collagen fibers. (Jee et al., 2010; Qi et al., 2018). Additionally, the addition of polyphosphate to the PILP system, given its propensity to form electrostatic bonds with collagen fibers, refines the control over apatite's sustained growth. This procedure culminates in the creation of hierarchical IMC, which boasts layered apatite formations reminiscent of those in natural bone. Under TEM, these formations are characterized by pronounced cross-banded patterns (Liu et al., 2011; Hu et al., 2016; Ye et al., 2016). It is this structural alignment of IMC with natural bone tissue that has amplified its acknowledgment and interest within the scientific community.

The ideal mineralized collagen bone substitute material should include both EMC and IMC, with fixed volume ratios (3:1 in bone, 2:1 in dentin). However, despite scientists around the world putting in tremendous effort, this high-level biomimetic preparation method has not yet achieved a breakthrough (Chen et al., 2023). Studies have demonstrated that, when employing the PILP method, the surface of IMC shows deposits of calcium phosphate particles, indicating the occurrence of extrafibrillar mineralization, i.e., I-EMC (Hu et al., 2016; Du et al., 2022). The preparation of I-EMC involves three essential components: Type-I collagen, minerals, and non-collagen analogs (NCP) (Oosterlaken et al., 2021). Various factors (Höhling et al., 1990; Kikuchi et al., 2004; Dhand et al., 2016; Du et al., 2018) influence these elements, including collagen diameter, orientation, crosslinking degree, phosphorylation level, and NCP molecular weight and concentration (Jee et al., 2010; Zhou et al., 2017; Qi et al., 2018). These factors can impact the *in vitro* biomimetic mineralization process, thereby influencing the degree of collagen mineralization and its microstructure. The biomineralization and microstructure of the material also play a significant role in determining its physicochemical properties and biological activity (Kim et al., 2021). Furthermore, the material's biological activity is closely tied to its physical and chemical properties (Perrier et al., 2010; Liu et al., 2014). Consequently, carefully considering and understanding these multifaceted factors is a crucial prerequisite for preparing I-EMC that effectively emulates the structure and function of natural bone and provides an optimal osteogenic microenvironment.

In preparing mineralized collagen, both the mineralization time and the concentration of the mineralizing solution are crucial parameters. They significantly impact the microstructure of the mineralized collagen, as well as the ratio of collagen to minerals (Liu et al., 2011). Importantly, by "mineralization time," we

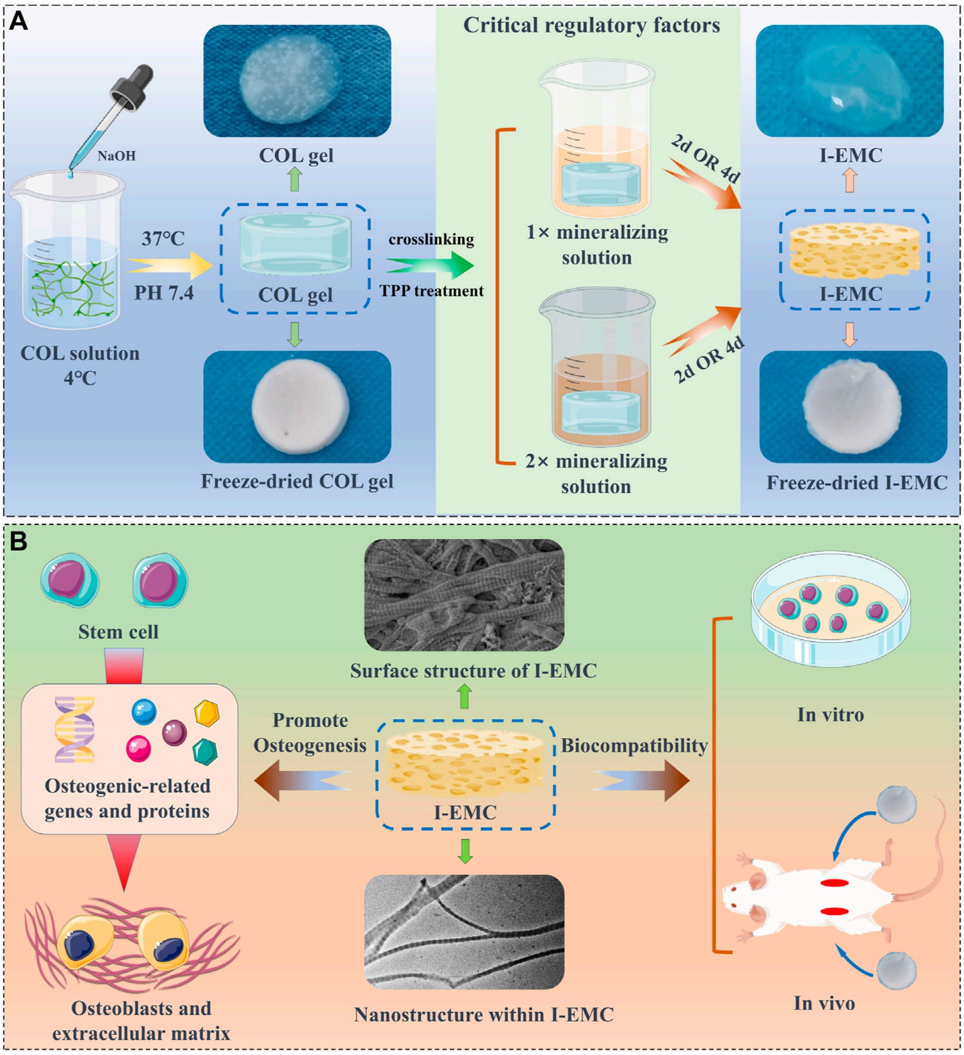

SCHEME 1
The fabrication of collagen (COL) and intra- and extra-mineralized collagen (I-EMC), exhibiting excellent biocompatibility in both *in vivo* and *in vitro* settings, along with remarkable performance in promoting osteogenic differentiation *in vitro*.

specifically mean the duration for which collagen fibers are exposed to the mineralizing solution. However, despite their significance, there remains considerable confusion regarding the use of these two parameters. Some studies use relatively low calcium phosphate concentrations and longer mineralization times to prepare mineralized collagen (Liu et al., 2011; Yu et al., 2020; Ye et al., 2021), while others opt for higher concentrations and significantly shortened mineralization times (Liu et al., 2011; Yu et al., 2020; Ye et al., 2021). It is worth mentioning that the latter did not provide a characterization of the nanostructure of the prepared mineralized collagen. As is well known, various physicochemical factors during the process of preparing mineralized collagen can affect its nanostructure, making it impossible to determine the specific type of mineralized collagen obtained. Notably, some studies do not specify the calcium phosphate concentrations or mineralization times (Xu et al., 2016; Zhang et al., 2018; Zhang et al., 2019; Xuan et al., 2021). The absence of standardized reporting presents challenges for cross-analyzing and comparing research findings. Furthermore, it hampers the clinical translation and progress of mineralized collagen products with a more biomimetic structure and enhanced osteogenic performance. In addition, there is a shortage of comparative studies that take into account both mineralization time and mineralization solution concentration simultaneously.

We aimed to utilize mineralization time and mineralization solution concentration as variables and adopted the PILP strategy to prepare I-EMC with distinct microstructures (Scheme 1). Through comprehensive characterization, we examined the physical and chemical properties of I-EMC under various mineralization conditions and assessed the *in vitro* and *in vivo* biocompatibility and osteogenic performance. By investigating the relationship between mineralization parameters, material physicochemical properties, and osteogenic performance, we revealed how microstructures influence cellular behaviors like biocompatibility and osteogenic microenvironment. This study has clarified the correlation between "conditions-structure-performance" in I-EMC. It establishes a foundation for the development of high-quality mineralized collagen-based bone substitute materials with improved osteogenic capabilities, and further advances their application in clinical settings. Our goal was to enhance the osteogenic microenvironment, facilitating more effective and enduring bone repair and regeneration, offering hope in the treatment of large bone defects.

2 Materials and methods

2.1 Fabrication of collagen gel

We procured a 5 mg/mL solution of Type-I collagen derived from rat tails, listed under the product number C8062, from Solarbio Life Sciences. To reconstitute the fibrils, the following steps were performed under ice bath conditions: 6 mL of Type-I collagen solution (5 mg/mL) was mixed with 3 mL of 10-fold phosphate buffered solution (PBS) buffer; deionized water was then added to adjust the collagen concentration to 1 mg/mL; after thorough mixing, 0.1 M NaOH solution was gradually added to adjust the pH to 7.4. The mixture was transferred into a 48-well culture plate with 300 μL per well and incubated at 37°C for 1 h to form a collagen gel. Subsequently, 1% glutaraldehyde solution was added for 30 min of crosslinking. After rinsing three times with deionized water, the samples were stored at 4°C for future use, and referred to as COL.

2.2 Preparation of I-EMC

We prepared 1 L of tris-buffered saline (TBS) buffer containing 8.77 g NaCl, 0.96 g Tris-base, and 6.61 g Tris-HCl. Before use, the buffer was filter sterilized. According to previous studies, the 1× mineralization solution is prepared as follows (Qi et al., 2018): a solution of 9 mM $CaCl_2$ and 4.2 mM K_2HPO_4 in TBS buffer was prepared. Equal volumes of the $CaCl_2$ solution and K_2HPO_4 solution were mixed using a syringe under magnetic stirring. Then, an appropriate amount of polyacrylic acid (PAA, MW ~2 kDa) was added to achieve a final PAA concentration of 0.25 mg/mL. The mixture was stirred for 30 min, and the resulting mineralization solution was stored at 4°C for later use. To prepare a 2× mineralization solution, the concentrations of calcium and phosphate ions were doubled, and the PAA concentration was adjusted to 1.0 mg/mL, following the same procedure. The collagen membrane was incubated in a 2.5% sodium tripolyphosphate (TPP) solution at 37°C for 1 h, followed by washing three times with deionized water. The pre-prepared 1× and 2× mineralization solutions were separately added, and mineralization was conducted for 2 days and 4 days, respectively, with daily solution replacement. The mineralized samples were named “1X-2D,” “1X-4D,” “2X-2D,” and “2X-4D.” After mineralization, the samples were washed three times with deionized water and stored at 4°C for later use. Additionally, the conventional crystallization method was used to prepare EMC materials for comparative study.

2.3 Characterizations of I-EMC

2.3.1 Scanning electron microscopy (SEM)

The morphologies of the collagen and I-EMC with varying microstructures were captured using a Merlin Compact SEM (Zeiss, Germany). We first processed the prepared collagen and I-EMC through freeze-drying. Subsequently, these were affixed onto the dedicated SEM sample stage using conductive adhesive and were treated via Pt sputtering before observation. Finally, the samples were placed into the SEM sample chamber and observed under an accelerating voltage of 15 kV. To identify the constituent in the samples, the energy-dispersive X-ray spectroscopy (EDS) spectra were obtained using the TEAM EDS point analysis software.

2.3.2 Transmission electron microscopy (TEM)

The internal morphologies of the collagen and I-EMC with varying microstructures were analyzed using a transmission electron microscope (Tecnai F20) operated at 200 kV. To prepare the samples for TEM, we initially immersed the previously prepared collagen and I-EMC specimens into deionized water, followed by homogenization to reduce the specimens into fibrous form. We then dropped 100 μL of the suspension onto the copper grid and allowed it to air dry overnight. Notably, we conducted the observations directly without any staining process on the samples. To prepare mineralization solution TEM samples, different concentration solutions were dropped onto the copper grid.

2.3.3 X-ray diffractometry (XRD)

XRD analysis of the collagen and I-EMC was meticulously conducted using a Rigaku Ultima IV X-ray diffractometer, outfitted with a copper target. Operating the diffractometer in a continuous scanning mode, with a precision step size of 0.02° across a testing range of 10°–60°, allowed for the procurement of comprehensive and uniform data.

2.3.4 Fourier transform infrared spectra (FTIR)

Characterization of the surface functional groups was achieved via FTIR, employing an attenuated total reflectance (ATR) mode. The infrared spectra (ATR-FTIR) were meticulously collected over the range of 500–4,000 cm^{-1} through a sequence of 32 scans, each with a resolution of 4 cm^{-1}. This process was facilitated using a Nicolet 6700 FTIR, specifically equipped with a flat-plate ATR from Thermo Fisher Scientific.

2.4 Water contact angle (WCA) measurements

The dynamic water contact angles of collagen and I-EMC were measured at 25°C using a dynamic contact angle analyzer (Theta Flex, Biolin Scientific). Building upon the methodologies employed by previous researchers (Ye et al., 2021), we first freeze-dried the collagen and I-EMC samples and then placed them between two glass slides to ensure their flatness. Next, the samples were carefully attached to glass slides. For the measurement process, we utilized 4 μL of distilled water. The WCAs were determined using a goniometer and the sessile drop method. Considering the superior hydrophilicity of the collagen material, we analyzed the dynamic WCA of different materials by capturing photographs at intervals of 0.03 s. Additionally, we performed measurements on three samples within the same group.

2.5 Thermogravimetric analysis (TGA)

The tested sample weighed between 3 and 5 mg, and a TGA was conducted utilizing a thermogravimetric analyzer (TGA2, Mettler Toledo, Switzerland). Considering the degradation temperatures of collagen and hydroxyapatite (HA), the TGA testing conditions were set as follows: the heating temperature ranged from 37°C to 800°C, with a heating rate of 10°C per minute. The TGA analysis was performed under air.

2.6 Isolation and culture of bone marrow stromal cells (BMSCs)

BMSCs were obtained from a healthy one-week-old female New Zealand rabbit and cultured in Dulbecco's modified eagle medium/nutrient mixture F-12 (DMEM/F12), enriched with 10% fetal bovine serum and 1% streptomycin-penicillin. The culture medium was replaced every 3 days, and the cell cultures were nurtured in a humidified incubator set to 37°C and 5% CO_2. Once the medium reached approximately 80% confluence, the cells were treated with trypsin at 37°C for 2 min prior to passaging. After three passages, the cells were conditioned for subsequent *in vitro* biocompatibility and osteogenesis experiments.

2.7 Cell viability, proliferation, and morphology

The fabricated COL and I-EMC were transferred into a new 48-well plate and subjected to sterilization with 75% ethanol. Over the next 3 h, the ethanol was refreshed hourly, followed by sterilization overnight. Before the process of cell seeding, all samples were ventilated and exposed to ultraviolet (UV) sterilization for 2 h. Subsequently, a rinse with PBS was performed to remove any potential residual solvents. The samples were then immersed in a complete culture medium for an additional 2 h. In the final step, taking cues from prior research, we seeded the third-generation BMSCs onto the membranes at a density of 5×10^4 cells per well (Wang et al., 2019). We renewed the culture medium bi-daily. After 24 h, the collagen and mineralized collagen membranes, with the attached BMSCs, were relocated to a new 48-well plate. Using the calcein-AM/PI double staining kit, we assessed the vitality of the BMSCs. For the CCK-8 assay, we seeded BMSCs at a density of 2×10^4 cells per well in a 48-well culture plate. One day later, we transferred the films to a new plate and evaluated cell proliferation using the CCK-8 assay (CCK8, Bioss, China) on days 1, 3, and 7 of culture. Additionally, we employed phalloidin staining to assess the morphology of cells on the membranes. The F-actin filaments and nuclei of the BMSCs were marked, respectively, using rhodamine-phalloidin and 4′,6-diamidino-2-phenylindole (DAPI). Specifically, after a 24-h incubation period, we relocated the membranes to a fresh 48-well plate, and then applied 4.0% paraformaldehyde to fix the samples. Next, we performed permeabilization using 0.5% Triton X-100. Subsequently, the samples were incubated with rhodamine-phalloidin for 30 min, followed by a 2-min counterstain with DAPI. All stained samples were captured using a fluorescence microscope (RVL-100-M, ECHO). The immunofluorescent intensity was quantified using ImageJ.

2.8 *In vivo* biocompatibility

Drawing upon the methods of prior researchers (Zandi et al., 2021), we conducted an *in vivo* biocompatibility study utilizing 11 male Sprague Dawley (SD) rats, each weighing approximately 200 g. Initially, we created two 1-cm incisions on the dorsal skin of each rat and prepared small subcutaneous pockets under sterile conditions. We then sequentially implanted COL, 1X-2D, 1X-4D, 2X-2D, and 2X-4D samples (four samples per group) into the subcutaneous pockets on the rat's back, implanting two identical samples in each rat. One rat served as the control group and did not receive any sample; its incisions were directly sutured. After 7 days of sample implantation, we euthanized the rats and collected the implants and the surrounding tissues, heart, liver, spleen, lung, and kidney tissues. We then conducted hematoxylin and eosin (HE) staining and histological analysis on these tissues to evaluate the extent of inflammation.

2.9 Alkaline phosphatase (ALP) activity

We seeded 1×10^5 BMSCs onto collagen or mineralized collagen membranes in a 48-well plate. After 1 day, we carefully transferred the membranes to a new well plate. Following prior research protocols (Zhao et al., 2020), we added osteogenic culture medium containing 10 mM of β-glycerophosphate, 50 μM of ascorbic acid-2-phosphate, and 0.1 μM of dexamethasone, with media changes every other day. After completing the 7-day osteogenic induction, ALP activity was evaluated using ALP staining and ALP assay kits.

2.10 Alizarin red S (ARS) staining

The procedures of cell seeding, medium replacement, and incubation followed the same steps as the ALP staining. After 14 days of osteogenic induction, the samples were fixed using 4% paraformaldehyde, washed with deionized water, and then stained for 10 min with 2% alizarin red S solution at pH 4.2. The samples were then repeatedly washed with deionized water to remove any residual alizarin red S. Finally, we observed the calcium deposits under a microscope (RVL-100-M, ECHO). Calcium phosphate in the I-EMC samples can interfere with ARS staining. Therefore, we cultured BMSCs in a blank plate and co-cultured them with the different samples. After 14 days of osteogenic induction, the cells at the bottom of the plate were stained with alizarin red. After thoroughly removing unbound dyes with deionized water, we captured images using a microscope (RVL-100-M, ECHO). The Alizarin Red-stained calcium nodules were then eluted from the cultures using the cetylpyridinium chloride method (Xiao et al., 2020)), and their absorbance at 540 nm was assessed for quantification.

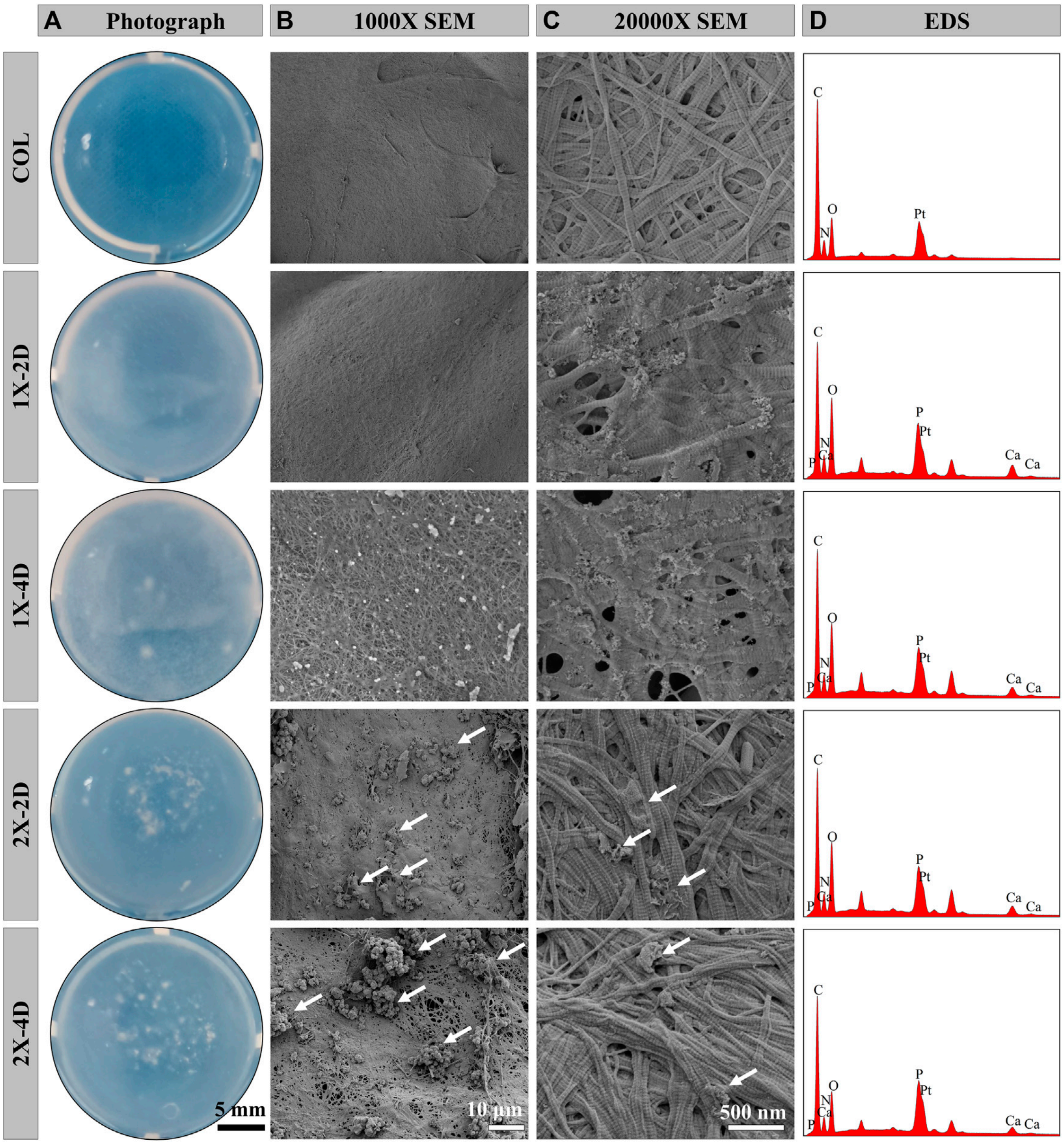

FIGURE 1
Characterizations of COL and I-EMC. Gross appearance **(A)** and SEM morphologies **(B, C)** and EDS analysis **(D)** of various samples. White arrows highlight the presence of large calcium phosphate particles.

2.11 Immunocytochemistry

After 14 days of osteogenic induction, immunocytochemical staining was performed to detect the expression of osteocalcin (OCN) and runt-related transcription factor 2 (RUNX-2). The samples were fixed with 10% paraformaldehyde at room temperature for 10 min, followed by cell permeabilization with 0.1% Triton X-100 at room temperature for 20 min. To block nonspecific binding, cells were incubated with 10% goat serum at room temperature for 30 min. Subsequently, primary antibodies against OCN (A14636, AB clonal) and RUNX2 (A2851, AB clonal) diluted at 1:180 were added and incubated overnight at 4°C. Secondary antibodies (AS053, AB clonal) diluted at 1:400 were then added and incubated for 1 h at 37°C. Subsequently, phalloidin and DAPI staining were performed as described. Throughout the entire experiment, the samples were rinsed with PBS-Tween between every step. Finally, the images were observed and captured using a fluorescence microscope (RVL-100-M, ECHO), and the fluorescence intensity of each bone-related protein was semi-quantitatively analyzed using ImageJ software.

2.12 Statistical analysis

All data are presented as mean ± standard deviation. For data comparison, we employed one-way analysis of variance, paired

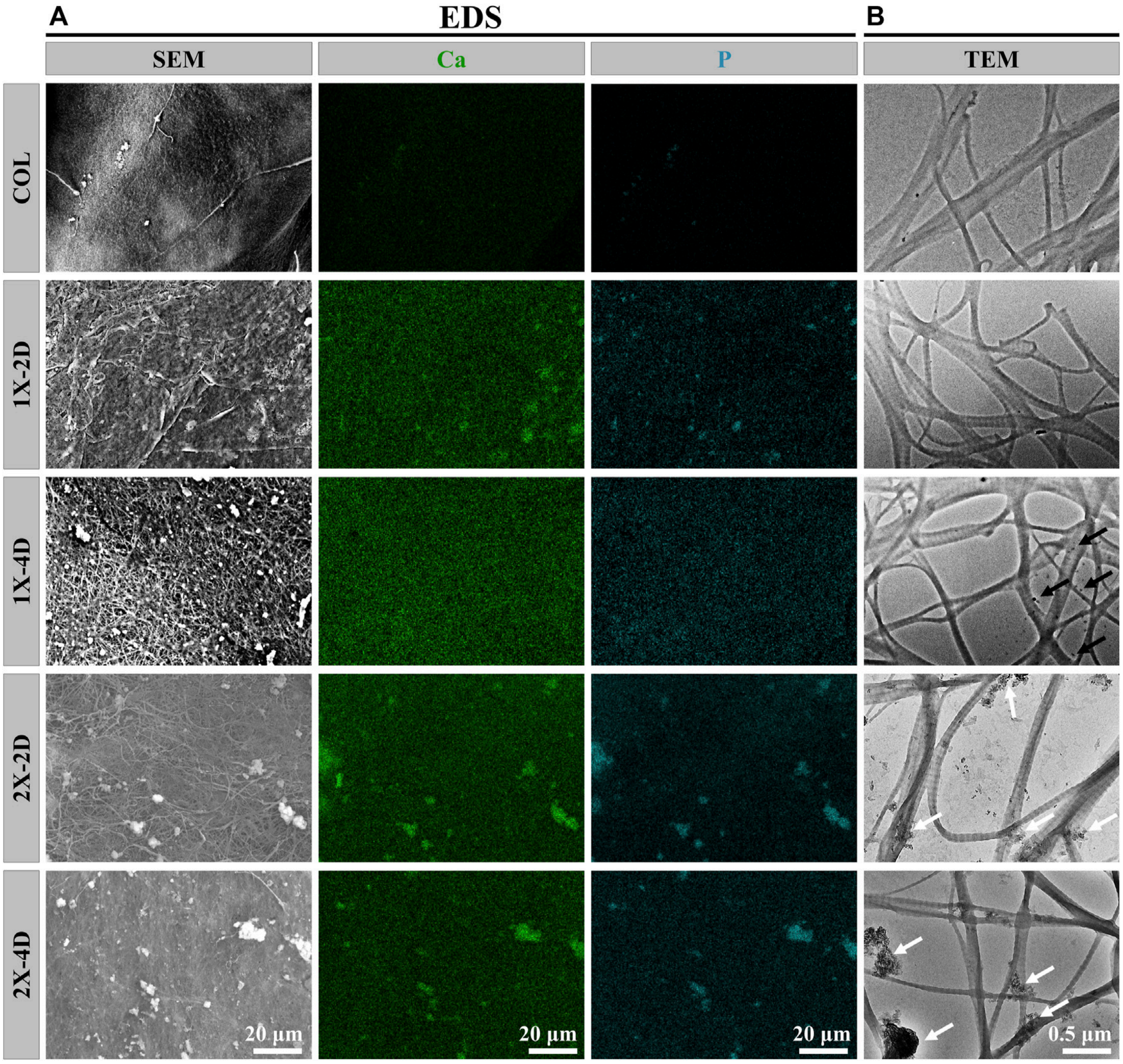

FIGURE 2
Characterization of COL and I-EMC. EDS mapping images **(A)** and TEM images **(B)** of different samples. White arrows indicate the presence of large calcium phosphate particles, while black arrows indicate the presence of small amorphous calcium phosphate nanoparticles.

t-test, and the Bonferroni–Dunn *post hoc* test. A significance level of $p < 0.05$ was considered statistically significant. All statistical analyses were performed using GraphPad Prism 9 (GraphPad Software). Each experiment was independently repeated at least three times.

3 Results and discussion

3.1 Microstructure and element distribution of I-EMC

We employed the PILP process to produce I-EMC with diverse microstructures. A collagen protein solution with a concentration of 1 mg/mL was prepared under 4°C conditions. After adjusting the pH, the solution was incubated at 37°C for 1 h, resulting in self-assembly of collagen proteins and the formation of collagen gel. Figure 1A shows the appearance of the collagen gel and different I-EMC samples. The collagen gel is initially transparent, but after mineralization, it transforms into a milky white, opaque appearance. Specifically, the samples mineralized with 1× mineralization solution exhibit a uniform milky white appearance, whereas the samples mineralized with 2× mineralization solution have more visible white particles scattered on the surface. The number of white particles increases with longer mineralization time. After freeze-drying, both collagen and I-EMC exhibit a white sponge-like structure, with no apparent difference in appearance between pre-mineralized and post-mineralized states (Scheme 1). Additionally, it should be noted that in the experiment, we observed that, after standard cleaning (using deionized water), some of the calcium phosphate particles on the surface of mineralized collagen were partially removed. However, during electron microscope observations (Figure 1B; Figure 2A), some residual calcium phosphate particles that were not completely eliminated from the surface were still visible. We speculate that these particles may have a relatively tight association with collagen.

Although increasing the number of cleaning cycles or enhancing cleaning intensity (such as introducing ultrasonic cleaning techniques) might remove some of these particles, it is important to note that this could potentially lead to structural damage to the mineralized collagen.

Under SEM, the surface morphology of the samples is clearly revealed in Figures 1B,C. Prior to mineralization, the COL sample exhibits a smooth surface, while after mineralization, the surface of collagen protein becomes rough. Among them, the 1X-2D and 1X-4D samples show dispersed small particles on the surface with uniform features, whereas the 2X-2D and 2X-4D samples exhibit dispersed larger calcium phosphate particles with uneven distribution. At high magnification, both COL and I-EMC are composed of reconstituted collagen fiber networks, and the process of biomineralization does not interfere with their fiber structure (Figure 1C). Compared to the IMC prepared without template analog TPP (Ye et al., 2021), the introduction of TPP allowed us to clearly observe the periodic band pattern in I-EMC (Jin et al., 2019). The EDS spectrum is shown in Figure 1D. The presence of calcium and phosphorus elements indicates the deposition of calcium phosphate on the collagen protein, demonstrating the successful preparation of mineralized collagen material.

To assess the uniformity of I-EMC sample mineralization, we conducted EDS to qualitatively map the distribution of calcium and phosphorus. The results depicted in Figure 2A demonstrate that the distribution of calcium and phosphorus elements is uniform in the 1X-2D and 1X-4D samples. However, in the 2X-2D and 2X-4D samples, calcium and phosphorus elements tend to cluster and exhibit lower density in specific areas, indicating poor uniformity. These findings are consistent with the observations and SEM results shown in Figure 1. It can be inferred that an increase in the concentration of the mineralization solution leads to uneven mineralization, resulting in a higher deposition of minerals outside the fibers.

On the other hand, the collagen fibers obtained from the five different samples exhibit distinct periodic patterns, as shown in Figure 2B, indicating successful mineral deposition within the interstitial regions of the collagen fibers, resembling the D-band pattern observed in natural bone (Jin et al., 2019). This D-band pattern observed through TEM aligns with the periodic banding pattern observed through SEM, which may be the result of intermittent deposition of nano-sized calcium phosphate within the fibers upon the introduction of the template analog TPP.

Moreover, the 1X-4D sample reveals the presence of nano-sized amorphous calcium phosphate (ACP) particles stabilized by PAA on the surface, while the 2X-2D and 2X-4D samples exhibit larger clusters of calcium phosphate deposited on the collagen surface, resembling the surface structure of EMC (Figures 3A,B). These findings demonstrate that mineralization within collagen fibers can be achieved with different concentrations of PAA-stabilized mineralizing solutions. However, this process also leads to varying degrees of mineralization occurring outside the fibers. With an increase in mineralizing solution concentration, the stabilizing effect of PAA decreased, leading to the formation of larger-sized clusters of calcium phosphate (Figures 3C,D). As these clusters could not penetrate the interior of the collagen fibers, more substantial deposits of calcium phosphate occurred on the outer surface of the fibers. It can be inferred that, due to the limited surface area of collagen fibers, the deposition of minerals outside the fibers has an impact on the progression of internal mineralization.

3.2 Chemical composition and organic and inorganic content of I-EMC

FTIR spectroscopy provides direct information about the conformational structure of compounds through the absorption peaks of characteristic functional groups. The infrared spectra of the five sample groups are shown in Figure 4A. In the FTIR spectra, COL exhibits typical amide bands, with the absorption peak at 1,650 cm^{-1} primarily attributed to the stretching vibration of the C=O bond (amide I band), the peak at 1,550 cm^{-1} mainly arising from the vibrations of the C-N and N-H bonds (amide II band), and the peak at 1,240 cm^{-1} mainly resulting from the stretching vibrations of the C-N and C-C bonds (amide III band). The different I-EMC samples exhibit similar infrared spectral patterns. Firstly, the absorption peaks corresponding to the triple helical structure of collagen are present, indicating that the triple helical structure of collagen is well-preserved after mineralization (Du et al., 2022). In the biomimetic mineralization process, calcium phosphate ions first aggregate to form ACP, which then deposits within the collagen fibers and eventually transforms into poorly crystalline hydroxyapatite and hydroxyapatite crystals. Therefore, in addition to the aforementioned collagen protein peaks, the I-EMC samples exhibit a strong absorption peak around 1,040 cm^{-1}, corresponding to the stretching vibration of phosphate groups (PO_4^{3-}), as well as absorption peaks around 595 cm^{-1} and 660 cm^{-1}, with the former corresponding to the vibrational absorption of phosphate groups (PO_4^{3-}) in ACP and the latter corresponding to the stretching vibration absorption of hydroxyl groups (OH) in hydroxyapatite. Thus, the ACP gradually converts into hydroxyapatite during the mineralization process (Du et al., 2022). Previous studies have reported similar results (Xia et al., 2013; Hu et al., 2016; Wang et al., 2019). The sharper the peak shape, the higher the crystallinity. By observing the changes in the absorption peaks of the phosphate groups in mineralized collagen under different conditions, we found that the characteristic peaks at 595 cm^{-1}, 660 cm^{-1}, and 1,040 cm^{-1} were highest and sharpest in the 1X-4D and 2X-4D samples, indicating a higher content and purity of the phosphate groups. This also implies that extending the mineralization time can promote the transformation of hydroxyapatite crystals. Additionally, compared to the 1X-2D sample, the 2X-2D samples exhibited relatively higher and sharper absorption peaks, indicating that increasing the mineralization solution concentration can also enhance the content and purity of the phosphate groups and promote the transformation of hydroxyapatite crystals. However, it should be noted that, as mentioned earlier, this is due to the decreased stabilizing effect of PAA on high-concentration mineralization solution, which accelerates the transformation of ACP to hydroxyapatite crystals, resulting in more mineralization occurring outside the fibers.

The XRD spectra of the sample groups are presented in Figure 4B. COL exhibits a broad characteristic diffraction peak, known as the “D peak,” around 13°, which reflects the fibrous structure and hierarchical features of collagen. Different I-EMC

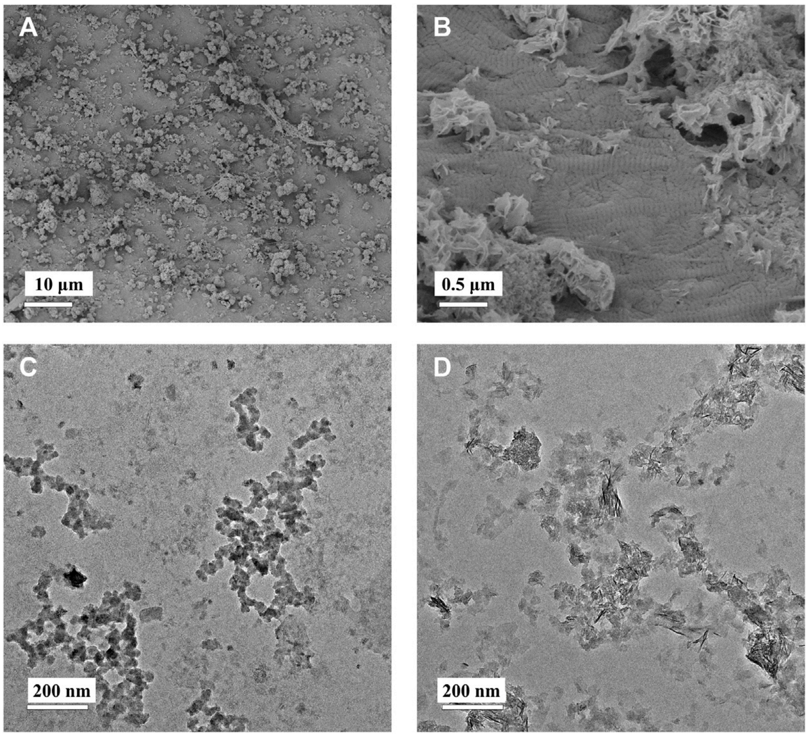

FIGURE 3
Low-magnification **(A)** and high-magnification **(B)** SEM images of EMC. PAA-stabilized 1× mineralization solution **(C)** and 2× mineralization solution **(D)** depicting TEM images of ACP.

samples display similar XRD spectra. The peak at 26.2° (2θ) corresponds to the (002) plane of HA. The main peak in the range of 2θ = 31.5°–33.5° corresponds to the overlapping of the (112) (211), and (300) crystal planes of apatite. This is similar to the XRD spectrum of natural cancellous bone (Li et al., 2012). The peak at 45.4° (2θ) corresponds to the (222) plane of HA. All diffraction peaks are sharp, indicating a high degree of crystallinity in the mineralized collagen. Furthermore, compared to samples mineralized for 2 days, the mineralized collagen after 4 days of mineralization exhibits relatively stronger diffraction peaks, which typically indicate higher crystallinity, consistent with the results of FTIR.

Thermogravimetric analysis (TGA) is a valuable technique used to investigate the composition, components, and stability of materials by monitoring their mass changes as the temperature increases. Figure 4C displays the TGA curves for the five sample groups, which exhibit two distinct weight loss stages. The initial weight loss, occurring within the range of 37°C–200°C, corresponds to the removal of bound water (highlighted in yellow box). Subsequently, between 200°C and 660°C, the weight loss corresponds to the degradation of collagen protein (highlighted in green box). Due to the fact that HA primarily loses weight through the release of bound water, the mass loss is minimal, with the majority occurring during the collagen degradation process. Notably, the I-EMC samples exhibit lower mass loss compared to the COL sample. A reduced weight loss in mineralized collagen suggests a higher remaining mass, indicating an elevated concentration of HA within the collagen matrix. Figure 3C depicts the mass residue rates of samples from each group at the conclusion of thermal gravimetric analysis. Based on this data, we can easily calculate the mass loss rates within the specified temperature range for each group of samples, namely, COL (74.3%), 1X-2D (61.8%), 1X-4D (52.6%), 2X-2D (46.3%), and 2X-4D (40.4%). This suggests that prolonging the mineralization time and increasing the concentration of the mineralization solution can enhance the mineral content, although higher solution concentration often leads to more mineralization occurring outside the fibers. Furthermore, it is noteworthy that the second weight loss stage of the COL sample occurs earlier than that of the I-EMC samples. This indicates that mineralized collagen exhibits higher thermal stability than pure collagen, which aligns with previous research findings [29]. The observed changes in decomposition temperature reflect a close structural relationship between collagen and HA, suggesting that most of the crystals are embedded within the collagen fibers (Li et al., 2012; Liu et al., 2014; Qi et al., 2018; Thrivikraman et al., 2019; Ye et al., 2021).

3.3 Hydrophilicity of I-EMC

Collagen protein, as a common biomaterial, exhibits excellent hydrophilicity. In this study, we utilized a compression molding method to prepare the samples and conducted WCA measurements. Based on the dynamic changes in WCA over time, we plotted the dynamic contact angle curves (Figure 4D) for all samples. Figure 4E shows representative images of water droplets on the test samples,

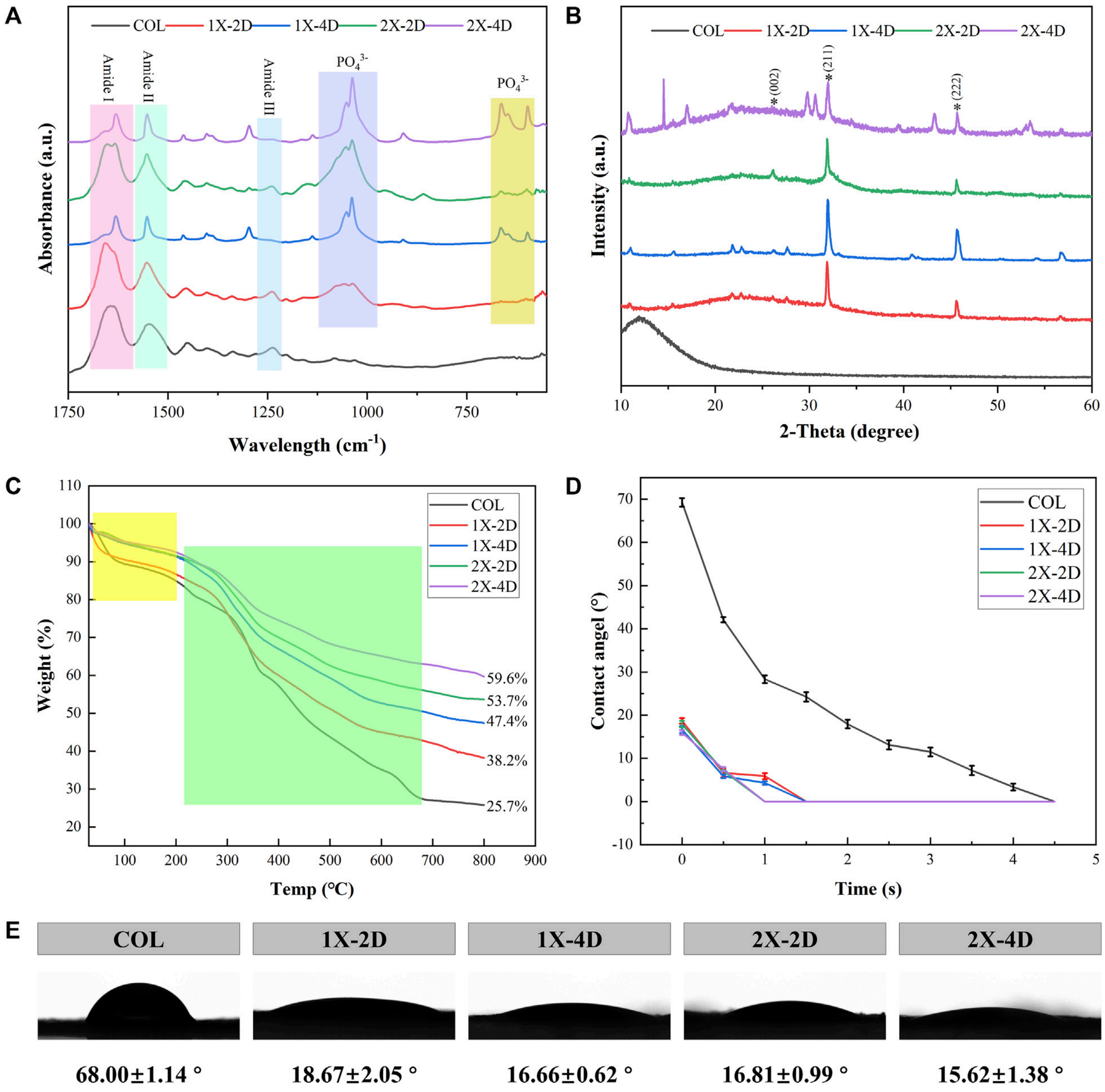

FIGURE 4
Characterization of COL and I-EMC. **(A)** FTIR spectra, **(B)** XRD spectra, **(C)** TGA curves, and **(D)** water contact angle (WCA) graph. **(E)** WCA images and average WCA.

along with the corresponding average WCA and standard deviations. Through the observation of dynamic contact angle curves, we noticed a gradual decrease in WCAs during the measurement process, attributed to droplet absorption and spreading. The WCA for pure collagen was maintained for 4.5 s, while after mineralization, the contact angle was reduced to 1.5 s, indicating that mineralization increased the collagen hydrophilicity. Importantly, after 5 s, all samples exhibited superhydrophilicity, consistent with previous findings (Ye et al., 2021; Du et al., 2022). However, some researchers suggest that the attachment of HA or ACP particles on collagen surfaces may cover hydrophilic groups and, thus, reduce the material's hydrophilicity (Du et al., 2022). We acknowledge that this could be related to the handling of samples during water contact angle testing. Overall, whether mineralized or not, all samples exhibited excellent hydrophilicity.

3.4 *In vitro* biocompatibility of I-EMC

The hydrophilicity, morphology, and roughness of materials play a pivotal role in influencing cell adhesion, migration, and proliferation. The biocompatibility of materials serves as the fundamental basis for their biological applications. To evaluate the biocompatibility of collagen and I-EMC samples, we employed calcein-AM/PI staining to analyze the cytotoxicity of the cells. The results demonstrated that BMSCs adhered well to

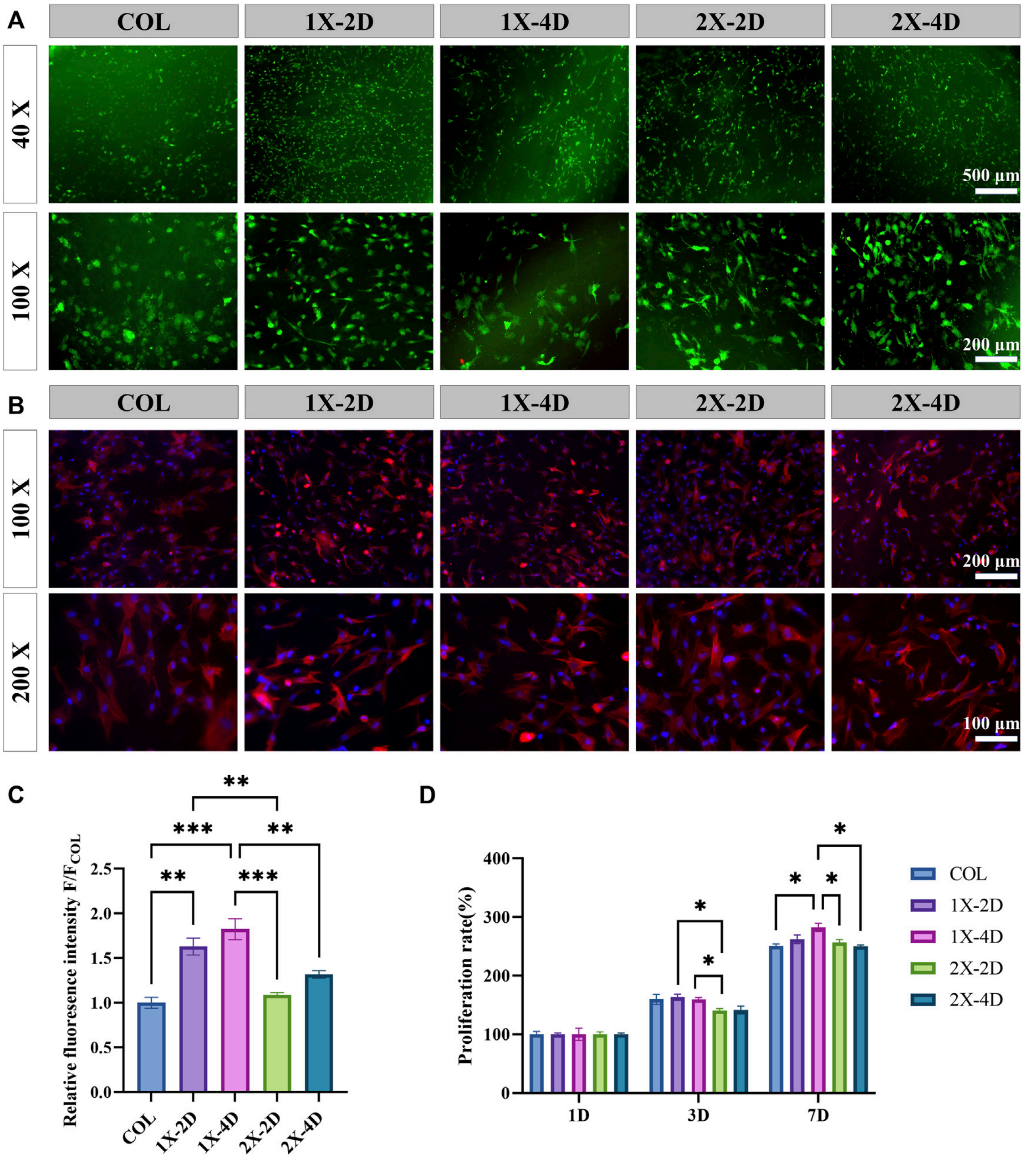

FIGURE 5
In vitro biocompatibility of COL and I-EMC. **(A)** Calcein-AM/PI staining of BMSCs at 24 h: live cells (green) and dead cells (red). **(B)** Fluorescent imaging with rhodamine-DAPI staining. **(C)** Quantitative analysis of F-actin fluorescence intensity (n = 3). **(D)** Cell proliferation within the different samples at 1, 3, and 7 days. (*$p < 0.05$, **$p < 0.01$, ***$p < 0.001$).

the surface of each sample and exhibited high cell viability after 24 h (Figure 5A), indicating good biocompatibility. Subsequently, we performed CCK-8 assays to analyze the effects of various samples on cell proliferation. BMSCs were seeded on samples, and cell proliferation was assessed after 1, 3, and 7 days after seeding. Figure 5D shows that the cell numbers in different samples significantly increased with prolonged culture time. Compared to the 2X-2D group, the 1X-2D and 1X-4D samples promoted cell proliferation on the third day, indicating better biocompatibility toward BMSCs. Furthermore, on the seventh day, the 1X-4D group significantly enhanced cell proliferation.

To observe the morphology of BMSCs adhering to the surfaces of different samples, we used rhodamine-phalloidin staining to label F-actin (Figure 5B). The results showed that, after 24 h of culture, most cells adhered to the samples and exhibited a spread-out state. Cells cultured on the COL sample had a more rounded morphology, consistent with the results observed in the live/dead staining, which may be attributed to the porous and loose structure of collagen, allowing BMSCs to easily penetrate into the collagen gel. In contrast, cells cultured on the four types of I-EMC samples exhibited an elongated morphology, indicating cell migration characteristics. We quantitatively analyzed the fluorescence intensity of F-actin using ImageJ software and

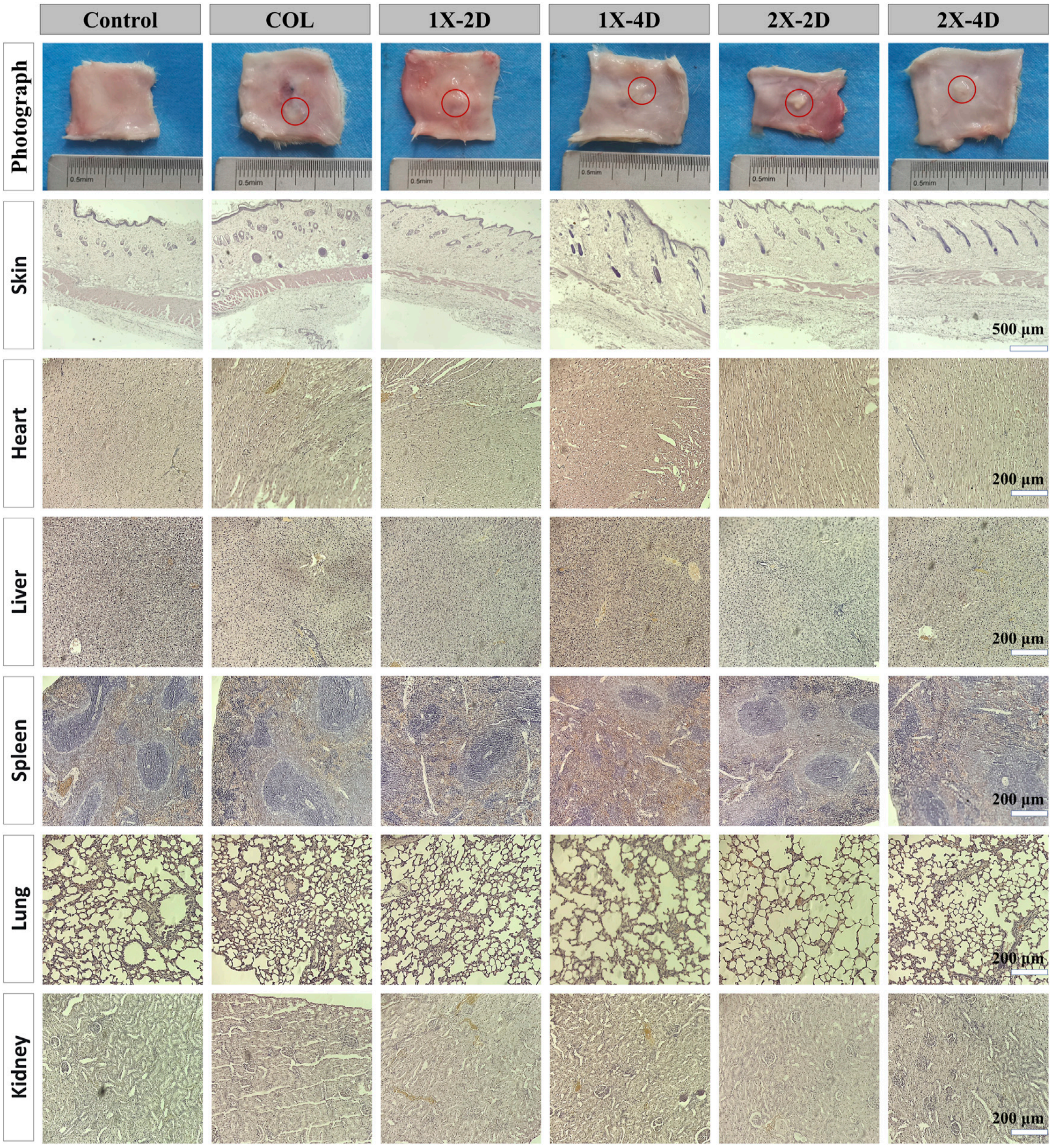

FIGURE 6
In vivo biocompatibility assessment of COL and I-EMC after subcutaneous implantation in rats. Macroscopic view and HE staining of the skin around the implant, as well as heart, liver, spleen, lung, and kidney tissues after 7 days of implantation. The control group comprised rats without any implanted materials. The red circle marks the location where COL and I-EMC were implanted.

presented the results in a bar graph (Figure 5C). The results showed that the F-actin fluorescence intensity was significantly higher in the 1X-2D and 1X-4D samples compared to the other groups, with no statistical difference between the two groups.

F-actin is a multifunctional protein and an important component of the cell cytoskeleton. It can form microfilaments, rapidly assemble and disassemble, providing mechanical support for cell morphology and movement (Pollard and Cooper, 2009; Cerutti and Ridley, 2017), and participate in key cellular processes such as cell migration and division (dos Remedios et al., 2003). Additionally, F-actin plays a crucial role in the osteogenic process of BMSCs (Chen et al., 2016), and the enhancement of its fluorescence intensity is beneficial for the early osteogenic differentiation of BMSCs (Wu et al., 2020). Therefore, the 1X-2D and 1X-4D samples may significantly enhance the expression of F-actin and the reorganization of the cell cytoskeleton, thereby inducing the migration and osteogenic differentiation of BMSCs. This may be attributed to the uniform mineralization and surface structure of these samples.

3.5 *In vivo* biocompatibility and toxicity of I-EMC

Our findings indicate that both COL and I-EMC materials exhibited no cytotoxicity *in vitro* and demonstrated excellent

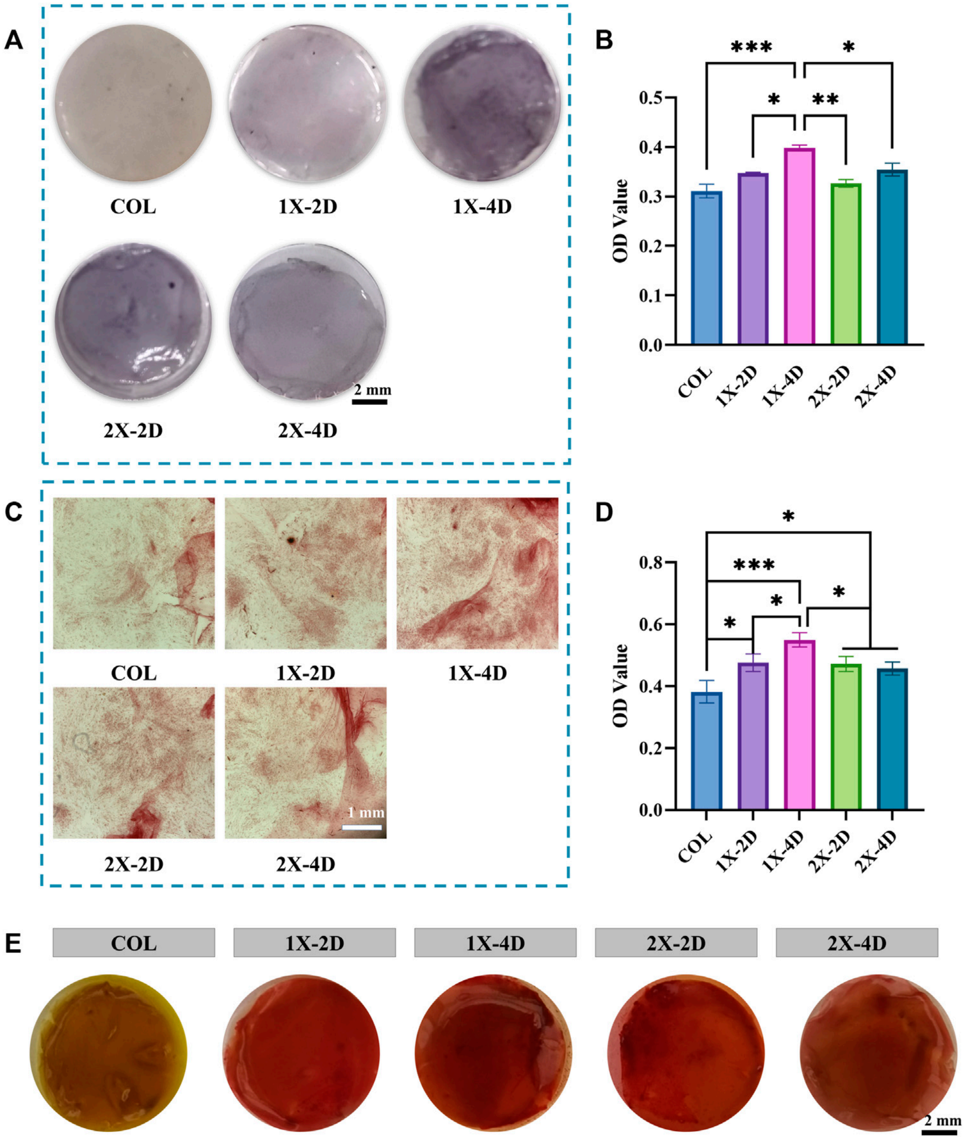

FIGURE 7
Evaluation of the osteogenic differentiation of BMSCs seeded on COL and I-EMC. **(A)** Alkaline phosphatase (ALP) staining and **(B)** ALP activity determination at 7 days post osteogenic differentiation induction. **(C)** Alizarin red staining and **(D)** quantification of alizarin red in BMSCs cultured with various samples in osteogenic media for 2 weeks. **(E)** Images of different groups post alizarin red S staining; (*$p < 0.05$, **$p < 0.01$, ***$p < 0.001$).

biocompatibility. However, it should be noted that *in vitro* results may not always reflect *in vivo* performance. To further evaluate the biocompatibility of COL and I-EMC materials, an *in vivo* study was conducted using a rat subcutaneous pouch model. During the 7-day period after implantation of various samples into the subcutaneous tissue of rats, no deaths or infections were observed. Additionally, all incisions in each group healed well. Figure 6 shows the macroscopic view and HE staining of the skin around the implant materials, heart, liver, spleen, lungs, and kidneys in each group. Macroscopic observation of the samples revealed no signs of redness or local exudation. HE staining of the skin confirmed the absence of any inflammatory reactions. Additionally, to assess the material toxicity to the organism, we collected samples from the rat's heart, liver, spleen, lungs, and kidneys, conducted sectioning, and performed HE staining. Compared to the control group, the rat's various organ tissues exhibited intact structures without any pathological changes. In conclusion, both collagen and I-EMC materials demonstrated excellent biocompatibility, both *in vivo* and *in vitro*, supporting cell adhesion and proliferation.

3.6 Effect on osteogenic differentiation of BMSCs

Osteogenic differentiation plays a pivotal role in maintaining the equilibrium of the bone microenvironment. An ideal bone graft material should possess excellent biocompatibility and exhibit outstanding activity during the process of bone formation. Alkaline phosphatase (ALP) is a crucial protein involved in the differentiation of osteoblasts, playing a key role in early bone

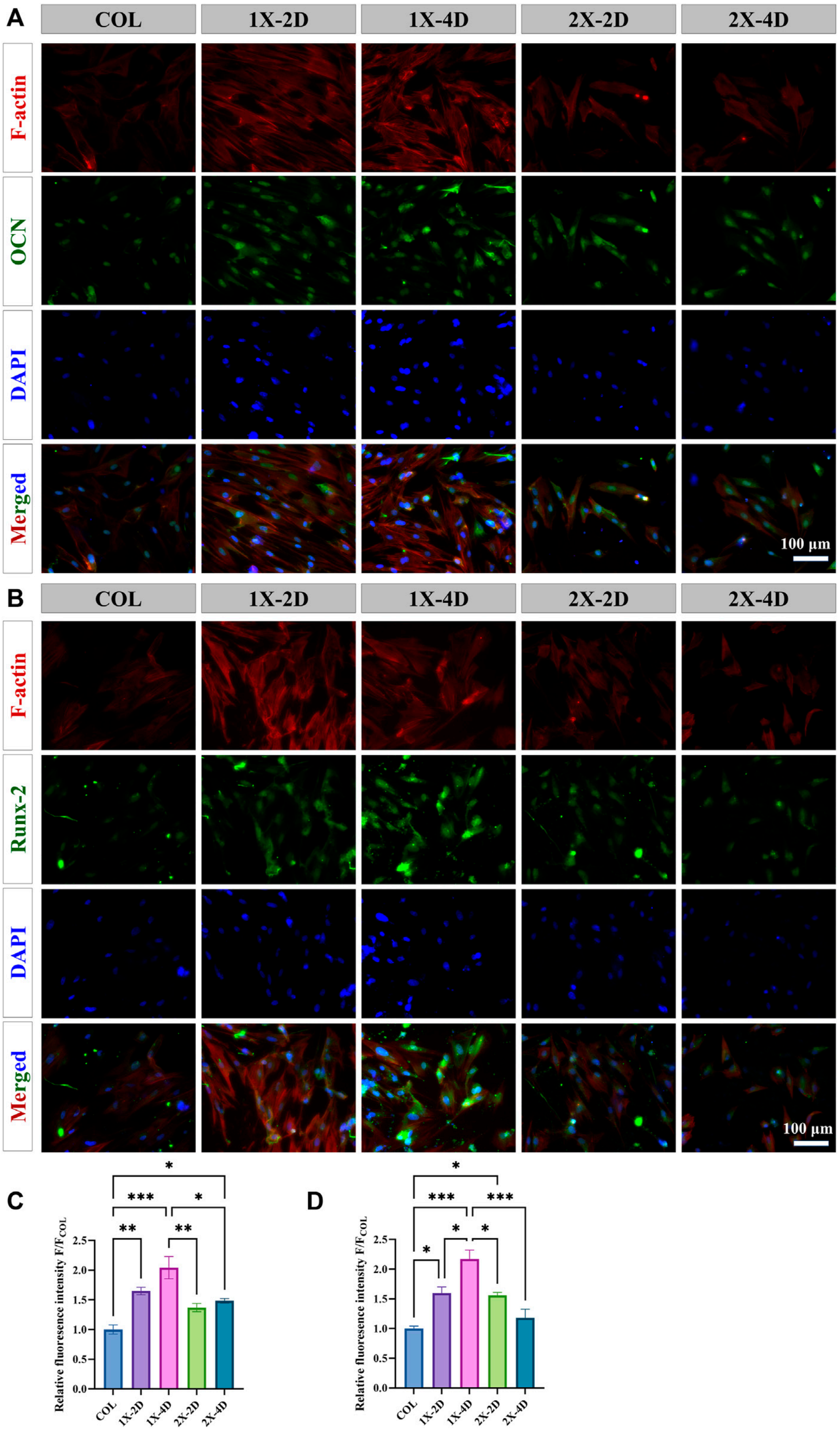

FIGURE 8
Immunohistochemical staining and quantitative analysis of osteogenic-related proteins in BMSCs cultured in different groups for 14 days, specifically focusing on **(A, C)** OCN and **(B, D)** RUNX-2. ($*p < 0.05$, $**p < 0.01$, $***p < 0.001$).

formation. Figure 7A displays the ALP staining results, where the COL surface shows fewer and lighter blue-purple areas, whereas the I-EMC surface exhibits increased and deeper ALP-positive regions, indicating a more significant ALP expression, especially in the 1X-4D and 2X-2D groups. Semi-quantitative analysis of ALP activity (Figure 7B) indicates that, compared to COL, the I-EMC material significantly enhances ALP activity, particularly in the 1X-4D group, with significant differences ($p < 0.05$). Therefore, compared to COL, I-EMC promotes the early differentiation of BMSCs toward osteogenesis. The 1X-4D sample exhibits remarkable osteogenic induction, with both ALP secretion and activity surpassing those of other groups, indicating the most favorable osteogenic effect, consistent with other study findings (Wang et al., 2019).

Calcium deposition serves as an indicator of late-stage osteogenic differentiation. To evaluate the osteogenic differentiation of BMSCs, we performed alizarin red staining. BMSCs were co-cultured with samples from each group, and after 14 days of osteogenic induction, the underlying cells were stained, as depicted in Figure 7C. The semi-quantitative results are in Figure 7D, revealing that BMSCs co-cultured with I-EMC had richer and denser calcium nodules. Notably, the 1X-4D sample showed the most pronounced calcium deposition. Figure 7E displays the staining images of these nodules. When compared to the COL samples, I-EMC exhibited significantly deeper red-stained areas, with the 1X-4D sample being especially vivid in staining depth and coverage. This evidence underscores the vital role of I-EMC in osteogenic differentiation, with the 1X-4D and 2X-2D samples emerging as the most illustrative.

During osteogenic differentiation, osteogenic-related proteins play a crucial role. We employed immunofluorescence staining to explore the effect of I-EMC on the osteogenic differentiation of BMSCs, specifically targeting osteocalcin (OCN) and runt-related transcription factor 2 (RUNX-2), both closely linked to bone formation. After 14 days of osteogenic induction, all BMSC groups exhibited OCN expression (Figure 8A) and RUNX-2 expression (Figure 8B). BMSCs cultured on the I-EMC surface showed significantly higher average fluorescence intensities of OCN and RUNX-2 compared to the COL group, particularly in the 1X-2D and 1X-4D samples with the most prominent fluorescence signals ($p < 0.05$). Quantitative analysis indicated that, under 1X-2D, 1X-4D, and 2X-4D culture conditions, BMSCs demonstrated significant increases in OCN expression by 1.64-fold, 2.04-fold, and 1.48-fold, respectively (Figure 8C). Additionally, under 1X-2D, 1X-4D, and 2X-2D culture conditions, the expression of RUNX-2 in BMSCs was also significantly upregulated by 1.59-fold, 2.17-fold, and 1.56-fold, respectively (Figure 8D) ($p < 0.05$), compared to the COL group.

Based on our comprehensive experimental results, all I-EMC samples significantly enhanced the ALP activity of BMSCs, promoted mineral deposition, and increased osteogenic-related protein expression compared to COL, showcasing excellent osteogenic performance. This is consistent with previous research findings. Compared to non-mineralized collagen, the addition of calcium phosphate in collagen significantly enhances the prolonged metabolic activity of BMSCs and amplifies the expression of osteogenesis-associated genes (Weisgerber et al., 2015; de Melo Pereira et al., 2020). *In vivo* studies also support the idea that the combination of HA with collagen more effectively promotes new bone formation (Liu et al., 2016b; de Melo Pereira et al., 2020). This effect is likely due to the inherent osteogenic potential of HA, providing both osteoconductivity and stimulating the expression of osteogenic-related factors (Chai et al., 2011; Huanhuan et al., 2013). Additionally, the characteristics of I-EMC, including the slow release of calcium and phosphate ions, directly influence the cell's osteogenic differentiation process (Pamela et al., 2010; Chai et al., 2011; Huanhuan et al., 2013; Danoux et al., 2015). These findings further underscore the potential and promising applications of I-EMC in bone tissue engineering and bone graft materials research.

The physicochemical properties of materials play a critical role in determining their biological characteristics. In mineralized collagen, the phase of the mineral substance and its manner of integration with collagen fibers influence the response of BMSCs (Liu et al., 2016c; Santhakumar et al., 2021). Compared to EMC, both hierarchical IMC and IMC exhibit a higher Young's modulus. Furthermore, they significantly enhance the adhesion, proliferation, and differentiation capabilities of osteogenic-related cells, promoting the expression of osteogenic-associated genes, new bone formation, and the repair of bone fractures (Liu et al., 2013; Liu et al., 2014; Wang Y.-F. et al., 2016; Jin et al., 2019). I-EMC, prepared under various conditions, exhibits distinct microstructures and material compositions. Surface morphology and roughness, influenced by hydroxyapatite, significantly impact cell responses and new bone formation (Liu et al., 2014; Roman et al., 2014; Costa-Rodrigues et al., 2016). Notably, the 1X-2D and 1X-4D samples show significantly higher ALP activity and mineral generation compared to the 2X-2D and 2X-4D samples. This difference can be attributed to the relatively smooth and uniform surface structure of the 1X-2D and 1X-4D samples, along with the presence of nano-sized apatites (Fukui et al., 2008). Additionally, the deposition of larger calcium phosphate particles on the surfaces of 2X-2D and 2X-4D samples significantly increased the surface roughness. Previous *in vivo* studies have suggested that a rough surface facilitates the polarization of monocytes toward M1, while a relatively smooth surface promotes M2 polarization (Sun et al., 2016; Jin et al., 2019). M1 polarization may release certain cytokines inhibiting the osteogenic process, whereas M2 polarization secretes cytokines that promote osteogenic differentiation, fostering bone formation. Furthermore, studies suggest that the composite material exhibits optimal osteogenic differentiation and bone tissue regeneration effects only when the collagen-to-hydroxyapatite ratio is appropriate (Roman et al., 2014; Wang Y. et al., 2016; Ma et al., 2018). Based on thermal gravimetric analysis, we found that the 2X-4D samples have higher mineral content, which might not be the optimal mineral-to-collagen ratio. Similar trends were observed in the expressions of OCN and RUNX-2.

Furthermore, when comparing the 1X-2D and 1X-4D samples, we found that the 1X-4D sample exhibited significantly enhanced osteogenic performance, especially in terms of ALP activity and RUNX-2 expression ($p < 0.05$). We posit that the enhanced osteogenic performance of 1X-4D is likely tied to its optimal mineral-to-collagen ratio. Drawing upon our past investigations, especially insights from EDS mapping images, we identified that 1X-4D displays a more uniform distribution of hydroxyapatite crystals compared to 1X-2D. Such uniformity likely plays a significant role in the enhanced osteogenic efficacy of 1X-4D. This indicates that extending the mineralization time during the preparation of I-EMC with 1× mineralization solution can enhance its osteogenic potential. However, in comparison, the 2X-4D did not show stronger osteogenic activity than 2X-2D. This is likely due to the rough surface structure and uneven mineralization of I-EMC prepared with the 2× mineralization solution. Additionally, the presence of a large amount of mineral outside the fibers and a decrease in the stabilizing effect of PAA may prevent a significant increase in nano-sized apatite within the fibers, even with extended mineralization time. These findings suggest that the mineralization time and concentration of mineralization solution play a crucial role in optimizing the osteogenic performance of I-EMC materials.

Mineralized collagen is a high-quality material for bone repair, with numerous products available on the market. Some have received regulatory approval and are in commercial production. In clinical practice, especially in the fields of orthopedics, dentistry, and neurosurgery, artificial bone has achieved significant success (Qiu et al., 2015). Mineralized collagen has demonstrated reliable effectiveness and fewer complications in clinical applications such as open reduction and internal fixation of bone fractures, grafting after benign bone tumor resection, total hip arthroplasty, and internal fixation fusion procedures (Huang et al., 2015; Ghate and Cui, 2017; Pan et al., 2018; Gao et al., 2020). However, current mineralized collagen protein products are primarily prepared using traditional methods, such as collagen mixture or co-precipitation with hydroxyapatite (Niu et al., 2023), emphasizing compositional biomimicry. In contrast, I-EMC, with both compositional and structural biomimicry, demonstrates superior mechanical performance and biological activity. Nonetheless, there is still a need for further exploration and research in clinical applications. This study found that increasing the concentration of the mineralization solution can shorten the mineralization time and achieve intrafiber mineralization, facilitating the commercial production and clinical application of mineralized collagen products with dual biomimicry. Additionally, the research revealed that the osteogenic performance of mineralized collagen is not only related to its degree of mineralization but also closely associated with its surface nanostructure. These findings provide crucial insights for advancing the development of mineralized collagen products with enhanced biomimetic and osteogenic properties.

4 Conclusion

In this research, the primary objective was to examine how specific parameters during collagen mineralization influence the material's microstructure, its physicochemical properties, and the creation of an essential osteogenic microenvironment. The role of microstructure in cell behavior was explored, aiming to define the "condition-structure-performance" relationship of I-EMC. The findings highlighted the optimal mineralization conditions for achieving the best bone-forming performance. While the study offers valuable insights, it also has limitations. Specifically, a bone repair model was not used when assessing the osteogenic potential of I-EMC, an area we aim to address in our future research. These findings will drive the commercial production and clinical application of mineralized collagen products with dual biomimicry. This lays the foundation for the development of the next-generation of bone substitute materials based on mineralized collagen protein. It provides robust support for the advancement of bone tissue engineering and transplant materials, highlighting a promising future in the treatment of various extensive bone defects.

Data availability statement

The original contributions presented in the study are included in the article/Supplementary Material, further inquiries can be directed to the corresponding author.

Ethics statement

The animal study was approved by the Animal Protection and Use Ethics Committee of Jilin University. The study was conducted in accordance with the local legislation and institutional requirements.

Author contributions

JW: Conceptualization, Funding acquisition, Methodology, Supervision, Writing–review and editing. XZ: Data curation, Formal Analysis, Methodology, Writing–original draft, Writing–review and editing. HB: Methodology, Supervision, Writing–review and editing. JZ: Software, Validation, Data curation, Writing–original draft. HL: Supervision, Validation, Writing–review and editing. ZW: Investigation, Supervision, Formal Analysis, Writing–review and editing. HW: Data curation, Writing–review and editing. JL: Data curation, Software, Writing–review and editing. YW: Conceptualization, Investigation, Supervision, Validation, Data curation, Writing–review and editing.

Funding

The author(s) declare financial support was received for the research, authorship, and/or publication of this article. This work was financially supported by the National Natural Science Foundation of China (Grant Nos. 82001971, 82102358, U23A20523, and 82202698); Scientific Development Program of Jilin Province (Grant Nos. 20200403088SF, 20220204117YY, YDZJ202201ZYTS086, 20200404202YY, and 20200802008GH); Program of Jilin Provincial Health Department (Grant No. 2020SC2T064 and 2020SC2T065); Project of "Medical + X" Interdisciplinary Innovation Team of Norman Bethune Health Science Center of Jilin University (Grant No. 2022JBGS06); China Postdoctoral Science Foundation (Grant No. 2021M701384); Bethune Plan of Jilin University (Grant No. 2022B27, 2022B03).

Conflict of interest

The authors declare that the research was conducted in the absence of any commercial or financial relationships that could be construed as a potential conflict of interest.

Publisher's note

References

Agarwal, R., and García, A. J. (2015). Biomaterial strategies for engineering implants for enhanced osseointegration and bone repair. *Adv. Drug Deliv. Rev.* 94, 53–62. doi:10.1016/j.addr.2015.03.013

Cerutti, C., and Ridley, A. J. (2017). Endothelial cell-cell adhesion and signaling. *Exp. Cell Res.* 358, 31–38. doi:10.1016/j.yexcr.2017.06.003

Chai, Y. C., Roberts, S. J., Schrooten, J., and Luyten, F. P. (2011). Probing the osteoinductive effect of calcium phosphate by using an *in vitro* biomimetic model. *Tissue Eng. Part A* 17, 1083–1097. doi:10.1089/ten.tea.2010.0160

Chen, L., Zeng, Z., and Li, W. (2023). Poly(acrylic acid)-assisted intrafibrillar mineralization of type I collagen: a review. *Macromol. Rapid Commun.* 44, e2200827. doi:10.1002/marc.202200827

Chen, Z., Luo, Q., Lin, C., Kuang, D., and Song, G. (2016). Simulated microgravity inhibits osteogenic differentiation of mesenchymal stem cells via depolymerizing F-actin to impede TAZ nuclear translocation. *Sci. Rep.* 6, 30322. doi:10.1038/srep30322

Costa-Rodrigues, J., Carmo, S., Perpétuo, I. P., Monteiro, F. J., and Fernandes, M. H. (2016). Osteoclastogenic differentiation of human precursor cells over micro- and nanostructured hydroxyapatite topography. *Biochimica Biophysica Acta* 1860, 825–835. doi:10.1016/j.bbagen.2016.01.014

Danoux, C. B. S. S., Bassett, D. C., Othman, Z., Rodrigues, A. I., Reis, R. L., Barralet, J. E., et al. (2015). Elucidating the individual effects of calcium and phosphate ions on hMSCs by using composite materials. *Acta Biomater.* 17, 1–15. doi:10.1016/j.actbio.2015.02.003

de Melo Pereira, D., Eischen-Loges, M., Birgani, Z. T., and Habibovic, P. (2020). Proliferation and osteogenic differentiation of hMSCs on biomineralized collagen. *Front. Bioeng. Biotechnol.* 8, 554565. doi:10.3389/fbioe.2020.554565

Dhand, C., Ong, S. T., Dwivedi, N., Diaz, S. M., Venugopal, J. R., Navaneethan, B., et al. (2016). Bio-inspired *in situ* crosslinking and mineralization of electrospun collagen scaffolds for bone tissue engineering. *Biomaterials* 104, 323–338. doi:10.1016/j.biomaterials.2016.07.007

dos Remedios, C. G., Chhabra, D., Kekic, M., Dedova, I. V., Tsubakihara, M., Berry, D. A., et al. (2003). Actin binding proteins: regulation of cytoskeletal microfilaments. *Physiol. Rev.* 83, 433–473. doi:10.1152/physrev.00026.2002

Du, T., Niu, X., Li, Z., Li, P., Feng, Q., and Fan, Y. (2018). Crosslinking induces high mineralization of apatite minerals on collagen fibers. *Int. J. Biol. Macromol.* 113, 450–457. doi:10.1016/j.ijbiomac.2018.02.136

Du, T., Niu, Y., Liu, Y., Yang, H., Qiao, A., and Niu, X. (2022). Physical and chemical characterization of biomineralized collagen with different microstructures. *J. Funct. Biomater.* 13, 57. doi:10.3390/jfb13020057

Fukui, N., Sato, T., Kuboki, Y., and Aoki, H. (2008). Bone tissue reaction of nano-hydroxyapatite/collagen composite at the early stage of implantation. *Bio-medical Mater. Eng.* 18, 25–33.

Gao, C., Qiu, Z. Y., Hou, J. W., Tian, W., Kou, J. M., and Wang, X. (2020). Clinical observation of mineralized collagen bone grafting after curettage of benign bone tumors. *Regen. Biomater.* 7, 567–575. doi:10.1093/rb/rbaa031

Ghate, N. S., and Cui, H. (2017). Mineralized collagen artificial bone repair material products used for fusing the podarthral joints with internal fixation-a case report. *Regen. Biomater.* 4, 295–298. doi:10.1093/rb/rbx015

Höhling, H. J., Barckhaus, R. H., Krefting, E. R., Althoff, J., and Quint, P. (1990). *Collagen mineralization: aspects of the structural relationship between collagen and the apatitic crystallites*. Springer US.

Hu, C., Zilm, M., and Wei, M. (2016). Fabrication of intrafibrillar and extrafibrillar mineralized collagen/apatite scaffolds with a hierarchical structure. *J. Biomed. Mater. Res. Part A* 104, 1153–1161. doi:10.1002/jbm.a.35649

Huang, C., Qin, L., Yan, W., Weng, X., and Huang, X. (2015). Clinical evaluation following the use of mineralized collagen graft for bone defects in revision total hip arthroplasty. *Regen. Biomater.* 2, 245–249. doi:10.1093/rb/rbv022

Huang, R. L., Kobayashi, E., Liu, K., and Li, Q. (2016). Bone graft prefabrication following the *in vivo* bioreactor principle. *EBioMedicine* 12, 43–54. doi:10.1016/j.ebiom.2016.09.016

Huanhuan, L., Peng, H., Wu, Y., Zhang, C., Cai, Y., Xu, G., et al. (2013). The promotion of bone regeneration by nanofibrous hydroxyapatite/chitosan scaffolds by effects on integrin-BMP/Smad signaling pathway in BMSCs. *Biomaterials* 34, 4404–4417. doi:10.1016/j.biomaterials.2013.02.048

Jee, S.-S., Thula, T. T., and Gower, L. B. (2010). Development of bone-like composites via the polymer-induced liquid-precursor (PILP) process. Part 1: influence of polymer molecular weight. *Acta Biomater.* 6, 3676–3686. doi:10.1016/j.actbio.2010.03.036

Jin, S.-S., He, D.-Q., Luo, D., Wang, Y., Yu, M., Guan, B., et al. (2019). A biomimetic hierarchical nanointerface orchestrates macrophage polarization and mesenchymal stem cell recruitment to promote endogenous bone regeneration. *Acs Nano* 13, 6581–6595. doi:10.1021/acsnano.9b00489

Kikuchi, M., Matsumoto, H. N., Yamada, T., Koyama, Y., Takakuda, K., and Tanaka, J. (2004). Glutaraldehyde cross-linked hydroxyapatite/collagen self-organized nanocomposites. *Biomaterials* 25, 63–69. doi:10.1016/s0142-9612(03)00472-1

Kim, J. W., Han, Y. S., Lee, H. M., Kim, J. K., and Kim, Y. J. (2021). Effect of morphological characteristics and biomineralization of 3D-printed gelatin/hyaluronic acid/hydroxyapatite composite scaffolds on bone tissue regeneration. *Int. J. Mol. Sci.* 22, 6794. doi:10.3390/ijms22136794

Li, D., Zhang, K., Shi, C., Liu, L., Yan, G., Liu, C., et al. (2018). Small molecules modified biomimetic gelatin/hydroxyapatite nanofibers constructing an ideal osteogenic microenvironment with significantly enhanced cranial bone formation. *Int. J. Nanomedicine* 13, 7167–7181. doi:10.2147/ijn.s174553

Li, Y., Thula, T. T., Jee, S., Perkins, S. L., Aparicio, C., Douglas, E. P., et al. (2012). Biomimetic mineralization of woven bone-like nanocomposites: role of collagen cross-links. *Biomacromolecules* 13, 49–59. doi:10.1021/bm201070g

Liu, S., Sun, Y., Fu, Y., Chang, D., Fu, C., Wang, G., et al. (2016a). Bioinspired collagen-apatite nanocomposites for bone regeneration. *J. Endod.* 42, 1226–1232. doi:10.1016/j.joen.2016.04.027

Liu, Y., Kim, Y.-K., Dai, L., Li, N., Khan, S. O., Pashley, D. H., et al. (2011). Hierarchical and non-hierarchical mineralisation of collagen. *Biomaterials* 32, 1291–1300. doi:10.1016/j.biomaterials.2010.10.018

Liu, Y., Liu, S., Luo, D., Xue, Z., Yang, X., Cu, L., et al. (2016b). Hierarchically staggered nanostructure of mineralized collagen as a bone-grafting scaffold. *Adv. Mater.* 28, 8740–8748. doi:10.1002/adma.201602628

Liu, Y., Luo, D., Kou, X.-X., Wang, X.-D., Tay, F. R., Sha, Y.-L., et al. (2013). Hierarchical intrafibrillar nanocarbonated apatite assembly improves the nanomechanics and cytocompatibility of mineralized collagen. *Adv. Funct. Mater.* 23, 1404–1411. doi:10.1002/adfm.201201611

Liu, Y., Luo, D., Liu, S., Fu, Y., Kou, X., Wang, X., et al. (2014). Effect of nanostructure of mineralized collagen scaffolds on their physical properties and osteogenic potential. *J. Biomed. Nanotechnol.* 10, 1049–1060. doi:10.1166/jbn.2014.1794

Liu, Y., Luo, D., and Wang, T. (2016c). Hierarchical structures of bone and bioinspired bone tissue engineering. *Small (Weinheim der Bergstrasse, Ger.* 12, 4611–4632. doi:10.1002/smll.201600626

Ma, L., Wang, X., Zhao, N., Zhu, Y., Qiu, Z., Li, Q., et al. (2018). Integrating 3D printing and biomimetic mineralization for personalized enhanced osteogenesis, angiogenesis, and osteointegration. *Acs Appl. Mater. Interfaces* 10, 42146–42154. doi:10.1021/acsami.8b17495

Niu, Y., Du, T., and Liu, Y. (2023). Biomechanical characteristics and analysis approaches of bone and bone substitute materials. *J. Funct. Biomater.* 14, 212. doi:10.3390/jfb14040212

Olszta, M. J., Douglas, E. P., and Gower, L. B. (2003). Scanning electron microscopic analysis of the mineralization of type I collagen via a polymer-induced liquid-precursor (PILP) process. *Calcif. Tissue Int.* 72, 583–591. doi:10.1007/s00223-002-1032-7

Oosterlaken, B. M., Vena, M. P., and de With, G. (2021). *In vitro* mineralization of collagen. *Adv. Mater.* 33, e2004418. doi:10.1002/adma.202004418

Pamela, H., David, C., Charles, J. B., Doillon, C., McKee, M. D., and Barralet, J. E. (2010). Collagen biomineralization *in vivo* by sustained release of inorganic phosphate ions. *Adv. Mater.* 22, 1858–1862. doi:10.1002/adma.200902778

Pan, Y. X., Yang, G. G., Li, Z. W., Shi, Z. M., and Sun, Z. D. (2018). Clinical observation of biomimetic mineralized collagen artificial bone putty for bone reconstruction of calcaneus fracture. *Regen. Biomater.* 5, 61–67. doi:10.1093/rb/rbx033

Perrier, A., Dumas, V., Linossier, M. T., Fournier, C., Jurdic, P., Rattner, A., et al. (2010). Apatite content of collagen materials dose-dependently increases pre-osteoblastic cell deposition of a cement line-like matrix. *Bone* 47, 23–33. doi:10.1016/j.bone.2010.03.010

Pollard, T. D., and Cooper, J. A. (2009). Actin, a central player in cell shape and movement. *Science* 326, 1208–1212. doi:10.1126/science.1175862

Qi, Y., Ye, Z., Fok, A., Holmes, B. N., Espanol, M., Ginebra, M. P., et al. (2018). Effects of molecular weight and concentration of poly(acrylic acid) on biomimetic mineralization of collagen. *ACS Biomater. Sci. Eng.* 4, 2758–2766. doi:10.1021/acsbiomaterials.8b00512

Qiu, Z.-Y., Cui, Y., Tao, C.-S., Zhang, Z.-Q., Tang, P.-F., Mao, K.-Y., et al. (2015). Mineralized collagen: rationale, current status, and clinical applications. *Mater. (Basel, Switz.* 8, 4733–4750. doi:10.3390/ma8084733

Reznikov, N., Shahar, R., and Weiner, S. (2014a). Bone hierarchical structure in three dimensions. *Acta Biomater.* 10, 3815–3826. doi:10.1016/j.actbio.2014.05.024

Reznikov, N., Shahar, R., and Weiner, S. (2014b). Three-dimensional structure of human lamellar bone: the presence of two different materials and new insights into the hierarchical organization. *Bone* 59, 93–104. doi:10.1016/j.bone.2013.10.023

Roman, S. M., Surmeneva, M. A., and Ivanova, A. A. (2014). Significance of calcium phosphate coatings for the enhancement of new bone osteogenesis--a review. *Acta Biomater.* 10, 557–579. doi:10.1016/j.actbio.2013.10.036

Santhakumar, S., Oyane, A., Nakamura, M., Yoshino, Y., Alruwaili, M. K., and Miyaji, H. (2021). Bone tissue regeneration by collagen scaffolds with different calcium phosphate coatings: amorphous calcium phosphate and low-crystalline apatite. *Materials* 14, 5860. doi:10.3390/ma14195860

Sun, Y., Liu, S., Fu, Y., Kou, X.-X., He, D.-Q., Wang, G.-N., et al. (2016). Mineralized collagen regulates macrophage polarization during bone regeneration. *J. Biomed. Nanotechnol.* 12, 2029–2040. doi:10.1166/jbn.2016.2296

Thrivikraman, G., Athirasala, A., Gordon, R., Zhang, L., Bergan, R., Keene, D. R., et al. (2019). Rapid fabrication of vascularized and innervated cell-laden bone models with biomimetic intrafibrillar collagen mineralization. *Nat. Commun.* 10, 3520. doi:10.1038/s41467-019-11455-8

Wang, J., Qu, Y., Chen, C., Sun, J., Pan, H., Shao, C., et al. (2019). Fabrication of collagen membranes with different intrafibrillar mineralization degree as a potential use for GBR. *Mater. Sci. Eng. C, Mater. Biol. Appl.* 104, 109959. doi:10.1016/j.msec.2019.109959

Wang, Y., Van Manh, N., Wang, H., Zhong, X., Zhang, X., and Li, C. (2016b). Synergistic intrafibrillar/extrafibrillar mineralization of collagen scaffolds based on a biomimetic strategy to promote the regeneration of bone defects. *Int. J. nanomedicine* 11, 2053–2067. doi:10.2147/ijn.s102844

Wang, Y.-F., Wang, C.-Y., Wan, P., Wang, S.-G., and Wang, X.-M. (2016a). Comparison of bone regeneration in alveolar bone of dogs on mineralized collagen grafts with two composition ratios of nano-hydroxyapatite and collagen. *Regen. Biomater.* 3, 33–40. doi:10.1093/rb/rbv025

Weisgerber, D. W., Caliari, S. R., and Harley, B. A. C. (2015). Mineralized collagen scaffolds induce hMSC osteogenesis and matrix remodeling. *Biomaterials Sci.* 3, 533–542. doi:10.1039/c4bm00397g

Wu, J., Chen, T., Wang, Z., Chen, X., Qu, S., Weng, J., et al. (2020). Joint construction of micro-vibration stimulation and BCP scaffolds for enhanced bioactivity and self-adaptability tissue engineered bone grafts. *J. Mater Chem. B* 8, 4278–4288. doi:10.1039/d0tb00223b

Xia, Z., Yu, X., Jiang, X., Brody, H. D., Rowe, D. W., and Wei, M. (2013). Fabrication and characterization of biomimetic collagen-apatite scaffolds with tunable structures for bone tissue engineering. *Acta Biomater.* 9, 7308–7319. doi:10.1016/j.actbio.2013.03.038

Xiao, Q., Zhang, Y., Qi, X., Chen, Y., Sheng, R., Xu, R., et al. (2020). AFF4 regulates osteogenic differentiation of human dental follicle cells. *Int. J. Oral Sci.* 12, 20. doi:10.1038/s41368-020-0083-9

Xu, S.-J., Qiu, Z.-Y., Wu, J.-J., Kong, X.-D., Weng, X.-S., Cui, F.-Z., et al. (2016). Osteogenic differentiation gene expression profiling of hMSCs on hydroxyapatite and mineralized collagen. *Tissue Eng. Part A* 22, 170–181. doi:10.1089/ten.tea.2015.0237

Xuan, Y., Li, L., Ma, M., Cao, J., and Zhang, Z. (2021). Hierarchical intrafibrillarly mineralized collagen membrane promotes guided bone regeneration and regulates M2 macrophage polarization. *Front. Bioeng. Biotechnol.* 9, 781268. doi:10.3389/fbioe.2021.781268

Ye, B., Luo, X., Li, Z., Zhuang, C., Li, L., Lu, L., et al. (2016). Rapid biomimetic mineralization of collagen fibrils and combining with human umbilical cord mesenchymal stem cells for bone defects healing. *Mater. Sci. Eng. C-Materials Biol. Appl.* 68, 43–51. doi:10.1016/j.msec.2016.05.104

Ye, Z., Zhu, X., Mutreja, I., Boda, S. K., Fischer, N. G., Zhang, A., et al. (2021). Biomimetic mineralized hybrid scaffolds with antimicrobial peptides. *Bioact. Mater.* 6, 2250–2260. doi:10.1016/j.bioactmat.2020.12.029

Yu, L., Rowe, D. W., Perera, I. P., Zhang, J., Suib, S. L., Xin, X., et al. (2020). Intrafibrillar mineralized collagen-hydroxyapatite-based scaffolds for bone regeneration. *Acs Appl. Mater. Interfaces* 12, 18235–18249. doi:10.1021/acsami.0c00275

Yu, L., and Wei, M. (2021). Biomineralization of collagen-based materials for hard tissue repair. *Int. J. Mol. Sci.* 22, 944. doi:10.3390/ijms22020944

Zandi, N., Sani, E. S., Mostafavi, E., Ibrahim, D. M., Saleh, B., Shokrgozar, M. A., et al. (2021). Nanoengineered shear-thinning and bioprintable hydrogel as a versatile platform for biomedical applications. *Biomaterials* 267, 120476. doi:10.1016/j.biomaterials.2020.120476

Zhang, Z., Li, Z., Zhang, C., Liu, J., Bai, Y., Li, S., et al. (2018). Biomimetic intrafibrillar mineralized collagen promotes bone regeneration via activation of the Wnt signaling pathway. *Int. J. nanomedicine* 13, 7503–7516. doi:10.2147/ijn.s172164

Zhang, Z., Zhang, S., Li, Z., Li, S., Liu, J., and Zhang, C. (2019). Osseointegration effect of biomimetic intrafibrillarly mineralized collagen applied simultaneously with titanium implant: a pilot *in vivo* study. *Clin. Oral Implants Res.* 30, 637–648. doi:10.1111/clr.13449

Zhao, Y., Li, Z., Jiang, Y., Liu, H., Feng, Y., Wang, Z., et al. (2020). Bioinspired mineral hydrogels as nanocomposite scaffolds for the promotion of osteogenic marker expression and the induction of bone regeneration in osteoporosis. *Acta Biomater.* 113, 614–626. doi:10.1016/j.actbio.2020.06.024

Zhou, Q., Ren, X., Bischoff, D., Weisgerber, D. W., Yamaguchi, D. T., Miller, T. A., et al. (2017). Nonmineralized and mineralized collagen scaffolds induce differential osteogenic signaling pathways in human mesenchymal stem cells. *Adv. Healthc. Mater.* 6. doi:10.1002/adhm.201700641

Zhu, X., Wang, C., Bai, H., Zhang, J., Wang, Z., Li, Z., et al. (2023). Functionalization of biomimetic mineralized collagen for bone tissue engineering. *Mater. Today Bio* 20, 100660. doi:10.1016/j.mtbio.2023.100660

frontiers | Frontiers in Bioengineering and Biotechnology

TYPE Original Research
PUBLISHED 10 January 2024
DOI 10.3389/fbioe.2023.1334072

EDITED BY
Zuhao Li,
Shanghai Jiao Tong University, China

REVIEWED BY
Kui Xu,
Anhui University of Chinese Medicine, China
Dankai Wu,
Second Affiliated Hospital of Jilin University, China
Jingwei Zhang,
Shanghai Jiao Tong University, China

*CORRESPONDENCE
Jincheng Wang,
✉ jinchengwang@hotmail.com
Zhihui Qian,
✉ zhqian@jlu.edu.cn

RECEIVED 06 November 2023
ACCEPTED 20 December 2023
PUBLISHED 10 January 2024

CITATION
Lu Y, Wang X, Chen H, Li X, Liu H, Wang J and Qian Z (2024), "Metal-bone" scaffold for accelerated peri-implant endosseous healing.
Front. Bioeng. Biotechnol. 11:1334072.
doi: 10.3389/fbioe.2023.1334072

"Metal-bone" scaffold for accelerated peri-implant endosseous healing

Yue Lu[1], Xianggang Wang[2,3], Hao Chen[2,3], Xin Li[2,3], He Liu[2,3], Jincheng Wang[2,3]* and Zhihui Qian[1]*

[1]Key Laboratory of Bionic Engineering, Ministry of Education, Jilin University, Changchun, China, [2]Orthopaedic Medical Center, The Second Hospital of Jilin University, Changchun, China, [3]Orthopaedic Research Institute of Jilin Province, Changchun, China

Restoring bone defects caused by conditions such as tumors, trauma, or inflammation is a significant clinical challenge. Currently, there is a need for the development of bone tissue engineering scaffolds that meet clinical standards to promote bone regeneration in these defects. In this study, we combined the porous Ti6Al4V scaffold in bone tissue engineering with advanced bone grafting techniques to create a novel "metal-bone" scaffold for enhanced bone regeneration. Utilizing 3D printing technology, we fabricated a porous Ti6Al4V scaffold with an average pore size of 789 ± 22.69 μm. The characterization and biocompatibility of the scaffold were validated through *in vitro* experiments. Subsequently, the scaffold was implanted into the distal femurs of experimental animals, removed after 3 months, and transformed into a "metal-bone" scaffold. When this "metal-bone" scaffold was re-implanted into bone defects in the animals, the results demonstrated that, in comparison to a plain porous Ti6Al4V scaffold, the scaffold containing bone tissue achieved accelerated early-stage bone regeneration. The experimental group exhibited more bone tissue generation in the early stages at the defect site, resulting in superior bone integration. In conclusion, the "metal-bone" scaffold, containing bone tissue, proves to be an effective bone-promoting scaffold with promising clinical applications.

KEYWORDS

metal-bone scaffold, Ti6Al4V, 3D-printing, osseointegration, porous scaffolds

1 Introduction

Bone defects often result from various causes such as trauma, tumors, inflammation, and more. Smaller defects can typically heal on their own, but larger bone defects often cannot undergo self-repair (Henkel et al., 2021). In clinical practice, autologous bone transplantation is considered as the gold standard for treating these challenging non-healing bone defects. However, due to the difficulty in sourcing autologous bone, this approach can lead to secondary injuries. Allogeneic bone grafts face issues related to immune rejection (Nayak et al., 2023). To promote bone regeneration at the site of bone defects, bone tissue engineering has emerged as a highly promising technique. Bone tissue engineering generally involves a scaffold, cells, and bioactive substances. Given the specific biological requirements of bone, the scaffold must possess adequate mechanical strength, excellent biocompatibility, and osteoconductivity (Wang et al., 2020). Hence, Ti6Al4V scaffolds have found wide application in bone tissue engineering. Nevertheless, since pure Ti6Al4V scaffolds can merely fill defects and have limited potential to enhance bone regeneration, it is essential to incorporate osteoinductive components into the scaffold (Li et al., 2023). Considering that the gold standard for bone defect treatment in clinical practice is bone transplantation, the development of a novel "metal-bone" scaffold that combines bone tissue with a metal scaffold holds the potential to significantly enhance bone regeneration outcomes.

Titanium alloy, Ti6Al4V, is a commonly used biomaterial in orthopedic surgery. Titanium alloys are favored due to their excellent biocompatibility, osseointegration properties, higher strength, and corrosion resistance compared to pure titanium (Gu et al., 2022; Liu et al., 2022). However, as a type of alloy, Ti6Al4V possesses a significantly higher strength than human bone tissue. Consequently, when Ti6Al4V implants are placed inside the body, stress shielding phenomena occur, leading to stress concentration and hindering optimal bone healing (Naghavi et al., 2023b). To address this issue, the current consensus suggests the use of porous Ti6Al4V scaffolds, effectively reducing the relative strength of the scaffold and mitigating stress shielding problems (Abbasi et al., 2020).

The preparation of porous Ti6Al4V scaffolds commonly involves the use of 3D printing technology, a method prevalent in current research (Subasi et al., 2023). 3D printing, also known as additive manufacturing, is a technology that fabricates three-dimensional objects layer by layer based on three-dimensional models. Utilizing 3D printing technology, it is possible to precisely and conveniently manufacture Ti6Al4V scaffolds with specific porous structures (Altunbek et al., 2023).

In previous research, extensive studies have been conducted on the optimal pore size of porous Ti6Al4V scaffolds for promoting osteogenesis (Zhang et al., 2022). Research has shown that pores that are too small (<400 μm) can lead to excessive scaffold strength, severe stress shielding, and hinder the ingrowth of new bone tissue (Chen et al., 2020). Conversely, pores that are too large (>1,000 μm) can result in insufficient scaffold strength, providing ineffective mechanical support, and impeding bone tissue ingrowth, ultimately causing loosening of the implant at the bone-tissue interface (Wang et al., 2021a). Some research findings have suggested that a pore size around 600 μm is considered optimal (Wang et al., 2017). However, for titanium alloy, strength is a crucial consideration as well. Smaller pores might lead to excessive strength and serious stress-shielding effects, while larger pores can mitigate stress-shielding effects (Zeng et al., 2022; Naghavi et al., 2023a). Taking into account both scaffold strength and pore size, in this study, 3D-Printed Ti6Al4V porous scaffolds were designed with a pore size of 800 μm, consistent with the previously established optimal pore size from experimental research (Wang et al., 2021b). The porosity was set at 70%, aligning with the porosity found in physiological bone trabeculae, ensuring the best osteogenic outcomes (Cui et al., 2021).

In this study, a novel "metal-bone" scaffold was developed for the treatment of bone defects. Initially, a porous Ti6Al4V scaffold was 3D printed. Subsequently, the scaffold was implanted into the bone defect site in experimental animals. After a sufficient amount of bone tissue had grown inside the scaffold, the scaffold was removed from the bone defect site, resulting in the formation of the "metal-bone" scaffold. This "metal-bone" scaffold was then implanted into the bone defect and compared with a control group using a porous Ti6Al4V scaffold without bone tissue, to evaluate the ultimate effects on bone regeneration and integration, as illustrated in Scheme 1.

2 Materials and methods

2.1 Materials

The Ti6Al4V powder was obtained from AK Medical Co., Ltd. (Beijing, China). The low Glucose Dulbecco's Modified Eagle's Medium (DMEM), streptomycin–penicillin dual Antibiotics, and fetal bovine serum (FBS) were purchased from Gibco (Grand Island, NY, United States). Pareformaldehyde and Phosphate buffer (PBS) were obtained from Solarbio (Beijing, China). The Live-Dead staining kit was obtained from Bioss (Beijing, China). The Hematoxylin and Eosin (H&E) stain, Masson's trichrome stain, and Van Gieson (VG) stain were purchased from Thermo Fisher Scientific (Shanghai, China). Rhodamine phalloidin and 4′,6-diamidino-2-phenylindole (DAPI) were obtained from Thermo Fisher Scientific (Shanghai, China). The double-distilled water used in this study was obtained from a Milli-QA10 filtration system (Milipore, Billerican, MA, United States). BMP-2 and OCN antibodies used in immunofluorescence were purchased from Abcam (Cambridge, United Kingdom).

2.2 Preparation and characterization of the 3D-printed porous Ti6Al4V scaffolds

The preparation method for the 3D-Printed porous Ti6Al4V scaffolds utilized in this study is consistent with the description provided in previously published articles (Bai et al., 2020). In brief, we initiated the process by creating a three-dimensional cylindrical model with a specified diameter of 5 mm and a height of 10 mm. Key parameters were set to include a pore size of 800 μm, a porosity of 70%, and a strut diameter of 300 μm. The material employed for printing the scaffolds was biomedical-grade Ti6Al4V powder, and the 3D printing equipment used was an Electron Beam Melting (EBM) printer (Q10, Arcam, Sweden). The scaffolds, characterized by a uniform pore structure, were printed layer by layer. Following the printing process, all scaffolds underwent ultrasonic cleaning to remove any unadhered Ti6Al4V powder from their surfaces. Subsequently, they were subjected to repeated cleaning with acetone, alcohol, and deionized water. Prior to cell experiments and *in vivo* implantation, the scaffolds were sterilized through high-pressure autoclaving. To validate the fidelity of the final printed scaffolds to the design specifications, post-printing visual inspections of scaffold morphology were conducted. Optical microscopy (Olympus Ⅸ, Japan) was employed to magnify observations, and scanning electron microscopy (SEM, JEOL, Tokyo, Japan) was utilized to scrutinize surface topography. Energy-dispersive X-ray spectroscopy (EDS, Aztec software, Oxford Instruments, Abingdon, United Kingdom) analysis was then performed to qualitatively assess the elemental composition of the material, ensuring the absence of impurities or contamination during the fabrication process.

To assess the surface hydrophilicity of the printed scaffolds, water contact angle measurements were conducted in this study

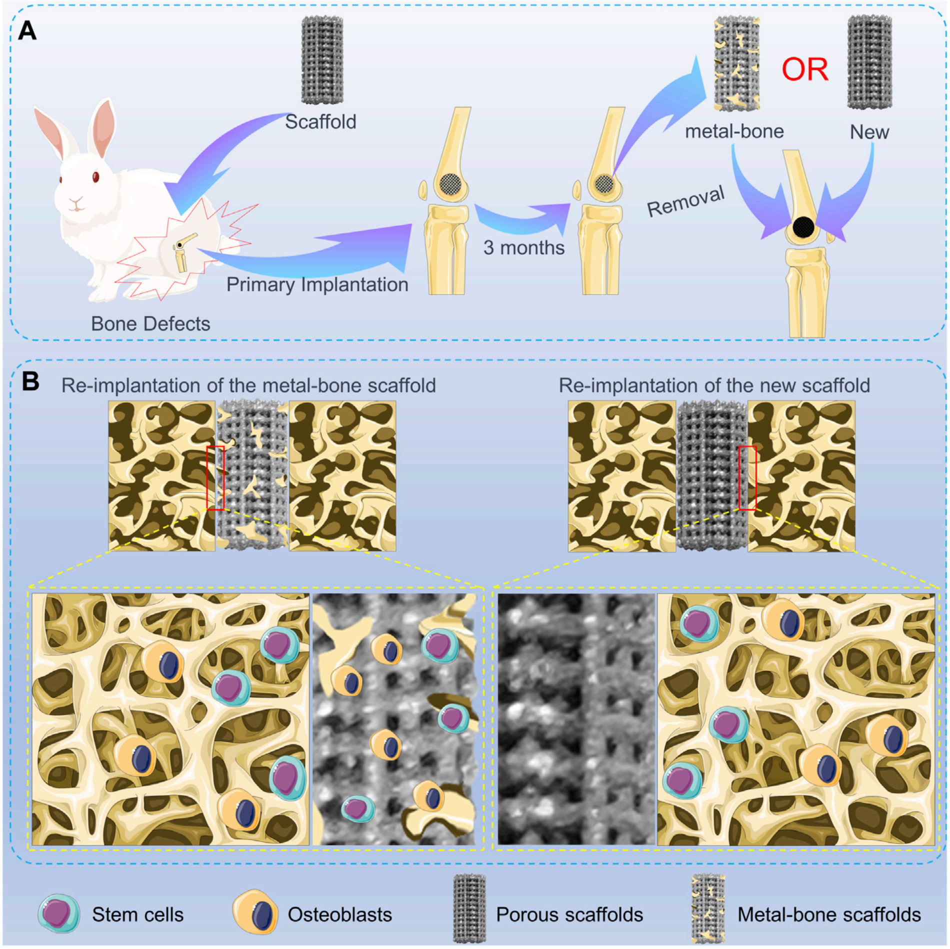

SCHEME 1
Schematic illustration of the metal-bone and new scaffolds in bone defects. **(A)** Animal experiments of metal-bone implants and new implants. **(B)** The interface between two types of implants and surrounding bone tissue.

using a water contact angle goniometer (DM-500, Kyowa Interface Science Co., Ltd.) Initially, the 3D-Printed Ti6Al4V scaffolds to be tested were prepared, ensuring that their surfaces were dry, clean, and free from impurities. A microliter syringe was employed to dispense a droplet of deionized water onto the material surface, and the shape of the water droplet on the material surface was recorded using the goniometer's integrated camera. Subsequently, the water contact angle was measured from the images using ImageJ 1.53c software (National Institutes of Health, Bethesda, MD, United States). Three samples were tested, with each sample subjected to three repeated measurements to obtain a reliable average contact angle value.

2.3 Extraction and cultivation of bone marrow mesenchymal stem cells

The method for extracting bone marrow mesenchymal stem cells (BMSCs) was as follows: New Zealand White rabbits aged 1 week were selected. The long bones of the rabbit's limbs were extracted, and bone marrow was flushed from the long bones using a sterile 1 mL syringe and sterile PBS. The flushed cells were then cultured in low-glucose DMEM medium containing 10% fetal bovine serum and 1% penicillin-streptomycin. The cell culture dishes were placed in a constant temperature incubator for cell cultivation. On the third day of cultivation, the cells in the culture dish underwent partial medium replacement, and subsequently, the medium was changed every 3 days. When the cells reached 80%–90% confluence, they were passaged after digestion with trypsin. In this study, the BMSCs used were all from the third generation or higher of mesenchymal stem cells.

2.4 Live/dead staining

In a 12-well plate, 40,000 BMSCs were seeded in each well. In the control group, only an equivalent number of BMSCs were seeded into the respective wells. In the experimental group, in addition to seeding an equivalent number of cells, sterile and disinfected Ti6Al4V porous scaffolds were placed in the corresponding wells of the plate. The plate was then placed in a constant temperature incubator for 24 h of cultivation, after which a live-dead staining assay was conducted.

Initially, the plate was centrifuged at 3,000 rpm for 2 min, and the culture medium was aspirated. Live staining solution was added, and the plate was returned to the constant temperature incubator for 30 min of staining. After live staining, the wells were washed three times with PBS. Subsequently, dead staining solution was added, and the plate was stained for 5 min. After staining was completed, the wells were again washed three times with PBS. The live-dead staining results were observed under a fluorescence microscope (Olympus IX71, Tokyo, Japan). All staining and observation procedures were conducted under subdued light conditions.

2.5 Immunofluorescence staining of the cell cytoskeleton

To observe the influence of Ti6Al4V porous scaffolds on the cellular morphology of BMSCs, in this study, staining and observation of the BMSCs' cytoskeleton were conducted using Rhodamine-labeled phalloidin staining solution. Initially, 10,000 BMSCs were seeded in each well of a 12-well plate. In the experimental group, Ti6Al4V porous scaffolds were placed in the corresponding wells, while the control group contained cells only. After 3 days, the staining and observation were performed as follows.

First, the culture medium in the wells was aspirated, and fixation was carried out using a 4% paraformaldehyde solution for 10 min. Subsequently, the cells were washed three times with PBS. Then, they were subjected to light-protected staining with Rhodamine-phalloidin staining solution for 30 min. After 30 min, the cells were washed three times with PBS. DAPI staining solution was applied for light-protected staining for 5 min. Following staining, the cells were washed three times with PBS. After the final washing, the staining results were observed using a fluorescence microscope. All procedures involving staining and observation were conducted under subdued light conditions.

2.6 Initial implantation of scaffolds

All animal experimental protocols were approved by the Animal Care and Use Ethics Committee of Jilin University (2022142). Twenty-four adult male New Zealand rabbits were selected for this study. The animals were anesthetized via intravenous injection of 0.5% pentobarbital sodium into the marginal ear vein. The surgical site was selected as the right distal femur for implantation. Prior to surgery, the fur around the knee joint area was shaved using clippers. During the surgical procedure, the rabbits were secured on the operating table. After standard sterilization procedures, a 1–2 cm incision was made on the outer edge of the rabbit's distal femur using a scalpel. Hemostatic forceps were used for blunt dissection of the subcutaneous muscles, ligaments, and blood vessels around the distal femur, exposing the lateral condyle. A specialized orthopedic core drill with an inner diameter of 4 mm and an outer diameter of 5 mm was then used to create a borehole with a depth of 10 mm, resulting in a bone defect matching the size of the printed scaffold precisely.

The bone debris at the defect site was carefully removed and the defect was rinsed with physiological saline. Subsequently, the scaffold was implanted into the distal femur. The incision was closed layer by layer, with absorbable sutures used for suturing muscles, tendons, ligaments, etc., in the inner layer, and non-absorbable sutures for suturing the skin in the outer layer. Postoperatively, penicillin was administered for 3 days, and the animals' condition was observed for 1 week.

2.7 Secondary implantation surgery

After 3 months from the initial implantation surgery, the same anesthesia, shaving, and sterilization procedures were performed on the rabbits. The 24 rabbits were randomly divided into two groups: the control group with the new scaffolds (Con) implanting consisting of 12 rabbits, the experimental group with the "metal-bone" scaffolds (MB) implanting group consisting of 12 rabbits. During the surgery, the Ti6Al4V scaffold from the right hind limb's distal femur was first removed. For the MB group, the removed scaffold, which contained bone tissue, was re-implanted into the same rabbit's opposite hind limb at an equivalent anatomical position in the distal femur. For the control group, after removing the scaffold from the right side, an identical new Ti6Al4V porous scaffold was implanted into the defect site in the other hind limb. Similar to the initial surgery, the incision was closed layer by layer. Postoperatively, penicillin was administered for 3 days to prevent infection, and the rabbits were closely observed for 1 week.

The scaffolds containing bone tissue, taken from the control group, were subjected to Micro-computed tomography (Micro-CT) scans (SkyScan 1076 scanner, Bruker Micro-CT NV, Kontich, Belgium), SEM observation, and mechanical testing. The mechanical testing was conducted using a universal testing machine (H25KS, Hounsfield, United Kingdom), with the scaffolds placed on the sample platform of the testing machine. Compression tests were performed at a rate of 1.0 mm/min until the scaffolds reached their maximum force and maximum deformation. The maximum compressive strength and maximum force that the Ti6Al4V scaffolds with and without bone tissue could withstand were recorded. The mechanical performance differences between the "metal-bone" scaffolds and the new scaffolds were compared.

2.8 Micro-CT analysis

At 6 and 12 weeks post the second implantation surgery, euthanasia of the rabbits was carried out using carbon dioxide asphyxiation. The left femoral scaffold implantation sites were then harvested for evaluation. Micro-CT scans were performed to assess bone regeneration at the implantation sites. A cylindrical region of interest with a diameter of 5 mm and a height of 10 mm was selected for three-dimensional reconstruction and subsequent analysis of bone tissue parameters. Specific analyses included volume/tissue volume ratio (BV/TV, %), trabecular thickness (Tb.Th, mm), trabecular separation (Tb.Sp, mm), and trabecular number (Tb.N, 1/mm).

2.9 Hard sectioning and staining

Following the completion of Micro-CT scanning, the specimens were fixed in 4% formalin solution. Subsequently, the scaffold implantation sites were subjected to hard sectioning and staining using Masson's trichrome staining and Van Gieson (VG) staining. Stained sections were then observed and photographed under an optical microscope.

2.10 H&E, Masson's trichrome, and immunohistochemical staining

After fixation, the specimens were subjected to decalcification using 10% EDTA. Following decalcification, sections were prepared using a microtome and subjected to H&E, Masson's trichrome, and immunohistochemical staining. The specific procedures were consistent with those described in previously published articles for immunohistochemical staining of osteogenic-related genes in the scaffold implantation sites. In brief, bone tissue sections were incubated with BMP-2 and OCN antibodies overnight at 4°C. Subsequently, the samples were washed three times with PBS. The scaffold implantation sites in the sections were then observed and photographed under an optical microscope. The expression intensity of the relevant proteins around the scaffold was quantitatively analyzed using image analysis software ImageJ.

2.11 Push-out tests

A standard mechanical push-out test was conducted to assess the interfacial strength between the scaffold and the surrounding bone tissue in each group. Mechanical push-out tests were performed using a universal testing machine. Initially, the samples were placed on the test platform for the mechanical push-out test, with a displacement rate of 1.0 mm/min. The force applied during the scaffold push-out process was recorded using software, with the endpoint being when the scaffold completely disengaged from the bone. By recording the maximum push-out force during the experiment, the interfacial strength between the scaffold and the surrounding tissue was validated.

2.12 Statistical analysis

All data are presented as the mean ± standard deviation of at least three independent experiments. Statistical analysis was performed using *t*-test followed by *post hoc* multiple comparison tests using SPSS 19.0 software (SPSS Inc., Chicago, Illinois, United States) to determine the minimum significant differences. Statistical significance was considered at $p < 0.05$.

3 Results and discussion

3.1 Characterizations of the 3D-printed porous scaffolds

The final 3D-Printed Ti6Al4V porous scaffold exhibited the characteristics shown in Figures 1A, B. It is evident that the scaffold, matching the model parameters, took the form of a porous cylinder with a diameter of 5 mm and a height of 10 mm. This scaffold's dimensions were entirely consistent with the bone defect size prepared for the subsequent animal experiments. Furthermore, as shown in Figure 1C from the scanning electron microscopy results, during the printing process of the scaffold, it was primarily formed through the fusion of powder particles. The scaffold's surface was filled with Ti6Al4V particles of varying sizes, resulting in a rugged surface structure.

On one hand, this rough surface structure enhances the adhesion of cells to the scaffold, particularly the migration and adhesion of mesenchymal stem cells, thereby promoting the bone formation process (Montero et al., 2020). On the other hand, the uneven surface structure provides a certain degree of fixation, making it more favorable for the scaffold to be firmly secured in the defect site, preventing implant displacement (Calore et al., 2023). From the scanning electron microscopy results, it can be observed that the pore size of the final printed scaffold was 789 ± 22.69 μm, which closely matched the parameters designed before printing.

Through EDS analysis, as shown in Figure 1D, the results indicated that the main component of this scaffold was Ti6Al4V. There were no impurity elements detected during the scaffold's preparation, meeting the clinical implantation requirements.

Furthermore, the hydrophilicity of the scaffold's surface was assessed using a water contact angle measurement device, with results displayed in Figure 1E. It can be observed that the water contact angle on the surface of the 3D-Printed Ti6Al4V porous scaffold was 71.26° ± 5.41°. In previous studies, when the water contact angle is less than 90°, it is considered that the material surface has a certain degree of hydrophilicity. A smaller water contact angle indicates better surface hydrophilicity. Good hydrophilicity suggests that the scaffold possesses excellent biocompatibility and promotes cell adhesion (Sokoot et al., 2023).

In this study, the 3D-Printed porous Ti6Al4V scaffold exhibited a water contact angle of less than 90°, indicating good surface hydrophilicity. This characteristic is beneficial for the adhesion of mesenchymal stem cells after implantation *in vivo*.

3.2 Cell viability and morphology

To validate the biocompatibility of the scaffold, it was co-cultured with the most commonly used orthopedic cells, BMSCs. The influence of the scaffold on BMSC growth was assessed by monitoring cell viability and morphology. The results of live-dead staining are shown in Figure 2A. It can be observed that, compared to the control group where BMSCs were growing normally, the addition of the scaffold did not significantly affect the viability of BMSCs, as indicated by the statistical results in Figure 2B. Quantitative analysis revealed that adding the scaffold did not impact the cell survival rate, suggesting that the scaffold material itself does not affect the normal survival of BMSCs.

Microfilaments are important components of the cell cytoskeleton (Jockusch et al., 2004; Muranova et al., 2022). In this study, immunofluorescence staining was used to observe cell morphology by staining the microfilaments in BMSCs. The results are displayed in Figures 2C, D. The F-actin filaments were stained by rhodamine-phalloidin in red, and nuclei were stained by DAPI in blue. It can be observed that in the control group, BMSCs exhibited good spreading, and the microfilament morphology within the cells

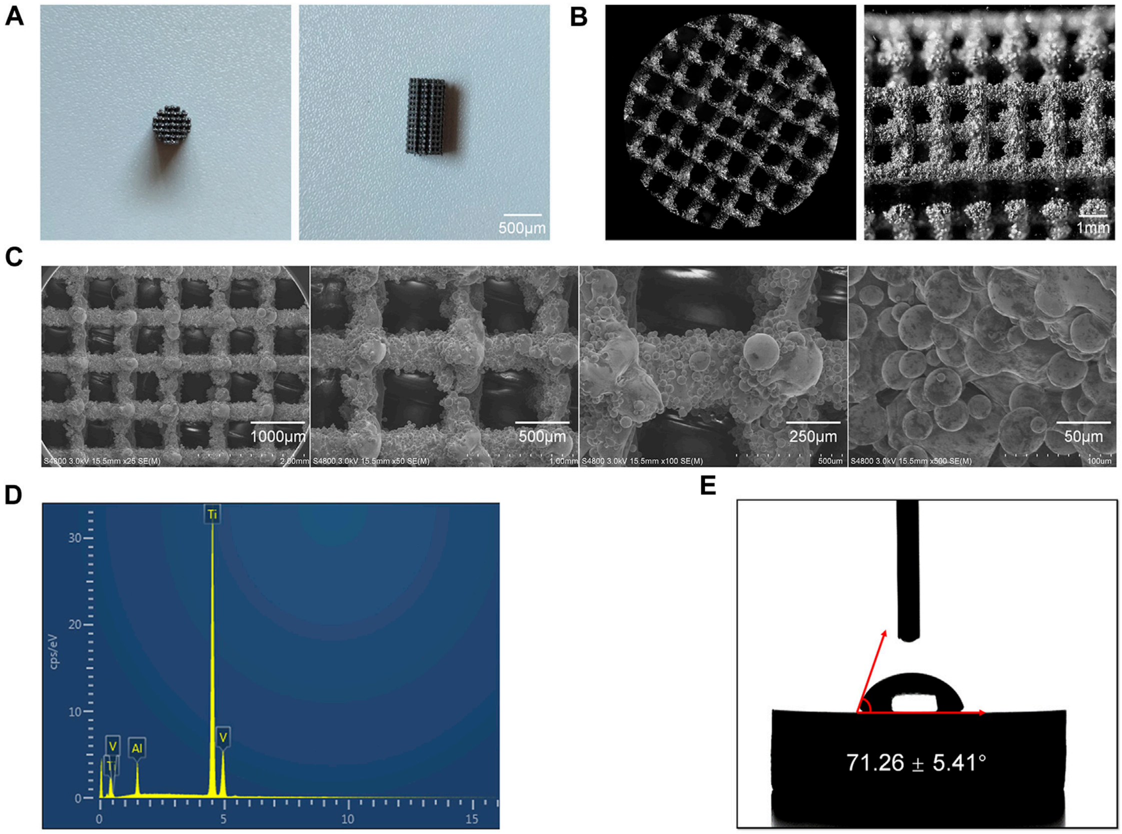

FIGURE 1
Characterization of the 3D-Printed Ti6Al4V porous scaffolds. **(A)** General appearance of the scaffold. **(B)** Microscopic images of the scaffold. **(C)** SEM images of the scaffolds at various magnifications. **(D)** Elemental composition of the Ti6Al4V scaffolds. **(E)** Water contact angle measurements of the Ti6Al4V scaffolds.

was clear. In the experimental group, BMSCs adhered well to the scaffold surface. While their cell size appeared slightly smaller, they exhibited longer extensions compared to the control group. The cells on the scaffold showed regular morphology, with a distinct spindle-shaped structure and longer pseudopods. Similar to the control group, the microfilament morphology within the cells was clear. This result suggests that the 3D-Printed porous Ti6Al4V scaffold used in this study allows BMSCs to effectively adhere to its surface. The adhered BMSCs exhibit typical cell morphology, and the cell cytoskeleton is clearly distinguishable.

Taken together, the results of live-dead staining and cell cytoskeleton staining demonstrate that the 3D-Printed Ti6Al4V scaffold used in this study exhibits excellent biocompatibility. It does not adversely affect the survival of BMSCs, and the scaffold surface promotes cell adhesion and spreading without affecting cell morphology.

3.3 Osseointegration of the porous scaffold with surrounding bone

This animal experiment consisted of two surgeries. The first surgery involved the routine implantation of the orthopedic prosthesis, as illustrated in Figure 3A. After a period of 3 months, the scaffold had tightly integrated with the surrounding bone tissue. The second surgery was depicted in Figure 3B. First, the scaffold from the initial surgery was removed. In the MB group, the removed scaffold was re-implanted into the corresponding site on the contralateral limb. This group simulated the process of using the "metal-bone" scaffold for re-implantation, a less common clinical practice. In contrast, the control group also removed the scaffold but discarded it, then used an entirely new scaffold to be implanted in the same location on the contralateral limb. This control group simulated the more commonly used clinical strategy of re-implanting a new scaffold into the original site.

In Figure 3B, it can be observed that the removed prosthesis had integrated well with the surrounding bone tissue, and there was evident ingrowth of new bone tissue into the pores of the scaffold. Three-dimensional reconstruction based on Micro-CT results is illustrated in Figure 3C. A comparison with the plain Ti6Al4V scaffold (a) reveals that the "metal-bone" scaffold is filled with bone tissue in the pore. It shows a tight integration between the scaffold and bone tissue (b). Upon removing the Ti6Al4V scaffold section, abundant bone tissue (c) is observed within the scaffold pores. Quantitative analysis indicates that the bone tissue is approximately 41.68% ± 2.53% of the scaffold volume. This result validates the expected composition of the "metal-bone" scaffold, demonstrating the stable presence of internal tissue within the scaffold. Further observation of the bonding between bone tissue and the scaffold in

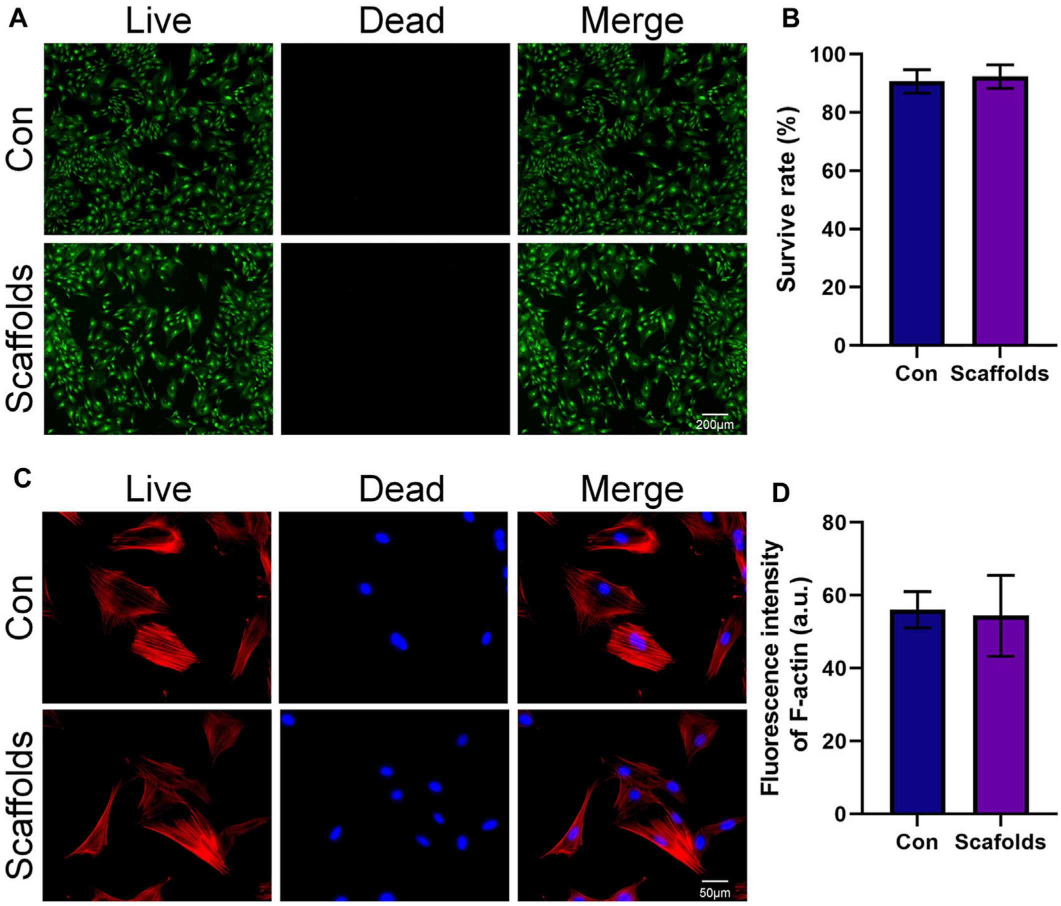

FIGURE 2
Biocompatibility of the porous scaffolds. **(A)** Calcein AM/PI staining of live cells (green) and dead cells (red). **(B)** Quantitative analysis of cell survival rate ($n = 3$). **(C)** Fluorescent images of the cellular morphology. **(D)** Quantitative analysis of the fluorescence intensity in different groups ($n = 3$). The data are expressed as the mean ± SD. *indicates significant differences between groups. *$p < 0.05$, **$p < 0.01$, and ***$p < 0.001$.

"metal-bone" scaffolds was conducted using SEM, as depicted in Figure 3D. It is evident that the porous Ti6Al4V scaffold is filled with bone tissue, and there is a tight integration between the bone tissue and the scaffold surface. During the removal of the prosthesis in the second surgery, it was also noted that the scaffold had a strong integration effect with the bone tissue interface, resulting in significant resistance when pulling out the scaffold. The mechanical testing of the removed scaffold, as shown in Figures 3E, F, revealed that in MB group when the Ti6Al4V scaffold contained bone tissue, its strength significantly increased, and it could withstand greater forces. On one hand, this result indicates that the scaffold indeed contained a certain amount of bone tissue. On the other hand, it suggests that the bone tissue inside the "metal-bone" scaffold was tightly integrated with the scaffold, providing stronger mechanical support. This finding aligns with previous research, which also demonstrated that Ti6Al4V porous scaffolds exhibit excellent bone integration effects, especially with pore sizes in the range of 600–900 μm and a porosity of 70% (Taniguchi et al., 2016). The appropriate pore size facilitates the ingrowth of new bone tissue and nutrient supply, while a 70% porosity rate closely resembles the porosity rate of physiological bone trabeculae, making it a biomimetic physiological condition that achieves optimal bone integration effects (Pan et al., 2021).

To validate the osseointegration effectiveness between the scaffold and the surrounding bone tissue at the site of bone defects, mechanical push-out tests were conducted on the scaffold to measure the maximum force exerted when pushing the scaffold out of the bone tissue, as depicted in Figure 3G. It is evident that in the early stages of implantation, at 6 weeks, the MB group exhibited significantly greater bonding strength with the surrounding bone tissue in comparison to the control group, displaying a statistically significant difference ($p < 0.5$). By 12 weeks, the MB group also experienced a significantly higher maximum push-out force compared to the control group ($p < 0.1$). These findings suggest that the MB scaffold, which incorporates bone tissue, demonstrates enhanced osseointegration effects, characterized by higher bonding strength with the surrounding tissues when contrasted with the control group.

In order to evaluate the formation of new bone in the control and MB groups, Micro-CT scans were conducted at 6 and 12 weeks, and the results are presented in Figure 4A. From the 3D reconstruction results, it is evident that at both 6 and 12 weeks, the scaffolds containing some bone tissue in the MB group, following the secondary surgery, had a greater amount of new bone tissue compared to the control group. Quantitative analysis, as shown in Figures 4B–E, indicates that the MB group had a higher

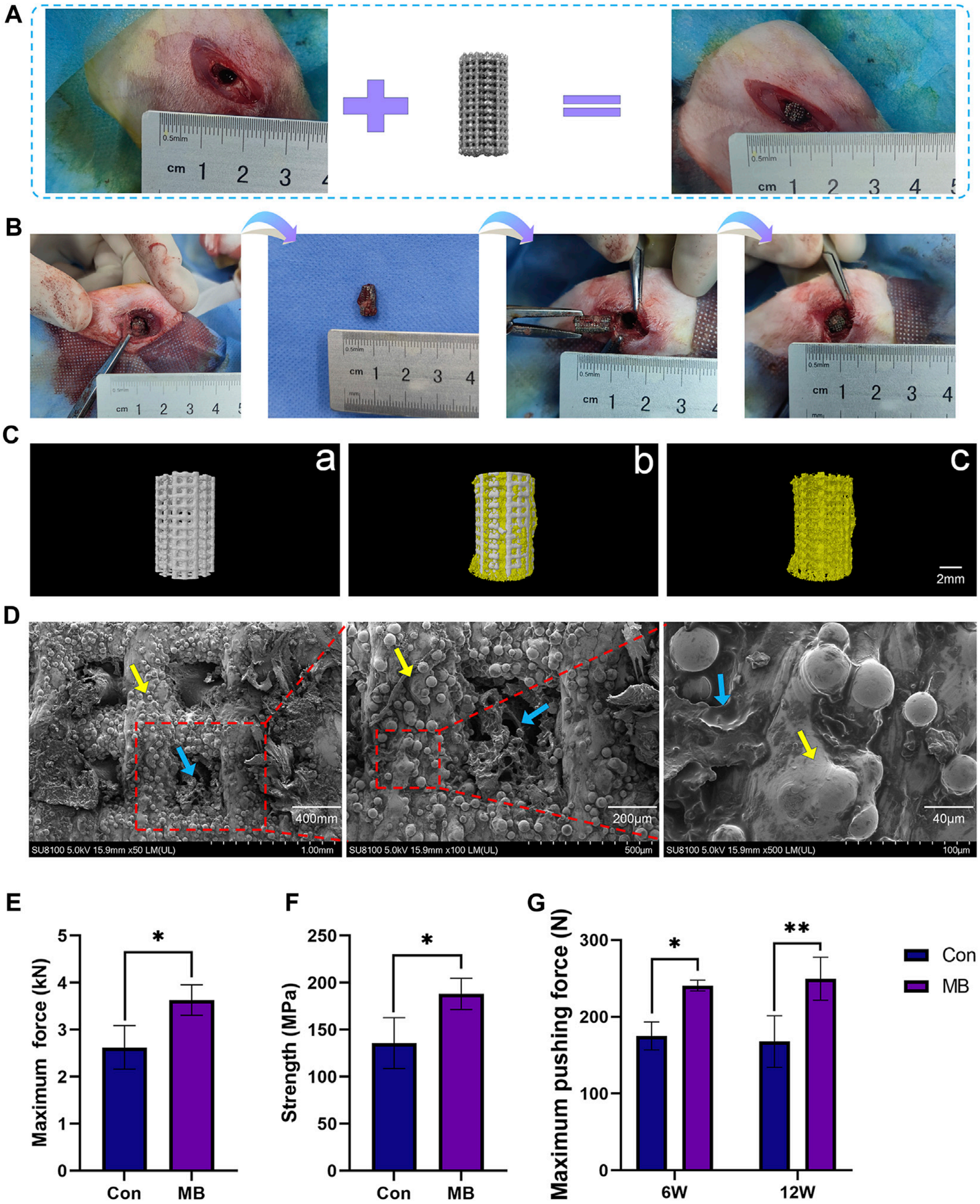

FIGURE 3
Two-Stage Surgical Procedure in Implantation. **(A)** Initial Implantation of Scaffolds. **(B)** Secondary implantation surgery procedure. **(C)** Micro-CT analysis: Representative 3D reconstruction image of a) the new scaffold (Con), b) the metal-bone scaffold (MB), c) the bone tissue inside the metal-bone scaffold. **(D)** SEM images of the bone tissue inside the metal-bone scaffolds (The area indicated by the yellow arrows is the Ti6Al4V scaffold region, and the area indicated by the blue arrows is the bone tissue region). **(E)** Compressive strength testing for the metal-bone scaffolds and new scaffolds (n = 3). **(F)** Maximum force in the biomechanical test of two types of scaffolds (n = 3). **(G)** Maximum pushing force of the Con and MB groups after implantation (n = 3). The data are expressed as the mean ± SD. *indicates significant differences between groups. *$p < 0.05$, **$p < 0.01$, and ***$p < 0.001$.

proportion of regenerative bone tissue and a greater number of bone trabeculae compared to the control group.

From the Micro-CT results at 6 weeks, it is apparent that the MB group had a higher content of newly formed bone tissue than the control group. This suggests that the bone tissue contained within the "metal-bone" scaffold survived and integrated well with the surrounding tissues of the new bone defect after the revision surgery. After the secondary surgery, the Micro-CT results at 6 weeks indicate that the bone tissue in the "metal-bone" scaffold group is approximately 37.97% ± 2.67% (BV/TV), while the control group exhibits about 31.75% ± 1.29% bone tissue. The increased regenerated bone tissue in the "metal-bone" scaffold group is likely attributed to the survival of the original bone tissue within the scaffold. This surviving bone tissue contributes to accelerated bone defect repair by integrating with surrounding newly formed bone tissues, while the remaining internal bone tissues within the

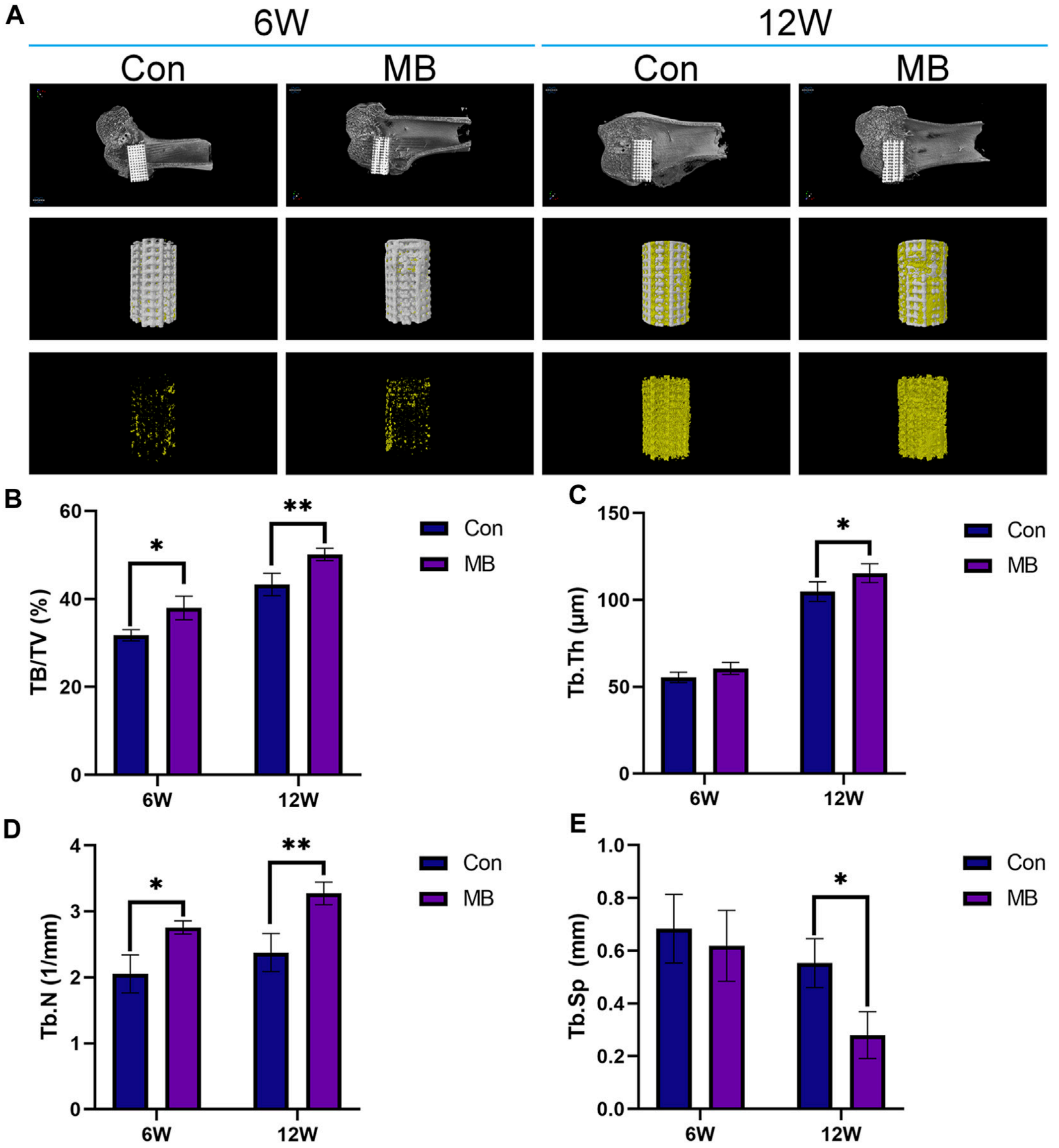

FIGURE 4
Micro-CT analysis of osseointegration around the prosthetic interfaces. **(A)** 3D reconstruction images around the prosthetic interfaces (The regenerated bone tissue is indicated in yellow and scaffolds are white). Quantitative analysis of **(B)** BV/TV, **(C)** Tb.Th, **(D)** Tb.N, and **(E)** Tb.Sp in two groups at 6 and 12 weeks after secondary implantation surgery ($n = 3$). The data are expressed as the mean ± SD. *indicates significant differences between groups. $^{*}p < 0.05$, $^{**}p < 0.01$, and $^{***}p < 0.001$.

scaffold undergo absorption. Therefore, it can be inferred that the "metal-bone" scaffold containing some bone tissue accelerated the regeneration process following the initial prosthesis implantation, leading to faster bone repair. Moreover, the bone tissue within the "metal-bone" scaffold is the patient's own tissue, eliminating the risk of immune rejection and allowing it to thrive.

To get a clearer view of the bone regeneration within the scaffold, hard sectioning was performed on specimens obtained 6 weeks after the second surgery, as illustrated in Figure 5A. The black area represents the location of the scaffold. The red areas in blue VG and blue areas in Masson's trichrome represents regenerated bones. Results from VG and Masson's trichrome staining show that in the MB group, the depth of bone ingrowth around the scaffold was greater than that in the control group, and there was also a higher amount of newly formed bone tissue surrounding the scaffold, consistent with the Micro-CT results.

To further assess the bone regeneration at the site of bone defect, Ti6Al4V scaffolds were removed six and 12 weeks after the second surgery, followed by decalcification and sectioning. H&E staining as well as immunohistochemical staining for bone regeneration-related proteins were performed. The results for the bone tissue around the scaffold stained by H&E and Masson's trichrome are shown in Figure 5B. From the H&E staining results, it can be observed that at 6 and 12 weeks, the bone trabeculae around the "metal-bone" scaffold containing bone tissue were more tightly integrated and there were more trabeculae compared to the control group. Masson's staining reveals a higher content of newly formed bone tissue around the "metal-bone" scaffold, with active

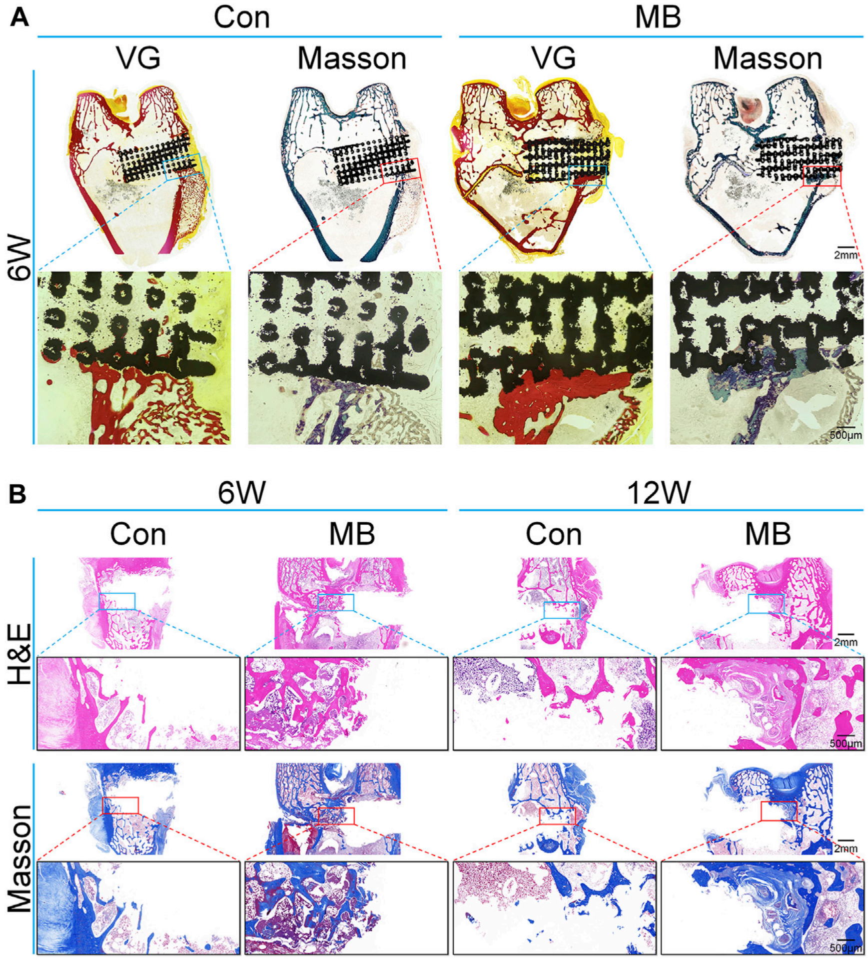

FIGURE 5
Histological analysis of bone regeneration around the scaffolds. **(A)** Van Gieson and Masson's trichrome staining of the regenerated bone around scaffolds at 6 weeks (without removal of the scaffold). **(B)** H&E and Masson's trichrome staining of the regenerated bone around scaffolds (after removal of the scaffold).

proliferation of bone trabeculae and the formation of more new bone trabeculae.

The results of immunohistochemistry are presented in Figure 6A, with OCN protein being a hallmark protein for bone formation (Zhou et al., 2023), and BMP-2 being an important protein in the bone regeneration process (Wang et al., 2022). Immunohistochemical staining for these two proteins has been widely used in previous studies to assess bone regeneration strength (Santinoni et al., 2021; Fiorin et al., 2022).

From the immunohistochemical results of each group, it can be seen that at 6 weeks, the expression levels of both bone-forming marker proteins were significantly higher in the MB group than in the control group, as shown in Figures 6B, C. These differences were statistically significant. This suggests that in the MB group, the pre-existing bone tissue within the scaffold remained viable, leading to a faster bone formation process at the site of the bone defect. At this point, the bone regeneration effect at the bone defect site was superior to that in the control group.

By the 12th week, the expression level of OCN protein in the MB group remained higher than that in the control group, but the expression of BMP-2 was lower than that in the control group. Considering that BMP-2 is an osteogenic growth factor that promotes bone formation (Zhang et al., 2019; Bi et al., 2023), this result suggests that the strong bone-promoting effect in the control group was achieved at 12 weeks, later than in the MB group.

The analysis of the animal experiment results leads to the conclusion that the MB scaffold containing some bone tissue is superior to a new scaffold. The reason for this could be the presence of host bone within the original scaffold. When re-implanted into the bone defect site, the tissue inside the scaffold can survive and integrate with the surrounding tissues, thereby accelerating the bone regeneration process. Compared to a new scaffold, the bone tissue around the MB scaffold can initiate the bone formation process more quickly, facilitating the migration of BMSCs and osteogenic cells to the scaffold site, thereby reducing the time required for bone repair and achieving better results.

In this study, we have combined the widely used Ti6Al4V scaffold in bone tissue engineering with clinical bone transplantation techniques to fabricate a "metal-bone" scaffold, which exhibits superior osteoinductive properties compared to

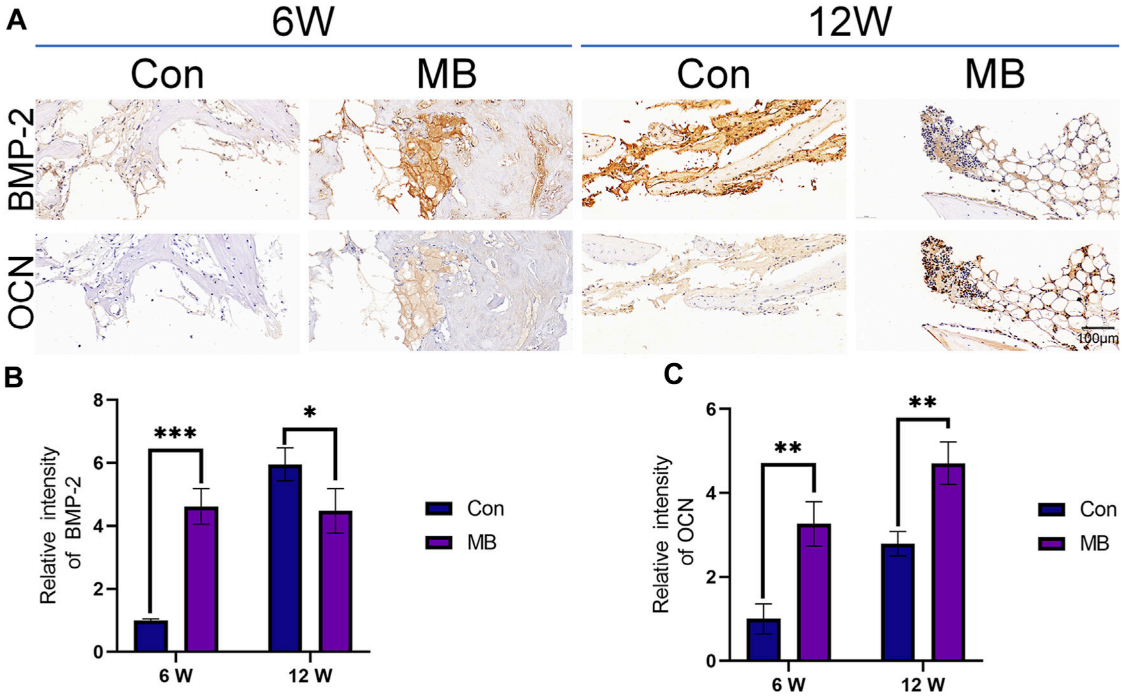

FIGURE 6
Immunohistochemical analysis of bone regeneration around the scaffolds. **(A)** Immunohistochemical staining of BMP-2 and OCN expression in each group. **(B)** Quantitative analysis of relative intensity of BMP-2 expression (n = 3). **(C)** Quantitative analysis of relative intensity of OCN expression (n = 3). The data are expressed as the mean ± SD. *indicates significant differences between groups. *p < 0.05, **p < 0.01, and ***p < 0.001.

pure Ti6Al4V scaffolds, thus accelerating bone healing. Ti6Al4V scaffolds are widely adopted in bone tissue engineering due to their excellent mechanical strength, biocompatibility, and osseointegration (Liao et al., 2021). However, their high mechanical strength often leads to stress shielding phenomena. To overcome this limitation, porous structures are commonly produced using 3D printing technology. On one hand, these porous structures mitigate stress shielding effects, while micro-porosities promote bone tissue ingrowth, enhance bone formation, and aid in scaffold fixation. Nevertheless, due to the biologically inert nature of Ti6Al4V, efficient bone regeneration often necessitates the incorporation of bioactive substances into porous scaffolds, especially in the case of larger bone defects (Koju et al., 2022).

Considering the clinical challenges associated with treating substantial bone defects, autografting is a well-established approach. However, in cases of extensive bone loss, autograft availability may be limited, and the excessive use of autografts can lead to iatrogenic damage, while allografts may trigger immune rejection responses (Baldwin et al., 2019). In this study, we have innovatively combined 3D-printed porous Ti6Al4V scaffolds with autografting techniques. Our findings confirm that the addition of a small amount of autograft within the porous scaffold can efficiently promote bone regeneration. Furthermore, our animal experiments demonstrate that the “metal-bone” scaffold outperforms plain porous Ti6Al4V scaffolds by expediting early-stage bone regeneration, thus reducing the time required for peri-implant endosseous healing. This research provides valuable clinical insights, substantiating the effectiveness of incorporating a small amount of viable autograft around Ti6Al4V scaffolds to accelerate bone healing and facilitate osteogenesis.

Compared to clinical implants, our study innovatively employs a 3D-printed porous Ti6Al4V scaffold, with its design parameters informed by prior research findings to optimize osteogenesis. Additionally, we integrate clinical bone grafting techniques with porous titanium alloy scaffolds in this study, creating a novel “Metal-Bone” scaffold through implantation. This scaffold contains bioactive bone tissue internally, and observations indicate a tight integration between the scaffold and its internal bone tissue. Following implantation into bone defects, it significantly enhances osteointegration, accelerates bone healing compared to titanium alloy scaffolds without bone tissue, promoting the integration of the implant with the surrounding bone tissues. In terms of clinical applications, considering the substantial extraction of bone tissue during orthopedic implant surgeries (Wazzan et al., 2023), incorporating a small amount of autologous bone tissue into implants is conceivable. This strategy has the potential to accelerate bone regeneration and strengthen the bone integration around the implanted prosthetic. The primary challenges lie in whether the bone tissue obtained during replacement surgery can maintain its vitality after fragmentation. Additionally, there is a requirement for the implant to be porous to accommodate sufficient bone tissue. In clinical translation, numerous challenges will be encountered, requiring further in-depth investigation for the potential clinical application of the “Metal-Bone” scaffold.

Furthermore, the “metal-bone” scaffold employed in this study shares similarities with the old scaffolds removed during orthopedic revision surgeries. Consequently, this research also furnishes empirical evidence regarding the choice between using old prostheses containing some bone tissue or opting for entirely new prostheses in orthopedic revision procedures.

Joint replacement surgery is one of the top five most common surgeries annually and one of the top five fastest-growing procedures (Schwartz et al., 2020; Pigeolet et al., 2021). The increasing number of patients receiving prosthetic joint replacement surgery is driven by factors such as osteoporosis, trauma, and tumors (Hunter and Bierma-Zeinstra, 2019). As the number of joint replacement surgeries rises, so do postoperative complications, including prosthesis sinking, loosening, and displacement (Howard et al., 2023). Currently, over 30% of joint replacement patients undergo one or more joint replacement surgeries in 20 years (Lee et al., 2023). In clinical practice, when addressing postoperative complications following joint replacement, it is common to replace the old prosthesis with a new one during revision surgery (Gong et al., 2023). However, intraoperatively, it is often observed that the original prosthesis remains intact, with complications primarily arising due to inadequate bonding between the prosthesis and surrounding bone tissue. Using new prostheses in revision surgery not only results in the wastage of medical materials but also imposes an economic burden on patients and their families (Cimatti et al., 2022). Currently, there is no definitive research comparing the efficacy of retaining the original prosthesis versus using a new one in revision surgery. This study addresses this clinical issue through experimental animal research by comparing the outcomes of these two prosthesis approaches. The results confirm that, in orthopedic revision surgeries, prostheses containing some bone tissue, when still viable, exhibit osteoinductive properties similar to new prostheses. Consequently, this study offers a novel perspective to some extent for revision surgeries, carrying certain clinical implications.

4 Conclusion

In summary, this study combines 3D-printed porous Ti6Al4V prostheses commonly used in bone tissue engineering with clinical bone transplantation techniques to create a novel "metal-bone" scaffold for promoting bone regeneration in cases of bone defects. Firstly, the scaffold's consistency with expectations was validated through SEM, EDS, and similar methods. Subsequently, cell experiments confirmed the scaffold's biocompatibility. Finally, through animal experiments involving a two-stage surgical approach, wherein a "metal-bone" scaffold with bone tissue was first prepared over 3 months and then implanted into the contralateral limb bone defect, it was compared against a new scaffold lacking bone tissue. The results substantiated the survival of bone tissue within the "metal-bone" scaffold post-transplantation, achieving more effective bone regeneration and expediting the healing process. This research opens up significant prospects for the clinical application of orthopedic prostheses preparation and revision surgeries.

Data availability statement

The original contributions presented in the study are included in the article/Supplementary material, further inquiries can be directed to the corresponding authors.

Ethics statement

The animal studies were approved by the Animal Care and Use Ethics Committee of Jilin University. The studies were conducted in accordance with the local legislation and institutional requirements. Written informed consent was obtained from the owners for the participation of their animals in this study.

Author contributions

YL: Conceptualization, Formal Analysis, Investigation, Methodology, Writing–original draft, Writing–review and editing. XW: Formal Analysis, Methodology, Writing–original draft. HC: Methodology, Resources, Supervision, Writing–original draft. XL: Methodology, Supervision, Writing–review and editing. HL: Methodology, Resources, Supervision, Writing–original draft. JW: Funding acquisition, Supervision, Writing–review and editing. ZQ: Conceptualization, Funding acquisition, Project administration, Writing–review and editing.

Funding

The author(s) declare financial support was received for the research, authorship, and/or publication of this article. This work was supported by the National Natural Science Foundation of China (52175270), the Project of Scientific and Technological Development Plan of Jilin Province (20220508130RC) and the Project of "Medical + X" interdisciplinary innovation team of Norman Bethune Health Science Center of Jilin University (2022JBGS06).

Conflict of interest

The authors declare that the research was conducted in the absence of any commercial or financial relationships that could be construed as a potential conflict of interest.

Publisher's note

References

Abbasi, N., Hamlet, S., Love, R. M., and Nguyen, N.-T. (2020). Porous scaffolds for bone regeneration. *J. Sci. Adv. Mater. Devices* 5 (1), 1–9. doi:10.1016/j.jsamd.2020.01.007

Altunbek, M., Afghah, S. F., Fallah, A., Acar, A. A., and Koc, B. (2023). Design and 3D printing of personalized hybrid and gradient structures for critical size bone defects. *ACS Appl. Bio Mater* 6 (5), 1873–1885. doi:10.1021/acsabm.3c00107

Bai, H., Zhao, Y., Wang, C., Wang, Z., Wang, J., Liu, H., et al. (2020). Enhanced osseointegration of three-dimensional supramolecular bioactive interface through osteoporotic microenvironment regulation. *Theranostics* 10 (11), 4779–4794. doi:10.7150/thno.43736

Baldwin, P., Li, D. J., Auston, D. A., Mir, H. S., Yoon, R. S., and Koval, K. J. (2019). Autograft, allograft, and bone graft substitutes: clinical evidence and indications for use in the setting of orthopaedic trauma surgery. *J. Orthop. Trauma* 33 (4), 203–213. doi:10.1097/BOT.0000000000001420

Bi, Z., Shi, X., Liao, S., Li, X., Sun, C., and Liu, J. (2023). Strategies of immobilizing BMP-2 with 3D-printed scaffolds to improve osteogenesis. *Regen. Med.* 18 (5), 425–441. doi:10.2217/rme-2022-0222

Calore, A. R., Srinivas, V., Groenendijk, L., Serafim, A., Stancu, I. C., Wilbers, A., et al. (2023). Manufacturing of scaffolds with interconnected internal open porosity and surface roughness. *Acta Biomater.* 156, 158–176. doi:10.1016/j.actbio.2022.07.017

Chen, Z., Yan, X., Yin, S., Liu, L., Liu, X., Zhao, G., et al. (2020). Influence of the pore size and porosity of selective laser melted Ti6Al4V ELI porous scaffold on cell proliferation, osteogenesis and bone ingrowth. *Mater Sci. Eng. C Mater Biol. Appl.* 106, 110289. doi:10.1016/j.msec.2019.110289

Cimatti, P., Andreoli, I., Busacca, M., Govoni, M., Vivarelli, L., Del Piccolo, N., et al. (2022). An observational prospective clinical study for the evaluation of a collagen-hydroxyapatite composite scaffold in hip revision surgery. *J. Clin. Med.* 11 (21), 6372. doi:10.3390/jcm11216372

Cui, Y., Wang, Z., Li, Z., Ji, X., Yuan, B., Sun, Y., et al. (2021). Functionalized anti-osteoporosis drug delivery system enhances osseointegration of an inorganic–organic bioactive interface in osteoporotic microenvironment. *Mater. Des.* 206, 109753. doi:10.1016/j.matdes.2021.109753

Fiorin, L. G., Matheus, H. R., Ervolino, E., Canciani, E., Pellegrini, G., Dellavia, C., et al. (2022). Tamoxifen improves homeostasis in the peri-implant bone remodeling of osseointegrated titanium implants. *J. Periodontal Res.* 57 (4), 880–890. doi:10.1111/jre.13026

Gong, L., Chen, X., Shao, H., Gu, J., Dong, R., and Ding, Y. (2023). Clinicopathological analysis of the periprosthetic tissue of revision total hip and knee arthroplasty. *Chin. Med. J. Engl.* 136 (15), 1870–1872. doi:10.1097/CM9.0000000000002219

Gu, Y., Sun, Y., Shujaat, S., Braem, A., Politis, C., and Jacobs, R. (2022). 3D-printed porous Ti6Al4V scaffolds for long bone repair in animal models: a systematic review. *J. Orthop. Surg. Res.* 17 (1), 68. doi:10.1186/s13018-022-02960-6

Henkel, J., Medeiros Savi, F., Berner, A., Fountain, S., Saifzadeh, S., Steck, R., et al. (2021). Scaffold-guided bone regeneration in large volume tibial segmental defects. *Bone* 153, 116163. doi:10.1016/j.bone.2021.116163

Howard, L. C., Day, C. W., Masri, B. A., and Garbuz, D. S. (2023). Comparison of clinical and functional outcomes in one versus two component revision for total knee arthroplasty. *J. Arthroplasty* 38 (6S), S275–S280. doi:10.1016/j.arth.2023.01.047

Hunter, D. J., and Bierma-Zeinstra, S. (2019). Osteoarthritis. *Lancet* 393 (10182), 1745–1759. doi:10.1016/S0140-6736(19)30417-9

Jockusch, B. M., Rothkegel, M., and Schwarz, G. (2004). Linking the synapse to the cytoskeleton: a breath-taking role for microfilaments. *Neuroreport* 15 (10), 1535–1538. doi:10.1097/01.wnr.0000131673.92694.58

Koju, N., Niraula, S., and Fotovvati, B. (2022). Additively manufactured porous Ti6Al4V for bone implants: a review. *Metals* 12 (4), 687. doi:10.3390/met12040687

Lee, J. J., Oladeji, K., Sweeney, B. F., Chakoma, T. L., Arora, P., Finlay, A. K., et al. (2023). Single, recurrent, synchronous, and metachronous periprosthetic joint infections in patients with multiple hip and knee arthroplasties. *J. Arthroplasty* 38 (9), 1846–1853. doi:10.1016/j.arth.2023.03.014

Li, S., Lei, H., Liu, H., Song, P., Fan, S., Wu, L., et al. (2023). Pulsed electrodeposition of MXenes/HAp multiple biological functional coatings on 3D printed porous Ti-6Al-4V bone tissue engineering scaffold. *Surf. Coatings Technol.* 464, 129532. doi:10.1016/j.surfcoat.2023.129532

Liao, B., Xia, R. F., Li, W., Lu, D., and Jin, Z. M. (2021). 3D-Printed Ti6Al4V scaffolds with graded triply periodic minimal surface structure for bone tissue engineering. *J. Mater. Eng. Perform.* 30 (7), 4993–5004. doi:10.1007/s11665-021-05580-z

Liu, B., Hou, G., Yang, Z., Li, X., Zheng, Y., Wen, P., et al. (2022). Repair of critical diaphyseal defects of lower limbs by 3D printed porous Ti6Al4V scaffolds without additional bone grafting: a prospective clinical study. *J. Mater Sci. Mater Med.* 33 (9), 64. doi:10.1007/s10856-022-06685-0

Montero, J., Fernandez-Ruiz, A., Pardal-Pelaez, B., Jimenez-Guerra, A., Velasco-Ortega, E., Nicolas-Silvente, A. I., et al. (2020). Effect of rough surface platforms on the mucosal attachment and the marginal bone loss of implants: a dog study. *Mater. (Basel)* 13 (3), 802. doi:10.3390/ma13030802

Muranova, L. K., Shatov, V. M., and Gusev, N. B. (2022). Role of small heat shock proteins in the remodeling of actin microfilaments. *Biochem. (Mosc)* 87 (8), 800–811. doi:10.1134/S0006297922080119

Naghavi, S. A., Tamaddon, M., Garcia-Souto, P., Moazen, M., Taylor, S., Hua, J., et al. (2023a). A novel hybrid design and modelling of a customised graded Ti-6Al-4V porous hip implant to reduce stress-shielding: an experimental and numerical analysis. *Front. Bioeng. Biotechnol.* 11, 1092361. doi:10.3389/fbioe.2023.1092361

Naghavi, S. A., Tamaddon, M., Garcia-Souto, P., Moazen, M., Taylor, S., Hua, J., et al. (2023b). A novel hybrid design and modelling of a customised graded Ti-6Al-4V porous hip implant to reduce stress-shielding: an experimental and numerical analysis. *Front. Bioeng. Biotechnol.* 11, 1092361. doi:10.3389/fbioe.2023.1092361

Nayak, V. V., Slavin, B., Bergamo, E. T. P., Boczar, D., Slavin, B. R., Runyan, C. M., et al. (2023). Bone tissue engineering (BTE) of the craniofacial skeleton, Part I: evolution and optimization of 3D-printed scaffolds for repair of defects. *J. Craniofac Surg.* 34 (7), 2016–2025. doi:10.1097/SCS.0000000000009593

Pan, C. T., Hsu, W. H., Cheng, Y. S., Wen, Z. H., and Chen, W. F. (2021). A new design of porosity gradient Ti-6Al-4V encapsulated hydroxyapatite dual materials composite scaffold for bone defects. *Micromachines (Basel)* 12 (11), 1294. doi:10.3390/mi12111294

Pigeolet, M., Jayaram, A., Park, K. B., and Meara, J. G. (2021). Osteoarthritis in 2020 and beyond. *Lancet* 397 (10279), 1059–1060. doi:10.1016/S0140-6736(21)00208-7

Santinoni, C. S., Neves, A. P. C., Almeida, B. F. M., Kajimoto, N. C., Pola, N. M., Caliente, E. A., et al. (2021). Bone marrow coagulated and low-level laser therapy accelerate bone healing by enhancing angiogenesis, cell proliferation, osteoblast differentiation, and mineralization. *J. Biomed. Mater Res. A* 109 (6), 849–858. doi:10.1002/jbm.a.37076

Schwartz, A. M., Farley, K. X., Guild, G. N., and Bradbury, T. L., Jr. (2020). Projections and epidemiology of revision hip and knee arthroplasty in the United States to 2030. *J. Arthroplasty* 35 (6S), S79–S85. doi:10.1016/j.arth.2020.02.030

Sokoot, E. A., Arkan, E., Khazaei, M., and Moradipour, P. (2023). A novel 3D-electrospun nanofibers-scaffold grafted with Royal Jelly: improve hydrophilicity of the nanofibers-scaffold and proliferation of HUVEC cell line. *Cell. Tissue Bank.* 24 (2), 329–340. doi:10.1007/s10561-022-10035-3

Subasi, O., Karaismailoglu, B., Ashkani-Esfahani, S., and Lazoglu, I. (2023). Investigation of lattice infill parameters for additively manufactured bone fracture plates to reduce stress shielding. *Comput. Biol. Med.* 161, 107062. doi:10.1016/j.compbiomed.2023.107062

Taniguchi, N., Fujibayashi, S., Takemoto, M., Sasaki, K., Otsuki, B., Nakamura, T., et al. (2016). Effect of pore size on bone ingrowth into porous titanium implants fabricated by additive manufacturing: an *in vivo* experiment. *Mater Sci. Eng. C Mater Biol. Appl.* 59, 690–701. doi:10.1016/j.msec.2015.10.069

Wang, C., Huang, W., Zhou, Y., He, L., He, Z., Chen, Z., et al. (2020). 3D printing of bone tissue engineering scaffolds. *Bioact. Mater* 5 (1), 82–91. doi:10.1016/j.bioactmat.2020.01.004

Wang, C., Xu, D., Lin, L., Li, S., Hou, W., He, Y., et al. (2021a). Large-pore-size Ti6Al4V scaffolds with different pore structures for vascularized bone regeneration. *Mater Sci. Eng. C Mater Biol. Appl.* 131, 112499. doi:10.1016/j.msec.2021.112499

Wang, J., Wei, Y., Zhou, Z., Yang, J., Jia, Y., Wu, H., et al. (2022). Deer antler extract promotes tibia fracture healing in mice by activating BMP-2/SMAD4 signaling pathway. *J. Orthop. Surg. Res.* 17 (1), 468. doi:10.1186/s13018-022-03364-2

Wang, X., Li, Z., Wang, Z., Liu, H., Cui, Y., Liu, Y., et al. (2021b). Incorporation of bone morphogenetic protein-2 and osteoprotegerin in 3D-printed Ti6Al4V scaffolds enhances osseointegration under osteoporotic conditions. *Front. Bioeng. Biotechnol.* 9, 754205. doi:10.3389/fbioe.2021.754205

Wang, Z., Wang, C., Li, C., Qin, Y., Zhong, L., Chen, B., et al. (2017). Analysis of factors influencing bone ingrowth into three-dimensional printed porous metal scaffolds: a review. *J. Alloys Compd.* 717, 271–285. doi:10.1016/j.jallcom.2017.05.079

Wazzan, A. L. J., Almusallam, M. H., Almosa, M. S., Bin Dukhi, M. M., Bin Akrish, A. M., Alaraidh, S. A., et al. (2023). Etiologies of orthopedic implant removal among patients who underwent orthopedic fixation surgeries in king abdulaziz medical city. *Cureus* 15 (8), e43809. doi:10.7759/cureus.43809

Zeng, S., Liu, G., Li, C., Ye, J., and Li, D. (2022). Porous structure design and mechanical properties analysis of femoral stem based on selective laser melting. *Chin. J. Lasers-Zhongguo Jiguang* 49 (2), 0202016. doi:10.3788/cjl202249.0202016

Zhang, X., Lou, Q., Wang, L., Min, S., Zhao, M., and Quan, C. (2019). Immobilization of BMP-2-derived peptides on 3D-printed porous scaffolds for enhanced osteogenesis. *Biomed. Mater* 15 (1), 015002. doi:10.1088/1748-605X/ab4c78

Zhang, Y., Sun, N., Zhu, M., Qiu, Q., Zhao, P., Zheng, C., et al. (2022). The contribution of pore size and porosity of 3D printed porous titanium scaffolds to osteogenesis. *Biomater. Adv.* 133, 112651. doi:10.1016/j.msec.2022.112651

Zhou, Y., Zhu, P., Shen, S., Wang, Y., Li, B., Guo, B., et al. (2023). Overexpression of fibroblast growth factor receptor 2 in bone marrow mesenchymal stem cells enhances osteogenesis and promotes critical cranial bone defect regeneration. *Front. Cell. Dev. Biol.* 11, 1208239. doi:10.3389/fcell.2023.1208239

Frontiers in
Bioengineering and Biotechnology

Accelerates the development of therapies, devices, and technologies to improve our lives

A multidisciplinary journal that accelerates the development of biological therapies, devices, processes and technologies to improve our lives by bridging the gap between discoveries and their application.

Discover the latest Research Topics

See more →

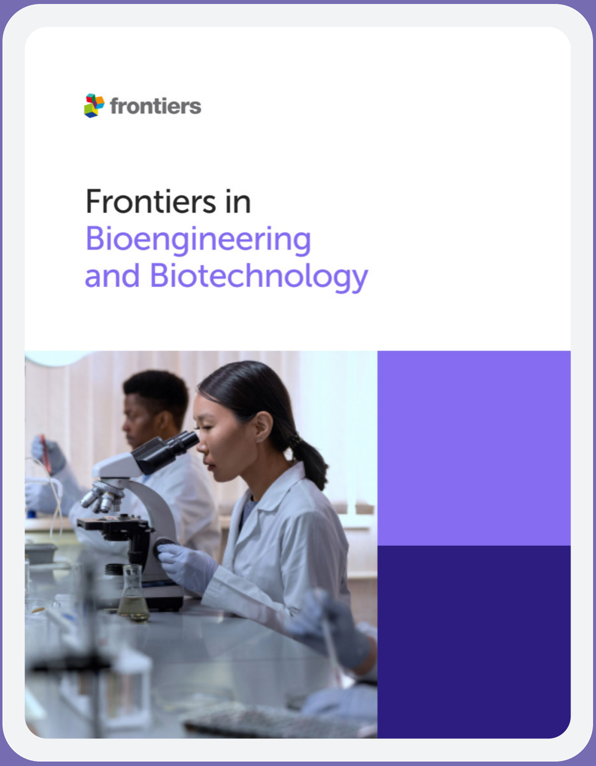

frontiers

Frontiers in
Bioengineering
and Biotechnology

Frontiers

Avenue du Tribunal-Fédéral 34
1005 Lausanne, Switzerland
frontiersin.org

Contact us

+41 (0)21 510 17 00
frontiersin.org/about/contact